

# **A Point Source High Power Converter Target to Produce Bremsstrahlung for Photonuclear Reactions**

Inaugural dissertation  
of the Faculty of Science,  
University of Bern

presented by

Mehran Vagheian

from Iran

Supervisor of the doctoral thesis:  
Prof. Andreas Türlér

Departement für Chemie und Biochemie (DCB)  
Universität Bern

The original document is available from the web server of the University of Bern  
(BORIS Theses, <https://boristheses.unibe.ch/>)



This work is licensed under a Creative Commons Attribution-NonCommercial-NoDerivatives (CC BY-NC-ND) Switzerland license, except where otherwise noted.

# **A Point Source High Power Converter Target to Produce Bremsstrahlung for Photonuclear Reactions**

Inaugural dissertation  
of the Faculty of Science,  
University of Bern

presented by

Mehran Vagheian

from Iran

Supervisor of the doctoral thesis:  
Prof. Andreas Türlér

Departement für Chemie und Biochemie (DCB)  
Universität Bern

Bern, ...

The Dean

Prof. Dr. Zoltan Balogh

# Acknowledgements

First of all, I would like to express my thanks to Prof. Andreas Türlér, my supervisor and head of the Radiochemistry of the Department for Chemistry, Biochemistry and Pharmacy at the University of Bern, for giving me the opportunity to carry out research in his group and providing valuable guidance and support. His knowledge, vision, sincerity, and motivation throughout this research have inspired me deeply, and I am grateful for his acceptance of working in his group. I believe that this study could not have been performed without his guidance, and both practical and mental support.

I would like to thank Mr. Ronald Zingg, whose work and enthusiasm for supporting me was highly inspiring.

In addition, I would also like to express my thankfulness to Prof. Prasser at ETH, who generously spent time reviewing my thesis.

An endless special thanks go to my wife (Dr. Nadia Zandi) for her love, constant support, and patience to complete this research work. She unconditionally supported me throughout the project and motivated me a lot to complete it.



# Contents

<b>Acknowledgements</b>	<b>I</b>
<b>List of figures</b>	<b>VI</b>
<b>List of tables</b>	<b>XX</b>
<b>Abbreviations</b>	<b>XXI</b>
<b>Nomenclature</b>	<b>XXII</b>
<b>Summary</b>	<b>XXIII</b>
<b>Aim of the thesis</b>	<b>XXIV</b>

<b>Chapter 1: Introduction</b>	<b>1</b>
1.1 Electrons passing through a medium	4
1.1.1 Electron interactions	7
1.1.1.1 Ionization	7
1.1.1.2 Scattering	8
Bhabha scattering	9
Moeller scattering	9
Single, plural, and multiple scattering	10
1.1.1.3 Cherenkov radiation	11
1.1.1.4 Electron-positron annihilation	12
1.1.1.5 Bremsstrahlung	13
Electron-nucleus Bremsstrahlung	15
Electron-electron Bremsstrahlung	16
Two/ Multiple photon Bremsstrahlung	17
Electron-positron Bremsstrahlung	17
Polarization Bremsstrahlung	18
Coherent and incoherent Bremsstrahlung	18
1.1.1.6 Electronuclear reaction	19
1.1.2 Electron energy loss	22
1.1.3 Linear energy transfer	23
1.1.4 Electron energy straggling	24
1.2 Photons passing through a medium	25
1.2.1 Photon beam attenuation	26
1.2.2 Total and mass attenuation coefficients	29
1.2.3 Mean free path	31
1.2.4 Radiation length	31
1.2.5 Half value layer and tenth value layer	32
1.2.6 Photon interactions	33

Thomson (classical) scattering.....	33
Rayleigh scattering.....	34
Compton effect (scattering).....	37
Photoelectric effect.....	43
Nuclear and electronic pair production.....	49
Photonuclear scattering, absorption and production.....	54
Summary of photon interactions.....	61
 1.3 Heat transfer mechanisms .....	64
1.3.1 Conduction .....	64
1.3.2 Convection .....	67
1.3.3 Radiation .....	74
Surface types .....	77
1.3.4 Simultaneous heat transfer mechanisms .....	79
1.3.5 Boundary and initial conditions .....	79
1.3.5.1 Boundary conditions in heat transfer.....	80
Specified heat flux boundary condition.....	80
Specified temperature boundary condition .....	82
Convection boundary condition .....	83
Radiation boundary condition.....	84
Interface boundary condition.....	85
Generalized simultaneous boundary condition.....	86
1.3.5.2 Boundary conditions in fluid dynamics.....	86
Inlet boundary condition.....	86
Outlet boundary condition.....	87
No-slip boundary condition.....	87
Symmetric boundary condition.....	87
Constant pressure boundary condition.....	88
Outflow boundary condition.....	88
1.3.6 Overview of theoretical heat transfer calculations.....	88
1.3.7 Overview of theoretical radiation transport calculations.....	97
1.3.8 Software for computational purposes.....	98
 1.4 Electron beam accelerators.....	100
1.4.1 Different types of high-energy electron beam accelerators.....	101
Dynamitron.....	101
Betatron.....	102
Microtron.....	103
Linac.....	105
Rhodotron.....	107

1.4.2 Comparison between the high-energy, high-power electron beam accelerators.....	109
1.5 Photonuclear irradiation setup.....	110
Electron beam.....	111
Entrance window.....	114
Converter target.....	115
Production targets.....	125
<b>Chapter 2: Modeling &amp; computations.....</b>	<b>127</b>
Photonuclear irradiation setup modeling.....	128
2.1 Electron beam.....	128
Electron beam modeling of a rotating target.....	130
2.2 Entrance window.....	131
Electron emergent coefficient.....	131
Bremsstrahlung yield.....	132
Energy deposition.....	133
Heat conduction modeling of the beryllium entrance window.....	134
Helium-cooled rotating beryllium disc modeling.....	138
2.3 Tantalum converter target.....	141
Bremsstrahlungs yield calculations of tantalum converter target.....	141
Electron emergent coefficient.....	143
Bremsstrahlungs energy spectrum.....	143
Distribution of angular Bremsstrahlung.....	144
Energy deposition.....	146
Heat conduction modeling of the tantalum converter target.....	147
2.4 Other irradiation setup components.....	157
2.4.1 Flattening filter.....	158
2.4.2 Production targets.....	159
2.4.3 Calculated yields of radionuclides (examples).....	161
Production of $^{67}\text{Cu}$ from $^{68}\text{Zn}$ .....	162
Production of $^{225}\text{Ra}$ from $^{226}\text{Ra}$ .....	165
Production of $^{224}\text{Ra}$ from $^{226}\text{Ra}$ .....	172
Production of $^{99}\text{Mo}$ from $^{100}\text{Mo}$ .....	178
Same and hybrid multiple simultaneous radionuclide production.....	183
2.4.4 Massive beam stop.....	183
2.4.5 Energy deposition in all components.....	186
2.5 Summary of the results .....	187

<b>Chapter 3: Conclusion &amp; outlook.....</b>	<b>189</b>
3.1 Conclusion.....	190
3.2 Outlook.....	192
 References.....	 193
Appendix A.....	208
Appendix B.....	211

# List of Figures

<b>1.1</b>	Block diagram of different radiation types [P16].....	2
<b>1.2</b>	A schematic representation of the transmission curve for monoenergetic electrons versus the absorber thickness, where $R_e$ stands the extrapolated range [K00].....	4
<b>1.3</b>	A schematic representation of the main electron interaction mechanisms a) Backscattering b) Secondary electron generation c) Photon production [WH19].....	5
<b>1.4</b>	A schematic representation of the backscattered electrons in a medium.....	5
<b>1.5</b>	Fraction of backscattered to incident electrons ( $\eta$ ) as a function of incident electron energy [K00].....	8
<b>1.6</b>	A schematic representation of the successive ionization process [A07].....	8
<b>1.7</b>	A schematic representation of secondary electron interactions in the medium, where $E_p$ and $E_s$ are the energy of the primary and secondary electrons, respectively. The polar angle $\theta$ is the angle of the electron (i.e., the scattered electron in the elastic scattering and the secondary generated electron in the inelastic scattering, respectively). Concerning the polar incident electron direction axis, the azimuthal angle $\phi$ is the rotation angle regarding the initial meridian plane, and the subscript numbers refer to the scattering interaction number [LMD11].....	9
<b>1.8</b>	A schematic representation of some of the electron and positron interactions [WH19].....	9
<b>1.9</b>	A quantitative representation of the fractional energy loss of electrons (and positrons) per radiation length in the lead versus the incident electron (and positron) beam energy. The radiation length for electrons ( $X_0$ ) is the mean distance over which a high-energy incident electron loses all but 1/e of its energy through the Bremsstrahlungs interaction in a medium. For lead, this value is $6.37 \text{ g. cm}^2$ [GK00].....	10
<b>1.10</b>	Angular distribution (as intensity) of multiple electron scattering in an aluminum target with different incident electron beam energy [NUE12].....	11
<b>1.11</b>	Cherenkov radiation in water-cooled nuclear reactors. The Cherenkov radiation spectrum is continuous. Its relative intensity per unit frequency was shown to be inversely proportional to the wavelength squared. Thus, the number of photons increases by decreasing the wavelength. That is the reason why most of the Cherenkov radiation appears blue and mainly in the UV range. In a water-cooled nuclear reactor, the blue radiation that appears in the reactor pool is Cherenkov radiation, where the emitted $\beta^-$ particles from fission results in the shock wave constructive interference that appears as a glow. Cherenkov radiation has been identified useful for many	

applications such as imaging, radiotherapy monitoring, optical-guided surgery, etc. [B16, V20, O19].....	12
<b>1.12</b> Electron-positron annihilation. In this process, the photons are emitted at under 180 degrees [TL15] .....	12
<b>1.13</b> A schematic representation of the Bremsstrahlungs process in the vicinity of atomic nuclei [L03, TMAYY17].....	13
<b>1.14</b> The Bremsstrahlung polar angle emission distribution from an electron beam [K03]. As the incident electron beam energy increases, the Bremsstrahlung tends to peak more in a forward direction [EGS05, BS70].....	14
<b>1.15</b> A schematic representation of the electron-nucleus Bremsstrahlungs process, where $\mathbf{k}$ is the momentum of the emitted photon. Moreover, $\mathbf{p}_0$ and $\mathbf{p}_e$ refer to the momentum of the incoming and outgoing electron, respectively. The initial momentum of the incoming electron, $\mathbf{p}_0$ , is shared between the outgoing electron, $\mathbf{p}_e$ , the emitted photon, $\mathbf{k}$ , and the nucleus, $\mathbf{q}$ , as: $\mathbf{p}_0 = \mathbf{p}_e + \mathbf{k} + \mathbf{q}$ [HN04].....	15
<b>1.16</b> A schematic representation of the produced relative number of Bremsstrahlung per energy interval versus the photon energy $h\nu$ in the electron-nucleus Bremsstrahlungs process [HN04].....	15
<b>1.17</b> A schematic representation of a qualitative comparison of electron-electron and electron-nucleus Bremsstrahlungs processes in different energy ranges. The recoil electron energy in the electron-electron Bremsstrahlung is appreciable in contrast to the energy recoil of the nucleus in the electron-nucleus Bremsstrahlung; therefore, the maximum photon energy for electron-nucleus Bremsstrahlung is always higher than for electron-electron Bremsstrahlung. Moreover, in the electron-electron Bremsstrahlung, the maximum photon energy is dependent on the photon emission angle [HN04].....	16
<b>1.18</b> Photon spectrum in electron-positron Bremsstrahlung [H03].....	17
<b>1.19</b> A schematic representation of a) the ordinary and b) the polarization Bremsstrahlungs process. In contrast to the ordinary Bremsstrahlungs process, in the polarization Bremsstrahlungs process, the photon emission is considered due to the virtual excitation of the target electrons by the projectile. Virtual excitation of the electrons translates to target polarization [KS14].....	18
<b>1.20</b> A schematic representation of constructive interference of coherent Bremsstrahlung in the periodic structure, where $\mathbf{k}$ is a wave vector. Moreover, $\mathbf{E}_1(\mathbf{k})$ and $\mathbf{E}_2(\mathbf{k})$ refer to the radiation field on the first and second period, respectively [P11].....	19
<b>1.21</b> The experimental photonuclear ( $\gamma, n$ ) and electronuclear ( $e^-, e'^-n$ ) cross-sections for $^{63}\text{Cu}$ [TFS20].....	20
<b>1.22</b> $^{99}\text{Mo}$ production yield as a function of electron beam energy through photonuclear and electronuclear reactions for a 20 mm $^{100}\text{Mo}$ cylindrical target (about 9.518 g). $^{100}\text{Mo}$ is used in this work as the converter/target	

for $^{99}\text{Mo}$ production [TFS20].....	21
<b>1.23</b> The ratio of electronuclear to photonuclear $^{99}\text{Mo}$ production yield for (a) 20 mm and (b) 1 mm thick $^{100}\text{Mo}$ target [TFS20].....	22
<b>1.24</b> Energy-loss (stopping power) for electrons in Pb [PT73].....	23
<b>1.25</b> a) Schematic representation of electron energy straggling when electron beam passes through a medium (where $R$ is the electron range, $E_0$ is the initial electron beam energy, and $X$ is the penetration distance in the medium). b) An illustration of the experimental measurements of the energy distribution of an electron beam that was performed through carbon foils with (a) 1.33 mm (b) 0.895 mm, and (c) 0.475 mm thickness [K10, S55].....	24
<b>1.26</b> Photon cross-section as a function of energy for (a) carbon and (b) lead. In this figure, $\sigma_{g.d.r}$ refers to the giant dipole resonance, which is discussed in section 1.2.6 [L17].....	25
<b>1.27</b> Attenuation of 0.662-MeV monoenergetic photons (solid lines) and of a heterochromatic photon beam (dotted line) [J17].....	27
<b>1.28</b> Measurements of photon beam attenuation under conditions of (a) a good geometry and (b) a poor geometry. In the case of a good geometry, ideally, it is assumed that the photon beam is well collimated and the photon source is located as far as possible from the detector. Additionally, it is assumed that the absorber, which is located between the photon source and the detector is thin enough to consider the probability of a second scattering of the photon to be negligible. In the case of poor geometry, as is observable, the probability of a second or multiple scattering of the incident photon is quite considerable. Thus, it can contribute to the registered detector signal [J17].....	28
<b>1.29</b> Spectrum of Bremsstrahlung for different endpoint energies where the converter target is tungsten [N13].....	28
<b>1.30</b> Schematic representation of the experimental attenuation coefficient measurement method for a) a narrow photon beam and b) broad photon beam. As can be seen, a slab of absorber with a thickness of $x$ is placed between the detector and the photon source. The absorber reduces the detector signal (photon intensity that is proportional to the number of photons reaching the detector) from $I_0$ measured without the absorber to $I(x)$ measured with absorber thickness $x$ in the photon beam. Considering a narrow beam is, in fact to exclude any scattered photon or any probably generated secondary radiation into the photon beam [P16].....	29
<b>1.31</b> Mass attenuation coefficient as a function of energy for different elements [J17].....	30
<b>1.32</b> Radiation length as a function of atomic number $Z$ [PT73].....	32
<b>1.33</b> Schematic representation of Rayleigh scattering. In this process, the incident photon interacts with the atom and transfers its energy by causing all (or some) of the atomic electrons	

to vibrate momentarily and then radiating their attained energy in the form of electromagnetic waves. These electromagnetic waves nondestructively combine with one another, forming an electromagnetic wave, which represents the scattered photon. The scattered photon is the same as the incident photon except for the emission angle that is generally less than 20 degrees (in respect to the direction of the original photon) [S14].	35
<b>1.34</b> A polar graph of the angular distribution of the Rayleigh scattering cross-section for aluminum and lead with different incident photon energies. Note that $d\Omega = 2\pi \sin \theta$ [C07].	35
<b>1.35</b> Angular distribution of the scattered photons through Rayleigh scattering as a function of photon energy for different elements. As the energy increases, the scattered photons tend to appear more in forward direction [C07].	36
<b>1.36</b> Cross-section for Rayleigh and Compton scattering of different elements as a function of photon energy [P09]. Note that for a given absorber, the photon energy $h\nu_{eq}$ , at which $\sigma_R = \sigma_C$ is shown as o	36
<b>1.37</b> Schematic representation of the Compton scattering [A07].	37
<b>1.38</b> The change in the photon's wavelength before and after Compton scattering as function of $\theta$ [A07].	38
<b>1.39</b> Average and maximum energies of outgoing electrons and average energy of scattered photons as a function of the incident photon energy (values are normalized to the incident photon energy) [C07].	40
<b>1.40</b> Energy distribution of the scattered electrons through Compton scattering for incident photons of 511, 1200, and 2760 keV [D88].	40
<b>1.41:</b> Electron Compton energy as a function of the Compton electron scattering angle $\theta_e$ for different incident photon energies [C07].	41
<b>1.42</b> Polar graph of the angular distribution of the Compton scattering cross-section (form a free electron) for different incident photon energies. Note that $d\Omega = 2\pi \sin \theta d\theta$ [C07] and $\theta$ is the photon scattering angles as shown in Fig.1.37	41
<b>1.43</b> Schematic representation of the dependency of electronic Compton scattering on the (a) photon energy, and (b) atomic number $Z$ [TL15].	42
<b>1.44</b> Theoretical (dashed curves) and experimental (solid curves) atomic Compton cross-section as a function of photon energy $h\nu$ for a wide range of materials [P09].	43
<b>1.45</b> Schematic representation of the photoelectric effect [P09].	45
<b>1.46</b> Schematic representation of electronic transmission in an excited atom in which an electron in the lower orbital is missing [NKV10]. It is worth pointing out that for photons with higher energies than the K-shell binding energy, about 80% of all photoelectric absorption occurs with K-shell electrons, and the remaining 20% with the less tightly bound outer electron shells [P09].	45



<b>1.47</b>	Ratio of total to K-shell photoelectric cross-section for photon energies higher than the K-shell binding energy as a function of atomic number of the absorber material [LR04].....	46
<b>1.48</b>	Schematic representation of X-ray photon generation and Auger electron emission in photoelectric effect [M16].....	46
<b>1.49</b>	Schematic representation of the dependency of photoelectric effect on (a) the photon energy, and (b) the atomic number $Z$ [TL15].....	47
<b>1.50</b>	Photoelectric cross-sections for various elements as a function of the photon energy [P09].....	48
<b>1.51</b>	Relative number of photoelectrons per unit angle $\frac{d\eta}{d\phi}$ as a function of the photoelectron ejection angle $\phi$ [P09].....	48
<b>1.52</b>	Schematic representation of the pair production mechanism [LR04].....	49
<b>1.53</b>	A schematic representation of a) the nuclear pair and electronic pair production mechanism and b) the electron-positron annihilation process [JC53].....	51
<b>1.54</b>	Dependency of the nuclear pair production process on the atomic number of a material for photons with energies higher than 20 MeV [A07].....	51
<b>1.55</b>	Atomic cross-section for nuclear pair production and electronic pair production as a function of photon energy for carbon and lead [P09]. As is shown, as the atomic number increases, the difference in nuclear pair production cross-section and the electronic one is increasing.....	52
<b>1.56</b>	Schematic representation of dependency of the atomic (including nuclear and electronic) pair production on the (a) photon energy, and (b) atomic number $Z$ [TL15].....	53
<b>1.57</b>	Atomic cross-section for pair production (as a sum of electronic and nuclear pair production cross-sections) versus photon energy for different materials [P09].....	53
<b>1.58</b>	A schematic representation of the photonuclear reaction with single neutron emission [S14].....	55
<b>1.59</b>	Cross-section data of the $^{93}\text{Nb}(\gamma, xn; x = 1 - 4)$ reaction as a function of photon energy [N13]. As is shown, emission of more than a single neutron due to photonuclear reactions is less probable and occurs at higher photon energies.....	55
<b>1.60</b>	Photonuclear absorption excitation function of deuterium, beryllium, zirconium and uranium. The thresholds for $(\gamma, n)$ reactions are 2.226, 1.666, 8.64 and 5.74 MeV for deuterium, beryllium, zirconium and uranium, respectively [IAEANO.2].....	56
<b>1.61</b>	Photoabsorption excitation function for different particle emissions of $^{29}\text{Si}$ (a) and $^{105}\text{Pd}$ (b) [IAEANO.2].....	57
<b>1.62</b>	Schematic representation of the Lorentzian distribution for (a) a single peak and (b) a double peak [TL15, IAEANO.2]. In the case of the double peak, the FWHM usually is larger than those of any two Lorentzian functions.....	57
<b>1.63</b>	Photoabsorption excitation function of $^{48}\text{Ti}$ [IAEANO.2].....	59
<b>1.64</b>	The $(\gamma, n)$ excitation function for holmium and erbium. The solid curve is the sum of two Lorentz curves (applied for fitting), and the dashed line is a smooth curve through the data points [H70].....	59

<b>1.65</b>	The $(\gamma, n)$ reaction cross-section for $^{141}\text{Pr}$ [H70].....	60
<b>1.66</b>	The peak width of the energy $\Gamma$ as a function of atomic mass number $A$ . The experimental data show that the average giant resonance width is about 5 MeV and that the dependency of $\Gamma$ on atomic mass number $A$ proceeds through several maxima. As is observable, these are associated with the three main regions of large intrinsic nuclear deformation, near $A = 25, 160$ , and $240$ [H70]. In general, $\Gamma$ changes from 3-4 MeV for magic nuclei to larger values for nonspherical or deformed nuclei [VVR99].....	60
<b>1.67</b>	Schematic representation of different photon interactions with matter. Note that electronic pair production in (E) refers the triplet production [P14, P16].....	62
<b>1.68</b>	Schematic block diagram representation of the interaction of photons with matter [E55].....	62
<b>1.69</b>	Major photon cross-section of different interactions with different atomic number and incident photon energy [FS20].....	63
<b>1.70</b>	Three mechanisms for the heat transfer [KBKW21, Z19].....	64
<b>1.71</b>	A schematic representation of heat flow through a wall [K50].....	66
<b>1.72</b>	Thermal conductivity ranges of some substances (all values are given at room temperature) [LQT18].....	66
<b>1.73</b>	Thermal conductivities variations versus temperature for different substances [H10].....	67
<b>1.74</b>	A schematic representation of the difference in mechanism for natural and forced convection. Natural convection (the LHS figure) is induced via a difference in hot and cold fluid density. In contrast, in forced convection (the RHS figure), fluid movement is forced by an external device (for example, by a cooling fan) [SOLID10].....	68
<b>1.75</b>	Schematic representation of uniform flow past a heated plate [J00].....	68
<b>1.76</b>	Schematic representation for (a) thermal-boundary layer thickness $\delta_T$ , (b) hydrodynamic boundary layer $\delta$ , and the temperature gradient at the surface [MSMD03].....	69
<b>1.77</b>	A schematic representation of the hydrodynamic and thermal boundary layers for (a) $Pr < 1$ , and (b) $Pr > 1$ [MMD16].....	70
<b>1.78</b>	Schematic representation for the hydrodynamic boundary layer $\delta$ , and the thermal-boundary layer thickness $\delta_T$ when there is a difference in the heat and flow starting point, shown as $X_0$ [YT].....	71
<b>1.79</b>	Schematic representation of the effects of the fluid flow regimes on hydrodynamic boundary layer $\delta$ [STACK]. For explanations about the buffer layer and viscous sublayer refer to [SG16, R82] for more details.....	71
<b>1.80</b>	Schematic representation of the fluid flow regimes as a function of the Reynolds number [L03].....	72
<b>1.81</b>	Variation of the convection heat transfer coefficient $h$ , and hydrodynamic boundary layer $\delta$ as a function of the flow regime. In the turbulent regime, fluid motion is highly irregular and can be characterized by velocity fluctuations that result in the enhancement of energy transfer. Because of fluid mixing, which results from fluctuations, the turbulent boundary layer is thicker compared to other regimes. Therefore, the temperature profile is flatter; however, the temperature	

gradient at the surface is steeper compared to laminar flow. So, the turbulent regime's local convection coefficient is more than the laminar regime [MSMD03].....	72
<b>1.82</b> The electromagnetic spectrum [ELEC19].....	74
<b>1.83</b> Schematic representation of the radiation energy reflection and absorption of an opaque surface, where $\dot{Q}_{incident}$ is the rate of incident radiation energy on the surface, $\dot{Q}_{ref}$ is the rate of radiation that is reflected back from the surface and $\dot{Q}_{ref}$ is the absorbed radiation energy within the body [LQT18].....	77
<b>1.84</b> Blackbody radiation emission intensity as a function of wavelength at given different temperatures [AST].....	78
<b>1.85</b> Schematic representation of the intensity of radiation emission at a given temperature for blackbody, graybody, and real surfaces [MBC17].....	79
<b>1.86</b> A schematic representation of the specified heat flux boundary conditions on both left and right surfaces of a slab with a length of $L$ at time $t$ [C02].....	80
<b>1.87</b> A schematic representation of a slab with an insulation heat flux boundary condition for a surface (the surface on the LHS) [P80].....	81
<b>1.88</b> A schematic representation of the thermal symmetry boundary condition in a slab [C02].....	82
<b>1.89</b> A schematic representation of the specified temperature boundary condition in a slab [C02].....	82
<b>1.90</b> A schematic representation of the convection boundary condition for a slab [C02].....	83
<b>1.91</b> A schematic representation of the convection boundary condition for different directions of heat transfer. As can be seen, the direction of heat transfer at a boundary has no impact on the surface energy balance [C02].....	83
<b>1.92</b> A schematic representation of different radiation boundary conditions for both boundary surfaces of a slab, in which $T_{surr}$ stands for the surrounding temperature and subscript numbers denote different surrounding mediums [C02].....	85
<b>1.93</b> A schematic representation of interface boundary conditions between two different layers of a body at the interface $x_0$ [C02].....	86
<b>1.94</b> Schematic representation of (a) no-slip boundary condition and (b) slip boundary condition. In this figure, BC is the abbreviation of boundary condition, $r$ and $R$ are the axis and radius of the tube, and finally $v(r)$ is the flow velocity [BCHS08].....	87
<b>1.95</b> A schematic representation of a) swirling flow in the cylindrical furnace and b) burner arrangement gaseous fuel that is injected through six symmetrical holes (swirl air directly enters through the outer burner's annulus). As is observable, a cyclic and periodic boundary condition can be considered for the cylindrical furnace and burner [VM07].....	88
<b>1.96</b> Mesh Terminology [MSM06].....	91
<b>1.97</b> Schematic representation of (a) orthogonal uniform, (b) orthogonally non-uniform, (c) non-orthogonal-structured, and (d) non-orthogonal unstructured meshes [MSM06].....	91

<b>1.98</b>	AAE of $k_{eff}$ resulting from a neutron diffusion calculation of a PWR reactor core using both mesh-edge and mesh-centered FDM. $k_{eff}$ is defined as the ratio of the neutrons produced in the next generation (through the fission reaction) to the sum of neutrons absorbed in fission reactions or non-fission reactions, plus those lost in this generation [A77, 19, 20]. Additionally, $N$ is the number of total applied meshes (or points) in the problem (which is a PWR nuclear reactor) [A77].....	92
<b>1.99</b>	Mesh configuration in the adaptive moving mesh method for two different cases (related to the gradient of reactor power for two different nuclear reactor cores). As can be seen, the mesh configuration is initially an orthogonal uniform form; however, it moved and deformed during the numerical calculations as the solution evolved [VOG19].....	93
<b>1.100</b>	A schematic representation of a quadrilateral mesh configuration in the moving mesh method, where $P$ is the central CV, $N$ (with subscripts 1 to 6) is the neighboring CVs and $C_p$ is the center of the sharing face between the two adjacent CVs [VT19].....	93
<b>1.101</b>	Two and three-dimensional cell/element types [MMD16].....	94
<b>1.102</b>	A schematic representation of the hybrid mesh configuration [LZXX13].....	94
<b>1.103</b>	A schematic representation of the time of solution as a function of geometry complexity for both Monte-Carlo and deterministic methods [B01].....	97
<b>1.104</b>	A close-up of the photon and electron trajectories in a thin plastic foil and a large NaI detector generated from a 20 MeV incident electron beam in an experiment presented in [B01].....	98
<b>1.105</b>	a) Schematic representation of the dynamitron b) 5 MeV, 300 kW dynamitron developed by Radiation Dynamics, Inc. [HH12].....	102
<b>1.106</b>	a) A schematic representation of the betatron b) A 35 MeV betatron at the University of Melbourne [HH12].....	103
<b>1.107</b>	Schematic representation of a) Circular and b) Racetrack microtron [BR81].....	104
<b>1.108</b>	Schematic representation of the cascade of three racetrack microtrons with the injector linac installed at the University of Mainz [T18].....	104
<b>1.109</b>	A schematic representation of a linac [H05].....	105
<b>1.110</b>	a) Two installed side by side linacs with 15kW and 10MeV incident electron beam energy in a medical products sterilization facility. b) a 3.2-kilometer linear accelerator installed at the Stanford Linear Accelerator Center that enables it to accelerate electrons to 50 GeV [HH12, SLAC].....	107
<b>1.111</b>	a) A schematic representation of the rhodotron where G, L, C, and D are electron gun, magnetic lens, accelerating cavity, and bending magnet, respectively. b) A cutaway schematic view of the rhodotron [HH12].....	108
<b>1.112</b>	A schematic representation of multiple beam lines (shown as $E_1... E_6$ ) of a rhodotron [K03, IBANO.1].....	109
<b>1.113</b>	The rhodotron models [ARIES18].....	109
<b>1.114</b>	Scheme of the proposed photonuclear setup.....	110
<b>1.115</b>	a) Photon flux distribution generated from a 40 MeV and 1 kW incident electron beam and 2mm thick tungsten. b) $^{67}\text{Cu}$ yield	

distribution in Zn target in units of MBq/g [HS15].....	111
<b>1.116</b> A 1D Gaussian distribution [TL15].....	112
<b>1.117</b> 1D Gaussian distribution for different FWHM [P16].....	113
<b>1.118</b> A 2D Gaussian distribution.....	113
<b>1.119</b> Variations of beam broadening under atmospheric and vacuum conditions. Although in a vacuum condition, electron beams are not visible to the human eye, a “beam glow” is produced as the ambient pressure increases because of the collisions between gas molecules and incident electrons. As is shown in this figure, this can eventually lead to the subsequent excitation of the ambient gas molecules and shows the beam broadening effect [HH12].....	114
<b>1.120</b> The $Z$ (atomic number) dependency for the production of Bremsstrahlung within 2 mrad angle at two different incident electron energies a) 20 MeV and b) 40 MeV as a function of thickness [DNA19].....	115
<b>1.121</b> The production of Bremsstrahlung (which corresponds to the photon yield in the $y$ axis) per incident electron is presented for various incident electron beam energies emerging from a 1 mm thick and 1.5 cm radius cylindrical shaped tungsten converter target [CV14].....	117
<b>1.122</b> Bremsstrahlungs spectrum for a tantalum converter target with 0.2 cm thickness with different electron energies and its impact on the production yield through the photonuclear reaction by increasing the number of impinging photons on the target in the GDR cross-section region depicted for some nuclides [RLK17].....	117
<b>1.123</b> Bremsstrahlungs production (per incident electron) as a function of tantalum thickness for a 10 MeV incident electron beam [EGS05].....	118
<b>1.124</b> Angular distribution of created Bremsstrahlung from a 60 MeV incident electron beam for various tungsten thicknesses, where $r_0$ is the electron mean range for 60 MeV in tungsten and equals $16.5 \text{ g} \cdot \text{cm}^{-2}$ , and $z$ is the thickness in $\text{g} \cdot \text{cm}^{-2}$ [BS70].....	119
<b>1.125</b> Spectrum of Bremsstrahlung emitted at different angles due to a 60 MeV incident electron beam impinging on a tungsten converter target, where $r_0$ is the electron mean range for 60 MeV in tungsten and equals $16.5 \text{ g} \cdot \text{cm}^{-2}$ , and $z$ is the thickness in $\text{g} \cdot \text{cm}^{-2}$ [BS70].....	119
<b>1.126</b> Variation of $^{67}\text{Cu}$ production rates in terms of specific activity ( $\text{MBq/g}$ ) for different production target masses as a function of their position away from the converter target (tungsten with a 2mm thickness) [HS15].....	120
<b>1.127</b> Energy deposition as a function of the incident electron beam energy in a 20 mm thick $^{100}\text{Mo}$ target [TFS20].....	121
<b>1.128</b> Variation of the energy deposition per incident electron in a tungsten target for different incident electron beam energies versus thickness. The energy deposition is $r_0 D(z)/T_0$ , in which, $D(z)$ is the energy deposition in units of $\text{MeV} \cdot \text{cm}^2 \cdot \text{g}^{-1}$ [BS70].....	121
<b>1.129</b> Photonuclear cross-section of $^{181}\text{Ta}(\gamma, n)^{180}\text{Ta}$ [KRSDFM19].....	122
<b>1.130</b> Excitation function of the neutron capture reaction on $^{226}\text{Ra}$ in dependence of the neutron energy [IAEANO.1] .....	122
<b>1.131</b> Ratio of photoneutron yield ( $Y_n$ ) to incident electron energy ( $T_0$ ) for different tantalum thicknesses and electron energies [BS70].....	123
<b>1.132</b> The number of emergent electrons per incident electron ( $T_N$ ) and the	

fraction of the emergent incident electrons with energy ( $T_E$ ) versus the tungsten thickness [BS70].....	124
<b>1.133</b> Fluence ( $F$ ) of electrons (1), photons (2) and neutrons (3) generated from 100 MeV incident electron beam energy in a 0.5 cm thick lead converter target [K20].....	124
<b>1.134</b> Neutron energy spectrum for different incident electron beam energies in a lead converter target [K20].....	125
<b>1.135</b> The photoabsorption cross-section of $^{43}\text{Ca}$ [IAEANO.2].....	126
<b>2.1</b> Two-dimensional Gaussian distribution for different FWHM modeled in MATLAB software.....	128
<b>2.2</b> A schematic representation of the arc-shaped energy deposition in a rotating target.....	129
<b>2.3</b> A schematic representation of incident electron beam profile, energy deposition profile, and total energy deposition profile.....	129
<b>2.4</b> A schematic representation for the proper location of the incident electron beam axis.....	130
<b>2.5</b> An illustration of the arc-shaped two-dimensional Gaussian function in a quarter of a circle with different FWHM (1 mm to 5 mm) obtained by the Matlab software.....	130
<b>2.6</b> Electron emergent coefficient ( $T_N$ ) as a function of beryllium thickness.....	131
<b>2.7</b> The fraction of the transmitted incident electron beam in the interval 39-40 MeV to 0-40 MeV.....	132
<b>2.8</b> Bremsstrahlung yield for different thickness of beryllium entrance window.....	132
<b>2.9</b> Dose due to the interactions of the electrons as a function of the beryllium thickness.....	133
<b>2.10</b> Total energy deposition due to the interaction of the electrons as a function of the beryllium thickness. Considering $1.9\text{E}16$ e/s emission via the rhodotron model TT300-HE, one can estimate about 14 to 77 Joule/s (Watt) for 20 to $100\mu\text{m}$ thickness, respectively.....	134
<b>2.11</b> Mesh distribution used in the COMSOL Multiphysics software for the stationary beryllium disc modeling of 0.2 s simulation time, 1 mm FWHM, and $20\mu\text{m}$ thickness.....	135
<b>2.12</b> The time distribution function of the electron beam.....	136
<b>2.13</b> Maximum temperature distribution versus 0.2 s simulation time for 1 mm FWHM of the electron beam and $20\mu\text{m}$ beryllium thickness.....	136
<b>2.14</b> 2D temperature distribution at 0.2 s simulation time for 1 mm FWHM electron beam and $20\mu\text{m}$ beryllium thickness.....	137
<b>2.15</b> Variation of maximum temperature versus beryllium thickness for different FWHM.....	137
<b>2.16</b> A schematic representation of the proposed rotation mechanism for the beryllium disc.....	138
<b>2.17</b> Mesh distribution used in the COMSOL Multiphysics software for modeling a rotating beryllium disc.....	139
<b>2.18</b> 2D temperature distribution at 0.06 s simulation time for 5mm FWHM of the electron beam and $20\mu\text{m}$ thickness.....	140
<b>2.19</b> Variation of maximum temperature versus beryllium thickness for different FWHM in the new design.....	140
<b>2.20</b> Bremsstrahlung yield for various tantalum thicknesses.....	142
<b>2.21</b> Range of electrons in tantalum for two different energies [Nucleonica20].....	142

<b>2.22</b>	Emergent electron per incident electron ratio for different tantalum converter thicknesses.....	143
<b>2.23</b>	Bremsstrahlungs spectrum for the optimum tantalum converter thickness.....	144
<b>2.24</b>	Angular distribution of the Bremsstrahlungs yield in the range of 0-40 MeV per incident electron.....	145
<b>2.25</b>	Angular distribution of the Bremsstrahlungs yield in the energy range of 8-30 MeV per incident electron.....	145
<b>2.26</b>	Energy deposition as dose (Joule/g) versus tantalum thickness due to the interactions of the electrons.....	146
<b>2.27</b>	Total Energy deposition (Joule) as a function of tantalum thickness due to the interactions of the electrons. Considering a $1.9\text{E}16$ e/s beam current from a rhodotron model TT300-HE, one can estimate about 47'000 Joule/s (Watt) for the optimum tantalum converter target thickness.....	147
<b>2.28</b>	Energy deposition as a function of tantalum converter target thickness for 200 $\mu\text{A}$ and 40 MeV electron beam [A07].....	147
<b>2.29</b>	Mesh distribution in the tantalum converter target of the optimum thickness (i.e., 4.5mm) for the time-dependent heat conduction modeling of 200ms simulation time and 1mm FWHM electron beam .....	149
<b>2.30</b>	2D temperature distribution of the tantalum converter target at 200ms simulation time for 1 mm FWHM of the electron beam.....	149
<b>2.31</b>	Maximum temperature distribution versus 200ms simulation time for the optimum thickness of the tantalum target with 1mm FWHM of the electron beam.....	150
<b>2.32</b>	Variation of maximum temperature as a function of FWHM for the optimum thickness of the tantalum converter target.....	151
<b>2.33</b>	A schematic representation of multidisc tantalum converter target design in a) 3D and b) 2D geometries.....	151
<b>2.34</b>	Energy deposition in the tantalum converter discs. Considering a $1.9\text{E}16$ e/s beam current from a rhodotron model TT300-HE, one can estimate about 47'000 Joule/s (Watt) energy deposition for the entire tantalum converter discs. Considering the heat capacity of helium ( $5.2 \text{ Joule. } g^{-1} K^{-1}$ ), and a 200K difference in temperature of helium's inlet and outlet, one can obtain about $250 \text{ l. } s^{-1}$ for cooling the converter targets.....	152
<b>2.35</b>	A schematic representation of tantalum disc rotation in the newly proposed helium-cooled multidisc rotating converter target design.....	153
<b>2.36</b>	Mesh density distribution used in the COMSOL Multiphysics software for the newly proposed multidisc rotating converter target design considering 5mm FWHM and 0.25ms simulation time .....	155
<b>2.37</b>	2D temperature distribution of the third tantalum converter disc for 5mm FWHM at 0.25ms simulation time.....	155
<b>2.38</b>	Variation of maximum temperature versus different FWHM of the electron beam for the third tantalum disc.....	156
<b>2.39</b>	Schematic representation of different irradiation setup components. The production targets are assumed to have 2cm diameter and placed 1cm apart. The aluminum column has a 1mm thickness (on each side) with a dimension of $0.5\text{cm} \times 2.2\text{cm} \times 20\text{cm}$ . The internal water thickness is 3mm. The distance between the last tantalum converter disc and the	

first production target (i.e., the first detector) is 1.5 cm. The distance between the aluminum column and the first production target (i.e., the first detector) is 0.5 cm. The converter discs are tightly enclosed in a water-cooled housing. The housing incorporates openings to allow gas circulation to and from the housing with a 3mm to 5mm thickness.....	157
<b>2.40</b> Electron energy spectrum before and after electron beam collision with the aluminum column. The reduction in electrons is 22.8% in the entire energy range.....	158
<b>2.41</b> a) Photon energy spectrum before and after the aluminum column. b) Absolute difference in number of transmitted photons/source-electron (i.e., subtraction of 'Before' and 'After', in Fig. 2.41a). The reduction of photons is 11.2% in the 0-8 MeV, 6.5% in the 8-30 MeV and 2.9% in the 30-40 MeV energy interval.....	159
<b>2.42</b> Schematic representation of the spatial photon emission distribution in the entire photonuclear irradiation setup.....	160
<b>2.43</b> Photon flux (with the units of photons per source-electron per cm <sup>2</sup> ) for the energy ranges of 8-30 MeV and 0-40 MeV, respectively.....	160
<b>2.44</b> Angular photon distribution (in units of photons per source-electron) for the energy range of 8-30 MeV.....	161
<b>2.45</b> Photon (per source-electron) energy spectrum for different production target positions.....	162
<b>2.46</b> Schematic representation of the <sup>67</sup> Cu photonuclear production routes and its decay chain and scheme [BNB16, Nucleonica20].....	163
<b>2.47</b> Photonuclear excitation function (mb) of the <sup>68</sup> Zn( $\gamma$ , p) <sup>67</sup> Cu reaction vs. photon energy (MeV). Data taken from the TENDL-2019 [KRSDFM19] and EXFOR database [EXFOR21].....	163
<b>2.48</b> Fitting curve (using a Gaussian distribution) for the experimental measurements of the photonuclear excitation function (mb) of the <sup>68</sup> Zn( $\gamma$ , p) <sup>67</sup> Cu reaction presented in Fig.2.47.....	164
<b>2.49</b> <sup>67</sup> Cu production for different production target position numbers considering a 1 (g. cm <sup>-2</sup> ) <sup>68</sup> Zn target thickness.....	164
<b>2.50</b> Schematic representation of the <sup>225</sup> Ra photonuclear production routes and its decay chain. The yellow, blue, and red colors imply that the radionuclide has an alpha, $\beta^-$ , and $\beta^+$ (or $\epsilon$ ) decay mode.....	165
<b>2.51</b> Photonuclear excitation function (mb) of the <sup>226</sup> Ra( $\gamma$ , n) <sup>225</sup> Ra reaction vs. photon energy (MeV). Data taken from the TENDL-2019 [KRSDFM19] (No data was found in the EXFOR database [EXFOR21]).....	166
<b>2.52</b> Photonuclear excitation function (mb) of the <sup>226</sup> Ra( $\gamma$ , p) <sup>225</sup> Fr reaction vs. photon energy (MeV). Data taken from the TENDL-2019 [KRSDFM19] (No data was found in the EXFOR database [EXFOR21]).....	166
<b>2.53</b> <sup>225</sup> Ra and <sup>225</sup> Ac production for the first production target position number considering a 0.1 (g. cm <sup>-2</sup> ) <sup>226</sup> Ra target thickness during irradiation and 20 days after EOB (called the waiting time).....	168
<b>2.54</b> Ratio of activity of <sup>225</sup> Ac at waiting time <i>t</i> to activity of <sup>225</sup> Ra at EOB (%) as a function of waiting time in units of days for different irradiation times.....	169
<b>2.55</b> Ratio of max. activity of <sup>225</sup> Ac reached at the optimal waiting time	



to activity of $^{225}\text{Ra}$ at EOB (%) for different irradiation times in units of irradiation time/half-life of $^{225}\text{Ra}$ .....	169
<b>2.56</b> Buildup and extraction of $^{225}\text{Ra}$ and $^{225}\text{Ac}$ from an irradiated $0.1\text{ g.cm}^{-2}\text{ }^{226}\text{Ra}$ target as a function of time.....	171
<b>2.57</b> Theoretical transient equilibrium of $^{225}\text{Ac}$ resulting from beta minus decay of $^{225}\text{Ra}$ (considering zero initial $^{225}\text{Ac}$ activity at EOB)[Nucleonica20] .....	171
<b>2.58</b> $^{224}\text{Ra}$ decay chain [J18].....	173
<b>2.59</b> $^{226}\text{Ra}$ photonuclear excitation functions for the reactions of $^{226}\text{Ra}(\gamma, n)^{225}\text{Ra}$ and $^{226}\text{Ra}(\gamma, 2n)^{224}\text{Ra}$ [KRSDFM19].....	173
<b>2.60</b> $^{224}\text{Ra}$ and $^{212}\text{Pb}$ production for the first production target position number considering a $0.1\text{ (g.cm}^{-2}\text{)}^{226}\text{Ra}$ target thickness during irradiation and 20 days after EOB (called the waiting time) .....	174
<b>2.61</b> Ratio of activity of $^{212}\text{Pb}$ at waiting time $t$ to activity of $^{224}\text{Ra}$ at EOB (%) as a function of waiting time in units of days for different irradiation times .....	175
<b>2.62</b> Ratio of max. activity of $^{212}\text{Pb}$ reached at the optimal waiting time to activity of $^{224}\text{Ra}$ at EOB (%) for different irradiation times in units of irradiation time/half-life of $^{224}\text{Ra}$ .....	175
<b>2.63</b> Buildup and extraction of $^{224}\text{Ra}$ and $^{212}\text{Pb}$ from an irradiated $0.1\text{ g.cm}^{-2}\text{ }^{226}\text{Ra}$ target as a function of time.....	176
<b>2.64</b> Decay of $^{224}\text{Ra}$ into different radionuclide daughters (considering zero initial $^{212}\text{Pb}$ activity at EOB) [Nucleonica20].....	177
<b>2.65</b> Decay of $^{224}\text{Ra}$ into $^{212}\text{Pb}$ (considering zero initial $^{212}\text{Pb}$ activity at EOB) [Nucleonica20].....	177
<b>2.66</b> Photonuclear excitation function (mb) of the $^{100}\text{Mo}(\gamma, n)^{99}\text{Mo}$ reaction vs. photon energy (MeV). Data taken from the TENDL-2019 [KRSDFM19] and EXFOR database [EXFOR21]... ..	179
<b>2.67</b> Schematic representation of the $^{99}\text{Mo}$ photonuclear production routes and its decay chain and scheme [Nucleonica20]. Note that the data given in the left part of $^{99}\text{Tc}$ (in the left hand side figure) apply to the metastable state, while those in the right part apply to the ground state. The blue color implies that the decay mode of the nuclide(s) is (are) $\beta^-$ . $^{100}\text{Mo}$ and $^{98}\text{Mo}$ (shown as a box containing a black part) are primordial nuclides; i.e., those formed in the build-up of terrestrial matter and still present today. The number which is written below the symbol of $^{100}\text{Mo}$ and $^{98}\text{Mo}$ in the left hand side figure (inside the black box) shows the abundance in naturally occurring elements (atom %). The red color in the top right of $^{100}\text{Tc}$ indicates that it is also decaying by EC to $^{100}\text{Mo}$ [MDS18] .....	179
<b>2.68</b> $^{99}\text{Mo}$ and $^{99\text{m}}\text{Tc}$ production for the first production target position number considering a $1\text{ (g.cm}^{-2}\text{)}^{100}\text{Mo}$ target during irradiation time and 20-day after EOB (called the waiting time).....	180
<b>2.69</b> Ratio of activity of $^{99\text{m}}\text{Tc}$ at waiting time $t$ to activity of $^{99}\text{Mo}$ at EOB (%) as a function of waiting time in units of days for different irradiation times .....	181
<b>2.70</b> Ratio of max. activity of $^{99\text{m}}\text{Tc}$ reached at the optimal waiting time to activity of $^{99}\text{Mo}$ at EOB (%) for different irradiation times in units of irradiation time/half-life of $^{99}\text{Mo}$ .....	181

<b>2.71</b>	Buildup and extraction of $^{99}\text{Mo}$ and $^{99\text{m}}\text{Tc}$ from an irradiated $1\text{ g.cm}^{-2}\text{ }^{99}\text{Mo}$ target as a function of time.....	182
<b>2.72</b>	Schematic representation of the simultaneous multiple target irradiation. The production targets are assumed to have a 2cm diameter and are placed 1cm apart.....	183
<b>2.73</b>	Energy spectrum of the impinging photons to the beam stop. In the simulation, no production target material is assumed in order to consider the most conservative conditions from the point of view of electron and photon shielding.....	185
<b>2.74</b>	Energy spectrum of the impinging photons on the beam stop .....	185
<b>2.75</b>	Energy deposition in all components of the photonuclear irradiation setup.....	186

# List of Tables

- 1.1 Cross-sections for photonuclear and electronuclear <sup>99</sup>Mo production on natural Mo [TFS20]..... 20
- 1.2 LET values for various low and high LET radiation beams [P16].....24
- 1.3 The Rayleigh characteristic angle  $\theta_R$  for different absorber materials and photon energies [P09] .....36
- 1.4 Photon interactions and their properties [P16].....63
- 1.5 Normal emissivity of different metals [J00].....75
- 1.6 Emissivity of different nonmetallic solids [J00].....76

# Abbreviations

RPM	Rotation Per Minute
GDR	Giant Dipole Resonance
FWHM	Full Width at Half Maximum
MCNP Code	Monte-Carlo N-Particle Transport Code
DC	Direct Current
RF	Radio Frequency
eV	Electron Volt

# Nomenclature

$E$	Energy	$Bq$	Becquerel
$R$	Range	$\nu$	Photon's frequency
$e$	Electron	$Z$	Atomic number
$e^+$	Positron	$\sigma$	Standard deviation
$q$	Atom's charge	$\Gamma$	Full Width at Half Maximum (FWHM)
$c$	Speed of light	$T_N$	Electron emergent coefficient
$n$	medium's refractive index	$b$	Barn ( $\cong 10^{-28}$ cm <sup>2</sup> )
$v$	charged particle's velocity	$A$	Activity
$h$	Planck constant	$\lambda$	Decay constant
$\lambda_p$	Photon's wavelength	$Y$	Radionuclide reaction yield
$mA$	Milli Ampere	$\nu$	Photon's frequency
$T_{1/2}$	Half-life	$s$	Second
$mrad$	Milliradian	$z$	Distance or depth
$Z$	Atomic number	$D$	Dose

# Summary

A continually growing number of applications of radionuclides are known in medicine and various industries. In industries, radionuclides can have different applications depending on the industry in which they are used. For example, they can be employed in the automotive industry for the quality control of the produced metal sheets or accurate thickness measurements; in the oil and gas industry to detect pipe cracks; in the aerospace industry for the use as compact sources of electrical power in spacecraft with long life and almost uniform performance. On the medical side, radionuclides are employed as radiopharmaceuticals to diagnose and treat diseases depending on the radiation that they emit. Three families of radionuclides that emit  $\alpha$ ,  $\beta^-$ , and Auger electrons are considered for therapy; the family of radionuclides that emit  $\beta^+$  is employed for diagnosis. A relatively new branch called theranostic has been introduced in recent years and is a combination of therapy and diagnostics. The term true theranostic pair refers to pairs of radioisotopes (one  $\beta^+$  emitter and another  $\beta^-$  emitter), of the same element conjugated with the same bio-molecule.

To fulfill the high demand for radionuclides, a reliable large-scale production facility that utilizes a low cost and highly efficient method is needed. Up to now, different ways for the production of different radionuclide families have been introduced and built. One of the most conventional methods is using nuclear reactors, which still are being used widely. However, the fleet of radionuclide producing reactors is relatively old and thus no longer reliable (they are scheduled to be taken offline in the next few years). The cyclotron is another method that accelerates protons, deuterons, and alpha particles in a circular path and is mainly used to produce a family of radionuclides that emit  $\beta^+$  with a relatively short half-life. Among the associated problems which they have, low production rates and specific activity are the main. Another radionuclide production method, which is relatively new, is based on photonuclear interaction and uses energetic photons for irradiation of the targets. In order to produce these photons, electron accelerators need to be employed, and then by using a converter, electrons produce photons in an interaction called Bremsstrahlung. This method has a relatively long history in radionuclide production; however, the problem that makes this method unsuitable is the considerable heat generation in the converter target. This problem made the use of this method restricted so that only research areas with a very low input power of incident electrons were of interest. Due to the many advantages of the photonuclear reactions over existing methods, including high production rate and specific activity, low material quantity, low impurities activation, and low post-processing, an in-depth investigation into possible new designs and optimization of the irradiation parts is essential and constitutes the motivation for this Ph.D. work.

This study was performed in the framework of the project entitled “Sinergia Project (SNSF): PHOtonuclear Reactions (PHOR): breakthrough research in radionuclides for theranostics” funded by the Swiss National Science Foundation and submitted to the European Patent Organisation (No 21212627.0).

# Aim of the thesis

Over the past few decades, a number of works have been performed to investigate the characteristics of generated Bremsstrahlung from converter targets [SQ82, S19, DNA19]. These characteristics include the energy and angular spectrum of the generated Bremsstrahlung from the collision of different incident electron beam energies with different converter target materials and thicknesses [HLB14, PBSKS07, D19, EGS05, CV14, SSSC10, HS15, DSFO18, TBAM16, GMHEM07, A61, P11, RLK17]. Work on such a complex problem could only be complemented by the development and employment of nuclear Monte-Carlo program-based codes [DSFO18, W09, EGS05].

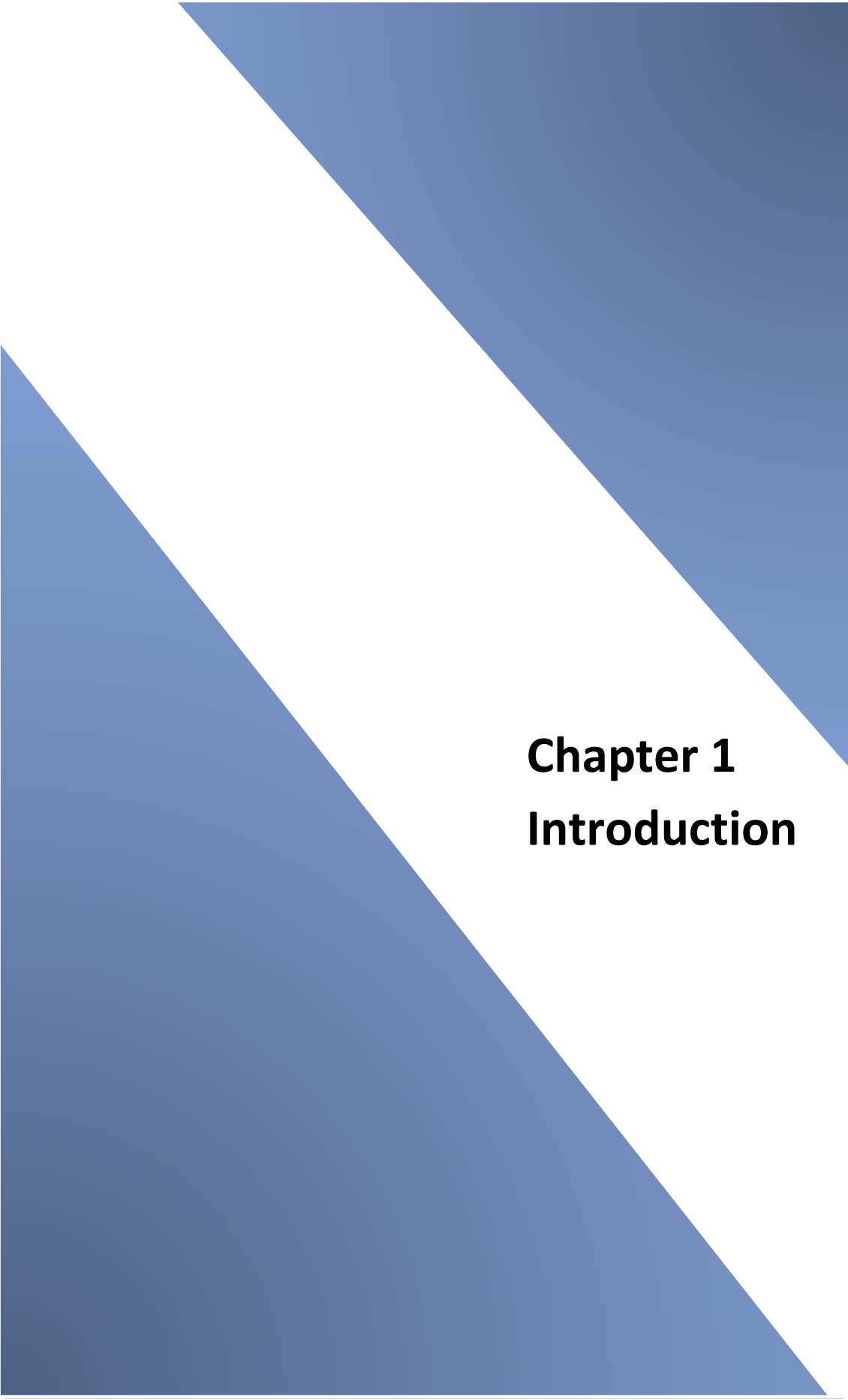
An electron accelerator suitable to induce photonuclear reactions has to fulfill a number of requirements concerning electron beam energy, beam intensity (beam power), time structure of the beam, and width of the beam [RLK17, HS15, K06, A07, S11, BS70, TFS20]. However, the lack of commercially available electron beam accelerators with energy and power suitable for the production of isotopes, made further studies of the photonuclear irradiation setups impractical. In recent years, two different electron beam accelerators, i.e., linac (offered by the company MEVEX) with 35 to 50 MeV and 4 mA average electron beam current and rhodotron (offered by the company IBA) with 40 MeV and 3.125 mA average electron beam current are now commercially available [M19, IBANO.1, IBANO.2, IBANO.3]. These recently developed high-power electron accelerators can be employed for viable radionuclide production. However, due to the higher repetition rates of a linac (800 Hz) compared to a rhodotron (50 Hz), much higher peak energies are deposited in a small area of the converter target resulting in significantly higher peak temperatures induced by the passage of the incident electron beam. Therefore, an irradiation setup design for a rhodotron is, in practice, more reasonable to implement compared to a linac. Nevertheless, to my best knowledge, the thermal analysis of the converter target has not been investigated so far, particularly for high-power electron beam accelerators. On this basis, designing an entire photonuclear irradiation setup (including entrance window, converter target, production targets, shielding, etc.) for a high-power rhodotron electron beam accelerator requires not only a nuclear assessment but also heat transfer analysis.

In order to produce radionuclides through photonuclear reactions, a high-energy electron beam derived from an electron accelerator impinges on a converter target to allow for photon production through the Bremsstrahlungs process (note that all of these parameters will be discussed in the introduction chapter). The generated high-energy Bremsstrahlung can then hit the production targets and produce the desired radionuclides through photonuclear interaction [JC83, D03]. Since, high-energy electrons and photons can interact through different interaction modes and deposit their energy in matter, a significant amount of heat is transferred to the target [A07]. On this basis, the introduction chapter (as the first of the three chapters of this thesis) focuses mainly on the electron and photon interaction mechanisms and the heat transfer analysis of the absorber. In addition, a brief review of different types of high-energy electron accelerators is presented in the introduction chapter. Chapter two is composed of different parts for simulation and modeling of the irradiation setup, with the first one providing details of electron beam modeling followed by the second part, which is the beryllium entrance window simulation. In the third part of chapter two, the

converter target design is presented. The rest of the irradiation components in the entire new proposed irradiation setup are provided in the fourth part, including the production targets and a massive beam stop. In the last chapter, the conclusion and outlook of this work are presented. Appendix A provides a series of benchmark problems to verify the calculations performed with the software used in this work. Appendix B includes a patent extracted from this work and the following selected papers related to this thesis's framework.

1. M. Vagheian et al., A new moving-mesh Finite Volume Method for the efficient solution of ..., Nuclear Engineering and Technology 51 (2019) 1181-1194.
2. M. Vagheian et al., Introduction to the non-orthogonal gradient-based Finite Volume Method for ..., Annals of Nuclear Energy 138 (2020) 107216.
3. M. Vagheian et al., Introduction to the Slide Modeling Method for the efficient solution of heat conduction calculations, Journal of Applied and Computational Mechanics, 5(4) (2019) 680-695.
4. M. Vagheian et al., Enhanced finite difference scheme for the neutron diffusion equation using the importance function, Annals of Nuclear Energy 96 (2016) 412–421.
5. M. Vagheian et al., Experimental and theoretical investigation into X-ray shielding properties of thin lead films, International Journal of Radiation Research, 18 (2) (2020) 263-274.
6. J. Jastrzębski, ..., M. Vagheian, Investigation of the production of the auger electron emitter <sup>135</sup>La using medical cyclotrons, Acta Physica Polonica B 51 (2020) 861-866.
7. M. Vagheian et al., On an improved box-scheme finite difference method based on the relative event probabilities, Progress in Nuclear Energy 88 (2016) 33-42.



The page features two large, solid blue triangles. One triangle is positioned in the top right corner, pointing towards the bottom left. The other triangle is in the bottom left corner, pointing towards the top right. These triangles are separated by a white diagonal band that runs from the top left to the bottom right, creating a stylized 'X' or 'Z' shape across the page.

# **Chapter 1**

## **Introduction**

In general, radiation is classified into two main categories, namely ionizing, and non-ionizing radiation, depending on its ability to ionize matter [CJ09, P16, J17]. The ionization energy of atoms is the minimum energy required for ionizing an atom and is specified in electron volts (eV)\*. Non-ionizing radiation is not able to ionize matter because its energy is lower than the ionization energy of the atoms of the absorber. Therefore, the term non-ionizing radiation refers to all types of electromagnetic radiation, which does not carry the required energy per quantum (i.e., photon) to ionize atoms or molecules of the absorber medium. This range of electromagnetic radiation is near to ultraviolet radiation, visible light, microwaves, and radio waves in descending order of energy [S07, P16].

Ionizing radiation is able to ionize matter either directly or indirectly, since its quantum energy is higher than the ionization potential of atoms and molecules [P16, J17, NUE12]. Ionizing radiation is categorized into two main groups, namely directly and indirectly ionizing radiation. The former group consists of charged particles (electrons, protons,  $\alpha$ -particles, and heavy ions), which deposit their energy in the absorber medium through a direct one-step process involving Coulomb interactions between the ionizing charged particle, and orbital electrons of the target atoms. The latter group, however, comprises neutral particles (photons and neutrons) that deposit energy in the absorber medium through a two-step process. In the first step of the process, a charged particle as the result of the interaction between the indirect radiation with the medium is released in the absorber, which in the case of photons are either electrons or electron/positron pairs, and in the case of neutrons, protons, or heavier ions. In the second step of the interaction process, the released charged particles deposit their energy in the medium through direct Coulomb interactions (with orbital electrons of the target atoms). Fig.1.1 presents a block diagram, which summarizes the above discussion [MG05, P16, J17].

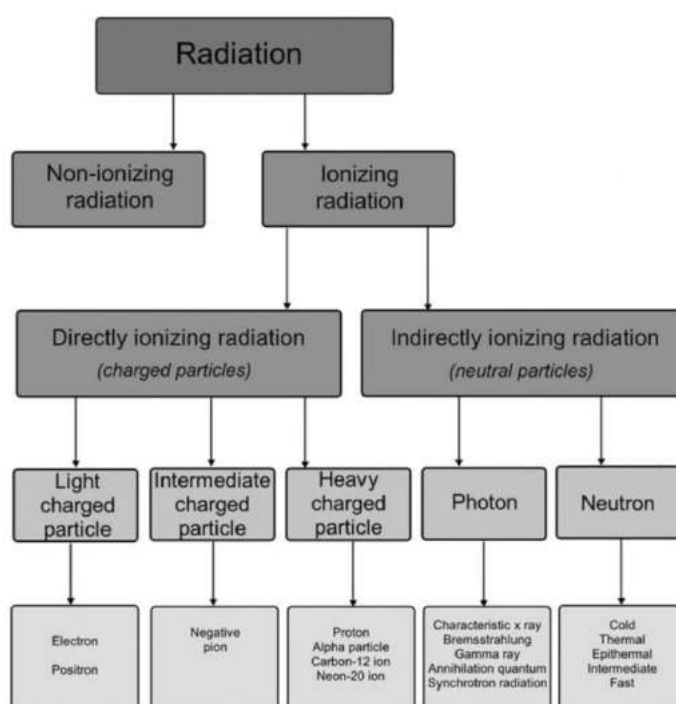


**Fig. 1.1:** Block diagram of different radiation types [P16]

\* eV is the amount of kinetic energy obtained by an electron accelerating from rest (i.e., zero kinetic energy) through an electric potential difference of one volt in vacuum [TL15, K10].

In order to produce radionuclides through photonuclear reactions, a high-energy electron beam derived from an electron accelerator impinges on a converter target to allow for photon production through the Bremsstrahlungs process (note that all of these parameters will be discussed in the introduction chapter). The generated high-energy Bremsstrahlung can then hit the production targets and produce the desired radionuclides through photonuclear interaction [JC83, D03]. Since high-energy electrons and photons can interact through different interaction modes and deposit their energy in matter, a significant amount of heat is transferred to the target [A07]. On this basis, the introduction chapter focuses mainly on the electron and photon interaction mechanisms and the heat transfer analysis of the absorber. In addition, a brief review about different types of high-energy electron accelerators is presented in the introduction chapter.

## 1.1 Electrons passing through a medium

When an electron passes through any medium, it loses its energy because of the interaction with atomic electrons and nuclei. Additionally, the direction of electron motion and its momentum is changed [F58]. The transmission curve for monoenergetic electrons versus absorber thickness is presented in Fig. 1.2. As is shown, the number of transmitted electrons begins to drop immediately and then approaches zero. The electron range is obtained by extrapolating the transmission curve's linear portion to zero, giving the extrapolated range  $(Re)^*$  [K00].

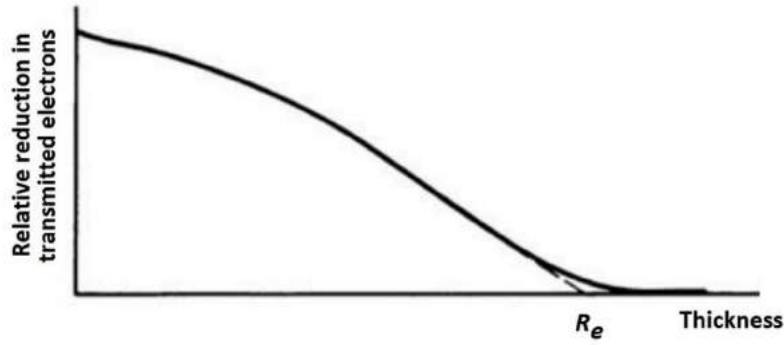


**Fig. 1.2:** A schematic representation of the transmission curve for monoenergetic electrons versus the absorber thickness, where  $Re$  stands the extrapolated range [K00]

Considering the range of incident electrons with the energy of  $E_o$  as  $R(E_o)$ , then for target thicknesses greater than  $R(E_o)$ , the target is considered as bulk material that leads to backscattering or absorption of incident electrons in the target. However, if the thickness is lower than  $R(E_o)$ , a fraction of the incident electrons can also be transmitted through the target. What is more, is that electromagnetic radiation can also be produced through these processes when the electron approaches the electric field of the nucleus or atomic electrons and is decelerated (see Fig.1.3). In the following, a detailed description of the electron's interaction mechanisms is presented [D03].

---

\* Besides the extrapolation range, some other range definitions can be defined, such as *path length* of an electron, which is the total distance along the actual electron's trajectory till it comes to rest (i.e., stop), regardless of its direction of motion. The projected range is the other range definition, which is the sum of individual path lengths projected onto the electron direction. One of the important range types is called the continuous slowing down approximation (CSDA) range and symbolized as  $R_{CSDA}$ . This comes from the approximation that assumes that since most of the collision and radiation interactions individually transfer only a small fraction of the incident electron's kinetic energy, it is possible to assume that the electron is moving through a medium as it is losing its kinetic energy gradually and continuously [P16]. Other range definitions have also been defined and can be found in literature, such as the maximum range  $R_{max}$ , the 50% range  $R_{50}$ , the therapeutic ranges  $R_{80}$  and  $R_{90}$ , the practical range  $R_p$ , etc. [P16].

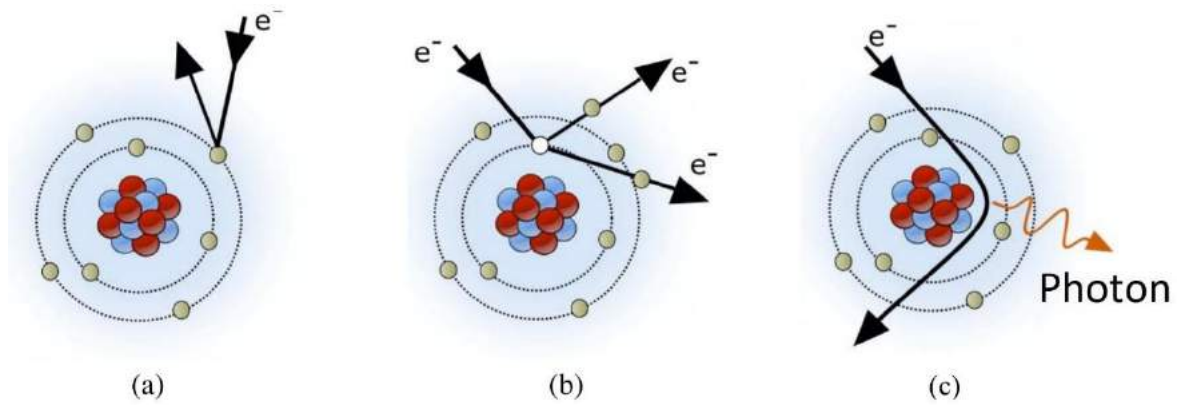


**Fig. 1.3:** A schematic representation of the main electron interaction mechanisms  
a) Backscattering b) Secondary electron generation c) Photon production [WH19]

Backscattered electrons are those electrons that scatter back or, in other words, undergo large-angle deflections along their tracks in a way that they re-emerge from the surface through which they entered (see Fig. 1.3a) [K00, WH19]. Backscattered electrons have lower energy than incident primary electrons since they dissipate a fraction of their energy in the target through different interactions, including ionization, electron excitations, scattering, etc. (see Fig. 1.4). The number of backscattered electrons relies on the target material, target thickness, and incident primary electron energies. Backscattering is mostly considered for low incident electron energy and high atomic numbers of the absorber targets [K00]. It also is needed to point out that if the target thickness is higher than the range of the incident primary electrons, the number of backscattered electrons reaches its maximum value [D03]. The fraction of the backscattered electrons to incident electrons ( $\eta$ ) for some materials and a wide energy range of electrons is presented in Fig. 1.5.

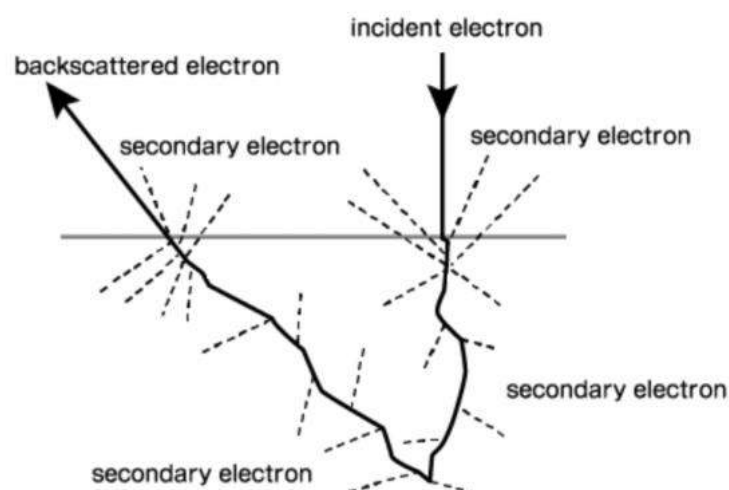


**Fig. 1.4:** A schematic representation of the backscattered electrons in a medium [PM]

Secondary electrons are created in the target due to the interaction of the primary electrons with the electrons from the atoms bound in the target or the other energetic secondary electrons that travel in the target (see Fig. 1.3b). Secondary electrons can emerge from the

target surface following many elastic and inelastic collisions\* with the target atoms (see Fig.1.4). It should be noted that the spectrum of the secondary electrons usually is contaminated by the contribution of the primary or backscattered primary electrons. This stems from the fact that secondary electrons, similar to the primary incident electrons, undergo many elastic or inelastic collisions with target atoms, and therefore, are able to emerge from the target surface. On this basis, the process of secondary electron production can be categorized into two main groups. The first one is due to interactions between primary electrons and electrons bound in the target's atoms, while the second one is due to interactions of the produced secondary electrons with the electrons bound in the target. Accordingly, a cascade of secondary electrons can be produced in the target, and this process continues until the energy of the secondary electrons reach lower than the required value for extracting new secondary electrons or until the produced secondary electrons reach the surface of the target and have enough energy to emerge from it [D03].

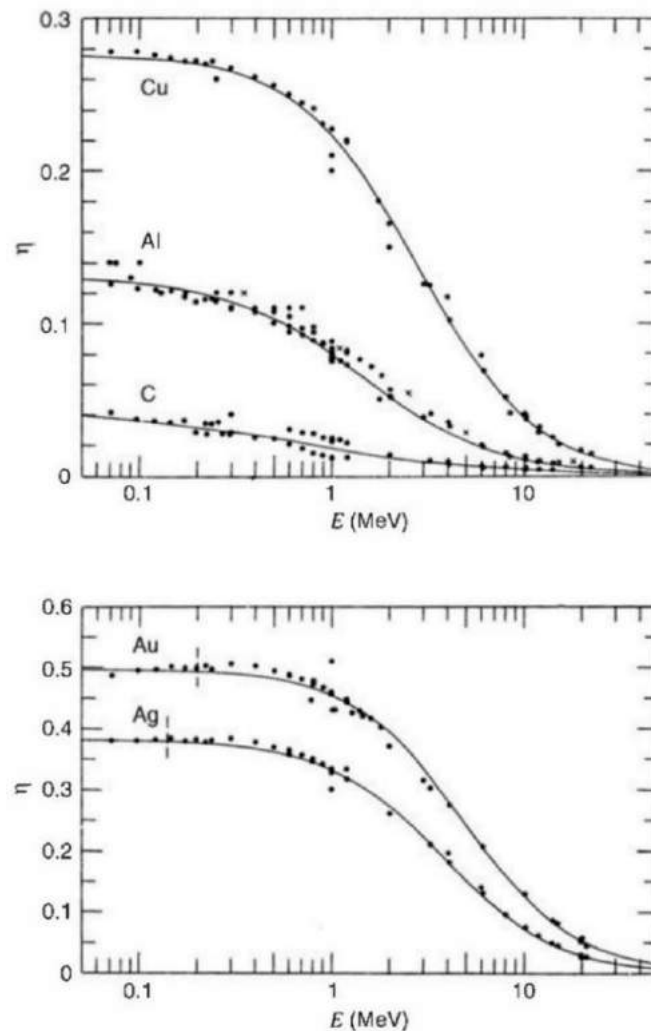


**Fig. 1.5:** Fraction of backscattered to incident electrons ( $\eta$ ) as a function of incident electron energy [K00]

\* In an elastic collision, the primary electron does not lose its energy despite its change in direction through the interaction. However, in an inelastic collision, in addition to the direction, the energy of the incident primary electron also changes [A07, AP18].

Bremsstrahlung refers to the process of electromagnetic radiation emission due to the deceleration of every charged particle (see Fig. 1.3c). The Bremsstrahlung intensity changes directly with the energy and inversely with the square of the incident particle mass. In addition, it depends on the atomic number and density of the converter's target material. As an illustration, for the X-ray tubes in which electrons have low energy, most of the energy of the incident electrons is converted to heat (around 99%), and only a small fraction (less than 1% of the energy) is converted to photons. However, in the case of electron accelerators, in which incident electrons have high energies, tens to even more than 90% of the energy are converted to photons [JC83].

If the thickness of the target is higher than the range of the incident electron in the target, the number of transmitted electrons is zero, whereas the fraction of backscattered electrons reaches its maximum (the backscattered coefficient). The remaining incident primary electrons are absorbed. Accordingly, if  $r$  stands as the backscattered coefficient,  $1 - r$  equals the fraction of absorbed electrons in the target material [D03].

### 1.1.1 Electron interactions

Electrons can undergo interactions with different interaction probabilities depending on their incident energy, atomic number, and target material density [A07, JC83]. Generally, the interactions are divided into scattering, ionization, electron-positron annihilation, Cherenkov radiation, and Bremsstrahlung emission [JC83, D03]. The Bremsstrahlung process dominates at high electron energies (which are of interest in electron accelerator design) and solid target materials (which are used in different irradiation setups for the photonuclear production at electron accelerators). In the following, each interaction is described briefly, and more details of the Bremsstrahlung process are presented due to its higher importance in this work. It is worth noting that in some of the electron interactions, positrons are also considered to have existed in the medium. This is due to the fact that when an energetic electron beam impinges on a high-Z target (which is expected to be used for the converter target material), high-energy photons are created through the Bremsstrahlung process. Then these photons can undergo the pair production interactions close to the atomic nuclei or atomic electrons and produce positrons [A07, HN04].

#### 1.1.1.1 Ionization

Ionization interaction refers to a process in which a primary incident electron can eject loosely bound electrons\* of an atom if it transferred enough energy to the atom. The ejected electron can also generate secondary ionization in the same manner if it carried away enough energy from the atom due to the first ionization. Until the ejected electrons' energy is higher than the atom's first ionization potential, the process can continue (see Fig. 1.6) [A07, C07]. Note that not all of the electrons with higher energies than the ionization potential can produce ionization; in fact, the probability in which the electrons can eject electrons through the ionization process relies on the cross-section, where the cross-section itself depends on the electron energy and target material [A07, P16].

---

\* Loosely bound electron is an atomic electron whose binding energy ( $E_B$ ) is considerably smaller than the incident photon energy ( $h\nu$ ) [K10, P09].

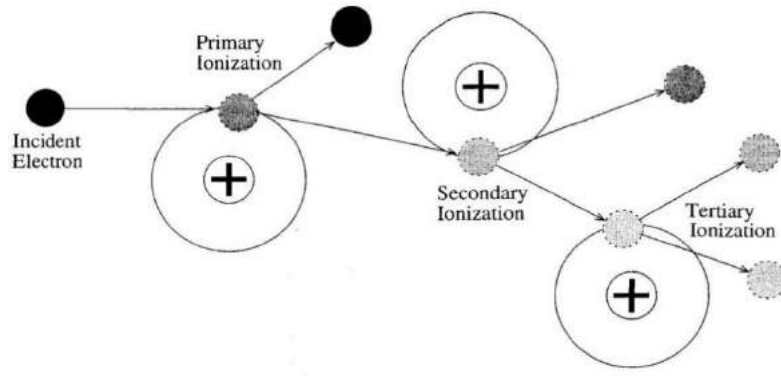


**Fig. 1.6:** A schematic representation of the successive ionization process [A07]

At low to moderate incident electron energies, the ionization process dominates among the electron interaction modes. Symbolically, the electron ionization process can be considered as:



where  $X_q$  refers to an atom and  $q$  is the atom's total positive charge [A07].

### 1.1.1.2 Scattering

Electrons can be scattered through interactions with electrons or atomic nuclei in the target. Generally, electron scattering interactions are divided into two main groups, elastic scattering, and inelastic scattering [HAT16]. The former happens when the primary electron does not lose its energy in spite of its change in direction through the interaction (see Fig. 1.7). However, in the latter case, in addition to the direction, the energy of the incident primary electron also changes (see Fig. 1.7). Accordingly, despite elastically scattered electrons, inelastically scattered electrons have a longer wavelength than the incident primary electrons [HAT16]. All in all, the electron path in a medium is nonlinear (see Figs. 1.4 and 1.7). The first reason is due to a large scattering angle with an orbital electron at the inelastic scattering interaction. The second reason is owing to a large deflection with a nucleus at the elastic scattering interaction [NUE12]. In the following, different scattering interactions of the incident electrons are presented (see Fig. 1.8).

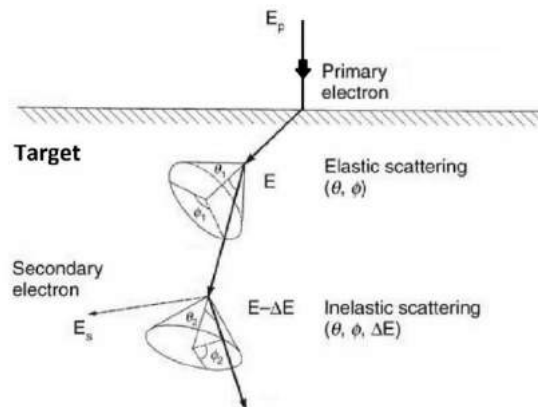


**Fig. 1.7:** A schematic representation of secondary electron interactions in the medium, where  $E_p$  and  $E_s$  are the energy of the primary and secondary electrons, respectively. The



polar angle  $\theta$  is the angle of the electron (i.e., the scattered electron in the elastic scattering and the secondary generated electron in the inelastic scattering, respectively). Concerning the polar incident electron direction axis, the azimuthal angle  $\phi$  is the rotation angle regarding the initial meridian plane, and the subscript numbers refer to the scattering interaction number [LMD11].

## Bhabha scattering

Bhabha scattering considers the scattering of an electron from a positron (see Fig. 1.8). Symbolically, the Bhabha scattering can be written as follows:

$$e^- + e^+ \rightarrow e^- + e^+. \quad (1.2)$$

Bhabha scattering is an elastic scattering, and the interaction can be considered due to the Coulomb attraction between the two particles. For high energetic electrons, the probability of the interaction is not considerable [A07, AP18]. Fig. 1.9 shows the fractional energy loss of electrons and positrons per radiation length  $(X_0)^*$  in lead versus the incident beam energy. In Fig. 1.9, for the Bhabha scattering, positrons are considered as projectiles. As can be seen, the contribution in energy loss for positrons with higher energy than about 10 MeV always is very low.

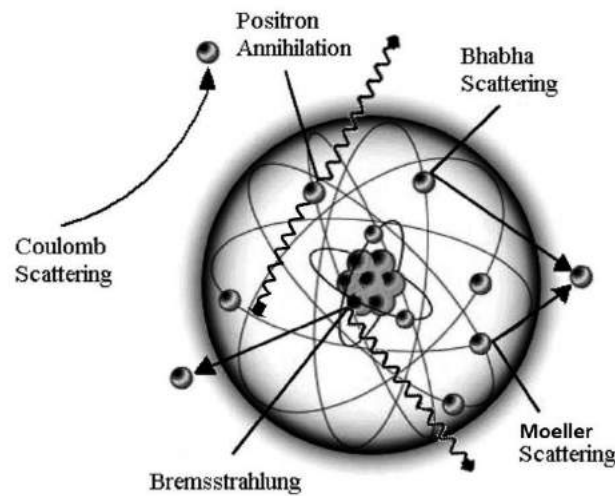


**Fig. 1.8:** A schematic representation of some of the electron and positron interactions [WH19]

## Moeller scattering

Moeller scattering is an elastic scattering of an electron from another electron (see Fig. 1.8). Symbolically, Moeller scattering can be written as:

$$e^- + e^- \rightarrow e^- + e^-. \quad (1.3)$$

---

\*  $X_0$  is the mean distance over which a high-energy incident electron loses all but  $1/e$  of its energy through the Bremsstrahlung interaction in a medium [GK00].

Moeller scattering can be considered due to the Coulomb repulsion between the two electrons [A07, AP18]. As is shown in Fig. 1.9, the Moeller scattering has the same trend of variations with the Bhabha scattering and has an almost negligible contribution in energy loss for energies above about 10 MeV of electrons.

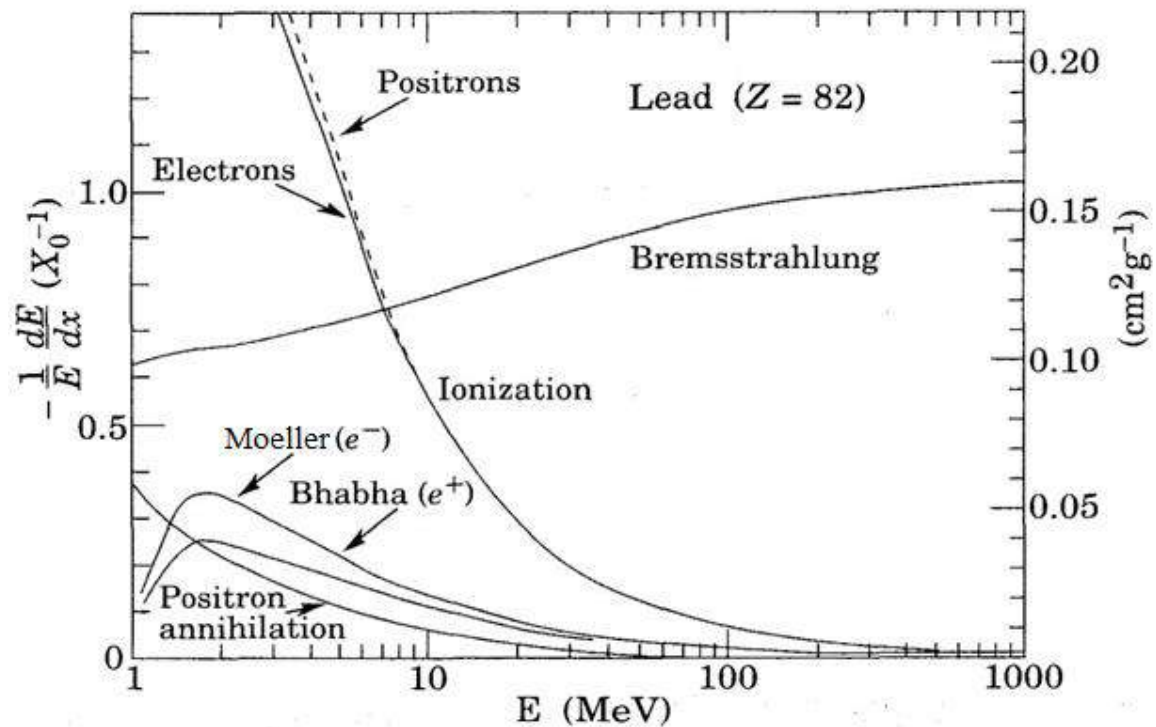


**Fig. 1.9:** A quantitative representation of the fractional energy loss of electrons (and positrons) per radiation length in the lead versus the incident electron (and positron) beam energy. The radiation length for electrons ( $X_0$ ) is the mean distance over which a high-energy incident electron loses all but 1/e of its energy through the Bremsstrahlungs interaction in a medium. For lead, this value is  $6.37 \text{ g} \cdot \text{cm}^{-2}$  [GK00].

## Single, plural, and multiple scattering

Single scattering occurs when an electron is scattered only once; however, plural and multiple scattering happens when the electron is scattered several times and often over. The probability for the number of scattering interactions depends on the ratio between target thickness and the mean free path length  $\lambda_{mfp}^*$  [ZLH06]. By increasing the target's thickness ratio to the mean free path length, the probability for plural and multiple scattering increases. Additionally, as the energy of the incident electron increases, the electrons are scattered in smaller angles through the medium (see Fig. 1.10) [BRS38, E70].

\* The mean free path is defined as the average distance that is traveled by an electron between two successive elastic or inelastic collisions [ZLH06].

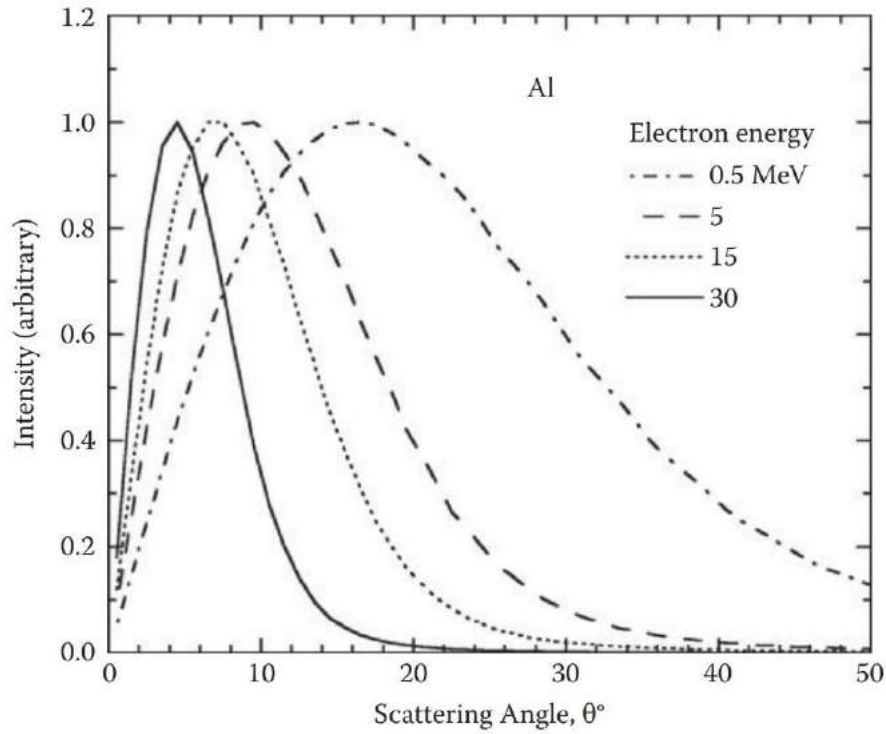


**Fig. 1.10:** Angular distribution (as intensity) of multiple electron scattering in an aluminum target with different incident electron beam energy [NUE12]

### 1.1.1.3 Cherenkov radiation

Cherenkov radiation is a special kind of radiation with a wavelength around the electromagnetic spectrum's visible region. Cherenkov radiation is emitted when a high-energy charged particle travels faster than the speed of light in a medium [A07]. It can be shown that the Cherenkov radiation is emitted when the velocity of the charged particle is significantly higher than a threshold value:

$$v > \frac{c}{n}, \quad (1.4)$$

where  $v$ ,  $c$ , and  $n$  refer to the charged particle's velocity, speed of light, and the medium's refractive index, respectively. It was shown that the energy (or velocity) limitation for Cherenkov radiation emission is 0.289 MeV and 539 MeV for electron and proton, respectively [A07]. Cherenkov radiation can be seen in water-cooled nuclear reactors where high energetic electrons ( $\beta^-$  particles) are produced from the fission\* process (see Fig. 1.11) [B16, DH91, and L65].

---

\* Nuclear fission refers to a process in which a heavy nucleus splits into two lighter nuclei, each with about half the heavy nucleus mass [L65, LB01].

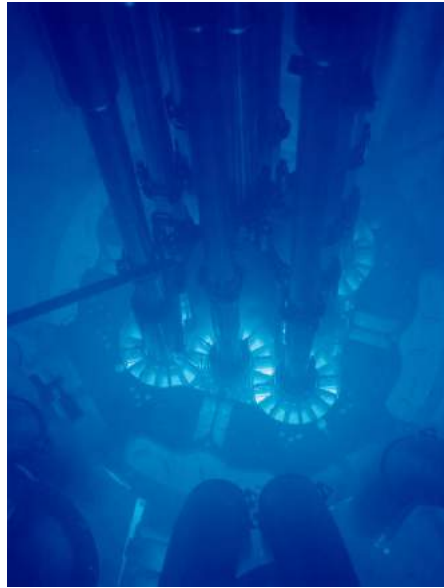


**Fig. 1.11:** Cherenkov radiation in water-cooled nuclear reactors. The Cherenkov radiation spectrum is continuous. Its relative intensity per unit frequency was shown to be inversely proportional to the wavelength squared. Thus, the number of photons increases by decreasing the wavelength. That is the reason why most of the Cherenkov radiation appears blue and mainly in the UV range. In a water-cooled nuclear reactor, the blue radiation that appears in the reactor pool is Cherenkov radiation, where the emitted  $\beta^-$  particles from fission results in the shock wave constructive interference that appears as a glow. Cherenkov radiation has been identified useful for many applications such as imaging, radiotherapy monitoring, optical-guided surgery, etc. [B16, V20, O19].

#### 1.1.1.4 Electron-positron annihilation

The electron-positron annihilation process results in at least two photon emission, each having 511 keV (see Fig. 1.12). Generally, more than two photons can be produced in this process; however, the probability decreases remarkably as the number of produced photons increases [A07]. For high energetic electrons, the cross-section for the electron-positron annihilation process is too low (almost zero), whereas it increases as the electron energy decreases. The main reason for the low cross-section of this interaction is the low abundance of positrons in the target, leading to a low contribution to the total energy loss, particularly at moderate to high electron energies [A07, H06, LP07].

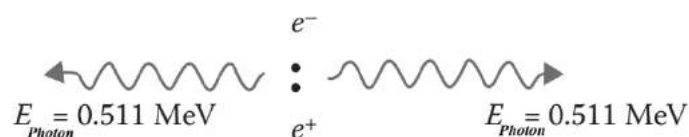


**Fig. 1.12:** Electron-positron annihilation. In this process, the photons are emitted at under 180 degrees [TL15].

### 1.1.1.5 Bremsstrahlung

As discussed before (section 1.1.1), Bremsstrahlung refers to the process of electromagnetic radiation emission due to the deceleration of every charged particle (see Fig. 1.13). However, as the mass of the charged particle increases, the Bremsstrahlungs intensity decreases due to the inverse relation of the Bremsstrahlungs intensity with the square of the radiating particle mass. When an electron has an energy much higher than its rest energy while moving through a medium, a Bremsstrahlung is probable to be emitted. The Bremsstrahlung created in the same target material (i.e., the same atoms) do not have the same energy necessarily. The energies of Bremsstrahlung can differ due to different electron energies (different primary, secondary, and tertiary generated electrons in the target) and different decelerations of the impinging electrons when encountering an electric field of a charged particle [L03, TMAYY17].

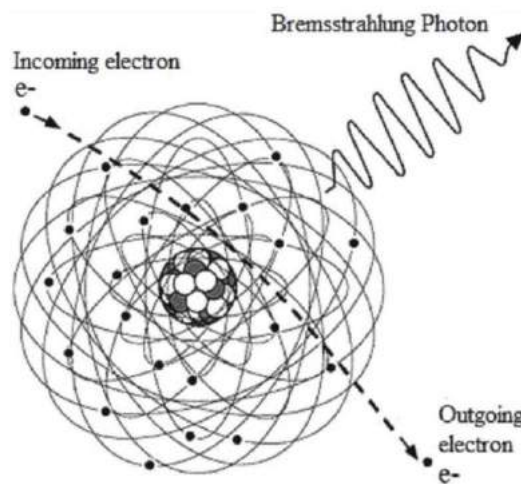


**Fig. 1.13:** A schematic representation of the Bremsstrahlungs process in the vicinity of atomic nuclei [L03, TMAYY17]

When an incident electron approaches an atom, the Coulomb field of the nuclear charge acts as the atom's main force leading to Bremsstrahlungs emission [A07]. Atomic electrons have a two-fold impact on the Bremsstrahlungs emission. On the one hand, these electrons can lead to Bremsstrahlungs emission if they act as individual particles and absorb the incident electron's recoil momentum through a collision called the electron-electron Bremsstrahlungs process (this process will be discussed later in more detail). On the other hand, the atomic electrons as a static charge distribution can screen the Coulomb field of the nucleus and cause a reduction in cross-section of the electron-nucleus Bremsstrahlung (this process will be discussed later in more detail) results in a reduction in photon emission. It is worth pointing out that in the latter case, the atomic electrons and the nucleus together as an atom absorb the collision's recoil momentum by the incident electron [A07, HN04].

The maximum attained energy of an accelerated electron through a potential  $V$  is (one)  $eV$  (where  $e$  refers to the unit electronic charge). Accordingly, the maximum Bremsstrahlungs energy, which an electron can emit, is also (one)  $eV$ . In general, the energy of Bremsstrahlung can be written as [P09, K03]:

$$E_{brems} \leq E_{max} = eV, \quad (1.5)$$

or can be given by:

$$\frac{hc}{\lambda_p} \leq eV, \quad (1.6)$$

where  $\lambda_p$  is the wavelength of the emitted photon and  $h$  is the Planck constant. Eq. 1.6 can be rewritten as:

$$\lambda_p \geq \frac{hc}{eV}. \quad (1.7)$$

Therefore, the minimum wavelength for the emitted photon is called the cutoff wavelength for Bremsstrahlung [A07, K03, P09, BS70].

The angular distribution of Bremsstrahlung depends on the incident electron beam energy. Moreover, the material and thickness of the converter target can also impact the number of photon emissions emitted at different angles. Fig. 1.14 shows the polar angle photon emission distribution depending on the incident electron beam energy [K03].

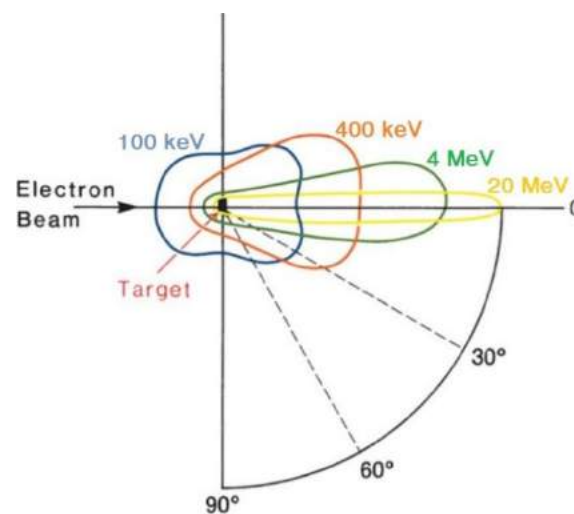


**Fig. 1.14:** The Bremsstrahlung polar angle emission distribution from an electron beam [K03]. As the incident electron beam energy increases, the Bremsstrahlung tends to peak more in a forward direction [EGS05, BS70].

As is observable in Fig. 1.14, the Bremsstrahlung is emitted mainly in forward direction when the incident electron beam energy increases to tens of MeV [MLA06].

Bremsstrahlungs production mechanisms due to the deceleration of an incident electrons can be categorized as electron-nucleus Bremsstrahlung, electron-electron Bremsstrahlung, two-photon Bremsstrahlung, electron-positron Bremsstrahlung, polarization Bremsstrahlung, incoherent Bremsstrahlung, and coherent Bremsstrahlung (from crystalline targets) [HN04]. In the following, the mechanisms mentioned above are explained in detail.

## Electron-nucleus Bremsstrahlung

Electron-nucleus Bremsstrahlungs mechanism refers to the process in which the Coulomb field of the nuclear charge acts as the main force on the incident electron. In the case of a not too highly energetic incident electron (consider it as  $E_0$ ), the nucleus' recoil energy is not considered because of its large mass (in comparison with the incident electron). On this basis [HN04]:

$$E_0 = E_e + h\nu, \quad (1.8)$$

where  $E_e$  is the electron energy after collision and  $h\nu$  is the energy of the emitted photon, which can be increased up to the kinetic energy of the incident electron. This happens when all of the incident electron's kinetic energy is carried away by the emitted Bremsstrahlung ( $h\nu_{max}$ ) [HN04, P09, BS70]. A schematic view of the electron-nucleus Bremsstrahlungs process is shown in Fig. 1.15. In addition, the relative number of produced Bremsstrahlung per energy interval versus the photon energy  $h\nu$  is presented in Fig. 1.16. As is observable, the emitted photon energy has a maximum value ( $h\nu_{max}$ ), which corresponds to the cutoff wavelength for Bremsstrahlung.

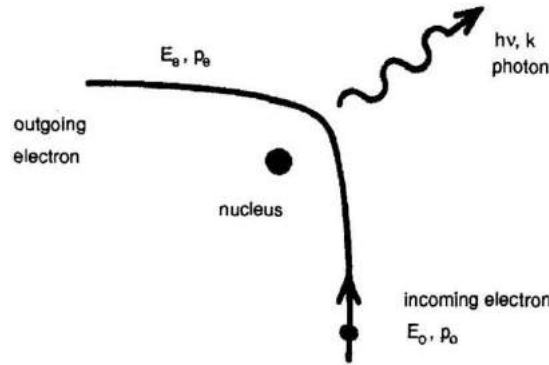


**Fig. 1.15:** A schematic representation of the electron-nucleus Bremsstrahlungs process, where  $k$  is the momentum of the emitted photon. Moreover,  $p_0$  and  $p_e$  refer to the momentum of the incoming and outgoing electron, respectively. The initial momentum of the incoming electron,  $p_0$ , is shared between the outgoing electron,  $p_e$ , the emitted photon,  $k$ , and the nucleus,  $q$ , as:  $p_0 = p_e + k + q$  [HN04].

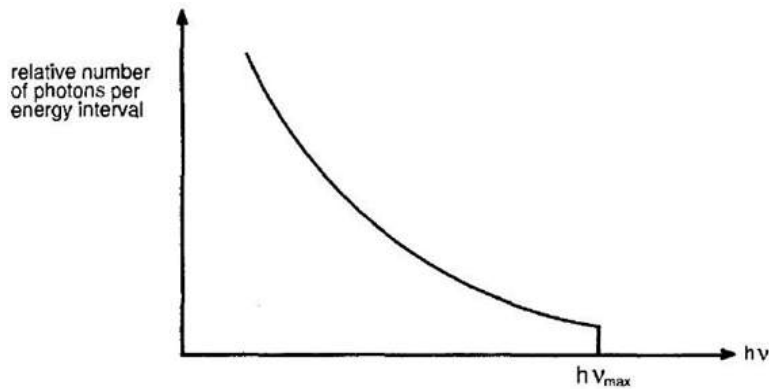


**Fig. 1.16:** A schematic representation of the produced relative number of Bremsstrahlung per energy interval versus the photon energy  $h\nu$  in the electron-nucleus Bremsstrahlungs process [HN04]

As discussed before, in the electron-nucleus Bremsstrahlungs process, the atomic electrons as a static charge distribution can screen the Coulomb field of the nucleus, and cause reduction of the Bremsstrahlungs cross-section and, therefore, a reduction of the photon emission. This process, known as the Screening Effect, is more effective in the Bremsstrahlungs production in the soft-photon end region of the energy spectrum; however, it contributes little to the hard-photon region of the energy spectrum [HN04].

## Electron-electron Bremsstrahlung

Electron-electron Bremsstrahlung refers to the process in which the Coulomb field of the electron charge acts as the main force on the incident electron. In contrast to electron-nucleus Bremsstrahlung, in electron-electron Bremsstrahlung, where the two colliding particles possess unity charges, Coulomb effects are not important, particularly when the target material is of low-Z [HN04].

To compare the electron-nucleus Bremsstrahlung and electron-electron Bremsstrahlung, it is worth pointing out that the former is a function of  $Z$  (i.e., atomic number); however, the latter is a function of  $Z^2$ . The difference between the two aforementioned processes can also be considered in the case of energy ranges. More precisely, at relativistic energies of the incident electron, the cross-section of the electron-electron Bremsstrahlung is comparable with the cross-section of the electron-nucleus Bremsstrahlung. However, in the nonrelativistic energy range, the cross-section of the electron-electron Bremsstrahlung reduces rapidly compared to the cross-section of the electron-nucleus Bremsstrahlung [HN04, H06]. On this basis, the radiative, electron-electron collision (i.e., electron-electron Bremsstrahlungs process) is usually ignored in the low to moderate electron energy ranges. A qualitative comparison of electron-electron and electron-nucleus Bremsstrahlungs processes in different energy ranges is presented in Fig.1.17.

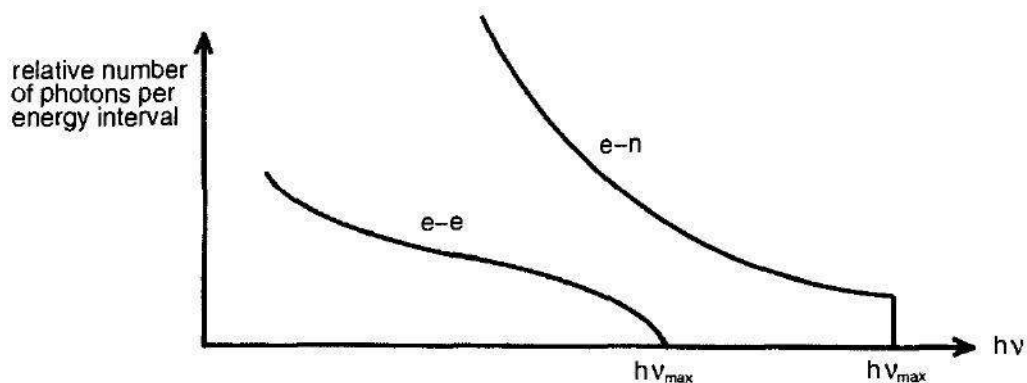


**Fig. 1.17:** A schematic representation of a qualitative comparison of electron-electron and electron-nucleus Bremsstrahlungs processes in different energy ranges. The recoil electron energy in the electron-electron Bremsstrahlung is appreciable in contrast to the energy recoil of the nucleus in the electron-nucleus Bremsstrahlung; therefore, the maximum photon energy for electron-nucleus Bremsstrahlung is always higher than for electron-electron Bremsstrahlung. Moreover, in the electron-electron Bremsstrahlung, the maximum photon energy is dependent on the photon emission angle [HN04].

As shown in Fig. 1.17, the maximum photon energy is higher in electron-nucleus Bremsstrahlung than in electron-electron Bremsstrahlung. This is due to the fact that the



recoil electron can have considerably higher energy in the former process compared to the other one. The contribution of the electron-electron Bremsstrahlung compared to the entire Bremsstrahlung in the photon emission spectrum is very low at nonrelativistic energies. Even for relativistic energies, the ratio is not significant, particularly for high-Z materials [H06].

## Two/multiple photon Bremsstrahlung

Two-photon Bremsstrahlung refers to a process in which two Bremsstrahlung is created simultaneously in a single collision of the incident electron with an atom. Multiple-photon Bremsstrahlung is also possible; however, the probability decreases as the number of photon Bremsstrahlung increases [G77, H76, MMD59, KS06, KM90, KS02]. It was shown that the probability of multiple Bremsstrahlungs production (consider  $n$  as the photons number) will always be smaller by a factor of  $\alpha^{n-1}$  (where  $\alpha = e^2/2hc$ ) than the single Bremsstrahlungs emission [MMD59]. As an illustration, in the case of the two-photon Bremsstrahlungs production, the probability of emission in comparison with the one-photon case is about  $\alpha = 1/137$  times less, resulting in a contribution completely buried by the dominant single Bremsstrahlungs emission background [MDV87].

## Electron-positron Bremsstrahlung

Electron-positron Bremsstrahlung refers to a process in which a Bremsstrahlung is created in the collision of an incident electron with a positron. Fig. 1.18 shows the spectrum of electron-positron Bremsstrahlung for an incident beam energy of 100 MeV [H03]. As discussed before (in section 1.1.1.4), the number of positrons can be considerable in the target; however, it is not comparable to the enormous number of electrons in the converter target material [HN04, H06]. Besides, the interaction probability between an incident electron and a positron leads to Bremsstrahlungs emission, in high quantity, compared to the ordinary Bremsstrahlungs process, in particular, in the GDR region, it seems to be relatively very low.

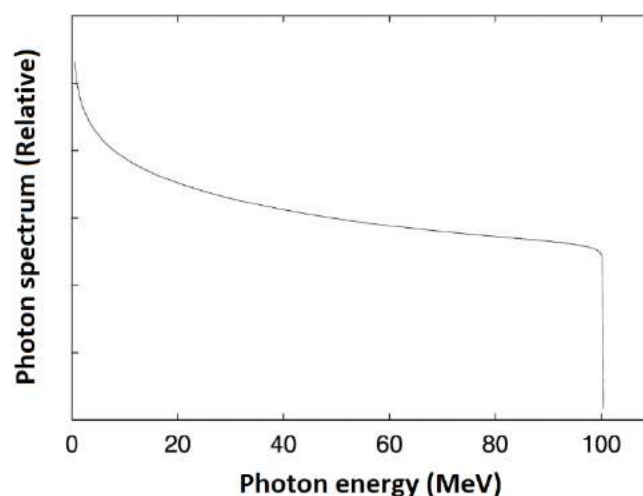


**Fig. 1.18:** Photon spectrum in electron-positron Bremsstrahlung [H03]

## Polarization Bremsstrahlung

Polarization Bremsstrahlung is a process in which the Bremsstrahlung is emitted due to a polarization of the structured atomic target in the collision of the incident electron with an atom. More precisely, the atom's internal structure is polarized or deformed during the process and causes an induced electric dipole moment in the atom. The result of this process is the creation of a continuous Bremsstrahlungs source in a time-dependent approach [HN04]. Fig. 1.19 shows the schematic representation of the difference of (a) the ordinary and (b) the polarization Bremsstrahlungs process. In contrast to the ordinary Bremsstrahlungs process, in the polarization Bremsstrahlungs process, photon emission is considered due to the virtual excitation of the target electrons. It is worth pointing out that the intensity of photons in polarization Bremsstrahlung depends on the intensity of the projectile's particle electric field and not the mass of the projectile particle. As an illustration, the polarization Bremsstrahlungs intensity of the collision of an electron and a proton (with the same energy) with an atom results in the same amount (for a wide range of incident projectile energies); however, in the case of ordinary Bremsstrahlung, the intensity of photon emission of the electron is  $(m_p/m_e)^2 \sim 10^6$  times more than for the proton [KS14].

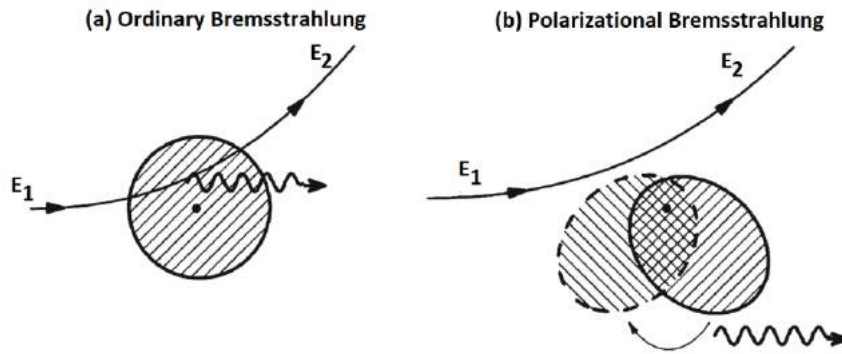


**Fig. 1.19:** A schematic representation of a) the ordinary and b) the polarization Bremsstrahlungs process. In contrast to the ordinary Bremsstrahlungs process, in the polarization Bremsstrahlungs process, the photon emission is considered due to the virtual excitation of the target electrons by the projectile. Virtual excitation of the electrons translates to target polarization [KS14].

## Coherent and incoherent Bremsstrahlung

Coherent Bremsstrahlung refers to a process in which the recoil is taken up by the whole lattice when the incident electron collides with a monocrystal. In contrast, incoherent Bremsstrahlung is the sum of all contributions from atoms acting independently. Fig. 1.20 shows a schematic representation of constructive interference of coherent Bremsstrahlung in the periodic structure of the monocrystalline target. As is shown in Fig. 1.20, the electron moves on a flat periodic trajectory, where  $E_1(\mathbf{k})$  refers to the radiation field on the first period, and  $\mathbf{k}$  is a wave vector. Additionally, one can obtain the time duration of the wave front passing from two consecutive identical periodic positions as  $\Delta t_K = d \cos \theta / c$  [P11]. Both coherent and incoherent Bremsstrahlungs mechanisms contribute to the Bremsstrahlungs emission from the monocrystalline target. However, coherent Bremsstrahlung may dominate

at a specified angle if the appropriate orientation of the monocrystalline target is considered [HN04].

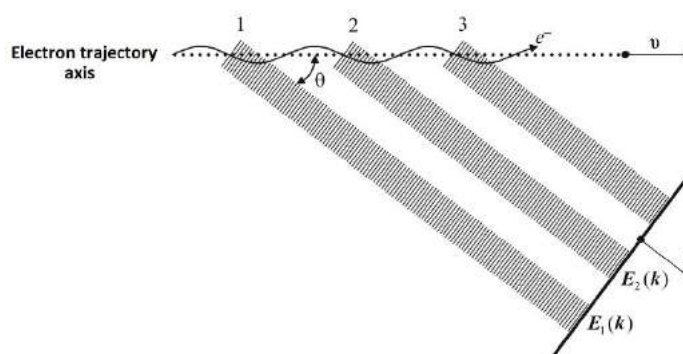


**Fig. 1.20:** A schematic representation of constructive interference of coherent Bremsstrahlung in the periodic structure, where  $\mathbf{k}$  is a wave vector. Moreover,  $\mathbf{E}_1(\mathbf{k})$  and  $\mathbf{E}_2(\mathbf{k})$  refer to the radiation field on the first and second period, respectively [P11].

### 1.1.1.6 Electronuclear reaction

Electronuclear reaction ( $e^-$ ,  $e^-'x$ ) refers to a reaction in which the incident electrons interact with the nuclei directly, without producing any Bremsstrahlung through the photonuclear reaction (see section 1.2.6). According to this reaction, the electrons interact directly with weakly-bound nucleons and knock them out of the nucleus [DK14]. The electronuclear reaction method usually refers to the one-stage approach for radionuclide production in comparison to the photonuclear production method, which refers to the two-stage radionuclide production method. The number of stages comes from the number of processes in which radionuclides can be produced via electron accelerators [TFS20]. In the photonuclear production method, the accelerated electrons hit the electron converter (such as tungsten or tantalum) as the first stage, and then the produced Bremsstrahlung interacts with the production targets, as the second stage. However, according to the electronuclear production method, no converter target is required, and the production target is used alone to allow accelerated electrons to hit the target and produce the desired radionuclide/s. As an illustration,  $^{99}\text{Mo}$  can be produced using  $^{100}\text{Mo}(\gamma, n)^{99}\text{Mo}$ , and  $^{100}\text{Mo}(e^-, e^-'n)^{99}\text{Mo}$  reactions via photonuclear and electronuclear reactions, respectively [TFS20]. For facilitating comparison, Table 1.1 gives some values for the  $^{99}\text{Mo}$  production cross-section via the photonuclear and electronuclear reactions. As is observable, the cross-section for the photonuclear production is much higher than that of electronuclear production at the same energy.

**Table 1.1**Cross-sections for photonuclear and electronuclear  $^{99}\text{Mo}$  production on natural  $\text{Mo}$  [TFS20]

Beam energy, MeV	$\sigma_{\text{photonuclear}}, \text{mb}$	$\sigma_{\text{electronuclear}}, \text{mb}$
150	6.5	0.16
200	6.3	0.17
225	6.4	0.21

An excitation function for  $^{63}\text{Cu}$  is presented in Fig. 1.21. As can be seen, the photonuclear cross-section shows a typical resonance behavior (which is discussed in section 1.2.6), in the energy range of 12-20 MeV and then drops sharply for higher energies. However, the electronuclear cross-section shows a monotonical increase as the incident electron energy increases.

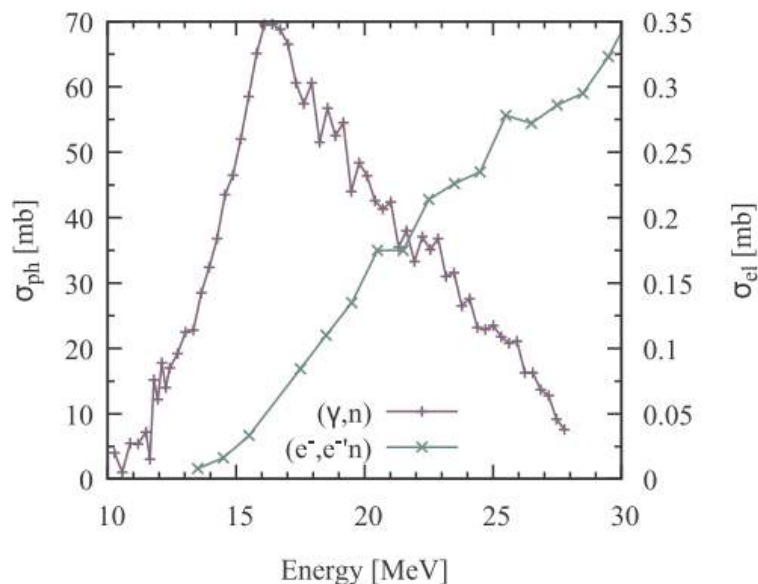


**Fig. 1.21:** The experimental photonuclear  $(\gamma, n)$  and electronuclear  $(e^-, e^{-'}n)$  cross-sections for  $^{63}\text{Cu}$  [TFS20]

In order to compare the production yield estimation, based on the photonuclear and electronuclear methods, Tsechanski et al. [TFS20] showed that the yields for  $^{99}\text{Mo}$  production via the photonuclear method are evidently much higher compared to the electronuclear method (see Fig.1.22). In general, the ratio of total production yield to the production yield via the photonuclear reaction can be given as:

$$\frac{Y_{\text{total}}}{Y_{\text{bremsstrahlung}}} = \left(1 + \frac{0.04}{T}\right), \quad (1.9)$$

where  $T$  is the target thickness in Radiation Lengths (see section 1.2.4). Accordingly, in thin targets, the production yield due to electronuclear reactions is considerably higher than for

thick targets [TFS20, MKN96]. In Fig.1.23, the ratio of the electronuclear to photonuclear  $^{99}\text{Mo}$  production yield for (a) 20 mm and (b) 1mm thick  $^{100}\text{Mo}$  target is presented. As is observable, for the thin  $^{100}\text{Mo}$  target, the electronuclear production yield is much higher than that of the thick target. Additionally, as can be seen, in the thin  $^{100}\text{Mo}$  target, the production yield due to the electronuclear is higher than that of the photonuclear reaction. This strong variation in the ratio of the production yield is due to the fact that the Bremsstrahlungs production yield\* (see section 2.3) and the consequent increase of the photonuclear reactions' intensity increases as the converter target (which here is the production target itself) increases [DK14, TFS20]. One should note that, although the cross-sections for the electronuclear reactions are significantly smaller in comparison with those of the photonuclear reaction, electrons are the primary particles in the electronuclear reaction while the Bremsstrahlung being the secondary particles for the photonuclear reactions. On this basis, even though cross-sections for the electronuclear reaction are lower than those of the photonuclear reaction, the intensity of the primary electrons at the entrance to the converter/target is remarkably higher than the generated secondary Bremsstrahlungs photon. More importantly, all electrons impinging on the production target are monoenergetic; however, the generated photon Bremsstrahlungs spectrum is continuous, ranging from zero to the kinetic energy of the incident electrons, with a considerable fraction of the Bremsstrahlung having energy below the photonuclear reaction threshold [TFS20, MKN96]. According to the above discussion, although the production yield due to electronuclear reaction is considerable in thin targets, the total production yield in such thin targets is not appropriate for large-scale production purposes. This makes the contribution of this reaction in total production yield for thick targets less important. More importantly, the direct interaction of the incident electrons with the production targets (which also serves as the converter in the electronuclear reaction) transfers a huge amount of heat to the target, which evidently is not desirable. This situation is getting worse when a high-energy and high-power electron beam is employed [TFS20].

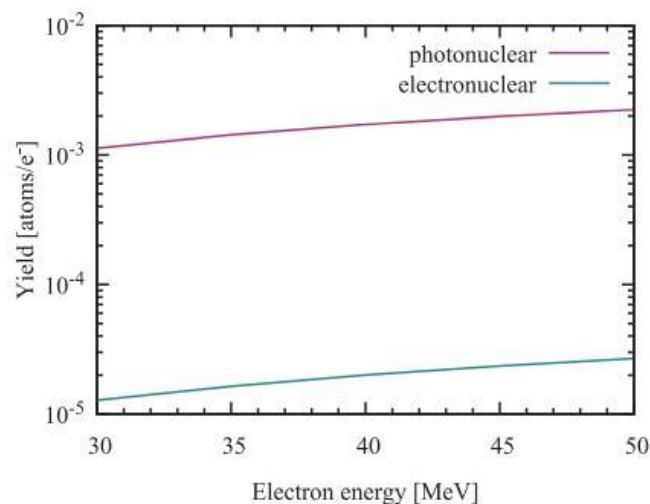


**Fig.1.22:**  $^{99}\text{Mo}$  production yield as a function of electron beam energy through photonuclear and electronuclear reactions for a 20 mm  $^{100}\text{Mo}$  cylindrical target (about 9.518 g).  $^{100}\text{Mo}$  is used in this work as the converter/target for  $^{99}\text{Mo}$  production [TFS20].

\* The Bremsstrahlung production yield is the ratio of the number of generated Bremsstrahlung photons per incident electron [SSSC10].

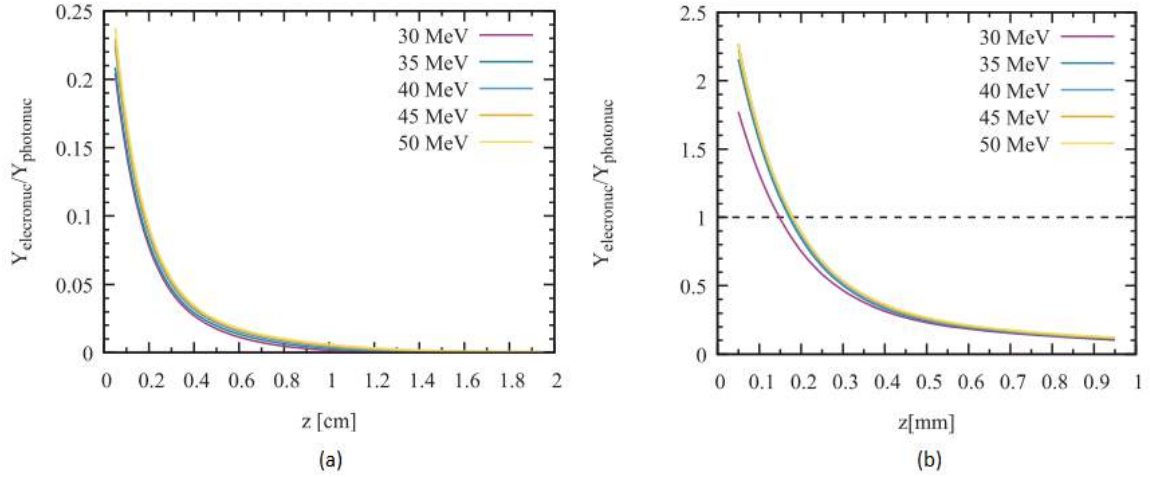


**Fig.1.23:** The ratio of electronuclear to photonuclear  $^{99}\text{Mo}$  production yield for (a) 20 mm and (b) 1 mm thick  $^{100}\text{Mo}$  target [TFS20].

### 1.1.2 Electron energy loss

As shown earlier in this chapter, there are a number of different interactions based on electronic and nuclear mechanisms through which an electron can interact with the medium [PT73, DK14]. As can reasonably be argued, the net result of all of these interactions is a reduction in incident particle energy as it passes through a medium. The rate of energy loss of an electron (or in general, a charged particle) as it passes through a medium depends on the electron energy and nature of the target. This quantity is referred to as the *stopping power* of the material. The stopping power represents the rate of energy loss of the incident electron per unit length of the target material that the electron traverses. The total stopping power is the sum of the stopping powers as a result of atomic collision and radiation emission (i.e., Bremsstrahlung emission due to interaction with the electric field of a nucleus) [DK14].

$$S_{Total} = -\frac{dE}{dx} = S_{Collision} + S_{Radiation} , \quad (1.10)$$

where the negative sign implies that the electron loses energy as it passes through the medium. For electrons, the term of the nuclear component can be ignored for most practical applications since it is only a small fraction of the total stopping power\*. Therefore, the total stopping power can be approximated as [DK14]:

$$-\frac{dE}{dx} \approx S_{Collision} . \quad (1.11)$$

Generally speaking,  $S_{collision}$  increases as the electron velocity is decreased [K10]. The energy-loss mechanisms for electrons in Pb as a function of energy are presented in Fig. 1.24. As can be seen at low energies which correspond to energies less than 1 MeV, the energy loss due to the ionization mechanism (i.e., collisions) is more important than that of the radiation [PT73].

---

\* In the case of alpha particles, the term of the nuclear component can be ignored if its energy is not high enough to penetrate so deep into the atom where the short range nuclear forces of nucleons become appreciable [A07].

The theoretical stopping power formula for collision and radiation can be found in [A07, PT73, K10].

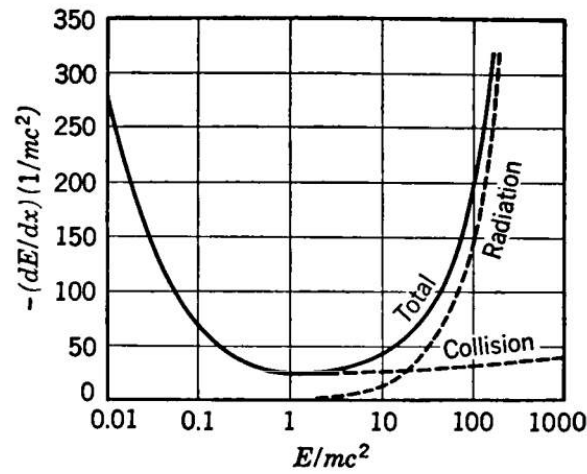


**Fig.1.24:** Energy-loss (stopping power) for electrons in Pb [PT73]

As can be seen in Fig. 1.24, there is a critical kinetic energy where the two mechanisms of the energy-loss are equal. This critical kinetic energy for a given absorber material with atomic number  $Z$  can be obtained as [P09]

$$(E_K)_{critical} \approx \frac{800 \text{ MeV}}{Z}. \quad (1.12)$$

The ratio of collision to radiation stopping power for electrons is given as [P09]:

$$\frac{S_{Collision}}{S_{Radiation}} = \frac{(E_K)_{critical}}{E_K}, \quad (1.13)$$

where  $E_K$  is the kinetic energy of the electron.

### 1.1.3 Linear energy transfer

Linear energy transfer (LET) is the mean amount of energy, which a given ionizing radiation imparts to a medium per unit path length and is used mostly in radiation protection and radiobiology to determine the quality of an ionizing radiation beam [P16, PT73]. The ionization density produced by ionizing radiation in an absorbing medium (such as tissue) relies on the LET of the ionizing radiation beam. Usually, ionization beams are categorized into low LET (which is also referred to as sparsely ionizing), and high LET (which is also referred to as densely ionizing) beams [P16, P09].

In contrast to stopping power (see section 1.1.2) that focuses on the energy loss by an energetic electron passing through a medium, the LET focuses on the linear energy absorption rate by the medium as the electron traverses the absorber [P16, P09]. The LET is given in units of keV/ $\mu\text{m}$ . In literature, 10 keV/ $\mu\text{m}$  separates the low LET radiation from the high LET radiation. In Table 1.2, low LET and high LET ionization radiation beams with different energies are presented [P16].

**Table 1.2**

LET values for various low and high LET radiation beams [P16]

Low LET radiation	LET ( $\text{keV}/\mu\text{m}$ )	High LET	LET ( $\text{keV}/\mu\text{m}$ )
Photons: 250 kVp	2	Electrons: 1 MeV	12.3
Photons: Co-60	0.3	Neutrons: 14 MeV	12
Photons: 3 MeV	0.3	Protons: 2 MeV	17
Electron: 10 keV	2.3	Carbon Ions: 100 MeV	160
Electrons: 1 MeV	0.25	Heavy Ions	100-2000

### 1.1.4 Electron energy straggling

Since the details of the microscopic interactions for electrons vary somewhat randomly, their energy-loss is a stochastic or statistical process. Accordingly, a spread in energies always occurs after a monoenergetic electron beam passes through an absorber material [K10]. To measure this energy straggling, the width of the electron energy distribution, which varies with the distance along the electron track, is employed. A schematic representation of the electron energy straggling is presented in Fig. 1.25a. As can be seen, the energy distribution of an initially monoenergetic electron beam at various points along its range is illustrated. From the beginning to near the end of the electron range, the energy distribution becomes wider and more skewed, with penetration distance denoting the increasing importance of electron energy straggling. Near the end of the electron range (see section 1.1), the electron energy distribution narrows again because the mean electron energy has been considerably reduced [K10, S55]. In Fig.1.25, experimental measurements of the energy distribution of an electron beam through graphite foils with (a) 1.33 mm, (b) 0.895 mm, and (c) 0.475 mm are displayed [S55]. As is observable, the experimental measurements clearly show the electron energy straggling when passing through a medium.

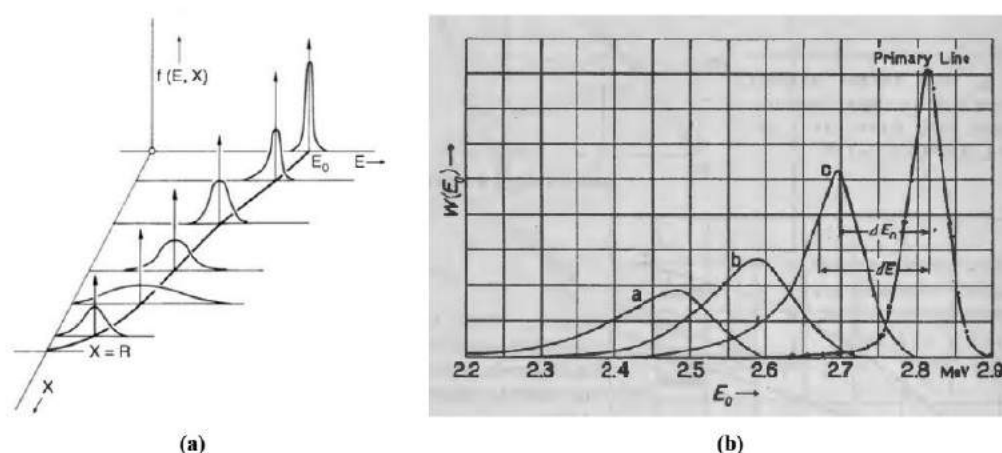


**Fig.1.25:** a) Schematic representation of electron energy straggling when electron beam passes through a medium (where  $R$  is the electron range,  $E_0$  is the initial electron beam energy, and  $X$  is the penetration distance in the medium). b) An illustration of the experimental measurements of the energy distribution of an electron beam that was performed through carbon foils with (a) 1.33 mm (b) 0.895 mm, and (c) 0.475 mm thickness [K10, S55].



## 1.2 Photons passing through a medium

Photons can interact with matter in different ways and mechanisms. The interaction mechanisms between the incident photon and matter have different incident photon energy thresholds and regions of cross-section for different materials. This is because not all of the incident photons go to the same type of interaction with matter. In fact, one should look at the process as a statistical process, in which each photon can interact with matter in different ways [A07, K10].

Photons as indirectly ionizing radiation deposit their energy in matter through a two-step process. In the first step, the energy of a photon is transferred to an energetic light (in weight) charged particle. While, in the second step, the transferred energy is deposited in matter through the interaction of the energetic charged particle with the medium [CJ09, P16, J17]. Note that the transferred energy of the energetic charged particle may also be radiated from it while passing through the medium. Photons may experience different interactions with the medium's atoms (which depends on the photon's incident energy, and the density and also the atomic number of the absorber material). These interactions of photons with atoms involve either the nuclei or the orbital electrons of the atoms. The interaction of the photon with atomic nuclei may be either a direct photon-nucleus interaction (*photonuclear*) or an interaction between the photon and the nucleus's static field (*pair production*). The interaction of the photon with electrons may be either an interaction with a loosely bound electron\* (*Compton effect*, *Thomson scattering*, *triple production*) or a tightly bound electron† (*Rayleigh scattering*, *photoelectric effect*). As mentioned earlier, these interactions have different regions of high cross-sections for different materials. Fig.1.26 shows the photon cross-section for (a) carbon and (b) lead as a function of energy. As is observable, regions of high cross-sections for different materials vary somewhat [S07, J17, NUE12, MG05].

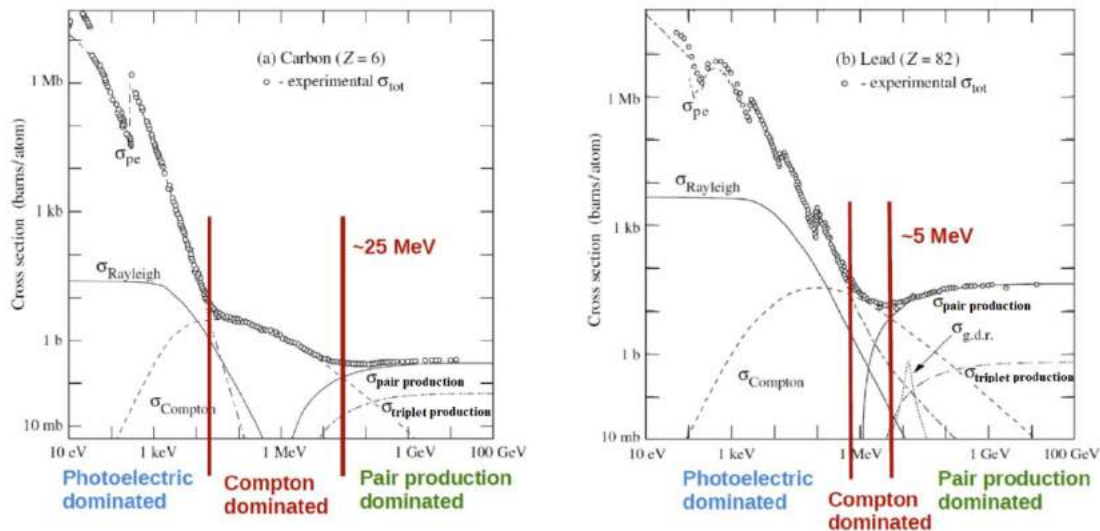


**Fig.1.26:** Photon cross-section as a function of energy for (a) carbon and (b) lead. In this figure,  $\sigma_{g.d.r.}$  refers to the giant dipole resonance, which is discussed in section 1.2.6 [L17]

\* A loosely bound electron is an atomic electron whose binding energy ( $E_B$ ) is considerably smaller than the incident photon energy ( $h\nu$ ) [K10, P09].

† A tightly bound electron is an atomic electron whose binding energy ( $E_B$ ) is larger than the incident photon energy ( $h\nu$ ) [K10, P09].

### 1.2.1 Photon beam attenuation

The attenuation of photons by an absorber material is qualitatively different from that of electrons. This is due to the fact that electrons have definite ranges in matter; therefore, they can be stopped completely [NUE12, P09]. However, photons can only be reduced in intensity as the absorber thickness increases; in fact, they can not be absorbed completely. In the case of conditions of good geometry, which is a well-collimated, narrow beam of radiation, it has been revealed that at any point in an absorber material, the reduction in the intensity of a photon beam per unit length (of the absorber material) relies on the intensity of the photon beam at that point, that is [J17, NUE12]

$$\frac{dI}{dx} \propto -I$$
$$\Rightarrow \frac{dI}{dx} = -\mu_t I, \quad (1.14)$$

where  $dI$  is the change in photon intensity as it passes through the absorber thickness of  $dx$ .  $\mu_t$  is the total linear attenuation coefficient, which depends on the photon energy and the absorber material. By integrating of Eq.1.14, one can obtain [P09, J17, S07]

$$I = I_0 e^{-\mu_t x}, \quad (1.15)$$

where  $I_0$  is the intensity of the photon beam before impinging to the absorber, and  $I$  is the intensity of photons at point (or depth)  $x$ . Fig. 1.27 shows the gamma-ray (monoenergetic) attenuation data for aluminum and lead, which is plotted in a semilog arithmic graph and results in a straight line. In the case of a heterochromatic photon beam (such as Bremsstrahlungs photons), a curve results, as represented by the dotted-line in Fig.1.27 [J17, P09] (as will be discussed later in this chapter).

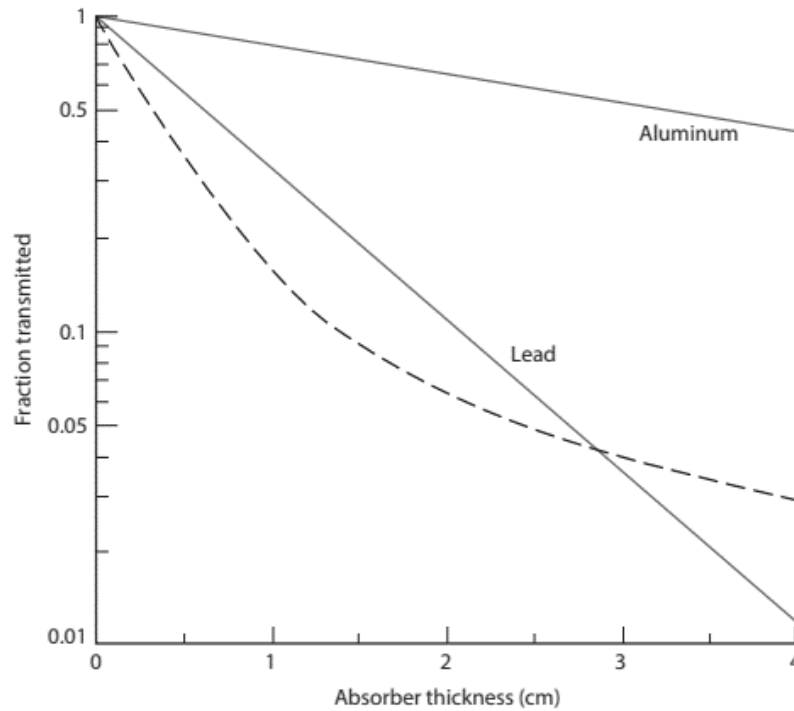


**Fig.1.27:** Attenuation of 0.662-MeV monoenergetic photons (solid lines) and of a heterochromatic photon beam (dotted line) [J17].

Under conditions of poor geometry, which is for a broad photon beam or a very thick absorber, Eq.1.15, underestimates the photon intensity reaching the detector (i.e.,  $I$ ). This stems from the fact that according to the good geometry conditions, it is assumed that every photon that interacts with the absorber is removed from the photon beam and thus is not able to reach the detector (see Fig. 1.28) [J17, JC53, R14, S07]. However, in the case of poor geometry, a considerable number of scattered photons from the broad beam can be scattered but are still able to reach the detector, or the photons that had been scattered by the thick absorber may scatter back after a second or multiple collisions and thus reach the detector [A07, J17]. In such cases, a *build up factor*  $B$  is introduced into Eq.1.15, which gives the final number of the photon intensity  $I$  as:

$$I = B \cdot I_0 e^{-\mu_t x}, \quad (1.16)$$

where  $B$  is always greater than unity and can be defined as [A07, J17, JC53]:

$$B = \frac{\text{primary+scattered radiation}}{\text{primary radiation}}. \quad (1.17)$$

The attenuation of a Bremsstrahlungs beam is more complicated to calculate compared to a monoenergetic photon beam due to its nonlinear energy-dependent intensity profile (see Fig.1.29).

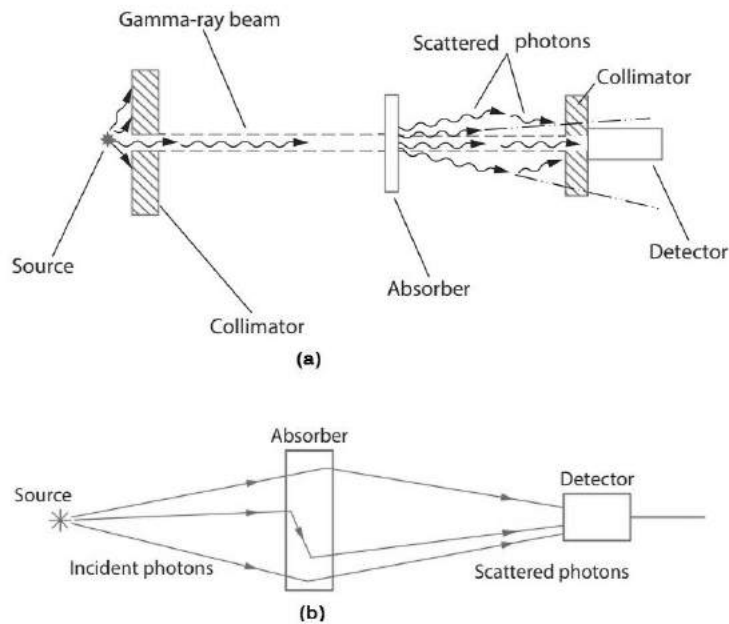


**Fig.1.28:** Measurements of photon beam attenuation under conditions of (a) a good geometry and (b) a poor geometry. In the case of a good geometry, ideally, it is assumed that the photon beam is well collimated\*, and the photon source is located as far as possible from the detector. Additionally, it is assumed that the absorber, which is located between the photon source and the detector is thin enough to consider the probability of a second scattering of the photon to be negligible. In the case of poor geometry, as is observable, the probability of a second or multiple scattering of the incident photon is quite considerable. Thus, it can contribute to the registered detector signal [J17].

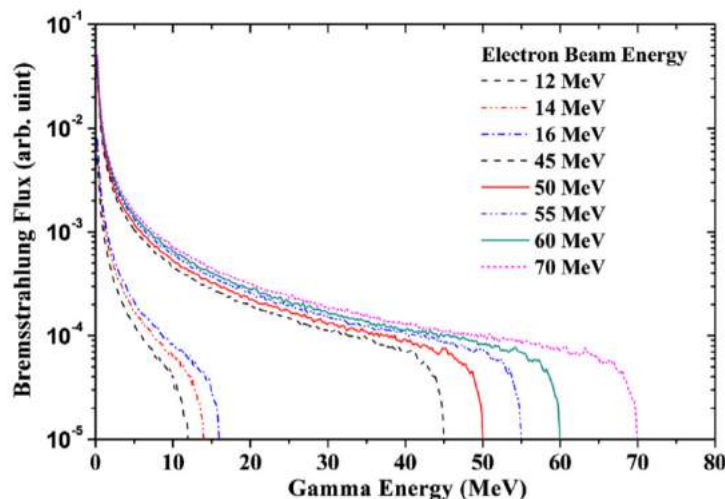


**Fig.1.29:** Spectrum of Bremsstrahlung for different endpoint energies where the converter target is tungsten [N13]

\* A collimator allows measuring the photon intensity from a well-defined or a small portion of the photon source and, therefore, reduces (or even completely excludes) the number of scattered photons reaching the photon detector [D88].

In principle, one possible way for calculating the attenuation of a Bremsstrahlung is to divide the Bremsstrahlung spectrum into appropriate photon energy intervals and then determine the corresponding mass (or) attenuation coefficient for each one of the intervals. Afterward, by considering the good geometry and if it is required to apply the corresponding build-up factor, one can determine the Bremsstrahlung properly. Another possible way to obtain the attenuation of Bremsstrahlung is to substitute the whole Bremsstrahlung energy spectrum with a single value of “effective photon energy”. As a rule of thumb, the effective photon energy is about one-third of the peak photon energy. For instance, it has been calculated that for a 20 MeV electron beam, the accurate, effective photon energy is 7 MeV [PT73].

### 1.2.2 Total and mass attenuation coefficients

The total attenuation coefficient is the fractional decrease or attenuation of the incident gamma-ray beam intensity per unit thickness of absorber material [J17, TL15, MG05]. In fact, the total linear attenuation coefficient  $\mu_t$  ascertains how quickly or slowly a photon beam is attenuated while passing through an absorber material. As mentioned earlier,  $\mu_t$  depends on the photon energy in addition to the absorber material features, including atomic number and density. Its dependence on the physical state of the material makes its use undesirable. Accordingly, instead of using the total linear attenuation coefficient, the mass attenuation coefficient  $\mu_m$  is employed that is defined by [TL15, LR04]

$$\mu_m = \frac{\mu_t}{\rho}, \quad (1.18)$$

where  $\rho$  is the material density [A07]. In the following, a brief description of the photon interactions with matter is presented. In the literature,  $\mu_t$  and  $\mu_m$  have units of  $\text{cm}^{-1}$  and  $\text{cm}^2/\text{g}$ , respectively [S07, J17].

The attenuation coefficient  $\mu_m$  determined by experimental measurements using the so-called narrow beam geometry method, which implies a narrowly collimated monoenergetic photon source and a narrowly collimated photon detector (see Fig.1.30).

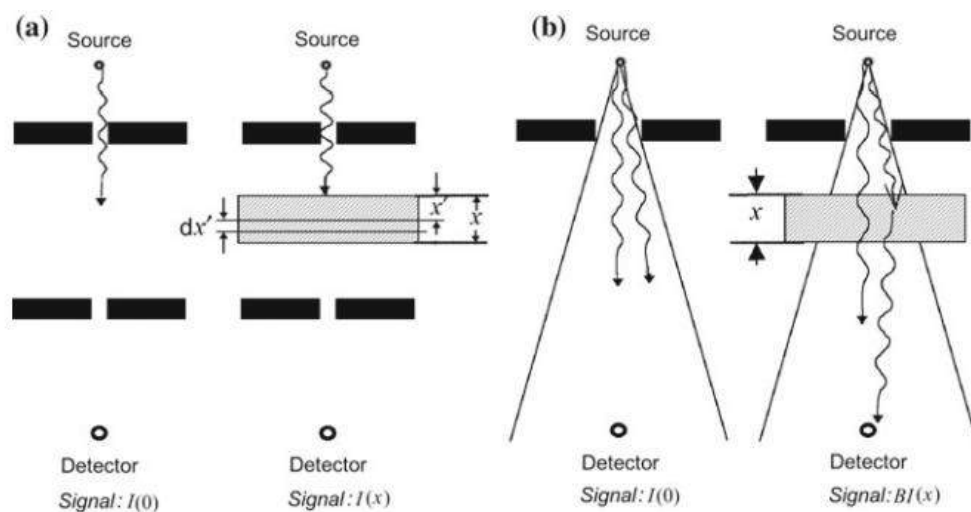


**Fig.1.30:** Schematic representation of the experimental attenuation coefficient measurement method for a) a narrow photon beam and b) broad photon beam. As can be

seen, a slab of absorber with a thickness of  $x$  is placed between the detector and the photon source. The absorber reduces the detector signal (photon intensity that is proportional to the number of photons reaching the detector) from  $I_0$  measured without the absorber to  $I(x)$  measured with absorber thickness  $x$  in the photon beam. Considering a narrow beam is, in fact to exclude any scattered photon or any probably generated secondary radiation into the photon beam [P16].

Since the total linear attenuation coefficient  $\mu_t$  determines the interaction probability of a given photon beam in an absorber material, and the total atomic photon cross-section  ${}_a\sigma_t$  also gives the interaction probabilities, these two quantities must be related. It is found that  $\mu_t$ , in terms of  ${}_a\sigma_t$ , can be written as [LR04, S14]:

$$\mu_t = \sigma_t N = \sigma_t \frac{\rho N_A}{A}, \quad (1.19)$$

where  $N$  (in units of  $atoms.cm^{-3}$ ) is the number of atoms per unit volume in the absorber material with atomic number  $A$  and weight density  $\rho$  (in units of  $g.cm^{-3}$ ). In Eq.1.19,  $N_A$  is Avogadro's number ( $6.0221409E+23$ ). It is also evident that if the units of  ${}_a\sigma_t$  are considered as  $cm^2.atom^{-1}$ , then the units of  $\mu_t$  are given as  $cm^{-1}$  [LR04, R14].

Considering Eqs.1.18 and 1.19, one can also formulate the total mass attenuation coefficient in terms of the total photon interaction cross-section as [R14, J17, S14]:

$$\mu_m = {}_a\sigma_t \frac{N_A}{A}. \quad (1.20)$$

Fig. 1.31 shows the mass attenuation coefficient as a function of energy for different elements [J17]. As is observable, it varies systematically with the atomic number of the absorber material in addition to the incident photon energy.

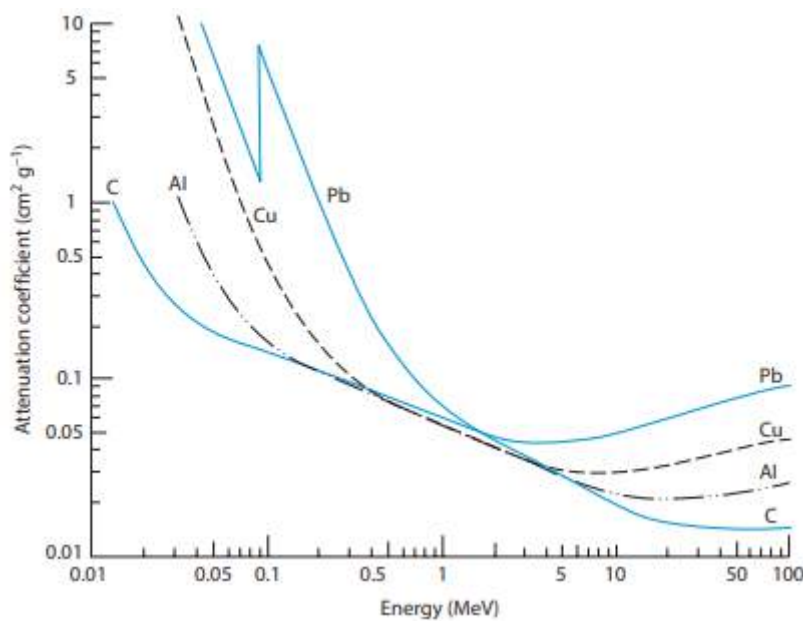


**Fig.1.31:** Mass attenuation coefficient as a function of energy for different elements [J17]

Since  $\mu_t$  and  $\mu_m$  can be obtained based on  ${}_a\sigma_t$ , it is of great importance to know how  ${}_a\sigma_t$  can be obtained. Considering the cross-section of any possible photon interaction mechanism, one obtains:

$${}_a\sigma_t = {}_a\sigma_{Th} + {}_a\sigma_R + {}_a\sigma_C + {}_a\sigma_{pp} + {}_a\sigma_{pe} + {}_a\sigma_{pn} + \dots, \quad (1.21)$$

where  ${}_a\sigma_{Th}$ ,  ${}_a\sigma_R$ ,  ${}_a\sigma_C$ ,  ${}_a\sigma_{pp}$ ,  ${}_a\sigma_{pe}$  and  ${}_a\sigma_{pn}$ , represent cross-sections of Thomson scattering, Rayleigh scattering, Compton scattering, pair production, photoelectric effect, and photonuclear reaction, respectively.

### 1.2.3 Mean free path

Mean free path ( $\lambda_m$ ) is the average distance between two successive interactions [TL15]. As the photon beam travels  $\lambda_m$ , its intensity reduced by  $1 - \frac{1}{e}$  corresponding to about 63% of the initial intensity. Considering  $I$  (see Eq.1.15), as the number of monoenergetic photons which travel a distance  $t$  without any interaction, and  $I_0$  as the number of initial monoenergetic photons, the probability of a photon to transverse a thickness  $t$  without any interaction is given as [TL15, P09, A07]:

$$\frac{\text{Number transmitted}}{\text{Number incident}} = \frac{I_0 e^{-\mu_t t}}{I_0} = e^{-\mu_t t}. \quad (1.22)$$

Regarding this probability, the average distance between two successive interactions is called the mean free path  $\lambda_m$  [TL15]:

$$\lambda_m = \frac{\int_0^\infty t e^{-\mu_t t} dt}{\int_0^\infty e^{-\mu_t t} dt} = \frac{1}{\mu_t}. \quad (1.23)$$

Considering  $\mu_m$ , the specific mean free path  $\lambda_p$  can be defined as [C07, P14]:

$$\lambda_p = \frac{1}{\mu_m} \quad (1.24)$$

### 1.2.4 Radiation length

Radiation length ( $X_0$ ) is a physical quantity employed to measure the absorber thickness traversed by high-energy photons or high-energy charged particles including electrons [R14]. Radiation length depends on the mass of charged particles and the atomic number  $Z$  of the absorbing material. Radiation length is defined as [C07, P14]:

- In the case of charged particles, as the average distance, a relativistic charged particle travels in an absorbing material while its energy, due to Bremsstrahlung losses\*, reduces to  $1/e$  ( $\sim 36.8\%$ ) of its initial value [P09, C07, A07].
- In the case of photons, as  $7/9$  fraction (78 %) of the mean free path for pair production mechanism by a high-energy photon traversing an absorbing material [P09, C07, A07].

---

\* Radiation energy loss, when expressed per  $g.cm^{-2}$ , is proportional to  $Z$ ; however, when expressed per atom, is proportional roughly to  $Z(Z + 1)$ . For more details, refer to [C07].

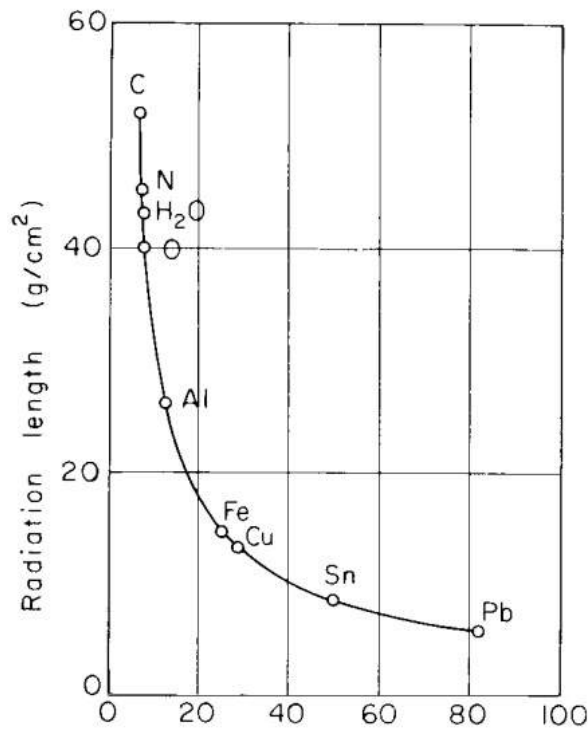


**Fig.1.32:** Radiation length as a function of atomic number Z [PT73]

### 1.2.5 Half value layer and tenth value layer thickness

The half-value layer (HVL) is the thickness of the absorber, which reduces the photon beam intensity by a factor of 2 to half of the initial level [P14, MG05, J17]. The HVL can be obtained using Eq. 1.15 as [J17]:

$$\begin{aligned}
 \frac{I}{I_0} &= \frac{1}{2} = e^{-\mu_t x} \\
 \Rightarrow \ln \frac{1}{2} &= -\mu_t x_{1/2} \\
 \Rightarrow x_{1/2} &= \frac{-0.693}{-\mu_t} = HVL.
 \end{aligned} \tag{1.25}$$

In the case of shielding thickness calculations, it is also convenient to obtain the number of HVLs required to reduce the initial photon beam intensity to a desired intensity level. In general, the number of HVLs ( $n$ ) in order to reduce the photon beam intensity from  $I$  to  $I_0$  can be obtained as [J17, P09, R14]:

$$\frac{I}{I_0} = \frac{1}{2^n} \tag{1.26}$$

The tenth value layer (TVL) is the thickness of the absorber, which can attenuate the radiation intensity to 10% of its initial level [J17].



### 1.2.6 Photon interactions

Photons may experience different interactions while passing through matter. These interactions may occur with atomic (loosely or tightly bound) electrons, the nucleus, or the atom as a whole. In the following, the most probable interactions are described [LR04, P09, P14].

#### Thomson (classical) scattering

Thomson scattering refers to an elastic scattering of low energy photons by loosely bound electrons (i.e., free electrons) when one can consider  $h\nu \ll m_e c^2$  (where  $m_e c^2$  is the electron rest mass energy). This interaction could be described by non-relativistic classical theory by *Joseph J. Thomson* whose assumed that the incident photon set each quasi-free electron of the medium atom into a forced resonant oscillation. More precisely, considering an electromagnetic wave in a classical sense, which passes near an electron can cause a momentarily acceleration of the electron by the electric field of the wave so that the electron radiates energy [JC53]. Thomson then employed classical theory to obtain the cross-section for re-emission of the electromagnetic radiation that can be considered as a result of the induced dipole oscillation of the electron [P09]. The electronic differential and total cross-sections can be written as [A07]:

$$\frac{d_e \sigma_{Th}}{d\Omega} = r_e^2 \sin^2 \theta \quad (1.27)$$

and

$$_e \sigma_{Th} = \frac{8\pi}{3} r_e^2 = 6.65 \times 10^{-29} m^2, \quad (1.28)$$

where  $\sigma_{th}$  is the total Thomson scattering cross-section,  $d_e \sigma_{Th}$  is the electronic differential Thomson scattering cross-section for re-emission of radiation into a solid angle  $d\Omega$ ,  $\theta$  is the photon scattering angle with respect to its initial direction of motion, and  $r_e$  is the electron's classical radius (2.82 fm [P09]). The result obtained in Eq.1.28, is noteworthy in that it contains not any energy-dependent terms. Additionally, no change in energy is predicted upon re-emission of the electromagnetic radiation. The electronic Thomson scattering cross-section has the same value ( $6.65 \times 10^{-29} m^2$ ) for all incident photon energies [P09].

The atomic cross-section for Thomson scattering  $_a \sigma_{Th}$  can be obtained in terms of the electronic Thomson scattering cross-section as:

$$_a \sigma_{Th} = Z _e \sigma_{Th}, \quad (1.29)$$

which shows a linear dependence of the atomic Thomson scattering cross-section upon  $Z$ . This result was experimentally discovered by *Charles Glover Barkla* who received the Nobel Prize in Physics in 1917\* [P09].

---

\* For his discovery of characteristic X-ray [P09].

Note that, as mentioned earlier, Thomson scattering as an elastic scattering predicts no change in energy upon re-emission of the electromagnetic radiation.

## Rayleigh scattering

Rayleigh scattering was first proposed by Lord Rayleigh in 1871 [A07]. Rayleigh scattering refers to the elastic scattering of a photon from an atom [P09]. As the incident photon through this process is scattered coherently from all the electrons, this process is also called coherent scattering (note that Compton scattering is incoherent scattering) [C07]. In fact, since all orbital electrons contribute to the scattering event and the photon is scattered by the constructive action of the entire tightly bound electrons of the whole atom, Rayleigh scattering refers to coherent scattering [P09].

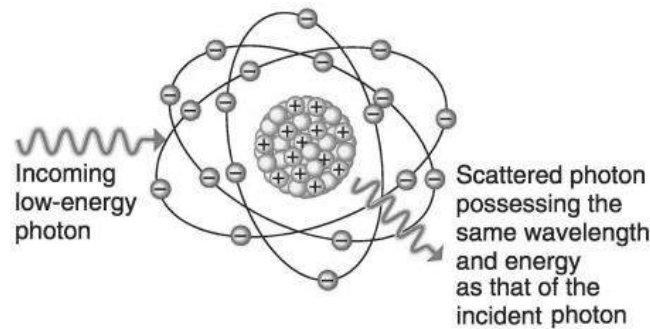


**Fig.1.33:** Schematic representation of Rayleigh scattering. In this process, the incident photon interacts with the atom and transfers its energy by causing all (or some) of the atomic electrons to vibrate momentarily and then radiating their attained energy in the form of electromagnetic waves. These electromagnetic waves nondestructively combine with one another, forming an electromagnetic wave, which represents the scattered photon. The scattered photon is the same as the incident photon except for the emission angle that is generally less than 20 degrees (in respect to the direction of the original photon) [S14]

Rayleigh scattering is applicable when the wavelength of the incident photon is much larger than the radius of the target atom [A07]. Through Rayleigh scattering, the target atom is neither excited nor ionized, and after the interaction, the bound electrons revert to their initial state [P09]. In fact, the atom as a whole absorbs the transferred momentum from the incident photon but its recoil energy is quite small, and the scattered photon (with scattering angle  $\theta$ ) possess essentially the same energy (and accordingly, the same wavelength) as the original incident photon. Note that the scattering angle of the scattered photon in Rayleigh scattering is relatively small (which depends inversely on the square of the photon energy and directly to the square of the absorber atomic number) since the recoil imparted to the atom causes no atomic excitation or ionization (see Figs.1.34 and 1.35) [P09]. The angular spread of Rayleigh scattering can be represented as [P09]:

$$\theta_R = 2\arcsin\left(\frac{0.026Z^{1/3}}{\varepsilon}\right), \quad (1.30)$$

where  $\theta_R$  refers to the characteristic angle for Rayleigh scattering, which represents the opening half-angle of a cone that includes 75 % of the entire Rayleigh-scattered photons. Additionally, In Eq.1.30,  $\varepsilon$  is the reduced photon energy and can be obtained as:  $\varepsilon = h\nu/m_0c^2$ . The Rayleigh characteristic angle  $\theta_R$  increases by increasing the atomic number  $Z$  for the same photon energy  $h\nu$  and decreases by increasing  $h\nu$  for the same  $Z$  (see Table 1.3) [P09].

It should be noted that for high photon energies when  $h\nu > 1 \text{ MeV}$ , Rayleigh scattering is confined to small angles for all absorbers. However, for low photon energies, in particular, for high  $Z$  materials, the angular distribution of Rayleigh-scattered photons is much broader (see Fig. 1.34) [P09].

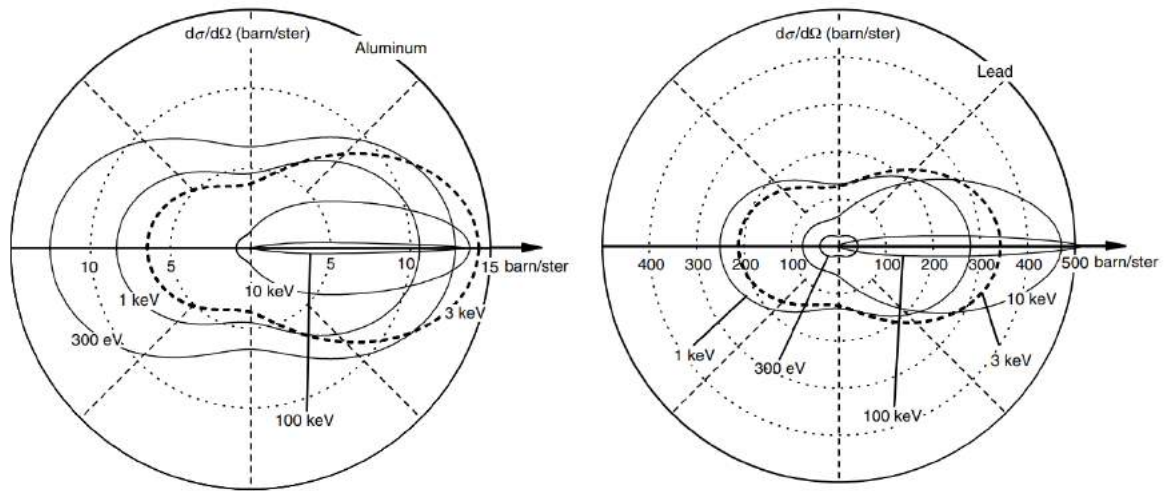


**Fig.1.34:** A polar graph of the angular distribution of the Rayleigh scattering cross-section for aluminum and lead with different incident photon energies. Note that  $d\Omega = 2\pi \sin \theta$  [C07]

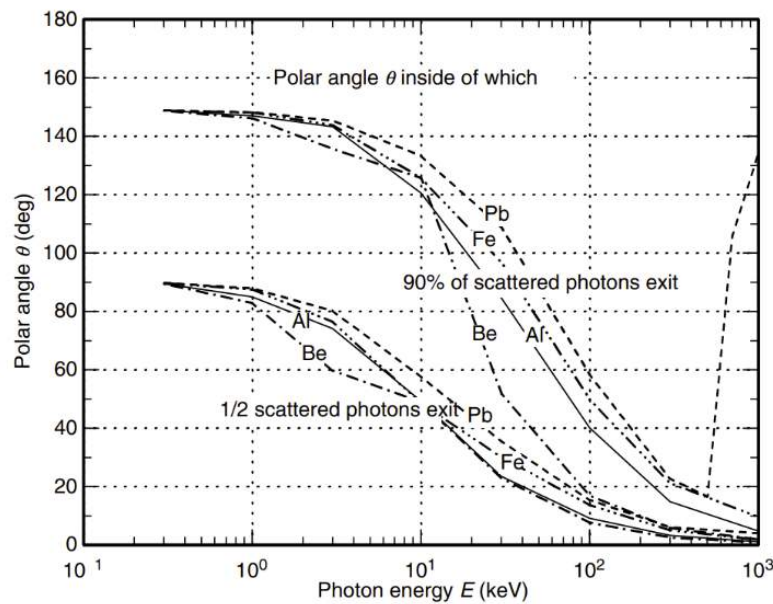


**Fig.1.35:** Angular distribution of the scattered photons through Rayleigh scattering as a function of photon energy for different elements. As the energy increases, the scattered photons tend to appear more in forward direction [C07].

**Table 1.3**

The Rayleigh characteristic angle  $\theta_R$  for different absorber materials and photon energies [P09]

Absorber	Symbol	Atomic number $Z$	Incident photon energy $h\nu$ (MeV)				
			0.1	0.5	1	5	10
Carbon	C	6	28°	6°	3°	0.6°	0.3°
Copper	Cu	29	48°	9°	5°	0.9°	0.5°
Lead	Pb	82	70°	13°	7°	1.3°	0.7°

It is worth pointing out that, Rayleigh scattering is the predominant mode of elastic scattering for most incident X-rays and low energy  $\gamma$ -rays in this energy region and for high atomic numbers  $Z$  of the absorber [P09]. Low energy photon regions mean that the electron binding effects severely decrease the Compton cross-sections. Therefore, as a result of a coherent contribution of the entire atomic electrons to the Rayleigh (i.e., coherent) atomic cross-section, the Rayleigh cross-section can exceed the Compton cross-section in this particular energy region [P09] (see Fig.1.36). On this basis, for a given absorber, the photon energy  $h\nu_{eq}$  at which  ${}_a\sigma_R = {}_a\sigma_C$  can be obtained. The photon energy  $h\nu_{eq}$  is proportional to the atomic number  $Z$  [P09]. As can be seen in Fig.1.36, for photon energies exceeding  $h\nu_{eq}$ , the Rayleigh atomic cross-section is inversely proportional to the square of  $h\nu$ , i.e.,

$${}_a\sigma_R \propto \frac{1}{(h\nu)^2}. \quad (1.31)$$

Also, as can be argued in Fig.1.36, for a given photon energy  $h\nu$ ,  ${}_a\sigma_R$  is proportional to the square of the atomic number  $Z$ , i.e.,  ${}_a\sigma_R \propto Z^2$  [P09].

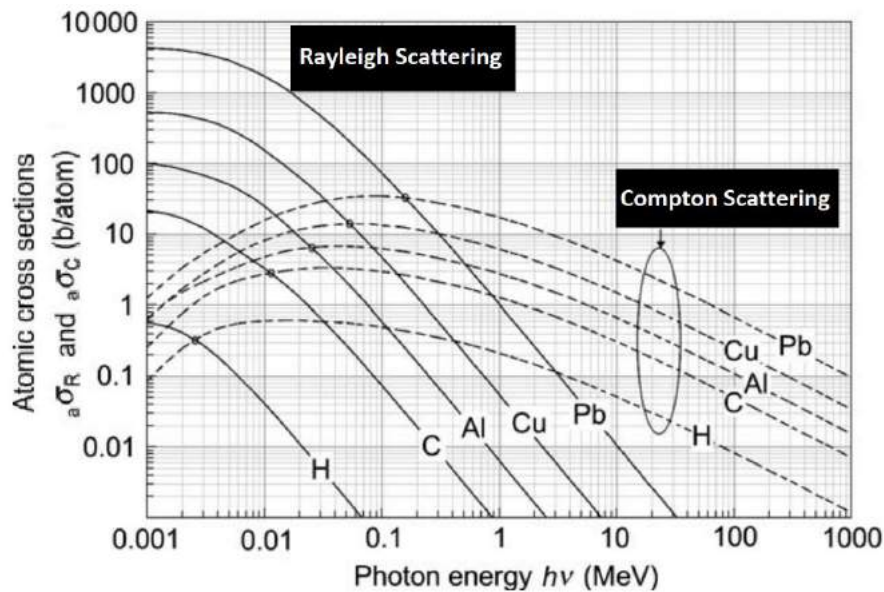


**Fig.1.36:** Cross-section for Rayleigh and Compton scattering of different elements as a function of photon energy [P09]. Note that for a given absorber, the photon energy  $h\nu_{eq}$ , at which  ${}_a\sigma_R = {}_a\sigma_C$  is shown as o.

## Compton effect (scattering)

In general, scattering of a photon from a free electron is described via Thomson scattering in the low-energy limit (i.e., non-relativistic energies in which  $h\nu \ll m_e c^2$ ), and via Compton scattering in the relativistic energy limit of the incident photon [GMBM04]. Accordingly, Compton scattering usually refers to the inelastic scattering of photons from a free (or a loosely bound) electron [M14]. This type of photon interaction was first discovered and described in 1923 by Compton [A07]. He could experimentally show that the wavelength of the scattered light was longer than that of the incident light. Moreover, he explained this phenomenon comprehensively by considering the fact that the light is consisting of quantized packets known as photons. Fig. 1.37 shows a schematic representation of the Compton scattering. Considering energy and momentum conservation laws, one can derive the relation between wavelengths of the incident and scattered photon as [JC53]:

$$\lambda = \lambda_0 + \frac{h}{m_0 c} (1 - \cos \theta), \quad (1.32)$$

where  $\lambda$  and  $\lambda_0$  are the wavelengths of the incident, and scattered photon, respectively,  $h$  is Planck's constant. In Eq.1.32,  $\theta$  is the angle between the incident and the scattered photon [JC53].

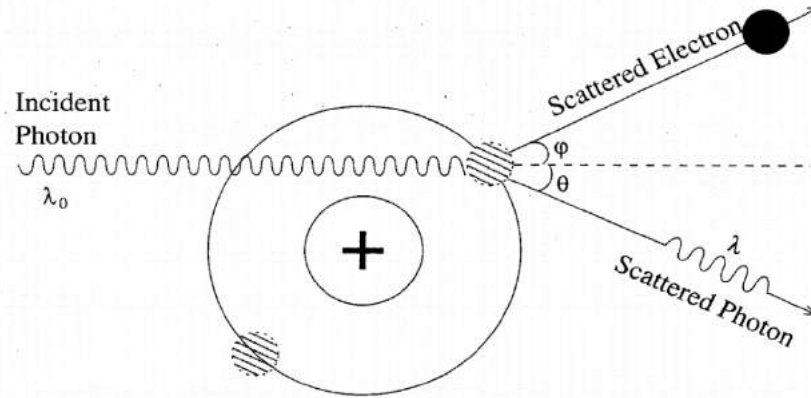


**Fig.1.37:** Schematic representation of the Compton scattering [A07]

Eq. 1.32 can also be rewritten in terms of the energy of the incident ( $E_{\gamma_0}$ ) and scattered ( $E_\gamma$ ) photon using  $E_\gamma = \frac{hc}{\lambda}$  as [A07, JC53, R14]:

$$E_\gamma = E_{\gamma_0} \left[ 1 + \frac{E_{\gamma_0}}{m_0 c^2} (1 - \cos \theta) \right]^{-1}. \quad (1.33)$$

According to Eq.1.33, the energy of the scattered photon depends on the incident photon energy and the scattering angle. Therefore, the scattering process is not isotropic. There are three extreme angles of the scattered photon, which are of interest to be investigated:  $0^\circ$ ,  $90^\circ$ , and  $180^\circ$  [LR04, A07].

- $\theta = 0^\circ$ :

In this case, since  $\cos \theta = 1$ , Eq. 1.33 gives [A07]:

$$E_\gamma = E_\gamma^{max} = E_{\gamma_0}. \quad (1.34)$$

This implies that the scattered photon carries all of the energy of the incident photon if it continues in the same direction as the incident photon. This is the upper bound of the scattered photon energy.

- $\theta = 90^\circ$ :

In this case, since  $\cos \theta = 0$ , Eq. 1.33 gives [A07]:

$$E_\gamma = E_{\gamma_0} \left[ 1 + \frac{E_{\gamma_0}}{m_0 c^2} \right]^{-1}. \quad (1.35)$$

This case happens when the scattered photon flies away at a right angle with respect to the incident electron direction of motion after scattering from the electron. The change in wavelength can then be obtained as:

$$\Delta\lambda = \frac{h}{m_0 c} = 2.432 \text{ fm}. \quad (1.36)$$

- $\theta = 180^\circ$ :

In this case, since  $\cos \theta = -1$ , Eq. 1.33 gives [A07]:

$$E_\gamma^{min} = E_{\gamma_0} \left[ 1 + \frac{2E_{\gamma_0}}{m_0 c^2} \right]^{-1}. \quad (1.37)$$

This implies that the scattered photon carries the minimum possible energy.

Using Eq.1.33, one can illustrate the change in the photon's wavelength before and after Compton scattering as a function of  $\theta$  (see Fig. 1.38). As can be seen in Fig. 1.38, the largest change in wavelength happens at  $\theta = 180^\circ$ , where, as was mentioned above, the scattered photon carries the minimum possible energy [A07, R14].

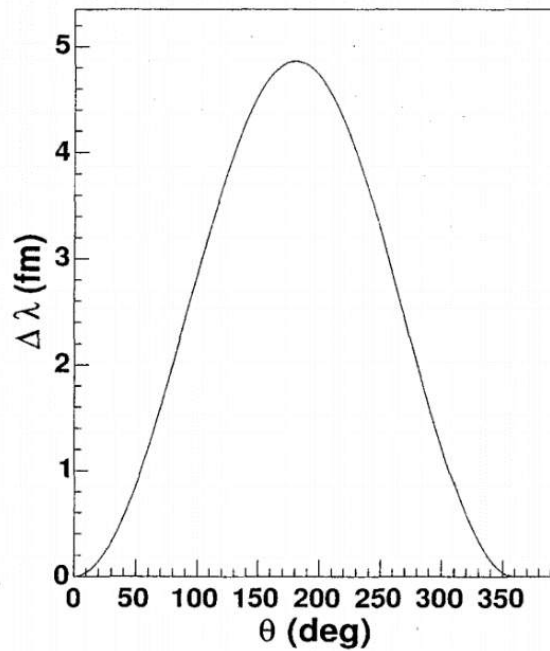


**Fig.1.38:** The change in the photon's wavelength before and after Compton scattering as function of  $\theta$  [A07]

As mentioned earlier and was shown in Eq.1.33, the energy of the scattered photon and therefore the electron depends on the incident photon beam energy. In Fig.1.39, the maximum and the average Compton electron kinetic energies, in addition to the average

energy of the scattered photon as a fraction of the incident photon is illustrated. Note that, in Fig.1.39, all values are averaged over all outgoing angles, which is the angle considered for either the scattered photon or the electron. Additionally, the maximum shown electron energy in Fig. 1.39 can be obtained as [C07]:

$$E_{electron}^{max} = \frac{h\nu_0}{1 + 1/2\alpha_{Compton}}, \quad (1.38)$$

where  $\alpha_{Compton}$  is defined as ratio of the incident photon energy to the electron rest energy ( $\frac{h\nu_0}{mc^2}$ ) [C07]. Fig.1.40 shows the energy distribution of the scattered electrons through Compton scattering for incident photons of 511, 1200, and 2760 keV. The electron energy can reach its maximum when the electron exits in forward direction and the photon is backscattered. As can be seen in Fig.1.40, by increasing the incident photon energy, the Compton electrons attain higher energies in Compton scattering than the lower incident photon energies. However, as is observable in Fig.1.39, the situation is opposite in the case of scattered photons [C07, P09].

The dependence of the emitted Compton electron energy on its emission angle  $\theta_e$  and the incident photon energy is presented in Fig.1.41. As can be seen, by increasing the incident photon energy, the energy of the emitted Compton electron in addition to its gradient\* to the angle  $\theta_e$  is increased [C07]. According to Fig.1.41, it can be argued that when the energy of the incident photon in Compton scattering is low, only a small amount of energy is transferred to the medium and most of the energy is merely scattered by the photons. However, when a high-energy photon (between 10 to 100 MeV) interacts through a Compton process with an electron, most of the energy is transferred to the Compton electron and very little is scattered by the photon [JC53, P09].

One of the other interesting graphical representations is the probability that the photon is scattered through Compton scattering to any given angle  $\theta$ . Fig. 1.42 shows the polar plot of the cross-section for Compton scattering with different incident photon energies. As is observable, the photons tend to scatter more in forward direction as the incident photon energy increases [D88].

---

\* Nabla  $\nabla$  is expressed by components as follows [KSKM18]:

$$\nabla = \begin{pmatrix} \frac{\partial}{\partial x} \\ \frac{\partial}{\partial y} \\ \frac{\partial}{\partial z} \end{pmatrix}.$$

Therefore, the nabla is expressed as a vector composed of the first partial derivatives of  $x$ ,  $y$ , and  $z$  directions. The gradient of an arbitrary function at a certain place can then be obtained by applying the nabla to the function at the position as follows [KSKM18]:

$$\nabla\phi = \begin{pmatrix} \frac{\partial\phi}{\partial x} \\ \frac{\partial\phi}{\partial y} \\ \frac{\partial\phi}{\partial z} \end{pmatrix},$$

where  $\frac{\partial\phi}{\partial x}$ ,  $\frac{\partial\phi}{\partial y}$ , and  $\frac{\partial\phi}{\partial z}$ , express the gradients in  $x$ ,  $y$ , and  $z$  directions, respectively [KSKM18].

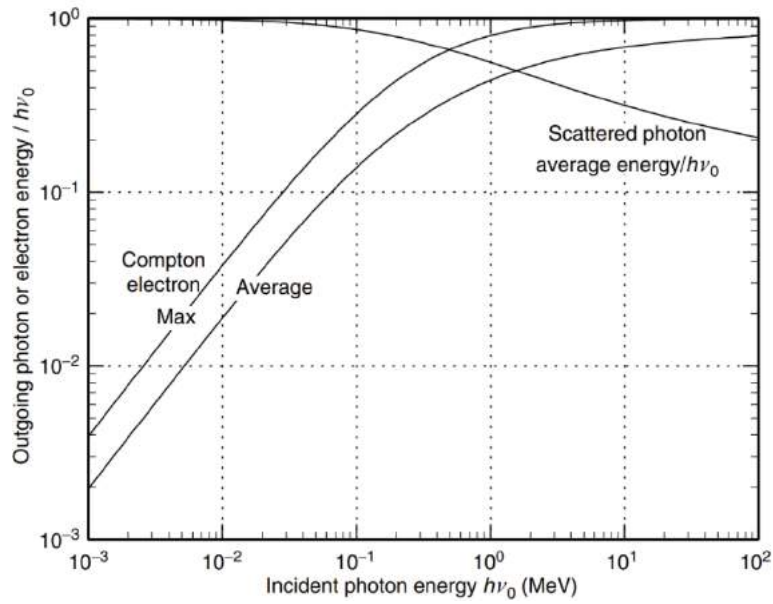


**Fig.1.39:** Average and maximum energies of outgoing electrons and average energy of scattered photons as a function of the incident photon energy (values are normalized to the incident photon energy) [C07].

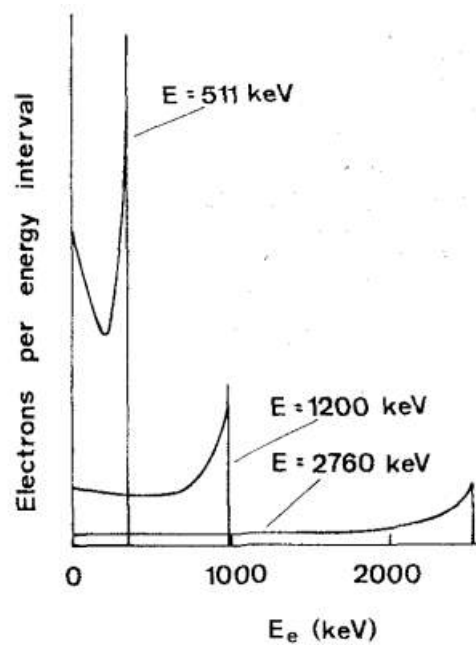


**Fig.1.40:** Energy distribution of the scattered electrons through Compton scattering for incident photons of 511, 1200, and 2760 keV [D88]



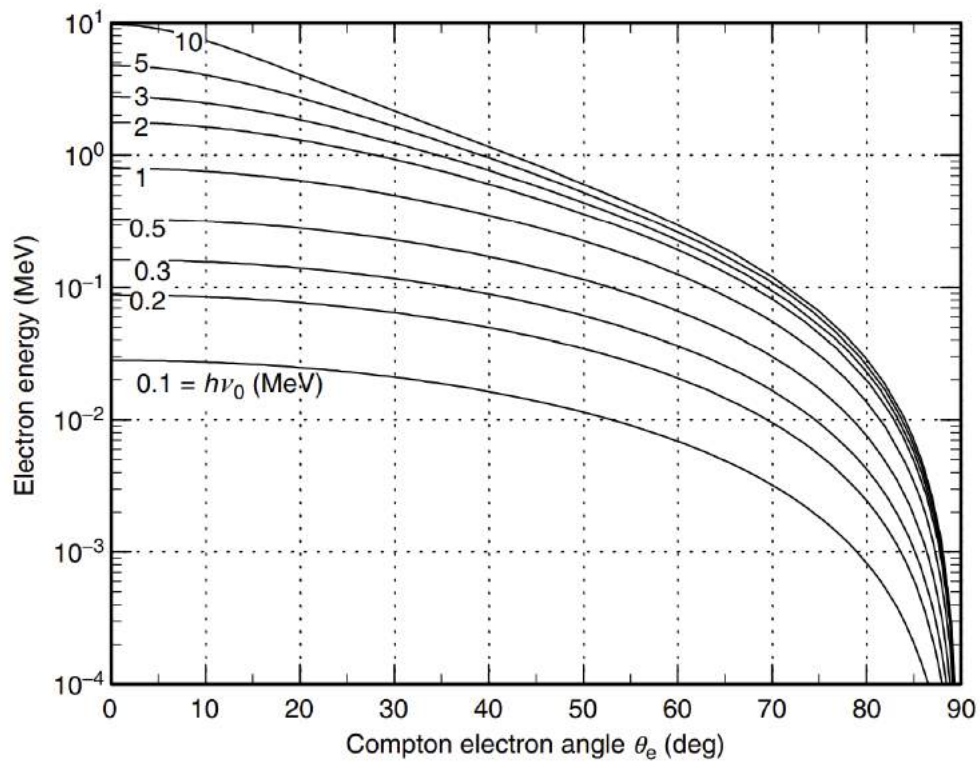


**Fig.1.41:** Electron Compton energy as a function of the Compton electron scattering angle  $\theta_e$  for different incident photon energies [C07].

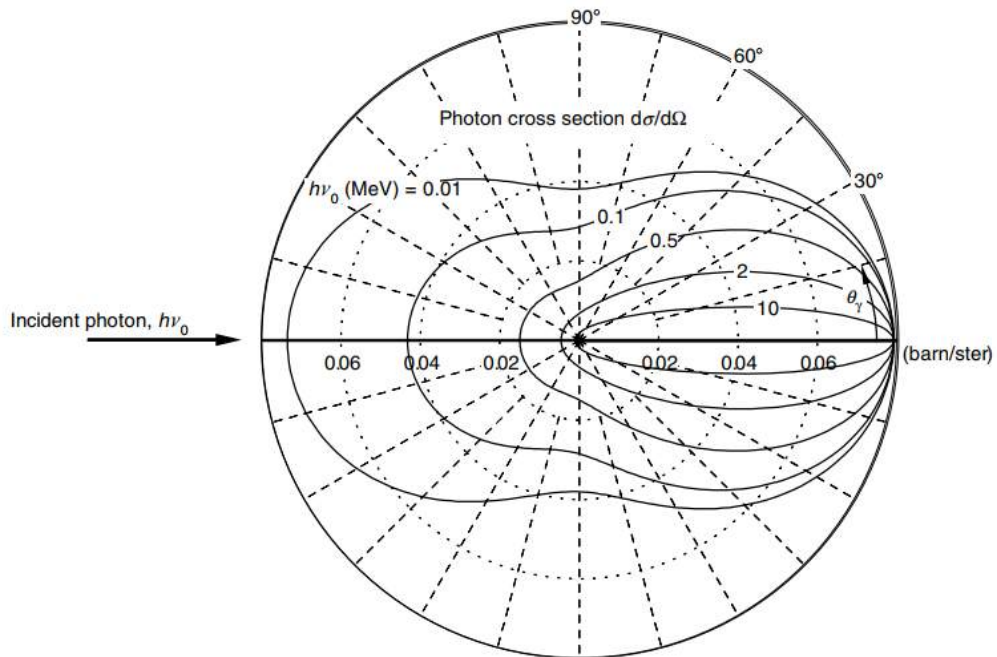


**Fig. 1.42:** Polar graph of the angular distribution of the Compton scattering cross-section (from a free electron) for different incident photon energies. Note that  $d\Omega = 2\pi \sin \theta d\theta$  [C07] and  $\theta$  is the photon scattering angles as shown in Fig.1.37

The atomic Compton cross-section  ${}_a\sigma_C$  is linearly proportional to the electronic Compton cross-section  ${}_e\sigma_C$  and can be obtained as:

$${}_a\sigma_C = Z {}_e\sigma_C. \quad (1.39)$$

Note that the electronic Compton cross-section is almost independent of the target atomic number  $Z$  [JC53] (see Fig. 1.43). However, the atomic Compton cross-section is linearly proportional to the atomic number  $Z$ . Additionally, the atomic and electronic Compton cross-section decreases by increasing photon energy  $h\nu$  [P16]. In general, one can write [D88]:

$${}_a\sigma_C \propto Z \cdot (h\nu)^{-1} \quad (1.40)$$

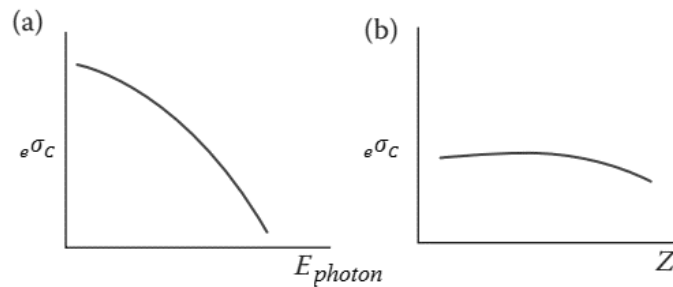


**Fig. 1.43:** Schematic representation of the dependency of electronic Compton scattering on the (a) photon energy, and (b) atomic number  $Z$  [TL15]

In general, for orbital electrons, Compton scattering is more probable than the photoelectric effect when the incident photon energy is higher in comparison with the binding energy of the innermost electron (i.e., K-shell) in the target absorber atom [A07]. More precisely, Compton scattering is the dominant process for incident photon energies ranging from hundreds of keV to several MeV [C07].

Since in the theoretical calculations of the Compton cross-section, the electron is considered as “free”, and thus, the binding energy is ignored, some discrepancies are observed between the experimental measurements and theoretical calculations. Fig.1.44, shows theoretical (dashed curves) and experimental (solid curves) atomic Compton cross-sections as a function of photon energy  $h\nu$  for a wide range of materials (from hydrogen to lead) [P09]. As can be seen, for high energies, the theoretical and experimental values are in good agreement; however, at low energies, considerable discrepancies can be observed. This stems from the fact that the assumption of the “free” electrons break down at low energies where the electron binding energy  $E_B$  is comparable with the photon energy  $h\nu$ . To be more precise, as closer  $h\nu$  to  $E_B$ , the larger the deviation of the theoretical values from experimental measurements [P09].

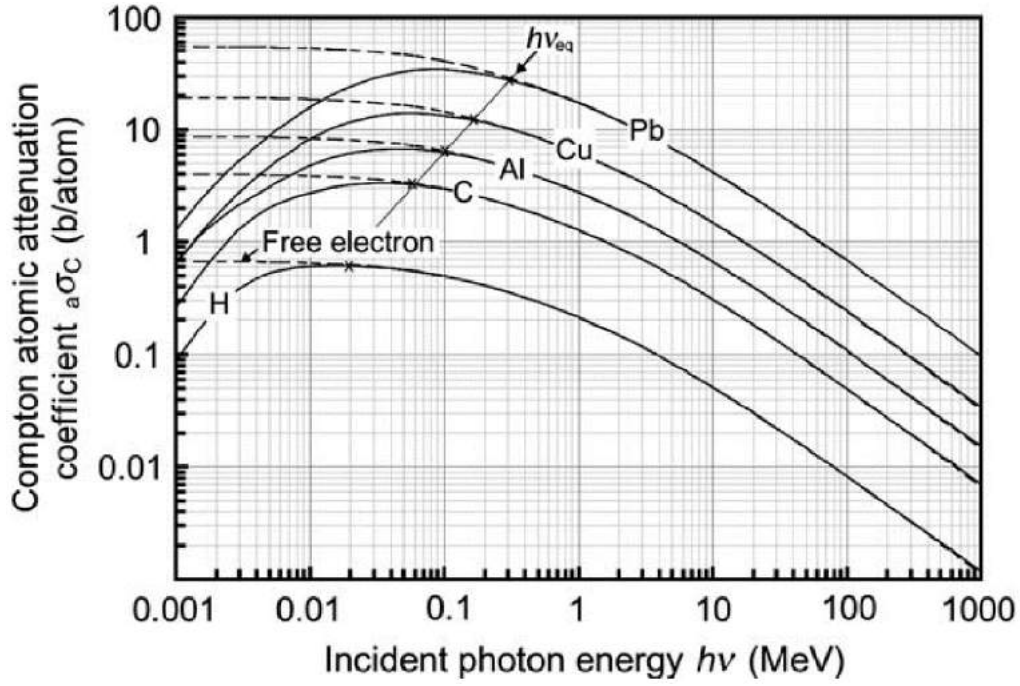


**Fig.1.44:** Theoretical (dashed curves) and experimental (solid curves) atomic Compton cross-section as a function of photon energy  $h\nu$  for a wide range of materials [P09].

## Photoelectric effect

The photoelectric effect (also known as photoeffect) refers to an interaction between a photon (with an energy of  $h\nu$ ) and a tightly atomic-bound orbital electron. The interaction is therefore between a photon and an atom as a whole [P16]. The photoelectric effect was originally explained by Einstein and earned him a Nobel Prize in 1921 [P09, NOBEL21]. The photoelectric effect is rather simple: when photons impinge on a material, electrons can be emitted. In the photoelectric effect, the emission of electrons, however, depends not on the intensity of the photons, but their frequency (or wavelength). If the frequency or energy is lower than a certain threshold value (for metals, this energy is called the *work function* [A07]), which depends on the target material, no electrons can be emitted from the target [P09]. Schematic diagram of the photoelectric effect is shown in Fig.1.45. As is observable, an incident photon interacts and is absorbed completely by a K-shell atomic electron (in general, one inner atomic shell) and then the electron is ejected from the atom as a photoelectron. The kinetic energy of the photoelectron,  $E_K$ , can then be obtained considering the binding energy of the K-shell atomic electron  $E_B$ , as:

$$E_K = h\nu - E_B. \quad (1.41)$$

Due to the fact that a free electron cannot absorb a photon\*, it can reasonably be expected that the photoelectric effect is larger for more tightly bound electrons, which are the inner

\* In the photoelectric interaction mechanism, the incident photon and a free electron alone are not able to simultaneously conserve the total momentum and energy. On this basis, the photoelectric interactions cannot occur between a photon and a free electron [P09]. The extra momentum and energy transported by the photon is transferred to a third particle, which is the parent atom of the

shell electrons. It has been revealed that for photons with higher energies than the K-shell binding energy of an absorber material, about 80% of all photoelectric absorption are with K-shell electrons, and only the remaining 20% is with the less tightly bound outer shell electron [LR04]. As can reasonably be argued, the electron binding energy depends on both the atomic number  $Z$  and the orbital. The binding energy decreases when proceeding towards the outer electron shells (see Fig.1.46). The following formula,  $e$  represents the binding energy in relation to the atomic number  $Z$  and the orbital shells K, L, and M [LR04]:

$$\begin{aligned} B_e(K) &\approx Ry(Z - 1)^2 [eV], \\ B_e(L) &\approx \frac{1}{4} Ry(Z - 5)^2 [eV], \\ B_e(M) &\approx \frac{1}{9} Ry(Z - 13)^2 [eV], \end{aligned} \tag{1.42}$$

where  $Ry = 13.61 \text{ eV}$  is the Rydberg energy [LR04]. In Fig.1.47, the ratio of total to K-shell photoelectric cross-section for photon energies higher than the K-shell binding energy of the absorber material is presented as a function of atomic number. As can be seen, the ratio is almost 1 for low atomic number nuclei and does not exceed more than 25% for heavy atomic number nuclei [LR04].

After ejection of the photoelectron, the atom (in fact the ion) is left in an excited state because a vacancy was created in its electronic shells [NKV10]. The atom then goes to a more stable electronic configuration in a process called *deexcitation* or *relaxation*, where the created vacancy in the K-shell (after ejection of the electron) is filled with an outer (or higher) orbit electron. The energy of the electronic transition (see Fig.1.46) can be emitted either as a characteristic photon or as an Auger electron (see Fig. 1.48). More precisely, since during the process of relaxation, the electrons depart from a higher to a lower energy state, this difference in energies can be emitted as characteristic X-ray photons (K, L, or M atomic shells), or an Auger electron as a result of absorption of the energy by an electron in one of the outer shells (L, M, or N atomic shells) [NKV10]. It is worth pointing out that for materials with low atomic number ( $Z < 20$ ), Auger electrons are predominantly produced compared to X-ray photons in the relaxation process. However, for medium to high atomic number materials, the relaxation process is performed preferentially by X-ray photon emission [NKV10]. It is also interesting to note that, in some cases, the energy uptake by the photoelectron during the photoelectric interaction process may be insufficient to allow its ejection from the target atom. This process is called atomic ionization. Nevertheless, the energy of the photoelectron may be sufficient to raise the photoelectron to a higher orbit in a process known as atomic excitation [P09].

---

photoelectron. However, this can happen only when the electron is tightly bound to the parent atom. That means the photon energy  $h\nu$  and the binding energy (of the electrons)  $E_B$  are of the same order of magnitude, with  $h\nu$  slightly exceeding  $E_B$  [P09].

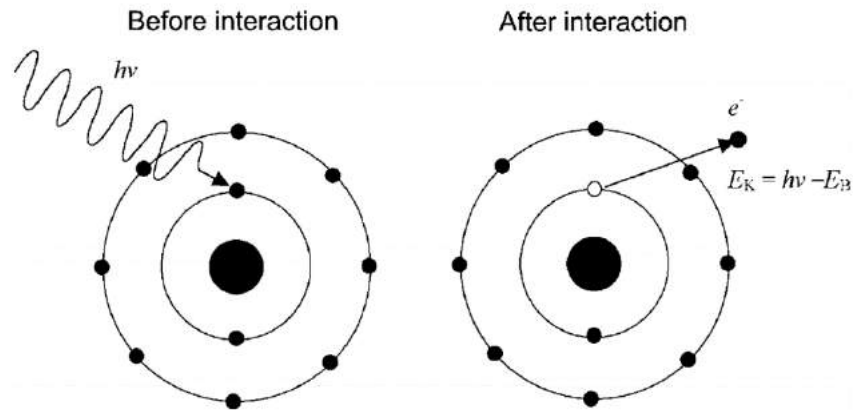


**Fig.1.45:** Schematic representation of the photoelectric effect [P09]

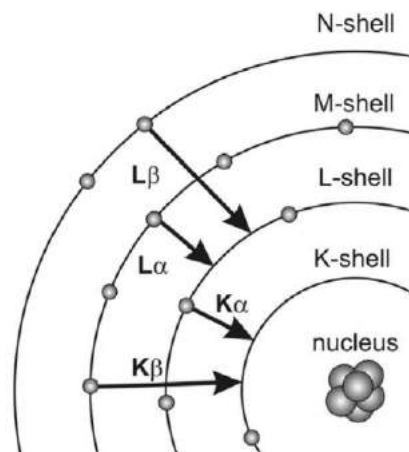


**Fig. 1.46:** Schematic representation of electronic transmission in an excited atom in which an electron in the lower orbital is missing [NKV10]. It is worth pointing out that for photons with higher energies than the K-shell binding energy, about 80% of all photoelectric absorption occurs with K-shell electrons, and the remaining 20% with the less tightly bound outer electron shells [P09].

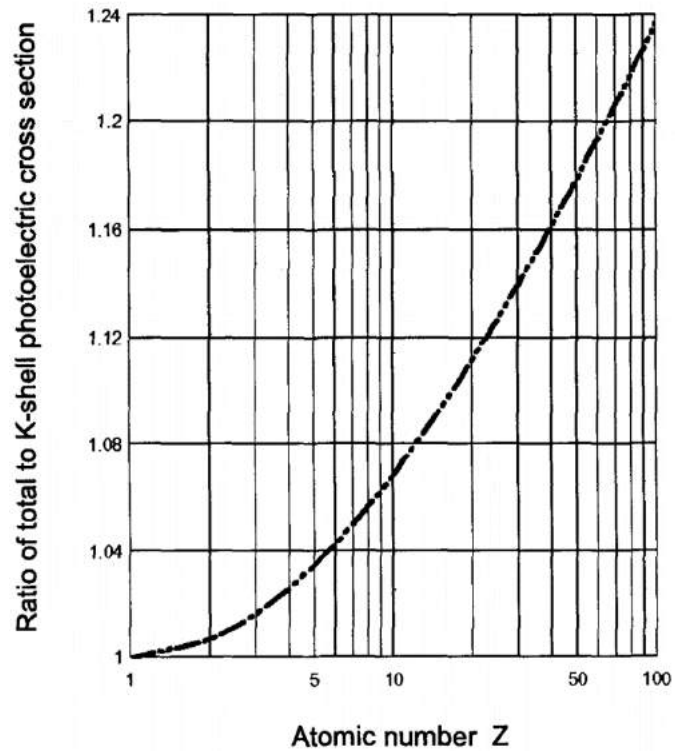


**Fig. 1.47:** Ratio of total to K-shell photoelectric cross-section for photon energies higher than the K-shell binding energy as a function of atomic number of the absorber material [LR04]

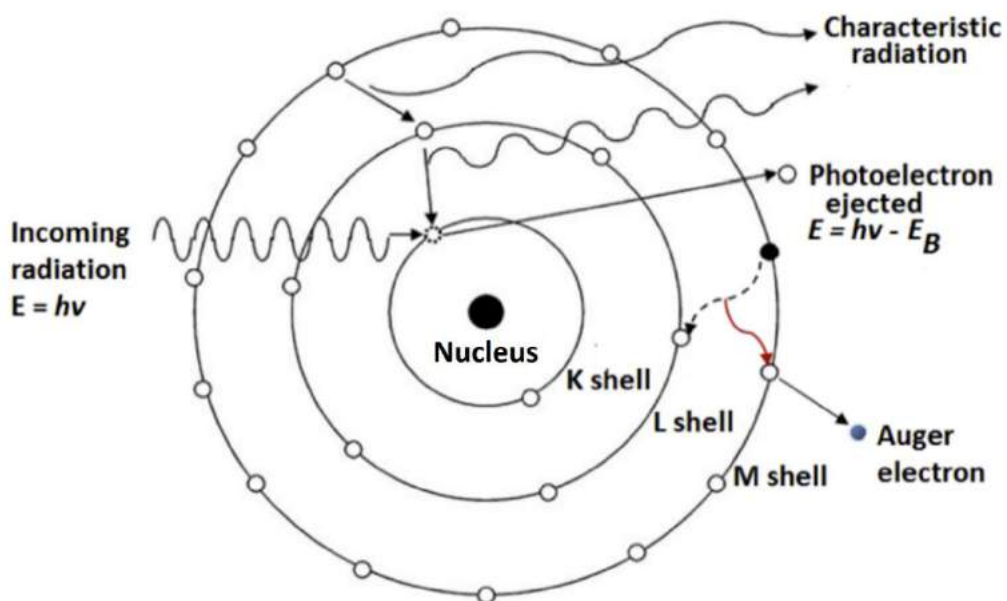


**Fig.1.48:** Schematic representation of X-ray photon generation and Auger electron emission in photoelectric effect [M16]

The photoelectric cross-section depends on the incident photon energy and the atomic number of the target material. Their dependencies can be written as [A07]:

$$\sigma_{pe} \propto \frac{Z^n}{E_\gamma^{3.5}}, \quad (1.43)$$

where  $\sigma_{pe}$  is the photoelectric cross-section. In Eq.1.43,  $n$  varies between 4 and 5 for low photon energies, and almost 1 in high energy regions [P09, A07]. This dependency on energy and atomic number is schematically presented in Fig.1.49.

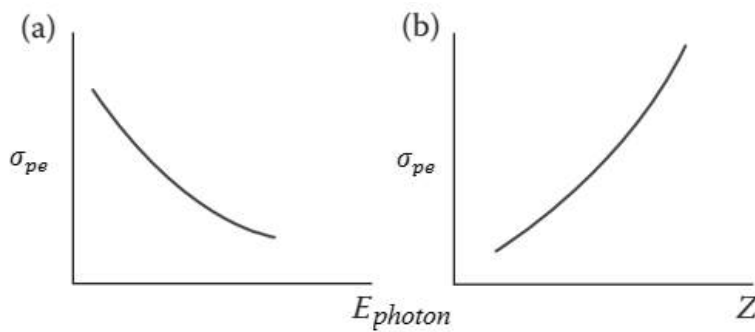


**Fig.1.49:** Schematic representation of the dependency of photoelectric effect on (a) the photon energy, and (b) the atomic number  $Z$  [TL15]

In Fig.1.50, cross-sections for the photoelectric effect of different elements are presented. As is observable, the magnitude of the cross-section increases by increasing atomic number of the absorber material. The angular distribution of the emitted photoelectrons depends on the incident photon energy  $h\nu$ . Fig. 1.51 shows the relative number of photoelectrons per unit angle  $\frac{d\eta}{d\phi}$  as a function of the photoelectron ejection angle  $\phi$  for different incident electron beam energies. Note that the angle  $\phi$  is the angle between the incident photon direction and that of the ejected photoelectron. As is shown in Fig.1.51, at low incident photon energies of the order of 10 keV, the ejected photoelectrons tend to be emitted at angles close to  $90^\circ$ . However, as the energy increases, the peak of the photoelectron emission angle moves progressively to angles that are more forward [P09].

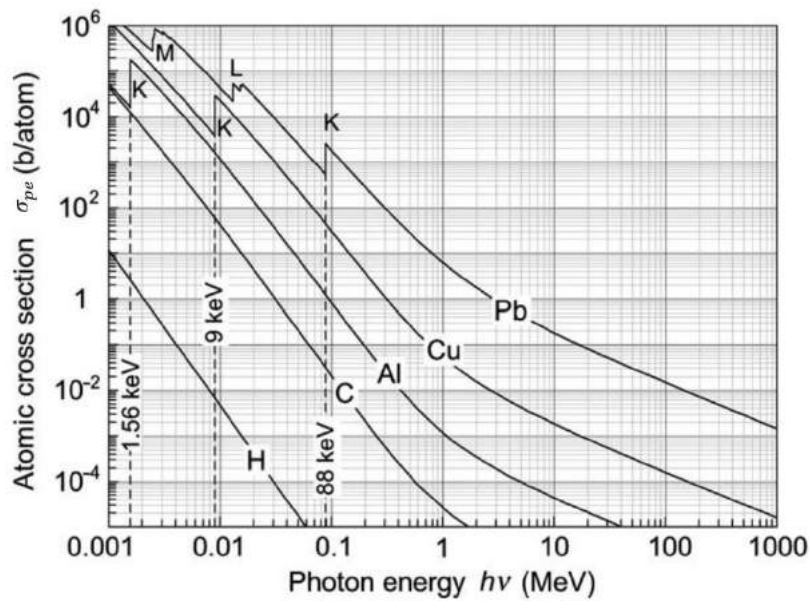


**Fig. 1.50:** Photoelectric cross-sections for various elements as a function of the photon energy [P09]

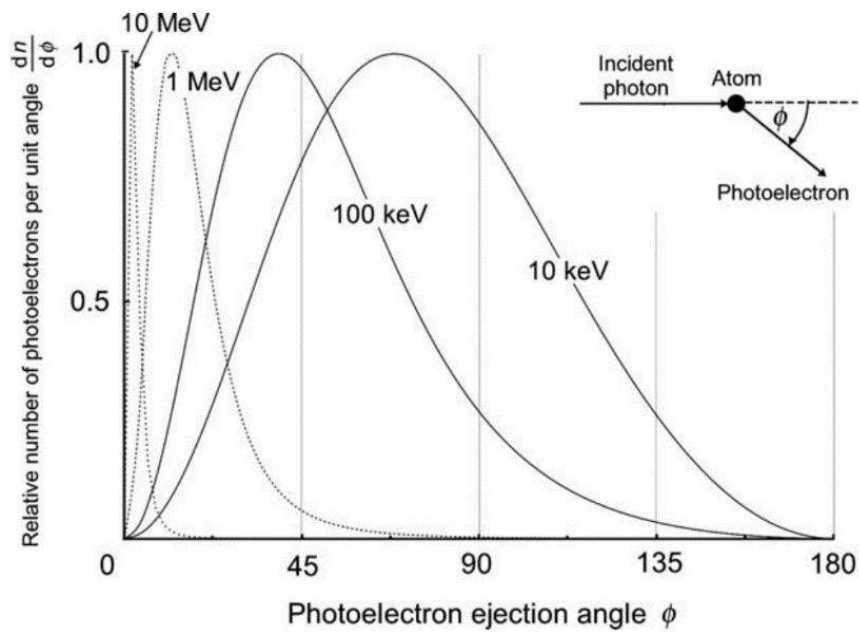


**Fig. 1.51:** Relative number of photoelectrons per unit angle  $\frac{d\eta}{d\phi}$  as a function of the photoelectron ejection angle  $\phi$  [P09]



## Nuclear and electronic pair production

Pair production mechanism refers to a process in which a high-energy incident photon (greater than 1.022 MeV) is absorbed when it passes near the nucleus of an atom and therefore is subjected to the strong field of it (so it is called nuclear pair production). In this mechanism, the incident photon suddenly disappears (as a photon) and becomes a negative and positive electron (i.e., a positron) (see Fig.1.52) [JC53].

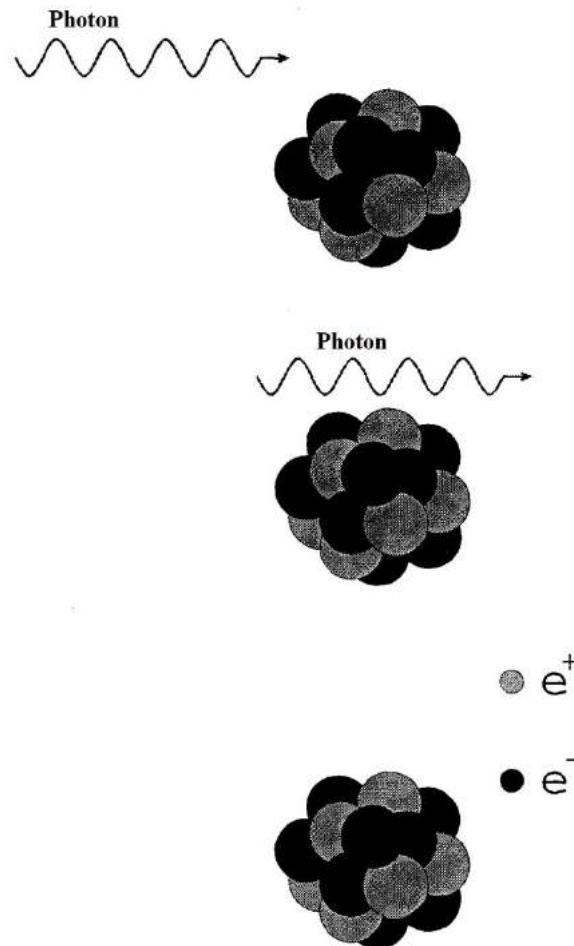


**Fig. 1.52:** Schematic representation of the pair production mechanism [LR04]

Intuitively thinking, one can say that since, one electron mass is 0.511 MeV, at least the energy of the incident photon must exceed 1.022 MeV (i.e.,  $E_{Photon}^{Threshold} \geq 2m_e c^2$ ). The actual threshold energy for the pair production process is given as [A07]:

$$E_{Photon}^{Threshold} \geq 2m_e c^2 + \frac{2m_e^2 c^2}{m_{nuc}}, \quad (1.44)$$

where  $m_{nuc}$  is the mass of the nucleus. One can also rewrite Eq.1.44, as follows [A07]:

$$E_{Photon}^{Threshold} \geq 2m_e c^2 \left[ 1 + \frac{m_e}{m_{nuc}} \right]. \quad (1.45)$$

Due to the fact that the mass of the nucleus is much greater than that of an electron (i.e.,  $m_{nuc} \gg m_e$ ), the second term in the parenthesis of Eq.1.45, can be neglected. Therefore, Eq.1.45, can be reduced and rewritten as [JC53, A07]:

$$E_{Photon}^{Threshold} \geq 2m_e c^2. \quad (1.46)$$

Eq.1.46 gives the threshold energy for the pair production process, which was mentioned earlier. For the incident photons whose energy is in excess of this value, this excess energy would be shared between the created positron and electron. The total energy given to the positron and electron can be divided in many ways with almost equal probabilities, except for an extreme one in which one obtains nearly all the excess energy and the other one none [JC53].

Besides the nucleus, the process of pair production can also occur in the vicinity of light particles [A07]. When the process of pair production occurs near the field of an electron rather than the nucleus, a positron, a created electron, and the original electron (in the photon interaction) appear (this process is known as electronic pair production). In fact, an electron-positron pair is produced; however, because the original electron scatters off, in the imaging detector, three tracks are visible [A07]. On this basis, this process is also called triplet production. Perrin in 1933 was the first who pointed out the possibility of the pair production process near the field of an atomic electron [E55]. The schematic representation of this process is shown in Fig.1.53 [JC53]. The probability of triplet production is much smaller than that of the pair production, and the energy threshold that the photon must have is 2.04 MeV, which is twice that of the pair production [TL15]. This value can be obtained using Eq.1.45, and replacing  $m_{nuc}$  in the denominator of the second term in the right hand side parenthesis by  $m_e$ .

Positrons produced in the pair and triplet production have very short half-lives\*. This is due to that fact that since these processes occurred in a material, which always have electrons in abundance, the positrons combine usually quickly with nearby electrons and produce photons in the process called annihilation [A07] (see Fig.1.53). As is shown in Fig.1.53, as a result of this process, two photons each having 0.511 MeV are produced which are emitted under 180 degrees of each other. It is interesting to point out that the process of pair production and electron-positron annihilation are inverse to each other. However, there is an operational difference between them. To be more precise, the pair production process requires taking part in a material and in fact in a vicinity of another particle to ensure momentum conservation. However, there is no such requirement for the electron-positron annihilation [P16, A07, TL15].

---

\* The time during which the activity of a nuclide reduces by a factor of two is known as the half-life and is symbolized as  $T_{1/2}$  [LB01].

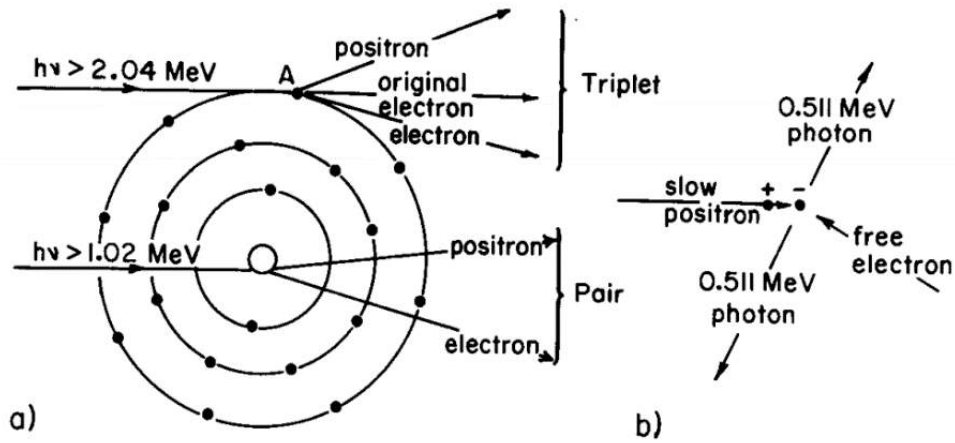


**Fig.1.53:** A schematic representation of a) the nuclear pair and electronic pair production mechanism and b) the electron-positron annihilation process [JC53]

Note that the cross-section of the nuclear pair production  $a\sigma_{Nuclear\ pp}$  is obtained from the integration of a very complex form of the differential cross-section of the process. The analytical integration can only be achieved when different approximations and assumptions are considered. Generally speaking, the atomic pair production cross-section  $a\sigma_{Nuclear\ pp}$  has roughly a  $Z^2$  dependence in the case of highly energetic incident photons where [E55]

$$m_0c^2 \ll h\nu \ll 137 m_0c^2 Z^{-\frac{1}{3}}. \quad (1.47)$$

As can be seen in Eq.1.47, this threshold also depends on the atomic number; e.g., for lead, this threshold is about 16 MeV [E55]. The trend of variation corresponding to Eq.1.47, for the atomic nuclear pair production cross-section has been shown in Fig.1.54, and is given as [A07, FS20, E55]:

$$a\sigma_{Nuclear\ pp} \propto Z^2 \ln(2E_{photon}). \quad (1.48)$$

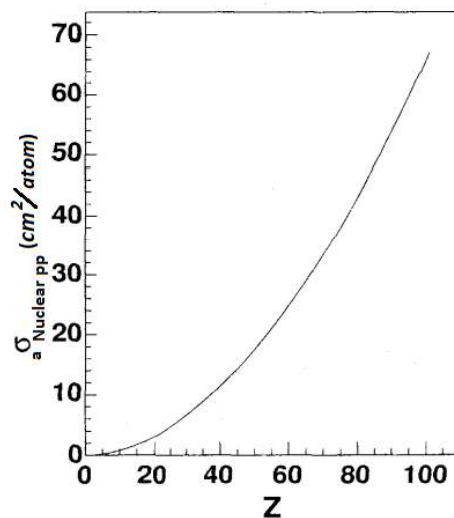


**Fig.1.54:** Dependency of the nuclear pair production process on the atomic number of a material for photons with energies higher than 20 MeV [A07]

For  $h\nu \gg 137 m_0 c^2 Z^{-\frac{1}{3}}$ , however, it is given by [E55]:

$$a\sigma_{Nuclear\ pp} \propto Z^2 \ln\left(Z^{\frac{1}{2}}\right). \quad (1.49)$$

In the case of the dependency of the atomic nuclear pair production cross-section on the incident photon energy, it should be noted that the cross-section increases rapidly as the energy exceeds the required threshold (i.e., 1.02 MeV) and then eventually increases approximately logarithmically with incident photon energy  $E_{photon}$  (see Eq.1.48). It is worth to point out that since the threshold for the electronic production is double that of the nuclear pair production, the cross-section of the electronic production is always smaller [A07, JC53]. It has been revealed that for any  $Z$  value, the ratio of the cross-section of the electronic pair production to the cross-section of the nuclear pair production can be given as [E55]:

$$\frac{a\sigma_{Electronic\ pp}}{a\sigma_{Nuclear\ pp}} = \frac{1}{CZ}. \quad (1.50)$$

In Eq.1.50, since the cross-section for the electronic pair production is summed up for all  $Z$  electrons in a target material, the atomic cross-section for the electronic pair production is presented as  $a\sigma_{Electronic\ pp}$  [E55]. Note that, in the case of nuclear pair production, since the cross-section is always obtained for the nucleus as a whole, the cross-section can be written either as  $\sigma_{Nuclear\ pp}$  or  $a\sigma_{Nuclear\ pp}$ , i.e.,  $\sigma_{Nuclear\ pp} = a\sigma_{Nuclear\ pp}$ . In Eq.1.50,  $C$  depends upon  $h\nu$ , but not upon  $Z$ . The value of  $C$  can be determined as [E55]:

$$\begin{aligned} C &\approx 1.3 + 0.3 \quad \text{for 5 to 20 MeV} \\ C &\approx 1.2 + 0.3 \quad \text{for 20 to 100 MeV} \end{aligned} \quad (1.51)$$

The value of  $C$  decreases by increasing the photon energy and eventually approaching (theoretically) unity when  $h\nu \rightarrow \infty$  [P09]. According to Eqs.1.50 and 1.51, one can observe that the cross-section for electronic pair production is at best 30% of the nuclear pair production for  $Z = 1$ , and less than 1% for high  $Z$  elements (see Fig. 1.55) [P09].

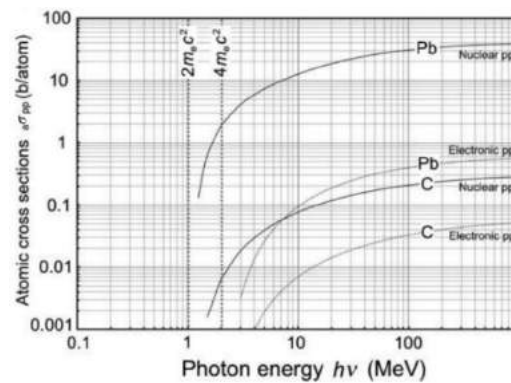


**Fig. 1.55:** Atomic cross-section for nuclear pair production and electronic pair production as a function of photon energy for carbon and lead [P09]. As is shown, as the atomic number increases, the difference in nuclear pair production cross-section and the electronic one is increasing.

Fig. 1.56 shows a schematic representation of the atomic (including nuclear and electronic) pair production cross-section as a function of energy and atomic number. The total atomic cross-section for pair production versus photon energy as the sum of nuclear and electronic pair production for different elements (in the range of hydrogen to lead) is presented in Fig.1.57. As is shown, by increasing the absorber atomic number  $Z$ , the total atomic pair production cross-section increases considerably.

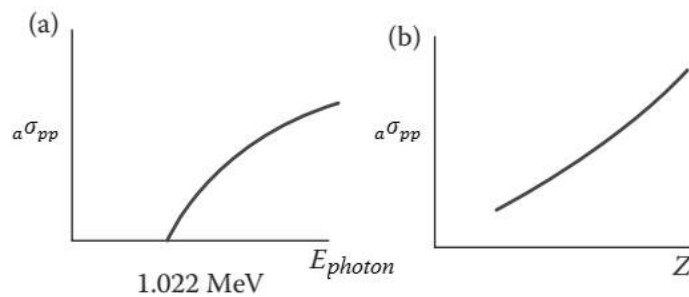


**Fig.1.56** Schematic representation of dependency of the atomic (including nuclear and electronic) pair production on the (a) photon energy, and (b) atomic number  $Z$  [TL15]

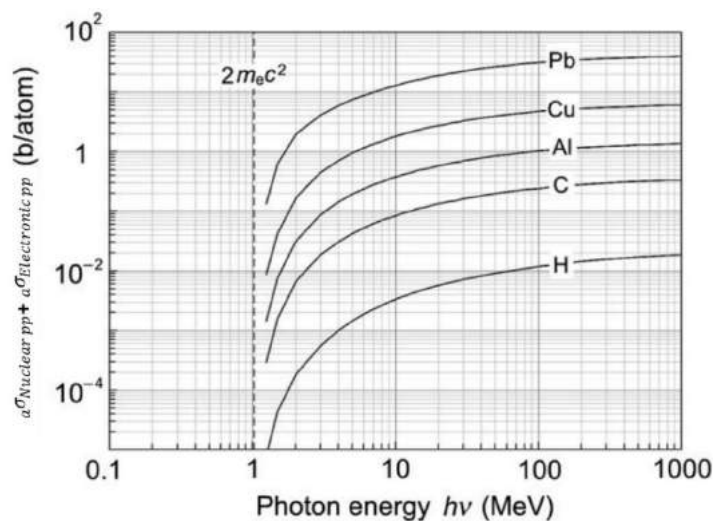


**Fig.1.57:** Atomic cross-section for pair production (as a sum of electronic and nuclear pair production cross-sections) versus photon energy for different materials [P09]

## Photonuclear scattering, absorption and production

There are different types of interaction between photons and nuclei. These interactions include photonuclear scattering such as nuclear Thomson scattering<sup>\*</sup>, nuclear photoelectric<sup>†</sup> and Delbrück scattering<sup>‡</sup> [LR04]. In general, the photonuclear scattering cross-sections are considerably smaller than other interactions of photons with matter, which have been discussed so far [LR04].

In contrast to the photonuclear scattering cross-section, the photonuclear absorption cross-section contributes to a considerable fraction of the total photon interaction cross-section (depending on the incident photon energy and atomic number) [C07]. Photonuclear absorption most likely results in an emission of a (or some) particle(s) (or  $\gamma$ -rays) if the energy of the incident photon is higher than a threshold (see Fig.1.58). This threshold energy is in fact the energy that is added to the absorber nucleus and must be at least equal to a nucleon's binding energy. For photon energies below the threshold, i.e., typically 7-8 MeV (except deuterium and beryllium with quite low energy thresholds for photoneutron emission: 2.226 and 1.666 MeV, respectively), only photonuclear scattering is possible [LR04]. Single neutron emission is preferential rather than proton emission since the neutron emission has no Coulomb potential barrier to overcome. However, it should be noted that apart from single neutron emission, emission of more than one neutron or emission of other charged particles is also possible (see Fig.1.59). In the case of other charged particle emission, proton emission is more probable in light nuclei where the photoneutron cross-section is smaller than the photoproton cross-section [AP18]. The range of energy thresholds for photoneutrons varies from 1.666 MeV for beryllium and 2.226 MeV for deuterium to about 8 MeV (see Fig. 1.60). In general, for light nuclei, the thresholds of energy fluctuate unsystematically; in the range of atomic mass numbers from 20 to 130, the thresholds increase gradually to about 8.5 MeV and

---

<sup>\*</sup> Nuclear Thomson scattering process is an elastic scattering which is quite similar to electron Thomson scattering in terms of interaction principle. The cross-section values of the nuclear Thomson scattering can also be obtained based on the electron Thomson scattering [LR04]. As a photon leaves the target atom unchanged, it is coherent with the Rayleigh scattering process. The amplitude of the nuclear Thomson scattering is smaller than that of the electronic Thomson contribution. In general, at low energies, for all elements, the nuclear Thomson scattering is always negligible in comparison with the scattering of photons from atomic electrons; however, at high energies ( $\sim 1$  MeV), its contribution can increase to some percent, particularly for high  $Z$  elements. At energies, around  $> 1$  MeV, for high  $Z$  elements, Thomson scattering can interfere also with atomic Rayleigh scattering [C07]. For more details, refer to [C07, LR04].

<sup>†</sup> Photonuclear reactions occur in a direct interaction between the incident photon and a nucleus resulting in nuclear disintegration. There are two other names, which are used for this effect, such as photodisintegration and nuclear photoelectric effect [P16].

<sup>‡</sup> Delbrück scattering is a type of elastic scattering from the Coulomb electric field, which exists surrounding the nucleus. The Delbrück scattering occurs via the virtual or real creation of an electron-positron pair that annihilates subsequently [LR04]. The Delbrück scattering requires enormous electric fields; as has been shown, this interaction is never the dominant photon-atom reaction mechanism. However, this interaction can be very important when attenuation is restricted to elastic scattering of photons from atoms. It has been revealed that in high  $Z$  elements, and at a few MeV energy, remarkable interference exists among nuclear Thomson, atomic Rayleigh and Delbrück scattering. For more details, refer to [C07]. Generally speaking, the coherent scattering processes, Rayleigh and Delbrück scattering, are associated with the photon absorption processes, the photoelectric effect, and pair production, respectively [H70].

afterward decrease slowly to about 6 MeV as the atomic mass numbers of target material increase; see Fig. 1.60 (Note that there are some exceptions that do not obey this trend) [J17].

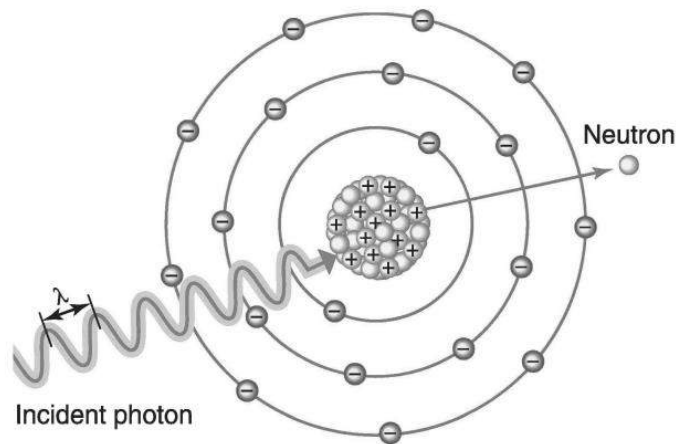


**Fig.1.58:** A schematic representation of the photonuclear reaction with single neutron emission [S14]

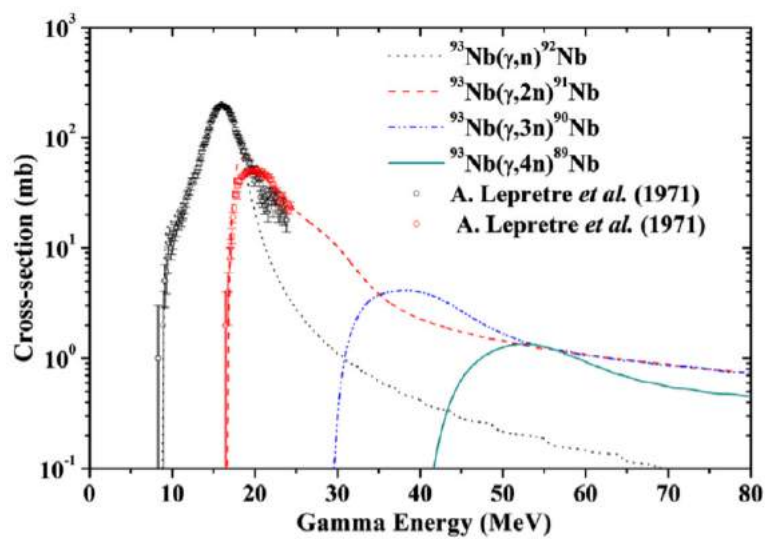


**Fig. 1.59:** Cross-section data of the  $^{93}\text{Nb}(\gamma, xn; x = 1 - 4)$  reaction as a function of photon energy [N13]. As is shown, emission of more than a single neutron due to photonuclear reactions is less probable and occurs at higher photon energies.

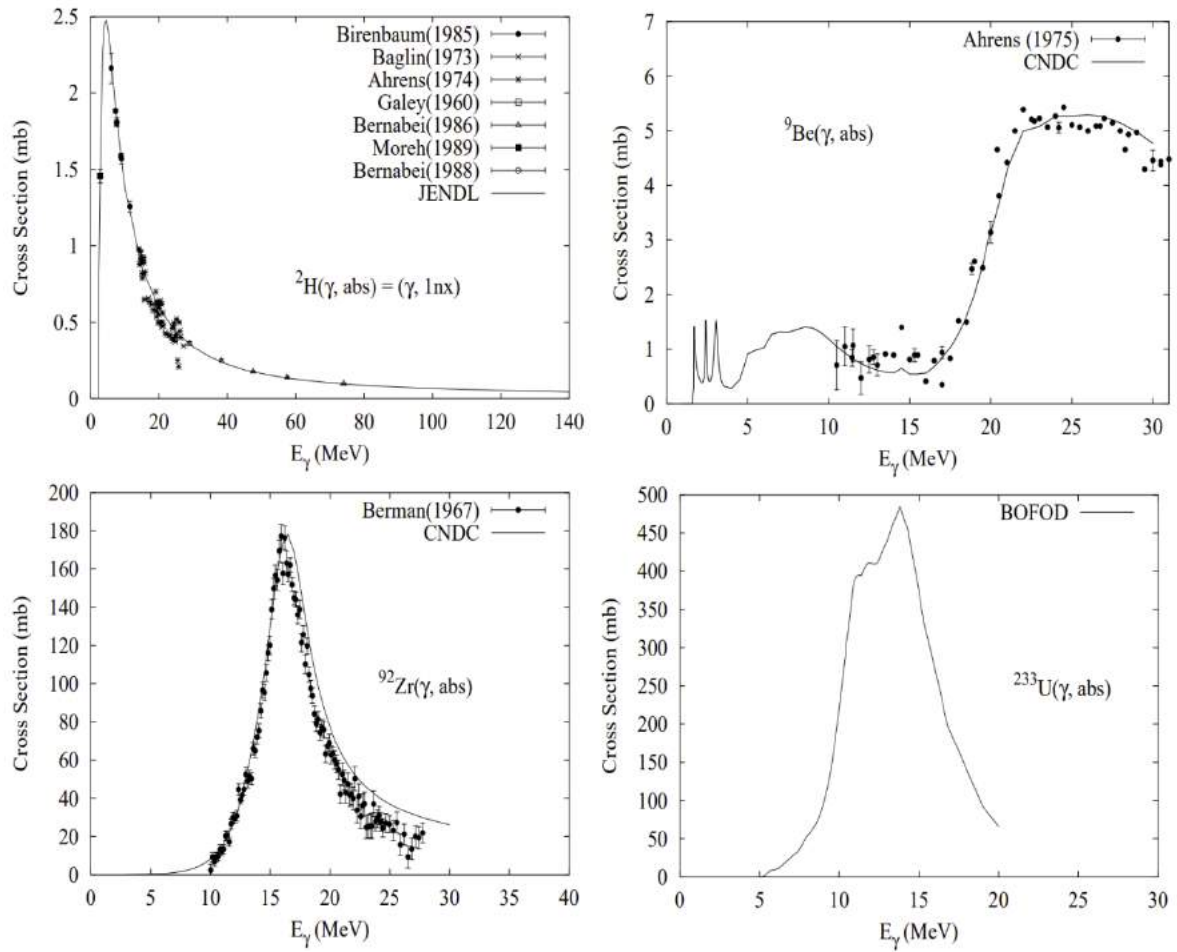


**Fig. 1.60:** Photonuclear absorption excitation function of deuterium, beryllium, zirconium and uranium. The thresholds for  $(\gamma, n)$  reactions are 2.226, 1.666, 8.64 and 5.74 MeV for deuterium, beryllium, zirconium and uranium, respectively [IAEANO.2].

Generally speaking, the threshold energy for photonuclear proton emission  $(\gamma, p)$  varies between 6 and 16 MeV [LR04]. It is of great importance to note that quantum energies greater than the energy threshold will appear as the kinetic energy of the emitted neutrons or, if large enough, may lead to the emission of charged particles from the nucleus [J17]. In Fig. 1.61, the cross-section of a)  $^{29}\text{Si}$  and b)  $^{105}\text{Pd}$  for different particle emissions due to photoabsorption is illustrated. As can be seen, in contrast to  $^{105}\text{Pd}$ , the probability of proton emission for  $^{29}\text{Si}$  is higher than that for neutron emission.



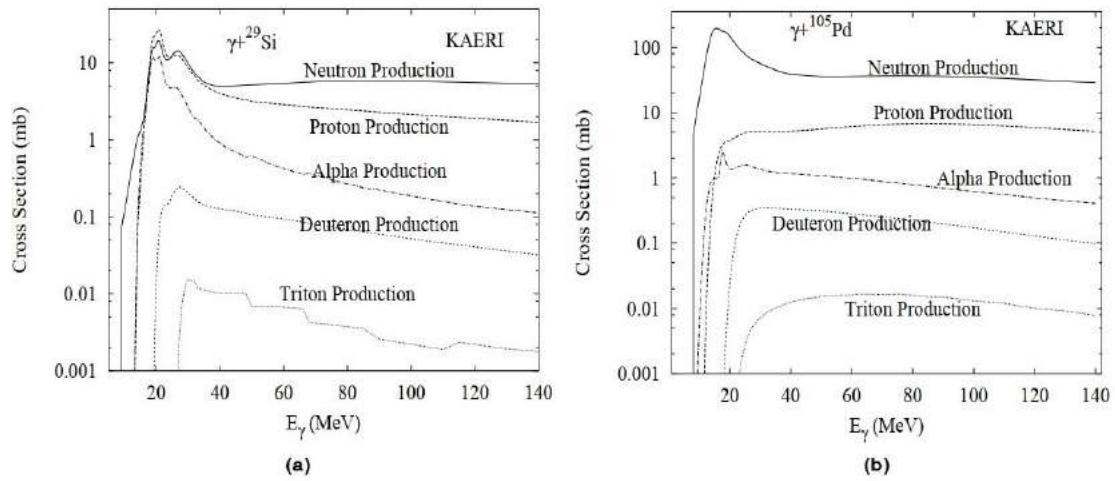


**Fig. 1.61:** Photoabsorption excitation function for different particle emissions of  $^{29}\text{Si}$  (a) and  $^{105}\text{Pd}$  (b) [IAEANO.2]

It has been revealed that the photonuclear absorption cross-section for most nuclei is similar to a Lorentzian distribution and can be fitted well with that (see Figs. 1.53 and 1.62a) [H07, TL15]. As can be seen later, there are some nuclei cases, where the shape of the excitation function is much more complicated so that instead of a single peak, a double, or even multiple peaks appear. However, regardless of the number of peaks, the shape of each peak in most cases follows a Lorentzian distribution (see Figs. 1.62b and 1.64) [H07, IAEANO.2].

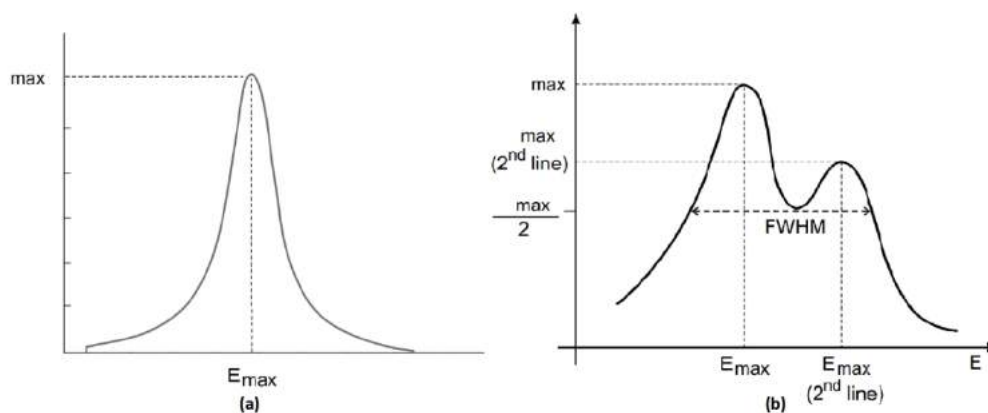


**Fig. 1.62:** Schematic representation of the Lorentzian distribution for (a) a single peak and (b) a double peak [TL15, IAEANO.2]. In the case of the double peak, the FWHM usually is larger than those of any two Lorentzian functions.

Most of the photonuclear absorption up to 30 MeV happens by dipole excitation of the nucleus known as Giant Dipole Resonance (GDR) [LR04]. More precisely, the GDR region is a range in cross-section in which most photoabsorption and other photonuclear interactions of almost all of the nuclei occur. In 1948, Goldhaber and Teller [G48] proposed that the peak in the cross-section was due to a nuclear resonance in which the neutrons in the nucleus move in one direction while the protons move in the opposite direction. These resonances are attributed to the enormous vibration of the neutrons as a collective against that of protons in the nucleus\* [H07, IAEANO.2]. Two years later (in 1950), Steinwedel and Jensen [SHJ50] proposed a two-fluid model of the giant resonance based on a similar idea in which two interpenetrating incompressible fluids are oscillating toward, and then away, from each other† [H07, G48]. This vibration process possesses a resonance frequency at which the absorbed photon is able to excite the nucleus, causing the nucleus to emit a neutron, a proton, etc. [H07]. The resonance happens for nuclei with mass number  $A$  around  $66 \times A^{-1/3} \text{ MeV}$  [R14]. For most middle and heavy mass nuclei, the GDR region is in the photon energy range of 8-30 MeV [VVRS99, IAEANO.2]. The dependence of the giant resonance energy on atomic mass number (i.e.,  $A^{-1/3}$ ) predicts a one-humped and a two-humped shape in cross-section for, spherical nuclei and deformed (nonspherical) nuclei, respectively (compare Figs. 1.63 and 1.64). This is due to the fact that the deformed nuclei have two characteristics of dimensions‡; therefore, two superpositions of resonance (which have an approximately 2:1 ratio of area for  $(\gamma, n)$  reactions) should appear in the cross-section [H70]. Fig. 1.64 shows the  $(\gamma, n)$  excitation function for holmium and erbium. As can be seen, the excitation function for these elements has two peaks denoting that they are deformed nuclei. Other examples of deformed nuclei are  $^{153}\text{Eu}$ ,  $^{159}\text{Tb}$ ,  $^{160}\text{Gd}$ ,  $^{165}\text{Ho}$ ,  $^{181}\text{Ta}$ ,  $^{186}\text{W}$ , and  $^{235}\text{U}$ . There are some nuclei having dynamic deformation, causing their photonuclear excitation function to appear much more complicated. Fig. 1.65 shows the  $(\gamma, n)$  excitation function for  $^{141}\text{Pr}$ . Refer to [H70] for more details. In the case of low atomic mass number, the GDR region is centered at 24 MeV, but decreases up to 12 MeV for the heaviest (i.e., high atomic mass number) stable nuclei. The peak width of the energy  $\Gamma$  (i.e., the energy difference between points around the peak where the photonuclear cross-section decreases by a factor two) changes between 3 and 9 MeV, depending on the target nucleus ( $\Gamma$  is in other words, the full-width-at-half-maximum FWHM) (see Fig. 1.66) [LR04, P16].

---

\* These resonance frequencies should be interpreted somewhat differently from those caused via definite nuclear levels and, in fact, analogous to the "reststrahl frequencies" of polar crystals. In the photonuclear absorption process, it is assumed that the photons excite a motion in the nucleus so that the bulk of the protons in the nucleus move in one direction, whereas the neutrons move in the opposite direction. This motion is called the "dipole vibration." Such a vibration has a high frequency due to the partial separation of the protons from the neutrons in the nucleus to which they are strongly bound. It has been shown that the magnitude of the integrated cross-section obtained from experimental measurements is too large to be explained as the result of the motion of a single proton or of a small fraction of the protons in the nucleus. This is the reason why in the photonuclear excitation function, only one peak (or two peaks, depending on the nucleus shape) is (are) observable. In fact, in the photonuclear absorption process, the nucleus vibrates as a whole [H07, G48, GT48].

† During dipole vibration, as a result of photonuclear absorption, the two neutron and proton fluids suffer a relative displacement at which, near the nucleus surface, the two neutron and proton fluids no longer overlap [G48, SHJ50].

‡ Most deformed nuclei are prolate ellipsoids [H07, G48].

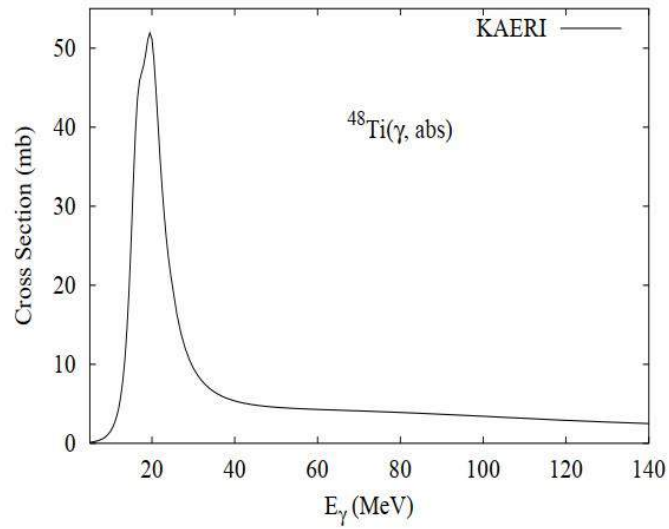


**Fig. 1.63:** Photoabsorption excitation function of  $^{48}\text{Ti}$  [IAEANO.2]

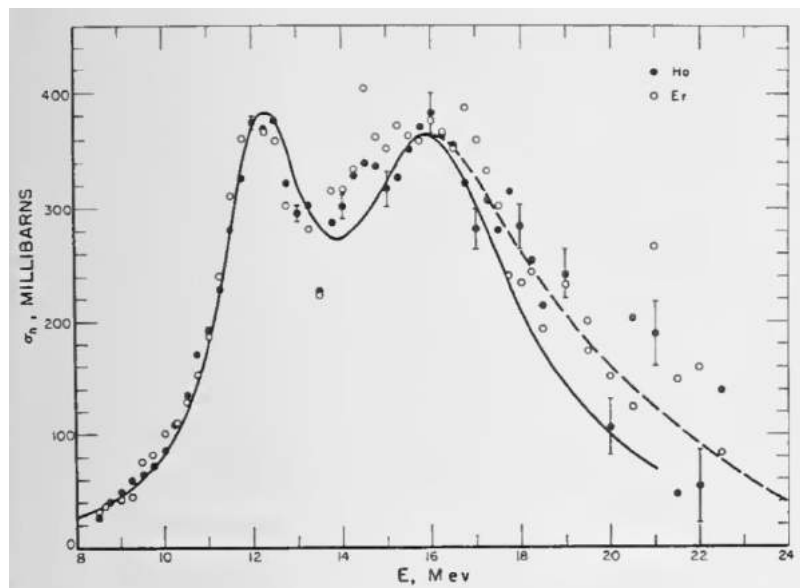


**Fig. 1.64:** The  $(\gamma, n)$  excitation function for  $^{165}\text{Ho}$  and  $^{166}\text{Er}$ . The solid curve is the sum of two Lorentz curves (applied for fitting), and the dashed line is a smooth curve through the data points [H70].

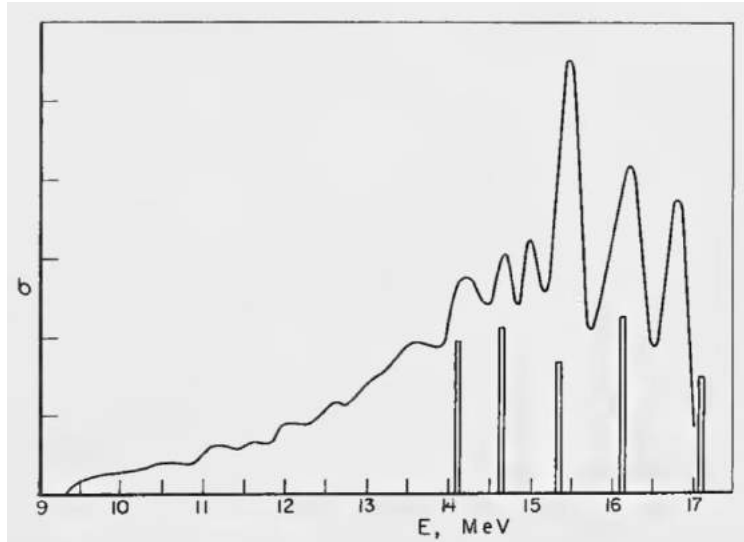


**Fig.1.65:** The  $(\gamma, n)$  reaction cross-section for  $^{141}\text{Pr}$  [H70]

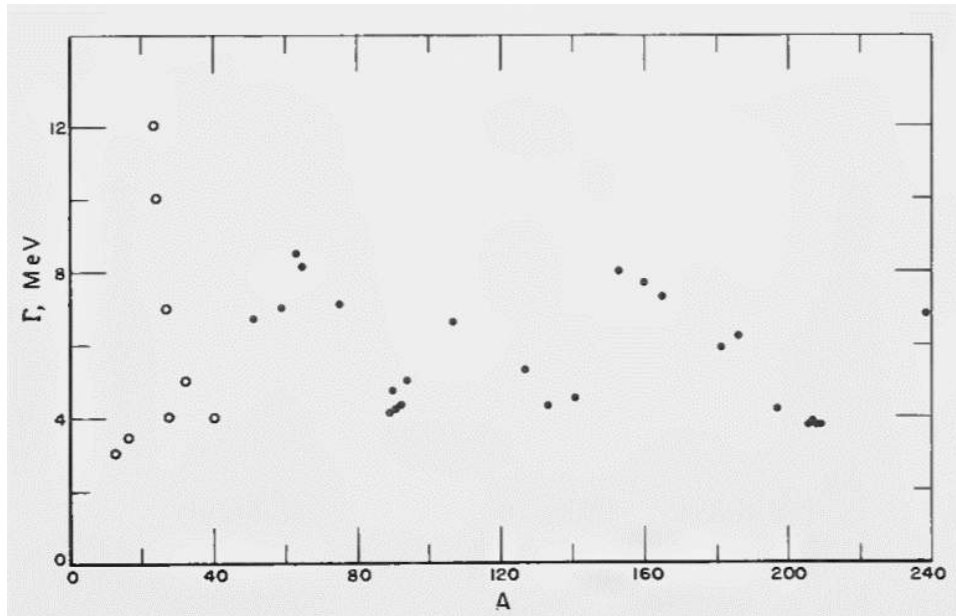


**Fig.1.66:** The peak width of the energy  $\Gamma$  as a function of atomic mass number  $A$ . The experimental data show that the average giant resonance width is about 5 MeV and that the dependency of  $\Gamma$  on atomic mass number  $A$  proceeds through several maxima. As is observable, these are associated with the three main regions of large intrinsic nuclear deformation, near  $A = 25$ , 160, and 240 [H70]. In general,  $\Gamma$  changes from 3-4 MeV for magic nuclei to larger values for nonspherical or deformed nuclei [VVR599].

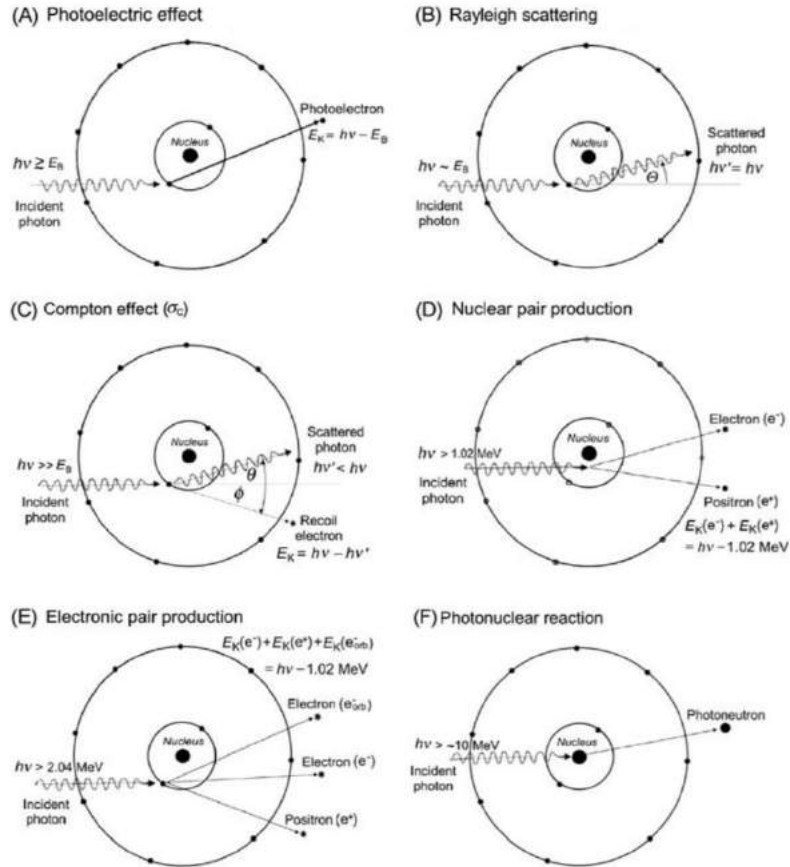
The photonuclear cross-section at the resonance peak is around 6% of the total atomic electron (electronic) cross-section for low mass number nuclei and is not higher than around 2% for high mass number nuclei [LR04].

In the case of photon energies corresponding to the giant resonance maximum (where the excitation function peaks), the angular distribution of emitted neutrons shows a symmetrical behavior centered around 90°; however, the angular distribution becomes less symmetric and more forward directed as the energy increases [LR04].

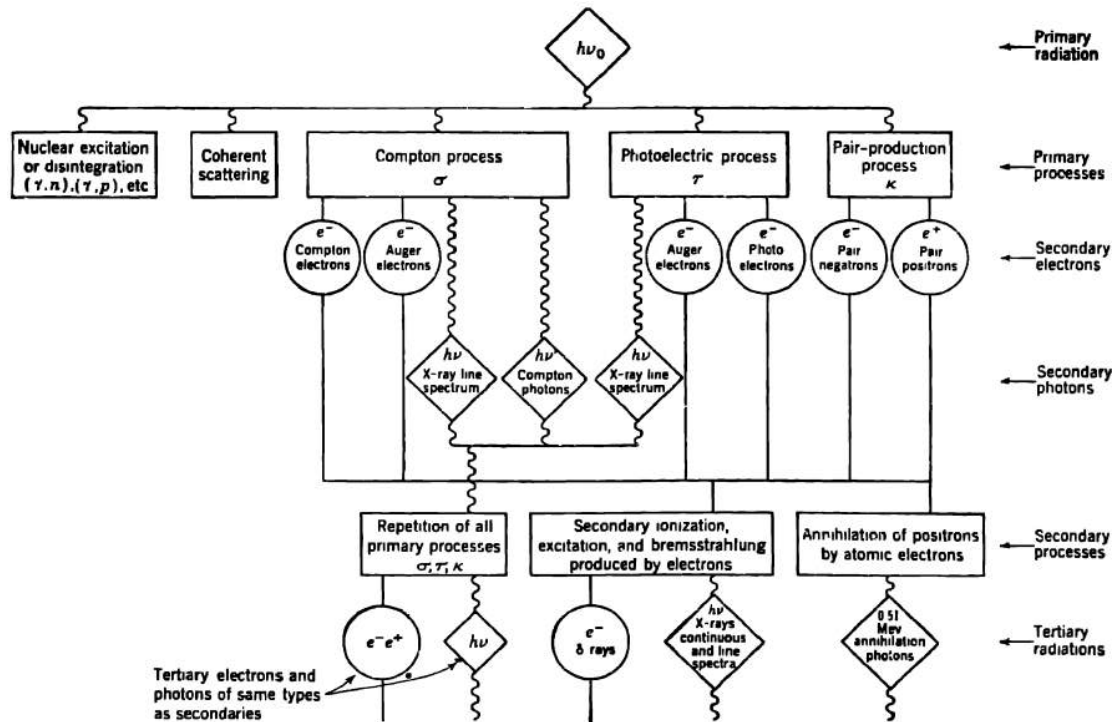
For energies below 30 MeV, the corresponding wavelength of the photon is in the range of the target nuclear dimension. However, as the energies increase above 30 MeV, the photon wavelength decreases to become smaller than the average inter-nucleon distance [LR04]. Therefore, the photon interaction can take place on a single or on few nucleons. It has been revealed that most of the reactions happen with nucleon pair (proton-neutron pair), so-called quasi-deuterons proposed by Levinger (1951) [LR04].

## Summary of photon interactions

In Figs.1.67 and 1.68, a brief representation of most of the photon interactions, which have been discussed earlier in this section, have been presented. Additionally, a summary of the important features for photon interaction mechanisms has been tabulated in Table 1.4. These features include the type of target, photon fate, and the possibility of charged particle production. As mentioned earlier, different photon interactions have different regions of high cross-sections for different materials. Fig.1.26 shows the cross-section as a function of photon energy for carbon and lead [S13]. In general, for low photon energies, the cross-section for Rayleigh scattering is higher than that for Compton scattering (the higher the atomic number  $Z$ , the larger the difference). Regardless of their difference, their values are negligible in comparison with the photoelectric cross-section [P09]. Generally speaking, for energies below 10 to 100 keV (which depends on the target atomic number), incident photons are absorbed by the photoelectric effect. At energies from tens of keV to around 10 MeV, or even lower energies in the case of very low atomic number of materials, the dominant interaction process can be considered as Compton scattering. Above these energies, the largest cross-section belongs to the pair production process. Among all other possible photon interaction types, the photonuclear process is more considerable and can contribute a few percent of the total cross-section (depending on the material) in its highest energy region (between 8 to 30 MeV) as was shown in Fig.1.26b [C07]. The largest and dominant cross-section for photon interaction with matter is presented in Fig.1.69, as a function of target atomic number and incident photon energy.



**Fig. 1.67:** Schematic representation of different photon interactions with matter. Note that electronic pair production in (E) refers the triplet production [P14, P16].

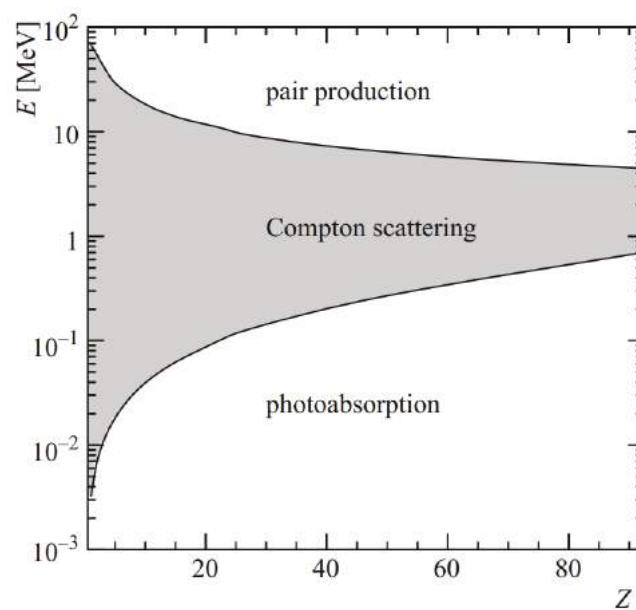


**Fig.1.68** Schematic block diagram representation of the interaction of photons with matter [E55]

**Table 1.4**

Photon interactions and their properties [P16]

Interaction	Type of targets		Photon fate after interaction		Production of charged particle after interaction			
	Orbital electron (bound, free, coulomb field)	Nuclei	Complete absorption	Scattering	No charged particle released	Only electron released	Electrons and positrons produced and released	Other charged particle produced and released
Nuclear pair production	✓	✓	✓				✓	
Compton effect	✓			✓		✓		
Photoelectric effect	✓		✓			✓		
Thomson scattering	✓			✓	✓			
Rayleigh scattering	✓			✓	✓			
Electronic pair production	✓	✓	✓				✓	
Photonuclear		✓	✓					✓

**Fig. 1.69:** Major photon cross-section of different interactions with different atomic number and incident photon energy [FS20]

### 1.3 Heat transfer mechanisms

Heat transfer is energy in transit that occurs because of a temperature gradient or difference. The temperature difference is thought of as a driving force, which causes heat to flow [J00]. The heat transfer mechanisms are generally classified into conduction, convection, and radiation, although most engineering applications are combinations of two or three of them (see Fig. 1.70) [K50].

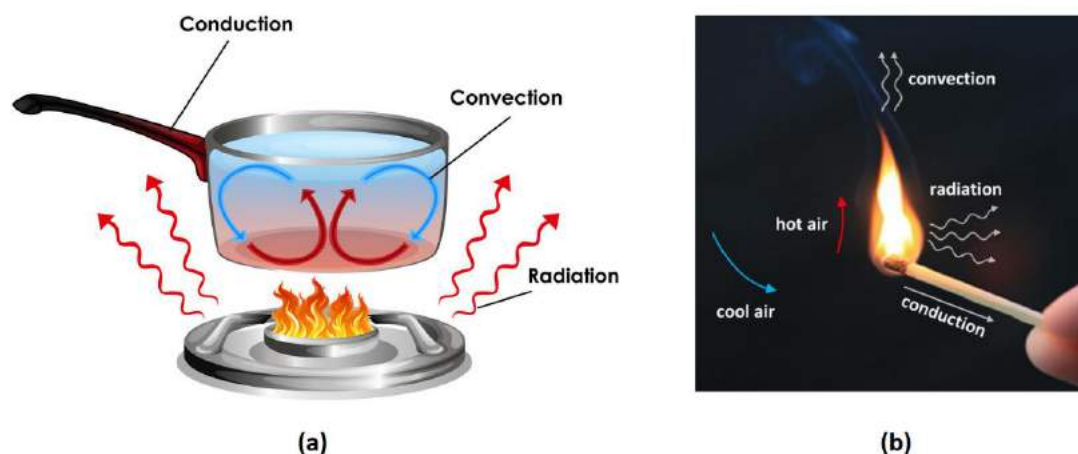


Fig.1.70: Three mechanisms for the heat transfer [KBKW21, Z19]

#### 1.3.1 Conduction

In 1822, Joseph Fourier published his book “Théorie Analytique de la Chaleur”, in which he formulated and presented a complete exposition of heat conduction theory [L03]. Conduction is a mechanism in which heat transfers through a substance without perceptible motion of the substance itself [J00]. Heat can be conducted through gases, liquids, and solids. In the case of gases, molecules have higher velocities in high-temperature regions compared to those in low-temperature regions. The random motion of molecules leads to collisions, and finally, an exchange of momentum and energy. Considering this random motion and a temperature gradient in the gas, molecules transfer some of their energy, through collisions, from the high-temperature region to molecules in the low-temperature region. This transport of energy is identified as heat transfer by the diffusive or conductive mechanism [J00]. In fluids, conduction is generally the primary heat transfer mechanism when the fluid poses zero bulk velocity. The conduction of heat in liquids is almost the same as for gases (i.e., random collisions of molecules with high energies with those molecules that have lower energies causing a transfer of heat). However, due to the fact that the molecules are more closely spaced in liquids compared to gases, the situation in liquids is more complex for the energy exchange between molecules. In opaque solids, conduction is considered as the only mechanism by which heat can be transferred. In the case of solids, the conduction of heat is due to the motion of free electrons, magnetic excitations, lattice waves, and electromagnetic radiation [J00]. Motion of free electrons occurs only in substances that are good electrical conductors, because the heat can be transported by electrons that are free to travel through



the lattice structure of these substances (i.e., the conductor), in the same way that electricity is conducted (this is usually considered for metals). In the case of magnetic excitations, magnetic dipoles of adjacent atoms (in some cases) could provide interactions between the magnetic moments, which may aid heat conduction in the solid. In the case of lattice waves, the molecular energy of vibration in a substance can be transmitted between adjacent solid molecules or atoms from a high-temperature region to a low-temperature region. In contrast to nonmetals, the lattice-wave mechanism is usually considered not to be a significant factor in the conduction of heat through metals. In translucent materials, electromagnetic radiation may have an influence on the conduction of heat (when the solid material has little capacity to absorb energy).

In Fig. 1.71, thermal conduction through a wall is presented. The direction of the heat flow is at a 90-degree angle to the wall (if the wall surfaces are considered isothermal\* and the body isotropic and homogeneous). The heat flow is proportional to the change of temperature through the wall (i.e., the temperature gradient, shown in general as  $\nabla T$  in the three-dimensional case) and the area of the wall (shown as  $A$ ). Considering  $T$ , as the temperature at any point in the wall, and  $x$  (in the one-dimensional case), as the wall thickness in the direction of heat flow, one can formulate the quantity of heat flow ( $dQ$ ) as [K50]:

$$dq = kA \left( -\frac{dT}{dx} \right), \quad (1.52)$$

where  $k$  is the constant of proportionality (called thermal conductivity, in units of W/m·K or J/m·s·K) and is evaluated experimentally [K50]. In Eq.1.52, the temperature gradient has a negative sign if the temperature in  $x = 0$ , has a higher value compared to the temperature where  $x = X$ . Although the thermal conductivities are usually associated with heat transfer in solids, they are also applicable with limitations in solids and liquids (as discussed above) [K50]. In Fig.1.72, the approximated ranges of the thermal conductivity (in units of W/m·°C) of some substances are presented. As can be seen, the difference in thermal conductivity is enormous (e.g.,  $k$  varies by a factor of  $10^5$  between diamond and gases at room temperature and can be increased up to  $10^7$  considering superinsulation). The thermal conductivity of substances usually depends on the temperature. Fig.1.73 shows variations in thermal conductivity versus temperature for some materials. As is observable, different substances show a different trend of variations against an increase in temperature [H86].

---

\* An isothermal surface is a surface in which all points of it have the same temperature [K50, J00].

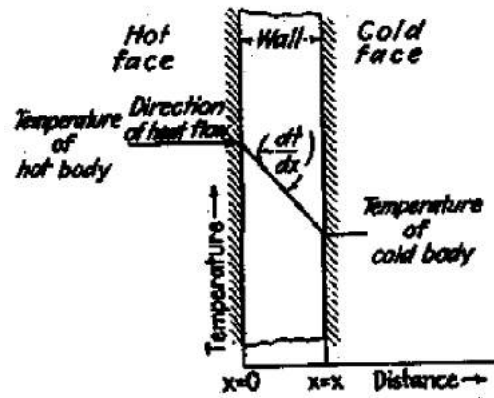


**Fig. 1.71:** A schematic representation of heat flow through a wall [K50]

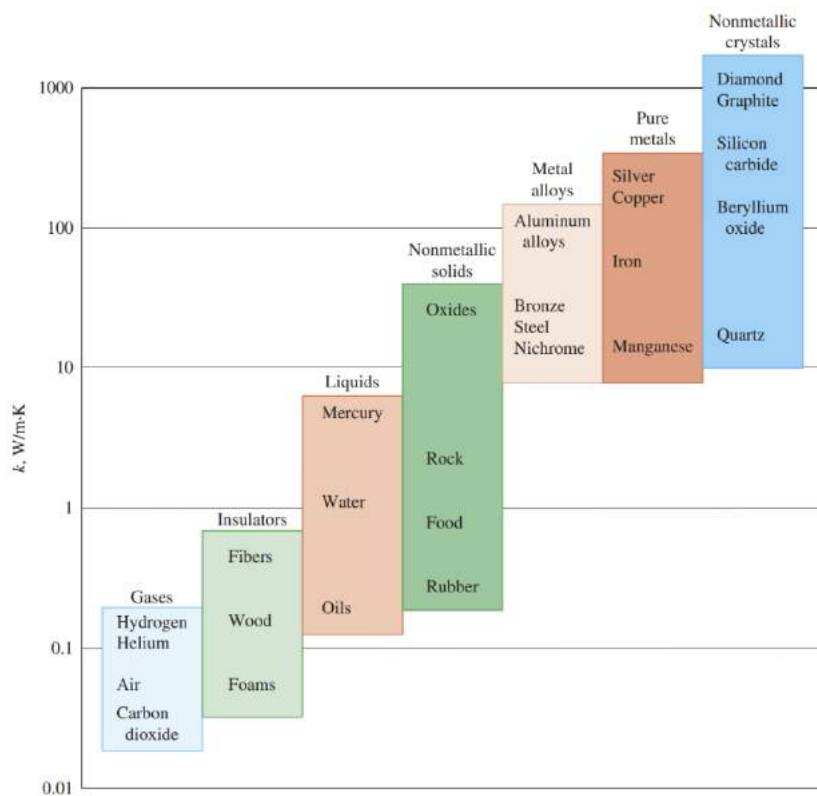


**Fig.1.72:** Thermal conductivity ranges of some substances (all values are given at room temperature) [LQT18]

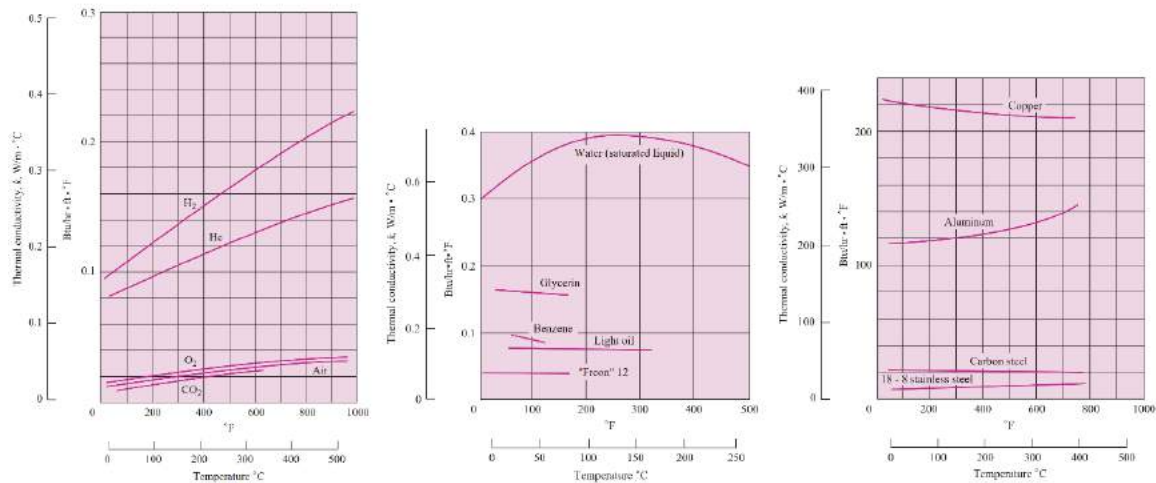


**Fig.1.73:** Thermal conductivities variations versus temperature for different substances [H10]

### 1.3.2 Convection

Thermal convection is applied to heat transfer as a result of the bulk movement of a fluid [J00]. In thermal convection, the heat being carried as internal energy due to the macroscopic motion of the fluid. Considering the heat transfer coefficient,  $h$ , the “wetted” surface area  $S$ , and surface-to-fluid temperature difference, convective thermal transport from a surface to a fluid in motion can be expressed as [BB03, K50]:

$$dq = hS dt. \quad (1.53)$$

The value of  $h$  is influenced by the nature of the fluid, the velocity of the flowing fluid, and temperature [BB03]. As an illustration, the value of  $h$  for air and water can differ up to 30 times in magnitude [KBKW21]. When Eq.1.53 is presented in integrated form, it is called Newton’s law of cooling (as Isaac Newton considered the convective process and formulated it in 1701 [L03, K50]). In general, there are two types of convection, natural (or free) convection, and forced convection. In the case of the former, a density difference resulting from temperature gradients in the fluid induces fluid motion. In the latter case, an external device (e.g., stirrers, pumps, and fans) provides fluid movement and, therefore, enhances heat transfer (see Fig. 1.74) [K50]. As can reasonably be argued, the convective heat transfer coefficient for forced convection is higher than natural convection. For example, in the case of air, the range of the convective heat transfer coefficient changes from 2.5-25 W/m<sup>2</sup>·K for natural convection to 10-500 W/m<sup>2</sup>·K for forced convection [KBKW21]. The forced convection mechanism is one of the main forms of heat transfer, which is used in cooling of electronics, heating, and air conditioning systems, and in numerous other technologies because of the large amounts of thermal energy that can be transferred efficiently [KBKW21].

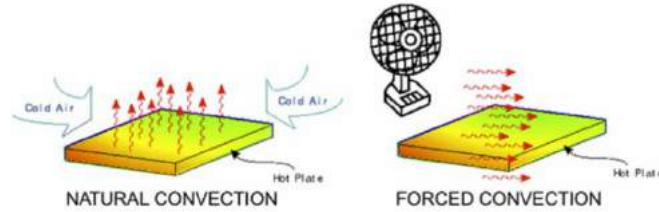


**Fig.1.74:** A schematic representation of the difference in mechanism for natural and forced convection. Natural convection (the LHS figure) is induced via a difference in hot and cold fluid density. In contrast, in forced convection (the RHS figure), fluid movement is forced by an external device (for example, by a cooling fan) [SOLID10].

Convection heat transfer is associated with fluid motion and is worth to be considered in more detail. Fig.1.75 shows an immersed plate in a uniform flow. As can be seen, the plate is heated to maintain the plate surface at a constant temperature  $T_w$  (uniformly). The fluid's uniform velocity and temperature (far from the heat plate, known as the *free-stream value*) are shown as  $V_\infty$  and  $T_\infty$ , respectively. As is observable, the velocity distribution (labeled as  $V$ ) at any location on the axes versus  $y$  is illustrated. As a result of the nonslip condition, which denotes that the fluid adheres to the wall because of viscous or friction effects, the velocity of the fluid at the wall is zero (see Fig.1.75). More precisely, the velocity of the fluid increases by increasing  $y$  from zero (at the wall) to nearly the free-stream value located at some vertical distance away, known as the *hydrodynamic boundary layer* (shown as  $\delta_h$  or simply as  $\delta$ ).

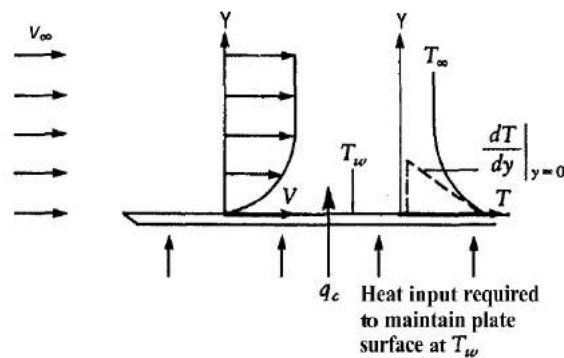


**Fig.1.75:** Schematic representation of uniform flow past a heated plate [J00]

In Fig.1.75, the temperature distribution versus  $y$  is also illustrated. As is shown, the temperature decreases from  $T_w$  (at the wall) to  $T_\infty$  (at some distances from the wall, known as the *thermal-boundary layer thickness*  $\delta_T$ ). According to Fig.1.75, heat is transferred from the plate wall to the fluid where (i.e., within the fluid) the mechanism of heat transfer at the plate wall is conduction due to the fact that the velocity of the fluid is zero there. The rate of heat transfer is proportional to the slope of  $T$  (i.e., temperature) versus the  $y$  curve at the plate wall ( $\frac{dT}{dy}$  at  $y = 0$ ). A steeper slope indicates a greater temperature difference (temperature gradient) at the fluid-solid interface and considerably relies on flow velocity. In fact, the distance from the wall in which the temperature reaches  $T_\infty$  is influenced by the flow velocity.

Considering  $q_c$  as the convection heat transfer and  $\bar{h}_c$  as the average convection heat transfer coefficient,  $q_c$  can be formulated as [J00]:

$$q_c = \bar{h}_c S (T_w - T_\infty). \quad (1.54)$$

Eq.1.54 is similar to Eq.1.53, except for  $\bar{h}_c$ . In Eq.1.54,  $\bar{h}_c$  accounts for the overall effects embodied in the convection heat transfer process, and the overbar notation indicates that the coefficient is an average over the length of the heated plate. Note that for some simple geometries,  $\bar{h}_c$  can be obtained analytically; however, in most cases, it must be measured. Additionally,  $\bar{h}_c$  can be affected by the flow velocity since, as mentioned above, the flow velocity influences the temperature gradient in the fluid-solid interface. Since viscosity and density (e.g., laminar versus turbulent flow, which is discussed later in this chapter) affect the flow velocity profile, they can also influence  $\bar{h}_c$  [J00].

In Fig.1.76, a schematic representation of the hydrodynamic boundary layer  $\delta$ , and thermal-boundary layer thickness  $\delta_T$  is presented. As is observable, there is a difference in magnitude between them, the thickness ratio denoted as  $\Delta$ , and therefore, they can be expressed based on each other as:

$$\delta_T = \Delta \cdot \delta. \quad (1.55)$$

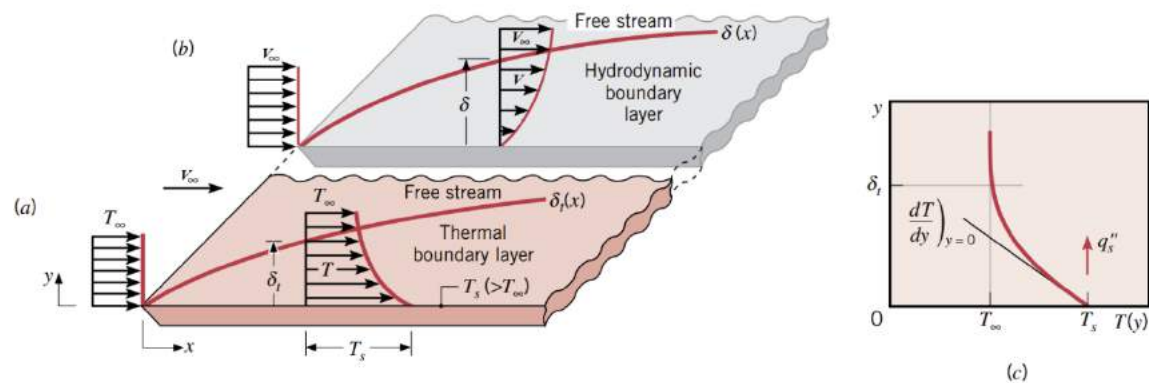


**Fig.1.76:** Schematic representation for (a) thermal-boundary layer thickness  $\delta_T$ , (b) hydrodynamic boundary layer  $\delta$ , and the temperature gradient at the surface [MSMD03]

The mathematical description of  $\delta$  was first made by Prandtl in 1904 [L03] and can be formulated in the case of a flat surface as:

$$\frac{\delta}{x} = \frac{4.92}{\sqrt{Re_x}}, \quad (1.56)$$

where  $Re_x$  is called the *Reynolds number* and characterizes the relative effects of inertial and viscous forces (in a fluid problem). The Reynolds number was introduced by Osborne Reynolds in the 1870s when he discovered the laminar-turbulent transition [L03].  $Re_x$  can be obtained as follows [L03]:

$$Re_x = \frac{\rho V_\infty x}{\mu} = \frac{V_\infty x}{\vartheta}, \quad (1.57)$$

where  $\mu$  is the dynamic viscosity (in units of  $\text{kg.m}^{-1}.\text{s}^{-1}$ ),  $\vartheta$  is the kinematic viscosity (in units of  $\text{m}^2\text{s}^{-1}$ , and is the ratio of the viscous force to the inertial force, i.e.,  $\frac{\mu}{\rho}$ ), and  $\rho$  is the fluid density (in units of  $\text{kg.m}^{-3}$ ).

$\Delta$  in Eq.1.55 can be determined based on the ratio of the thermal and the momentum diffusivity (of the fluid) that is expressed using the dimensionless *Prandtl number* ( $Pr$ ), obtained as:

$$Pr = \frac{c_p \cdot \mu}{k}. \quad (1.58)$$

In Eq.1.58,  $C_p$  is the heat capacity of the fluid (in units of  $\text{J.kg}^{-1}.\text{K}^{-1}$ ) and  $k$  the heat conductivity (in units of  $\text{W.K}^{-1}.\text{m}^{-1}$ ). In the case of gases, mostly  $Pr \approx 1$ , which results in  $\delta_T = \delta$ . However, for most liquids  $Pr > 1$ , that leads to  $\Delta < 1$ , and therefore  $\delta_T < \delta$  [SIP13]. In general, the *Prandtl number* is the ratio of the hydrodynamic boundary layer  $\delta$  to the thermal boundary layer  $\delta_T$ . As is shown in Fig.1.77a, if  $Pr < 1$ , the thermal boundary layer is larger than the hydrodynamic boundary layer ( $\delta_T > \delta$ ), and if  $Pr > 1$ , the opposite is true (see Fig.1.77b) [MMD16].

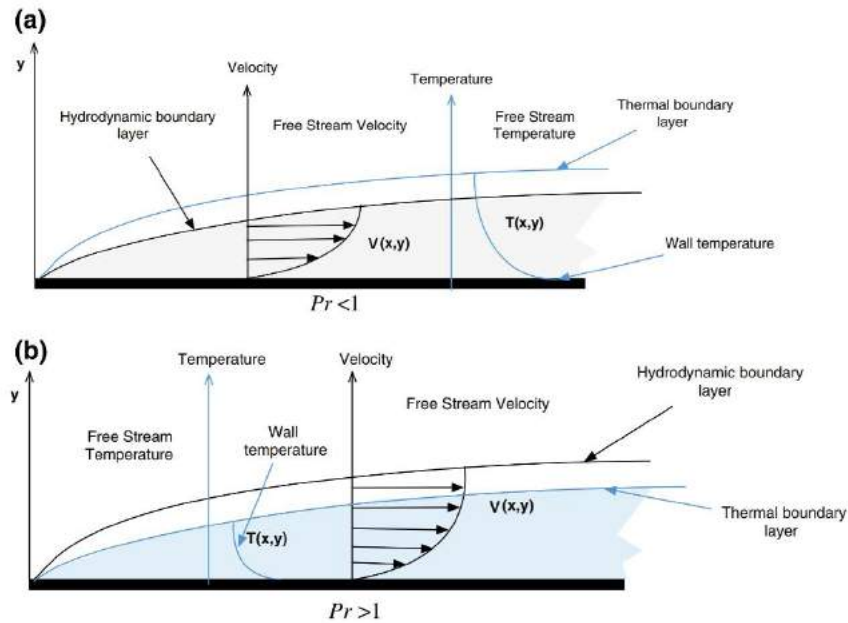


**Fig. 1.77:** A schematic representation of the hydrodynamic and thermal boundary layers for (a)  $Pr < 1$ , and (b)  $Pr > 1$  [MMD16]

Note that in Fig.1.75, it was assumed that the plate is heated from  $x = 0$ ; however, in a more complex condition, it is also possible that there is a difference in distance from the heating and flow starting point as is shown in Fig 1.78 ( $X_0$  in Fig. 1.78). Through the passing of a fluid on a plate, different flow regimes are developed. These flow regimes can significantly be

influenced by the boundary layer, and, therefore, by the convection heat transfer coefficient,  $h$ .

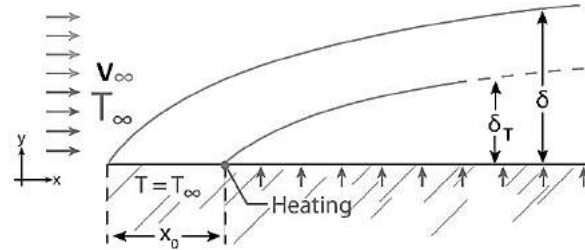


**Fig.1.78:** Schematic representation for the hydrodynamic boundary layer  $\delta$ , and the thermal-boundary layer thickness  $\delta_T$  when there is a difference in the heat and flow starting point, shown as  $X_0$  [YT].

Fig.1.79 shows a schematic representation of the developed flow regimes including laminar, transition, and turbulent flow for a flat surface. In the laminar regime, fluid motion is considered highly ordered and characterized by velocity. After the laminar regime, some disturbances in the flow are created, and therefore, transition to the turbulent regime occurs. In the turbulent regime, fluid motion is highly irregular and can be characterized by velocity fluctuations that result in enhancement of the energy transfer [MSMD03]. The flow regimes of a fluid can be determined based on the Reynolds number. Accordingly, one can find a critical value for  $x$  (shown as  $x_{cr}$  in Fig.1.79) and accordingly obtain a critical value for the Reynolds number (expressed as  $Re_{x_{cr}}$ ) in which the flow regime changes from laminar flow to turbulent flow. Considering Eq.1.59, one can obtain  $Re_{x_{cr}}$  as [L03]:

$$Re_{x_{cr}} = \frac{V_{\infty} x_{cr}}{\nu}. \quad (1.59)$$

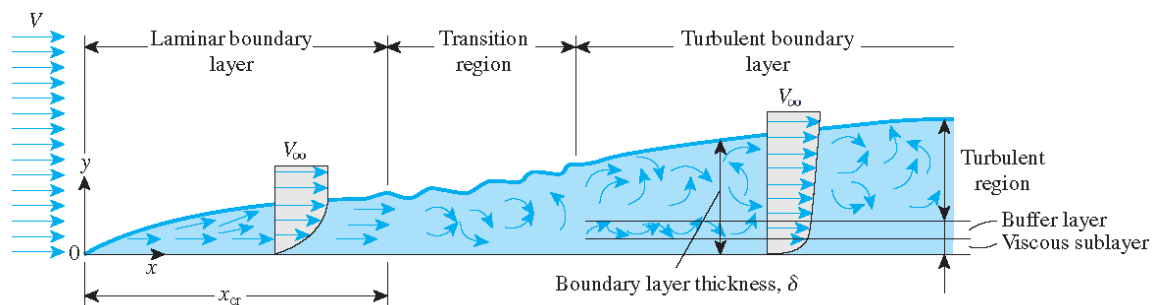


**Fig.1.79:** Schematic representation of the effects of the fluid flow regimes on hydrodynamic boundary layer  $\delta$  [STACK]. For explanations about the buffer layer and viscous sublayer refer to [SG16, R82] for more details.

According to the above discussion, one can also illustrate the flow regime as a function of the Reynolds number (see Fig.1.80). In Fig.1.80, the corresponding Reynolds number for each flow regime is presented. According to this figure,  $Re_{x_{cr}} = 3.5 \times 10^5$ ; however, the actual value depends significantly on the roughness of the wall, the shape of the leading edge of the plate, the probable presence of acoustic or structural vibration, etc. [L03].

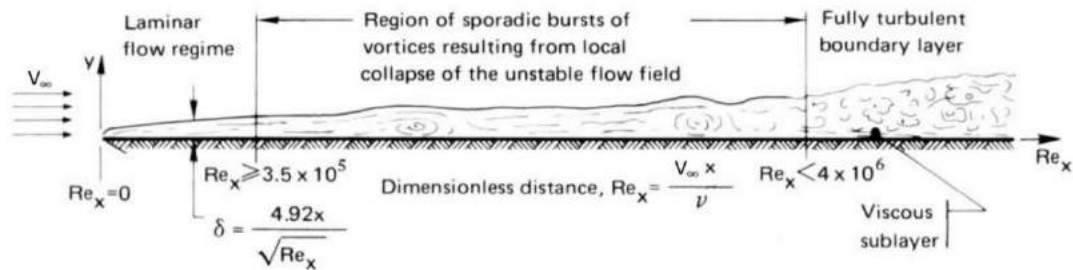


**Fig. 1.80:** Schematic representation of the fluid flow regimes as a function of the Reynolds number [L03]

As was discussed before, the change in density and viscosity of the fluid affects the convection heat transfer coefficient  $h$ . On this basis, it can reasonably be argued that  $h$  can significantly be influenced by the flow regime (see Fig.1.81).

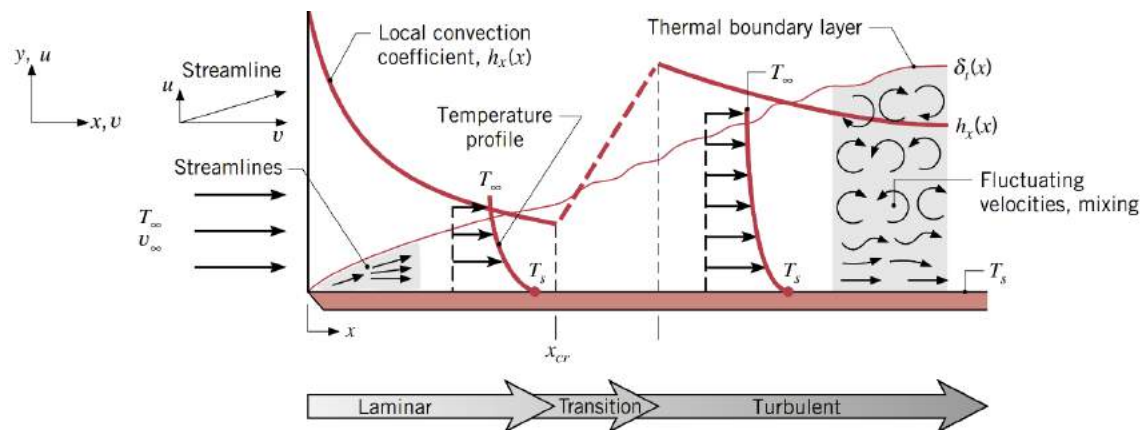


**Fig.1.81:** Variation of the convection heat transfer coefficient  $h$ , and hydrodynamic boundary layer  $\delta$  as a function of the flow regime. In the turbulent regime, fluid motion is highly irregular and can be characterized by velocity fluctuations that result in the enhancement of energy transfer. Because of fluid mixing, which results from fluctuations, the turbulent boundary layer is thicker compared to other regimes. Therefore, the temperature profile is flatter; however, the temperature gradient at the surface is steeper compared to laminar flow. So, the turbulent regime's local convection coefficient is more than the laminar regime [MSMD03].



As is observable in Fig.1.81, the convection heat transfer coefficient  $h$  increases suddenly as the flow regime changes from laminar to transition and then to turbulent due to a considerable mixing of different fluid layers in the flow (see caption of Fig.1.81). According to Fourier's law of the fluid (see Eq. 1.52), at any distance  $x$  from the leading edge, where  $y = 0$ , using the temperature gradient and the thermal conductivity of the fluid  $k$ , one can obtain the local heat flux as [MSMD03] (see Fig. 1.77c):

$$q_s'' = -k \frac{\partial T}{\partial y} \Big|_{y=0}. \quad (1.60)$$

As mentioned above,  $k$  is the fluid's thermal conductivity and is appropriate as the result of the nonslip condition. Considering that the surface heat flux also equals the convective heat flux that is mentioned by [MSMD03]:

$$q_s'' = q_{conv}'' = h_x(T_s - T_\infty), \quad (1.61)$$

one can obtain the local convection coefficient by combining Eqs.1.60 and 1.61 as [MSMD03]:

$$h_x = \frac{-k \frac{\partial T}{\partial y} \Big|_{y=0}}{T_s - T_\infty}. \quad (1.62)$$

Another important point is that in each flow regime, the convection heat transfer coefficient  $h$  decreases in a gradual manner over the surface thickness (see Fig.1.81). Considering Fig.1.77a, as the thermal boundary layer increases with  $x$ , the temperature gradient (in the boundary layer) must decrease with  $x$ , which, according to Eq.1.61, results in a decrease of  $q_s''$  and therefore, by considering Eq.1.62, a decrease of  $h_x$  (see Fig.1.81).

### 1.3.3 Radiation

Radiation refers to the transfer of energy via electromagnetic radiation that has a defined range of wavelengths [J00]. The entire electromagnetic spectrum is presented in Fig.1.82. Considering the gamma rays, their energy is very high, and the corresponding wavelength is very low. In contrast, radio waves, at the other end of the spectrum, have very low energy and, therefore, high wavelength. At a given temperature, a body emits radiation not only of a single wavelength but also at a wide range of wavelengths. Using a dispersing prism or thermopile, the intensity of the emitted radiation at each wavelength can be determined [K50].

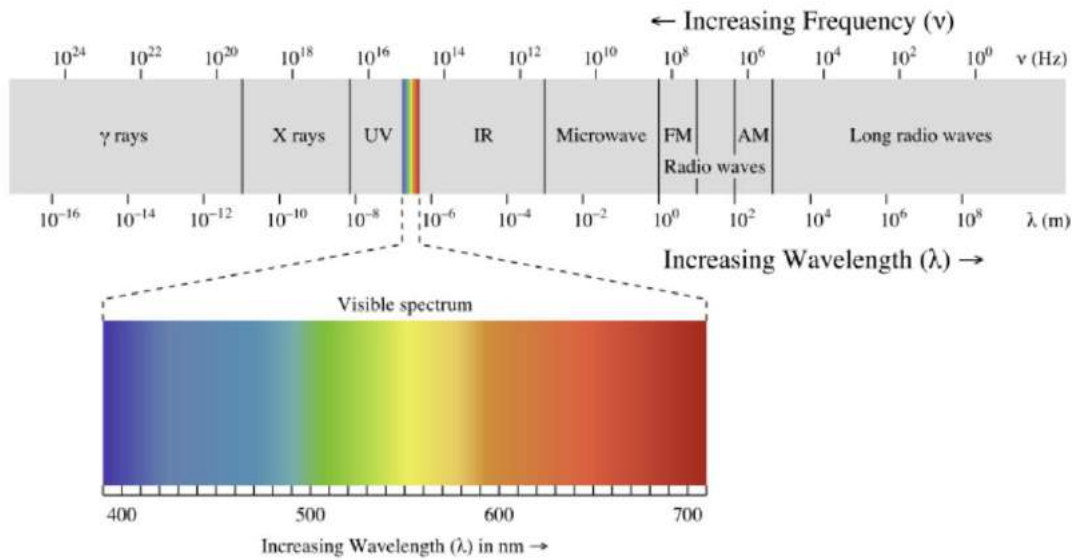


**Fig.1.82:** The electromagnetic spectrum [ELEC19]

Part of this energy is absorbed by the material and partially reflected by it. Boltzmann established that the rate of heat that a source gives off could be described as [K50]:

$$dq = \varepsilon \sigma dA T^4, \quad (1.63)$$

where  $T$  is the absolute temperature,  $\sigma$  refers to a dimensional constant (called *Stefan–Boltzmann constant* and is equal to  $5.670 \times 10^{-8} \text{ W} \cdot \text{m}^{-2} \cdot \text{K}^4$ ), and  $\varepsilon$  is called emissivity, a factor peculiar to radiation.  $\varepsilon$  is in the range  $0 \leq \varepsilon \leq 1$ . Accordingly, one can obtain the maximum rate of radiation that a surface at temperature  $T$  can emit as [LQT18]:

$$dq = \sigma dA T^4, \quad (1.64)$$

The idealized surface, which is able to emit such a maximum rate of radiation, is called a blackbody ( $\varepsilon = 1$ ), and therefore, the radiation that is emitted by a blackbody is called blackbody radiation. Similar to  $k$  (the thermal conductivity) and  $h$  (the convective heat transfer coefficient),  $\varepsilon$  (the emissivity) is determined experimentally [K50].  $\varepsilon$  value can significantly be influenced by the surface of a substance. To realize the difference in  $\varepsilon$  for a

material, one can consider Gold. Gold with a polished surface has a normal  $\varepsilon$  of 0.025, whereas an unpolished gold surface has a  $\varepsilon$  of 0.47 [J00]. The emissivity of some metallic solids is presented in Table 1.5. As is shown, the emissivity value not only depends on the type of material, but also on the surface condition [J00]. For facilitating comparison, the emissivity of some nonmetallic solids is presented in Table 1.6. According to the values presented in Tables 1.5 and 1.6, the emissivity values of metallic solids are much lower than those for other materials.

**Table 1.5**

Normal emissivity of different metals [J00]

Material	Surface condition	Temperature (K)	Emissivity, $\varepsilon$
Aluminum	Polished plate	296	0.040
		498	0.039
	Rolled and polished	443	0.039
		298	0.070
Chromium	Polished	423	0.058
Copper	Black oxidized	293	0.780
	Tarnished lightly	293	0.037
	Polished	293	0.030
Gold	Not polished	293	0.47
	Polished	293	0.025
Iron	Smooth oxidized	398	0.78
	Ground bright	293	0.24
	Polished	698	0.144
Lead	Gray oxidized	293	0.28
	Polished	403	0.056
Nickle	Oxidized	373	0.41
	Polished	373	0.045
Silver	Polished	293	0.025
Steel	Rough oxidized	313	0.94
	Ground	1213	0.520
Tungsten	Filament	3300	0.39
Zinc	Tarnished	293	0.25
	Polished	503	0.045

**Table 1.6**

Emissivity of different nonmetallic solids [J00]

Material	Temperature (K)	Emissivity, $\epsilon$
<b>Asphalt pavement</b>	300	0.85-0.93
<b>Building materials</b>		
<b>Red brick</b>	300	0.93-0.96
<b>Gypsum or plasterboard</b>	300	0.90-0.92
<b>Wood</b>	300	0.82-0.92
<b>Concrete</b>	300	0.88-0.93
<b>Cloth</b>	300	0.75-0.90
<b>Glass, window</b>	300	0.90-0.95
<b>Ice</b>	273	0.95-0.98
<b>Paint</b>		
<b>Black</b>	300	0.98
<b>White</b>	300	0.90-0.92
<b>Paper, white</b>	300	0.92-0.97
<b>Skin</b>	300	0.95
<b>Snow</b>	273	0.82-0.90
<b>Water</b>	300	0.96

By considering Eq.1.64, one can also reasonably argue that a non-linearity exists in Eq.1.64, due to the proportionality of  $q$  to the fourth power of temperature [B14]. This implies that the importance of the radiation heat transfer mechanism increases non-linearly by increasing temperature so that it is the dominant mechanism of heat transfer for temperatures beyond 1200 °C or 1500 °C. Even at low temperatures, if convection in the air is the case, free or forced, radiation cannot be neglected. If instead of air, water is used, the radiation contribution can be neglected due to the significant thermal conductivity of water (0.6 W/mK) [B14].

Another important point about the radiation term is that there is no material medium needed for the propagation of radiation. To be more precise, radiation travels best in vacuum compared to other mediums due to the absence of any distortion (including absorption or scattering) in vacuum [B14].

Absorptivity  $\alpha_{ab}$  of a surface is another important radiation property of a surface and is defined as the fraction of the radiation energy that impinges on a surface and is absorbed. Similar to the emissivity,  $\alpha$  is in the range of  $0 \leq \alpha_{ab} \leq 1$  [LQT18]. Generally, both  $\alpha_{ab}$  and  $\epsilon$  are dependent on the temperature of the surface and the wavelength of the radiation. According to Kirchhoff's law of radiation, the absorptivity and emissivity of a surface at a given temperature and radiation wavelength are equal. In the case of opaque surfaces, the portion of incident radiation that is not absorbed is reflected back (see Fig.1.83) [LQT18, H10].

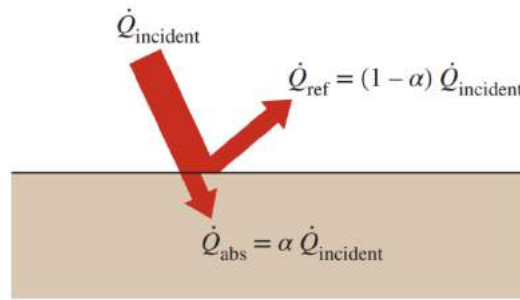


**Fig. 1.83:** Schematic representation of the radiation energy reflection and absorption of an opaque surface, where  $\dot{Q}_{incident}$  is the rate of incident radiation energy on the surface,  $\dot{Q}_{ref}$  is the rate of radiation that is reflected back from the surface and  $\dot{Q}_{abs}$  is the absorbed radiation energy within the body [LQT18].

In general, the net radiation heat transfer can be considered as the difference between the radiation absorbed and emitted by the surface. Therefore, a surface is gaining energy (by radiation) if the rate of radiation emission is less than the rate of radiation absorption. Otherwise, one can say that the surface is losing energy by radiation.

## Surface types

In general, any surface at a given temperature (consider it as  $T_s$ ) emits radiation with an intensity varying with direction and wavelength. Considering radiation emission per unit area, a surface can be categorized as a black, gray, or non-gray surface [B14, K13].

Blackbody refers to a surface that allows all incident radiation (all wavelengths with all incident directions) to be absorbed (i.e., no reflection and no transmittance,  $\alpha_{ab} = 1$ ) [B14]. Accordingly, there can be no body that absorbs more radiation compared to a blackbody, and this implies that any real body can only absorb radiation that is lower than that of the blackbody. The concept of maximum absorption of the blackbody regardless of incident direction and wavelength is considered central to the understanding of radiative heat transfer. In fact, a black body is considered as the benchmark or the gold standard against which all other real surfaces are to be compared. What is more important is that a black body emits the maximum radiation for any given temperature as a consequence of being the perfect absorber. The reason behind the word “black” for the black body is that the black bodies are, in fact, very poor reflectors that result in them appearing visually black. Note that if a body appears visually black, it can not be considered as a black body because the eye is only able to detect a very narrow range of the radiation spectrum (0.4  $\mu\text{m}$  to 0.7  $\mu\text{m}$ ) and therefore, for an entire verification, special equipment (such as spectrometer) is needed. However, since a black body absorbs the entire range of the radiation spectrum (including visible light as a part of the radiation spectrum), it can be concluded that any black body appears visually black [B14]. As discussed before, compared to all bodies, the blackbody emits the maximum radiation for any given temperature as a consequence of it being the perfect absorber. Fig.1.84 shows the blackbody radiation emission intensity as a function of wavelength at given different temperatures [K13, B14]. As can be seen, at a given temperature, a blackbody emits radiations not only in a single wavelength but also in a wide range of wavelengths. More importantly, by increasing the temperature, the minimum wavelength of the emitted radiation spectrum and the wavelength at which the maximum peak appears are shifted to

lower values. Besides, the intensity of radiation emission for all wavelengths also increases by increasing the temperature. Also, it can be observed that the radiation spectrum can also cover the narrow part of the visible light if the temperature is as high as required [K13].

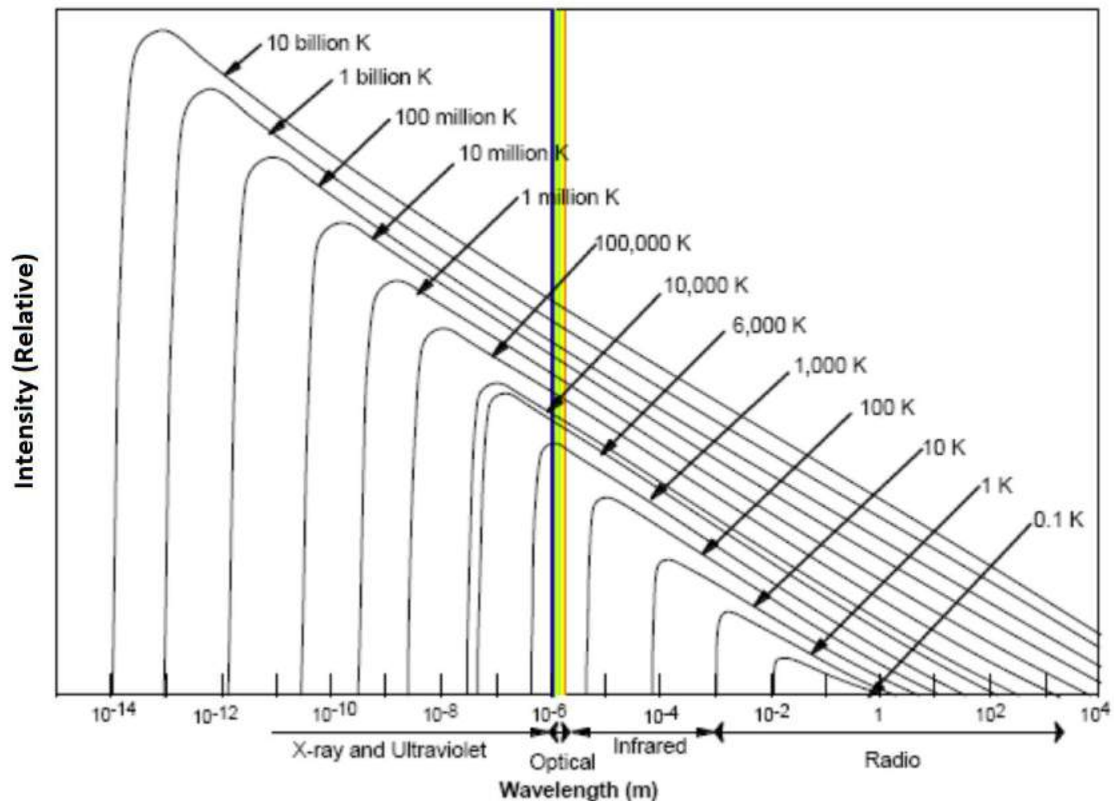


**Fig. 1.84:** Blackbody radiation emission intensity as a function of wavelength at given different temperatures [AST]

As mentioned above, compared to a blackbody which refers to a black surface, any other surface emits lower radiation energy per unit area at a given surface temperature  $T_s$ . So, considering the emitted intensity as a constant fraction (i.e., independent of wavelength) of that emitted from a black surface at  $T_s$ , the surface is called a gray surface. If the fraction depends on the wavelength, the surface is called a non-gray surface. The non-gray surface is more complicated to characterize and assess compared to other types of surfaces. In Fig.1.85, a schematic representation of the intensity of radiation emission at a given temperature for blackbody, graybody, and real surfaces is presented. In the case of blackbody radiation emission, the wavelength dependency is given by the Planck distribution (due to the discovery of Max Planck in the early 20<sup>th</sup> century) [MBC17]. As can be seen, the radiation emission from the graybody is a scaled version of a blackbody radiation emission with a constant (not dependent on the radiation wavelength) scaling factor [V21]. Conversely, in the case of a real surface, the radiation distribution depends on the wavelength [MBC17].

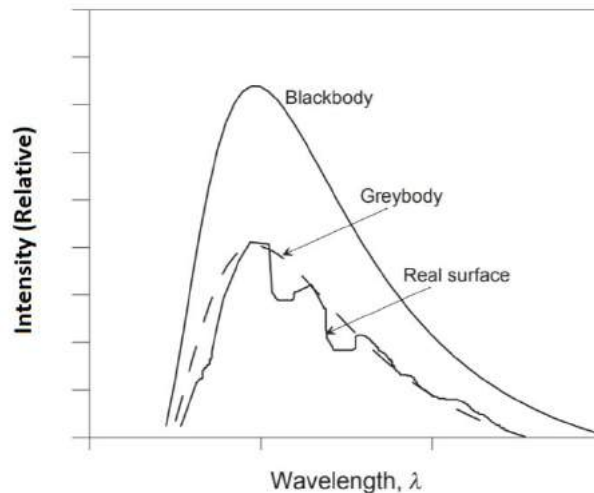


**Fig.1.85:** Schematic representation of the intensity of radiation emission at a given temperature for blackbody, greybody, and real surfaces [MBC17]

### 1.3.4 Simultaneous heat transfer mechanisms

A simultaneous heat transfer mechanism is usually considered in most actual engineering applications. For example, a solid may have both conduction and radiation heat transfer mechanisms; however, it may also involve convection and/or radiation heat transfer mechanisms on its surface that is exposed to a fluid (or other surfaces) [LQT18, E75]. In *still fluid* (no bulk fluid motion), the mechanism of heat transfer is by conduction and possibly by radiation. However, in the case of a *flowing fluid*, heat transfer is by convection and possibly by radiation. Therefore, regardless of radiation, the mechanism of heat transfer through a fluid is either by conduction, or convection (but not both), which depends on the presence of bulk fluid motion. In the case of gases, it should be noted that most of the gases are practically transparent to radiation, except for those that absorb radiation at certain wavelengths. For example, ozone absorbs ultraviolet radiation significantly; however, in general, radiation absorption is not taking into account for a gas when it is present between two surfaces, and the gas acts practically as a vacuum. In contrast to gases, liquids strongly absorb radiation. In a vacuum, heat transfer is only by radiation, since convection and conduction require a medium [LQT18].

### 1.3.5 Boundary and initial conditions

From the mathematical point of view, in order to obtain a unique solution from the governing differential equations, one has to specify boundary or initial conditions [P80, NK09]. The boundary conditions are the physical conditions of the system in space and the initial conditions are those related to physical conditions in time. The initial condition is considered for transient or time-dependent problems. It specifies, for example, in heat transfer problems, the temperature distribution at an instant of time (that usually is at the beginning of time) in the computational physical domain [MS06]. In fluid dynamics, the initial condition can be the flow direction and pressure field in the complete domain [B15].

### 1.3.5.1 Boundary conditions in heat transfer

The boundary conditions that are mostly encountered in practical applications are specified heat flux, specified temperature, radiation, and convection boundary conditions [MSMD03, NK09]. In the following, the most common boundary conditions encountered in heat transfer problems are described briefly.

#### Specified heat flux boundary condition

A specified heat flux boundary condition, which is a *Newmann condition*, is considered when there is information on the surface about the rate of heat transfer and therefore, the heat flux  $q''$  (defined as the rate of heat transfer per unit surface area, e.g.  $\text{W.m}^{-2}$ ) [C02, MS06]. For example, by irradiating a body surface using a heat lamp, or patch electric heater to a surface [MSMD03].

Considering the heat flux formula (according to the Fourier's Law, see section 1.3.2) on the one-dimensional  $x$ -axis as [C02]:

$$q'' = -k \frac{\partial T}{\partial x}, \quad (1.65)$$

one can consider a known specified heat flux at the boundary of a surface by setting it equal to  $-k \frac{\partial T}{\partial x}$ . Note that the sign of the specified heat flux is considered by inspection; i.e., it is positive if the heat flux is in the positive direction with respect to the coordinate axis, and it is negative in the opposite direction [P80]. Fig.1.86 shows the specified heat flux boundary conditions on both left and right surfaces of a one-dimensional planar slab. Note that in Fig.1.86, the specified heat flux at  $x = L$  is in the negative direction of the  $x$ -axis and therefore the sign of  $q''_L$  is negative [C02].

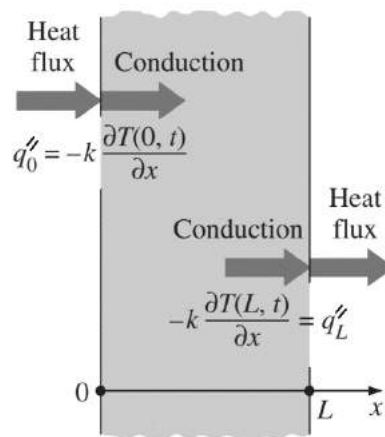


**Fig. 1.86:** A schematic representation of the specified heat flux boundary conditions on both left and right surfaces of a slab with a length of  $L$  at time  $t$  [C02]

There are some special cases in the specified heat flux boundary conditions. One of these cases is when one (or some) surface of a body is insulated. The insulation is in place to



minimize heat loss (or heat gain) through the surfaces, and therefore, one can consider the heat transfer (or heat flux) through the insulated surface as zero. In this case, the specified heat flux is equal to zero (mathematically, this translates as  $-k \frac{\partial T}{\partial x} \bigg|_{x=x_0} = 0$ , or  $\frac{\partial T}{\partial x} \bigg|_{x=x_0} = 0$ , where  $x_0$  is a surface location in an axis) [P80]. Fig. 1.87 shows the specified heat flux boundary condition for an insulated surface on the left side.

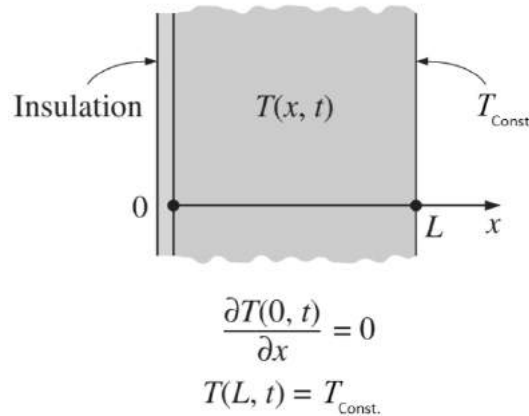


**Fig.1.87:** A schematic representation of a slab with an insulation heat flux boundary condition for a surface (the surface on the LHS) [P80]

As can be seen in Fig.1.87, the temperature gradient at the LHS slab in the direction normal to the insulated surface is equal to zero. This can result in a temperature profile because the slope of the temperature profile is zero on the insulated surface, and therefore, the temperature function is perpendicular to the surface [C02].

Another special type of the specified heat flux boundary condition is thermal symmetry that can be considered as a result of the symmetry in imposed thermal conditions (see Fig.1.88). The thermal symmetry boundary condition can also be applied in problems in which the entire geometry can be divided into smaller geometries to reduce the computational time for the solution of the governing equations [F20, P80]. As is shown in Fig.1.88, the slab has symmetry at  $x = L/2$  and it causes no heat flow through the center plane. Additionally, one can conclude that the heat flow direction at any point in the slab will be toward the boundary surface closer to the point. Moreover, considering Eq.1.66 or Fig.1.88, one can reasonably assume insulation or zero heat flux boundary conditions at the center plane of the slab [C02, NK09].

$$\frac{\partial T(L/2, t)}{\partial x} = 0. \quad (1.66)$$

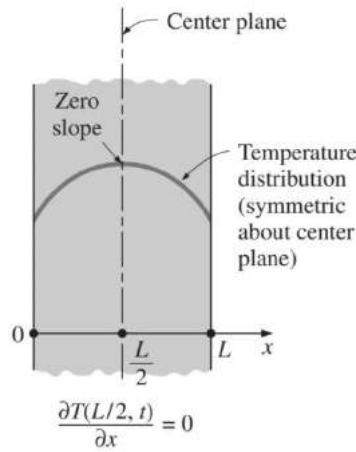


**Fig.1.88:** A schematic representation of the thermal symmetry boundary condition in a slab [C02]

### Specified temperature boundary condition

Specified temperature boundary condition, which is a *Dirichlet boundary condition*, refers to conditions when the temperature of an exposed surface is known (e.g., from measurements) [MS06]. Fig. 1.89 shows a schematic representation of a slab with the specified temperature boundary conditions on the surfaces.

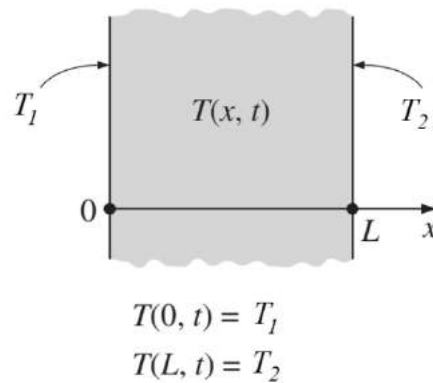


**Fig.1.89:** A schematic representation of the specified temperature boundary condition in a slab [C02]

The specified temperature boundary condition can mathematically be formulated as [SG16, C02]:

$$T(0, t) = T_1, \text{ \& } T(L, t) = T_2, \quad (1.67)$$

where  $T_1$  and  $T_2$  are the specified temperature boundary conditions for the left hand side and right hand side surfaces of the slab, respectively. Note that the specified temperatures may have a constant value (which is more relevant for the steady-state simulation) or a time-dependent value (for the transient simulation) [C02, F20]. Besides, this boundary condition

can also be a space-dependent function for both steady-state and time-dependent problems [P80].

## Convection boundary condition

Convection boundary condition is one of the most encountered boundary conditions in practice when dealing with heat transfer problems [FT08, P80]. This is due to the fact that usually surfaces of any body are exposed to an environment, and therefore, convection heating or cooling at the surfaces is considered (usually, depending on the temperature) the most dominant heat transfer mechanism [MSMD03, C02].

As shown in Fig.1.90, both surfaces of the slab are exposed to different environments with different convection coefficients  $h_1$ , and  $h_2$ , and different specified temperatures  $T_{\infty 1}$  and  $T_{\infty 2}$ .

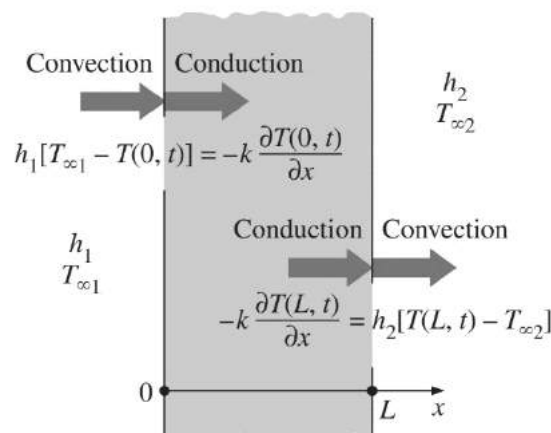


**Fig. 1.90:** A schematic representation of the convection boundary condition for a slab [C02]

In Fig.1.90, it can be observed that the direction for the convection boundary conditions is considered at both surfaces on the positive  $x$ -axis. However, when the opposite direction for one or both surfaces is desired, the signs are reversed for both convection and conduction terms (see Fig.1.91) [C02, MMD16].

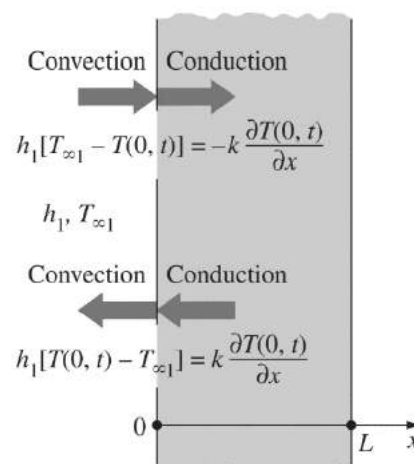


**Fig.1.91:** A schematic representation of the convection boundary condition for different directions of heat transfer. As can be seen, the direction of heat transfer at a boundary has no impact on the surface energy balance [C02]

As can reasonably be argued, the convection boundary condition can be expressed as the surface energy balance, which expresses that at the shared surface, the heat conduction (in a selected direction) is equal to the heat convection (in the same direction) as [L03]

$$q_{convection} = q_{conduction \text{ at the wall}}. \quad (1.68)$$

Therefore, for the slab depicted in Fig.1.91, the convection boundary condition encountered at  $x = 0$  is [C02]:

$$h_1[T_{\infty 1} - T(0, t)] = -k \frac{\partial T(0, t)}{\partial x}, \quad (1.69)$$

and similarly at  $x = L$ :

$$-k \frac{\partial T(L, t)}{\partial x} = h_2[T(L, t) - T_{\infty 2}], \quad (1.70)$$

Since the shared surface (similar to other boundary surfaces) has no thickness and therefore no mass, it cannot store any energy [MMD16]. This translates to the observation that the entire heat entering from one side of the surface leaves from the other side of the surface. On this basis, the convection boundary condition states that heat is flow from a body to its surrounding at the same rate (or vice versa for the opposite direction) [C02].

## Radiation boundary condition

Radiation boundary condition usually is considered for space and cryogenic applications where the boundary surface is surrounded by an evacuated space or medium in which the radiation mechanism is the predominant heat transfer mechanism between the surface and its surroundings [MMD16]. Considering the energy balance at the shared surface that states heat conduction in a selected direction is equal to radiation exchange in the same direction, one can mathematically formulate this boundary condition regarding Fig.1.92, as [C02]:

$$-k \frac{\partial T(0, t)}{\partial x} = \varepsilon_1 \sigma [T_{surr,1}^4 - T(0, t)^4], \quad (1.71)$$

and

$$-k \frac{\partial T(L, t)}{\partial x} = \varepsilon_2 \sigma [T(L, t)^4 - T_{surr,2}^4], \quad (1.72)$$

where  $T_{surr}$  is the surrounding temperature and subscript numbers denote different surrounding mediums. In Eq.1.72, all other parameters and variables have their usual meaning. What is important in Eqs.1.71 and 1.72 is, that the temperature has a power of four, which results in considering the radiation boundary condition as a nonlinear condition. The fourth power of temperature means powers of unknown coefficients, and therefore difficulties in their determination and complexities in mathematical calculations (due to the associated nonlinearities) [NK09, C02, LS09, P80]. Due to the mentioned associated mathematical implementation of radiation boundary conditions, usually it is tempting to

ignore radiation exchange at a body surface during the heat transfer assessment; in particular, at low temperatures in which heat transfer is dominated by convection mechanisms [C02].

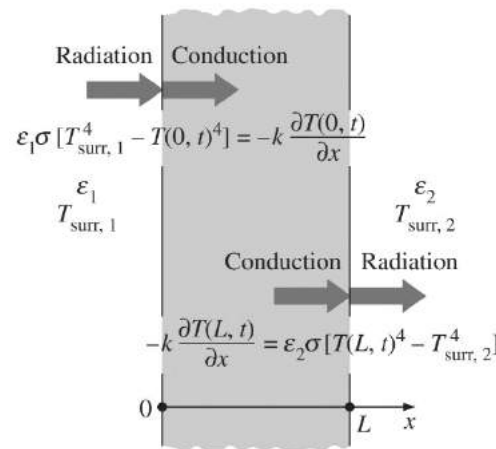


**Fig. 1.92:** A schematic representation of different radiation boundary conditions for both boundary surfaces of a slab, in which  $T_{surr}$  stands for the surrounding temperature and subscript numbers denote different surrounding mediums [C02].

## Interface boundary condition

Interface boundary condition is applied when some bodies are made up of different material layers (as is shown in Fig.1.93) [NK09]. In such cases, the heat transfer solution requires the solution of the heat transfer problem in each different material layer with the specification of boundary conditions in the interface. The interface boundary condition is based on two assumptions; the first one is that the two bodies must have the same temperature at the interface. The second one is that the interface of the layers in contact cannot store any energy, and therefore, the heat flux on the two sides of the interface must be the same [LS09, F20]. Accordingly, by considering Fig.1.93, the boundary conditions at the interface  $x_0$  can be written as [C02]:

$$T_A(x_0, t) = T_B(x_0, t), \quad (1.73)$$

and

$$-k_A \frac{\partial T_A(x_0, t)}{\partial x} = -k_B \frac{\partial T_B(x_0, t)}{\partial x}, \quad (1.74)$$

where, as shown in Fig.1.93, subscripts  $A$  and  $B$  refer to material  $A$ , and material  $B$ , respectively; and all other parameters and variables have their usual meaning.

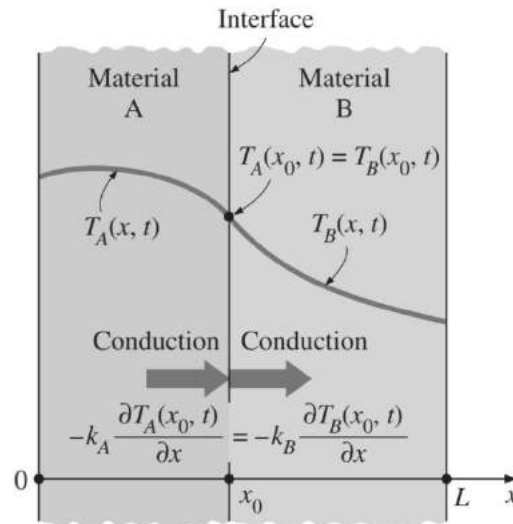


**Fig. 1.93:** A schematic representation of interface boundary conditions between two different layers of a body at the interface  $x_0$  [C02]

### Generalized simultaneous boundary condition

Generalized simultaneous boundary condition refers to problems when the surfaces under study are not only subjected to a single-mode heat transfer (such as convection, radiation, specified heat flux, etc.), but involve multiple heat transfer mechanisms [MMD16, LS09]. The boundary conditions can therefore be obtained from a surface energy balance, as heat transfer to the body surface in all modes must be equal to heat transfer from the surface in all modes [C02]. For more details about the combined heat transfer mechanisms, refer to [F20].

#### 1.3.5.2 Boundary conditions in fluid dynamics

Boundary conditions in fluid dynamics can be specified as an inlet boundary condition, outlet boundary condition, symmetric boundary condition, constant pressure boundary condition, and no-slip boundary condition. In the following, a brief description of these boundary conditions is presented [B15, GGH16].

##### Inlet boundary condition

Inlet boundary condition refers to the condition in which all inlet scalar properties and variables of flow, in particular, flow velocity (applied in the case of incompressible flows\* and known as velocity inlet boundary condition), or pressure (known as pressure inlet boundary condition) are specified for the problem. The latter is usually employed when the inlet pressure of the flow is known in contrast to the inlet velocity (or flow rate). Alternatively, in cases when the outlet velocity (or flow rate) is known [B15, Q22].

---

\* Incompressible flow refers to fluid flow where its density remains constant even with pressure changes (almost all liquids). In contrast, compressible flow refers to fluid flow that undergoes a considerable variation in density by changing pressure (e.g., gases) [B15, Q22].

## Outlet boundary condition

With the inlet flow boundary condition, it is common practice to define the outlet boundary condition. Outlet boundary is an exit of flow, on which usually, flow velocity, pressure value, or mass flow outlet are specified [KSKM18]. It should be noted that a pressure outlet must always be employed when the model under study is set up with a pressure inlet [B15, VM07].

## No-slip boundary condition

No-slip boundary condition or no velocity-offset boundary condition says that fluids in direct contact with a wall (or in general a boundary) will possess the same velocity as the wall, which in general, is zero (see Fig.1.94 and Eq.1.75, where in Eq.1.75,  $v_f$  and  $V_{Wall}$ , are the velocity of the fluid and the wall, respectively) [Q22, R17]. The “no-slip” comes from the fact that no relative movement between the fluid in contact and the boundary is considered according to this boundary condition, so there is no slip [R17]. The no-slip boundary condition assumption works well in the case of viscous fluids [HP97].

$$v_f|_{at\ the\ boundary} = V_{Wall} . \quad (1.75)$$

Slip boundary condition or velocity-offset boundary condition is applied when there is a discontinuity in the flow velocity function (see Fig.1.94). This is assumed mostly as the result of variations in the roughness of the wall. Considering this boundary condition, a relative movement is assumed between the boundary and the fluid in direct contact (so there is slip) [R17]. For more information about the no-slip and slip boundary condition, refer to [HP97, BCHS08, KSKM18]. Additionally, as mentioned earlier, the wall is considered stationary herein. In the case of moving walls and their influence on in contact flow, refer to [VM07].

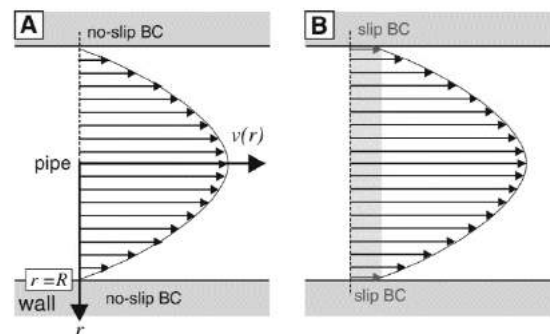


**Fig.1.94:** Schematic representation of (a) no-slip boundary condition and (b) slip boundary condition. In this figure, BC is the abbreviation of boundary condition,  $r$  and  $R$  are the axis and radius of the tube, respectively, and finally  $v(r)$  is the flow velocity [BCHS08].

## Symmetric boundary condition

The symmetric boundary condition is considered in some fluid dynamic problems in which a plane of symmetry can be considered [KSKM18]. According to this boundary condition, all the variables and gradients have the same value at the same distance from the plane of symmetry. For example, in the case of the fluid velocity field, since it is the same on either side of the symmetric plane, it must reach a minimum or maximum at the plane of symmetry. On this basis, one can consider the first derivative of the fluid velocity as zero at the plane of symmetry

(see Eq.1.76). In other words, the plane of symmetry acts as a mirror, which reflects all the fluid flow distribution to the other side of the plane [R17, KSKM18].

$$\left. \frac{\partial v_f}{\partial x} \right|_{\text{at the boundary}} = 0. \quad (1.76)$$

Note that the conditions at a symmetry boundary (or symmetry plane) can be specified as no flow across the boundary and, no scalar flux across the boundary [VM07]. Moreover, it should be mentioned that different types of symmetry can be applied to fluid dynamic problems as a result of different geometries. In such cases, different types of symmetries such as periodic or cyclic boundary conditions can be applied (see Fig.1.95) [VM07].

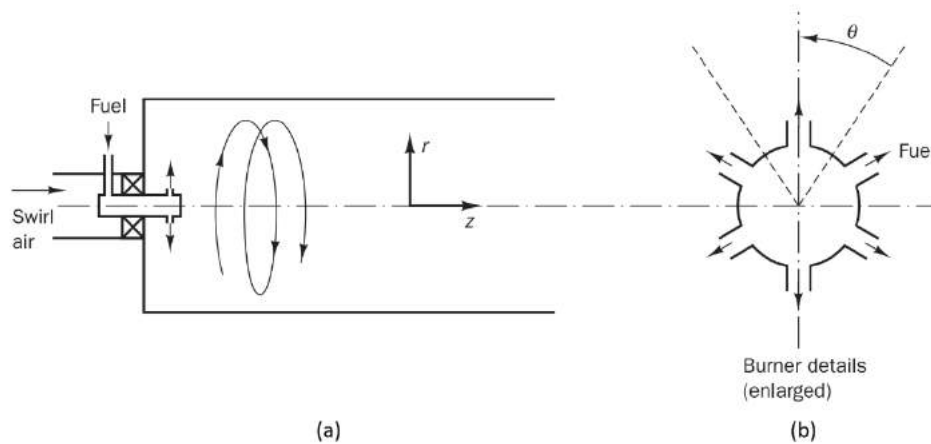


**Fig.1.95:** A schematic representation of a) swirling flow in the cylindrical furnace and b) burner arrangement gaseous fuel that is injected through six symmetrical holes (swirl air directly enters through the outer burner's annulus). As is observable, a cyclic and periodic boundary condition can be considered for the cylindrical furnace and burner [VM07].

### Constant pressure boundary condition

The constant pressure boundary condition is applied when exact details of flow distribution are not specified, and instead, the boundary values of flow pressure are known (this usually includes pressure inlet and outlet conditions). This boundary condition can be applied, for example, to external flows around objects, internal flows with multiple outlets, and free surface flows [VM07].

### Outflow boundary condition

The outflow boundary condition is applied to model flow exists in which the details of the pressure and flow velocity are not known. This boundary condition can not be employed for compressible flows. In addition, it can not be used with the inlet pressure boundary condition, and instead, a velocity inlet boundary condition should be employed [VM07, R17, KSKM18].

## 1.3.6 Overview of theoretical heat transfer calculations

Theoretical heat transfer calculations work out the consequences of a mathematical model consisting of a set of differential equations for the physical process of interest. There are many



advantages of theoretical calculations over experimental investigations, such as low cost (compared to experimental measurements, the cost of a computer run is almost negligible), speed (compared to an experimental design and investigation, a computational investigation with different configurations and designs can be carried out with remarkable speed), complete information (in contrast to an experimental investigation, a computer solution can give details and complete information about all the relevant variables in the entire domain of interest), simulation based on realistic conditions (in theoretical calculations, almost no simplicity for the assumption is required including, dimensions, temperatures, process speed, etc.), and design optimization (this feature is usually of interest in designing and studying a heat transfer problem) [P80, T11, BFB16]. Besides the advantage of theoretical calculations over experimental measurements, the validity of the mathematical model used in the computational investigation can be considered as a disadvantage of the theoretical calculation [P80, T11].

The mathematical calculation of the governing heat transfer equations for simple geometries and specified straightforward conditions is rather simple and can be carried out using classical methods [SM03, BFB16]. However, by considering classical methods based on the exact analytical mathematical approach, there would be only little hope for solving the governing equations corresponding to many phenomena of practical interest [PC18, IJ09, SM03, P80, B16]. In addition, having a look at the theoretical solution of the tiny fraction of the range of problems leads to the conclusion that these solutions often contain special functions, infinite-series, transcendental equations for eigenvalues, etc., so their assessment may present a tedious task [P80, PC18, BFB16].

The mathematical calculations of heat and mass transfer usually include a set of simultaneous algebraic equations obtained by approximating the governing equations with different discretization methods (discussed later in this chapter). This set of simultaneous algebraic equations can range in complexity from a few numbers to some thousands or even more in a complex time-dependent system [MS06, SM03, E13]. One of the very well-known simple mathematical methods that can be implemented using hand calculations for a set of algebraic equations is the *method of elimination of unknowns*. This algebraic mathematical approach involves multiplying the algebraic equations by one (or several, depending on the number of equations) constant value to eliminate one of the unknowns when combining the two equations (in the case of a set of two algebraic equations). This procedure can reduce the two equations to one equation with only one unknown that can be solved simply. Then, by substitution of the obtained value of the unknown into one of the original equations, one can simply obtain the other remaining unknown [SM03, BFB16]. This process of mathematical solution can be performed for a number of equations; however, as the number of equations increases, the implementation of the mathematical solution based on the elimination of unknowns becomes extremely complex and tedious. Therefore, other numerical approaches for the solution of a large set of simultaneous algebraic equations are required to be employed. In general, two numerical approaches are employed for the solution of such a set of simultaneous equations, named *direct methods* and *iterative methods* [MS06, MSM06, SW06].

Direct methods employ a finite number of steps for the solution of equations. These steps usually include the elimination of unknowns and combining the equations. Direct methods can be categorized into different subgroups: Gaussian elimination, Lu decomposition, Gauss-

Jordan elimination or factorization, diagonally dominant system, and Cholesky decomposition [MS06, E13, BFB16]. For more details about the direct methods and their solution procedure, refer to [MS06, MSM06, SM03, BFB16, S12, SW06].

Iterative methods are those approximate methods that start with an initial pre-determined guess solution and then calculate the simultaneous algebraic equations iteratively until the obtained solution converges\* using some pre-specified tolerance limits [CC15]. In other words, the iterative methods work based on a guess-and-correct philosophy that progressively (by increasing the iterations) updates and improves the guessed solution by repetitively calculating the discrete equations and replacing new solutions [MSM06, BFB16]. Many different iterative methods have been developed for the solution of a large system of equations such as: successive over relaxation (SOR) method, Gauss-Seidel method, conjugate gradient (CG) method, Jacobi method, generalized minimal residual (GMRES) method, transpose free quasi-minimal residual (TFQMR), and bi-conjugate gradient stabilized (Bi-CGSTAB) method. For more details about the aforementioned methods, refer to [MS06, BFB16, S12, SW06]. The former approach is usually only effective if the number of equations is small (in the order of several hundred); and is inadequate for a larger set of equations due to the associated problems with them, such as computational time and storage (i.e., memory) [CC15]. In practical heat transfer and fluid flow simulations in which the system of equations is as large as several thousand or even more, iterative methods should be employed for more effective implementation. This is mainly due to the lower storage requirements and computational time of the iterative methods compared to the direct methods [PC18, P80, LQT18]. The availability of large, high-performance computers, and the development of different discretization methods, lead to widely used theoretical heat transfer calculations for almost all practical applications [PC18, BFB16].

Fluid flow and heat transfer analysis starts with the basic conservation laws†. These laws can be formulated based on infinitesimal or finite systems and Control Volumes (CVs). Infinitesimal system and CV-based formulation that leads to differential formulation give point-to-point behavior and detailed knowledge of the system under study. However, the integral formulation resulting from the finite system, or CV gives only a gross or average behavior. Therefore, the solution of differential equations is usually the center of attention [P80, S12]. There were different discretization methods developed for the solution of differential equations [LQT18, E13, CC15]. The discretization of the physical domain can be performed by meshing it, which means, dividing the entire domain into smaller, usually polyhedral volumes (see Fig.1.96). The *cell* that also is called an *element*, considers the fundamental unit of the mesh. A *Cell centroid* is associated with each cell. As can be seen in

---

\* The convergence term in numerical methods refers to a sequence of model solutions in which the solution can approach a fixed value by increasingly refined solution domains [T92, MSM06].

† The governing equations of fluid flow represent mathematical statement of the conservation laws of physics [VM07].

The mass of a fluid is conserved (the continuity equation) [VM07].

The rate of change of momentum equals the sum of the forces on a fluid particle (Newton's second law; the momentum continuity) [VM07].

The rate of change of energy is equal to the sum of the rate of heat addition to and the rate of work done on a fluid particle (first law of thermodynamics; the energy equation) [VM07].

For more details about the conservation laws (the continuity, momentum, and energy equations) in fluid dynamics, refer to [B15, VM07].

Fig.1.96, each cell is surrounded by *faces* that meet at *vertices* or *nodes* (in the case of three-dimensional geometries, the face is a surface surrounded by edges). In two dimensions, faces, and edges, are considered the same. A variety of mesh types have been developed, as can be seen in Fig.1.97 [MSM06, EGH00].

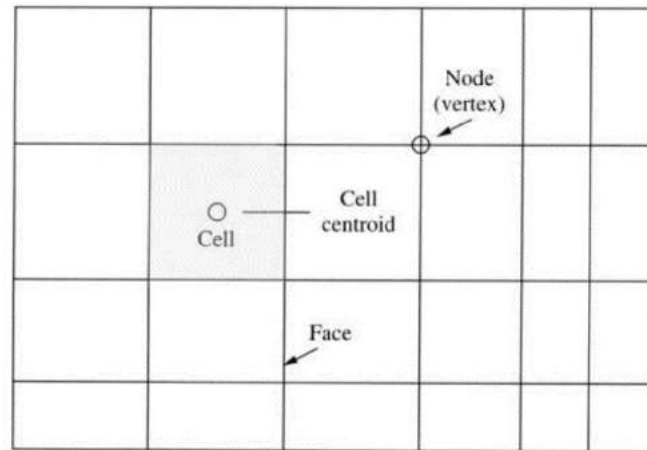


**Fig.1.96:** Mesh Terminology [MSM06]

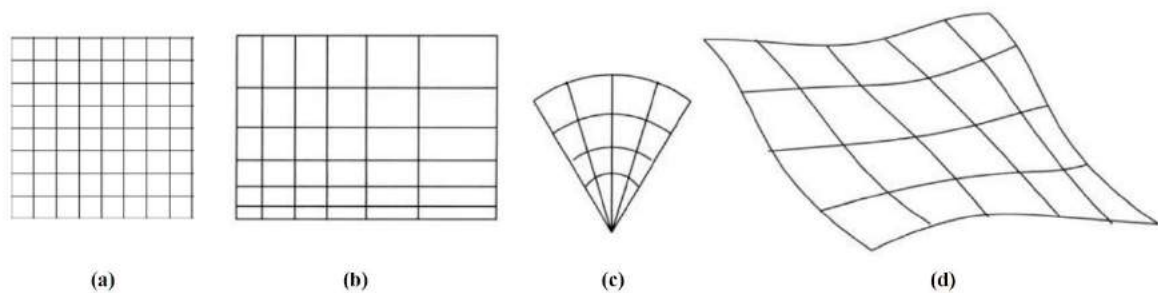


**Fig.1.97:** Schematic representation of (a) orthogonal uniform, (b) orthogonally non-uniform, (c) non-orthogonal-structured, and (d) non-orthogonal unstructured meshes [MSM06]

The mesh type can be orthogonal, which means the grid lines are orthogonally shaped and discretized in the physical domain and conform to the domain boundaries (see Figs.1.97a and b). This regular shape discretization approach is usually considered for regularly shaped geometries. In Fig.1.97, the difference between (a) and (b) is that in some practical applications in the computational model, some regions of the entire domain are of more interest compared to other regions (due to, for example, the difference in a temperature gradient, mechanical stress variations, etc.), and increasing the mesh number uniformly (as shown in Fig.1.97a) in the entire physical domain results in increasing computational cost significantly [THLZ17, CC15, B16]. Therefore, the orthogonal non-uniform discretization shape can give accurate results at reasonable computational cost by distributing the meshes in regions of interest adaptively. For more details, refer to references [VOG16, VVG16, VT19]. The discretization scheme of numerical methods can also be presented based on the location of storing of unknowns in the CV/element (see Fig.1.96) [LLGC04, CC15, P18]. Node-based/vertex-based/edged-based/mesh-edge schemes refer to those where the primary unknowns are stored in the node or vertex locations. In contrast, cell-based/mesh-centered schemes are those that store the unknowns at the cell centroid. Most of the discretization

methods can be written based on both schemes (such as FEM and FVM, which will be discussed later in this chapter). However, there are also some methods that have been developed for a specified scheme (e.g., FEM) [MSM06, LLGC04, DNK11, DT11]. For the same method (e.g., FDM) and problem, the mesh-centered scheme usually gives more accurate results than the mesh-edge scheme [VOG16, VVG16, VT19]. In Fig.1.98, the apparent absolute error (AAE; see Eq.1.77 [VVG16]) of the obtained effective multiplication factor (shown as  $k_{eff}$ ) resulting from a neutron diffusion calculation of a Pressurized Water Reactor (PWR) using both mesh-edge and mesh-centered FDM is presented [A77]. As can be seen, as the number of meshes (or points) increases, more accurate results are obtained. Moreover, for the same number of meshes, the mesh-centered scheme gives more accurate results compared to the mesh-centered scheme.

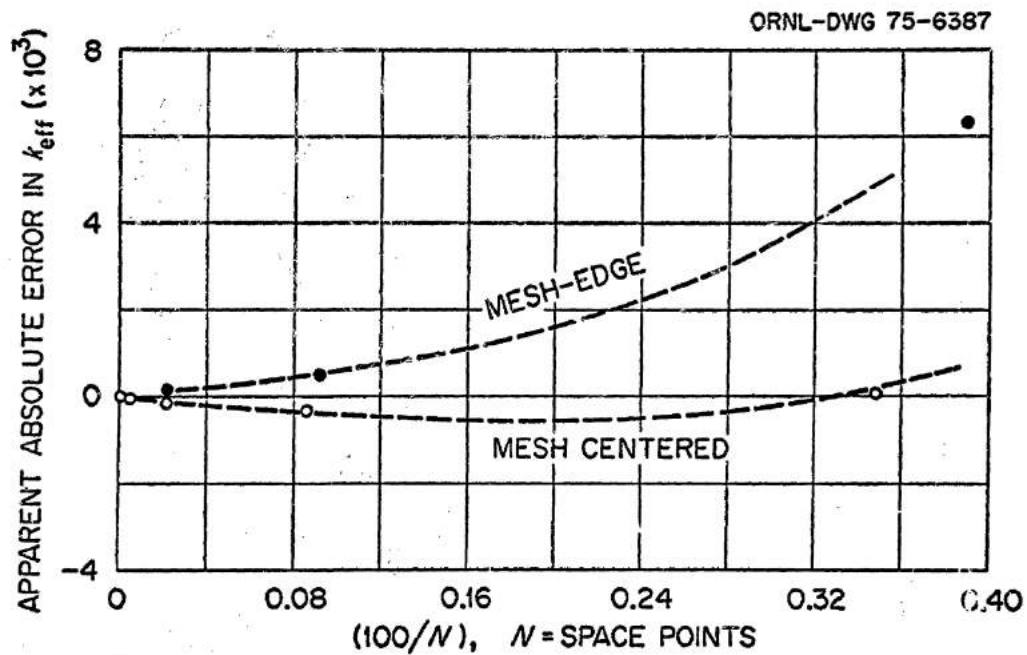


**Fig.1.98:** AAE of  $k_{eff}$  resulting from a neutron diffusion calculation of a PWR\* reactor core using both mesh-edge and mesh-centered FDM.  $k_{eff}$  is defined as the ratio of the neutrons produced in the next generation (through the fission reaction) to the sum of neutrons absorbed in fission reactions or non-fission reactions, plus those lost in this generation [A77, L65, LB01]. Additionally,  $N$  is the number of total applied meshes (or points) in the problem (which is a PWR nuclear reactor) [A77]

$$AAE (\times 10^3) = (\text{calculated value} - \text{reference value}) \times 10^3 \quad (1.77)$$

Although the orthogonal-shaped discretization approach seems to be straightforward, in many practical applications, the physical geometry is irregularly shaped, and therefore, a non-orthogonal mesh type discretization scheme is of interest [MSM06, EGH00]. In recent years, there have been some interests in the development of a new mesh type called the *moving mesh method*. According to this method, first, the meshes are generated in an orthogonal or non-orthogonal shape and then move without any restriction in orthogonality and

\* Pressurized Water Reactor

deformation along with (only a part of the entire or the entire) physical domain moving during the simulation time [VOG20, VOG19]. Also, there have been some new efforts to introduce an *adaptive moving mesh method* that is able to move the meshes not only due to the movement of the physical domain but also due to the change in evolution of solutions in regions of interest. As can be seen in Fig.1.99, the meshes are moved and deformed adaptively from an initial orthogonal uniform form. Fig.1.100 shows a schematic representation of a CV ( $CV_p$ ) with its corresponding neighbors ( $N_1$  to  $N_6$ ) in a three-dimensional form. Discretization of the governing equation with this method is more complicated compared to conventional methods; however, the efficiency of the computations is much better [J96, S11, W13].

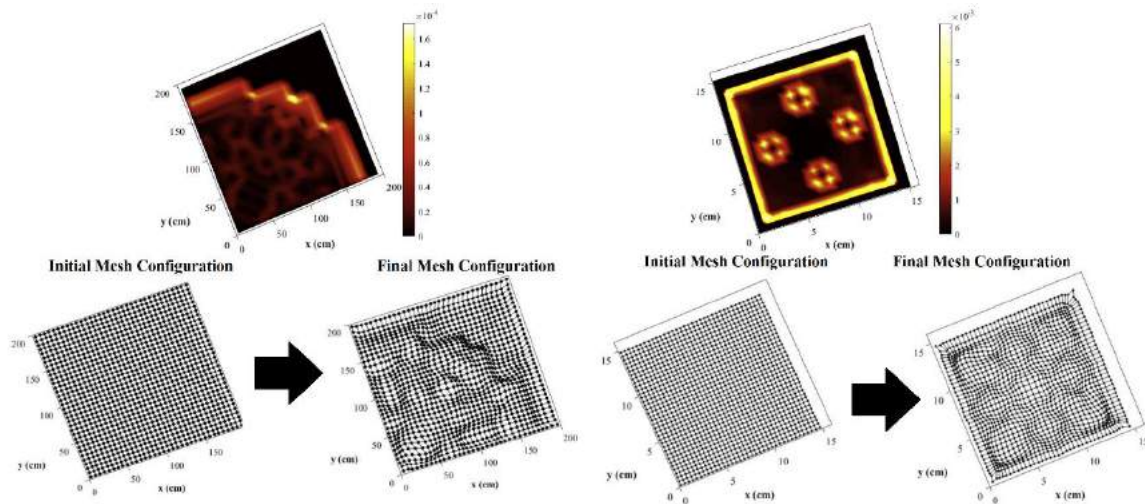


**Fig.1.99:** Mesh configuration in the adaptive moving mesh method for two different cases (related to the gradient of reactor power for two different nuclear reactor cores). As can be seen, the mesh configuration is initially an orthogonal uniform form; however, it moved and deformed during the numerical calculations as the solution evolved [VOG19].

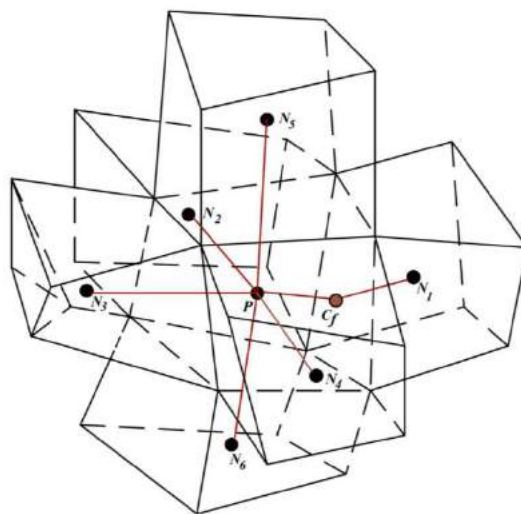


**Fig. 1.100:** A schematic representation of a quadrilateral mesh configuration in the moving mesh method, where  $P$  is the central CV,  $N$  (with subscripts 1 to 6) is the neighboring CVs and  $C_p$  is the center of the sharing face between the two adjacent CVs [VT19]

Note that cell or element shapes can be in very different forms and most of the discretization methods support a variety of them. Among all possible cell shapes, quadrilaterals, hexahedral, triangles, and tetrahedrals are the most widely used. In Fig.1.101, some of the cell shape types in two and three dimensions are presented [MMD16]. Another recently developed mesh type is called hybrid mesh that uses a variety of mesh types that can be employed (see Fig.1.102) [WM16].

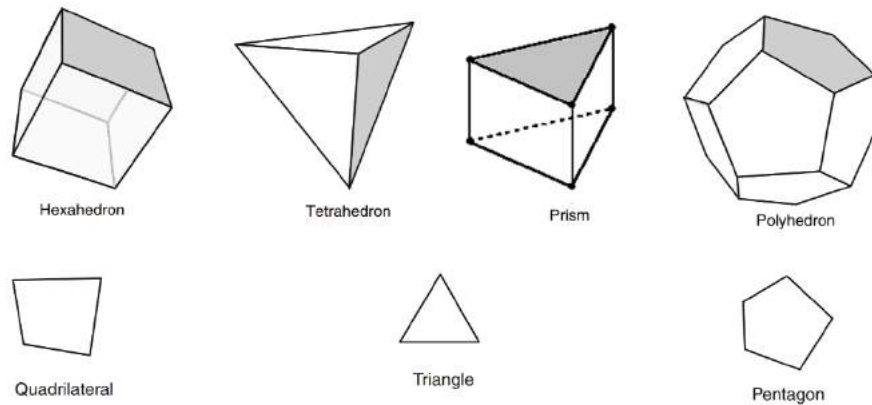


**Fig.1.101:** Two and three-dimensional cell/element types [MMD16]

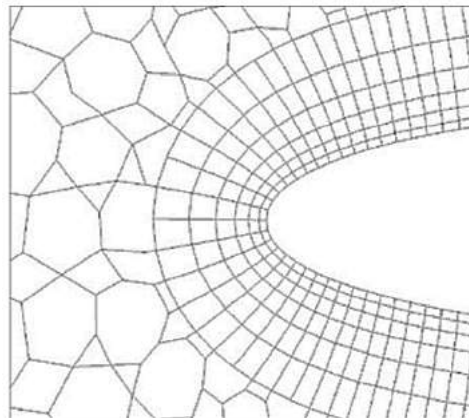


**Fig. 1.102:** A schematic representation of the hybrid mesh configuration [LZXX13]

During the last decades, different discretization methods have emerged as standard techniques for solving the governing equations for heat transfer and fluid flow. Among all of the developed methods, the Finite Difference Method (FDM), Boundary Element Method (BEM), Finite Volume Method (FVM), and Finite Element Method (FEM) are the most used approaches for the equation discretization [SB08, M17]. According to these methods, the original differential equations are reduced into a set of coupled algebraic equations using different approximation or local profile assumptions. In contrast to these methods of discretization, the Boundary Element Method (BEM), which has been employed for different heat transfer problems, uses Green's identities in order to convert the original differential equations into an integral form of the equation that involves only surface quantities, which afterward is discretized and solved [SM03, P18].

In the case of the FDM, to formulate the discretized form of the governing differential equations, the Taylor series expansions\* are used [IJ09, P18]. When modeling of multidimensional geometries is of interest, these formulas are employed for each coordinate. Using the FDM, the meshing is performed in most of the cases as orthogonal-uniform or orthogonally non-uniform meshes (see Figs.1.97a and 1.97b) [MC14, BFB16]. Therefore, the FDM is not usually applicable for irregular geometries, in particular for fluid flow modeling [S85, L07]. Moreover, in most of the problems, FDM can give acceptable, accurate results only if the mesh size is fine enough. Importantly, it was shown that refining meshes in FDM does not necessarily always guarantee to achieve more accurate results. Such associated problems with the FDM for the fluid flow and heat transfer modeling made the use of this method limited (usually in very simple geometries and special simple conditions) [MSM06, LQT18, L07].

BEM can be used in the calculations of steady and unsteady state heat conduction problems, different linear and nonlinear boundary conditions, source nonlinearities, temperature-dependent properties, and phase change. In BEM, the diffusion equation is an integral equation involving surface derivatives via Green's identities [L21], which is then calculated numerically. Therefore, the BEM's implementation procedure is discretizing the physical domain surface into small area elements, and afterward, converting the surface integral into a sum over the surface elements. Moreover, the function that is integrated on the surface, needs to be discretized using shape or interpolation functions. As the final result, a set of discrete algebraic equations, which relate the surface nodal values of the elements to each other, is obtained that is required to be solved numerically [WB92, B11, K16].

FVM is based on the integration of the governing differential equations over a central CV (see Figs.1.96 and 1.100). In FVM, the divergence theorem is applied in order to compute the discrete residual in each CV [BO04, P18]. The discrete residual considers a balance of the generation of the conserved variables, storage, diffusion fluxes, and convection within the CV. On this basis, using the FVM, an underlying conservation principle is considered and established on each CV, regardless of the mesh (or CV) size (in contrast to the FDM) [M19]. Note that conservation is different from accuracy, and therefore, for achieving an accurate solution, fine mesh size is usually required. Due to the fact that in FVM, the physical domain is discretized into smaller sizes (is called CVs in FVM), which does not necessarily have to be in a regular shape [T02], unstructured mesh types for a variety of mesh shapes have been developed and also applied for fluid flow and heat transfer analysis [SMM10, LWZ16]. However, until recent years, the possibility of the development of this method for a moving mesh approach was not developed and widely used (in our work [VOG20, VOG19]). This stems from the fact that the discretization of the governing equations based on the moving mesh

---

\* Taylor theorem mentions that if function  $f$  is  $k + 1$  times continuously differentiable between  $x$  and  $x_0$  (by considering them as real numbers), then there would be a number  $c$  between (between  $x$  and  $x_0$ ) so that:

$$f(x) = f(x_0) + f'(x_0)(x - x_0) + \frac{f''(x_0)}{2!}(x - x_0)^2 + \frac{f'''(x_0)}{3!}(x - x_0)^3 + \dots + \frac{f^{(k)}(x_0)}{k!}(x - x_0)^k + \frac{f^{(k+1)}(c)}{(k+1)!}(x - x_0)^{k+1}.$$

The terms up to degree  $k$  in  $x - x_0$  (the polynomial part of the result), are called degree  $k$  Taylor polynomials for the function  $f$  centered at point  $x_0$  [S12].

approach encounters some difficulties in derivation and implementation from the mathematical point of view [O17, Q18].

In FEM, likewise FVM, the physical domain is discretized into smaller regular or irregular volumes (is called elements in FEM). Accordingly, the FEM can be formulated based on unstructured meshes for a variety of mesh types [RG10, P18]. The difference between FEM and FVM is in the discretization method, i.e., how the governing differential equations are treated and then formulated in each discrete element/volume. More precisely, in FEM, minimization of some weighted residuals of governing differential equations is performed over each element. Weighted residuals are calculated by integrating the product of a weighting function and the residual of the (governing) differential equation [MSM06, HU94, P18]. The discrete algebraic equations for each unknown nodal can accordingly be obtained by considering shape and weight functions in terms of the nodal values of the unknown variable. Similar to FDM, the conservation property on coarse meshes does not exist; however, consistent\* formulations can be obtained by refining the applied meshes [MSM06, LQT18, SM03, NLS16].

Besides the aforementioned deterministic method, the probabilistic Monte-Carlo Method (MCM) can also be employed for heat transfer calculations. MCM is a statistical method, which uses random numbers as a base to carry out simulation and modeling for any specified situation (mostly in steady-state conditions for complex problems) [B17a, B17b]. The name of the method was chosen from the World War II Manhattan Project due to its close connection to chance-based games and the location of a famous casino in Monte Carlo. MCM modeling only requires that the system, in addition to the associated physical processes, be modeled using known probability density functions (pdfs)<sup>†</sup>. Accurately, pdfs definition can lead to simulation modeling via random sampling from the pdfs. Therefore, in contrast to the deterministic methods, discretization of the governing differential equations that lead to difficulties in discretization and meshing is not needed in the MCM. In the MCM simulations, a large number of histories are required to obtain an accurate estimation of the parameters, which significantly impact the execution time and, therefore, computational efficiency [LSK98]. In Fig.103, time to solution as a function of the complexity of the problem in terms of geometry for Monte-Carlo and deterministic methods is presented. As is observable, for simple geometries, deterministic methods can reach the solution faster compared to MCM. However, in the case of complex geometries, it is the opposite. This is due to the fact that the number of discretized algebraic equations in deterministic methods are small and therefore converge too fast for the simple geometries, while the number of histories that the MCM is needed to reach is still high. The situation is the opposite in the case of complex geometries because the number of discretized algebraic equations increases significantly, which impacts efforts to converge and, therefore, the time of solution [B01]. MCM shows its applicability in heat transfer problems, including conduction [FH77, B18], convection [TK87], and radiation mechanisms [M19, D03], in particular, when the system is in a steady-state condition [V17]. However, MCM is not widely used for coupled heat transfer and fluid flow problems [BK10]

---

\*The term of consistency in a numerical method refers to a discretization scheme if the sequence of the numerical solutions converges to the solution of the continuous equations (that govern the understudy physical phenomenon being modeled) [T92, MSM06].

<sup>†</sup>The probability density function refers to a function that describes the relative likelihood for a random variable to fall within a given particular range of values [K17].



when the system is strongly time-dependent, and it includes moving objects and the environment.

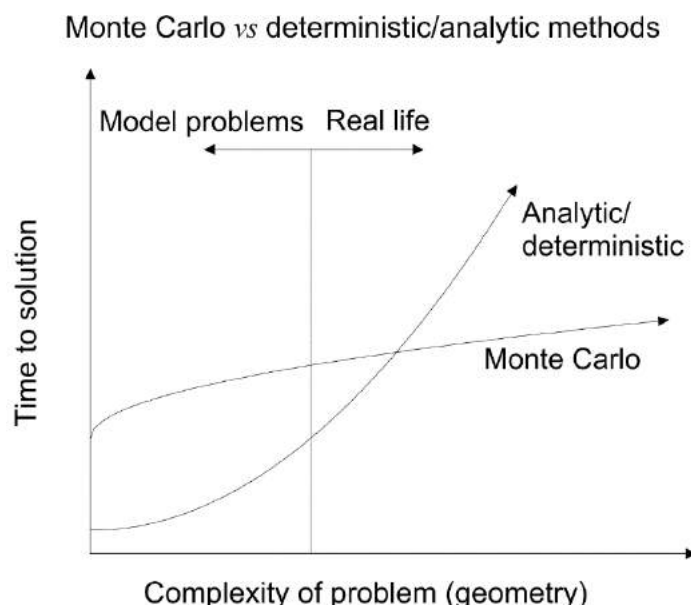


**Fig. 1.103:** A schematic representation of the time of solution as a function of geometry complexity for both Monte-Carlo and deterministic methods [B01]

### 1.3.7 Overview of theoretical radiation transport calculations

As was discussed before (see sections 1.1.1 and 1.2.6), as an incident particle emitted from a source, goes through a number of interactions with different probabilities depending on the medium and the projectile properties (see Fig.1.104) [B01]. On this basis, a deterministic approach based on numerical calculations of the discretized governing differential equations is not usually of interest, in particular, for complex systems and geometries [V17]. Additionally, the deterministic approach in radiation transport calculations contains uncertainties that are associated with the discretization of the independent variables of the transport equations, such as energy, space, and angle [W11]. Nevertheless, many works have been performed on radiation transport using the deterministic approach for mostly simple geometries and limited, specified conditions. For more details, refer to [P85, RR92, W03, BG70].

As mentioned earlier (section 1.3.6), the MCM (i.e., Monte-Carlo Method) is a numerical solution to a problem based on the probabilistic approach. To be more precise, MCM gives a solution to a macroscopic system based on simulation of its microscopic interactions (i.e., interactions of an object with other objects or environments) [B01]. In the radiation transport mechanism used in the MCM, the particle is tracked from its birth that corresponds to its emission from the source until its death, which corresponds to either absorption through a reaction or escaping (i.e., leakage) from a defined computational volume [LSK98]. The MCM can be detailed, accommodate different geometries, angular and energy representations, and therefore, is considered the most accurate method for the solution of complex radiation transport problems [W11, H21, L21, D19, GGOP21]. Fig.1.103 shows a schematic representation of the time of solution as a function of geometry complexity for both Monte-Carlo and deterministic methods. As can be seen, as the complexity of the problem tends to

real practical problems, the computational time of MCM is remarkably lower than that of deterministic/analytical methods [B01].

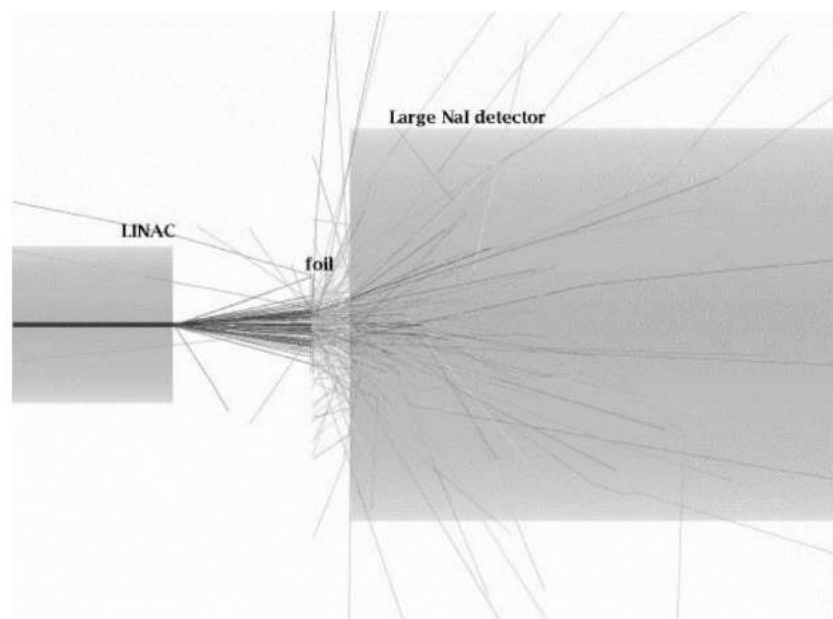


**Fig. 1.104:** A close-up of the photon and electron trajectories in a thin plastic foil and a large NaI detector generated from a 20 MeV incident electron beam in an experiment presented in [B01]

### 1.3.8 Software for computational purposes

In each component, incident electrons interact with different atoms under different interaction mechanisms and produce different particles/rays with various energies and angles [P09, A07]. These secondary rays can also undergo different interactions with different atoms (and nuclei), leading to the production of tertiary particles/rays. Therefore, one can reasonably assume that the accurate evaluation of Bremsstrahlungs production depends on the entire electron-photon cascade set up in all components, notably; the converter target. Therefore, a theoretical assessment must include the slowing down in addition to multiple scattering of the primary electrons and the secondary electrons produced in knock-on collisions, photoelectric absorption, Compton scattering, and pair-production mechanisms. It must also include the production, multiple Compton scattering, and absorption of continuous Bremsstrahlung, annihilation radiation, and characteristic X-rays [A07, C07, P14, P16]. Owing to the complexity of the solution based on the deterministic approach, the Monte-Carlo method (based on the probabilistic approach) is always of interest to be employed. On this basis, a few Monte-Carlo program-based codes have been developed, named MCNP, GEANT, FLUKA, PENELOPE, PHITS, and EGS codes. The difference between these codes is mostly in the algorithm used for radiation transport, cross-section data, computational cost, limitation in transporting different radiation and particles, limitation in projectile energy, the used programming language, and the required operating system for operation. To date, a number of works have been carried out to compare the results of simulations using Monte-Carlo codes. However, it was shown that almost all the codes give close results in electron and photon transport modeling problems [ST10, A18, VGGAL07]. In this project, the MCNP code is

used for Monte-Carlo calculations. MCNP is a general-purpose Monte-Carlo N-particle code that can be used for the transports of neutrons, photons, electrons, and other 29 particles (including all leptons, baryons, and mesons) [P11]. The upper energy limits for electrons and photons are 1 and 100 GeV, respectively. A lower limit of 1 keV is fixed for these particles [VGGAL07]. As mentioned above, in this project, the MCNP code was employed for electron and photon transport calculations in different components of irradiation setups optimizing the nuclear-based parameters required for obtaining an efficient design of the irradiation setup.

ANSYS and COMSOL Multiphysics software are the most powerful and well-known software, used extensively for heat transfer and fluid dynamic calculations. Both software give accurate results; however, ANSYS is oriented more towards the industry while COMSOL is academia-oriented. This is due to the fact that in COMSOL, more physical modules and different tools for a coupled model with very different physics are provided compared to the ANSYS [COMSOL, ANSYS]. In this project, the COMSOL Multiphysics software is employed for the heat transfer analysis. This software allows considering the heat transfer analysis in a three-dimensional and time-dependent problem. The COMSOL Multiphysics software also provides different physical modules that enable the possibility of simultaneous combination and modeling of different joint physical phenomena. The COMSOL Multiphysics software is a deterministic code, which relies on a numerical solution of the governing equations based on the Finite Element Method (FEM). This discretization method enables efficient, unstructured, adaptive meshing in different geometries [COMSOL, VOG19, VT19, VOG20, VOG16, VVG16].

## 1.4 Electron beam accelerators

Over the years (since the 1900s), many types of electron accelerators have been developed. To date (2014), about 25'000 electron accelerators are in use, most of them being linear accelerators (linacs). The contribution of circular cavity-shaped electron accelerators is limited to about 1000 [CV14, M98]. Electron accelerators can be used for different applications, such as sterilization, thin-film analysis, polymer chemistry, food treatment, environment, and Bremsstrahlungs production. Electron accelerators can be categorized based on different criteria, including electron beam energy, electron beam current, electron beam power, acceleration method, beam shape, etc. Classification based on the electron beam energy seems the most appropriate since energy determines the range of penetration depth and, therefore, possible applications [M98].

Low-energy electron beam accelerators are those where the electron beam has a lower energy than 500 keV. These accelerators usually have a long-evacuated linear tube connected to a direct current (dc) high voltage generator. Electron acceleration is performed inside the evacuated tube where the (dc) high voltage is produced (usually) by a rectifier circuit and a low-frequency iron-core transformer. A single gap exists between the thermionic cathode and the anode in most of the employed tubes in the low-energy electron accelerators. The cathode produces the electrons. The anode usually is a thin window in metallic form, which is at ground potential and allows the accelerated electrons to exit the evacuated tube. Low-energy electron beam accelerators are simple in design, compact in size, and self-shielded from the radiation protection point of view. Despite their low electron beam energy, a high-power electron beam is one of their advantages, i.e. for electron beam welding applications [M98, BSKS99].

Medium-energy electron beam accelerators are considered those that can produce electrons with less than 5 MeV. In this energy range, the acceleration tube typically contains a number of electrodes called dynodes to distribute the high (dc) voltage and prevent internal sparking. Most of the medium-energy electron beam accelerators are high current dc potential-drop devices, in addition to the pulsed radiofrequency linacs. In the case of dc medium-energy electron beam accelerators, it is not practical to use a flexible high voltage cable for the connection of the generator and the accelerator. Therefore, for systems operating at higher voltages of 800 keV, both the high-voltage generator and the acceleration tube are combined within the same enclosure. The use of compressed (pressures of ~6–7 atm) sulfur hexafluoride gas is usually appropriate for insulation purposes. The dynamitron was one of the earliest and most widely used in the category of medium-energy electron beam accelerators. A dynamitron can produce a beam power of 300 kW at 5.0 MeV (IBA Industrial, Inc., Dynamitron). An example of using RF linear accelerators in the medium-energy electron beam range is the family of linear accelerators at the Budker Institute of Nuclear Physics in Russia, which can produce 0.6-4 MeV electron beam energies with beam powers of 50 kW [HH12, G77]. Medium-energy electron beam accelerators are being utilized in various fields of sterilization, material modifications, cross-linking of cables, etc. [G77].

High-energy electron beam accelerators are those where the electron beam energy is higher than 5 MeV. High-power and high-energy electron beam accelerators use electric fields generated by radio frequency (RF) power to accelerate electrons. High-voltage dc generators with a high-power electron beam could also be constructed for high electron beam energies; however, their size is much larger than for RF type accelerators. This type of accelerator is

more expensive to make and house than RF type electron accelerators. The most widely used high-energy electron beam accelerators are linacs. Almost all of these linacs consist of a series of small coupled cavities that are energized via a microwave generator. High energy electron beam accelerators have many applications in food irradiation, medical device sterilization, radionuclide production, etc. In the following, some high-energy electron beam accelerators are described briefly.

#### **1.4.1 Different types of high-energy electron beam accelerators**

Different types of high-energy electron beam accelerators have been developed. In the following, some of the most widely-used high-energy electron beam accelerators are described.

##### **Dynamitron**

A dynamitron is a particle accelerator which depending on its configuration, can accelerate electrons or positrons. In 1959, the dynamitron was originally patented. Then, the dynamitron developed considerably at Radiation Dynamics, Inc., which was acquired later by IBA. In the last 20 years, some Chinese companies have also built these accelerators [HH12]. The tube in the dynamitron consists of two semi-cylindrical RF electrodes. A series of semicircular corona rings are located between the two semi-cylindrical electrodes, and a high-frequency oscillating voltage is applied between them. The corona rings in the dynamitron are connected to the rectifier junctions, where the rectifier stages themselves are connected between the high voltage terminal and the ground (see Fig. 1.105a). This results in a voltage inducement in the rings mentioned above and, finally, particle acceleration. For insulation purposes in the dynamitron,  $\text{CF}_6$  gas was usually employed [S13]; however, in the new models offered by IBA, the tube is under ultra-high vacuum ( $1\text{E-}8$  mbar range) [IBANO.1]. There are some dynamitrons providing either a high beam power (300 kW) or high electron beam energy (30 MeV); however, attaining both features at the same time, which would be suitable for efficient radionuclide production purposes, was not attainable so far [S13, B89, CF65]. IBA's available commercial dynamitrons offered are those that have beam energies up to 5 MeV with a beam current of 160 mA. Dynamitron electron accelerators are mainly used for cross-linking of wire and cable insulation, tire industry, sterilization, etc.; however, dynamitron proton accelerators are used mostly for photovoltaic slicing and cancer treatment (using Boron Neutron Capture Therapy) [IBANO.1].

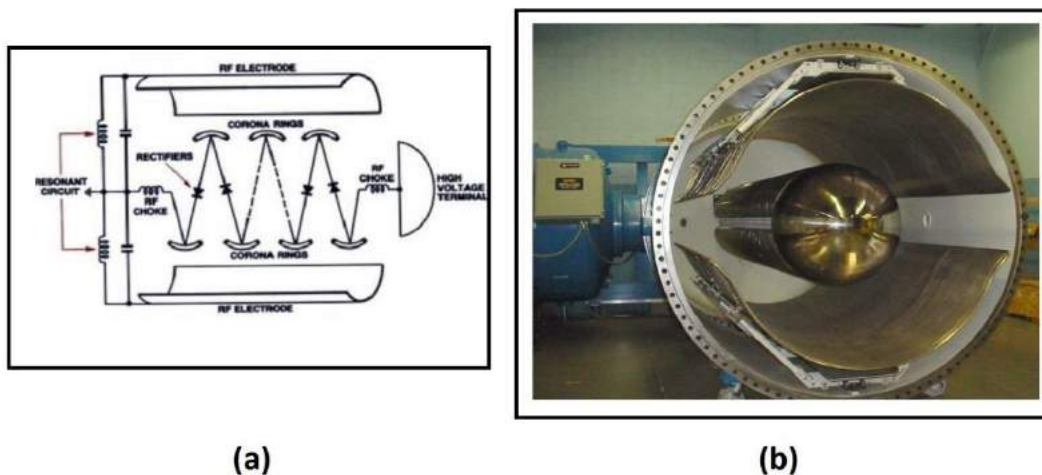
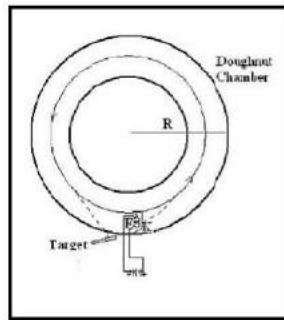


**Fig. 1.105:** a) Schematic representation of the dynamitron b) 5 MeV, 300 kW dynamitron developed by Radiation Dynamics, Inc. [HH12]

## Betatron

The principal design of a betatron was first formulated in 1928 by Widerøe; however, the device was not able to work properly. In 1940, D.W. Kerst constructed a 2.35 MeV betatron as the first circular electron accelerator after realizing that the magnetic field requires to be shaped so that it provides focusing and preventing the escape of the electrons. For several years, the betatrons played a significant role in electron-beam therapy since they were able to deliver X-ray beams up to an energy of 40 MeV. At most, at the beginning of the 1970s, about 200 units were installed and used in hospitals [H05]. A betatron is a cyclic electron accelerator that is based on the transformer technique of magnetic induction. A torus-shaped vacuum chamber and an alternating current allow the electrons to be accelerated in a circular path many thousands of times (see Fig. 1.106). The vacuum chamber is placed between the electromagnet poles (50 or 60 Hz sinusoidal voltage is supplied) [HH12]. The betatron magnet field plays a dual role. First, it confines the electron beam inside of an evacuated donut-shaped chamber. Secondly, it can accelerate the electrons using the electric field induced via the change in the magnetic flux, which passes through the circular-shape electron orbit [H05, B69]. As was mentioned above, Kerst built the first betatron, a 2.35 MeV machine. Then, he built a 20 MeV betatron, and finally, a 300 MeV machine, as the largest betatron ever built [V20]. The betatron can produce high electron beam energy (up to 300 MeV); however, the electron beam current is relatively small due to the applied confinement technique. High weight and cost are also among their major disadvantages. The betatron can be employed for the production of energetic photons if the accelerated high-energy electron beam impinges on a metal target [HH12, MI60, B69]. Recently, JME Company (in England) has constructed many portable (up to 9 MeV) compact in size betatrons, which produce X-ray beams and can be a substitution for  $^{60}\text{Co}$  gamma sources [JME].



(a)



(b)

**Fig. 1.106:** a) A schematic representation of the betatron b) A 35 MeV betatron at the University of Melbourne [HH12]

## Microtron

A microtron is an electron accelerator that was first proposed by Veksler in 1944. The first microtron, which was able to work properly was constructed in Canada in 1948. The microtron, also called an electron cyclotron, features a cyclotron (constant magnetic field), and a linac (resonant cavity). In a microtron, electrons are accelerated in a resonance cavity (a single microwave cavity) with repeated circular passes. In the first microtron, the injection system was based on a field emission technique; however, a thermionic electron gun mounted close to the cavity entrance aperture of the microtron is usually employed [BR81]. The extraction of the beam in a microtron is straightforward and is usually performed by insertion of a field-free tube, called the extraction tube, tangentially (as is shown in Fig. 1.107a) to the orbit. Microtrons are categorized into two types: circular and racetrack. These two types of microtron operate almost in the same way, and the difference is only in the magnet shape (see Fig. 1.107) [H05, BR81, K65, C06]. A microtron can produce electrons with an energy range of up to some tens of MeV and some hundreds of MeV in circular microtrons and racetrack microtrons, respectively. This difference stems from the fact that the increase in electron beam energy increases the weight and size in circular microtrons (because of the low value of the field) and causes magnetic field inhomogeneity. In racetrack microtrons, the circular microtron splits into two similar halves that are connected with a linear accelerator, located in the straight section between the two dipoles, as shown in Fig. 1.107b. The linear accelerator tube length (which corresponds to the acceleration magnitude) can be chosen freely depending on by how much energy is needed to be imparted to the electron. The electron injection in the racetrack microtrons is somewhat similar to circular microtrons. The difference is that in addition to the possibility of direct injection by an electron gun mounted at the side of the linac's entrance-end (see Fig. 1.107b), the beam can be injected in a relativistic energy range from a pre-accelerator. In Fig. 1.108, a schematic representation of the cascade of three racetrack microtrons with the injector linac installed at the University of Mainz is presented. This setup of cascade accelerators consists of a linear accelerator as an

injector in addition to a cascade of three microtrons, which can provide a maximum beam energy of 855 MeV and 100  $\mu\text{A}$  beam current with 100% duty cycle [T18].

Thanks to the well-separated orbits in the racetrack microtrons, the beam extraction is straightforward and usually is carried out using a small magnet to deflect the orbit and allow the beam to be extracted into a designed extraction tube. Microtrons depending on their beam energies have different applications in research and industry, such as medical applications (radiation therapy, radiography, etc.), nuclear physics, radionuclide production (through photonuclear reactions), etc. [BR81].

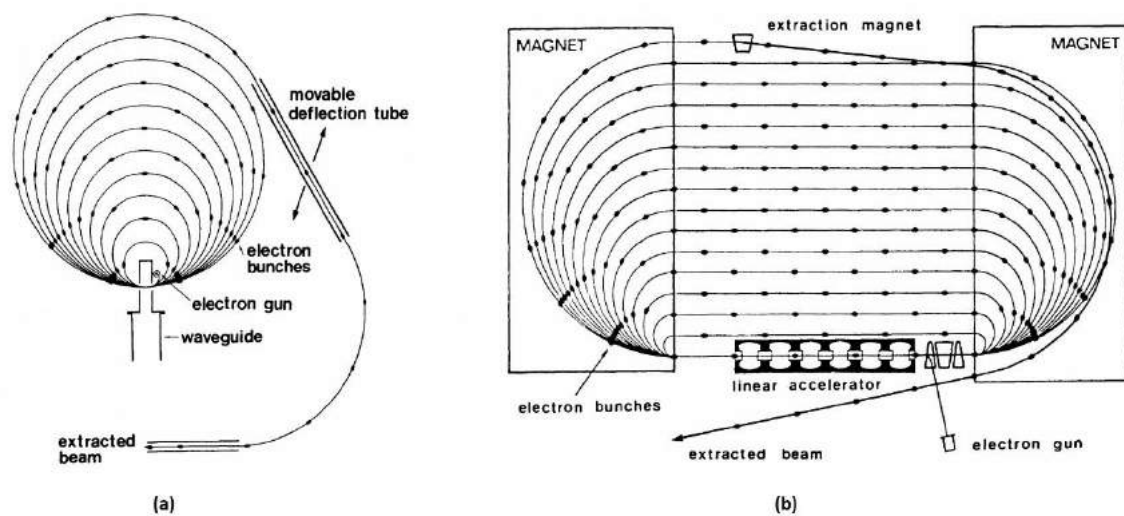


**Fig. 1.107:** Schematic representation of a) Circular and b) Racetrack microtron [BR81]

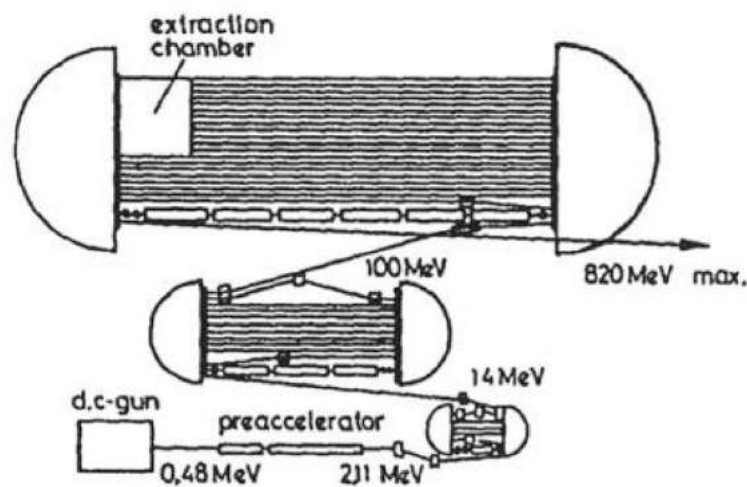


**Fig. 1.108:** Schematic representation of the cascade of three racetrack microtrons with the injector linac installed at the University of Mainz [T18]



Microtrons with high electron beam energy and high beam power have been developed and constructed in the last decades; however, the main problem associated with them is the high radiofrequency range (in the range of GHz) that makes them unsuitable for radionuclide production from the heat removal point of view (will be discussed later) [R58, KBM62]. Previous and current companies, which work on microtron construction and development, are the R&D 'AGAT' Corporation, Scanditronix, Photon Production Laboratory (Mirrorcle Analysis Center), and Racetrack Microtron Systems AB.

## Linac

In 1928, Rolf Widerøe built the first linear accelerator [H05]. Linac, a contraction of the term linear accelerator, accelerates electrons in a straight line while gaining energy as they move along the line from the accelerating electric field [HH12, A01]. Linear electron accelerators consist of different parts, including an electron source, accelerator tube, cylindrical electrodes, etc. As is shown in Fig. 1.109, the electron beam travels (from the left hand in Fig. 1.109) straight through a series of electrodes (in a hollow and tubular shape with progressively increasing length) connected to opposite poles (in alternating form) of a voltage source (RF). As the electrons cross the gaps (between the electrodes), they are accelerated and reach a certain energy. Once the electron beam enters an electrode, it drifts in a field-free region for a while that equals half the period of the applied RF voltage. When the electrons are within a drift tube, the voltage polarity is reversed, and then, the electron is accelerated as it crosses the following gap. On this basis, the applied oscillating voltage to alternate cylindrical electrodes has the opposite polarity. Since the adjacent cylindrical electrodes have opposite voltages, this leads to an oscillating electric field (E) in the gap located between each adjacent pair of cylindrical electrodes. As is shown in Fig. 1.109, the straight hollow pipe vacuum chamber is evacuated with a vacuum pump to prevent collision of the accelerated electrons with air molecules.

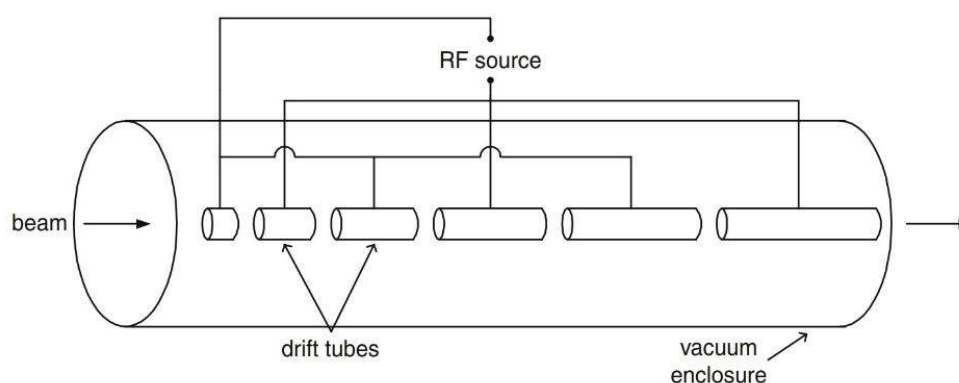


**Fig. 1.109:** A schematic representation of a linac [H05]

It is worth pointing out that the development of linacs was always relied on the available RF technology [H05].

The tube's length in linacs depends on the application and the energy of the accelerated electron beam (from a fraction of a meter to thousands of meters). As linacs have many applications in solid-state physics, medicine, biology, etc., the size of the tube and the

number of spherical electrodes are variable. As an illustration, in the case of sterilization of medical products, the tube length and the number of required spherical electrodes are much lower compared to those employed in high-energy physics. To facilitate a comparison, in Fig.1.110, two different facilities, first (see Fig. 1.110a), in a medical products sterilization facility, and second (see Fig. 1.110b), at the site of the Stanford Linear Accelerator Center for physics research are presented. Due to wide applications of linacs, many companies produce them, such as Mevex, Mitsubishi, L-3 Services Inc., Pulse Sciences (L-3 PS), Budker Institute (BINP), etc.

The electron source design could be different. It can be a cold cathode, a hot cathode, a photocathode, or a radiofrequency (RF) ion source [S13, H05]. For high electron beam energy purposes, the beamline needs to be very long. They are more expensive to manufacture and house than circular chamber-type electron accelerators (such as betatron, rhodotron, microtron, dynamitron, etc.). Besides, for large-scale radionuclide production, a high duty cycle of electron accelerators is a prerequisite parameter. However, linacs are typically operated in a low duty cycle from a few tenths of a percent up to about one percent. This causes a remarkable heat loading in a very small fraction of time, leading to a significant sharp temperature increase in a very small fraction of time in the converter target [HH12, S13, H05].



**Fig. 1.110:** a) Two installed side by side linacs with 15kW and 10MeV incident electron beam energy in a medical products sterilization facility. b) a 3.2-kilometer linear accelerator installed at the Stanford Linear Accelerator Center that enables it to accelerate electrons to 50 GeV [HH12, SLAC]

## Rhodotron

A rhodotron is an electron accelerator developed for high-energy and high-power electron beam applications. In the 1980s, researchers from the French Atomic Energy Agency (CEA) proposed the underlying accelerating principle of the rhodotron. After that, in the early 1990s, the patent was licensed to the IBA, where it was further developed and built into commercial rhodotron systems [HH12]. In the rhodotron, electrons are accelerated in a single coaxial resonant cavity under vacuum. The electron beam passes in the coaxial lines shorted at both ends, and the external magnets bend back and redirect them to the cavity center to let them again accelerate in the next line. This process repeats until the electron beam energy reaches the desired energy. In other words, whenever the electron beam crosses the cavity, it gains a

certain energy; therefore, multiple successive crossings are required to obtain a desired exit electron beam energy [HH12, TAHS12, AJPB04, P89] (see Fig. 1.111). The rhodotron consists of different components, including a cavity, an electron gun, an RF system, the deflection magnets, and a cooling water system [AJPB04]. The cavity of the rhodotron is composed of roll-shaped and welded plates of steel which are electrochemically copper-plated. The electron gun in a rhodotron is located at the cavity's outer wall and is pulsed at the RF frequency since electrons must be injected into the cavity when the field is accelerating; therefore, the electrons are drawn away and accelerated by means of the radial field. The cathode is a low work function indirectly heated flat cathode with a modulation grid structure (i.e., a gold-plated tungsten wire grid) [AJPB04]. The RF system is made up of a voltage-controlled oscillator afterward of a chain of amplifiers [J96]. The deflection magnets bend back and redirect the electron beam emerging from the accelerating cavity to the cavity-center and preserve electron focusing properties in both  $R$  and  $Z$  directions. A cooling water system efficiently cools down the cavity and subsystems in order to keep the temperature of the entire parts below 35°C. At the exit of the rhodotron, the cylindrical-shaped accelerated electron beam is guided through the beamlines from the cavity of the accelerator to the radiation vault [AJPB04]. The design of a rhodotron also allows the extraction of multiple beam lines (not concurrently) when different beamlines with different electron beam energies are required (see Fig. 1.112) [K03]. As is shown in Fig. 1.112, the electron beam can be extracted from the cavity whenever it reaches a certain energy. In comparison with linacs, which can produce an average beam power of 100 kW (depending on the final electron beam energy and current), rhodotrons are able to generate up to 200 kW at 10.0 MeV and even 700 kW at 7.0 MeV. Such high-power multi-beam line rhodotrons have already been installed in the U.S. Postal Service in order to sanitize critical governmental mails [HH12]. Since the invention of the rhodotron, several models have been commercially available (Fig. 1.113). As is shown in Fig. 1.113, the main difference is in electron beam energy and beam-power. Among the developed rhodotron models, the rhodotron model TT300-HE can be considered as the best option for radionuclide production purposes due to the high electron beam energy, high electron beam power and low RF system (i.e., low beam repetition rates) [IBANO.2, IBANO.3, BGGNB19].

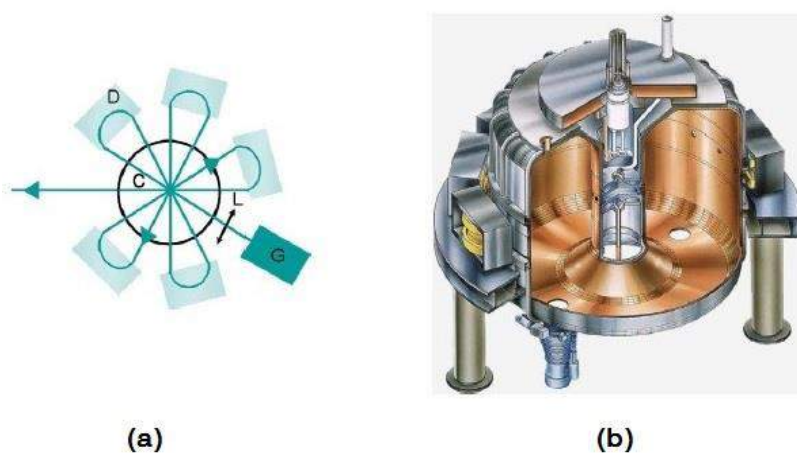


**Fig. 1.111: a)** A schematic representation of the rhodotron where G, L, C, and D are electron gun, magnetic lens, accelerating cavity, and bending magnet, respectively. **b)** A cutaway schematic view of the rhodotron [HH12]

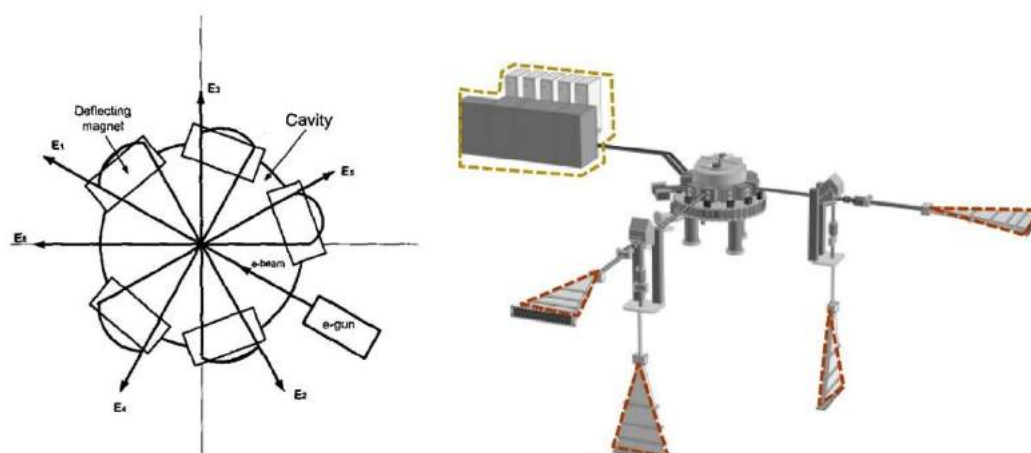


**Fig. 1.112:** A schematic representation of multiple beam lines (shown as  $E_1... E_6$ ) of a rhodotron [K03, IBANO.1]

New TT50	TT100	TT200/TT300	TT1000	TT300-HE New High Energy
				
1 to 10MeV	2.5 to 10MeV	1 to 10MeV	1 to 7MeV	Up to 40MeV
10 passes	12 passes	10 passes	6 passes	12 passes
2mA	4mA	10mA/35mA+	80mA	3.1mA
<b>10 to 20kW</b>	<b>20 to 40kW</b>	<b>20 to 480kW</b>	<b>560kW</b>	<b>125kW</b>
<b>Pulsed</b>	Continuous wave	<b>CW or pulsed</b>	<b>CW or Pulsed</b>	<b>Pulsed</b>

**Fig. 1.113:** The rhodotron models [ARIES18]

## 1.4.2 Comparison of high-energy, high-power electron beam accelerators

For radionuclide production purposes using electron accelerators, there are two main requirements; beam energy, and beam current. The beam energy of an electron accelerator should be higher than the reaction threshold, and the beam current must be as high as possible to produce an adequate quantities of radionuclides. In the case of using a high-energy and high-power (or high-current) electron beam accelerator, a considerable amount of heat is deposited in the converter target, which causes a very high local temperature increase and, therefore, failure of its mechanical stability. Therefore, the time structure and width of the beam (RF system), in addition to the above-mentioned considerations, are of great importance.

In this section, a comparison of the aforementioned high-energy, high-power electron accelerators is presented. A betatron can produce high electron beam energy (up to 300 MeV); however, the electron beam current is relatively small due to the applied confinement



technique. Some dynamitrons provide either a high beam power (300 kW) or high electron beam energy (30 MeV); however, attaining both features simultaneously, which is suitable for efficient radionuclide production purposes, was not attainable, so far. For large-scale radionuclide production, the high duty cycle of electron accelerators is a prerequisite parameter; however, linacs are typically operated in a low duty cycle from a few tenths of a percent up to about one percent [S13], which are not appropriate for large-scale radionuclide production purpose. A microtron can accelerate electrons up to some hundreds of MeV, which is relatively high. The disadvantage of a microtron is that their RF system operates usually from 1 GHz to 10 GHz, making it inappropriate due to the high beam repetition rates. Rhodotrons can produce high electron beam energy (up to 40 MeV) because electrons are accelerated through repeated passes in a cavity, making the rhodotron relatively small and compact in size. Additionally, a high-power electron beam (up to 700 kW) can be achieved (depending on the model and provided beam energy). The recirculating electron beam allows the capability of having multiple electron beamlines that have different electron beam energies extracted from the same accelerator (applicable for different target irradiation at different locations; see Fig. 1.112). High duty cycle and relatively low operational radiofrequency system are among other advantages that make the rhodotron interesting for promising efficient radionuclide production in the future. However, due to the bending of the electron beam back into the cavity, shielding requirements are very high.

## 1.5 Photonuclear irradiation setup

In general, the main photonuclear irradiation setup components are entrance window, electron to photon converter target, production target(s), shielding and a massive beam stop (against various radiations), and coolant (for cooling down any irradiated components) (see Fig. 1.114).

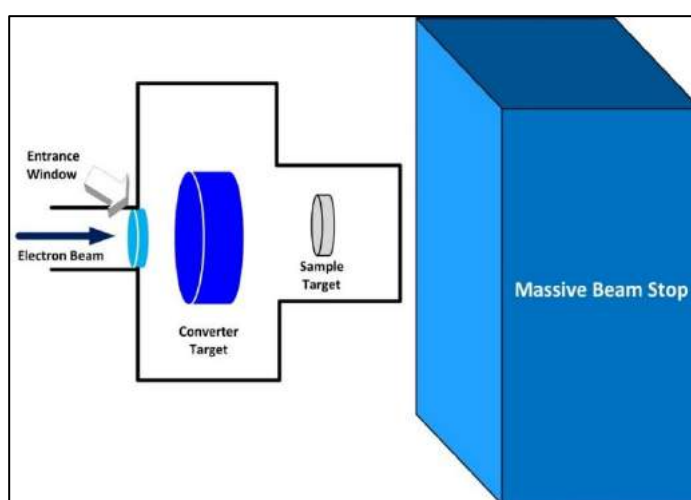


**Fig. 1.114:** Scheme of the proposed photonuclear setup

The idea of using electron accelerators for radionuclide production is not new and was investigated previously [SSSC10, HS15]. The function of the entrance window is to separate the cooling circuit of the converter from the vacuum of the accelerator. In literature, most of the works focused on the efficient design of a Bremsstrahlungs converter target as the major

component of a photonuclear irradiation setup. The Bremsstrahlungs converter target transforms the electron's energy into photons via the Bremsstrahlungs interaction mechanism (see section 1.1.1.5). The production target irradiation for the radionuclide production purpose also needs to be investigated to illustrate the amount of attainable radionuclide production yield through the designed photonuclear irradiation setup. The shielding of the transmitted electrons and photons from the system is an essential part of the study to ensure safe operational conditions from the radiation protection point of view. In the following, some of the foremost relevant studies to each discussed irradiation setup component are presented.

## Electron beam

The electron beam can be produced by an electron gun in electron accelerators. The electron gun is an essential part of every electron accelerator and can shape the electrons' current in a proper shape. Electron guns work in a continuous or a pulsed mode of a DC or RF type. They can produce electrons in different ways, such as thermionic, photoelectric, and electric field emissions. The two former cases are considered mostly in electron accelerators; however, the latter is more applicable in electron microscopy.

Electron guns consist of a cathode, an energy source, an electric field, and a vacuum environment. The cathode refers to a material for electron extraction. The energy source is utilized to excite electrons above the work function of the cathode; the electric field is applied for electron acceleration in addition to beam collimation; and finally, a vacuum environment prevents electron scattering and cathode contamination [GSS08, ADGGRZ14].

Electron beams are usually formed with a Gaussian shape. The Gaussian shape focuses electrons more in the beam's center, leading to a narrower conic-shaped photon emission angle. The photon shape emission can also affect the specific activity of the produced radionuclides in the target. In Fig. 1.115a, the photon flux distribution (generated from a 40 MeV and 1 kW incident electron beam in 2mm tungsten) and the specific activity of  $^{67}\text{Cu}$  in the Zn target (Fig. 1.115b) are presented [HS15].

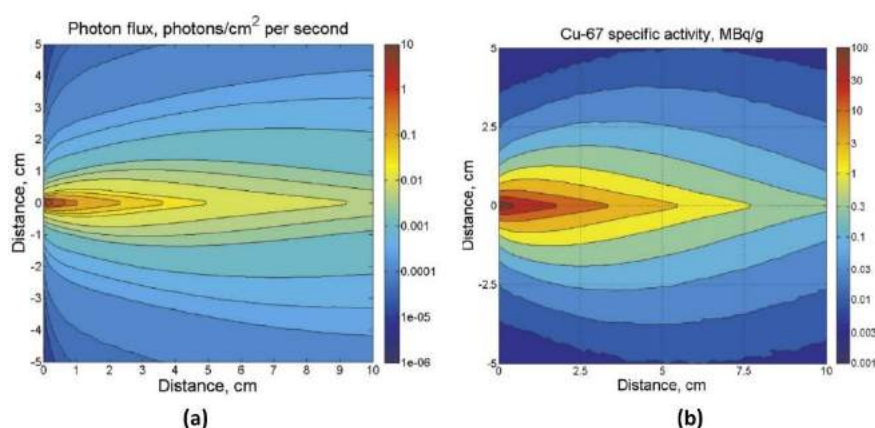


**Fig. 1.115:** a) Photon flux distribution generated from a 40 MeV and 1 kW incident electron beam and 2mm thick tungsten. b)  $^{67}\text{Cu}$  yield distribution in Zn target in units of MBq/g [HS15]

Besides the benefit of more photon interaction probabilities with the target material, in some cases, the target size is limited due to availability and radioactivity (e.g.,  $^{226}\text{Ra}$ ) or material cost (e.g., high enrichment), which makes the electron beam shape essential. Gaussian distributions can be different from each other based on height and width. On this basis, the area of the target in which the incident electrons make interactions can differ. This results in a different amount of heat deposition per unit area and, therefore, a significant difference in a temperature gradient. In the case of a rhodotron, the amount of heat deposited on the converter target is significant. Accordingly, the electron beam shape can play a significant role. The incident electron beam is considered to fall at a 90 degree angle on the target surface. The distribution of electrons inside the beam is taken Gaussian with various full width at half maximum (FWHM), which refers to the width of the Gaussian distribution at the position of half of its maximum (see Fig. 1.116) [TL15].

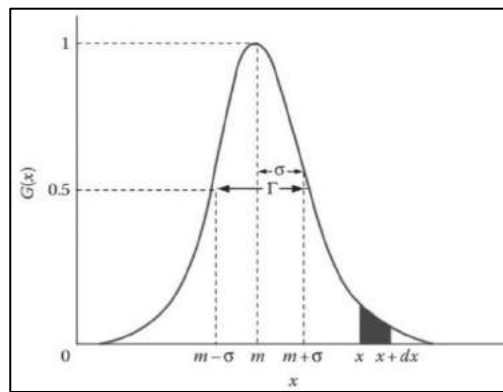


**Fig. 1.116:** A 1D Gaussian distribution [TL15]

As shown in Fig. 1.116, the FWHM denoted by the symbol  $\Gamma$  is wider than the Gaussian distribution's standard deviation ( $\sigma$ ). The Gaussian function formula can be written in one dimension as [TL15]:

$$G(x)dx = \frac{\sqrt{4 \ln(2)}/\pi}{\Gamma} \exp\left(\frac{-4 \ln(2)(x-m)^2}{\Gamma^2}\right) dx; \Gamma \neq 0, \quad (1.78)$$

where  $G(x)dx$  is the probability that the value of  $G(x)$  lies between  $x$  and  $x + dx$ . This is represented as the shaded area in Fig. 1.116 [TL15]. Fig. 1.117 shows the Gaussian distribution for different FWHMs. As can be seen, the height and width of the Gaussian function can significantly be influenced by considering different values of the FWHM. A Gaussian distribution can also be considered in two-dimension (see Fig. 1.118). The Gaussian distribution with equal standard deviation (or FWHM) in each dimension can be represented as:



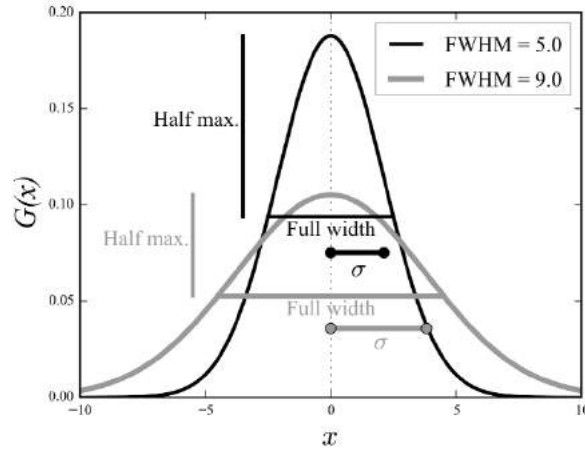


**Fig. 1.117:** 1D Gaussian distribution for different FWHM [P16]

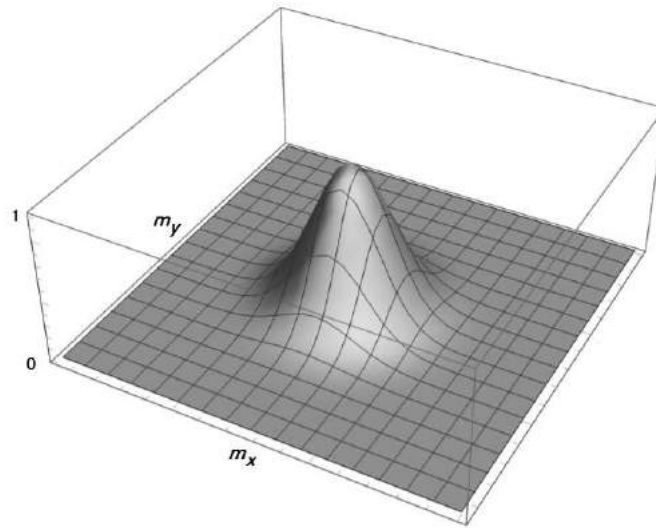


**Fig. 1.118:** A 2D Gaussian distribution

$$G(x, y)dxdy = \frac{4 \ln(2)}{\Gamma^2} \pi \exp \left( \frac{-4 \ln(2) \left\{ (x - m_x)^2 + (y - m_y)^2 \right\}}{\Gamma^2} \right) dxdy; \Gamma \neq 0. \quad (1.79)$$

According to the above discussion, it can be concluded that the electron beam Gaussian shape is able to affect the results of heat transfer simulation considerably. On this basis, in heat transfer modeling (which is discussed in the next chapter), more detail regarding the beam shape and its associated considerations are presented.

## Entrance window

The entrance window has a significant impact on the performance of the irradiation setup since it should tolerate a significant pressure difference across the window. The pressure difference is due to the vacuum condition in the electron beam exit of the accelerator and the atmospheric (or higher pressure) cooling circuit condition in the irradiation setup. The vacuum condition requirement in the electron accelerator exit is to prevent collisions of the electron beam with the gas molecules, which is called the beam broadening effect and increases with the increase of pressure (see Fig.1.119). Moreover, the vacuum condition allows for higher voltages [HH12].

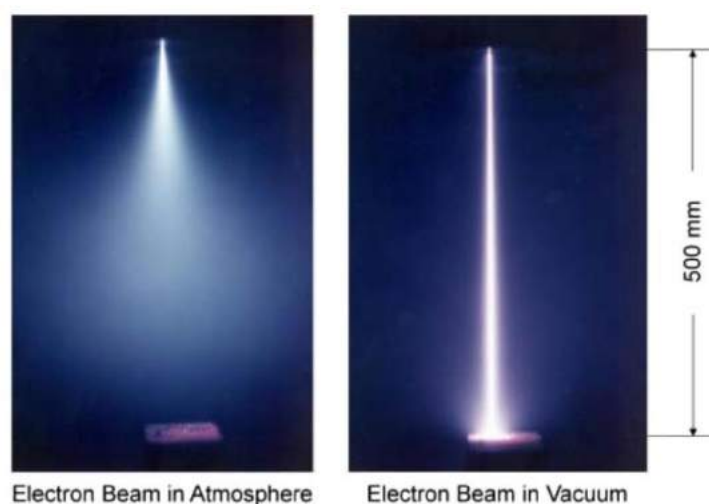


**Fig. 1.119:** Variations of beam broadening under atmospheric and vacuum conditions.

Although in a vacuum condition, electron beams are not visible to the human eye, a “beam glow” is produced as the ambient pressure increases because of the collisions between gas molecules and incident electrons. As is shown in this figure, this can eventually lead to the subsequent excitation of the ambient gas molecules and shows the beam broadening effect [HH12].

High transmission of electrons, high mechanical strength, and gas tightness are among the essential characteristics that the entrance window’s material should have. Among all the candidate materials, beryllium is the most commonly used material for the entrance window. The characteristics which make beryllium attractive are low density (around  $1.85 \text{ g.cm}^{-2}$ ), low atomic number ( $Z = 4$ ), high tensile strength, good thermal conductivity, and also relatively high melting point (around  $1287 \text{ }^{\circ}\text{C}$ ) [HLB14, CS95]. The beryllium thickness should be at least  $8\mu\text{m}$  to be gas-tight; however, it is usually manufactured with higher thickness to tolerate the difference in pressure [HMKPK15, NASA, W15, NMR15].

Beryllium also has some drawbacks such as limited supply, chemical reactions (with some chemicals), and toxicity, which the latter one requiring safety procedures for manufacturing [HMKPK15, EGKLLPRS20]. While beryllium poses these drawbacks, no alternative material is available. Most other alternatives pose much more severe drawbacks, such as lack of a high mechanical strength (which is essential for the entrance window), low electron absorption, and high melting point [HMKPK15, NASA, L03].

## Converter target

The converter target is the essential component in a photonuclear irradiation setup. There are some important features, which a converter target material must have. The first one is a high atomic number. According to section 1.1.1.5, the Bremsstrahlungs production increases by increasing the atomic number and density of the converter target material [SQ82, S19, DNA19]. In Fig. 1.120, Bremsstrahlungs production within 2 mrad\* angle for different materials (atomic numbers) at two different incident electron energies a) 20 MeV and b) 40 MeV as a function of thickness is presented [DNA19]. As is shown in Fig.1.120, the Bremsstrahlungs production also depends on the converter thickness. Besides, as is observable, the Bremsstrahlungs production increases by increasing the incident electron beam energy.

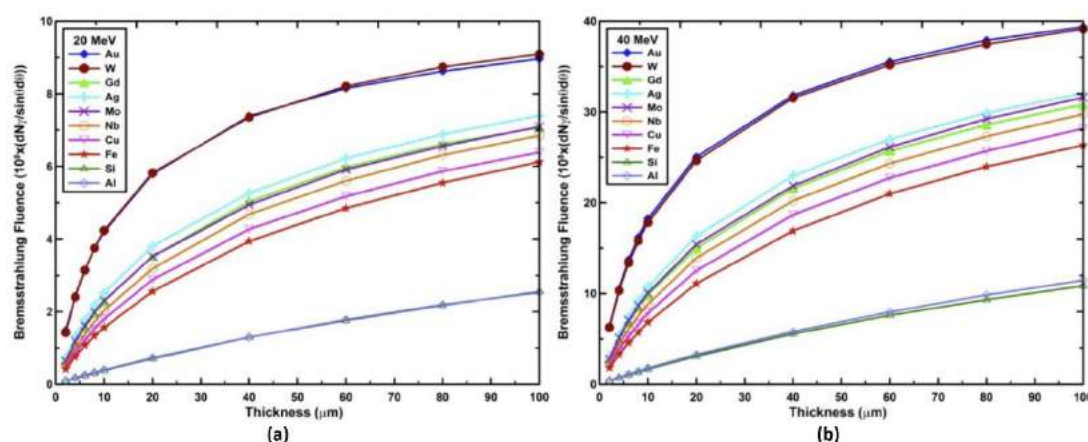
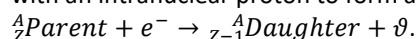


**Fig. 1.120:** The Z (atomic number) dependency for the production of Bremsstrahlung within 2 mrad angle at two different incident electron energies a) 20 MeV and b) 40 MeV as a function of thickness [DNA19]

The converter target must be a material with a high melting point due to the huge radiation heating power, which stems from collisions of the incident high-power, high-energy electron beam with the converter target. Among the candidate materials, tantalum, tungsten, and gold are the suitable choices [DSFO18]. Gold has a low melting point (around 1064°C) and is not cost-effective. Tungsten has high brittleness and accordingly is difficult to machining and fabrication. However, tungsten has a high melting point (3422 °C) and good corrosion resistance. Natural tungsten consists of 5 isotopes;  $^{180}\text{W}$  with a natural abundance of 0.12%,  $^{182}\text{W}$  with 26.50% natural abundance,  $^{183}\text{W}$  with 14.31% natural abundance,  $^{184}\text{W}$  with 30.64% natural abundance, and  $^{186}\text{W}$  with 28.43% natural abundance. In  $(\gamma, n)$  or  $(\gamma, 2n)$  reactions on  $^{180}\text{W}$  either  $^{179}\text{Ta}$  with 665 d half-life that decays to stable  $^{179}\text{Hf}$ , or relatively short-lived  $^{178}\text{W}$  ( $T_{1/2} = 22 \text{ d}$ ) that decays to  $^{178}\text{Ta}$  is formed, respectively. In  $(\gamma, n)$  or  $(\gamma, 2n)$  reactions on  $^{182}\text{W}$  and  $^{183}\text{W}$ ,  $^{181}\text{W}$  with a half-life of 121,2 d is formed, which decays by electron capture<sup>†</sup> to stable

\* 1 mrad is a thousandth of a radian, or 0.057296° degrees.

<sup>†</sup> In this radioactive transformation, one of the orbital electrons is captured by the nucleus and unites with an intranuclear proton to form a neutron according to the following equation [CJ09, J17, S07]:



According to this process, the atomic number Z of the daughter is one less than that of the parent, whereas the atomic mass number remains unchanged [CJ09, J17]. It is worth pointing out that when a

$^{181}\text{Ta}$  under the emission of X-rays and a very low energy gamma-ray. In  $(\gamma, n)$  reactions on  $^{186}\text{W}$ ,  $^{185}\text{W}$  with a half-life of 75.1 d is formed that decay by beta-minus\* emission (0.4 MeV) and gamma-ray of 125 keV with low branching ratio† to stable  $^{185}\text{Re}$ . The formation of  $^{182}\text{Ta}$  with 114.43 d half-life needs in  $(\gamma, p)$  or  $(\gamma, pn)$  reactions on  $^{183}\text{W}$  and  $^{184}\text{W}$  needs to be investigated; its dose rate may contribute significantly to the total dose rate even after an extended decay period. Of no big concern are  $(n, \gamma)$  reactions on the various W isotopes.

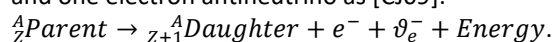
Tantalum with a high melting point (around 3017 °C), high atomic density ( $16.6 \text{ g.cm}^{-3}$ ), and high resistance against corrosion (by cooling) is one of the most suitable choices for the converter target material [HLB14]. Besides, the suitable physical and mechanical properties of the tantalum make it simple for fabrication. However, it is worth pointing out that tantalum is very sensitive to oxidation. Natural tantalum consists only of 2 isotopes;  $^{181}\text{Ta}$  with a natural abundance of 99.98799% natural abundance, and  $^{180\text{m}}\text{Ta}$  with 0.01201% natural abundance. In  $(\gamma, n)$  or  $(\gamma, 2n)$  reactions on  $^{181}\text{Ta}$  will form either very  $^{180}\text{Ta}$  or  $^{179}\text{Ta}$  with 665 days half-life to stable  $^{179}\text{Hf}$ , respectively. The latter nuclide decays by an electron-capture without the emission of gamma-rays. The formation of  $^{180}\text{Ta}^\ddagger$  with an 8.15 h half-life needs to be investigated, but its decay leads to either stable  $^{180}\text{W}$  or stable  $^{180}\text{Hf}$ . In  $(\gamma, p\text{xn})$ -reactions on Ta, stable Hf isotopes are being formed. $^{182}\text{Ta}$  can be formed by  $(n, \gamma)$  reaction on naturally abundant  $^{181}\text{Ta}$  (99.988%). The half-life of  $^{182}\text{Ta}$  that emits gamma-rays§ of 1.2 MeV is 114 days. This makes the tantalum converter target a source of gamma-rays [PBSKS07, D19]. In general, W activation is expected to be much higher than for Ta.

As was shown in Fig. 1.120, the Bremsstrahlungs spectrum also depends on the incident electron beam energy [EGS05, CV14, SSSC10, HS15, DSFO18, TBAM16, GMHEM07, A61, D19, P11]. In Fig. 1.121, the Bremsstrahlungs production (which corresponds to the photon yield in Fig. 1.121) per incident electron is presented for various incident electron beam energies emerging from a 1 mm thick cylindrical shape tungsten converter target [CV14]. As is shown, besides the difference in the end-point energy of the produced photons, the magnitude in photon production in the entire energy spectrum also is affected by changing the incident electron beam energy. On this basis, an increase in incident electron beam energy can result in a significant rise in radionuclide production rate. The importance of the electron energy beam on photonuclear production has been discussed in [C07]. Fig.1.122 is extracted from their paper and clearly shows that Bremsstrahlung that are generated from higher incident electron beam energies can significantly impact the production yield through the photonuclear reaction by increasing the number of impinging photons on the target nucleus

---

neutron-deficient atom that attains stability by positron emission does not exceed the weight of its daughter by at least two electron masses (i.e., 1.02 MeV), the neutron deficiency is overcome by the electron capture process [CJ09].

\* In this radioactive transformation, an intranuclear neutron decays into a proton (p), an electron ( $e^-$ ), and one electron antineutrino as [CJ09]:



Beta-minus decay occurs in the nuclides that are neutron-rich [CJ09, S07].

† Branching Ratio (BR) is the ratio of the number of particles that decay via a specific decay mode with respect to the total number of particles that decay via all decay modes [CJ09, J17].

‡  $^{180}\text{Ta}$  emits gamma-rays of 93 and 104 keV [PBSKS07, D19].

§ Gamma rays are monochromatic electromagnetic radiations that are emitted from the nuclei of excited atoms. These radioactive transformations provide a mechanism for ridding excited nuclei of their excitation energy without affecting either the atomic mass number or the atomic number of the atom [CJ09, J17].

in the GDR cross-section region [C07]. In the literature, some works have been performed regarding this issue. As an illustration, in one study, it has been shown that the increase in production yield of  $^{67}\text{Cu}$  due to an increase in electron beam energy from 30 to 45 MeV could triple [A07]. In addition, in 1969, the impact of the incident electron beam energy on the photonuclear reaction rate in titanium and vanadium targets was investigated [OKS69]. Similarly, in 2020, Khushvaktov et al. investigated the rate of photonuclear reactions in the  $^{165}\text{Ho}$  nucleus [K20]. Moreover,  $^{88}\text{Y}$  production rate investigations were conducted experimentally (with a 44 MeV pulsed electron linac) and theoretically (using the MCNP code) in reference [DSFO18].

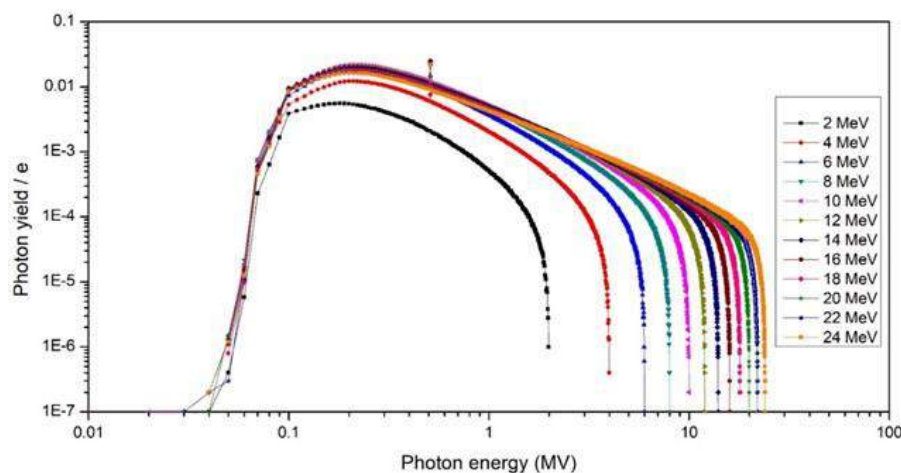


**Fig. 1.121:** The production of Bremsstrahlung (which corresponds to the photon yield in the y axis) per incident electron is presented for various incident electron beam energies emerging from a 1 mm thick and 1.5 cm radius cylindrical shaped tungsten converter target [CV14].

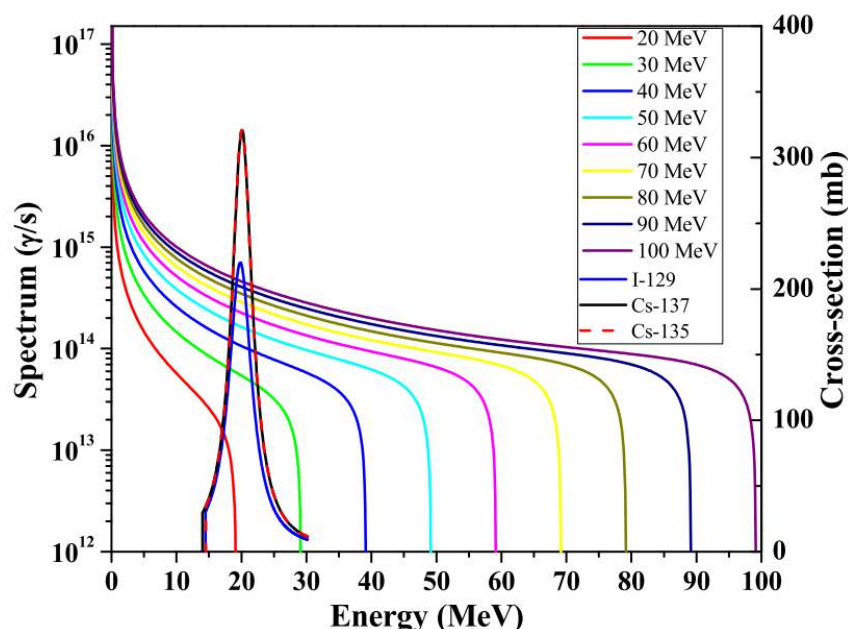


**Fig. 1.122:** Bremsstrahlungs spectrum for a tantalum converter target with 0.2 cm thickness with different electron energies and its impact on the production yield through the photonuclear reaction by increasing the number of impinging photons on the target in the GDR cross-section region depicted for some nuclides [RLK17]

As indicated before and shown in Fig.1.120, the Bremsstrahlungs production is a function of the converter target thickness [EGS05, PBSKS07, TBAM16]. In Fig. 1.123, the Bremsstrahlungs production as a function of tantalum thickness for an incident electron beam energy of 10 MeV is presented.

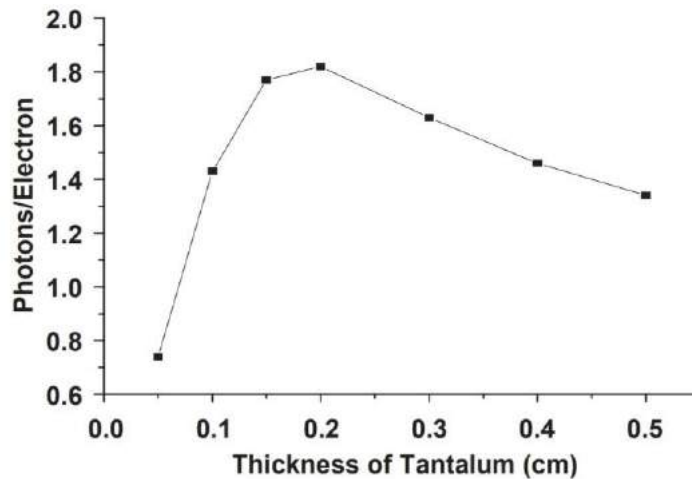


**Fig. 1.123:** Bremsstrahlungs production (per incident electron) as a function of tantalum thickness for a 10 MeV incident electron beam [EGS05]

As can be seen, the Bremsstrahlungs production reaches a maximum for a certain target thickness and then decreases again. This stems from the fact that, in the case of a thin target, electrons pass through the target fairly readily, leading to the production of relatively little Bremsstrahlung. If the target is too thick, the impact of photon attenuation is much larger than the small increase in photon production [BS70]. More precisely, in the case of a thick target, photons produced in the first part of the converter target will be attenuated by the rest of the remaining material. There is an optimum thickness for a particular target material and incident electron beam energy [W09].

The angular distribution of the produced Bremsstrahlung is also of interest. In Fig. 1.124, the angular distribution of the created Bremsstrahlung from a 60 MeV incident electron beam for various tungsten thicknesses is presented. In this figure,  $r_0$  is the electron mean range of 60 MeV in tungsten and equals  $16.5 \text{ g.cm}^{-2}$ , and  $z$  is the thickness in  $\text{g.cm}^{-2}$ . As can be seen, almost for all thicknesses, a sharp peak in forward angles is observed. Afterward a rapid decrease in larger angles with a dip around  $90^\circ$ , is followed by a rather flat distribution in angles beyond  $90^\circ$ . Additionally, Fig.1.124 shows that by increasing the thickness, the number of photons emitted at the smaller angles decreases and, in fact, is added to the photons emitted at larger angles [BS70].

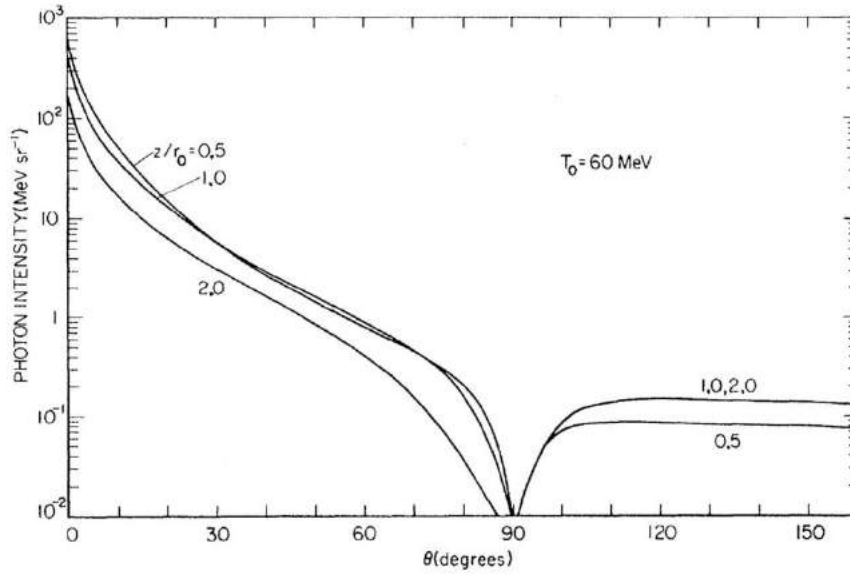


**Fig. 1.124:** Angular distribution of created Bremsstrahlung from a 60 MeV incident electron beam for various tungsten thicknesses, where  $r_0$  is the electron mean range for 60 MeV in tungsten and equals  $16.5 \text{ g.cm}^{-2}$ , and  $z$  is the thickness in  $\text{g.cm}^{-2}$  [BS70].

As was discussed in section 1.1.1.5 (Fig. 1.14), the angular distribution of the created photons significantly depends on the incident electron beam energy; in such a way that higher energetic photons are emitted at lower angles in a forward direction [GMHEM07, BS70, LM20]. Fig. 1.125 shows the spectrum of the Bremsstrahlung emitted at different angles due to a 60 MeV incident electron beam impinging on a tungsten converter target, where the parameters have the same usual meaning as stated in Fig. 1.124. As can be seen, higher energetic photons are emitted at smaller angles and vice versa [BS70].

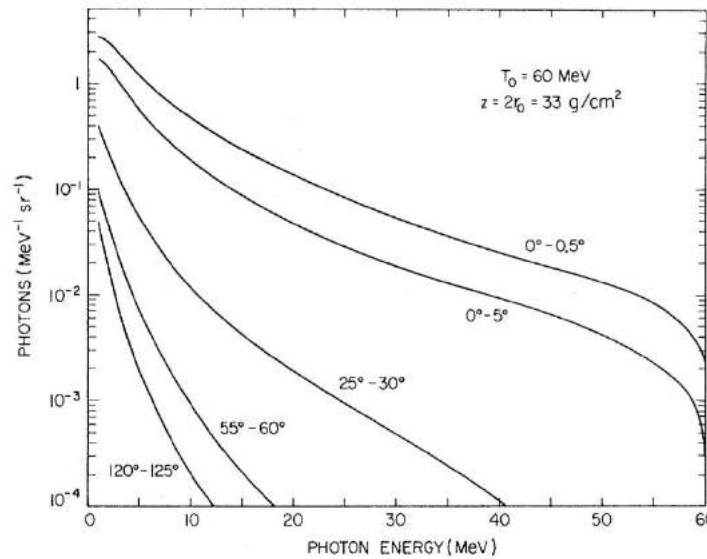


**Fig. 1.125:** Spectrum of Bremsstrahlung emitted at different angles due to a 60 MeV incident electron beam impinging on a tungsten converter target, where  $r_0$  is the electron mean range for 60 MeV in tungsten and equals  $16.5 \text{ g.cm}^{-2}$ , and  $z$  is the thickness in  $\text{g.cm}^{-2}$  [BS70].

Due to the angular photon distribution, approaching the production targets to the converter target gives rise to a higher radionuclide production rate. In Fig. 1.126, the change of the  $^{67}\text{Cu}$  production rate in terms of specific activity ( $\text{MBq/g}$ ) for different production target masses as a function of their position from the converter target (tungsten with 2mm thickness) is presented. As is observable, the production rate decreases by increasing the distance [HS15].

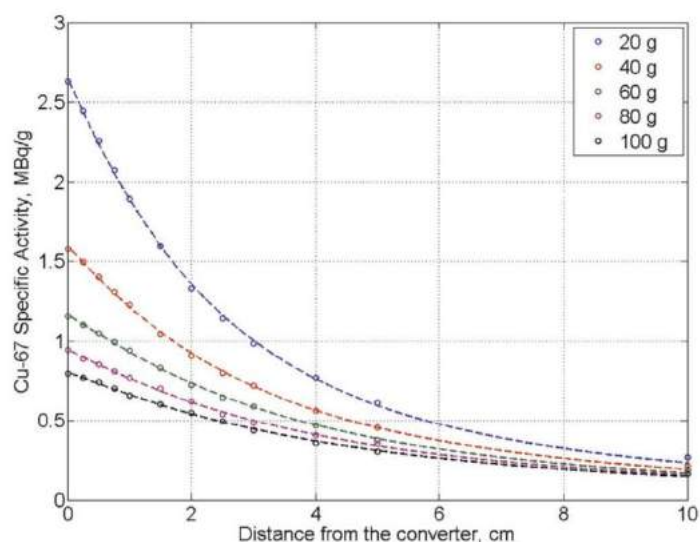


**Fig. 1.126:** Variation of  $^{67}\text{Cu}$  production rates in terms of specific activity ( $\text{MBq/g}$ ) for different production target masses as a function of their position away from the converter target (tungsten with a 2mm thickness) [HS15]

Photonuclear production rate dependencies on the converter target parameters of other medically relevant radionuclides were studied recently for  $^{47}\text{Sc}$  [A20],  $^{186}\text{Re}$  [L16],  $^{67}\text{Cu}$  [A19],  $^{225}\text{Ra}/^{225}\text{Ac}$  [MLA06] and  $^{99}\text{Mo}/^{99\text{m}}\text{Tc}$  [TBAM16, FT19]. One of the studied converter target parameters is, for example, geometry. A recent study showed that optimization in the converter target geometry allows an increase in  $^{99}\text{Mo}$  production by 2.8% [TFSG19].

As a significant fraction of the incident electron beam energy is transferred to the converter target, a heat transfer study is of great importance. Serious problems occur in the case of high-energy, high-power electron beam accelerators, in which a high heat load on the target makes target cooling a challenging problem. In 2020, Tsechanski et al. showed that the fraction of the transferred energy to a 20 mm thick  $^{100}\text{Mo}$  target increases linearly with increasing the incident electron energy (see Fig. 1.127) [TFS20].



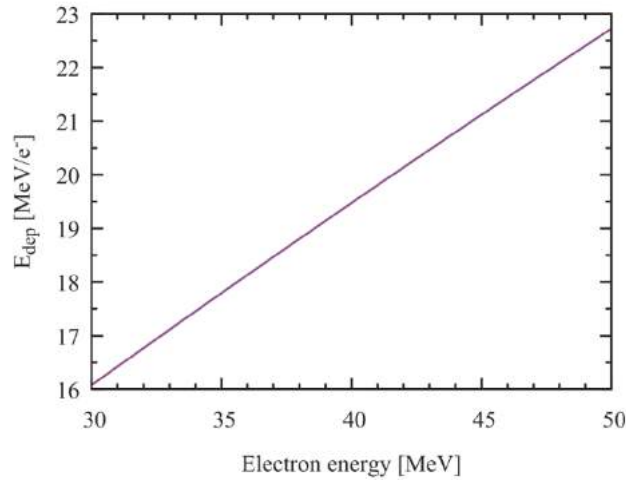


**Fig. 1.127:** Energy deposition as a function of the incident electron beam energy in a 20 mm thick  $^{100}\text{Mo}$  target [TFS20]

In 2009, Williams studied the energy density distribution and cumulative energy deposition for a 2-14 MeV incident electron beam energy in a 6 mm thick tantalum converter target using the MCNP code [W09]. It was shown that for a 6 mm thickness tantalum, the peak of energy deposition appears in different depths by changing the incident electron energy. However, it was revealed that the cumulative energy deposition changes proportionally with the incident electron energy with almost the same factor. In Fig. 1.128, energy deposition per incident electron ( $r_0 D(z)/T_0$ , where  $D(z)$  is the energy deposition in units of  $\text{MeV} \cdot \text{cm}^2 \cdot \text{g}^{-1}$ , all the other parameters have their usual meaning) in a tungsten target for various incident electron beam energy as a function of the depth in the target is presented. The results shown in Fig.1.128 include the contributions of electrons (primary and higher-generations), and generated Bremsstrahlung. As can be seen, the curves extend to rather great depths owing to the transport of energy by the produced Bremsstrahlung [BS70].

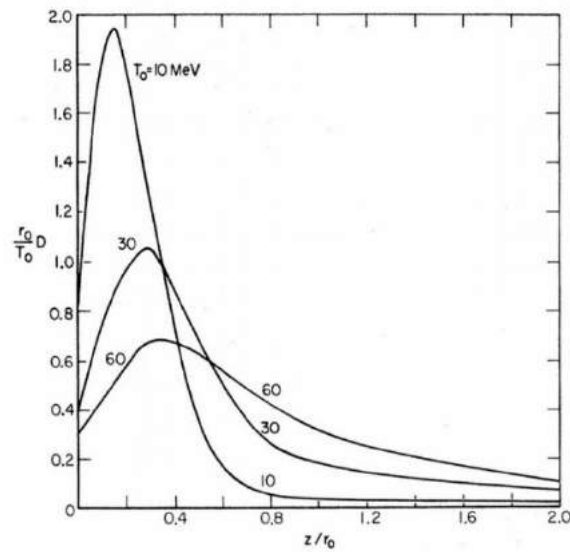


**Fig. 1.128:** Variation of the energy deposition per incident electron in a tungsten target for different incident electron beam energies versus thickness. The energy deposition is  $r_0 D(z)/T_0$ , in which,  $D(z)$  is the energy deposition in units of  $\text{MeV} \cdot \text{cm}^2 \cdot \text{g}^{-1}$  [BS70].

The investigation of photoneutron production in the tantalum converter target is also essential from the radiation protection point of view. The necessity of its investigation stems from the fact that the neutron interaction mechanisms and, therefore, the shielding considerations and appropriate material selection are different for either electrons, photons and neutrons [EGS05, BS70, PBSKS07, K20, FT19, D19]. Additionally, the produced neutrons are able to induce reactions in the production targets and produce radionuclide impurities. Photoneutron production through the  $(\gamma, n)$  reaction of  $^{181}\text{Ta}$  is the result of produced Bremsstrahlung interacting with the tantalum converter target [PBSKS07, D19]. Fig. 1.129 shows the photoneutron cross-section of  $^{181}\text{Ta}$  as a function of energy.

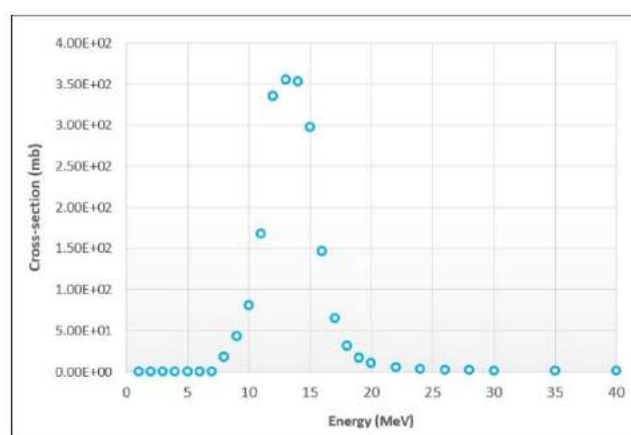


**Fig. 1.129:** Photonuclear cross-section of  $^{181}\text{Ta}(\gamma, n)^{180}\text{Ta}$  [KRSDFM19]

A relatively considerable  $(\gamma, n)$  cross-section (see Fig. 1.129) and a high isotopic abundance of  $^{181}\text{Ta}$  (99.988%) make the photoneutron production investigation in the tantalum target important. These photoneutrons can lead to, for example,  $^{227}\text{Ac}$  (half-life of 21.8 years) production as a radionuclide impurity in  $^{226}\text{Ra}$  target irradiations [DR21, KKVMV15].  $^{227}\text{Ac}$  produced as a beta decay of  $^{227}\text{Ra}$  from the irradiation of  $^{226}\text{Ra}$  target through the reaction of  $^{226}\text{Ra}(n, \gamma)^{227}\text{Ra}$ . Fig. 1.130 shows the neutron capture cross-section in  $^{226}\text{Ra}$  [IAEANO.1].

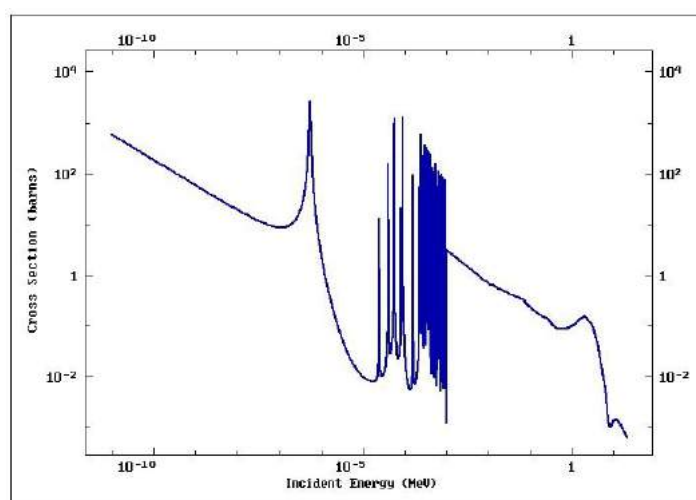


**Fig. 1.130:** Excitation function of the neutron capture reaction on  $^{226}\text{Ra}$  in dependence of the neutron energy [IAEANO.1]

In Fig. 1.131, the ratio of photoneutron yield to incident electron energy for different tantalum thicknesses and electron energies is presented [BS70]. As is shown, the photoneutron yield increases by increasing the incident electron beam energy and target thickness. In 2018, it was shown that for an incident electron beam energy ranging from 10 to 34 MeV, and 3.7 mm thick tantalum, the neutron yield increases from 0.88 to 18.0  $n/e$  [D19].

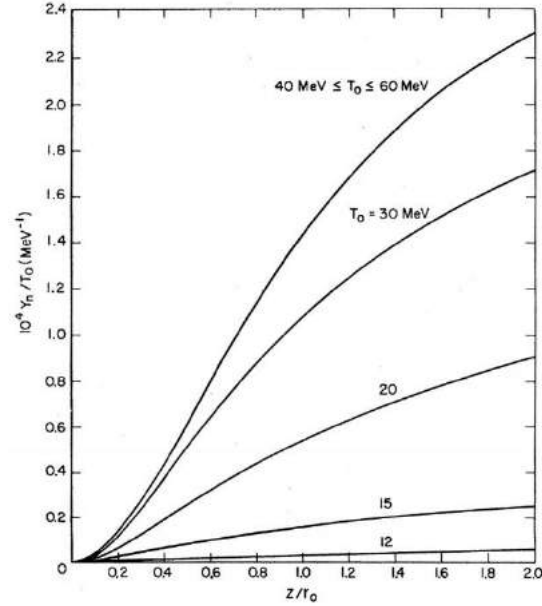


**Fig. 1.131:** Ratio of photoneutron yield ( $Y_n$ ) to incident electron energy ( $T_0$ ) for different tantalum thicknesses and electron energies [BS70]

The transmission and absorption of electrons in the Bremsstrahlungs converter target is also interesting to be considered. As discussed in section 1.1, the Bremsstrahlungs production in the converter target is always accompanied by some transmitted electrons so that for thin targets, these are mostly primary electrons, while for thick targets, electrons are set in motion by produced Bremsstrahlung. In Fig. 1.132, the number of emergent electrons per incident electron ( $T_N$ ) and the fraction of the emergent incident electron energy ( $T_E$ ) versus tungsten thickness is presented. As can be seen, in the case of thin targets,  $T_N$  is higher than unity because of the contribution of secondary electrons [BS70].

In Fig. 1.133, the spectrum of electrons, photons and neutrons generated in a 0.5 cm converter lead target for a 100 MeV incident electron beam energy is shown. As can be seen, the magnitude of the generated neutrons is much lower than for photons and electrons. Moreover, as shown in Fig.1.134, by changing the incident electron beam energy, the shape of the neutron spectrum remains the same in contrast to the magnitude. By comparison between Figs. 1.134, 1.122, it can be revealed that this trend of variations (i.e., the same neutron spectrum's shape for different energies) is different from the photons.

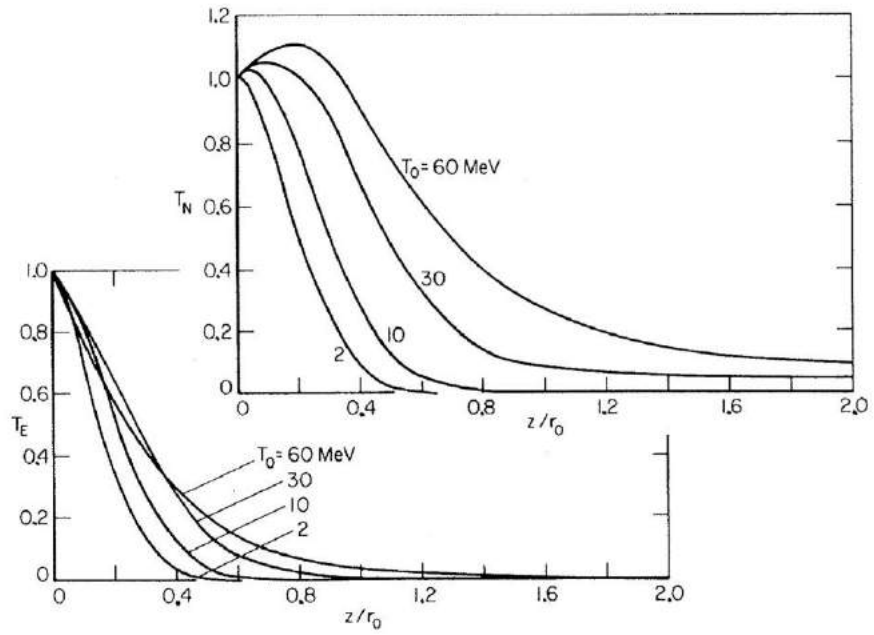


**Fig. 1.132:** The number of emergent electrons per incident electron ( $T_N$ ) and the fraction of the emergent incident electrons with energy ( $T_E$ ) versus the tungsten thickness [BS70]

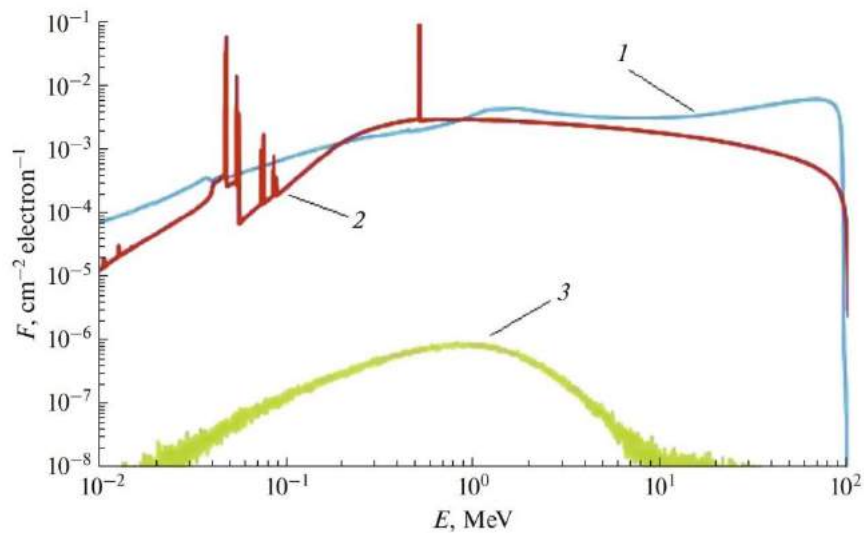


**Fig. 1.133:** Fluence ( $F$ ) of electrons (1), photons (2) and neutrons (3) generated from 100 MeV incident electron beam energy in a 0.5 cm thick lead converter target [K20]

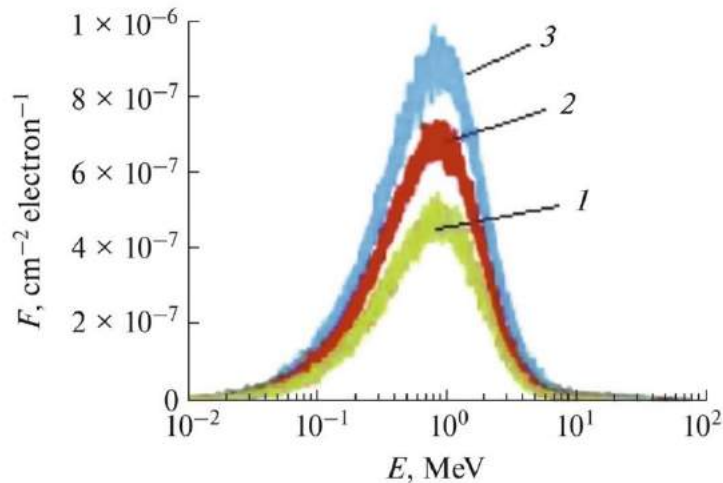


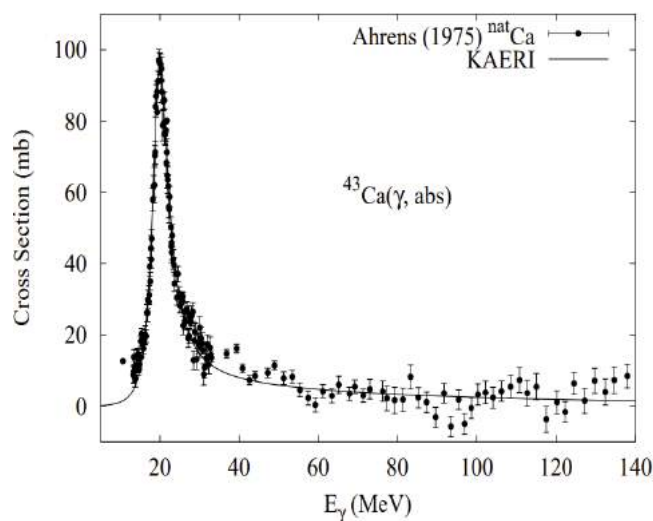
**Fig. 1.134:** Neutron energy spectrum for different incident electron beam energies (i.e., 1)60, 2)80, and 100 MeV) in a lead converter target [K20]

Aside from the radionuclide production purpose, the design of a photonuclear irradiation setup, particularly the converter target, can be based on other applications of interest. Bremsstrahlung generated from the electron to photon converter target can also be employed to produce tertiary particles through the photonuclear reaction with an additional converter target material. Photoneutron, photoproton, photodeuteron, and photoalpha particles can be produced by putting an additional converter target in front of the Bremsstrahlung converter target. In 2005, photoneutron yield calculations from a beryllium target irradiated by Bremsstrahlung were investigated. The beryllium target was irradiated via produced Bremsstrahlung from a 0.188 cm tantalum target with 10 MeV incident electron beam energy and modeled using MCNP and EGS4 codes [EGS05]. Another design of a Bremsstrahlung converter target can be based on the application of photons in the radiation processing of food products in addition to the sterilization of medical items [PBSKS07]. Besides, Bremsstrahlung can be employed to treat deeply located tumors where other particles can not be used [KKK17]. As mentioned previously, the idea of using electron accelerators for radionuclide production is not new and was investigated before. However, there are a few literature bodies in this field since efficient and large-scale radionuclide production via photonuclear reaction requires a high-energy and high-power electron beam accelerator. The lack of these types of accelerators and the associated problems with the heat removal of the converter target made their further studies rather impractical.

## Production targets

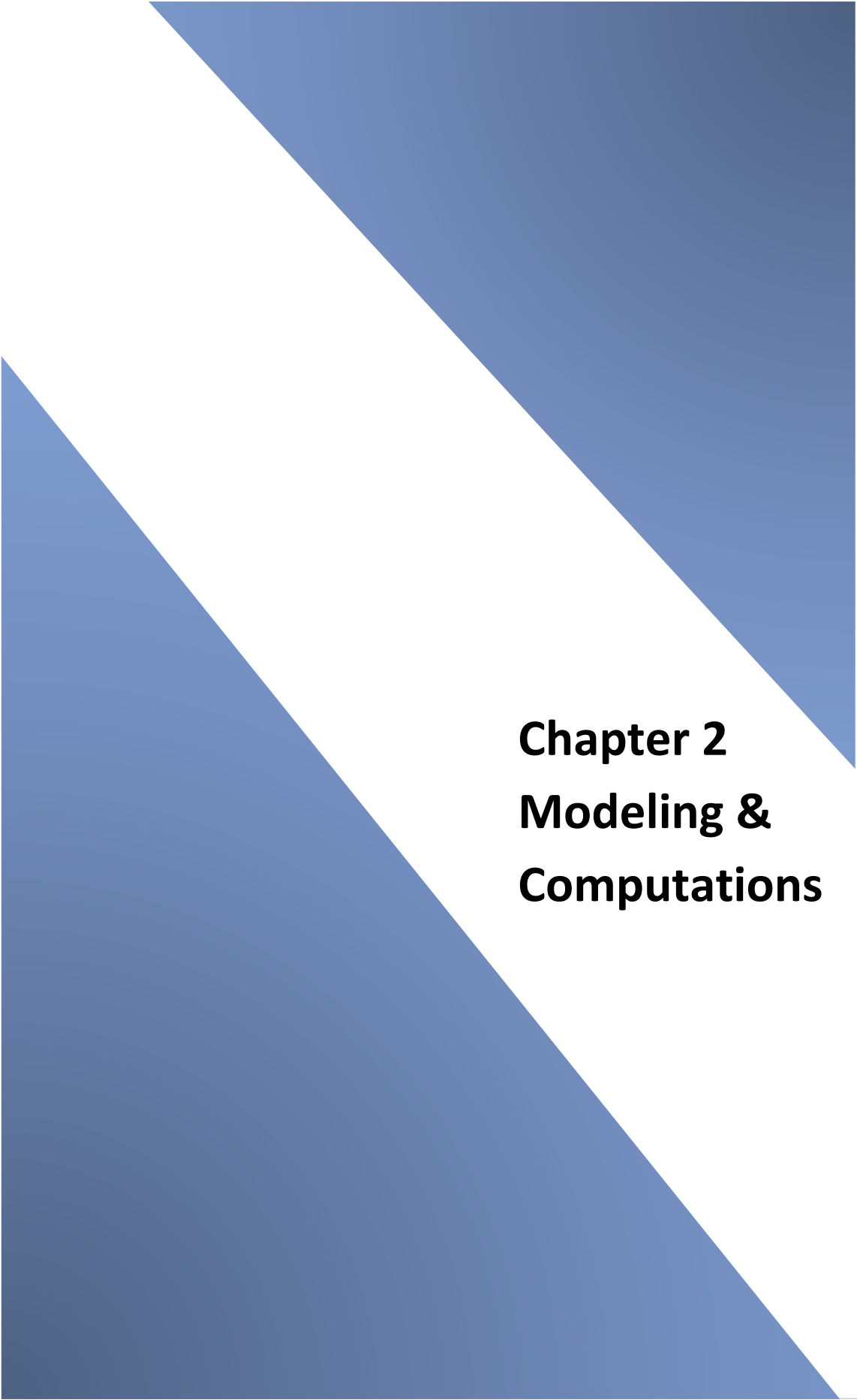
Production targets refer to the samples, which are irradiated by Bremsstrahlung. A wide range of samples with different material properties, dimensions, and geometries can be installed. Although different target materials have different photonuclear cross-sections, the range of photon's energy in which the cross-sections appear are almost the same and known as GDR, as mentioned earlier (in section 1.2.6). For most middle and heavy mass nuclei, the GDR region is in the photon energy range of 8-30 MeV [VVR99, IAEANO.2] (as an illustration for the shape of GDR region cross-section see Fig. 1.135). Although middle and heavy mass nuclei almost

show similar GDR cross-section range, but the magnitude of the cross-sections and the emission probabilities of different particles are different [IAEANO.2].



**Fig. 1.135:** The photoabsorption cross-section of  $^{43}\text{Ca}$  [IAEANO.2]

Aside from the converter target parameters on the radionuclide production in the production targets, the shape and geometry of the production targets can also be of great importance. In 2015, Howard and Starovoitova investigated the target optimization shape for the photonuclear production of  $^{67}\text{Cu}$  [HS15]. It was revealed that different parameters could affect the optimized shape determination, including production target material, incident electron beam energy, electron beam shape, etc. Additionally, as was discussed before, the distance between the converter target and the production targets affects the radionuclide production rate. This issue was investigated for  $^{99}\text{Mo}$  [K06] and  $^{67}\text{Cu}$  [A07, S11] as well.

The page features two large, overlapping blue triangles. One triangle is positioned in the top right corner, pointing downwards and to the left. The other triangle is in the bottom left corner, pointing upwards and to the right. They meet in the center of the page, creating a white diamond-shaped area where the chapter title is located.

## **Chapter 2**

## **Modeling &**

## **Computations**

## Photonuclear irradiation setup modeling

This section presents considerations for the modeling of a point-source like converter target using the electron beam of a rhodotron electron accelerator (model TT300-HE). The irradiation setup consists of different components, including the entrance window, the electron to photon converter target, shielding (against various radiations), coolant, etc. before the created Bremsstrahlung impinges on the production targets to induce photonuclear reactions. In the following, modeling, simulation, and designing of the different aforementioned components are presented.

### 2.1 Electron beam

For facilitating comparison between different FWHMs, the two-dimensional normalized Gaussian distribution of different FWHM (1mm to 3mm) are presented in Fig.2.1. The results of the calculations were normalized using Eq. 2.1.

$$\int_{-\infty}^{+\infty} G(x)dx = 1. \quad (2.1)$$

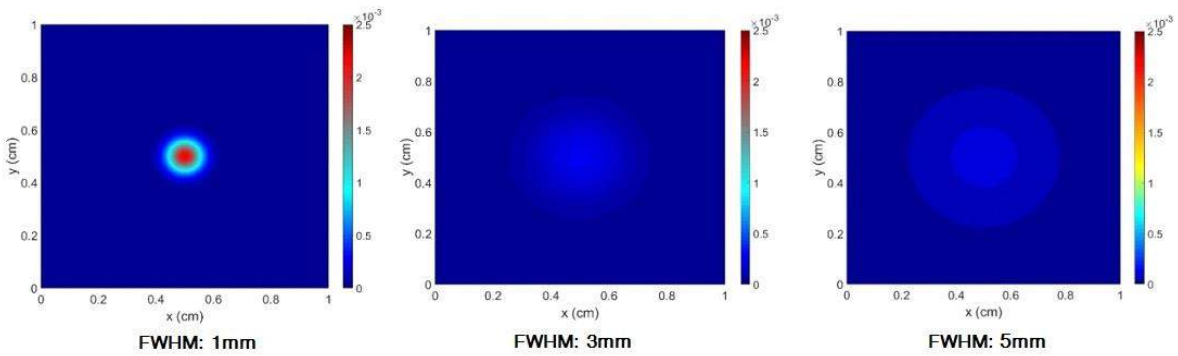


**Fig. 2.1:** Two-dimensional Gaussian distribution for different FWHM modeled in MATLAB software

As discussed above, Eq. 1.79 represents the two-dimensional Gaussian distribution and is applicable for electron beam modeling if the position of the beam and the converter target is fixed and do not change with time. However, as will be discussed later, it will be shown that the target needs to rotate while the beam is impinging on it (see Fig. 2.2). During the change of position, the heat is summed up in each one of the single spatial points and makes the mathematical modeling of the heat deposition sophisticated (see Fig. 2.3). In this case, the Matlab software is employed to obtain the Gaussian spatial distribution in a moving circular pattern [MATLAB20, SB15]. Accordingly, a comparison of different FWHMs in a rotational target can be obtained mathematically.



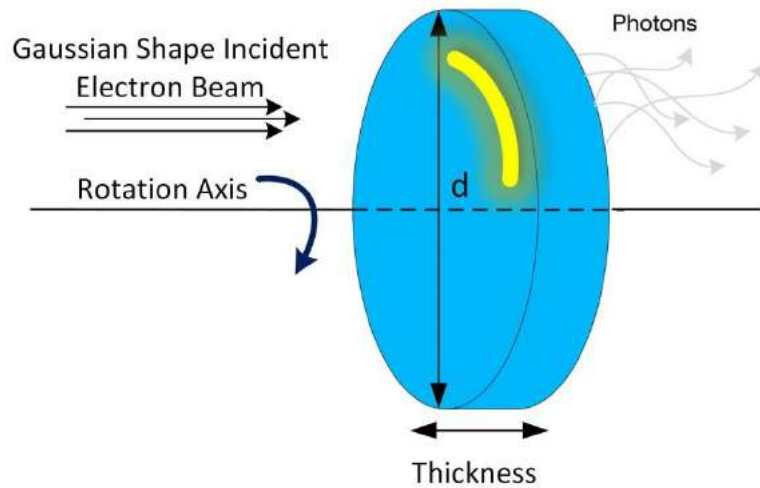


**Fig. 2.2:** A schematic representation of the arc-shaped energy deposition in a rotating target

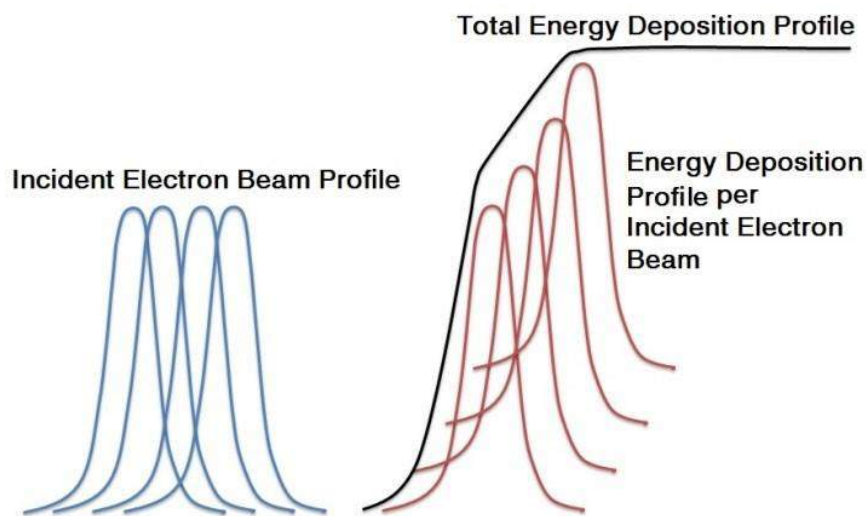


**Fig. 2.3:** A schematic representation of incident electron beam profile, energy deposition profile, and total energy deposition profile

Circular-shaped target irradiation requires the incident electron beam to hit the target at a distance from the target's edge ( $r$  in Fig. 2.4). Therefore, a minimum of  $r = 3\sigma$  (standard deviation) of the electron beam is considered to ensure approximately 99.7 % coverage of the Gaussian-shaped electron beam [TL15]. On this basis, a proper electron beam axis can be considered in the modeling of the irradiation setup components.

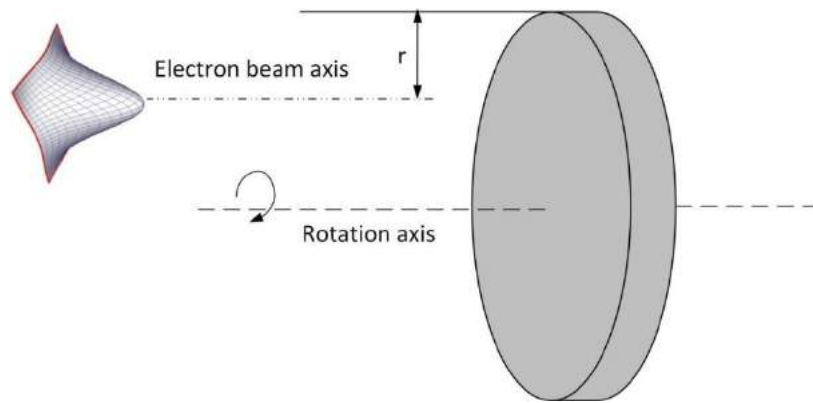


**Fig. 2.4:** A schematic representation for the proper location of the incident electron beam axis

### Electron beam modeling of a rotating target

Electron beam modeling of a rotating target can be obtained according to Eq. 1.79 using the Matlab software [MATLAB20]. Regarding this equation, a two-dimensional Gaussian function can be obtained for each centered point (considered as  $m$ , see Figs. 1.116 and 1.117). However, in the case of a rotating target, there would not be a single point. More precisely, the beam continuously impinges on the target for a while (which depends on the beam's frequency, the rotation speed of the target, and the target dimensions). Additionally, in the case of the energy deposition on the target, continuous irradiation results in a pile-up shape profile (see Figs. 2.4 and 2.5). To obtain the energy distribution profile, one can employ the Matlab software for different FWHMs ranging from 1mm to 5mm. As can be seen, the total energy deposition profile can significantly be influenced by various FWHMs.

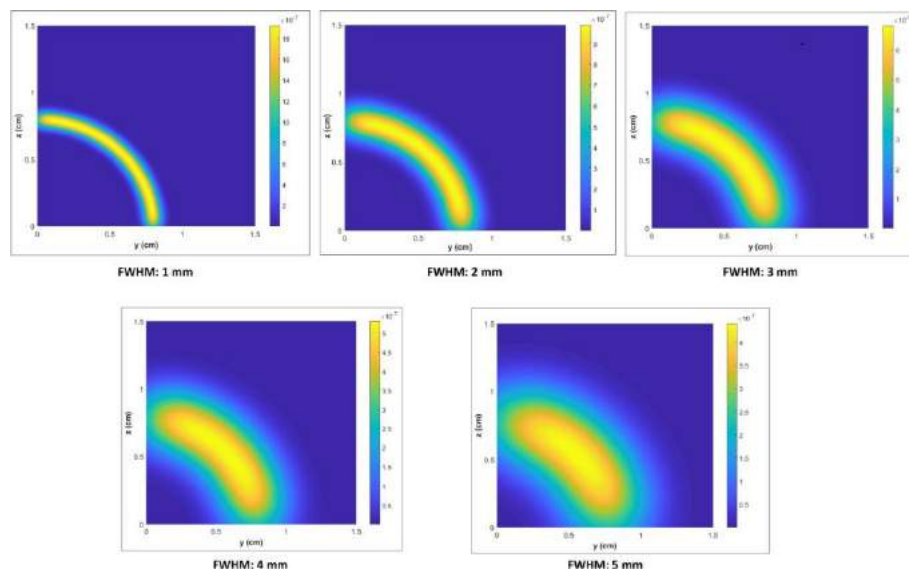


**Fig. 2.5:** An illustration of the arc-shaped two-dimensional Gaussian function in a quarter of a circle with different FWHM (1 mm to 5 mm) obtained by the Matlab software

## 2.2 Entrance window

In the following, the beryllium entrance window is modeled first in the MCNP code to yield the required, nuclear physics based information and then is modeled in the COMSOL Multiphysics software to investigate the heat conduction modeling.

For the MCNP code modeling, the incident mono-energetic and mono-directional electron beam is considered to fall normally on the fixed target surface (see Fig. 2.4). The electron beam energy and current are 40 MeV and 3.125 mA (which gives 125 kW). In the MCNP code, various 'Tally Card's are employed to collect the required information such as the number of electrons and photons with different energy and angle, energy deposition, etc. In the following, different important parameters for modeling the beryllium entrance window are presented.

### Electron emergent coefficient

The electron emergent coefficient ( $T_N$ )<sup>\*</sup> of the beryllium entrance window is able to show how it is influenced by the beryllium thickness. Ideally, the beryllium entrance window must not considerably change the number of transmitted electrons compared to the number of incident electrons. Since beryllium is a light mass nuclei in addition to the low material density, the number of emergent electrons for low thicknesses should vary significantly [CS95, NASA, W15, NMR15, L03]. Fig. 2.6 shows  $T_N$  as a function of beryllium thickness<sup>†</sup>. As is observable, the ratio is more than one; additionally, it does not change considerably by changing the thickness. This stems from the fact that as the incident electron beam impinges on the beryllium entrance window, secondary electrons can be produced and exit (in addition to the transmitted electrons) easily from the beryllium due to the very low beryllium thicknesses.

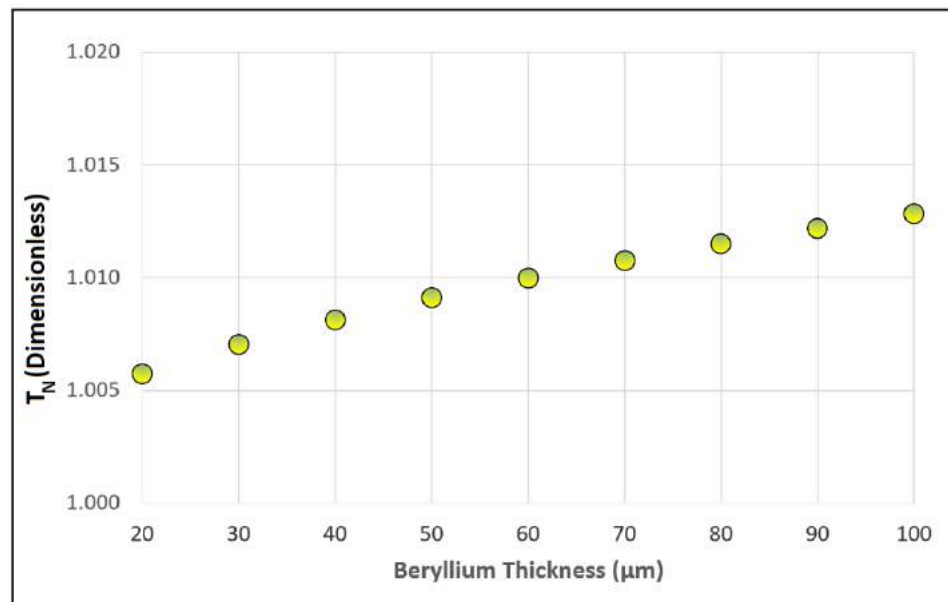


**Fig. 2.6:** Electron emergent coefficient ( $T_N$ ) as a function of beryllium thickness

<sup>\*</sup> The electron emergent coefficient ( $T_N$ ) is defined as the ratio of the number of emergent electrons (from the output surface through which they have emerged) to the incident number of electrons [BS70].

<sup>†</sup> For 3 cm diameter. It should be noted that the converter target's diameter does not affect the results as it is quite large compared to the incident electron point source.

The fraction of the transmitted incident electron beam in the interval 39-40 MeV to 0-40 MeV is presented in Fig. 2.7. As can be seen, it decreases as the beryllium thickness increases; however, it remains almost unchanged due to the low thickness and low atomic number.

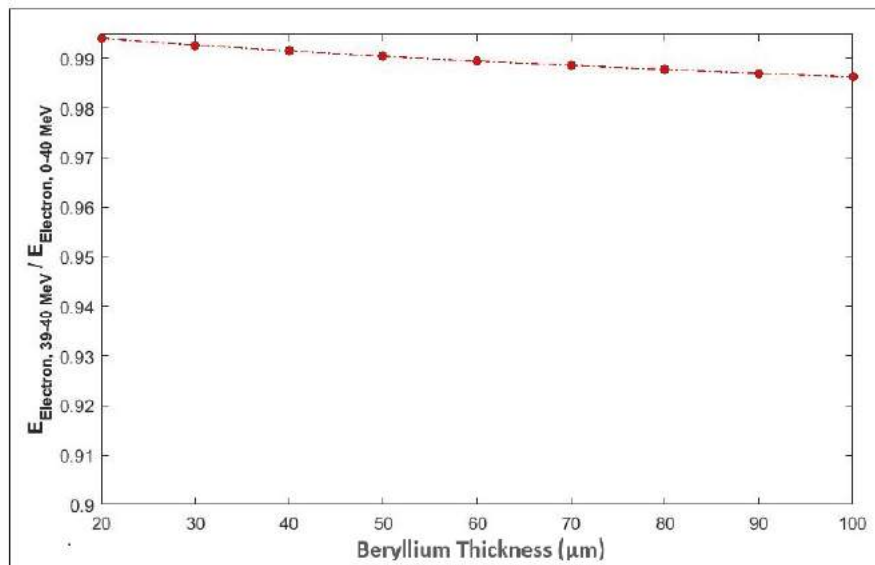


**Fig. 2.7:** The fraction of the transmitted incident electron beam in the interval 39-40 MeV to 0-40 MeV

## Bremsstrahlungs yield

The Bremsstrahlungs yield of the beryllium entrance window as a function of thickness is presented in Fig. 2.8. As can be seen, the ratio increases remarkably by increasing the thickness of the beryllium; however, the magnitude is too low compared to the tantalum converter target (see Fig. 2.20) due to the lower atomic number and density of beryllium.

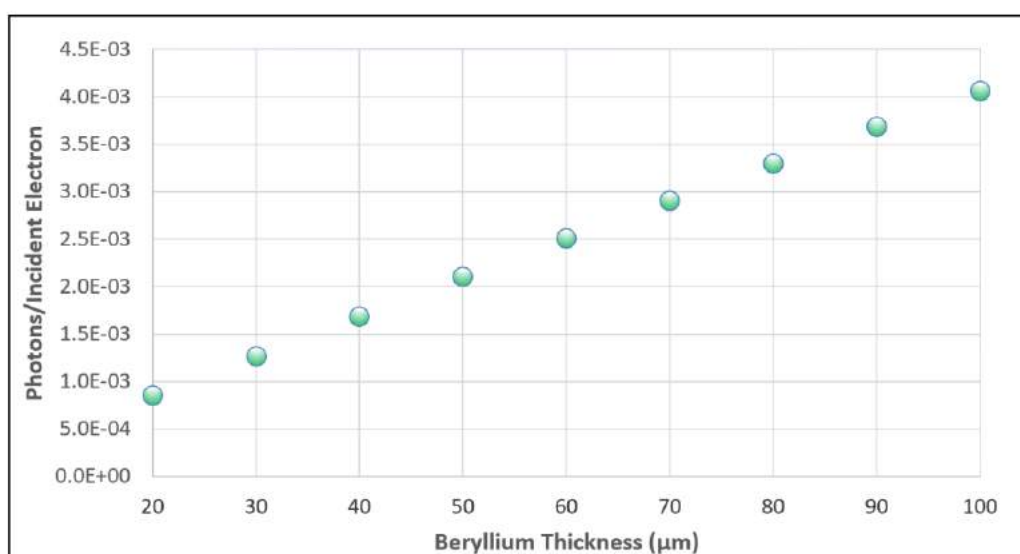


**Fig. 2.8:** Bremsstrahlungs yield for different thickness of beryllium entrance window

The low Bremsstrahlungs yield of the beryllium entrance window also could reasonably be argued from the low interaction rate of beryllium with the incident electron beam (see Fig.2.7). These results can together give a quantitative view of the impact of the beryllium entrance window on the transport of incident electrons and the produced photons.

## Energy deposition

Energy distribution as dose (Joule/g)\* for the beryllium entrance window is investigated in this part of the work. Fig. 2.9 shows variations of dose due to the electron interactions as a function of beryllium thickness. As can be seen, the energy deposition increases with increasing the thickness. This stems from the fact that compared to low thicknesses, more secondary electrons and Bremsstrahlung are produced at high thicknesses. The higher electron and photon production leading to higher probable interactions and, finally, higher energy deposition. Total energy deposition due to the electron interactions as a function of the beryllium thickness is shown in Fig. 2.10. The linear upward trend of energy deposition is due to the multiplication of almost linear dose variations (see Fig. 2.9) and linear mass versus thickness changes<sup>†</sup> (which are independent variables).

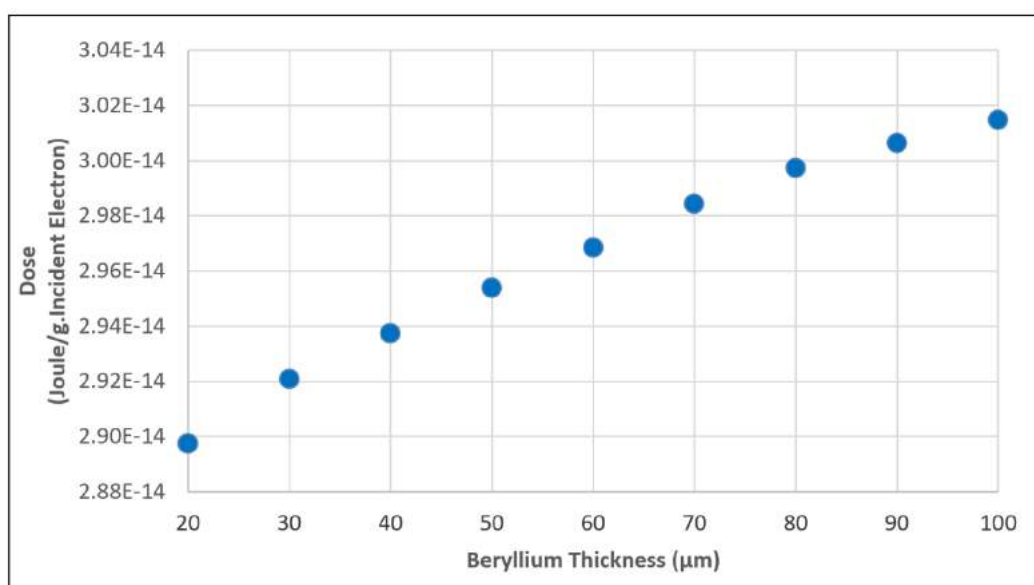


**Fig. 2.9:** Dose due to the interactions of the electrons as a function of the beryllium thickness

\* The unit of dose is the gray (Gy) which mentioned how much of energy (in the unites of Joule) is absorbed in 1 kg of radiation exposed material [E01].

<sup>†</sup> Since mass can be obtained as  $m = At/\rho$  (where here  $\rho$  is density and  $A$  is area of the front face with respect to the incident beam), and only  $t$  (as the thickness) can be varied; therefore,  $m$  is a linear function of  $t$ .

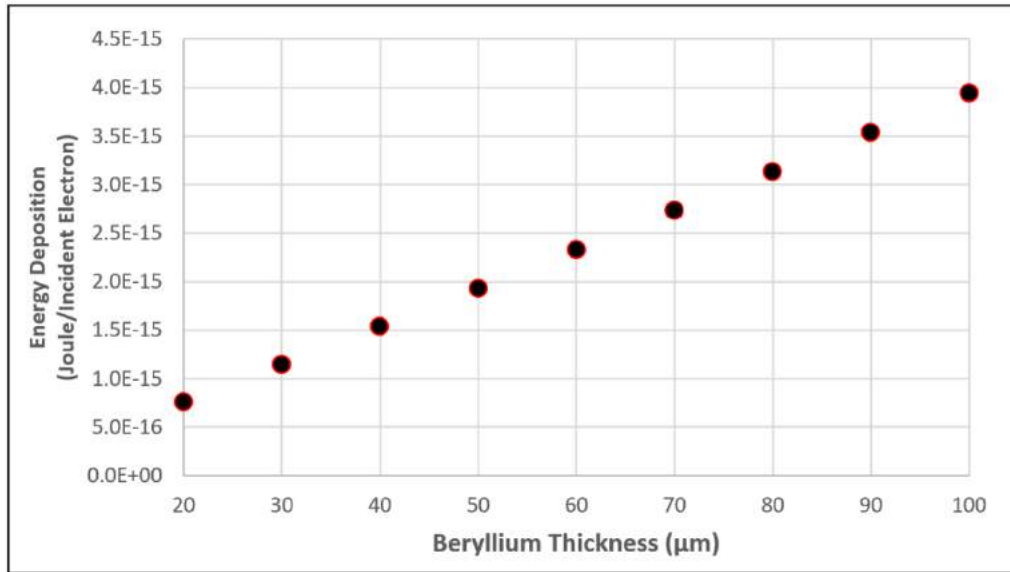


**Fig. 2.10:** Total energy deposition due to the interaction of the electrons as a function of the beryllium thickness. Considering  $1.9E16$  e/s emission via the rhodotron model TT300-HE, one can estimate about 14 to 77 Joule/s (Watt) for 20 to 100μm thickness, respectively.

In 2008, Williams investigated the energy deposition as a function of thickness for aluminum for different incident electron energy beams [W09]. According to the obtained results, it was shown that the energy deposition increased linearly at low thickness to finally reach a plateau for high thicknesses, in the range of some centimeters (that means almost all the incident electrons and generated photons deposited their energy in the very thick target).

## Heat conduction modeling of the beryllium entrance window

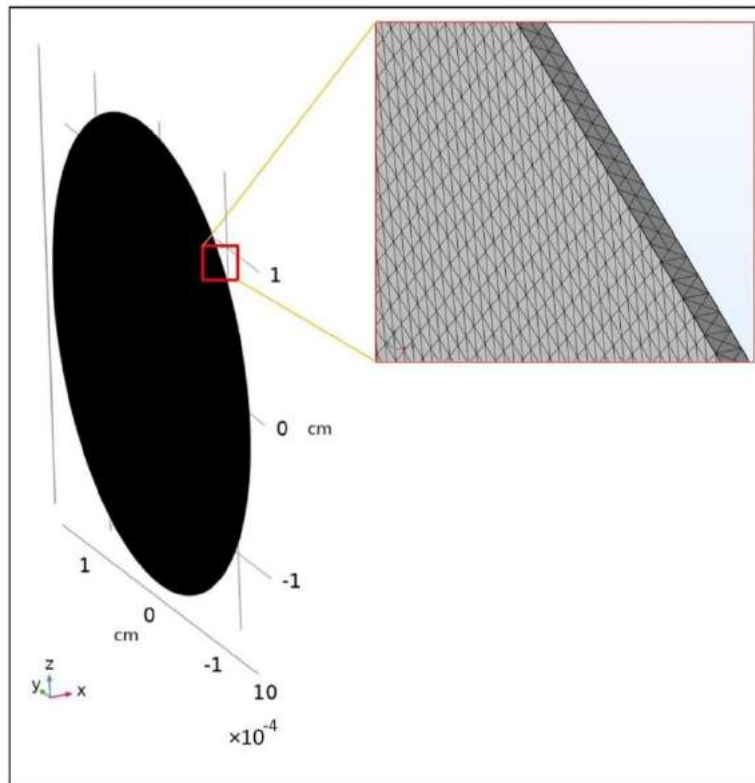
In this section, the heat conduction modeling of the beryllium entrance window is studied. Since, according to my best knowledge, there is no similar heat conduction modeling and modeling on beryllium discs that are irradiated with electron beams, the heat conduction modeling and results could not be compared or discussed with other works. On this basis, only the process of modeling implementation and results of this work are presented in the following.

To investigate heat conduction modeling, first, the beryllium disc is considered fixed (i.e., without rotation), and the incident electron beam irradiates the middle of the disc. Then, to reduce temperature, the beryllium disc is rotated and the rotation speed is synchronized with the time structure of the electron beam pulses. Moreover, the helium gas flows to cool down further the beryllium disc\*. The analysis was carried out for different thicknesses (from 20μm to 100μm) and different FWHMs (from 1mm to 5mm).

According to the above discussion, the heat conduction modeling for the fixed beryllium disc is performed in the following. Moreover, to investigate the change of variations as a function of thickness, different beryllium thicknesses (from 20μm to 100μm) are considered for modeling. The heat conduction modeling is carried out for a 40 MeV and 3.125 mA electron

\* The reason for choosing helium will be discussed in the section of '*Helium-cooled rotating beryllium disc modeling*'.

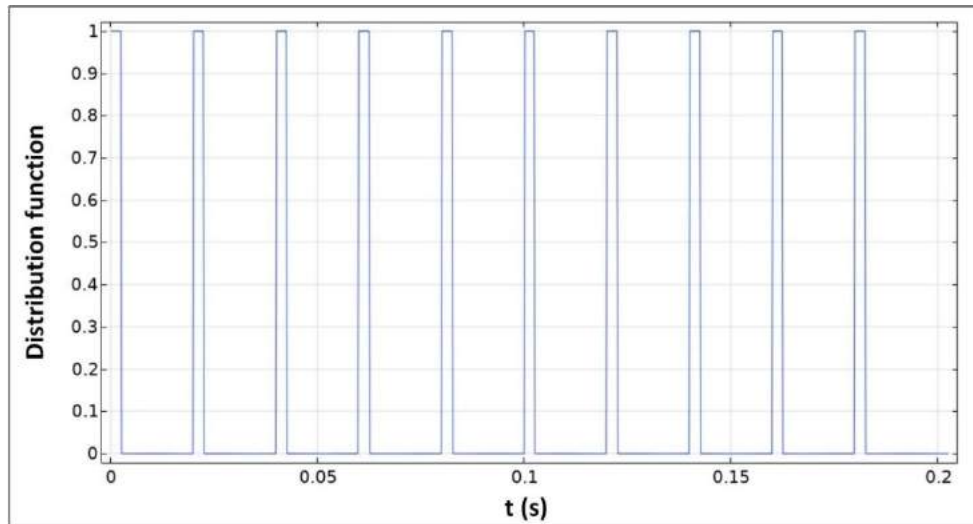
beam energy and electron beam current, respectively. It was assumed that the electron beam impinges perpendicularly with 50Hz frequency and 12.5% duty cycle to the middle of the beryllium disc (according to the beam characteristics of a rhodotron model TT300-HE). To perform the heat conduction modeling, the energy deposition, which was already obtained using the MCNP code, was used as an input for the COMSOL Multiphysics software, and then the maximum temperature was calculated. Fig. 2.11 shows the mesh configuration used for the beryllium disc modeling of 0.2 s simulation time, 1 mm FWHM, and 20 $\mu$ m thickness. As is shown, a fine-mesh size was considered to allow for accurate heat conduction calculations.



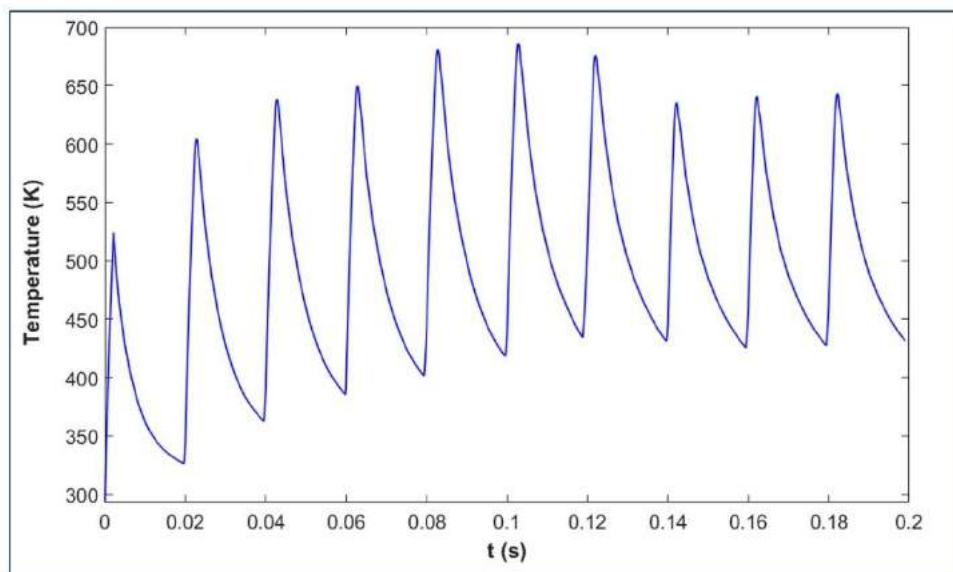
**Fig. 2.11:** Mesh distribution used in the COMSOL Multiphysics software for the stationary beryllium disc modeling of 0.2 s simulation time, 1 mm FWHM, and 20 $\mu$ m thickness

Fig. 2.12 shows the electron beam irradiation function versus time for 200 ms. As can be seen, the 50Hz electron beam frequency and 12.5% duty cycle give an irradiation time of 2.5 ms and the time between the two consecutive irradiations as 17.5 ms. The results of the heat conduction simulation of the COMSOL Multiphysics software corresponding to the electron beam irradiation function (Fig.2.12) for 1mm FWHM and 20 $\mu$ m beryllium thickness are presented in Fig. 2.13. As is shown, heat is dissipated by conduction during the pause between pulses, and it can reasonably be argued that the disc can dissipate most of the energy between the pulses. Therefore, one can conclude that without cooling, the temperature will not approach infinity, when heating is continued. Fig. 2.14 shows a 2D temperature distribution of 1mm FWHM and 20 $\mu$ m beryllium thickness at 200ms simulation time (the modeled flow domain is 5cm  $\times$  4cm  $\times$  1mm). As is observable, the maximum temperature appears in the middle of the beryllium disc, where the Gaussian-shaped electron beam impinges. In order to investigate the maximum attainable temperature as a function of the beryllium thickness, the

results of the heat conduction simulation using the COMSOL Multiphysics software are presented in Fig. 2.15. As can be seen, the maximum temperature does not significantly increase with increasing the thickness. This stems from the low energy deposition in the beryllium disc, even for the high thicknesses, as was discussed before.



**Fig. 2.12:** The time distribution function of the electron beam



**Fig. 2.13:** Maximum temperature distribution versus 0.2 s simulation time for 1 mm FWHM of the electron beam and 20μm beryllium thickness



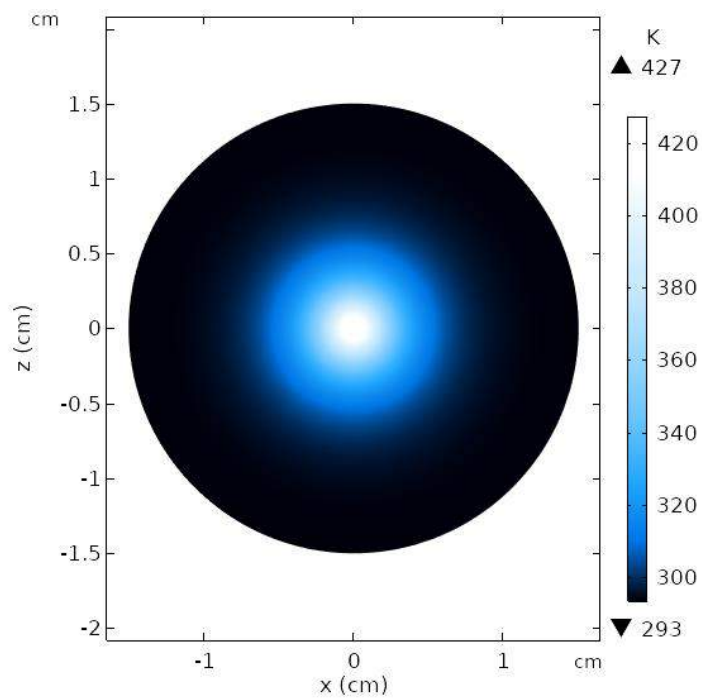


**Fig. 2.14:** 2D temperature distribution at 0.2 s simulation time for 1 mm FWHM electron beam and 20 $\mu$ m beryllium thickness

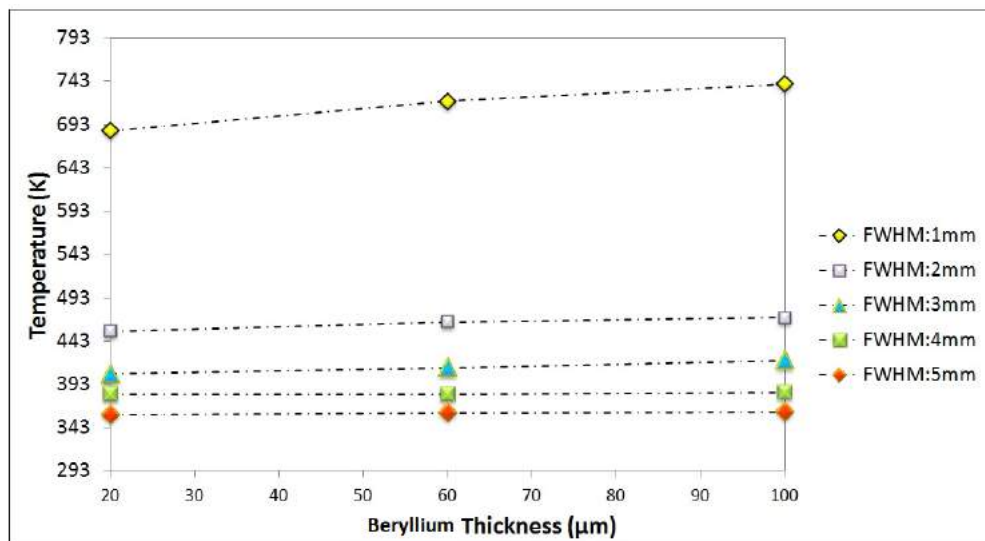


**Fig. 2.15:** Variation of maximum temperature versus beryllium thickness for different FWHM

## Helium-cooled rotating beryllium disc modeling

To reduce the temperature rise in the beryllium entrance window, two different approaches are considered. The first one is to rotate the beryllium disc, and the second one is to apply a forced gas flow through the irradiation setup components. The rotation speed of the beryllium disc affects the amount of heat that is deposited in a single volume of it. This can change the temperature distribution and the maximum temperature the beryllium reaches. Considering the beam repetition rate and the duty cycle, the rotation speed can be determined so that there would be a relatively long time between the irradiation of the same area of the beryllium target. Considering this issue and a possible speed limitation of the available beryllium disc commercial entrance window, one can propose the design presented in Fig. 2.16 as the best option.

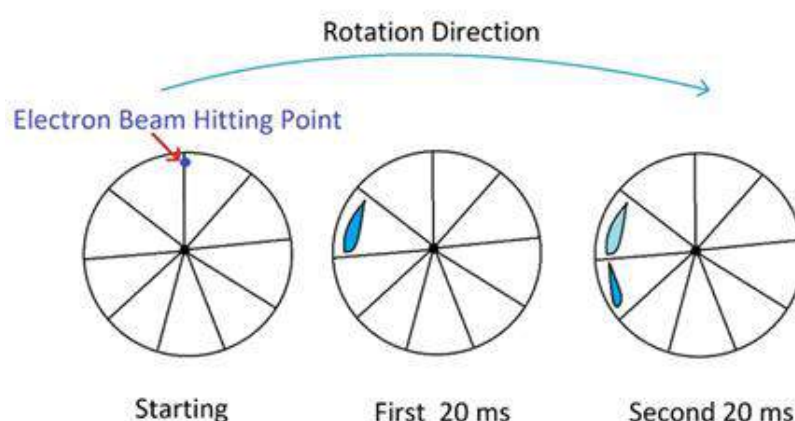


**Fig. 2.16:** A schematic representation of the proposed rotation mechanism for the beryllium disc

As can be seen in Fig. 2.16, the electron beam irradiates different slices in consecutive rotations. Therefore, each irradiated slice can cool down during the irradiation of the other slices. The corresponding rotation speed can simply be obtained by considering the irradiation time in each electron spot (2.5 ms) and the fraction of the irradiated beryllium disc (i.e., the number of slices, which is 9 for this design). The result of these calculations was obtained as 2'666.67 rpm.

As discussed above, in addition to the disc rotation, a gas flow mechanism (just one beryllium disc side; see Fig. 2.39) can also help to cool down the beryllium disc. Different gases can be employed for the cooling purposes. Among the candidates, argon, helium, and hydrogen could be the most attractive options. The specific heat (at constant pressure or volume)\* of hydrogen is about three times more than for helium and about thirty times more than for argon, making hydrogen more attractive from the heat removal capability point of view [K84]. However, associated problems with hydrogen, such as flammability, storage, cost, and probable chemical reactions, make it inappropriate for practical and routine usage in a

---

\* Specific heat at constant pressure and volume can be defined respectively as the derivative of enthalpy and internal energy respecting the temperature [K84, H86]. Enthalpy is the sum of internal energy and the product of its volume and pressure of a system [D09].

photonuclear irradiation setup. So, helium gas has been chosen due to its low atomic number and density, its chemical inertness and its reasonable heat capacity. Furthermore, helium is not reacting with the high energy Bremsstrahlungs photons.

Modeling of moving/deformed computational domain(s) within stationary computational geometries during the simulation time via the COMSOL software is not straightforward, and this is done by solving PDEs for the mesh displacement. It should be noted that in the COMSOL software there are two physics interfaces implementing different types of moving/deformed meshes: the Moving Mesh interface and the Deformed Geometry interface. In the former case, solid materials follow the mesh deformation and deform in the same way as the mesh. However, in the latter case, the material does not follow the change in shape. Therefore, deformation of the geometry boundaries corresponds to removal or addition of material [COMSOL]. The mesh distribution used in the COMSOL Multiphysics software for the rotating beryllium disc is presented in Fig. 2.17.

According to the above discussion, two mechanisms are considered for cooling down the beryllium entrance window. The first one is the rotation, and the second one is the helium gas flowing. Fig. 2.18 shows a modeling 2D temperature distribution at 0.06s simulation time for 5mm FWHM of the electron beam and 20 $\mu$ m beryllium thickness.

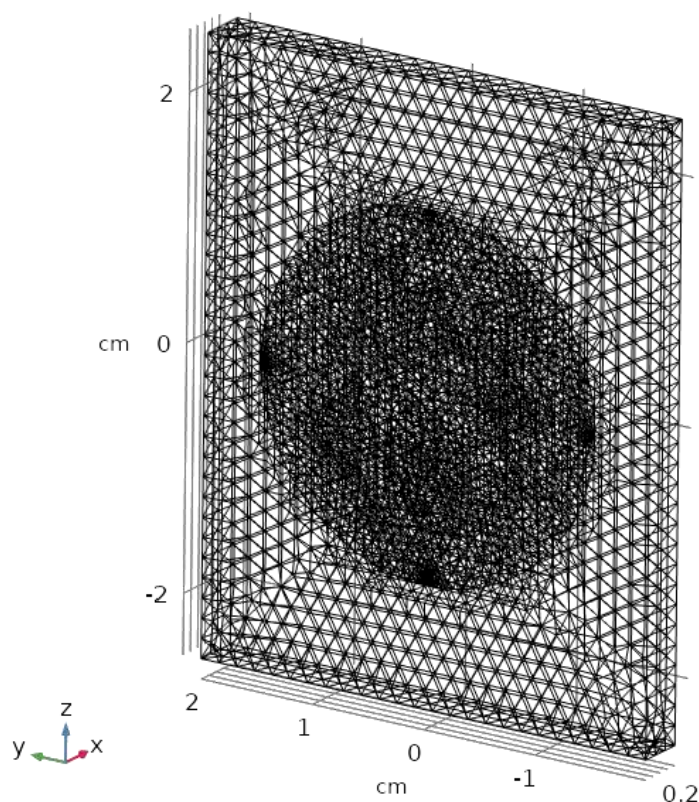


**Fig. 2.17:** Mesh distribution used in the COMSOL Multiphysics software for modeling a rotating beryllium disc

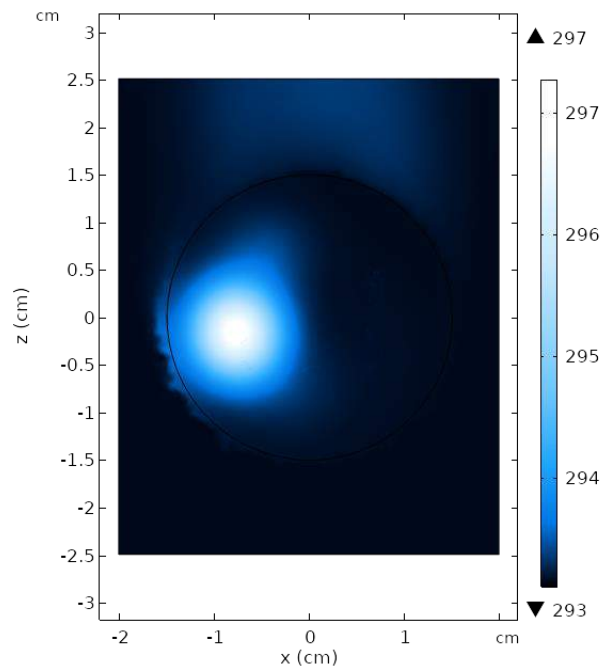


**Fig. 2.18:** 2D temperature distribution at 0.06 s simulation time for 5mm FWHM of the electron beam and 20 $\mu$ m thickness

The results of the simulation via the COMSOL Multiphysics software for different FWHMs are presented in Fig. 2.19. From a comparison between Figs 2.15 and 2.19, it can reasonably be argued that the temperature for almost all thicknesses and FWHMs is reduced by up to 200K. In Fig. 2.19, the highest temperature is around 531K for the 100 $\mu$ m beryllium thickness when impinged by a 1mm FWHM electron beam. Considering the melting point of beryllium, which is 1580K (1287°C), the maximum temperature accordingly reaches approximately one-third of the beryllium melting point, which seems to be acceptable.

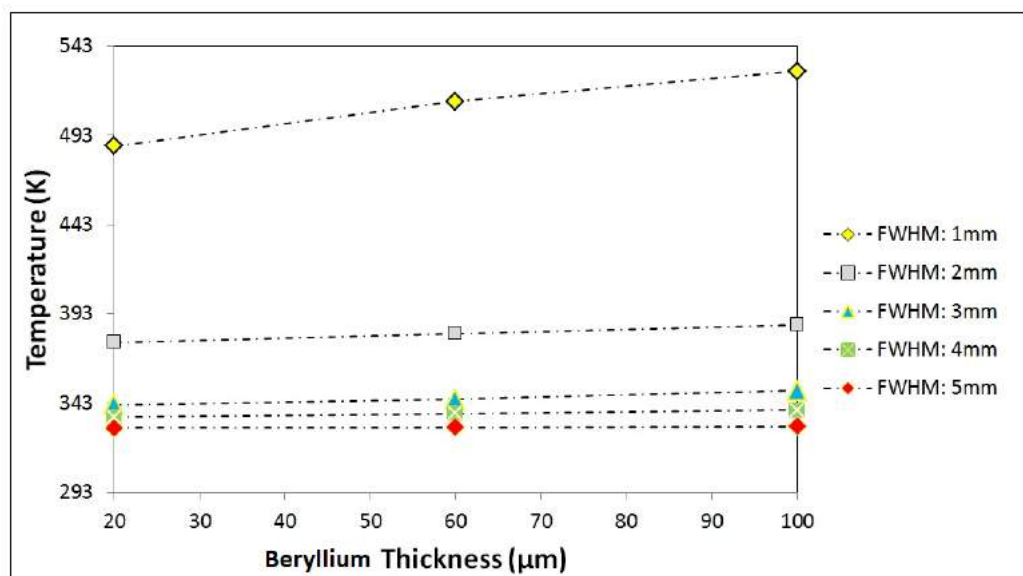


**Fig. 2.19:** Variation of maximum temperature versus beryllium thickness for different FWHM in the new design

## 2.3 Tantalum converter target

This section of work deals with the modeling of the Bremsstrahlungs converter target. In the following, the MCNP Code is used to obtain different parameters such as Bremsstrahlungs yield, optimum thickness, and Bremsstrahlungs spectrum. After that, the heat conduction modeling is performed using the COMSOL Multiphysics software. Finally, a new design and modeling of the Bremsstrahlungs converter target are presented and assessed.

### Bremsstrahlungs yield calculations of a tantalum converter target

Bremsstrahlungs yield calculations of different converter materials and incident electron beam energies have been studied in the literature. In 2005, Eshwarappa et al. obtained the Bremsstrahlungs yield for 10 MeV (generated by a Microtron electron accelerator) electron beam energy and different thicknesses of a tantalum converter target. They found that the maximum Bremsstrahlungs yield (for photons ranging from 0 to 10 MeV) appears at around 2 mm tantalum thickness [EGS05]. In a similar work, Shvetsov et al. in 2010 investigated the Bremsstrahlungs yield for a 30 MeV electron beam energy for different tungsten thicknesses. According to their results, the optimum thickness appears around 2.5 mm (considering photons ranging from 8 to 20 MeV) [SSSC10]. The Bremsstrahlungs yield can also be found for other converter target materials in [DNA13].

The Bremsstrahlungs yield of a tantalum converter target with various thicknesses is calculated, and the results are presented in Fig. 2.20. As can be seen, the Bremsstrahlungs yield for two different photon energy ranges of 0-40 MeV (black) and 8-30 MeV (red) is shown. This is due to the fact that the GDR for most middle and heavy mass nuclei is in the photon energy range of 8-30 MeV. According to Fig. 2.20, the maximum Bremsstrahlungs yield appears around 0.55 and 0.45 cm for the photon energy range of 0-40 and 8-30 MeV, respectively\*. Fig. 2.21 shows the range of electrons with 40 and 8 MeV energies in tantalum obtained from Nucleonica [Nucleonica20]. It can be observed that about 0.45 cm of tantalum is required to reduce the electrons' energy from 40 MeV to 8 MeV. This thickness is equivalent to that obtained using the MCNP code.

---

\* The tantalum converter has a 15 cm diameter. However, it should be noted that the converter target's diameter does not affect Bremsstrahlungs yield as it is quite large compared to the incident electron point source.

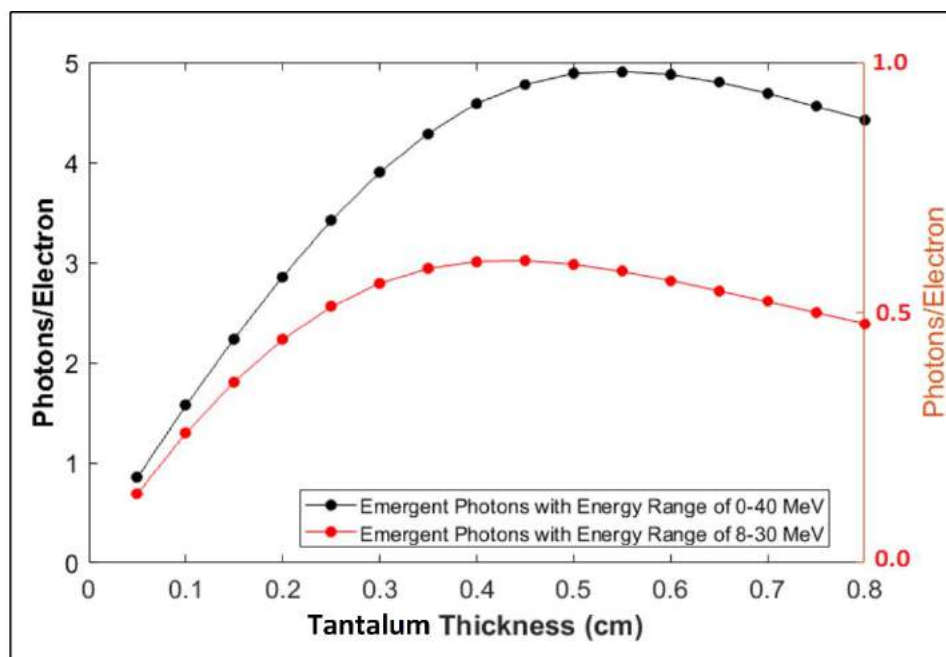


Fig. 2.20: Bremsstrahlung yield for various tantalum thicknesses

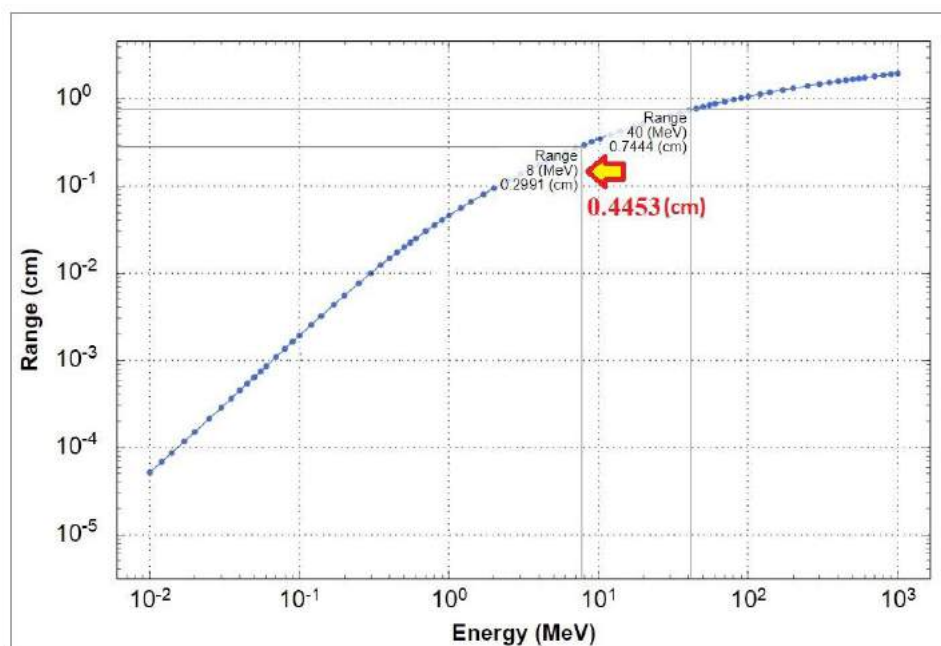
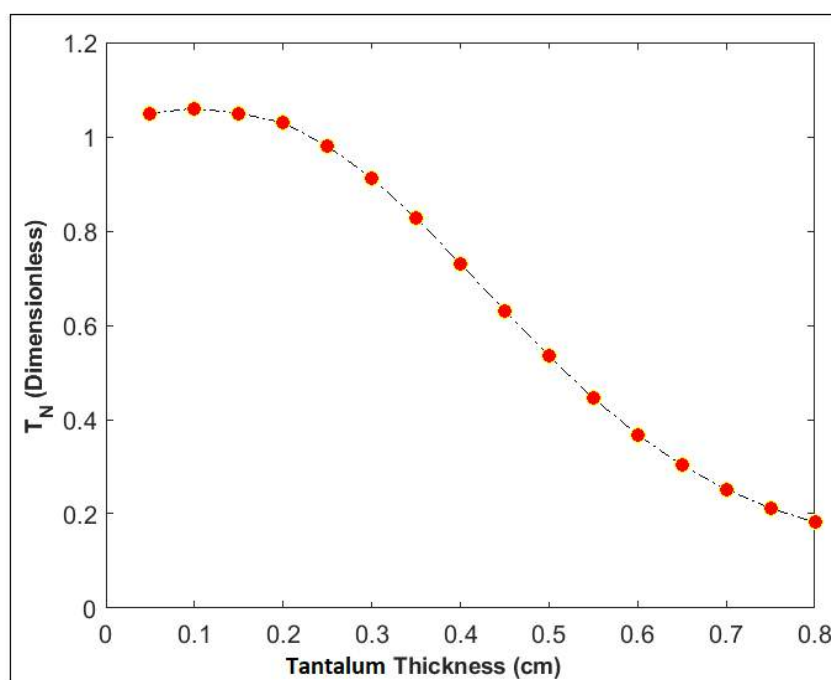


Fig. 2.21: Range of electrons in tantalum for two different energies [Nucleonica20]

## Electron emergent coefficient

The electron emergent coefficient ( $T_N$ ) of the tantalum converter disc for various thicknesses is obtained using the MCNP code and presented in Fig. 2.22. According to Fig. 2.22, it can be observed that for thin targets,  $T_N$  is significantly higher than unity due to the combination of transmitted and also generated secondary electrons in the tantalum converter target. However, at higher thicknesses, the electron population decreases due to increases in electron interactions and absorption. Comparing Figs. 1.132 (tungsten) and 2.22 (tantalum), it can be observed that the shape of variations is similar. This is due to the fact that the atomic number and material density for tantalum is close to tungsten (atomic number and density of tungsten and tantalum are 74 and  $19.28 \text{ g.cm}^{-3}$ , and, 73 and  $16.6 \text{ g.cm}^{-3}$ , respectively).



**Fig. 2.22:** Emergent electron per incident electron ratio for different tantalum converter thicknesses

## Bremsstrahlungs energy spectrum

The Bremsstrahlungs energy spectrum for a 0.45 cm tantalum target thickness is calculated using the MCNP code, and the results are shown in Fig. 2.23. As is shown, the emergent relative photons with low energies are much more than at high energies. This is due to the fact that most photons appear at low energies in the Bremsstrahlungs mechanism (see Figs.1.121 and 1.122). The shape of variations is almost the same as in other works. The Bremsstrahlungs spectrum for various converter target materials and different incident electron beam energies have been investigated extensively [DNA13, K20, A19, and KKK17]. In the case of tantalum, also one can find the Bremsstrahlungs spectrum for different electron beam energies and target thicknesses. As an illustration, in 2005, Eshwarappa et al. investigated the Bremsstrahlungs spectra for 8-12 MeV incident electron beam energy at the corresponding optimum thicknesses [EGS05]. The Bremsstrahlungs spectrum due to the incident of 30 MeV electron beam energy with 2.5 mm tantalum thickness was obtained in



2011 [S11]. In 2019, also, Bremsstrahlungs spectra for 10 and 100 MeV incident electron beam energies impinging on a 0.1 and 30 mm tantalum thick tantalum were investigated [D19].

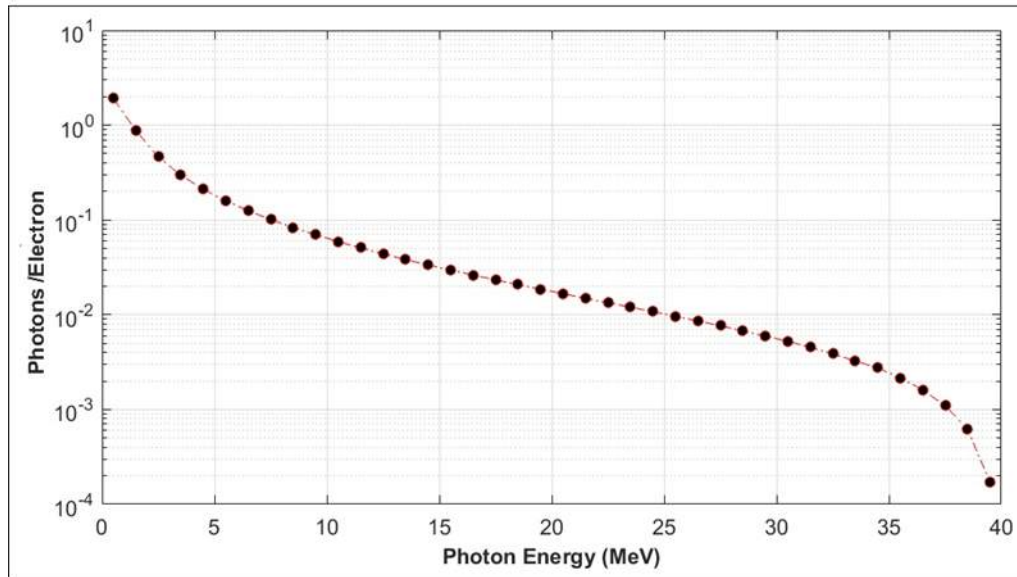


**Fig. 2.23:** Bremsstrahlungs spectrum for the optimum tantalum converter thickness

### Distribution of angular Bremsstrahlung

The distribution angle of the emitted angular Bremsstrahlung is considered in this part of the work. Considering theta (denotes as  $\theta$ ) as the angle between the electron beam axis and the Bremsstrahlung from the surface from which they have emerged, the angular Bremsstrahlungs distribution can be obtained using the MCNP code. In Figs. 2.24 and 2.25, the angular Bremsstrahlungs distribution per incident electron versus Cosine of theta for the energy ranges of 0-40 MeV and 8-30 MeV are presented. As can be seen, at all angles, the Bremsstrahlungs yield increases by increasing the converter target from 0.05cm to around 0.45cm thickness (which is the optimum target thickness for Bremsstrahlungs production). Additionally, as is observable in Figs. 2.24 and 2.25, except at small angles (or high  $\cos \theta$ ), spectra are almost flat in a wide range of angles. This change of variation in angular distribution is consistent with that presented in Fig. 1.125 (for 60 MeV incident electron beam energy on a tungsten converter target). As was observed in Fig. 1.125, almost for all thicknesses, a sharp peak appears at the smaller angles; afterward a rapid decrease at larger angles followed by a rather flat distribution of angles can be observed. By comparison between Figs. 2.24 and 2.25, it was also revealed that the shape of the variations is almost the same; however, the changes between the tantalum thicknesses are fewer in the energy range of 8-30 MeV compared to 0-40 MeV. Additionally, it can be seen from Fig. 2.25 that in contrast to the energy range of 0-40 MeV (Fig. 2.24), the spectra are almost zero at medium to large angles for the energy range of 8-30 MeV. This is due to the fact that low energy electrons that appear at large angles are excluded from the energy range of presented photons in Fig. 2.25.



The most evident result that can be observed from Figs. 2.24 and 2.25 is that Bremsstrahlung is emitted in forward direction for the 40 MeV incident electron beam. These results are in consistent with expectations mentioned earlier (see Figs. 1.14, 1.124, and 1.125).

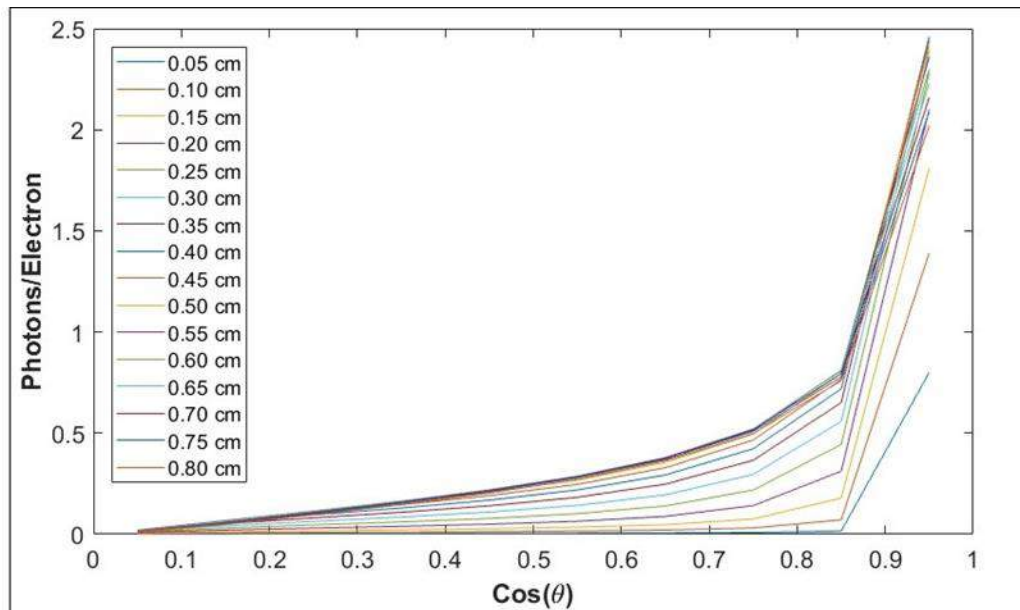


**Fig. 2.24:** Angular distribution of the Bremsstrahlungs yield in the range of 0-40 MeV per incident electron

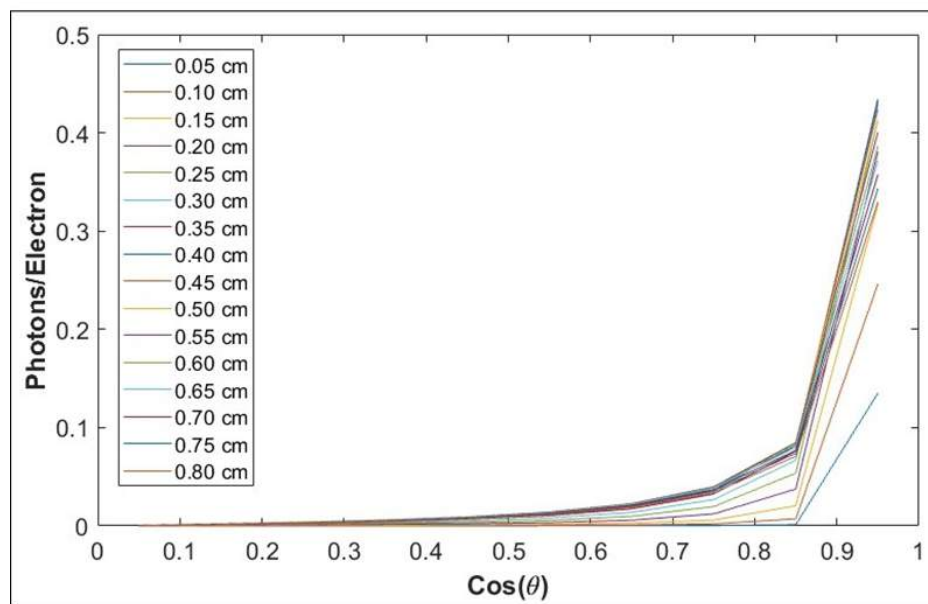


**Fig. 2.25:** Angular distribution of the Bremsstrahlungs yield in the energy range of 8-30 MeV per incident electron

## Energy deposition

Energy deposition as dose (Joule/g) per incident electron due to the incident electron beam interaction in a tantalum target is presented in Fig. 2.26. As is observable, the dose due to electron interaction's increases by increasing the thickness and reaches an approximately constant value and then decreases again. The shape of variation in Fig. 2.26 is similar to Fig.2.20. This stems from the fact that by increasing the thickness up to the optimum target thickness, the Bremsstrahlungs production due to the interactions of the electrons reaches its maximum value and decreases again. Therefore, the energy deposition changes in a similar trend.

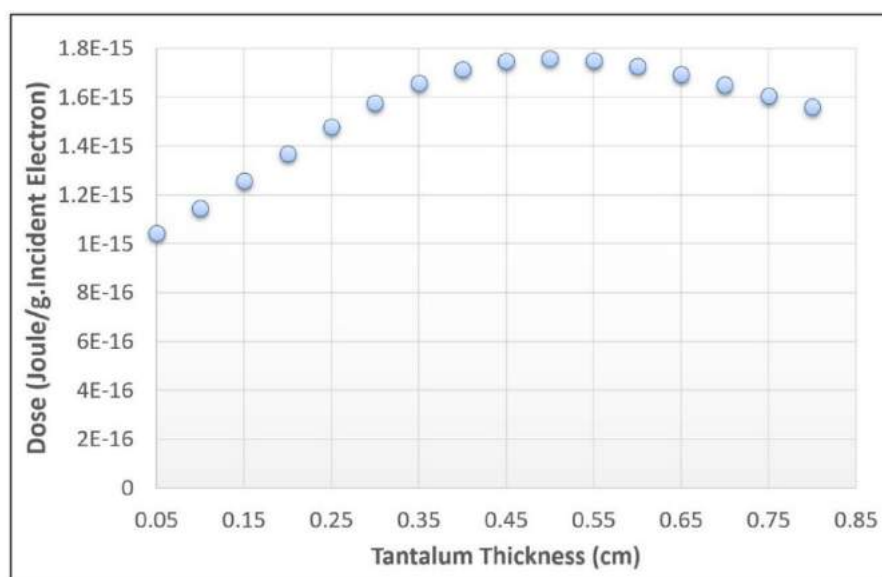


**Fig. 2.26:** Energy deposition as dose (Joule/g) versus tantalum thickness due to the interactions of the electrons

The total energy deposition is of great importance from the point of view of heat removal and target designing. The total energy deposition has been presented in Fig. 2.27 and obtained as the result of the multiplication of dose by the target mass in each thickness. Since the mass linearly corresponds with the thickness, from the mathematical point of view, the multiplication of mass in dose to give the total energy deposition leads to approximately a linear change of variations. From the physical point of view, the total energy deposition increases with the thickness and therefore the electron interaction increase; however, the trend of variations is not exactly linear because the rate of electron (and Bremsstrahlung) interactions and absorption is not changing linearly (see Figs. 2.20 and 2.22). More precisely, the slope of changes in Fig. 2.27 is higher at thicknesses below 0.5 cm and then decreases as the tantalum thickness increases. This shape of variation is consistent with that obtained by Williams for the tantalum converter target (for 14 MeV, as the highest electron beam energy that was investigated in that work) [W09]. More importantly, not only the shape of variations but also the magnitude of the heat deposition (as power) is quite close to results that Ayzatskiy et al. obtained in 2007 for a 40 MeV incident electron beam and different tantalum converter target thicknesses (see Fig.2.28) [A07]. More precisely, the power deposition that is obtained based

on our work is about 47 kW (see caption of Fig. 2.27), compared to approximately 46.9 kW from [A07] for a 3.125 mA (converting 200  $\mu$ A to 3.125 mA) beam current.

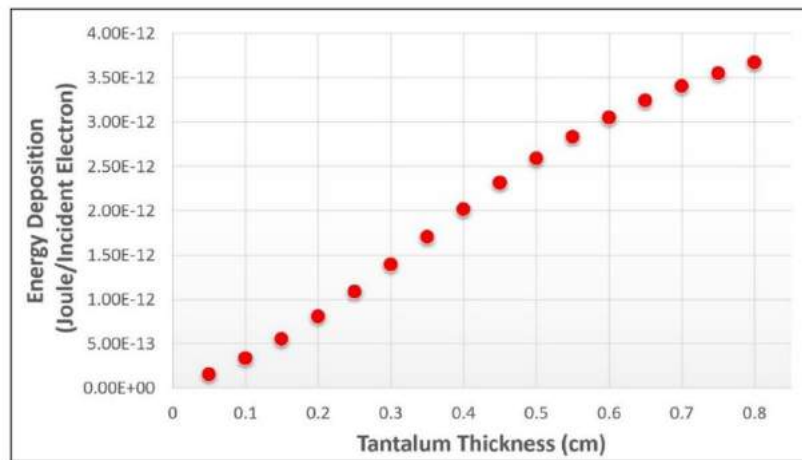


**Fig. 2.27:** Total Energy deposition (Joule) as a function of tantalum thickness due to the interactions of the electrons. Considering a  $1.9E16$  e/s beam current from a rhodotron model TT300-HE, one can estimate about 47'000 Joule/s (Watt) for the optimum tantalum converter target thickness.

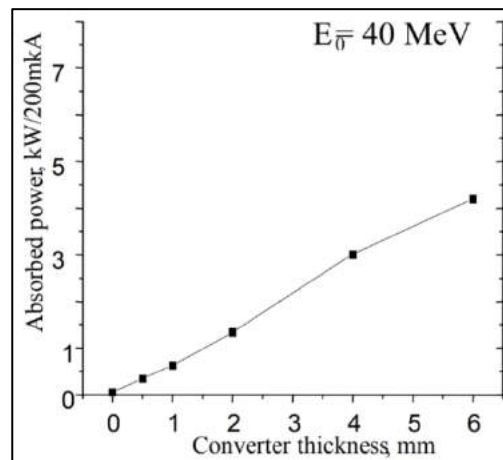


**Fig.2.28:** Energy deposition as a function of tantalum converter target thickness for 200  $\mu$ A and 40 MeV electron beam [A07]

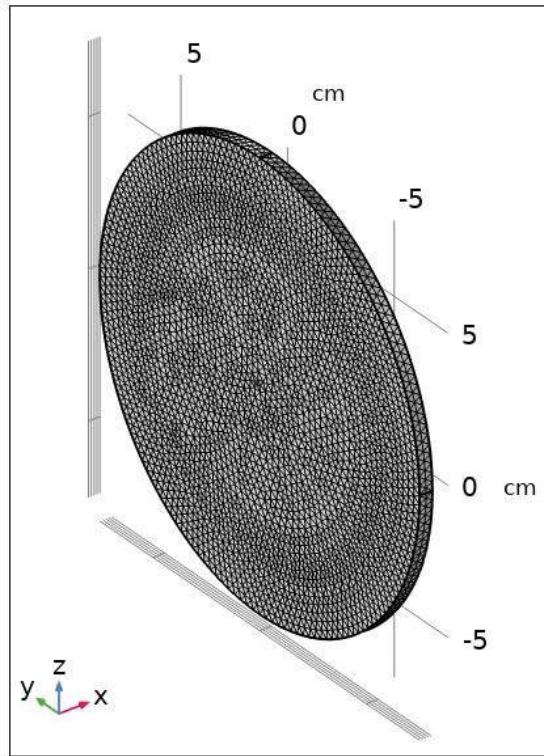
### Heat conduction modeling of the tantalum converter target

In this part of the study, a heat conduction modeling of the tantalum converter target is presented. In the first step, a fixed (i.e., without rotation) tantalum disc without any cooling mechanism is considered to give the maximum temperature that the converter target reaches. After that, three different mechanisms are applied to reduce the tantalum converter target temperature.

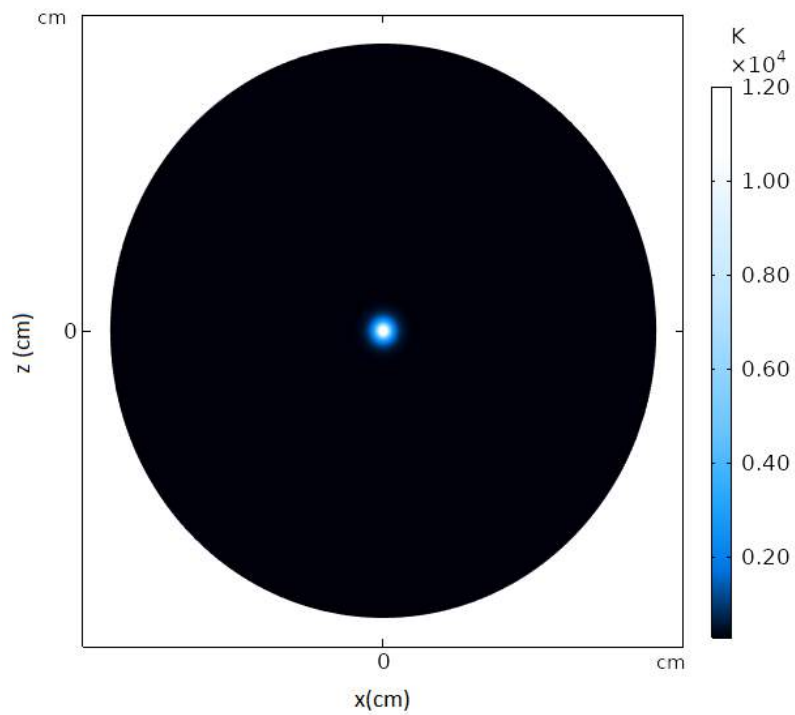
As was shown previously, a huge amount of heat is deposited in the tantalum converter target due to the electron beam's interaction (see Fig 2.27). Although a few works can be found in

the literature that investigated the heat conduction modeling of converter targets (for example, see [C18]), to my best knowledge, there is no similar heat conduction modeling and analysis existing on simulating a converter target that is irradiated with a high-energy and high-power electron beam. Therefore, only the modeling, results, and the corresponding discussion have been presented in the following.

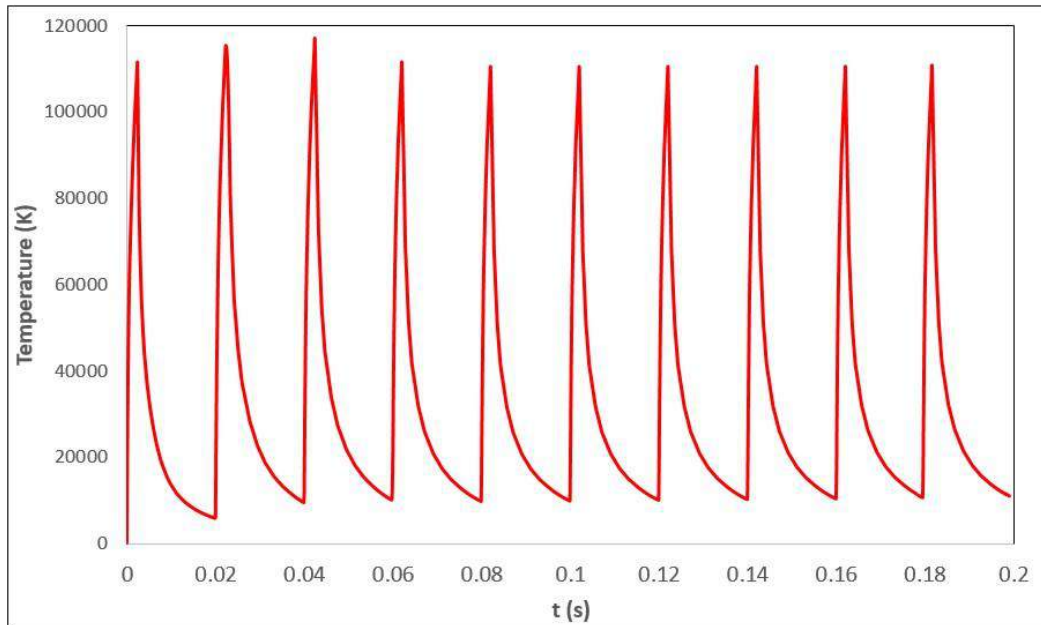
For modeling of the rotating converter target, the Moving Mesh interface should be employed (similar to the rotating beryllium disc). The term moving refers to the situation where a part of the geometry is moving while other parts remain fixed during simulation time [VOG19, VT19, VOG20, VOG16, VVG16]. Fig. 2.29 shows mesh distribution in the tantalum converter target, built in the COMSOL Multiphysics software for the time-dependent heat conduction modeling of 200ms simulation time and 1mm FWHM electron beam. For high accurately modeling of the converter target, a fine mesh structure was employed. In Fig. 2.30, the 2D temperature distribution of the tantalum converter target at 200ms simulation time and 1mm FWHM is presented. It is worth pointing out that the tantalum solid target material employed in the simulation was imported from the built-in solid structure material library of the COMSOL software. The maximum temperature variations, which the tantalum converter target reaches during the 200ms simulation time corresponding to the electron beam frequency are shown in Fig.2.31. As is observable, the maximum temperature changes periodically and corresponds to the incident electron beam frequency presented in Fig. 2.12. Although one can assume that without cooling, the temperature should approach infinity when heating is continued, it has to be considered that heat can be dissipated by conduction during the pause between pulses and that the disk can dissipate most of the energy between the pulses. Moreover, as is shown in Fig. 2.31, the temperature approached around 120'000 K, which can not be tolerated by any material (even tantalum). This example was provided to indicate that a new design for the converter target needs to be considered so that the temperature decreases below the tantalum melting point (as much as possible). Since the rhodotron works at 50 Hz and has a 12.5% duty cycle, it hits the converter for 2.5 ms, and for 17.5 ms, the converter has time to cool (one cycle is 20 ms). As was shown in Fig.2.31, the simulation is performed for 10 cycles (200ms) to show the magnitude of the temperature. It is worth pointing out that the rhodotron should work in principle for any desired target bombardment time (see section 2.4.3). This is due to the fact that radionuclide yield is a function of bombardment time. In reality, despite the fact that performing the simulation for a long time was not possible (due to the lack of a high-performance computer machine), it was even impractical to model it for a longer simulation time since the temperature is too high (around 120'000 K).



**Fig. 2.29:** Mesh distribution in the tantalum converter target of the optimum thickness (i.e., 4.5mm) for the time-dependent heat conduction modeling of 200ms simulation time and 1mm FWHM electron beam



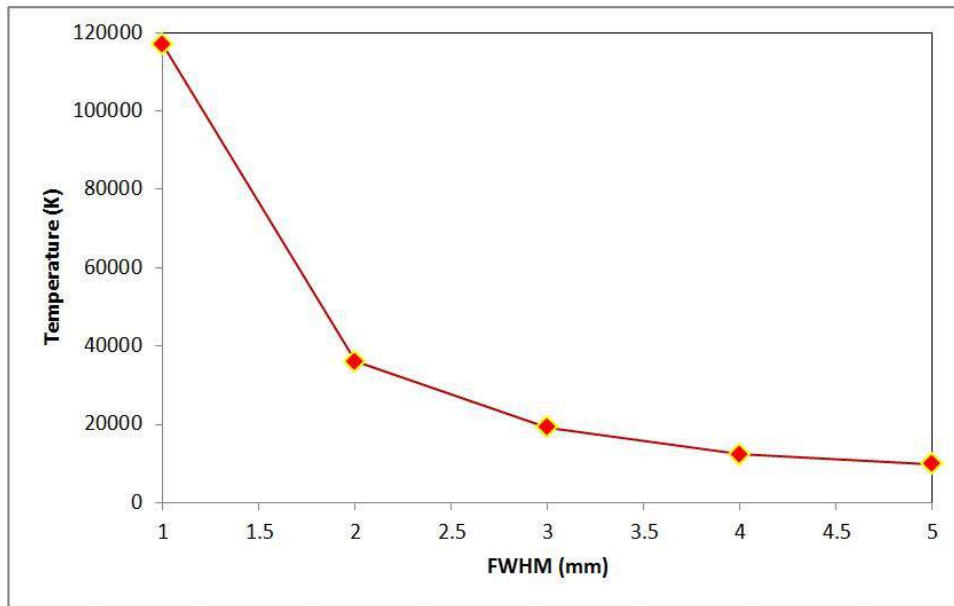
**Fig. 2.30:** 2D temperature distribution of the tantalum converter target at 200ms simulation time for 1 mm FWHM of the electron beam



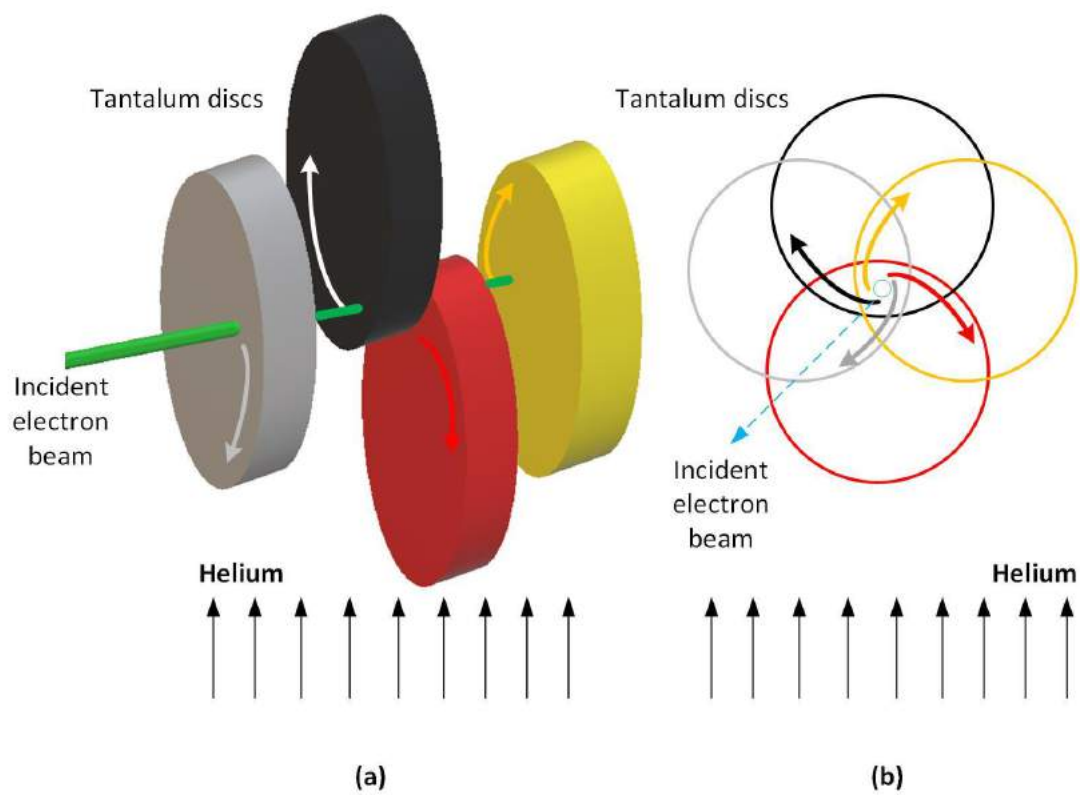
**Fig. 2.31:** Maximum temperature distribution versus 200ms simulation time for the optimum thickness of the tantalum target with 1mm FWHM of the electron beam

Fig. 2.32 reveals the effect of the incident electron beam shape (as FWHM) on the maximum temperature, which the tantalum target reaches. As can be seen, the maximum temperature decreases as the FWHM increases. After the performed heat conduction modeling of the conventional converter target design, it can reasonably be argued that practical use of such a design is impossible due to the significant temperature rise. On this basis, three different mechanisms for temperature reduction in the tantalum converter target are presented.

A helium-cooled multidisc rotating converter target design is proposed in the new design (see Fig.2.33). The idea behind using the multidisc converter target technique is to divide the conventional one-disc tantalum converter target with the optimum thickness into four discs while the sum of the thicknesses remains the same. This technique allows to divide the total amount of significant energy deposition in the tantalum and, therefore, reduce the temperature. A helium flow through the multidisc converter target also provides cooling and reduces the converter target's final temperature. Besides, the converter discs are rotating, which means that the electron beam does not hit the same position at the center of the converter target over and over, and impinges on a large area that should result in a lower maximum temperature of the converter target. Fig. 2.33 shows a) a 3D and b) 2D schematic representation of the multidisc converter target design. As shown in Fig. 2.33, the tantalum discs are considered to not be stacked on a single shaft in order to minimize overlap and mutual heating (considering the radiation heat transfer term).



**Fig. 2.32:** Variation of maximum temperature as a function of FWHM for the optimum thickness of the tantalum converter target (i.e., 4.5mm)



**Fig. 2.33:** A schematic representation of multidisc tantalum converter target design in a) 3D and b) 2D geometries.

In the following, the heat conduction modeling of the helium-cooled multidisc rotating converter target is performed using the COMSOL Multiphysics software. Since the main purpose is to investigate the maximum temperature, which the converter target(s) reaches, the energy deposition in each tantalum disc is obtained using the MCNP code. Then, the heat conduction modeling is carried out for the disc with the highest energy deposition. Fig. 2.34 shows the results of the MCNP code simulation and shows the energy deposition for each tantalum disc. As can be seen, in the third disc, the energy deposition is higher than in the other discs. On this basis, according to the above discussion, the heat conduction modeling is performed only for the third disc using the COMSOL Multiphysics software.

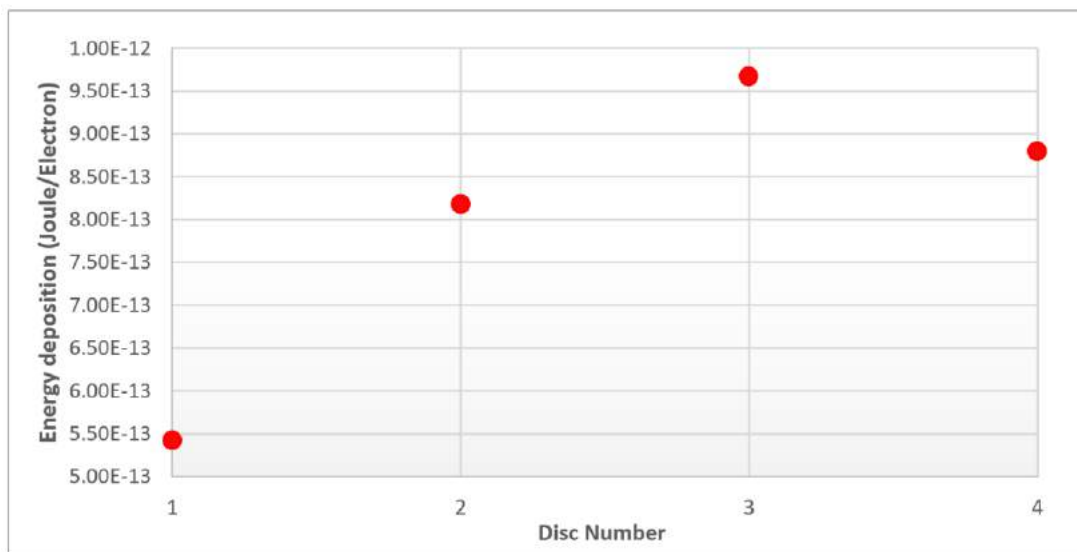


**Fig. 2.34:** Energy deposition in the tantalum converter discs. Considering a  $1.9\text{E}16$  e/s beam current from a rhodotron model TT300-HE, one can estimate about 47'000 Joule/s (Watt) energy deposition for the entire tantalum converter discs. Considering the heat capacity of helium ( $5.2 \text{ Joule} \cdot \text{g}^{-1} \text{K}^{-1}$ ), and a 200K difference in temperature of helium's inlet and outlet, one can obtain about  $250 \text{ l} \cdot \text{s}^{-1}$  for cooling the converter targets.

In order to model the new design in the COMSOL Multiphysics software, the distance between the discs is considered 2 mm. Additionally, a vertical helium flow is considered to enter the housing of the irradiation setup in order to cool down the disc with a volumetric flow rate of 250 L/s (see the caption of Fig. 2.34 for more details). No-slip conditions were considered at the surfaces of the converter target. The helium flows according to Fig.2.39 and streams in gaps of 2 mm between the rotating discs. As illustrated in Fig. 2.33, a fraction of the surfaces of the discs overlap with each other.

Instead of modeling the entire tantalum converter discs, a single disc could only be modeled due to the lack of a high-performance computer. Actually, higher accurate results could be obtained if the entire discs could be modeled. In the simulation, the no-slip conditions were applied and its effect on heat transfer was considered in the calculations. In the case of modeling of the proposed new design via the COMSOL Multiphysics software, it should be noted that the COMSOL Multiphysics offers physics interfaces for heat transfer and fluid flow



calculations. These interfaces have model inputs that make it possible to couple the physics. Moreover, the COMSOL Multiphysics and the Heat Transfer Module contain multiphysics coupling interfaces, facilitating the coupling between fluid flow and heat transfer interfaces [COMSOL]. Using the COMSOL Multiphysics software, primarily some initial information can be given as the starting point, such as the fluid flow regime, velocity/volumetric flow rate, temperature, etc. The COMSOL then asks the user for permission to change the assumptions whenever applicable during simulation time (for example, due to fluid flow passing between the discs, etc.). One of the options (to activate or not) is also giving the permission to solve the energy transport equations coupled to the Navier-Stokes equations, which has been activated in my work to give permission to the software in order to use it if it is required during the heat transfer calculations. Therefore, when the COMSOL start to solve the problem and, for example, see in the middle of the calculations that with the given method, it could not be matched or even converge the equations, it comes back (particularly, in the transient calculations, which was used in my work), and change the applied method (if it has the permission) and continue again to perform the calculations. This is a little bit different from the Ansys software that asks the user before the start of modeling to specify exactly which method must be used for the problem [COMSOL, ANSYS].

The angular rotation speed of the tantalum converter disc is considered as 24'000 rpm. Considering 50Hz frequency of the electron beam and 12.5% duty cycle of the rhodotron, the complete perimeter of the tantalum disc is exposed with each electron beam pulse, and seven complete rotations are free of electron beam exposure allowing the disc to cool down (see Fig. 2.35). According to Fig. 2.35, instead of exposing only one part of the tantalum disc, the entire disc is affected, which results in a lower energy density deposition.

As discussed above, in addition to the rotation of the tantalum targets and using a multidisc technique, a helium flow is considered to allow for heat removal and a temperature reduction of the tantalum converter discs.

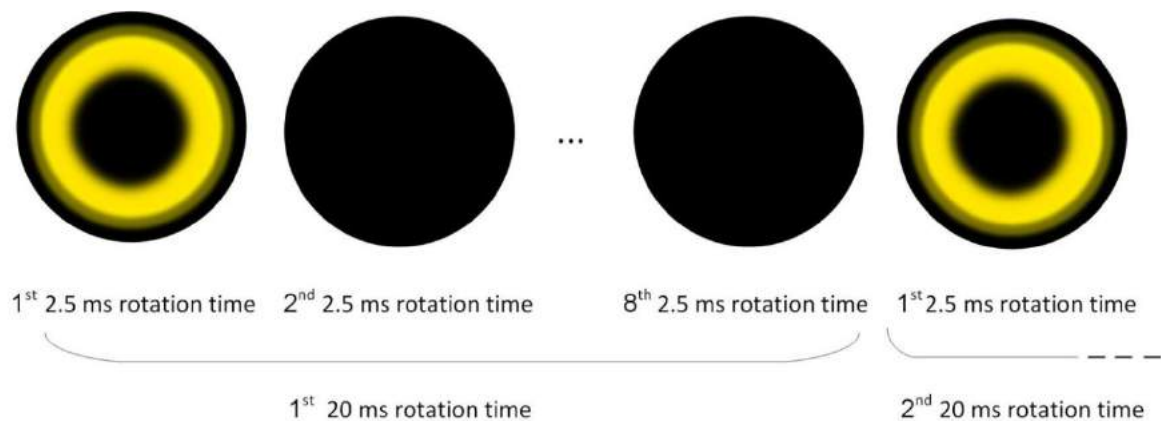


**Fig. 2.35:** A schematic representation of tantalum disc rotation in the newly proposed helium-cooled multidisc rotating converter target design

In the modeling with COMSOL Multiphysics software, all these mechanisms are applied together for the third tantalum disc, which is the target with the highest energy deposition.

In the case of discs number 1 and 4, the thermal radiation term can reduce the temperature much more efficiently compared to discs number 2 and 3. Moreover, since in terms of energy deposition (as was shown in Fig. 2.34), the disc number 1 and 4 do not have the highest amount of heat deposition (according to the MCNP code modeling, see Fig.2.34), their modeling was ignored (due to the lack of a high performance computer), and only the modeling of the disc number 3 was taken into account. This is due to the fact that, as mentioned above, disc number 3 has the highest energy deposition among all other discs, and in terms of thermal radiation, it can not be cooled efficiently. To continue, first, it should be mentioned that the rhodotron pulsed time in each cycle takes only 2.5 ms, and considering 24'000 rpm of the tantalum discs, it covers an entire disc uniformly during a single pulse irradiation (see Fig. 2.35). For the COMSOL modeling of the tantalum disc, since it was very difficult and even impossible for the employed computer to simulate 2.5 ms (i.e., an entire irradiating part of a single cycle), only a small fraction of it (0.25 ms) was modeled (see Figs.2.36 and 2.37). However, this short simulation time does not significantly affect the results regarding a completely single irradiating cycle modeling (i.e., 2.5 ms). This is due to the fact that the energy deposition profile is uniform for a given single shot (of course, if it was possible to model several cycles, it would be a different story, but for even a small fraction of a single pulse irradiation time, it took some weeks, and the memory of the computer was saturated so that it was even impossible to model a single complete cycle irradiating time). If I come back to the discussion about the modeling of the third disc, it has to be mentioned that I had to model only a small fraction of a single irradiating cycle (0.25 ms compared to 2.5ms; it also is observable by comparing Fig. 2.35, with Figs.2.36 and 2.37), corresponding to a fraction of the third disc, where it was covered by the discs number 2 and 4 (see Fig.2.33). Since, in spite of the thermal radiation, which is considered by the COMSOL software, I could not consider the heating up of the disc that is exposed by the other discs (i.e., discs number 2 and 4), and see their effect on the disc number 3, I changed the emissivity of the disc so that it was able to reduce the thermal radiation emission. This also helped to overestimate the temperature, which is fine from the conservative point of view.

The Moving Mesh interface has been employed to model the rotating converter target. Therefore, the converter target is rotating (and is continuously exposing). At the same time, the helium domain (with dimensions of 200mm × 200mm × 3.125mm) is fixed, and the helium flows (with a volumetric flow rate of 250 L/s) from the bottom up. Besides the conduction, the converter target is cooled by the helium flow (convection) and thermal radiation during the simulation time. Fig. 2.36 shows the mesh density distribution built in the COMSOL Multiphysics software for the time-dependent modeling of the third disc tantalum converter target considering 5mm FWHM and 0.25ms simulation time. As can be seen, an adaptive moving mesh method is used, which allows for a higher mesh density resolution in regions of interest. In Fig. 2.37, a 2D temperature distribution is presented for 5mm FWHM at 0.25ms simulation time. In addition, variations of maximum temperature as a function of FWHM for the third tantalum disc are shown in Fig. 2.38. As can be seen, the maximum temperature decreases significantly by increasing the FWHM. Although the obtained temperatures are all below the melting point of tantalum, the temperature should not be close to the melting point and is needed to be kept as low as possible. Therefore, instead of using a very low FWHM, a higher value is preferable for practical applications.

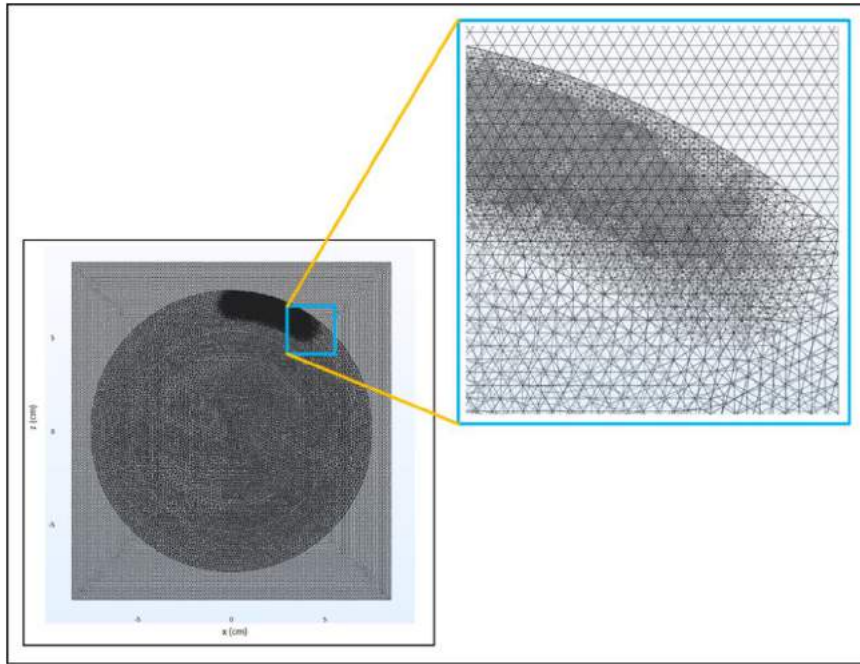


**Fig. 2.36:** Mesh density distribution used in the COMSOL Multiphysics software for the newly proposed multidisc rotating converter target design considering 5mm FWHM and 0.25ms simulation time

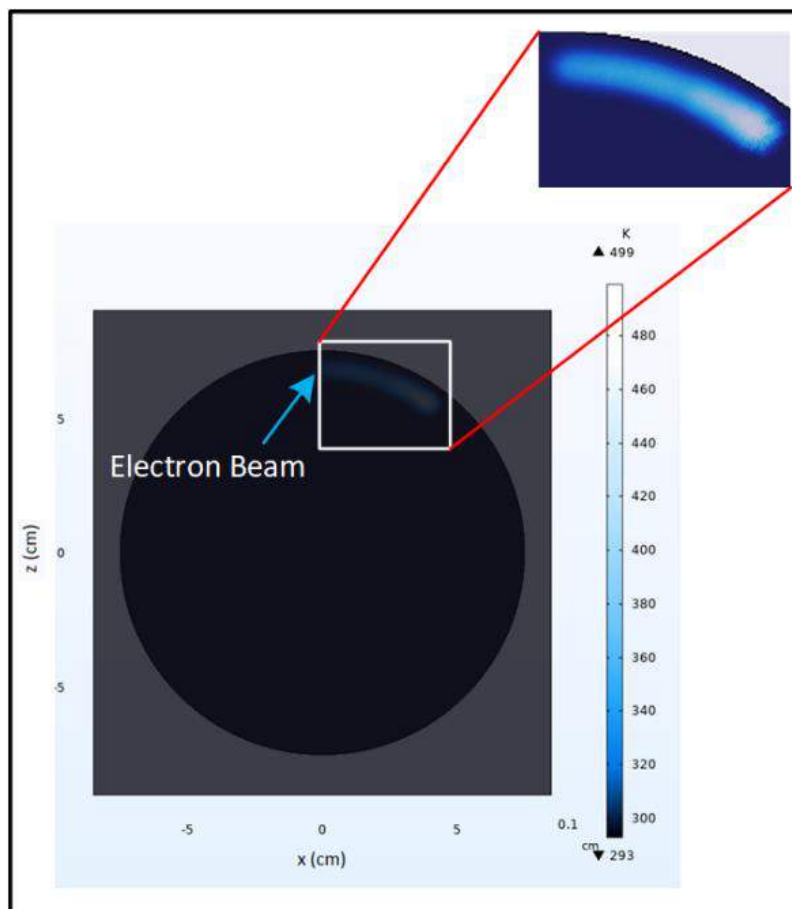


**Fig. 2.37:** 2D temperature distribution of the third tantalum converter disc for 5mm FWHM at 0.25ms simulation time

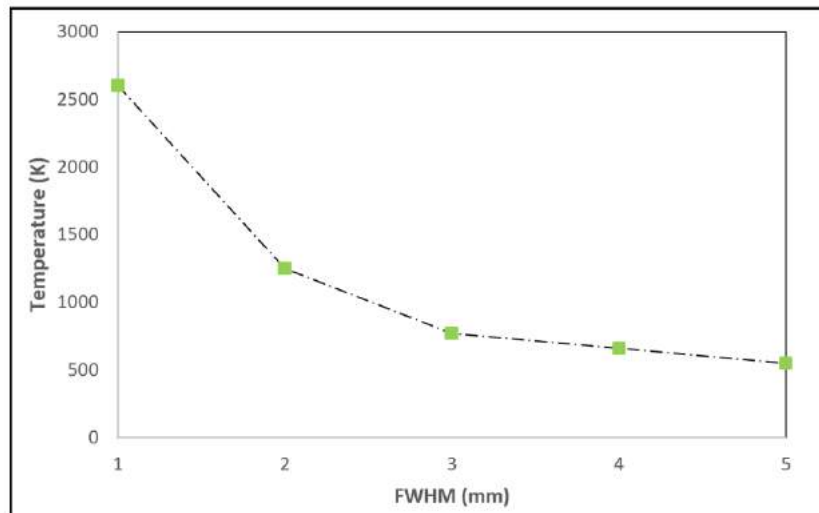


**Fig. 2.38:** Variation of maximum temperature versus different FWHM of the electron beam for the third tantalum disc

It should be noted that, in this section of work, the optimum target thickness refers to the optimum thickness that was obtained from the MCNP code regarding the highest Bremsstrahlung production in the range of the GDR region (8 to 30 MeV) for efficient photonuclear production (as was discussed in section 2.3). This optimum thickness is around 4.5 mm for the tantalum converter target (see Fig. 2.20). Therefore, the total tantalum discs thicknesses are 4.5 mm (each having 1.125 mm). The thickness of each disc also could be optimized from the point of view of heat deposition/temperature. This could change the maximum temperature that each disc reaches. However, because the temperature of the worst disc (i.e., disc number 3) is much less than the tantalum melting point, and the temperature was reduced significantly (from 2700K to around 500K) by changing of FWHM (from 1 to 5 mm) (see Fig. 2.38), no further investigation was considered to see the influence of changing the thickness regarding the heat deposition. However, optimization of the thickness of each tantalum disc can also be another option to reduce the temperature.

All in all, from the point of view of accuracy, it would be much better to model the entire irradiation setup, including all the converter discs, for a quite long time (perhaps around 2'000ms compared to 20ms of a single rhodotron cycle, including the irradiation time and cooling time that is 2.5 and 17.5 ms per each cycle, respectively). In this case, it would be possible to not only see the maximum immediate temperature but also to see the temperature growth versus time evolution (for all discs). However, as mentioned before, the lack of a high performance computer forced me to think about priorities in the simulation that I was looking for, which was an estimation of the maximum temperature that the discs would reach. For this reason, instead of modeling all of the discs, I considered the most challenging disc, which is disc number three. Disc number 3 is the most important one since, on the one hand, as the Monte-Carlo calculations showed (see Fig.2.34), the highest energy is deposited on this disc among all other discs. On the other hand, in terms of heat transfer, it would be partially exposed to the thermal radiation emitted from discs number 2 and 4 (similar to disc number 2, which is exposed by discs number 1 and 3). Therefore, since I had to choose one disc, I selected disc number 3. Moreover, it was also impossible to even model an entire cycle (i.e., 20ms including 2.5ms irradiation time and 17.5ms cooling time), so I chose the time range

between 0 to 0.25 ms, since in this range of time, as was mentioned before, it would be exposed by thermal radiation emitted from discs number 2 and 4. Considering the above discussion, I considered the most conservative possible case that could also be modeled by the employed computer. By thermal radiation the discs can be cooled; however, they can also heat up each other by the same effect (in particular, in the aforementioned range of time that was modeled). To consider this, I changed the emissivity of the disc to reduce the effect of cooling the disc by the thermal radiation emission term. In the case of the evolution of temperature, which could only be seen when a lot of irradiation rhodotron cycles were modeled (that, of course, was not possible), the helium flow rate considered so that it can remove the deposited heat from all of the discs (the heat deposition obtained by the MCNP code). This issue has been discussed in the caption of Fig. 2.34 and the discussion following that. Therefore, from the point of view of the maximum temperature that the converter reaches, and from the point of view of temperature growth over a long time, the obtained results have not been affected (and as was mentioned before, they even have been obtained conservatively).

## 2.4 Other irradiation setup components

Modeling and designing of other irradiation setup components are presented in this section of the study. Accordingly, this section of work has been divided into three different parts corresponding to each irradiation setup component (see Fig. 2.39). In the first part, designing an aluminum column containing water, which allows shielding of the low energy photons and electrons before impinging on the production targets is presented. In the second part, radionuclide production of some promising and high in demand radionuclides attainable by the photonuclear production method is discussed in detail. In the final part of this section, a lead shield modeling via the MCNP code is presented to ensure complete protection against the transmitted electrons and photons from the production targets.

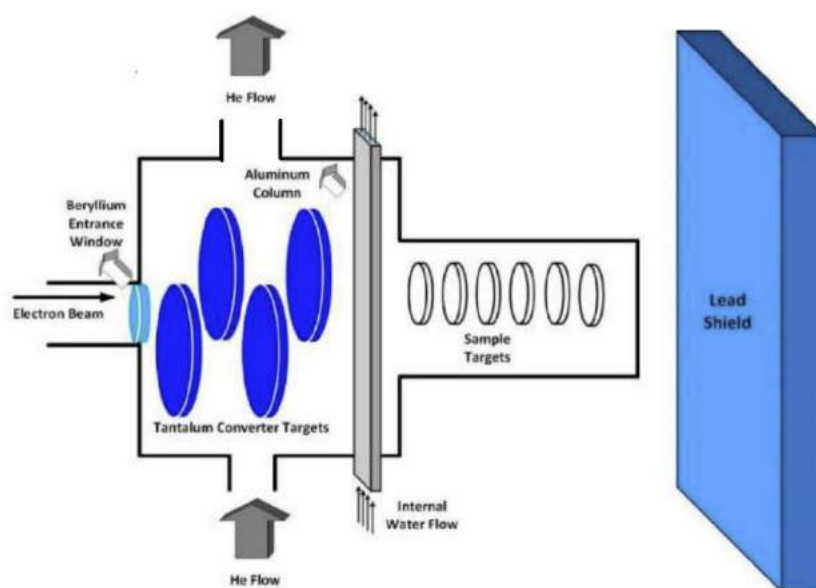


**Fig. 2.39:** Schematic representation of different irradiation setup components. The production targets are assumed to have 2cm diameter and placed 1cm apart. The aluminum column has a 1mm thickness (on each side) with a dimension of 0.5cm×2.2cm×20cm. The

internal water thickness is 3mm. The distance between the last tantalum converter disc and the first production target (i.e., the first detector) is 1.5 cm.

The distance between the aluminum column and the first production target (i.e., the first detector) is 0.5 cm. The converter discs are tightly enclosed in a water-cooled housing. The housing incorporates openings to allow gas circulation to and from the housing with a 3mm to 5mm thickness.

### 2.4.1 Flattening filter

The exit window of the converter target assembly can be made either from beryllium foil or constructed as a flattening filter in order to protect the targets from irradiation with electrons, X-rays and low energy gamma-rays. The flattening filter is made from a rectangular aluminum profile with 1 mm wall thickness (see Fig.2.39). The inside of the profile is flushed with cooling water of 3 mm thickness. The task of this unit is to filter out and therefore considerably reduce the flux of low energy photons that are not contributing to photonuclear reactions and the heat generation in the production targets (see Fig. 2.39) [PBSKS07, W09]. An internal water flow can be employed to provide an active heat removal from the aluminum column. The low atomic number of aluminum provides considerable shielding against low-energy photons and electrons while allowing passage of high-energy photons and, to some extent, high-energy electrons [W09, TAKVCGBM12]. In the simulation, the aluminum column has a 1mm thickness (for each side) with a dimension of 0.5cm×2.2cm×20cm. The internal water thickness is 3mm. Distance between the aluminum column and the first production target (i.e., the first detector) is 0.5 cm. In Fig. 2.40, the electron energy spectrum before and after passing through the column is presented. As is observable, the aluminum column shields electrons in the entire energy range, particularly, in the low-energy region.

In Fig. 2.41, the photon energy spectrum before and after passing through the column is presented. As is shown in Fig. 2.41, different than for electrons (see Fig. 2.40), the attenuation of photons is not evident in the entire energy range; and, in fact, is more considerable in the low energy range (i.e., lower than 8 MeV). Low attenuation of photons, particularly, in the GDR region (and beyond, i.e., higher than 30 MeV), allows the radionuclide production keeps high as before.

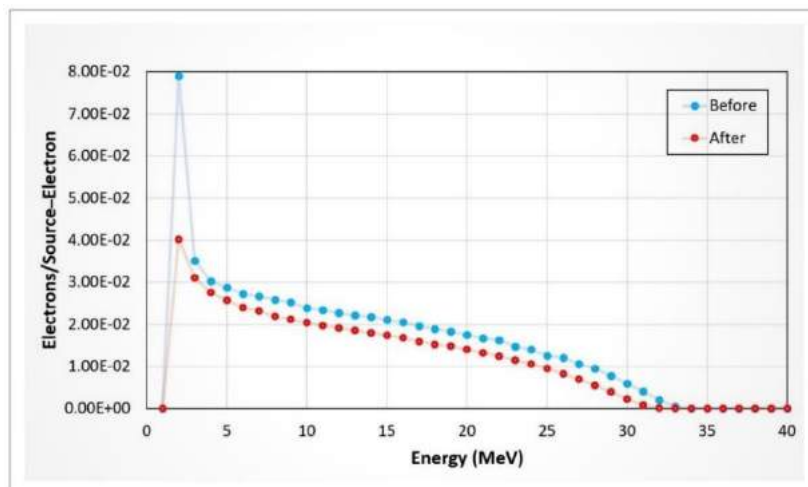


**Fig. 2.40:** Electron energy spectrum before and after electron beam collision with the aluminum column. The reduction in electrons is 22.8% in the entire energy range.

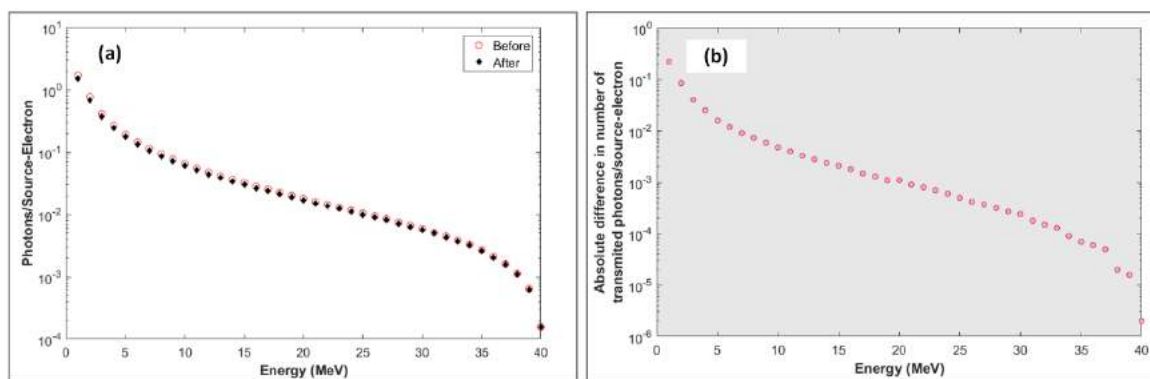


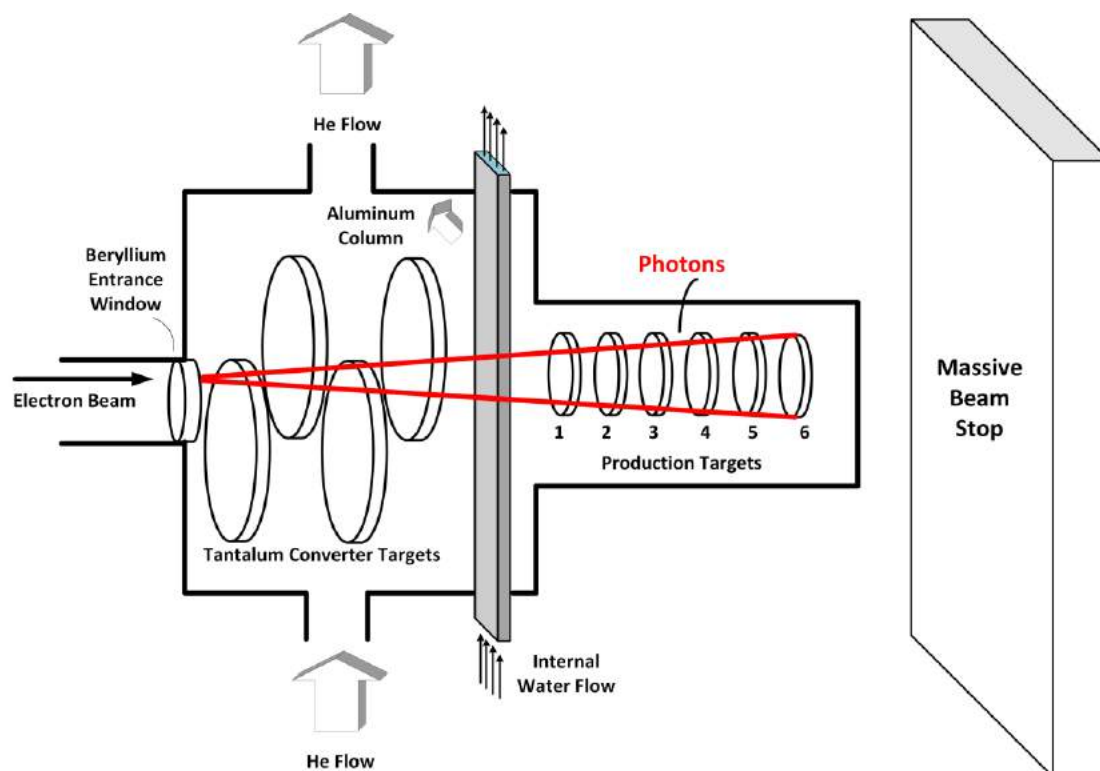
**Fig. 2.41:** a) Photon energy spectrum before and after the aluminum column. b) Absolute difference in number of transmitted photons/source-electron (i.e., subtraction of 'Before' and 'After', in Fig. 2.41a). The reduction of photons is 11.2% in the 0-8 MeV, 6.5% in the 8-30 MeV and 2.9% in the 30-40 MeV energy interval.

## 2.4.2 Production targets

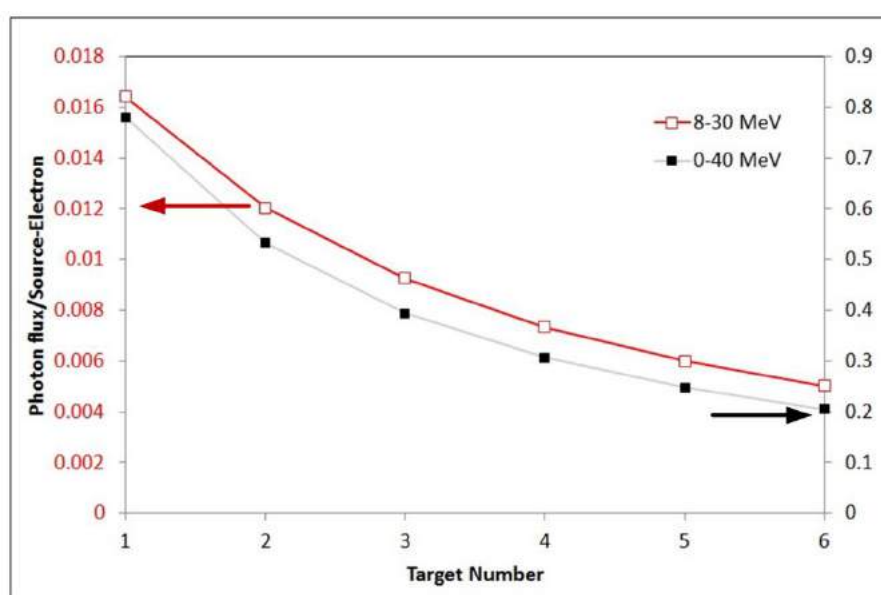
As was mentioned before, production targets refer to the samples, which are irradiated by the Bremsstrahlung. These production targets can be placed in different positions considering different distances from the aluminum column. To investigate the radionuclide yield (which will be defined later), the photons flux needs to be obtained in different positions. As was discussed before (see section 1.1.1.5), the generated high-energy Bremsstrahlung tend to move mainly in a forward conical-shaped direction as shown in Fig.2.42. In order to obtain the photon flux in different aforementioned positions, the MCNP code is employed. In the MCNP code, different "Tallies" (which work as different detectors) are considered to obtain the photon flux (see Fig. 2.43). Fig. 2.43 shows the photon flux (per source-electron) for the Tallies located at a one-centimeter distance from each other and have an energy range of 8-30 MeV and 0-40 MeV. As can be seen, the photon flux decreases by increasing the target position number (or, in other words, the distance).

Fig. 2.44 shows the angular photon flux (per source-electron) passing through the Tallies in the energy range of 8-30 MeV (i.e., the GDR region). As was expected, the Bremsstrahlung in the energy range of the GDR travel almost in a forward direction. However, even a small angular photon beam broadening can result in a reduction in photon population as photons travel farther. Fig. 2.44 shows a reduction of photons when the distance (target position number) increases.





**Fig. 2.42:** Schematic representation of the spatial photon emission distribution in the entire photonuclear irradiation setup



**Fig. 2.43:** Photon flux (with the units of photons per source-electron per  $\text{cm}^2$ ) for the energy ranges of 8-30 MeV and 0-40 MeV, respectively



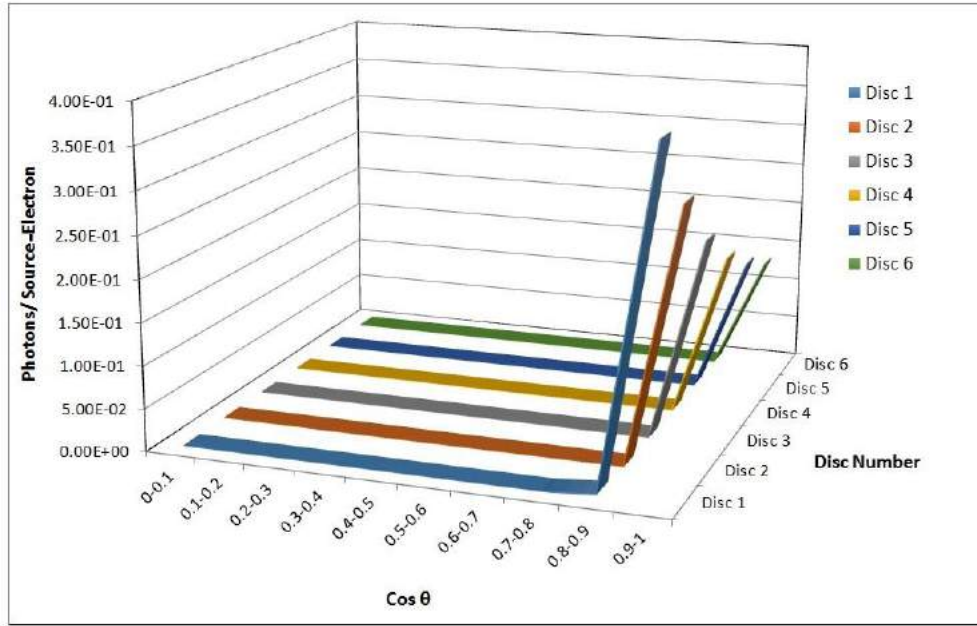


**Fig. 2.44:** Angular photon distribution (in units of photons per source-electron) for the energy range of 8-30 MeV

The yield for the production of  $^{99}\text{Mo}$ ,  $^{225}\text{Ac}$ , and  $^{67}\text{Cu}$  as the most interesting and promising radionuclides for the photonuclear production method are presented.

### 2.4.3 Calculated yields of radionuclides (examples):

The radionuclide reaction yield can be obtained as follows [A19, MLA06, VSSO20, V13]:

$$Y(\text{atoms/day}) = B \int_{E_1}^{E_2} NL\sigma(E)\phi(E) dE, \quad (2.2)$$

where  $Y$  is the yield of a radionuclide in atoms per day,  $N$  is the number of target atoms per gram,  $\phi$  is the incident photon flux per second,  $L$  is the target thickness in units of gram per  $\text{cm}^2$ , and  $\sigma$  is the cross-section in  $\text{cm}^2$ . Moreover, in Eq.2.2,  $B$  is a constant number and represents the conversion factor of seconds to days. Using the radionuclide reaction yield, one can obtain the radionuclide production rates as follows:

$$A = Y \times \lambda, \quad (2.3)$$

where  $\lambda$  is the decay constant, and  $A$  is the activity of the produced radionuclide in units of GBq per day (per 125kW) for 125 kW electron beam power and 40 MeV incident electron beam energy.

According to Eq.2.2, specifying photon spectra in different production target positions (see Fig. 2.42) is essential, which can be obtained using the MCNP code (note that the production targets are assumed to have 2cm diameter and are placed 1cm apart). Fig. 2.45 shows the photon energy spectrum in different production target positions in the entire energy range. As can be seen, the change of variations in photon spectra for energies higher than 30 MeV is less compared to the lower energies. This is due to the fact that high energetic photons travel

mostly in forward direction, and this reduce the escaping probability of photons from the position of the production targets. In other words, the population of high-energy photons is less dependent on the distance that they are traveling. In the following, calculated yields and activities of some radionuclides are presented.

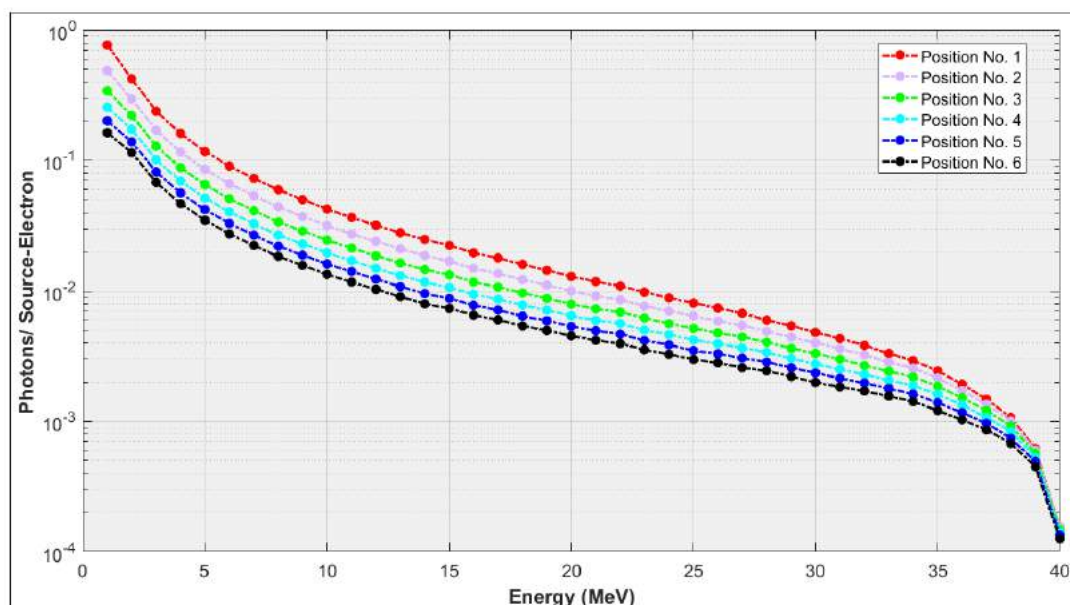


**Fig. 2.45:** Photon (per source-electron) energy spectrum for different production target positions

### Production of $^{67}\text{Cu}$ from $^{68}\text{Zn}$

$^{67}\text{Cu}$  can be produced through the  $^{68}\text{Zn}(\gamma, p)^{67}\text{Cu}$  reaction (see Fig. 2.46). In Fig. 2.47, photonuclear excitation function (mb) for  $^{67}\text{Cu}$  production through the reaction  $^{68}\text{Zn}(\gamma, p)^{67}\text{Cu}$  is presented. As can be observed, a significant difference exists between the data taken from the TENDL-2019 and EXFOR databases (probably due to the difference in theoretical modeling and experimental measurements). On this basis, experimental data are considered for the yield calculations. Due to the lack of sufficient experimental data (see Fig.2.47), a fitting Gaussian distribution curve is employed using the Matlab software (see Fig.2.48). Using Eqs. 2.2 and 2.3, and the photon energy spectrum (see Fig. 2.45),  $^{67}\text{Cu}$  production for one-day irradiation time can be obtained for different production target positions as shown in Fig. 2.49. As can be seen, the obtained  $^{67}\text{Cu}$  activity decreases as the production target number is increased.

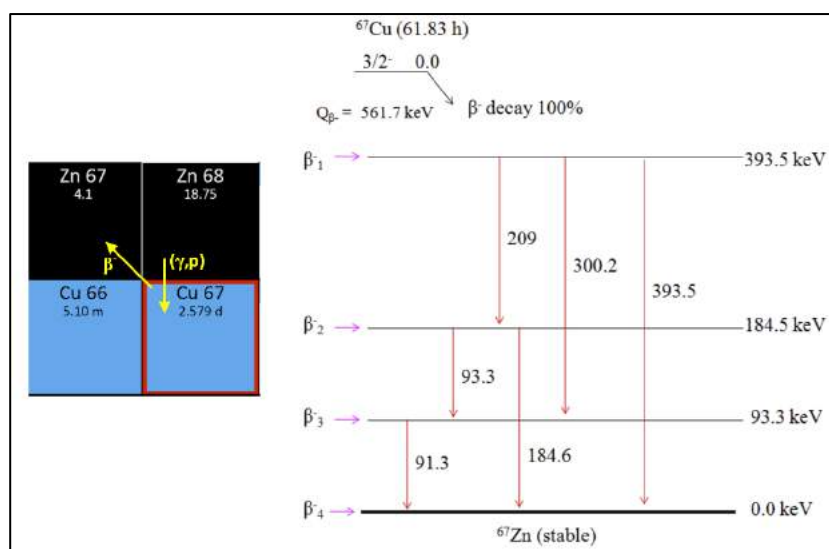


**Fig. 2.46:** Schematic representation of the  $^{67}\text{Cu}$  photonuclear production routes and its decay chain, and scheme [BNB16, Nucleonica20]

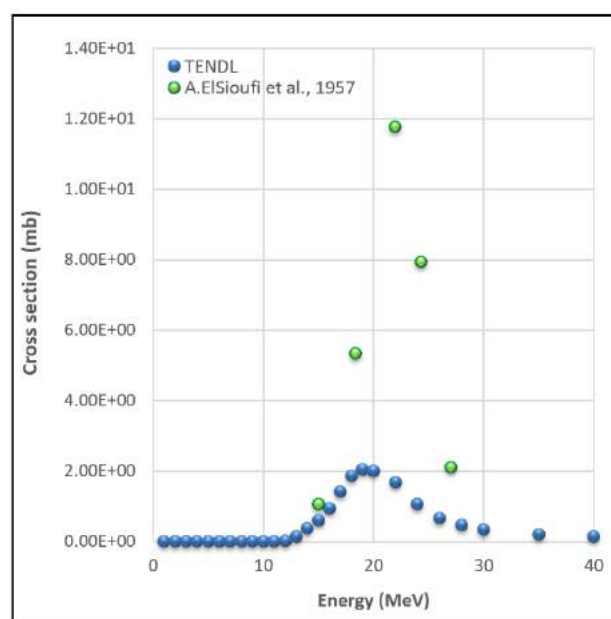


**Fig. 2.47:** Photonuclear excitation function (mb) of the  $^{68}\text{Zn}(\gamma, p)^{67}\text{Cu}$  reaction vs. photon energy (MeV). Data taken from the TENDL-2019 [KRSDFM19] and EXFOR database [EXFOR21].

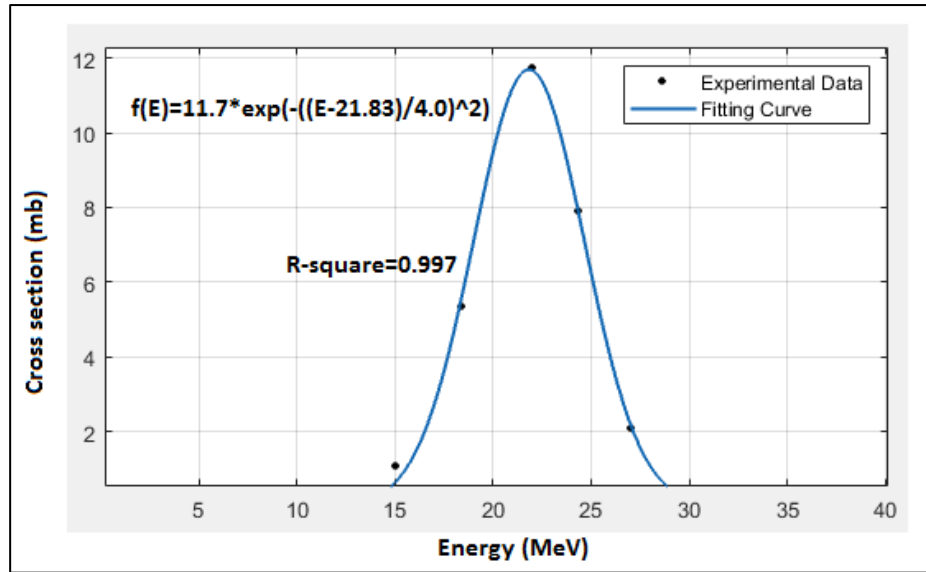


**Fig. 2.48:** Fitting curve (using a Gaussian distribution) for the experimental measurements of the photonuclear excitation function (mb) of the  $^{68}\text{Zn}(\gamma, p)^{67}\text{Cu}$  reaction presented in Fig.2.47

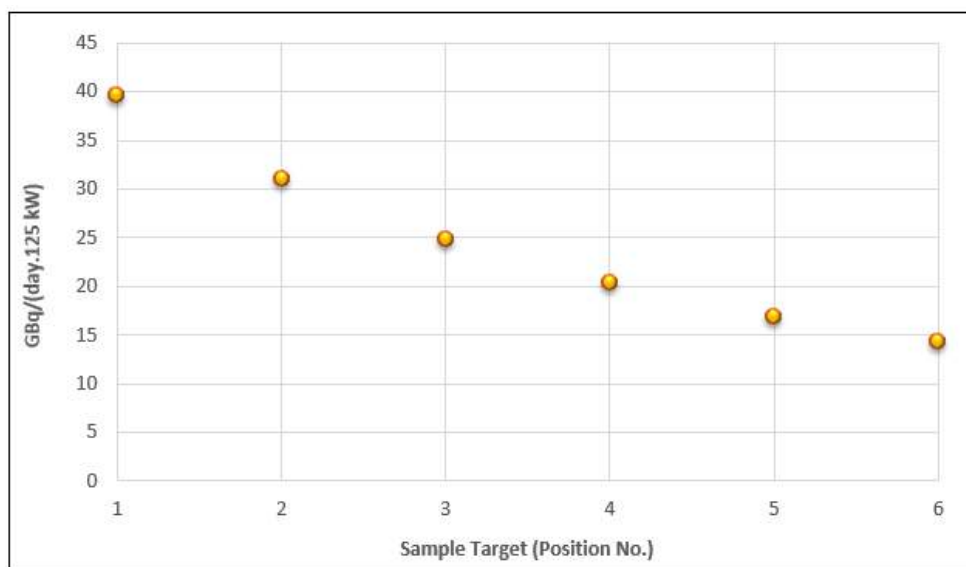


**Fig. 2.49:**  $^{67}\text{Cu}$  production for different production target position numbers considering a  $1 \text{ (g.cm}^{-2}\text{)}$   $^{68}\text{Zn}$  target thickness

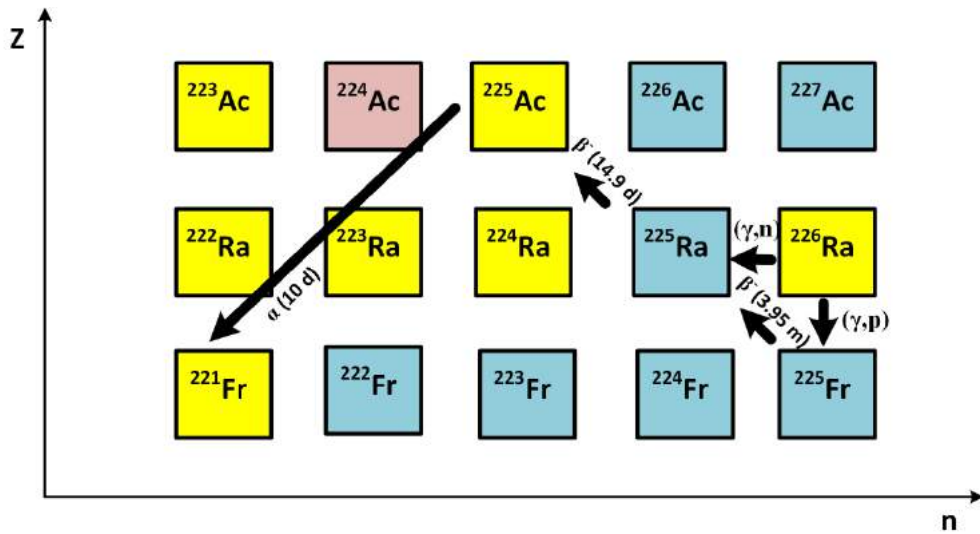
## Production of $^{225}\text{Ra}$ from $^{226}\text{Ra}$

$^{225}\text{Ac}$  can be obtained as the result of  $^{225}\text{Ra}$  beta-minus decay; once  $^{225}\text{Ra}$  is produced through the  $^{226}\text{Ra}(\gamma, n)^{225}\text{Ra}$ , and  $^{226}\text{Ra}(\gamma, p)^{225}\text{Fr} \xrightarrow{\beta^-(4.0\text{m})} ^{225}\text{Ra}$  reactions (see Fig.2.50) [CJ09, MLA06].  $^{225}\text{Ra}$  production calculations through the photonuclear reaction can be performed using the corresponding photonuclear excitation functions of  $^{226}\text{Ra}$  (see Figs. 2.51 and 2.52) and the Bremsstrahlungs spectrum (see Fig. 2.45). The time rate of change of the number of atoms of  $^{225}\text{Ra}$  and  $^{225}\text{Ac}$  can be given by the coupled differential equations

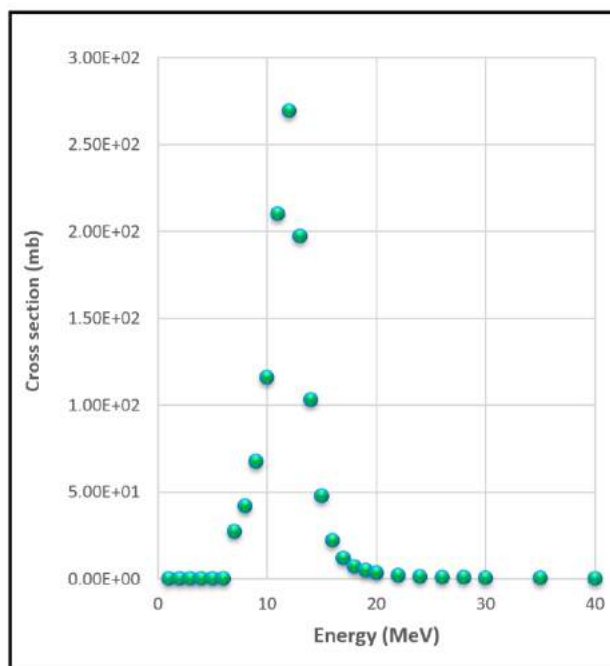
$$\begin{aligned} \frac{dN_{Ra225}}{dt} &= N_{Ra226} \cdot L \cdot \sigma_{(\gamma, n)}^{Ra226} \cdot \phi + N_{Ra226} \cdot L \cdot \sigma_{(\gamma, p)}^{Ra226} \cdot \phi - N_{Ra225} \lambda_{Ra225} \\ \frac{dN_{Ac225}}{dt} &= N_{Ra225} \lambda_{Ra225} - N_{Ac225} \lambda_{Ac225} , \end{aligned} \quad (2.4)$$

where  $\lambda_{Ra225}$  and  $\lambda_{Ac225}$  are decay constants of  $^{225}\text{Ra}$  and  $^{225}\text{Ac}$ , respectively. In Eq.2.4, all other parameters and variables have their usual meaning. Photonuclear excitation functions of the  $^{226}\text{Ra}(\gamma, n)^{225}\text{Ra}$  and  $^{226}\text{Ra}(\gamma, p)^{225}\text{Fr}$  reactions versus photon energy are presented in Figs. 2.51 and 2.52, respectively (MLA06, DR21). As shown, the photonuclear excitation function of the  $^{226}\text{Ra}(\gamma, n)^{225}\text{Ra}$  reaction is significantly higher compared to the  $^{226}\text{Ra}(\gamma, p)^{225}\text{Fr}$  reaction. Accordingly, Eq. 2.4 can be reduced to

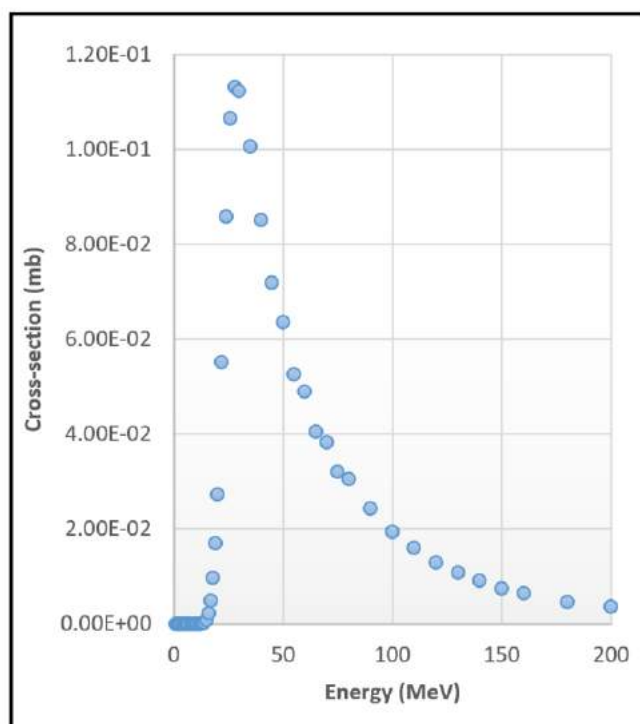
$$\begin{aligned} \frac{dN_{Ra225}}{dt} &= N_{Ra226} \cdot L \cdot \sigma_{(\gamma, n)}^{Ra226} \cdot \phi - N_{Ra225} \lambda_{Ra225} \\ \frac{dN_{Ac225}}{dt} &= N_{Ra225} \lambda_{Ra225} - N_{Ac225} \lambda_{Ac225} . \end{aligned} \quad (2.5)$$



**Fig. 2.50:** Schematic representation of the  $^{225}\text{Ra}$  photonuclear production routes and its decay chain. The yellow, blue, and red colors imply that the radionuclide has an alpha,  $\beta^-$ , and  $\beta^+$  (or  $\epsilon$ ) decay mode, respectively.

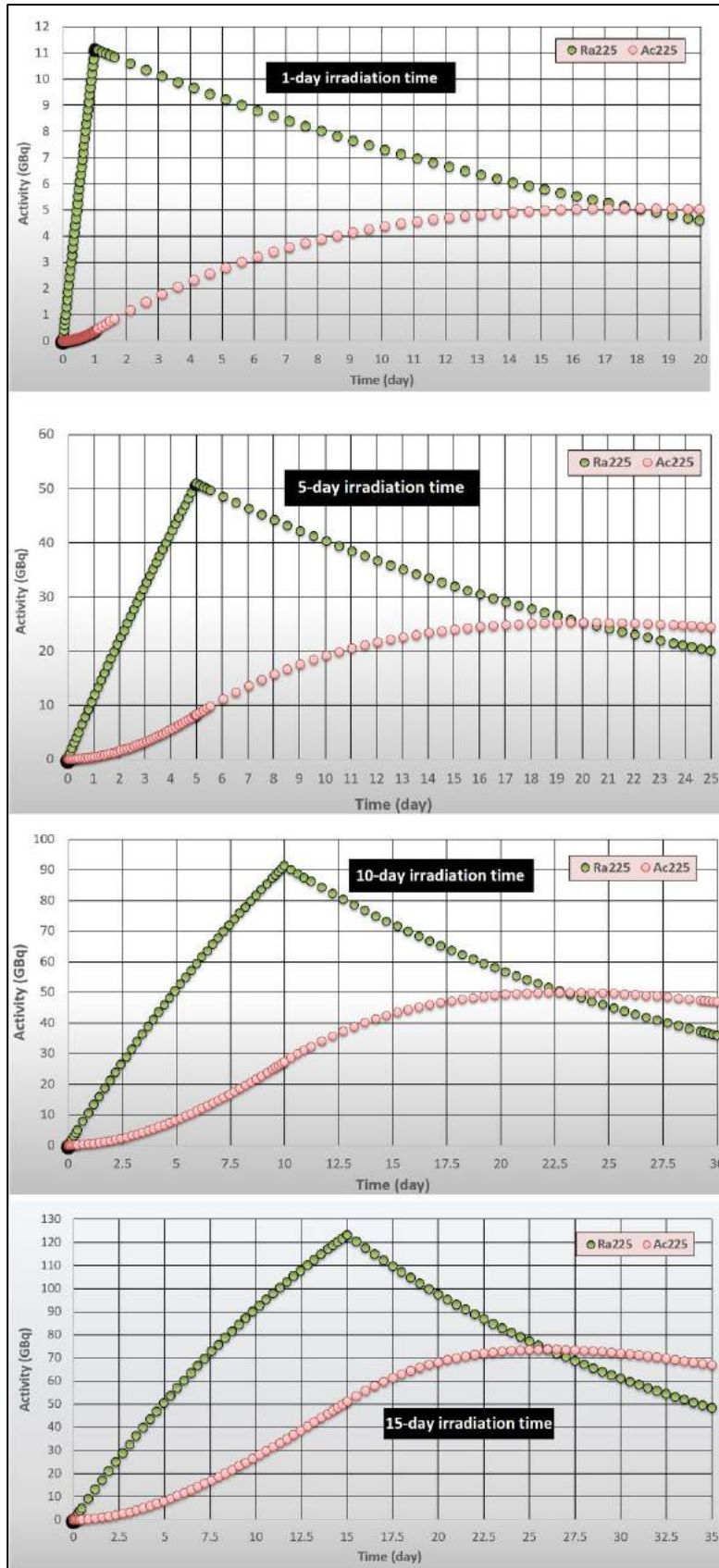


**Fig. 2.51:** Photonuclear excitation function (mb) of the  $^{226}\text{Ra}(\gamma, n)^{225}\text{Ra}$  reaction vs. photon energy (MeV). Data taken from the TENDL-2019 [KRSDFM19] (No data was found in the EXFOR database [EXFOR21]).



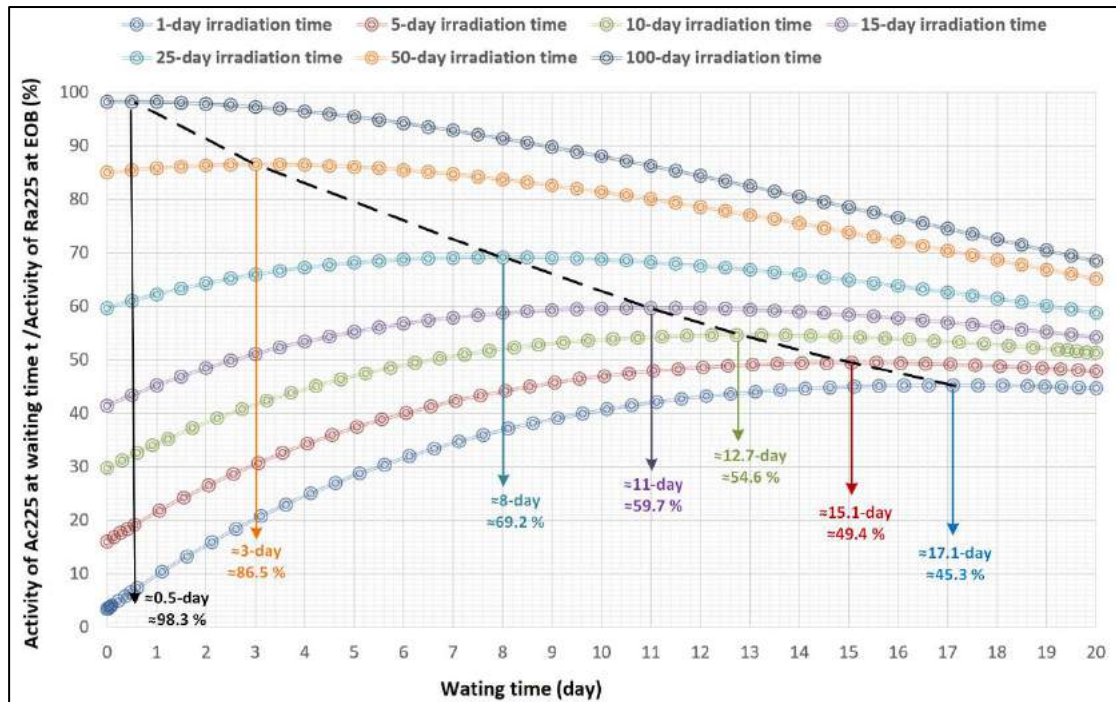
**Fig. 2.52:** Photonuclear excitation function (mb) of the  $^{226}\text{Ra}(\gamma, p)^{225}\text{Fr}$  reaction vs. photon energy (MeV). Data taken from the TENDL-2019 [KRSDFM19] (No data was found in the EXFOR database [EXFOR21]).

Fig. 2.53 shows the results of numerical calculations of Eq.2.5 using the Matlab software [MATLAB20]. Regarding the half-life of  $^{225}\text{Ra}$  (14.9 days) and  $^{225}\text{Ac}$  (10 days), one can consider the transient equilibrium condition in which the half-life of the daughter radionuclide is shorter than the parent radionuclide and results in an increase of  $^{225}\text{Ac}$  production from zero to a maximum value. Fig.2.53 shows  $^{225}\text{Ra}$  and  $^{225}\text{Ac}$  production for the first production target position number considering a  $0.1\text{ (g. cm}^{-2}\text{)}$   $^{226}\text{Ra}$  target thickness during irradiation time and 20 days after end of bombardment (EOB) (or waiting time). As can be seen, increasing the irradiation time results in an increase of  $^{225}\text{Ra}$  and  $^{225}\text{Ac}$  production. However,  $^{225}\text{Ra}$  and  $^{225}\text{Ac}$  production per day remain almost constant for different irradiation times. Moreover, Fig.2.53 clearly shows that the  $^{225}\text{Ac}$  buildup increases with an increase in waiting time and reaches a broad maximum when the production and decay rates of  $^{225}\text{Ac}$  are almost equal. According to Fig.2.53, the time at which the maximum production of  $^{225}\text{Ac}$  occurs after EOB depends significantly on the  $^{225}\text{Ac}$  production at EOB [CJ09], and therefore, on the  $^{226}\text{Ra}$  target irradiation time. It is also interesting to obtain the ratio of activity of  $^{225}\text{Ac}$  at waiting time  $t$  to activity of  $^{225}\text{Ra}$  at EOB (%) as a function of waiting time in units of days for different irradiation times. As is shown in Fig.2.54, the ratio increases from 45.3 (%) to 98.3 (%) as irradiation time is increased from 1-day to 100-day. Moreover, the time at which the maximum production of  $^{225}\text{Ac}$  occurs shifts to a lower waiting time as the  $^{226}\text{Ra}$  target irradiation time is increased. Fig.2.55 shows the ratio of max. activity of  $^{225}\text{Ac}$  reached at the optimal waiting time to activity of  $^{225}\text{Ra}$  at EOB (%) for different irradiation times in units of irradiation time/half-life of  $^{225}\text{Ra}$ . As is shown in Fig.2.55, the maximum activity of  $^{225}\text{Ac}$  increases as irradiation time is increased.



**Fig. 2.53:**  $^{225}\text{Ra}$  and  $^{225}\text{Ac}$  production for the first production target position number considering a  $0.1 \text{ (g.cm}^{-2}\text{)}$   $^{226}\text{Ra}$  target thickness during irradiation and 20 days after EOB (called the waiting time)





**Fig.2.54:** Ratio of activity of  $^{225}\text{Ac}$  at waiting time  $t$  to activity of  $^{225}\text{Ra}$  at EOB (%) as a function of waiting time in units of days for different irradiation times

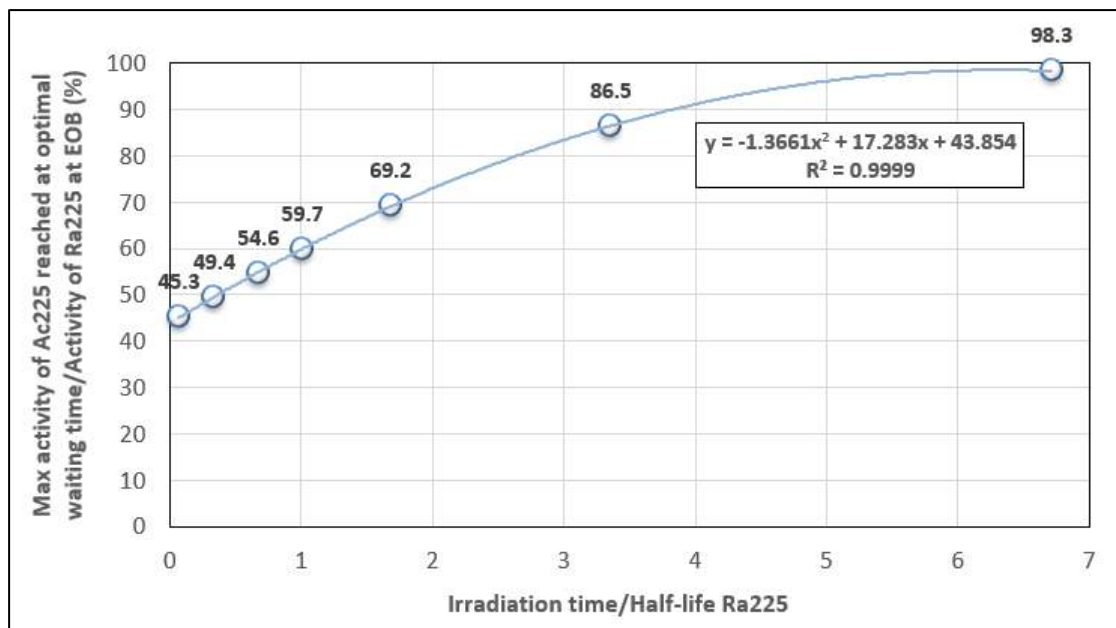


**Fig. 2.55:** Ratio of max. activity of  $^{225}\text{Ac}$  reached at the optimal waiting time to activity of  $^{225}\text{Ra}$  at EOB (%) for different irradiation times in units of irradiation time/half-life of  $^{225}\text{Ra}$

As shown in Fig. 2.53, the  $^{225}\text{Ac}$  buildup increases with an increase in waiting time, and reaches a broad maximum. At the time in which the maximum  $^{225}\text{Ac}$  buildup is reached, extraction of the produced  $^{225}\text{Ac}$  can take place. This procedure can eventually lead to an efficient  $^{225}\text{Ra}$ - $^{225}\text{Ac}$  generator production system. Fig. 2.56 shows the  $^{225}\text{Ra}$  and  $^{225}\text{Ac}$  buildup for 15 days of irradiation time. As was shown in Fig. 2.54, after 11 days of waiting time, the  $^{225}\text{Ac}$  buildup reaches its maximum value (about 73.7 GBq). Afterward, a second  $^{225}\text{Ac}$  buildup can be obtained by numerical calculations of Eq.2.5, considering the initial activity of  $^{225}\text{Ac}$  of zero at 26 days. As is shown in Fig.2.56, the second  $^{225}\text{Ac}$  buildup can be reached after about 17.35 days from the first milking day. This leads to another about 32.9 GBq extraction of  $^{225}\text{Ac}$ . In the case of the second and further milking cases, the time at which the maximum production of  $^{225}\text{Ac}$  occurs can also be obtained analytically using Eq. 2.5, which results in 17.35 days waiting time [CJ09].

$$t_{\max} = \frac{1}{\lambda_2 - \lambda_1} \cdot \ln \frac{\lambda_2}{\lambda_1} . \quad (2.6)$$

In Eq. 2.6,  $\lambda_1$  and  $\lambda_2$  refer to the decay constants of  $^{225}\text{Ra}$  and  $^{225}\text{Ac}$ , respectively. The production of  $^{225}\text{Ac}$  at time  $t$  resulting from beta-minus decay of initial production of  $^{225}\text{Ra}$  can be obtained using Eq.2.6 as [CJ09]:

$$A_2^t = \frac{A_1^0 \lambda_2}{\lambda_2 - \lambda_1} \cdot (e^{-\lambda_1 t} - e^{-\lambda_2 t}) , \quad (2.7)$$

where  $A_1^0$  denotes the initial production of  $^{225}\text{Ra}$ . Considering Eqs. 2.6 and 2.7, one can obtain the maximum production of  $^{225}\text{Ac}$ , which results in 44.1% of the initial  $^{225}\text{Ra}$  production (at the beginning time of milking) after 17.35 days waiting period of the first (second, etc.) milking. Fig. 2.57 shows the change of  $^{225}\text{Ra}$  and  $^{225}\text{Ac}$  radionuclides with time obtained by [Nucleonica20]. The analytical results and those obtained from [Nucleonica20] are in good agreement with my numerical results, which showed a 17.35-day required time. Moreover, according to the numerical calculations, the 73.8 GBq  $^{225}\text{Ra}$  activity obtained at the beginning time of milking (i.e., 26-day) and the 32.9 GBq  $^{225}\text{Ac}$  activity produced after 17.35-day of the first  $^{225}\text{Ac}$  extraction (milking), results in an about 44.6 (%) activity ratio. Therefore, the numerical results obtained here are also in good agreement in terms of the maximum ratio of the  $^{225}\text{Ac}$  activity (produced after 17.35 days of the first extraction) to the  $^{225}\text{Ra}$  activity (produced at the beginning time of milking) with the analytical result. The third  $^{225}\text{Ac}$  buildup after 17.35 days of waiting time can result in about 14.5 GBq activity.

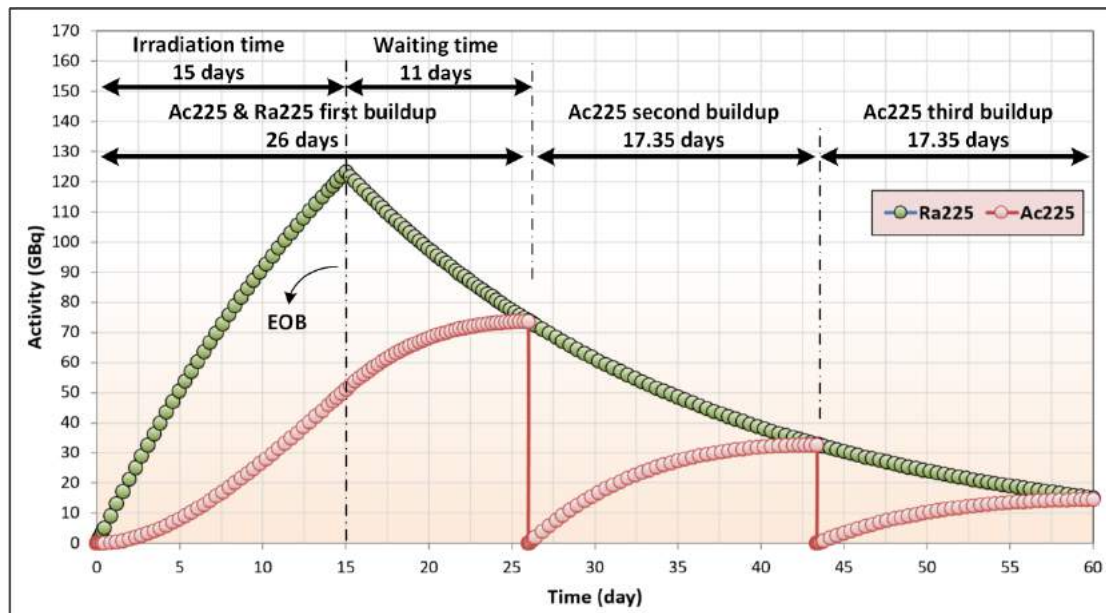


**Fig. 2.56:** Buildup and extraction of  $^{225}\text{Ra}$  and  $^{225}\text{Ac}$  from an irradiated  $0.1 \text{ g.cm}^{-2} \text{ }^{226}\text{Ra}$  target as a function of time

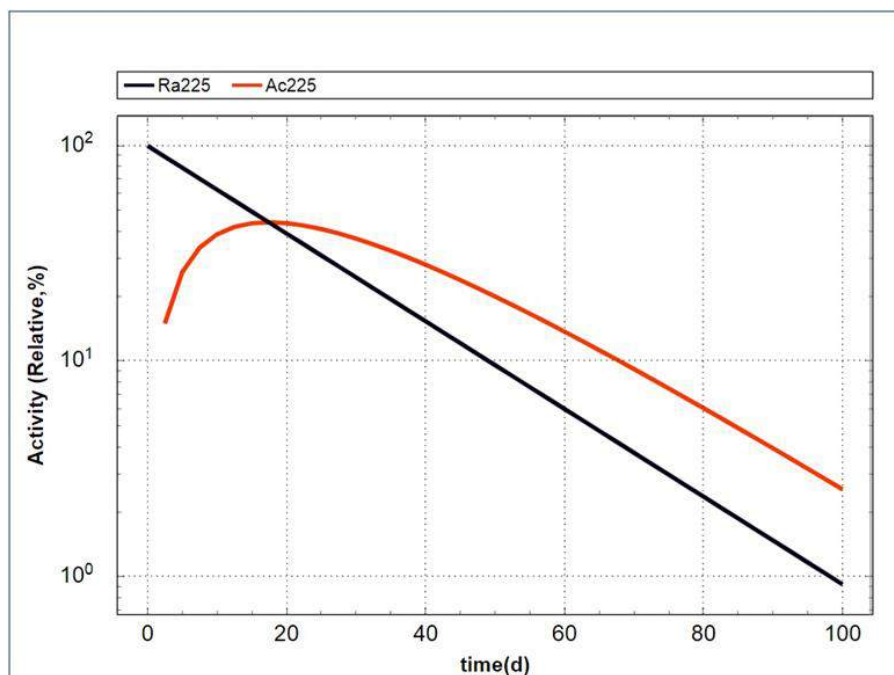


**Fig. 2.57:** Transient equilibrium of  $^{225}\text{Ac}$  resulting from beta minus decay of  $^{225}\text{Ra}$  (considering zero initial  $^{225}\text{Ac}$  activity at EOB)[Nucleonica20]

## Production of $^{224}\text{Ra}$ from $^{226}\text{Ra}$

During photonuclear production of  $^{225}\text{Ra}$  from a  $^{226}\text{Ra}$  target,  $^{224}\text{Ra}$  can also be produced through a  $^{226}\text{Ra}(\gamma, 2n)^{224}\text{Ra}$  reaction (see Fig. 2.50) (DR21). Fig. 2.58 shows the decay scheme of  $^{224}\text{Ra}$ . As can be seen,  $^{224}\text{Ra}$  decays into  $^{220}\text{Rn}$ , producing  $^{216}\text{Po}$ , which decays into  $^{212}\text{Pb}$ . As shown in Fig. 2.59, for photon energies beyond 13 MeV, the photonuclear cross-section for the  $(\gamma, 2n)$  reaction is higher than for the  $(\gamma, n)$  reaction. Accordingly, from the cross-section point of view,  $^{224}\text{Ra}$  production is quite probable (MLA06, DR21). From the medical point of view,  $^{212}\text{Pb}$  is a promising candidate for target alpha therapy, as  $^{212}\text{Pb}$  decays to alpha-particle emitting\*  $^{212}\text{Po}$ , which has been used, e.g., in the treatment of breast cancer patients with bone metastases [J18]. Accordingly,  $^{212}\text{Pb}$  production yield as a byproduct of  $^{226}\text{Ra}$  target irradiation is interesting to be investigated. The time rate of change of the number of atoms of  $^{224}\text{Ra}$  and  $^{212}\text{Pb}$  can be given by the coupled differential equations

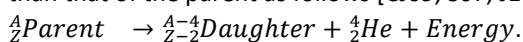
$$\begin{aligned}\frac{dN_{Ra224}}{dt} &= N_{Ra226} \cdot L \cdot \sigma_{(\gamma, 2n)}^{Ra226} \cdot \phi - N_{Ra224} \lambda_{Ra224} \\ \frac{dN_{Pb212}}{dt} &= N_{Ra224} \lambda_{Ra224} - N_{Pb212} \lambda_{Pb212},\end{aligned}\quad (2.8)$$

where  $\lambda_{Ra224}$  and  $\lambda_{Pb212}$  are decay constants of  $^{224}\text{Ra}$  and  $^{212}\text{Pb}$ , respectively. Note that in Eq.2.8, the rate of formation and transformation of  $^{220}\text{Rn}$  and  $^{216}\text{Po}$  has been ignored due to their relatively short half-live compared to  $^{224}\text{Ra}$  and  $^{212}\text{Pb}$ . Fig.2.60 shows the results of numerical calculations of Eq. 2.8 using the Matlab software [MATLAB20]. Regarding the half-life of  $^{224}\text{Ra}$  (3.63 days) and  $^{212}\text{Pb}$  (10.64 h), one can consider the transient equilibrium condition in which the half-life of the daughter radionuclide is shorter than the parent radionuclide and results in an increase of  $^{212}\text{Pb}$  production from zero to a maximum value [MLA06]. In Fig. 2.60, the results of  $^{224}\text{Ra}$  and  $^{212}\text{Pb}$  production are shown for the first production target position number considering a  $0.1 \text{ (g.cm}^{-2}\text{)}$   $^{226}\text{Ra}$  target thickness during (1, 5, 10, and 15 days) irradiation time and 20 days after EOB (waiting time). As can be seen, increasing the irradiation time results in an increase of  $^{224}\text{Ra}$  and  $^{212}\text{Pb}$  production. Moreover, Fig. 2.60 clearly shows that the  $^{212}\text{Pb}$  buildup increases with an increase in waiting time and reaches a maximum. According to Fig.2.60, the time at which the maximum production of  $^{212}\text{Pb}$  occurs after EOB depends significantly on the  $^{212}\text{Pb}$  production at EOB [CJ09], and therefore, on the  $^{226}\text{Ra}$  target irradiation time (and  $^{224}\text{Ra}$  production).

It is also interesting to obtain the ratio of activity of  $^{212}\text{Pb}$  at waiting time  $t$  to activity of  $^{224}\text{Ra}$  at EOB (%) as a function of waiting time in units of days for different irradiation times. As can be seen, the ratio increases from 81.1 (%) to 99.16 (%) as irradiation time is increased from 1-day to 15-day. Moreover, the time at which the maximum production of  $^{212}\text{Pb}$  occurs shifts to lower waiting time as the  $^{226}\text{Ra}$  target irradiation time is increased. Fig. 2.61 shows the ratio of max. activity of  $^{212}\text{Pb}$  reached at the optimal waiting time to activity of  $^{224}\text{Ra}$  at EOB(%) for different irradiation times in units of irradiation time/half-life of  $^{224}\text{Ra}$ . As is shown in Fig.2.62, the maximum activity of  $^{212}\text{Pb}$  increases as irradiation time is increased.

---

\* Alpha decay occurs in heavy nuclides with many nucleons when the neutron-to-proton ratio is too low. An alpha particle is a highly energetic helium nucleus. The result of alpha emission is a daughter whose atomic mass number is four less than that of the parent and whose atomic number is two less than that of the parent as follows [CJ09, S07, J17]:



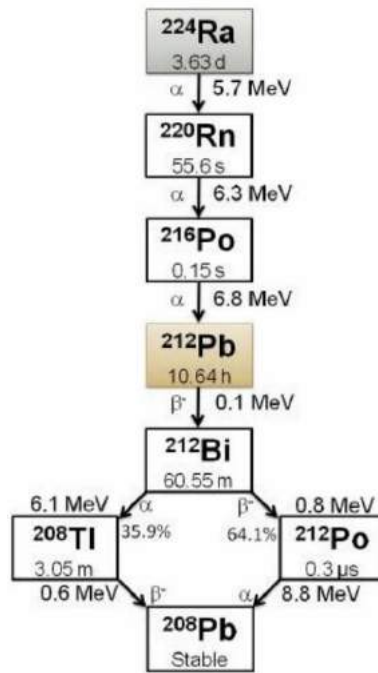


**Fig. 2.58:**  $^{224}\text{Ra}$  decay chain [J18]

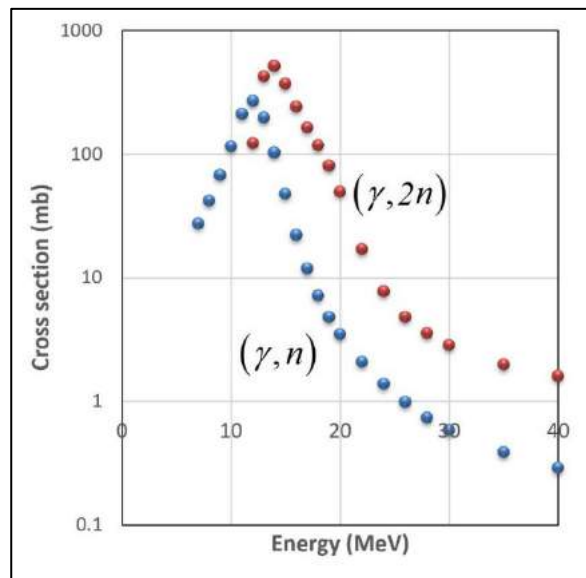


**Fig. 2.59:**  $^{226}\text{Ra}$  photonuclear excitation functions for the reactions of  $^{226}\text{Ra}(\gamma, n)^{225}\text{Ra}$  and  $^{226}\text{Ra}(\gamma, 2n)^{224}\text{Ra}$  [KRSDFM19]

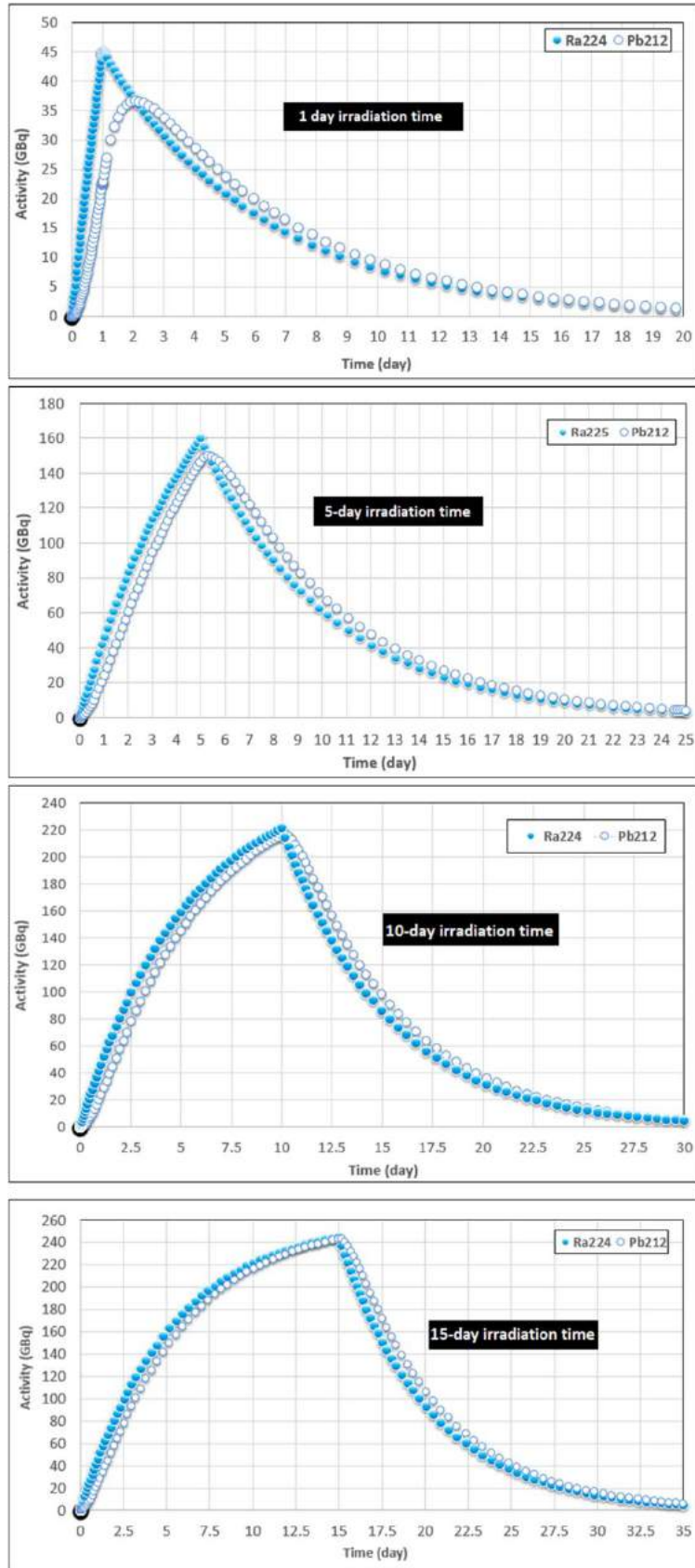


**Fig. 2.60:**  $^{224}\text{Ra}$  and  $^{212}\text{Pb}$  production for the first production target position number considering a  $0.1 \text{ (g.cm}^{-2}\text{)}$   $^{226}\text{Ra}$  target thickness during irradiation and 20 days after EOB (called the waiting time)

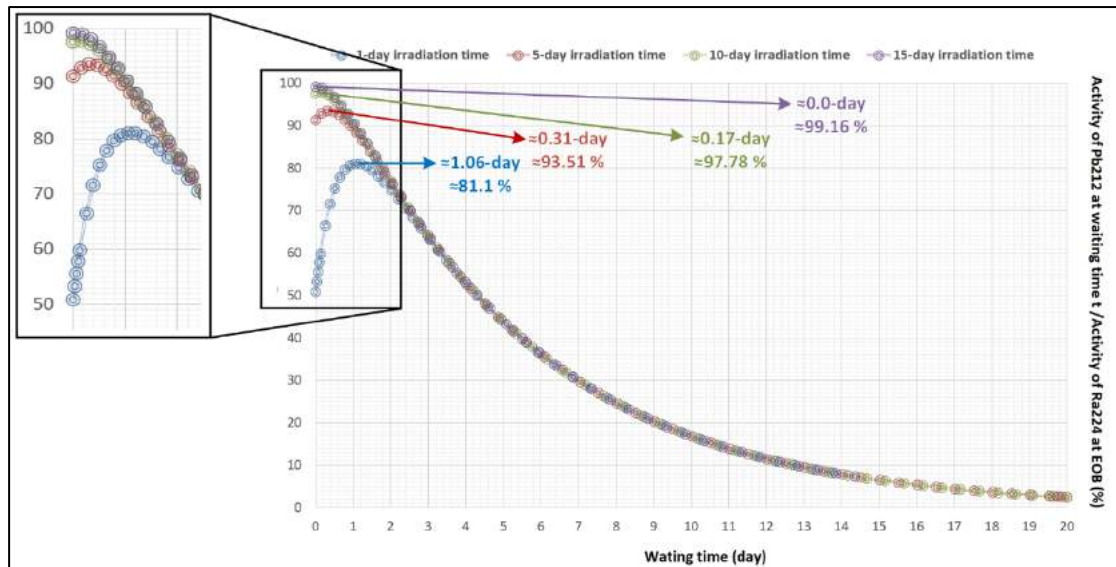


**Fig. 2.61:** Ratio of activity of  $^{212}\text{Pb}$  at waiting time  $t$  to activity of  $^{224}\text{Ra}$  at EOB (%) as a function of waiting time in units of days for different irradiation times

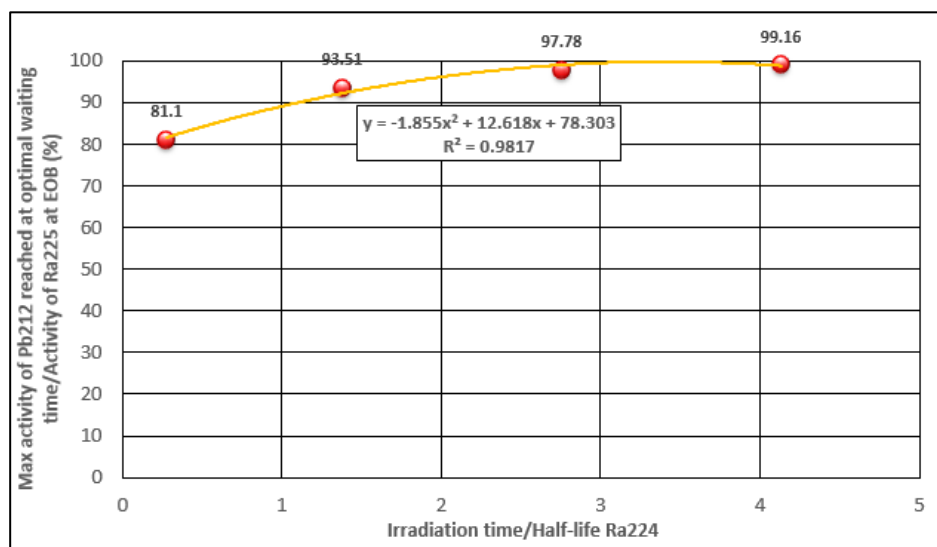


**Fig. 2.62:** Ratio of max. activity of  $^{212}\text{Pb}$  reached at the optimal waiting time to activity of  $^{224}\text{Ra}$  at EOB (%) for different irradiation times in units of irradiation time/half-life of  $^{224}\text{Ra}$



As shown in Fig.2.60, the  $^{212}\text{Pb}$  buildup increases with an increase in waiting time, and reaches a maximum. At the time in which the maximum  $^{212}\text{Pb}$  buildup is reached, extraction of the produced  $^{212}\text{Pb}$  can take place. This procedure can eventually lead to an efficient  $^{224}\text{Ra}$ - $^{212}\text{Pb}$  generator production system. Fig. 2.63 shows the  $^{224}\text{Ra}$  and  $^{212}\text{Pb}$  buildup for 1 day of irradiation time. As was shown in Fig.2.61, after 0.06 day of waiting time, the  $^{212}\text{Pb}$  buildup reaches its maximum value (about 24.9 GBq). Afterward, a second  $^{212}\text{Pb}$  buildup can be obtained by numerical calculations of Eq.2.8, considering the initial activity of  $^{212}\text{Pb}$  of zero at 1.06 days. As is shown in Fig.2.63, the second  $^{212}\text{Pb}$  buildup can be reached after about 1.5 days from the first milking day. This leads to another about 33.4 GBq extraction of  $^{212}\text{Pb}$ . In the case of the second and further milking cases, the time at which the maximum production of  $^{212}\text{Pb}$  occurs can be obtained using Eq. 2.6. In Eq. 2.6,  $\lambda_1$  and  $\lambda_2$  refer to the decay constants of  $^{224}\text{Ra}$  and  $^{212}\text{Pb}$ , respectively. Figs. 2.64, 2.65 show the change of  $^{224}\text{Ra}$  and  $^{212}\text{Pb}$  radionuclides with time obtained by [Nucleonica20]. The theoretical results and those obtained from [Nucleonica20] are in good agreement with my numerical results (both indicate 1.5 days required waiting time to reach the maximum  $^{212}\text{Pb}$  production considering the initial activity of  $^{212}\text{Pb}$  of zero at the beginning time of milking). Moreover, by using Eq.2.7, (where  $A_1^0$  denotes the initial production of  $^{224}\text{Ra}$ ), it is possible to obtain the maximum production of  $^{212}\text{Pb}$ , which results in 75% of the initial  $^{224}\text{Ra}$  production (at the beginning time of milking) after 1.5 days waiting period of the first (second, etc.) milking. According to the numerical calculations, the 44.7 GBq  $^{224}\text{Ra}$  activity obtained at the beginning time of milking (i.e., 1.06-day) and the 33.4 GBq  $^{212}\text{Pb}$  activity produced after 1.5 days of the first  $^{212}\text{Pb}$  extraction (milking), results in an about 75 (%) activity ratio. Therefore, the numerical calculations performed here are also in good agreement in terms of the maximum ratio of the  $^{212}\text{Pb}$  activity (produced after 1.5 days of the first extraction) to the  $^{224}\text{Ra}$  activity (produced at the beginning time of milking) with the analytical result. The third  $^{212}\text{Pb}$  buildup after 1.5-day waiting time can result in about 25.1 GBq activity.

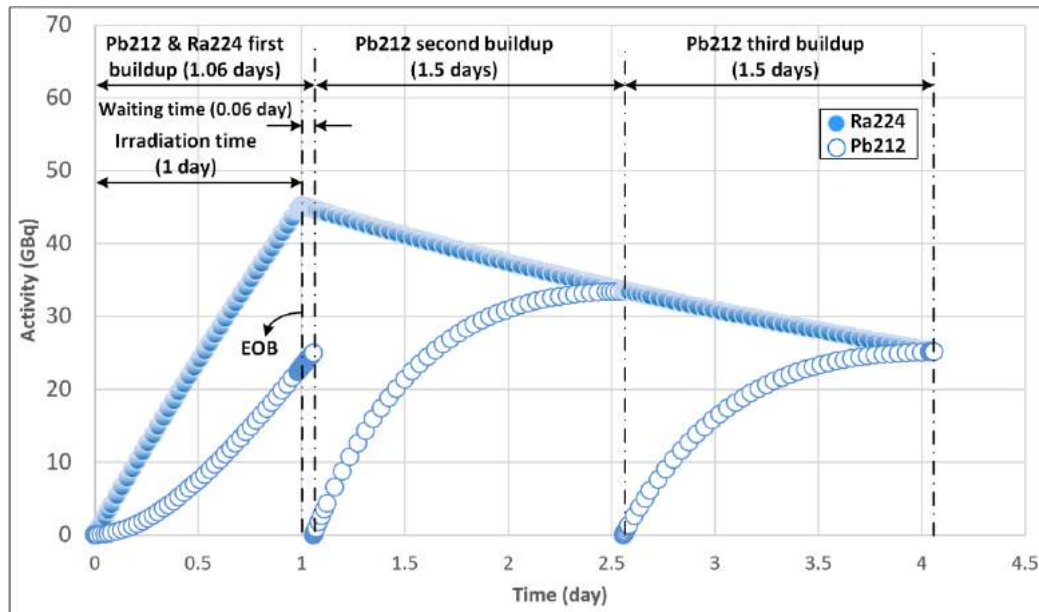


**Fig. 2.63:** Buildup and extraction of  $^{224}\text{Ra}$  and  $^{212}\text{Pb}$  from an irradiated  $0.1 \text{ g.cm}^{-2} \text{ }^{226}\text{Ra}$  target as a function of time



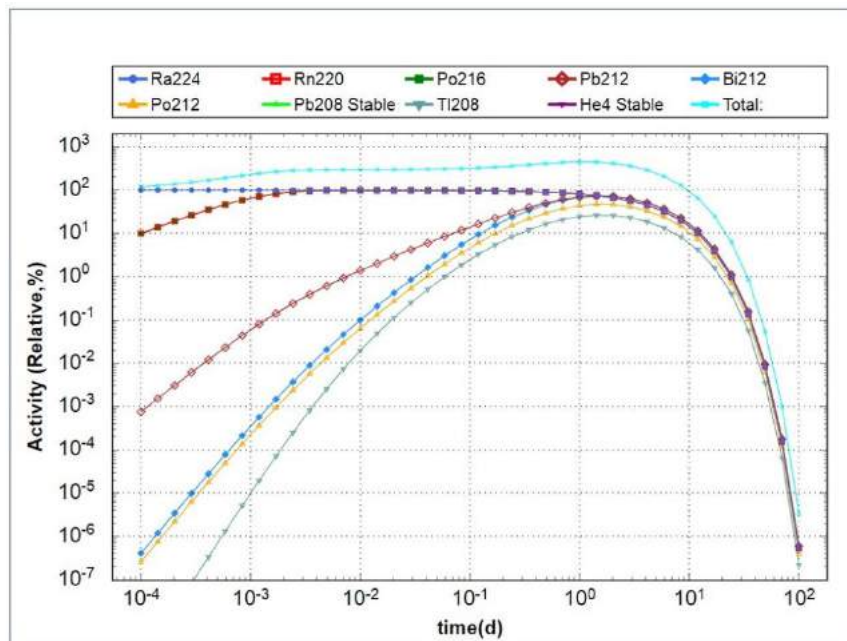


**Fig. 2.64:** Decay of  $^{224}\text{Ra}$  into different radionuclide daughters (considering zero initial  $^{212}\text{Pb}$  activity at EOB) [Nucleonica20]

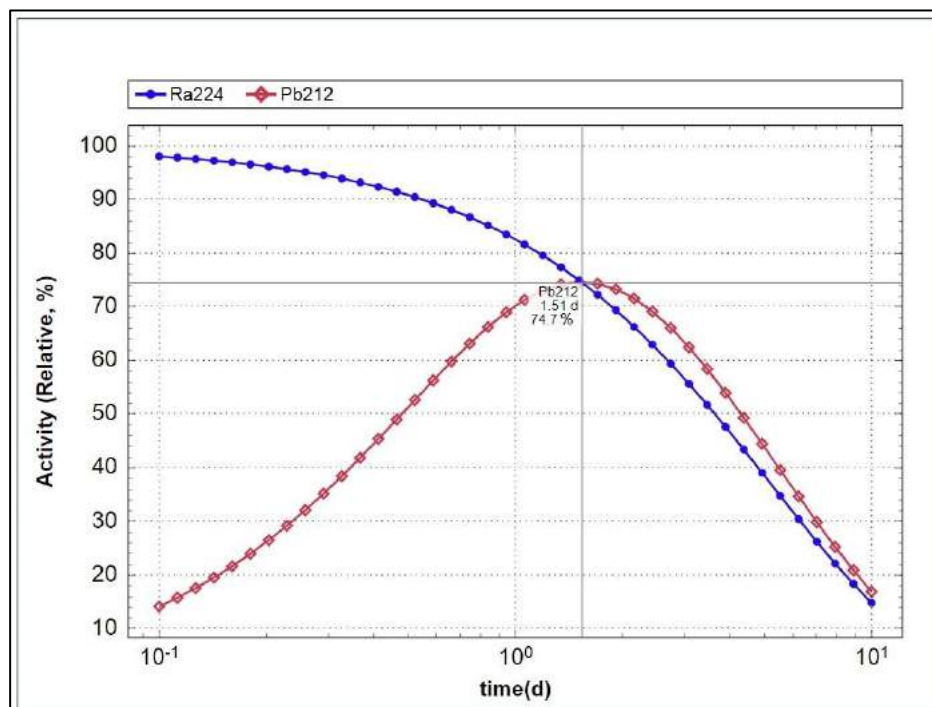


**Fig. 2.65:** Decay of  $^{224}\text{Ra}$  into  $^{212}\text{Pb}$  (considering zero initial  $^{212}\text{Pb}$  activity at EOB) [Nucleonica20]

## Production of $^{99}\text{Mo}$ from $^{100}\text{Mo}$

The photonuclear excitation function in mb for  $^{99}\text{Mo}$  production through the reaction  $^{100}\text{Mo}(\gamma, n)^{99}\text{Mo}$  is shown in Fig. 2.66. As can be seen, the data taken from the TENDL-2019 and EXFOR databases are in good agreement with each other; however, due to the lack of sufficient experimental data, the TENDL data was used for the yield and activity calculations. Fig. 2.67 shows a schematic representation of the  $^{99}\text{Mo}$  photonuclear production routes, decay chain, and scheme [Nucleonica20]. The time rate of change of the number of atoms of  $^{99}\text{Mo}$  and  $^{99\text{m}}\text{Tc}$  can be given by the coupled differential equations

$$\begin{aligned}\frac{dN_{Mo99}}{dt} &= N_{Mo100} \cdot L \cdot \sigma_{(\gamma, n)}^{Mo100} \cdot \phi - N_{Mo99} \lambda_{Mo99} \\ \frac{dN_{Tc99m}}{dt} &= N_{Mo99} \lambda_{Mo99} - N_{Tc99m} \lambda_{Tc99m},\end{aligned}\quad (2.9)$$

where  $\lambda_{Mo99}$  and  $\lambda_{Tc99m}$  are decay constants of  $^{99}\text{Mo}$  and  $^{99\text{m}}\text{Tc}$ , respectively. Fig.2.68 shows the results of numerical calculations of Eq. 2.9 using the Matlab software [MATLAB20]. Regarding the half-life of  $^{99}\text{Mo}$  (66 h) and  $^{99\text{m}}\text{Tc}$  (6.01 h), one can consider the transient equilibrium condition in which the half-life of the daughter radionuclide is shorter than the parent radionuclide and results in an increase of  $^{99\text{m}}\text{Tc}$  production from zero to a maximum value [MLA06]. In Fig.2.68, the results of  $^{99}\text{Mo}$  and  $^{99\text{m}}\text{Tc}$  production are presented for the first production target position number considering a  $1 (g \cdot cm^{-2})$   $^{100}\text{Mo}$  target thickness during (1, 2.5, 5, 7.5, and 10 days) irradiation time and 20 days after EOB (waiting time). As can be seen, increasing the irradiation time results in an increase of  $^{99}\text{Mo}$  and  $^{99\text{m}}\text{Tc}$  production. Moreover, Fig.2.68 clearly shows that the  $^{99\text{m}}\text{Tc}$  buildup increases with an increase in waiting time and reaches a maximum. According to Fig.2.68, the time at which the maximum production of  $^{99\text{m}}\text{Tc}$  occurs after EOB depends significantly on the  $^{99\text{m}}\text{Tc}$  production at EOB [CJ09], and therefore, on the  $^{100}\text{Mo}$  target irradiation time. Fig. 2.69 shows the ratio of activity of  $^{99\text{m}}\text{Tc}$  at waiting time  $t$  to activity of  $^{99}\text{Mo}$  at EOB (%) as a function of waiting time in units of days for different irradiation times. As can be seen, the ratio increases from 86.6(%) to 99.2(%) as irradiation time is increased from 1-day to 10-day. Moreover, the time at which the maximum production of  $^{99\text{m}}\text{Tc}$  occurs shifts to a lower waiting time as the  $^{100}\text{Mo}$  target irradiation time is increased. Fig. 2.70 shows the ratio of max. activity of  $^{99\text{m}}\text{Tc}$  reached at the optimal waiting time to activity of  $^{99}\text{Mo}$  at EOB (%) for different irradiation times in units of irradiation time/half-life of  $^{99}\text{Mo}$ . As is shown in Fig. 2.70, the maximum activity of  $^{99\text{m}}\text{Tc}$  increases as irradiation time is increased.

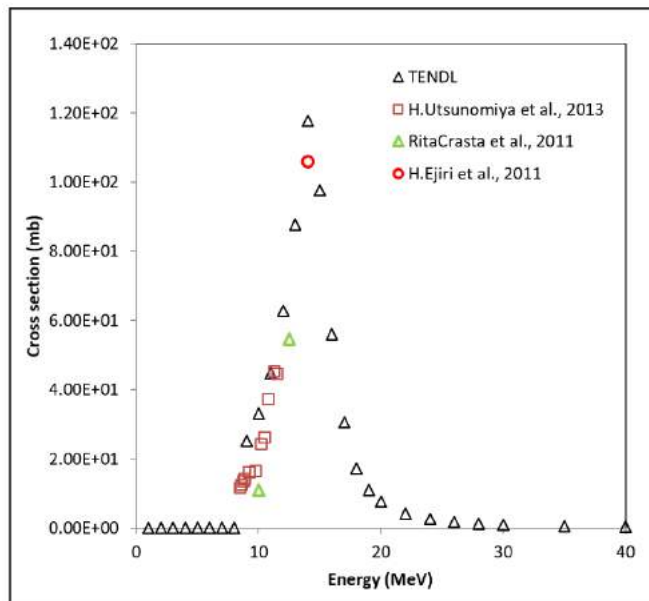


**Fig. 2.66:** Photonuclear excitation function (mb) of the  $^{100}\text{Mo}(\gamma, n)^{99}\text{Mo}$  reaction vs. photon energy (MeV). Data taken from the TENDL-2019 [KRSDFM19] and EXFOR database [EXFOR21].

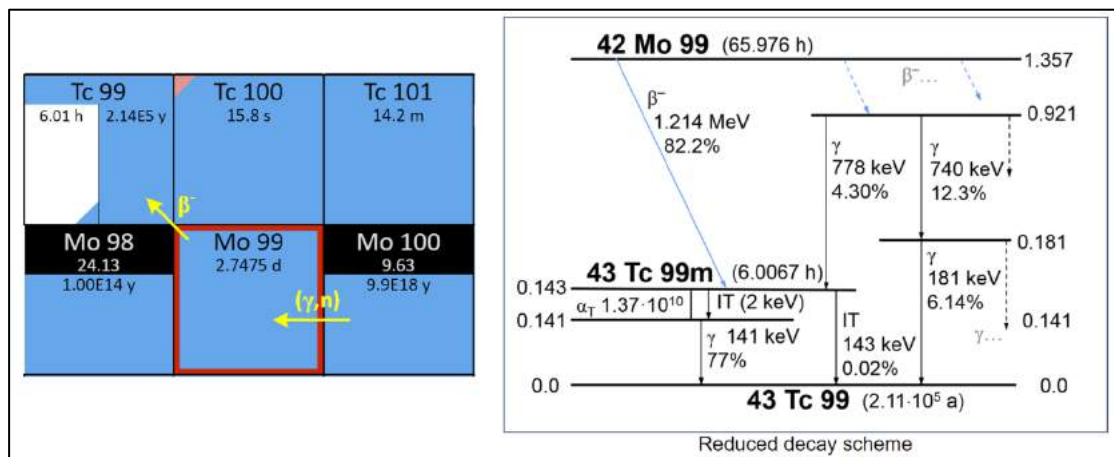


**Fig. 2.67:** Schematic representation of the  $^{99}\text{Mo}$  photonuclear production routes and its decay chain and scheme [Nucleonica20]. Note that the data given in the left part of  $^{99}\text{Tc}$  (in the left hand side figure) apply to the metastable state\*, while those in the right part apply to the ground state. The blue color implies that the decay mode of the nuclide(s) is (are)  $\beta^-$ .  $^{100}\text{Mo}$  and  $^{98}\text{Mo}$  (shown as a box containing a black part) are primordial nuclides; i.e., those formed in the build-up of terrestrial matter and still present today. The number which is written below the symbol of  $^{99}\text{Mo}$  and  $^{98}\text{Mo}$  in the right hand side figure (inside the black box) shows the abundance in naturally occurring elements (atom %). The red color in the top right of  $^{100}\text{Tc}$  indicates that it is also decaying by EC to  $^{100}\text{Mo}$  [MDS18].

\* Decays to the ground state or excited levels via isomeric transition. Isomeric transition (IT) is a process by which a metastable state nuclide decays through gamma-ray emission to a lower energy level of the same isotope [MDS18].

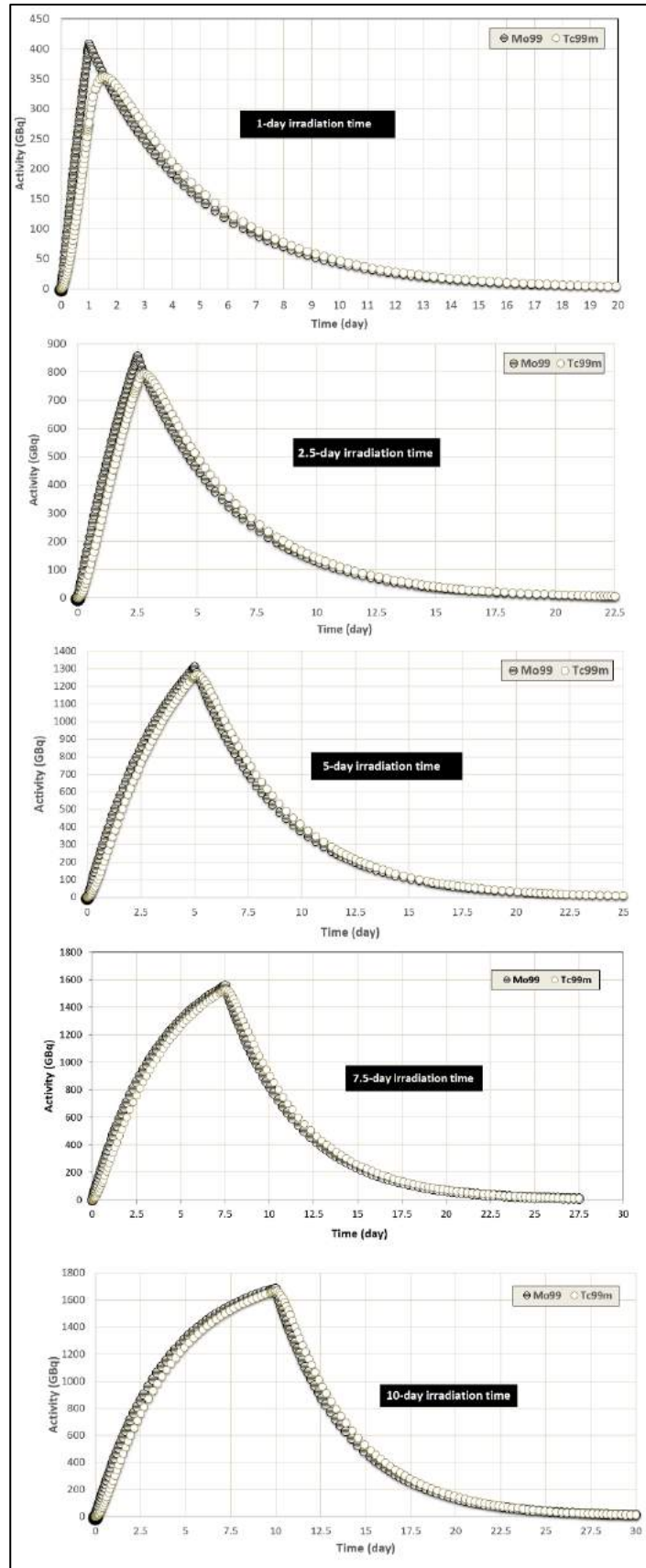


**Fig. 2.68:**  $^{99}\text{Mo}$  and  $^{99\text{m}}\text{Tc}$  production for the first production target position number considering a  $1\text{ (g.cm}^{-2}\text{)}$   $^{100}\text{Mo}$  target during irradiation and 20-day after EOB (called the waiting time)

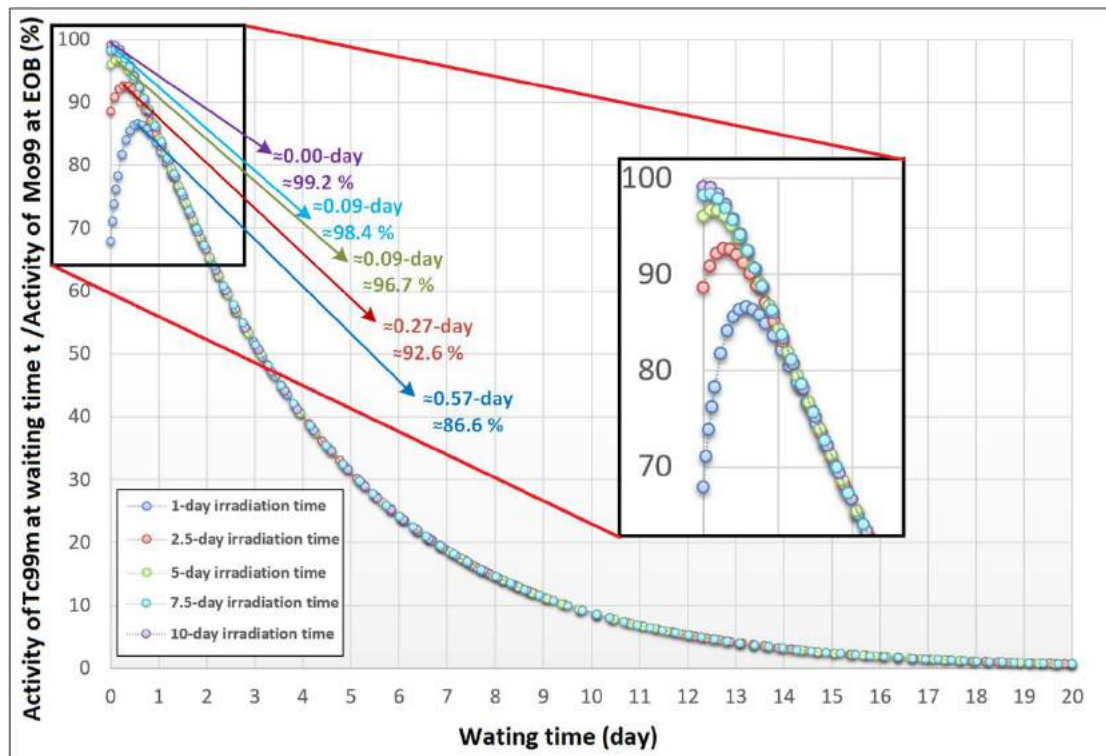


**Fig. 2.69:** Ratio of activity of  $^{99m}\text{Tc}$  at waiting time  $t$  to activity of  $^{99}\text{Mo}$  at EOB (%) as a function of waiting time in units of days for different irradiation times

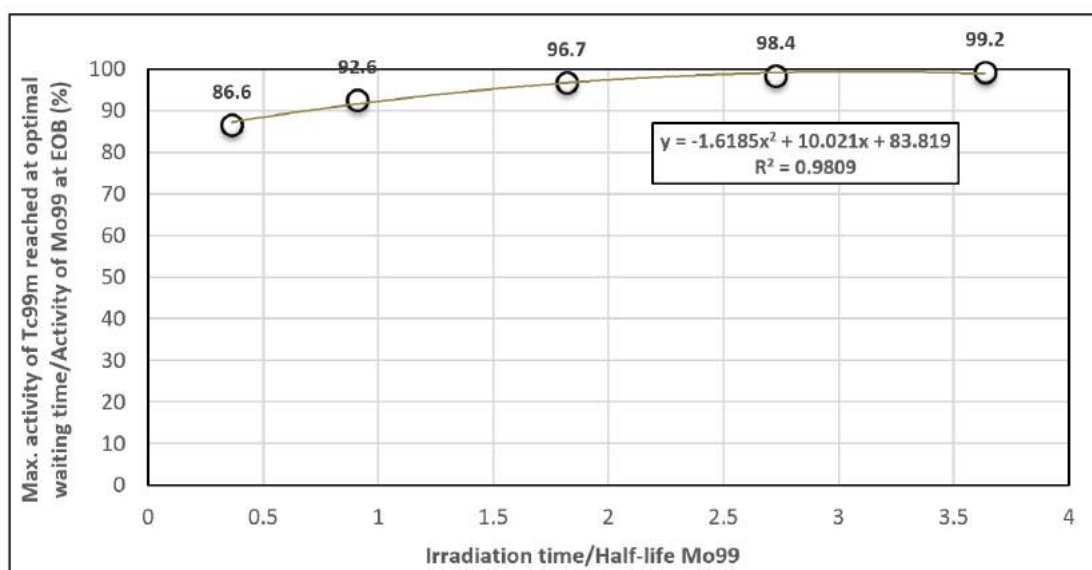


**Fig. 2.70:** Ratio of max. activity of  $^{99m}\text{Tc}$  reached at the optimal waiting time to activity of  $^{99}\text{Mo}$  at EOB (%) for different irradiation times in units of irradiation time/half-life of  $^{99}\text{Mo}$

As shown in Fig.2.68, the  $^{99m}\text{Tc}$  buildup increases with an increase in waiting time, and reaches a maximum. At the time in which the maximum  $^{99m}\text{Tc}$  buildup is reached, extraction of the produced  $^{99m}\text{Tc}$  can take place. This procedure can lead to an efficient  $^{99}\text{Mo}$ - $^{99m}\text{Tc}$  generator production system. Fig.2.71 shows the  $^{99}\text{Mo}$  and  $^{99m}\text{Tc}$  buildup for 10-day of irradiation time. As was shown in Fig.2.69, after 10-day of irradiation time (without any waiting time), the  $^{99m}\text{Tc}$  buildup reaches its maximum value (about 1668 GBq). Afterward, a second  $^{99m}\text{Tc}$  buildup can be obtained by numerical calculations of Eq.2.9, considering the initial activity of  $^{99m}\text{Tc}$  of zero at 10-day. As is shown in Fig.2.71, the second  $^{99m}\text{Tc}$  buildup can be reached after about 0.95-day from the first milking day. This leads to another about 1323 GBq extraction of  $^{99m}\text{Tc}$ . In the case of the second and further milking cases, the time at which the maximum production of  $^{99m}\text{Tc}$  occurs can also be obtained analytically using Eq. 2.6. In Eq. 2.6,  $\lambda_1$  and  $\lambda_2$  refer to the decay constants of  $^{99}\text{Mo}$  and  $^{99m}\text{Tc}$ , respectively. The time at which the maximum production of  $^{99m}\text{Tc}$  occurs, can be obtained 0.95-day using Eq.2.6 [CJ09]. As is revealed, the analytical results are in good agreement with my numerical results. Moreover, by using Eq.2.7, (where  $A_1^0$  denotes the initial production of  $^{99}\text{Mo}$ ), it is possible to obtain the maximum production of  $^{99m}\text{Tc}$  analytically, which results in about 79% of the initial  $^{99}\text{Mo}$  production (at the beginning time of milking) after 0.95-day waiting period of the first (second, etc.) milking. According to the numerical calculations, the 1683 GBq  $^{99}\text{Mo}$  activity obtained at 10-day (irradiation time) and the 1323 GBq  $^{99m}\text{Tc}$  activity produced after 0.95-day of the first  $^{99m}\text{Tc}$  extraction (milking), results in an about 79 (%) activity ratio. Therefore, the numerical result obtained here are also in good agreement in terms of the maximum ratio of the  $^{99m}\text{Tc}$  activity (produced after 0.95 days of the first extraction) to the  $^{99}\text{Mo}$  activity (produced at the beginning time of milking) with the analytical result. The third  $^{99m}\text{Tc}$  buildup after 0.95-day waiting time can result in about 1041 GBq activity.

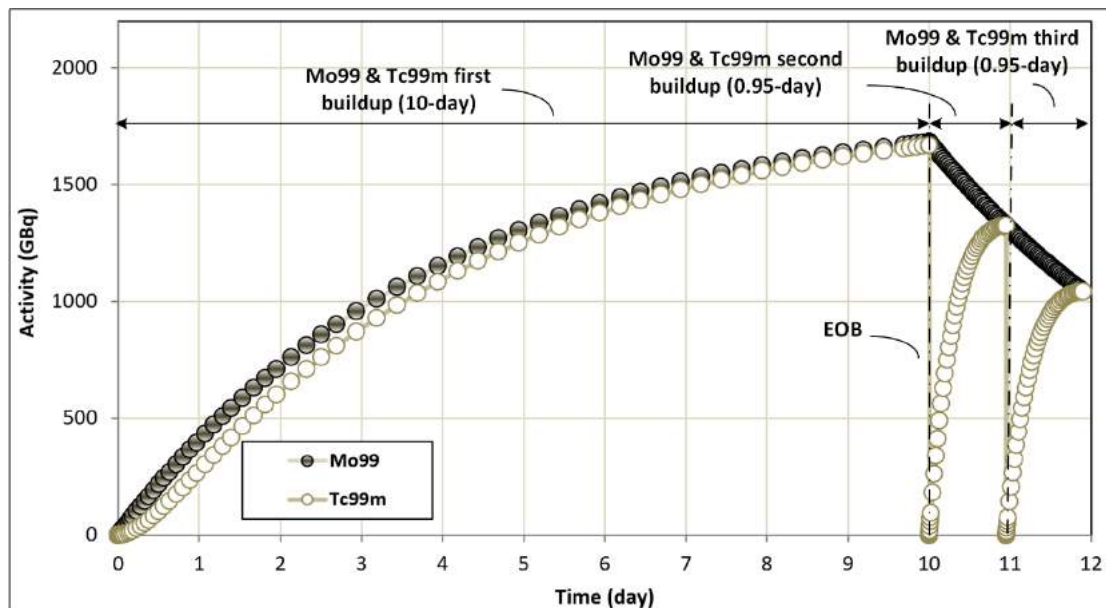


**Fig. 2.71:** Buildup and extraction of  $^{99}\text{Mo}$  and  $^{99m}\text{Tc}$  from an irradiated  $1 \text{ g.cm}^{-2} \text{ }^{100}\text{Mo}$  target as a function of time



## Same and hybrid multiple simultaneous radionuclide production

A simultaneous same (see Fig. 2.72a) or hybrid stack of target materials (see Fig. 2.72b) can be irradiated since photons in the GDR region (higher than 8 MeV) are deeply penetrating. This allows an efficient way for radionuclide production compared to other methods such as charged particle induced reactions. As is apparent, only the transmitted photons from a production target (within the GDR energy range) are able to effectively irradiate the next production target (see Fig. 2.42). Accordingly, for a multiple target irradiation, accurate knowledge of the photon spectra and their attenuation is required. As is obvious, a large number of different simulations need to be performed to consider all possible configurations, including different production target material, different thicknesses, different possible dimensions, and different probable production target ordering (see Fig. 2.72). Due to lack of space, they are not address within this thesis.

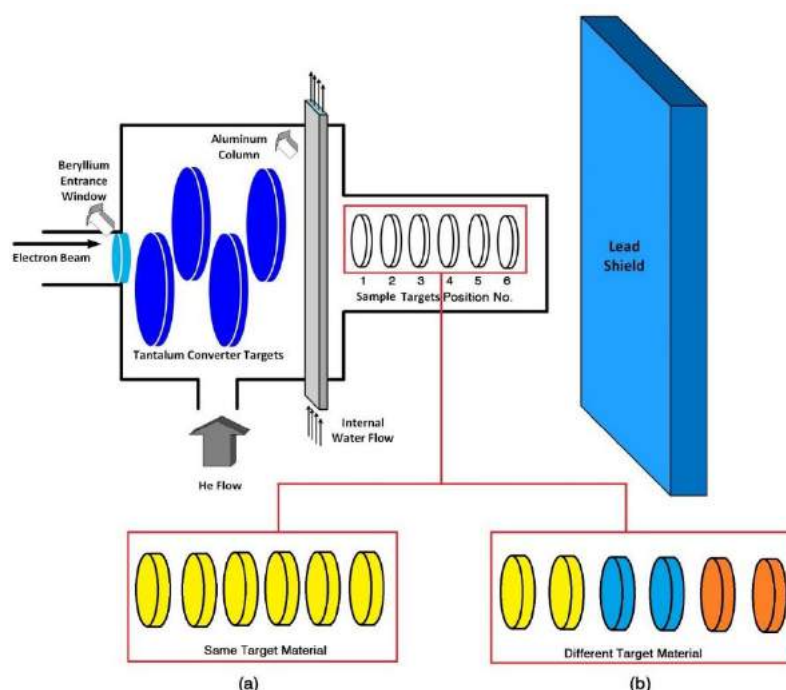


**Fig. 2.72:** Schematic representation of the simultaneous multiple target irradiation. The production targets are assumed to have a 2cm diameter and are placed 1cm apart.

### 2.4.4 Massive beam stop

A massive beam stop is needed to shield the remaining photons and electrons. Electrons have a relatively short range in almost all materials compared to photons. The problem associated with the electrons is that during their passage through matter and before their absorption, they may produce Bremsstrahlung that is able to penetrate deeper in matter, and if there is not sufficient material in front of them, they probably are able to escape. To reduce the chance of Bremsstrahlungs production, materials with low atomic numbers are usually considered. According to the above discussion, the beam stop must be able to absorb all of the incident electrons as well as those photons that are transmitted through the production targets or produced during the passage of electrons in the beam stop itself. Materials with high atomic numbers and high density can attenuate photons effectively. Among all of the candidate materials, lead has always been considered highly effective due to its high density, high atomic

number, and availability in different forms [JC83, JM20, K00, M67, CSF84]. Besides the electrons and photons, a number of photoneutrons created in the tantalum converter target must also be stopped in the beam stop. To shield the emitted photoneutrons, as a first step, materials with low atomic numbers such as hydrogen (in the form of water), boron carbide, beryllium, or paraffin are used for slowing-down purposes. Then, as a second step, materials with high thermal neutron absorption cross-sections such as gadolinium, silver, cadmium, and indium are used to stop the photoneutrons effectively. Using concrete containing one or some other aforementioned materials is also recommended for shielding purposes of photoneutrons and gamma-rays in many practical applications [CSF84, L65, LB01].

According to the above discussion, it can reasonably be argued that the design of the beam stop is complicated. In the following, the Monte-Carlo simulation for a simple geometry (box) of lead (for instance) as the massive beam stop is performed using the MCNP code. This allows for an estimation of the energy spectrum of the electrons and photons that reached the beam stop, in addition to an approximation of the amount of energy deposition due to different electrons and photons interactions within the beam stop. In the simulation, it is assumed, for instance, that the massive beam stop is located at a distance of 10 cm from the last production sample and has a front face dimension of 50cm×50cm with respect to the beam direction. The thickness of the beam stop should be in the order of some tens of centimeters. In the simulation, the beam stop is made of lead with the same front face dimension (i.e., 50cm×50cm) and 50cm thickness (for instance). The simulation results for impinging electrons and photons on the beam stop as energy spectrum are presented in Figs. 2.73 and 2.74, respectively. The results clearly show that high-energy electrons and photons can still have a significant contribution to the spectrum. As can reasonably be argued, electrons, photons (and neutrons) in the entire energy range must be completely shielded by the beam stop to ensure a safe operation of the proposed photonuclear irradiation setup from the radiation protection point of view. However, the Monte-Carlo calculations for such a complex problem and relatively big geometry (including the beam stop) require a High-Performance Computing (HPC) machine.



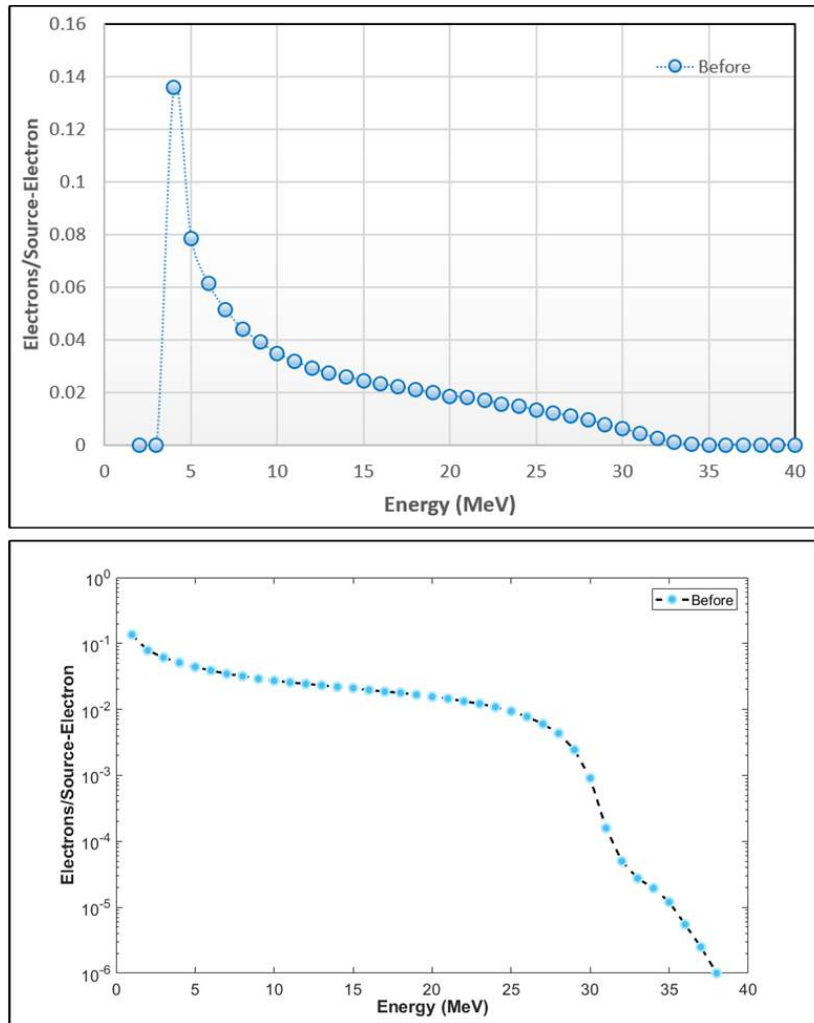


**Fig. 2.73:** Energy spectrum of the impinging photons to the beam stop. In the simulation, no production target material is assumed in order to consider the most conservative conditions from the point of view of electron and photon shielding.

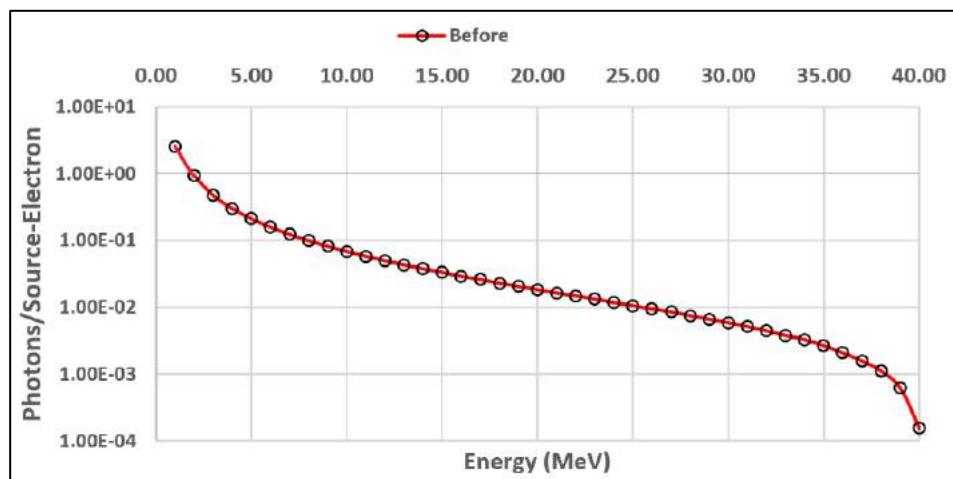


**Fig. 2.74:** Energy spectrum of the impinging photons on the beam stop

## 2.4.5 Energy deposition in all components

Energy deposition in all components of the irradiation setup illustrated in Fig. 2.72 is calculated and presented in Fig. 2.75. In Fig. 2.75, the beryllium thickness is 100  $\mu\text{m}$  (however, the energy deposition for all thicknesses was calculated in Fig. 2.10). The converter discs are tightly enclosed in a water-cooled housing. The housing incorporates openings to allow gas circulation to and from the housing. In the simulation, the housing is a box of aluminum (as an example), called "Wall" in Fig. 2.75, with a 3 cm thickness except the backward face between the last production target and the lead beam stop (which is considered as 1 mm). This is due to the fact that if one considers the thickness of this face too thick, this leads to significant energy deposition in this face due to the low range of the transmitted electrons. This high-energy deposition in the aluminum wall is not desirable due to the associated problems with heat removal, and it is more suitable to be deposited in a separate component (i.e., the massive beam stop). It is worth pointing out that when the energy deposition in all components is summed up (see Fig. 2.75), it reaches about 122 kW; however, as mentioned earlier, the rhodotron beam power is 125 kW. The missing energy deposition is the energy that is carried out by scattered photons and electrons from the system. When the thickness of the aluminum walls increases from 3 mm to 5 mm, the energy deposition is increased from 6.1 to about 7.0 kW. Moreover, as was discussed earlier, the thickness of the lead beam stop was not considered optimally to stop all of the photons. This stems from the fact that the Monte-Carlo calculations did not perform accurately (due to the non-availability of an HPC). Accordingly, there might be a chance that the beam stop is not able to stop all of the photons that pass through it. Therefore, by changing the thickness of the aluminum wall, it would be possible to eliminate (almost all) chances of radiation exposure to the environment of the system. As is shown in Fig. 2.75, since significant energy is deposited in the lead beam stop, a cooling system design is required to ensure sustainable performance and mechanical properties. Moreover, as mentioned before, a considerable neutron production in the tantalum converter target makes the beam stop design more complicated and requires to be investigated in more detail. However, due to the lack of the MCNP code library for photoneutron reactions, it is not addressed within this thesis.

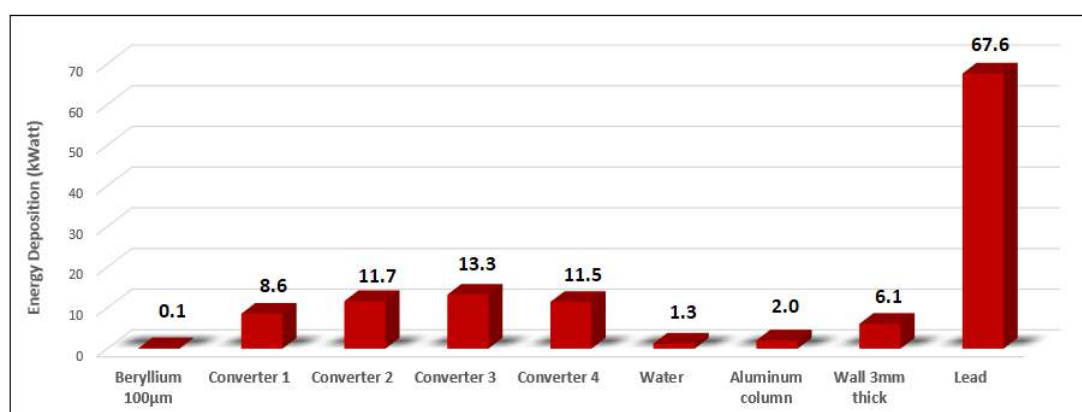


**Fig. 2.75:** Energy deposition in all components of the photonuclear irradiation setup

## 2.5 Summary of the results

In this part of the work, a summary of the most important obtained results is presented. As was shown in section 2.1 (i.e., the electron beam modeling), electron beam intensity variations as a function of FWHM for a fixed and rotating target are significant (was simulated via the MATLAB software). Since this parameter changes the electron beam distribution, it can affect the generated Bremsstrahlung production distribution and energy deposition profile.

In section 2.2, beryllium entrance window modeling as a function of beryllium thickness (ranging from 20  $\mu\text{m}$  to 100  $\mu\text{m}$ ) was performed via the MCNP code and COMSOL Multiphysics software. The Monte-Carlo simulation showed that the beryllium entrance window not only does not decrease the number of electrons but also it increases the number of them slightly. This is due to the fact that besides the primary incident electrons, the produced secondary electrons within the beryllium window are also able to pass through it (because of low atomic number, density, and considered low thicknesses). More importantly, the beryllium window does not affect the energy of the incident electrons considerably since, as the Monte-Carlo simulation showed, the fraction of the transmitted incident electron beam in the interval 39-40 MeV to 0-40 MeV varies from almost 0.992 to 0.985 when the thickness changes from 20  $\mu\text{m}$  to 100  $\mu\text{m}$ . The Monte-Carlo simulation also showed that the magnitude of the obtained Bremsstrahlung yields for the beryllium entrance window (all thicknesses) is low due to the low atomic number and density of beryllium; however, the energy deposition changes significantly from 14 to 77 Watt when the thickness increases from 20  $\mu\text{m}$  to 100  $\mu\text{m}$ . The COMSOL multiphysics software showed that for a fixed, not cooled rotating beryllium disc, the maximum temperature reaches around 750K in the worst case that belongs to the 100  $\mu\text{m}$  beryllium thick and 1 mm FWHM. Moreover, it was shown that for FWHMs ranging from 2mm to 5mm, the maximum temperature in the beryllium disc does not vary considerably (around 100K). Additionally, except for 1 mm FWHM, the beryllium thickness variations did not affect the maximum temperature significantly. According to the new proposed design, the beryllium disc was rotated. The rotation speed was synchronized with the time structure of the electron beam pulses generated from the rhodotron accelerator. Analytical investigation showed that 2'666.67 rpm was the best rotation speed considering the limitations of the commercial entrance windows options. The COMSOL Multiphysics software modeling for the new proposed rotating, helium-cooled, beryllium entrance design showed that the temperature for almost all thicknesses and FWHMs is reduced by up to 200K. In the worst case (that belongs to the 100  $\mu\text{m}$  thick and 1 mm FWHM), the maximum temperature reached around 531K, which is much lower than the melting point of beryllium (1580K).

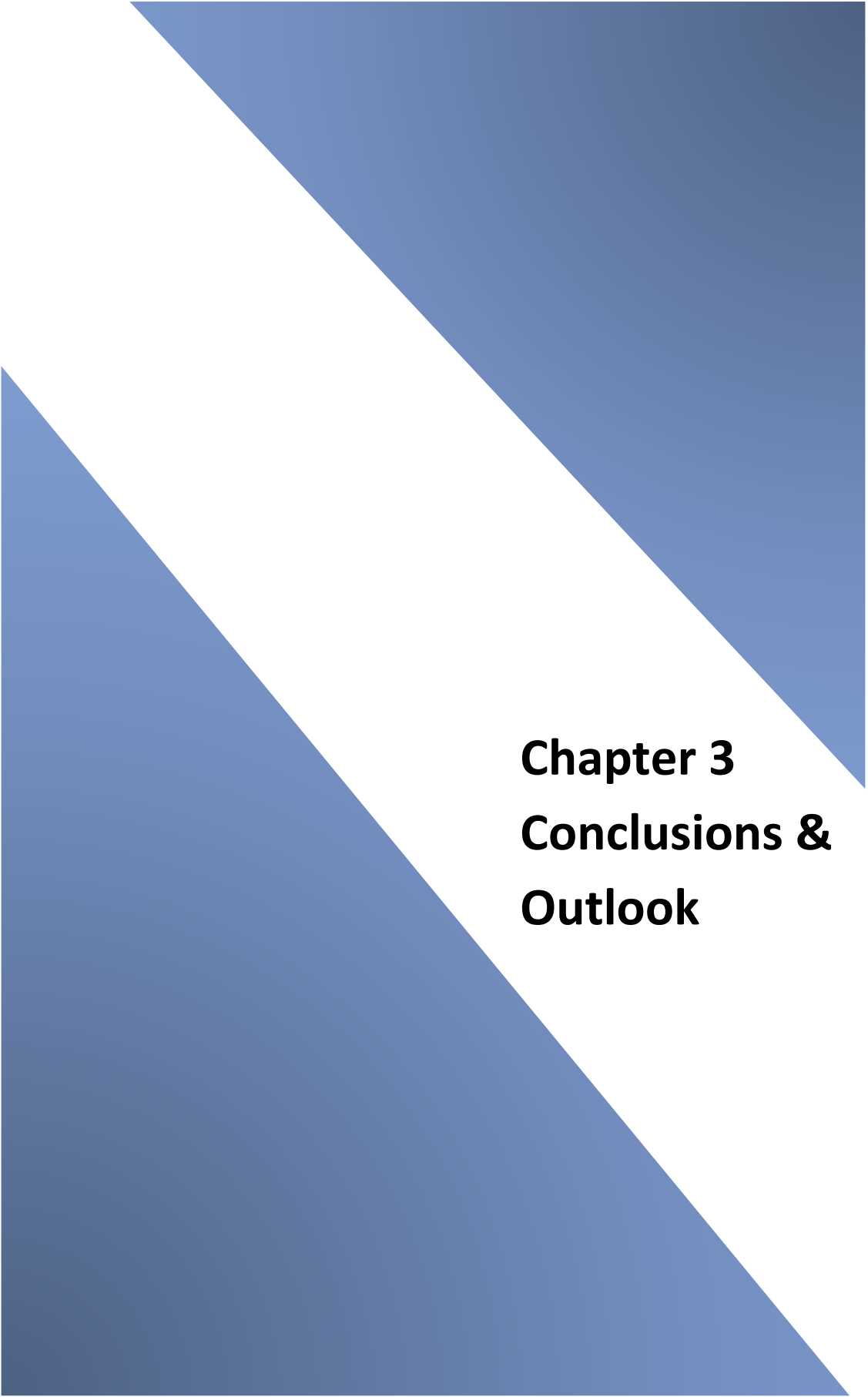
In section 2.3, Monte-Carlo simulation was performed to investigate the optimum tantalum converter thickness to maximize the number of Bremsstrahlung generated in the range of the GDR region (i.e., 8-30 MeV). Moreover, the Bremsstrahlungs angular and energy spectrum was obtained to be employed for further required mathematical calculations presented in the section of radionuclide production. The energy deposition obtained by the MCNP code showed that around 47 kW energy is deposited in the optimum thickness of the tantalum converter target. According to the results obtained via the COMSOL multiphysics software for the fixed, non-cooled converter target, the maximum temperature immediately increased to around 10'000K and 120'000K for 5mm and 1mm FWHM, respectively. It is evident that these temperatures are beyond the melting point of tantalum (that is, around 3300 K). According to the new proposed design, the converter target was rotated, and the rotation speed was

synchronized with the time structure of the electron beam pulses generated from the rhodotron accelerator. Analytical investigation showed that 24'000 rpm is the best rotation speed according to the converter and time structure of the beam. Besides the rotation mechanism, the optimum thick converter target disc is divided into 4 parallel discs to decrease the deposited energy instead of 1 disc to 4 discs. Moreover, a helium flow was considered to cool the converter discs. The simulation results obtained by the COMSOL multiphysics revealed that the maximum temperature is decreased compared with the conventional design remarkably. As an illustration, the maximum temperature reached around 500K, significantly lower than the tantalum melting point. According to the obtained results, beam widening is an effective method and therefore was applied to reduce the temperature in the converter targets (and the beryllium entrance window).

In section 2.4.1, an innovative flattening filter was proposed. The flattening filter comprised internal water-cooled aluminum to absorb a fraction of the number of electrons and photons with photon energy less than 8 MeV. This flattening filter can reduce the irradiation of the production targets with electrons and low-energy photons that can not contribute to the photonuclear reactions in the production targets. According to the Monte-Carlo simulation, the electrons' reduction is 22.8% in the entire energy range. In the case of photons, the results showed that the reduction was 11.2% in the 0-8 MeV.

In section 2.4.2, the Bremsstrahlungs energy spectrum for different production target positions was calculated using the MCNP code in order to be employed in the radionuclide activity estimation through photonuclear reactions.

In section 2.4.3, numerical calculations of coupled governing differential equations (using MATLAB software) for radionuclide production estimation were presented. Moreover, production estimation for some promising candidates of radionuclides that are high in demand was investigated. The results of numerical calculations for  $^{225}\text{Ac}$  production showed that for a  $0.1 \text{ g.cm}^{-2}$   $^{226}\text{Ra}$  target thickness, a target diameter of 2 cm, and 15 days irradiation time, around 74 (GBq)  $^{225}\text{Ac}$  can be produced. Assuming a patient dose of 10 MBq, around 7'400 patient doses can be produced from one  $^{226}\text{Ra}$  target. Considering a few milking cases, around 125 GBq of  $^{225}\text{Ac}$  can be produced for 15 days irradiation time per  $^{226}\text{Ra}$  target, corresponding to around 12'500 patient doses and roughly 37 Million Swiss Francs (CHF) benefits per target. Production estimation for some other radionuclides has also been investigated in section 2.4.3. Thanks to the high penetration of high-energy photons through different materials, simultaneous multiple production targets with the same photon beam can also be considered to maximize radionuclides production.

The page features two large, overlapping blue triangles. One triangle is positioned in the top right corner, pointing downwards and to the left. The other triangle is in the bottom left corner, pointing upwards and to the right. They meet in the center of the page, creating a white diamond-shaped area where the chapter title is located.

## **Chapter 3**

## **Conclusions & Outlook**

### 3.1 Conclusion

Increasing interest in the current and prospective application of various radionuclides in nuclear medicine makes the production of radionuclides crucial and high in demand. Among all the radionuclide production methods, promising results achieved with the photonuclear reaction method revealed a possibility for a large-scale radionuclide production if a high-energy and high-power electron accelerator is employed. However, very little research has been performed to explore the possibility of radionuclide production through photonuclear production, due to the non-availability of high-energy and high-power electron beam accelerators. The recent development of new types of modern electron beam accelerators calls now for a feasibility investigation for efficient photonuclear radionuclide production. Among them, the rhodotron accelerator (model TT300-HE) with an electron beam energy and power of 40 MeV and 125 kW, respectively, can provide a wide variety of medical radionuclides attainable on a large-scale. On this basis, designing a photonuclear irradiation setup is essential for efficient radionuclide production. The largest problem associated with this purpose, is the enormous heat generation in the converter target material.

The main objective of this thesis was the feasibility assessment and development of a novel photonuclear irradiation setup for a high-energy and high-power rhodotron accelerator (model TT300-HE) for the first time. A detailed investigation and in-depth assessment were also studied to ensure a safe operation and thoroughly reliable working conditions of the designed photonuclear irradiation setup.

The calculations presented here were conducted with a Monte-Carlo program, called the MCNP code. This code allowed calculations of the Bremsstrahlungs yield of the converter target, optimum target thickness determination, electron beam energy dissipation calculations, estimations of the angular Bremsstrahlungs distribution, energy deposition computation due to the electron and photon interactions, a design of the photon and electron shielding, and an approximation of the radionuclide production yield using photonuclear reactions.

As discussed above, the enormous heat generation in the converter target is the major problem associated with high-energy and high-power electron beam accelerators. Accordingly, calculations of heat deposition in the converter target and beryllium entrance window were performed using the COMSOL Multiphysics software to ensure mechanical stability and sufficient heat removal of the irradiated components. According to the carried out assessment, the maximum temperature in the beryllium entrance window reached about 750 K, lower than its melting point (around 1500 K). Low energy deposition in the beryllium entrance window resulted from the low atomic number and the low density of beryllium in a way that, according to the performed Monte-Carlo assessment, more than 98 percent of the incident electrons passed through the beryllium window with almost no interaction. Nevertheless, the possibility of heat removal and cooling of the beryllium entrance window was investigated. Rotation of the beryllium disc in addition to active helium flow resulted in around 200K reduction of the maximum temperature.

In the case of the tantalum converter target, the maximum temperatures reached approximately 20'000-120'000 K (depending on the FWHM of the electron beam), which is much higher than the tantalum melting point (around 3300 K), and made a new design for the converter target assembly essential. The new design of the tantalum converter target consisted of different mechanisms, first: rotating the tantalum converter target disc, second:

dividing the single tantalum converter target disc into four parallel discs, and third: cooling the discs by helium gas. The results of the heat transfer calculations confirmed a significant decrease in temperature to about a fraction of the melting point of tantalum (depending on the FWHM of the electron beam).

From the radiation protection point of view, the Monte-Carlo calculations ensured that half of a meter thick lead is able to stop almost all of the electrons and photons in all energy ranges. Therefore, the Monte-Carlo and heat transfer assessment revealed that the designed photonuclear irradiation setup is feasible from the heat removal and radiation protection point of view.

Radionuclide yield production via the designed photonuclear irradiation setup was addressed, and estimates of the yield of each nuclide were provided. These were  $^{67}\text{Cu}$ ,  $^{99}\text{Mo}$ , and  $^{225}\text{Ac}$  produced in the reactions  $^{68}\text{Zn}(\gamma, p)^{67}\text{Cu}$ ,  $^{100}\text{Mo}(\gamma, n)^{99}\text{Mo}$ , and  $^{226}\text{Ra}(\gamma, n)^{225}\text{Ra} \xrightarrow{\beta^-(14.9 \text{ days})} ^{225}\text{Ac}$ , respectively. The photonuclear radionuclide yield estimation for different radionuclides indicated for the first time, that a large-scale production via electron accelerators is attainable using the designed irradiation setup.

### 3.2 Outlook

The feasibility of a large-scale medical radionuclide production via electron accelerators was demonstrated in this study. Reliability in performance and safe operation of the designed photonuclear irradiation setup enabled us to ensure the promising application of high-energy and high-power electron beam accelerators for radionuclide production purposes. Apart from the investigated yield estimation of important isotopes, co-produced radionuclide impurities such as  $^{227}\text{Ac}$  in the  $^{226}\text{Ra}(n,\gamma)^{227}\text{Ra} \rightarrow ^{227}\text{Ac}$  activation/decay sequence are envisaged to be studied in the future. As the feasibility of a simultaneous multiple target irradiation configuration was demonstrated and proposed in the thesis, an in-depth investigation for an efficient and large-scale radionuclide production purpose is an area of interest as well. Simultaneous multiple different targets irradiation necessitated upmost attention to entire reaction routes investigation for some probably induced reactions through various particle emission (such as p and  $\alpha$  particles) of different production targets irradiation. Besides, the availability of updated experimental cross-sections in the employed MCNP code would allow for more realistic and accurate radionuclide yield estimation, particularly towards investigating the envisioned simultaneous multiple target irradiation method.

Within the thesis framework, in-depth entire electron-photon cascade interactions were analyzed via a Monte-Carlo program-based method. However, photons produced due to electron irradiation of tantalum induces  $^{181}\text{Ta}(\gamma,n)^{180}\text{Ta}$  reactions that result in additional radionuclide impurities through the neutron bombardment of the production targets. Photoneutrons can also be produced from the production targets (e.g., radium target), and consequently, induce probable neutron reactions that lead to producing radionuclide impurities in the production targets. More importantly, high energetic neutron penetration into the materials makes the entire neutron interactions in all irradiated components essential from the radiation protection point of view. Moreover, the scattering of electrons, photons, and photoneutrons in all angles makes designing a vessel containing all the irradiation setup components important in both radiation protection and heat transfer approaches. To establish a more complementary result, beta particle and gamma-ray emissions through the formation of two radionuclides  $^{180}\text{Ta}$  and  $^{182}\text{Ta}$  by  $(\gamma,n)$  and  $(n,\gamma)$  reactions in the tantalum converter target, and any other probable source of radiations from each irradiation setup component including the production targets requires to be investigated. It has to be kept in mind that probably active cooling of the vessel is needed due to the relatively long half-life and considerable induced activity of the produced radionuclides in each irradiation setup component. All these considerations have to be part of further investigations, which will require a high-performance computing system. Such a system is currently being installed.



# References

- [F58] S. Fluegge, Encyclopedia of physics, Springer-Verlag, 1958, Berlin, Germany.
- [K00] G.F. Knoll, Radiation detection and measurement. John Wiley and Sons, Inc. 2000, New York.
- [D03] M. Dapor, Electron-beam interactions with solids, Springer, 2003, USA.
- [WH19] K. Wilson and H. Schaub, X-ray spectroscopy for electrostatic potential and material determination of space objects. IEEE TRANSACTIONS ON PLASMA SCIENCE, Vol. 47, No. 8, 2019, 3858-3866.
- [LMD11] Y.G. Li, S.F. Mao and Z.J. Ding. Monte-Carlo simulation of SEM and SAM images, applications of Monte Carlo method in science and engineering, Shaul Mordechai, 2011, IntechOpen, DOI:10.5772/16171. <https://www.intechopen.com/books/applications-of-monte-carlo-method-in-science-and-engineering/monte-carlo-simulation-of-sem-and-sam-images>
- [JC83] H.E. Johns, J.R. Cunningham, The physics of radiology, Charles C Thomas, 1983, USA.
- [A07] S.N. Ahmed, Physics and engineering of radiation detection, Elsevier, 2007, USA.
- [HN04] E. Haug, W. Nakel, The elementary process of Bremsstrahlung. World Scientific Publishing Co., 2004, Singapore.
- [OH18] M. Omer and R. Hajima, Geant4 physics process for elastic scattering of  $\gamma$ -rays. JAEA-Data/Code 2018-007, 2018.
- [TL15] N. Tsoulfanidis, S. Landsberger, Measurement & detection of radiation, 4<sup>th</sup> edition, CRC Press Taylor & Francis Group, 2015, USA.
- [HAT16] G. Hubschen, I. Altpeter, R. Tschuncky, H. Herrmann, Materials characterization using nondestructive evaluation (NDE) methods, Elsevier, 2016, USA.
- [NUE12] H. Nikjoo, S. Uehara, D. Emfietzoglou, Interaction of radiation with matter, 2012, Taylor & Francis Group.
- [AP18] A. De Angelis, and M. Pimenta, Introduction to particle and astroparticle physics, Second edition, Springer International Publishing AG, part of Springer Nature, 2018.
- [E01] A. Edward et al. Encyclopedia of physical science and technology, third edition. Elsevier Science Ltd., 2001.
- [GK00] D. E. Groom, S. R. Klein, Passage of particles through matter, The European Physical Journal C, 2000 Vol. 15, Iss. 1-4 (2000) 163-173.
- [ZLH06] B. Ziaja, R. A. London, and J. Hajdu, Ionization by impact electrons in solids: Electron mean free path fitted over a wide energy range, Journal of Applied Physics. 99, 033514 (2006); doi:10.1063/1.2161821.
- [BRS38] H.A. Bethe, M.E. Rose, L.P Smith, The multiple scattering of electrons, Proceedings of the American Philosophical Society, **78**, (1938).
- [E70] P. Erman, Differences in single, plural and multiple scattering of electrons and positrons through intermediate angles, Physica Scripta, Vol. 1 (1970) 93-103.
- [B16] G. L. Bennett, Destination universe: some thoughts on faster-than-light (FTL) travel. Propulsion and Energy Forum July 25-27, 2016, Salt Lake City, UT 52nd AIAA/SAE/ASEE Joint Propulsion Conference.
- [DH91] J.J. Duderstadt, L.J. Hamilton, Nuclear reactor analysis, John Wiley & Sons, 1991, New York.

- [L65] J.R. Lamarsh, Introduction to nuclear reactor theory. Addison-Wesley Publishing Company, 1965.
- [LB01] J.R. Lamarsh and A. J. Baratta, Introduction to nuclear reactor engineering (third edition), Prentice-Hall, Inc., United States, 2001.
- [V20] M. Vollmer, Cherenkov radiation: why is it perceived as blue?, European Journal of Physics 41 (2020) 065304.
- [O19] S. A. Othman, Radiation Biophysics, Publisher: Universiti Tun Hussein Onn Malaysia, (2019) Malaysia.
- [H06] E. Haug, Electron-electron and electron-positron Bremsstrahlung, Radiation Physics and Chemistry **75**, (2006) 1330-1345.
- [LP07] T.W. Leadbeater, D.J. Parker, A positron camera with flexible geometry for the study of industrial processes, 5th World Congress on Industrial Process Tomography, Bergen, Norway, 2007.
- [L03] M. F. L'annunziata, Handbook of radioactivity analysis (Second Edition), 2003, Academic Press. USA.
- [TMAYY17] H.O. Tekin, T. Manici , E.E. Altunsoy, K. Yilancioglu and B. Yilmaz, An artificial neural network-based estimation of bremsstrahlung photon flux calculated by MCNPX, Acta Physica Polonica A, Vol. 132 (2017) No. 3-II, Special issue of the 3rd International Conference on Computational and Experimental Science and Engineering (ICCESEN 2016).
- [K03] F. M. Khan, The physics of radiation therapy, Lippincott Williams & Wilkins, 3<sup>rd</sup> edition, (2003), USA.
- [EGS05] K.M. Eshwarappa, Ganesh, K. Siddappa, Yogesh Kashyap, Amar Sinha, P.S. Sarkar, B.K. Godwal, Estimation of photoneutron yield from beryllium target irradiated by variable energy microtron-based Bremsstrahlung radiation, Nuclear Instruments and Methods in Physics Research A 540 (2005) 412–418.
- [BS70] M.J. Berger and S.M. Seltzer, Bremsstrahlung and photoneutrons from thick tungsten and tantalum targets, Physical Review C 2 (1970) 621-631.
- [MLA06] G. Melville, S.F. Liu, B.J. Allen, A theoretical model for the production of Ac-225 for cancer therapy by photon-induced transmutation of Ra-226, Applied Radiation and Isotopes 64 (2006) 979-988.
- [G77] S. Geltman, Stimulated multiphoton Bremsstrahlung in electron-ion collisions, Journal of Research of the National Bureau of Standards Vol. 82, No.3, 1977.
- [H76] R.G.L. Hewitt, A comparison of one photon and two photon Bremsstrahlung processes in hydrogen plasmas, (1976) Plasma Physics 18 219.
- [MMD59] R.C. Majumdar, V.S. Mathur and J. Dhar, Multiple photon production in Compton scattering and Bremsstrahlung, IL NUOVO CIMENTO ORGANO DELLA SOCIETA ITALIANA DI FISICA SOTTO GLI AUSPICI DEL CONSIGLIO NAZIONALE DELLA RICERCA, VOL. XII, N. 2, 1959, 97-105.
- [KS06] A.V. Korol, A. Solovjev, Relativistic two-photon Bremsstrahlung, Radiation Physics and Chemistry, Volume 75, Issue 10 (2006) 1346-1357.
- [KM90] R. Kleiss, S. Marck, Two-photon Bremsstrahlung, Nuclear Physics B, Vol. 342, Iss. 1, (1990), 61-94.
- [KS02] A.V.Korol, A.Solovjev, Relativistic calculation of the two-photon Bremsstrahlung process, Surface Review and Letters Vol. 09, No. 02 (2002) 1185-1190.

- [MDV87] A. Maquet, A. Dubois, V. Vénard. Some new perspectives in Bremsstrahlung research, *Journal de Physique Colloques*, 1987, 48 (C9), pp.C9-799-C9-809. [ff10.1051/jphyscol:19879141ff](https://doi.org/10.1051/jphyscol:19879141ff). [ffjpa-00227252](https://arxiv.org/abs/00227252).
- [H03] E. Haug, Photon energy spectrum of electron–positron Bremsstrahlung in the center-of-mass system, *The European Physical Journal C*, 31, (2003) 365–369.
- [KS14] A.V. Korol A.V. Solov'yov, *Polarization Bremsstrahlung*, Volume 80, Springer-Verlag Berlin Heidelberg 2014.
- [P11] A.P. Potylitsyn, *Electromagnetic radiation of electrons in periodic structures*, Springer Tracts in Modern Physics Volume 243, Springer-Verlag Berlin Heidelberg 2011.
- [CV14] A. P. Chernyaev and S. M. Varzar, Particle accelerators in modern world, *Physics of Atomic Nuclei*, Vol. 77, No. 10, (2014) 1203–1215.
- [M98] W. Mondelaers, Low-energy electron accelerators in industry and applied research, *Nuclear Instruments and Methods in Physics Research B* 139 (1998) 43-50.
- [BSKS99] B. Bogdanovitch, V. Senioukov, A. Koroliov, K. Simonov, Application of low energy electron beams for technology and medicine, *Proceedings of the 1999 Particle Accelerator Conference*, 1999, New York.
- [HH12] R. W. Hamm and M. E. Hamm, *Industrial accelerators and their applications*, World Scientific Publishing Co. Pte. Ltd (2012).
- [S13] A. A. M. El-Saftawy, *Regulating the performance parameters of accelerated particles*. Thesis Doctoral of philosophy, Department of Physics Faculty of Science Zagazig University 2013.
- [IBANO.1] PART V: Accelerators for industrial applications, IBA Industrial Solution, See: <https://indico.cern.ch/event/356897/contributions/1769242/attachments/710048/974734/handout-Part-5.pdf>.
- [B89] K. Brand, The dynamitron tandem accelerator-a useful tool for ion beam applications, *Materials Science and Engineering B* 2 (1989) 237-242.
- [CF65] M.R. Cleland and P. Farrell, Dynamitrons of the future, *IEEE* (1965) 227-234.
- [H05] R. Hellborg, *Electrostatic accelerators*, Springer-Verlag Berlin Heidelberg 2005.
- [B69] D. Brune, Application of a betatron in photonuclear activation analysis, *Analytica Chimica Acta* 44 (1969) 9-14.
- [MI60] H. Morinag, and T. Izuizotanagi, Internal target for a betatron, *Nuclear Instruments and Methods* 6 (1960) 66—71.
- [JME] JME Advanced Inspection System Company, A betatron accelerator builder company, see: <https://www.jme.co.uk/products/Betatron-Portable-Xray/betatron-9mev.html>.
- [BR81] A. Brahme and D. Reistad, Microtrons for electron and photon, *IEEE Transactions on Nuclear Science*, Vol. NS-28, No. 2, 1981.
- [K65] S.P. Kapitsa, The microtron and areas of its application, *Atomnaya Energya* 18 (1965) 203-209.
- [C06] A. Wu Chao, *Handbook of accelerator physics and engineering*, 3th edition (2006) World Scientific Publishing Co. Pte. Ltd
- [T18] Y. M. Tsipenyuk, *The microtron, development and application*, CRC Press Taylor & Francis Group, 2018.
- [R58] A. Roberts, The microtron as a high-Energy, high current particle accelerator, *Annals of Physics*: 4, (1958) 115-165.

- [KBM62] S. P. Kapitza, V. P. Bykov, and V. N. Melekhin, AN efficient high-current microtron, Soviet Physics JETP, Vol. 14, No. 2, (1962) 265-277.
- [A01] K.I. Antipov, et al., High-power electron linac for irradiation applications, Proceedings of the 2001 Particle Accelerator Conference, Chicago, 2805-2807.
- [SLAC] SLAC National Accelerator Laboratory, see: <https://www6.slac.stanford.edu/about/contact-slac>.
- [TAHS12] F. Tabbakh, M.M. Aldaavati, M.S. Hoseyni, K.R.E. Saraee, Induced photonuclear interaction by Rhodotron-TT200 10 MeV electron beam, PRAMANA 78 (2012) 257–264.
- [AJPB04] M. Abs, Y. Jongen, E. Poncelet, J. L. Bol, The IBA rhodotron TT1000: a very high power E-beam accelerator, Radiation Physics and Chemistry 71 (2004) 285–288.
- [P89] J. Pottier, A new type of electron accelerator: the rhodotron, Nuclear Instruments and Methods in Physics Research B40/41 (1989) 943-945.
- [J96] Y. Jongen et al., Rhodotron accelerators for industrial electron-beam processing: A progress report, 5th European Particle Accelerator Conference, Sitges, Barcelona, Spain, 1996, pp.e-proc. 268.
- [IBANO.2] Rhodotron TT300-HE datasheets, iba, See: [www.iba-industrial.com](http://www.iba-industrial.com)
- [IBANO.3] Rhodotron TT300-HE high energy electron generator, iba, See: [www.iba-industrial.com](http://www.iba-industrial.com)
- [BGGNB19] S. Bertrand, J. Geets, C. Gameiro, B. Nactergal, J. Brison, A new compact high power e-beam accelerator for radioisotopes production: a first evaluation, International symposium on trends in radiopharmaceuticals, Abstract ID n°199 ISTR 2019, Vienna, Austria.
- [K03] S. Korenev, The concept of beam lines from rhodotron for radiation technologies, Proceedings of the 2003 Particle Accelerator Conference, 1015-1016
- [ARIES18] ARIES Annual Meeting, Riga, IBA TT300-HE for radioisotopes production, (2018); see: [https://indico.cern.ch/event/699219/contributions/2929577/attachments/1655382/2649737/IBA\\_Presentation\\_Aries\\_Annual\\_Meeting.pdf](https://indico.cern.ch/event/699219/contributions/2929577/attachments/1655382/2649737/IBA_Presentation_Aries_Annual_Meeting.pdf).
- [SSSC10] V.N. Shvetsov, E.I. Sharapov, S.L. Stephenson, B.E. Crawford, comparison of calculated and measured yields of medical isotopes produced by electron Bremsstrahlung. XVII International Seminar on Interaction of Neutrons with Nuclei (Neutron Spectroscopy, Nuclear Structure, Related Topics), Dubna, May 27-29, 2009, JINR, E3-2010-36 (Dubna, 2010).
- [HS15] S. Howard and V. N. Starovoitova, Target optimization for the photonuclear production of radioisotopes, Applied Radiation and Isotopes 96 (2015) 162-167.
- [GSS08] C. Hernandez-Garcia, P. G. O'Shea, and M. L. Stutzman, Electron sources for accelerators, Physics Today 61, 2, 44 (2008); doi: 10.1063/1.2883909.
- [ADGGRZ14] S. Ahmadiannamin, F. Abbasi Davani, R. Ghaderi, F. Ghasemi, M. Lamahi Rachti, S. Zarei, Simulation study of electron gun for six MeV linac for x-ray Cargo inspection, IPAC2014, Dresden, Germany, 5th International Particle Accelerator Conference, 5th International Particle Accelerator Conference, doi:10.18429/JACoW-IPAC2014-THPRI038.
- [P16] T.C. Pataky et al. (2016), Region-of-interest analyses of one-dimensional biomechanical trajectories: bridging 0D and 1D theory, augmenting statistical power. PeerJ 4:e2652; DOI 10.7717/peerj.2652.
- [HLB14] W.M. Haynes, D.R. Lide, and T.J. Bruno, CRC Handbook of chemistry and physics, 95<sup>th</sup> edition, CRC Press, Taylor & Francis Group, (2014), New York, USA.

- [CS95] C. T. Chantler, and J. L. Staudenmann, Energy dependences of absorption in beryllium windows and argon gas, *Review of Scientific Instruments* 66 (1995)1651-1654.
- [HMKPK15] S. Huebner, N. Miyakawa, S. Kapser, A. Pahlke, and F. Kreupl. High Performance X-Ray Transmission Windows Based on Graphenic Carbon. *IEEE Transactions on Nuclear Science*, March 4 2015, Issue 99, <http://dx.doi.org/10.1109/TNS.2015.2396116>.
- [NASA] Beryllium thin films for resistor applications, NASA TECH BRIEF, Ames Research CenterB72-10021, ARC-10485.
- [W15] E.E. Wisniewski et al., Multiple scattering effects of a thin beryllium window on a short, 2 nC, 60 MeV bunched electron beam, 6<sup>th</sup> International Particle Accelerator Conference IPAC2015, Richmond, VA, USA.
- [NMR15] S. Nayak, M. Mapes, D. Raparia, Design of beryllium window for Brookhaven linac isotope producer, (2015) U.S. Department of Energy Office of Science, Office of Nuclear Physics NY, USA.
- [EGKLLPRS20] J. Engel, M. Gross, G. Koss, O. Lishilin, G. Loisch, S. Philipp, D. Richter, and F. Stephan. Polymer foil windows for gas–vacuum separation in accelerator applications. *AIP Advances* 10, 025224 (2020); doi: 10.1063/1.5143258.
- [L03] Y. Li, A thin beryllium injection window for CESR-C, *Proceedings of the 2003 Particle Accelerator Conference*, 2264-2266.
- [SQ82] M. Semaan and C. Quarles, Z dependence of atomic-field Bremsstrahlung, *PHYSICAL REVIEW A*, VOLUME 26, NUMBER 6 DECEMBER 1982, 3152-3154.
- [S19] S.J. Sharma, et al., Modified atomic number dependence of total Bremsstrahlung spectra in compounds *Turkish Journal of Physics*, (2019) 43: 365 – 371.
- [DNA19] N. Demir, Z. Nur Kuluöztürk, İ. Akkurt, FLUKA Monte Carlo calculations for angular distribution of Bremsstrahlung photons from thin targets, *Nuclear Inst. and Methods in Physics Research B*, 433 (2019) 19-24.
- [D09] J.P. Dalton, Researches on the Joule–Kelvin effect, especially at low temperatures. I. Calculations for hydrogen. *KNAW Proceedings*. 11, 863–873, 1909.
- [DSFO18] D.S. Dale, V.N. Starovoitova, T.A. Forest, E. Oliphant, Photonuclear production of yttrium-88 – A high energy gamma emitter for hydrocarbon extraction applications, *Applied Radiation and Isotopes* 139 (2018) 137-140.
- [TBAM16] A. Tsechanski, A.F. Bielajew, J.P. Archambault, and E. Mainegra-Hing, Electron accelerator-based production of molybdenum-99: Bremsstrahlung and photoneutron generation from molybdenum vs. tungsten, *Nuclear Instruments and Methods in Physics Research B* 366 (2016) 124-139.
- [GMHEM07] J. Galy, M. Maucec, D.J. Hamilton, R. Edwards and J. Magill, Bremsstrahlung production with high-intensity laser matter interactions and applications, *New Journal of Physics* 9 (2007) 23.
- [A61] P. Axel, Bremsstrahlung converter consideration, Technical report No. 22, Supplement to technical report No. 21, Office of naval research contract nonr 1834(05), Physical research laboratory, Physics department of Illinois, Urbana, Illinois, 1961.
- [D19] O.S. Deiev, et al., Bremsstrahlung of electrons and yield of neutrons from thick converters, passing of gamma-radiation and neutrons through biological shielding, *Problems of Atomic Science and Technology*, 2019, N3 (212), Series: Nuclear Physics Investigations (71) 65-73.

- [P11] S.H. Park, et al., Gamma-ray generation using laser-accelerated electron beam, *Proc. Of SPIE* (2011) 8075 8075Y1-8075Y7.
- [A07] N.I. Ayzatskiy et al., Comparison of Cu-67 production at cyclotron and electron accelerator, *Cyclotrons and Their Applications 2007*, Eighteenth International Conference, (2007) 243-245.
- [PBSKS07] V.C. Petwal, S.C.Bapna, R.S. Sandha, S. Kotaiah, K.V. Subbaiah, Bremsstrahlung converter for high power EB radiation processing facility, *APAC 2007*, Raja Ramanna Center for Advanced Technology (RRCAT), Indore, India. THPMA088, 767-769.
- [W09] T.J. Williams, Axial energy distribution in disc-shaped tantalum and aluminum Bremsstrahlung conversion targets, *Acta physica polonica A* 115 (2009) 1180-1182.
- [LM20] V.V. Lisovska, and T.V. Malykhina, Computer simulation of the angular distribution of electrons and Bremsstrahlung photons in tantalum converter, *East European Journal of Physics* (2020) 2 89-93.
- [KAY17] M.E. Korkmaz, O. Agar, and M. Yigit, Investigation of spherical and cylindrical natural Iridium targets by photonuclear reaction, *EPJ Web of Conferences* 154, 01027 (2017).
- [K20] J.H. Khushvaktov et al., Study of the rate of photonuclear reactions in  $^{165}\text{Ho}$  nucleus, *Physics of Particles and Nuclei Letters*, (2020) 17 821-825.
- [FT19] D.V. Fedorchenko, and A. Tsechanski, Photoneutronic aspects of the molybdenum-99 production by means of electron linear accelerators, *Nuclear Instrument and Methods in Physics Research B* 438 (2019) 6-13.
- [KRSDFM19] A.J. Koning, D. Rochman, J. Sublet, N. Dzysiuk, M. Fleming and S. van der Marck, "TENDL: Complete Nuclear Data Library for Innovative Nuclear Science and Technology", *Nuclear Data Sheets* 155 (2019).
- [DR21] W.T. Diamond and C.K. Ross, Actinium-225 production with an electron accelerator, *Journal of Applied Physics* 129 (10) 104901, 2021.
- [KKVMV15] E. Kukleva, J. Kozempel, M. Vlk, P. Mičolová, and D. Vopálka, Preparation of  $^{227}\text{Ac}/^{223}\text{Ra}$  by neutron irradiation of  $^{226}\text{Ra}$ , *Journal of Radioanalytical and Nuclear Chemistry*, 304, (2015) 263–266.
- [IAEANO.1] See: <https://www.iaea.org/resources/databases/atlas-of-neutron-capture-cross-sections> for IAEA Evaluated Data Library of Neutron Capture Cross-sections, 2010.
- [KKK17] J. Ko, B.Y. Kim, Y.S.Kim, Characteristic analysis of a photon converter in a medical Linac using GEANT4, *JVE International LTD. Vibroengineering Procedia*. 14 (2017) 256-259.
- [VVRS99] A. V. Varlamov, V. V. Varlamov, D. S. Rudenko, M. E. Stepanov, Atlas of Giant Dipole Resonances. International Atomic Energy Agency, Vienna 1999, INDC(NDS)-394.
- [IAEANO.2] Handbook on photonuclear data for applications: Cross-sections and spectra, IAEA, Vienna 2000, TECDOC-1178.
- [OKS69] Y. Oka, T. Kato, and N. Sato, The yields of photonuclear reactions in titanium and vanadium with Bremsstrahlung up to 60 MeV, *Bulletin of the Chemical Society of Japan* 42 (1969) 387-393
- [A20] R.A. Aliev et al., Photonuclear production of medically relevant radionuclide  $^{47}\text{Sc}$ , *Journal of Radioanalytical and Nuclear Chemistry* (2020) 326:1099-1106.
- [L16] W. Luo, et al., Production of radioisotopes of medical interest by photonuclear reaction using ELI-NP  $\gamma$ -ray beam, *Acta Physica Polonica B* (2016) 47 763-769.

- [A19] R.A. Aliev, et al., Photonuclear production and radiochemical separation of medically relevant radionuclides:  $^{67}\text{Cu}$ , *Journal of Radioanalytical and Nuclear Chemistry* (2019) 321: 125-132.
- [TFSG19] A.Tsechanski, D. Feorchenko, V. Starovoitova, and A. Galperin, Converter optimization for photonuclear production of Mo-99, *Nuclear Instruments and Methods in Physics Research B* 461 (2019) 118-123.
- [K06] S.P. Karasyov et. al., High-intensity Bremsstrahlung monitoring system for photonuclear technologies, *Proceeding of EPAC 2006, Edinburgh, Scotland TUPCH096* 1235-1237.
- [S11] V. Starovoitova et al., Cu-67 photonuclear production, *AIP Conference Proceedings* 1336, (2011) 502-504.
- [ST10] V. Sidlova, T. Trojek, Testing Monte Carlo computer codes for simulations of electron transport in matter, *Applied Radiation and Isotopes* 68 (2010) 961-964.
- [A18] J.P. Archambault, Monte Carlo calculations of electrons impinging on a copper target: A comparison of EGSnrc, Geant4 and MCNP5, *Applied Radiation and Isotopes* 132 (2018) 129-134.
- [VGGAL07] M. Vilches, S. Garcia-Pareja, R. Guerrero, M. Anguiano, A.M. Lallena, Monte Carlo simulation of the electron transport through thin slabs: A comparative study of PENELOPE, GEANT3, GEANT4, EGSnrc and MCNPX, *Nuclear Instrument and Methods in Physics Research B* 254 (2007) 219-230.
- [P11] D.B. Pelowitz, Ed., "MCNPX Users Manual Version 2.7.0" LA-CP-11-00438 (2011).
- [COMSOL] COMSOL Multiphysics® v. 5.4. [www.comsol.com](http://www.comsol.com). COMSOL AB, Stockholm, Sweden.
- [ANSYS] P. Kohnke, ANSYS: Theory reference, eleventh edition, (1999), ANSYS Inc., USA.
- [VOG19] M. Vagheian, D. R. Ochbelagh, M. Gharib, A new moving-mesh Finite Volume Method for the efficient solution of two-dimensional neutron diffusion equation using gradient variations of reactor power. *Nuclear Engineering and Technology* 51 (2019) 1181-1194.
- [VT19] M. Vagheian, S. Talebi., Introduction to the slide modeling method for the efficient solution of heat conduction calculations, *Journal of Applied and Computational Mechanics* 5(4) (2019) 680-695.
- [VOG20] M. Vagheian, D. R. Ochbelagh, M. Gharib, Introduction to the non-orthogonal gradient-based finite volume method for three-dimensional neutron diffusion calculations with application to the rectangular reactor core configurations. *Annals of Nuclear Energy* 138 (2020) 107216.
- [VOG16] M. Vagheian, D. R. Ochbelagh, M. Gharib, On an improved box-scheme finite difference method based on the relative event probabilities. *Progress in Nuclear Energy* 88 (2016) 33-42.
- [VVG16] M. Vagheian, N. Vosoughi, M.Gharib, Enhanced finite difference scheme for the neutron diffusion equation using the importance function, *Annals of Nuclear Energy* 96 (2016) 412–421.
- [BHOS10] C. Belavý, G. Hulkó, K. Ondrejkoš and D. Šišmišová, FEM Based Modeling in COMSOL Multiphysics and Design of Control of Distributed Parameter Systems, Excerpt from the Proceedings of the COMSOL Conference 2010 Paris.
- [MATLAB20] The Math Works, Inc. MATLAB. Version 2020a.
- [Nucleonica20] Nucleonica GmbH, Nucleonica Nuclear Science Portal ([www.nucleonica.com](http://www.nucleonica.com)), Version Version 3.0.297.0001, Karlsruhe (2020).

[TAKVCGBM12] T.D. Thiep, T.T An, N.T. Khai, N.T. Vinh, P.V.Cuong, Y.P. Gangrski, A.G. Belov, O.D. Maslov, Determination of the total Bremsstrahlung photon flux from electron accelerators by simulations activation of two monitors, *Physics of Particles and Nuclei Letters* 9(8) 104-114, 2012.

[VSSO20] M. Vagheian, D. Sardari, S. Saramad, D. R. Ochbelagh, Experimental and theoretical investigation into X-ray shielding properties of thin lead films. *International Journal of Radiation Research*, 18 (2) (2020) 263-274.

[V13] P. D. VanSant, Medical isotope production of actinium-225 by linear accelerator photon irradiation of Radium-226, Thesis master of science in mechanical engineering, Faculty of the Virginia Polytechnic Institute and State University 2013.

[CJ09] H. Cember, T.E.Johnson, Introduction to health physics, McGraw-Hill, fourth edition, 2009, New York.

[J18] A. Juzeniene et al., Antitumor activity of novel bone-seeking,  $\alpha$ -emitting  $^{224}\text{Ra}$ -solution in a breast cancer skeletal metastases model, *ANTICANCER RESEARCH* 38: 1947-1955 (2018).

[JM20] J. Jastrzębski, ..., M. Vagheian, Investigation of the production of the auger electron emitter ..., *Acta Physica Polonica B* 51 (2020) 861-866.

[M67] W.E. Meyerhof, Elements of nuclear physics. McGrawHill, (1967), New York.

[CSF84] A.B. Chilton, J.K. Shultis, R.E. Faw, Principles of radiation shielding, Prentice-Hall, Inc, (1984), Englewood Cliffs.

[J00] W. S. Janna, Engineering heat transfer. CRC Press LLC, second edition, 2000, USA.

[K50] D. Q. Kern, Process heat transfer. McGraw-Hill, 1950, Singapore.

[KBKW21] P. Kosky, R. Balmer, W. Keat, G. Wise, Exploring engineering: An introduction to engineering and design (fifth edition), Elsevier Inc., Academic Press, 2021, USA.

[Z19] D. Zeinali, Flame spread and fire behavior in a corner configuration. Ph.D. thesis, Ghent University, Belgium, 2019.

[L03] J. H. Lienhard, A heat transfer textbook, Third edition, Phlogiston Press, USA, 2003.

[H86] J.P. Holman, Heat transfer (sixth edition). McGraw-Hill Book Co. Singapore 1986.

[LQT18] Z. Li, Z. Qiao, and T. Tang, Numerical solution of differential equations: introduction to Finite Difference and Finite Element Methods. Cambridge University Press. United Kingdom, 2018.

[H10] J.P. Holman, Heat transfer (tenth edition). McGraw-Hill Companies Inc. USA, 2010.

[BB03] A. Bejan, A.D. Bejan, Heat transfer handbook. John Wiley & Sons, Inc., USA 2003.

[SOLID10] [Exces\_thermal31] See: [https://www.solidworks.com/sw/docs/thermal\\_2010\\_eng\\_final.pdf](https://www.solidworks.com/sw/docs/thermal_2010_eng_final.pdf)

[TLLBBE00] N.R.Tas, T.S.J. Lammerink, P.J. Leussink, J.W. Berenschot, H-E. de Bree, M. Elwenspoek, Towards thermal flowsensing with pL/s resolution. *Proceedings of SPIE - The International Society for Optical Engineering*, 2000. DOI: 10.1117/12.395619

[STACK] See: <https://physics.stackexchange.com/questions/281281/about-the-definition-of-boundary-layer>

[MMD16] F. Moukalled L. Mangani, M. Darwish, The finite volume method in computational fluid dynamics. Springer International Publishing, Switzerland, 2016.

[MSMD03] M. J. Moran, H. N. Shapiro, B. R. Munson, and D. P. DeWitt, Introduction to thermal systems engineering: thermodynamics, fluid mechanics, and heat transfer. John Wiley & Sons, Inc. USA, 2003.

[YT] See: [https://www.youtube.com/watch?v=aqUWsU\\_IsK4](https://www.youtube.com/watch?v=aqUWsU_IsK4)



- [SG16] H. Schlichting, K. Gersten, Boundary-layer theory (ninth edition). Springer Nature, Germany, 2016.
- [R82] M.D. Raisinghania, Fluid dynamics with complete hydrodynamics and boundary layer theory. S. Chand & Company PVT. LTD., India, 1982.
- [NW06] J. Nocedal. S.J. Wright, Numerical optimization (second edition), Springer Science+Business Media, LLC, 2006.
- [ELEC19] See: <https://www.noteshatke.com/2019/10/24/electromagnetic-spectrum-the-trick-to-memorize-the-order-of-wavelengths-and-frequencies/>
- [B14] C. Balaji, Essentials of radiation heat transfer. John Wiley & Sons Ltd., United Kingdom, 2014.
- [AST] See: <http://astronomyonline.org/Science/RadioAstronomy.asp>
- [K13] M. KuriaKose, Thermal investigations on polymer dispersed liquid crystal composites & thermo-electric polymer composites using photothermal techniques. Ph.D. thesis, L'Universite Du Littoral-C'ote D'opale, 2013.
- [V21] S. P. Venkateshan, Heat transfer (third edition). Springer Nature, Switzerland, 2021.
- [MBC17] C. Meola, S. Boccardi, and G. M. Carlomagno, Infrared thermography in the evaluation of aerospace composite materials. Woodhead Publishing, Elsevier Ltd., 2017.
- [P80] S. V. Patankar, Numerical heat transfer and fluid flow. Hemisphere Publishing Corporation, USA, 1980.
- [HW20] J. Han, and L. M. Wrigh, Experimental methods in heat transfer and fluid mechanics, Taylor & Francis Group, LLC, USA, 2020.
- [MSM06] W. J. Minkowycz, E. M. Sparrow, J.Y. Murthy, Handbook of numerical heat transfer (second edition). John Wiley & Sons Inc., USA, 2006.
- [MMD16] F. Moukalled, L. Mangani, M. Darwish, The Finite Volume Method in computational fluid dynamics: an advanced introduction with OpenFOAM® and Matlab®, Fluid mechanics and its applications, Vol. 13. Springer International Publishing, Switzerland, 2016.
- [WM16] Wang, and L. di Mare, Hybrid meshing using constrained Delaunay triangulation for viscous flow simulations. International Journal for Numerical Methods in Engineering. Published by John Wiley & Sons Ltd., 2016. DOI: 10.1002/nme.5272
- [LZXX13] Z. Laiping, Z. Zhong, C. Xinghua, H. Xin, A 3D hybrid grid generation technique and a multigrid/parallel algorithm based on anisotropic agglomeration approach. Chinese Journal of Aeronautics, 26 (1) 47-62 (2013).
- [SM03] E. Süli, and D. F. Mayers, An introduction to numerical analysis. Cambridge University Press, United Kingdom, 2003.
- [IJ09] S.R.K. Iyengar, and R. K. Jain, Numerical methods. New Age International (P) Ltd., India, 2009.
- [MC14] C. G. Mingham, D. M. Causon, Introductory finite difference methods for PDEs (first edition). Bookboon, United Kingdom, 2014.
- [S85] G. D. Smith, Numerical solution of partial differential equations: finite difference methods (third edition). Oxford University Press, USA, 1985.
- [L07] R. J. LeVeque, Finite difference methods for ordinary and partial differential equations steady-state and time-dependent problems. Society for Industrial and Applied Mathematics, USA, 2007.
- [LQT18] Z. Li, Z. Qiao, T. Tang, Numerical solution of differential equations: introduction to finite difference and finite element methods. University of Cambridge, United Kingdom, 2018.

- [L21] J. Lobry, A FEM-Green approach for magnetic field problems with open boundaries. *Mathematics*, 9 (2021) 1662.
- [WB92] L. C. Wrobel, and C. A. Brebbia, *Boundary element methods in heat transfer*, Elsevier Science Publishers Ltd, United Kingdom, 1992.
- [B11] A. Belmiloudi, *Heat transfer-mathematical modelling, numerical methods and information technology*. InTech, Croatia, 2011.
- [K16] J. T. Katsikadelis, *The boundary element method for engineers and scientists (second edition)*. Elsevier Ltd., USA, 2016.
- [BO04] T. Barth, and M. Ohlberger, *Finite volume methods: foundation and analysis*, *Encyclopedia of Computational Mechanics*, John Wiley & Sons, Ltd., USA, 2004.
- [AFO15] E.V. Avdeev, V.A. Fursov V.A. Ovchinnikov, An adaptive mesh refinement in the finite volume method. *Proceedings of Information Technology and Nanotechnology (ITNT-2015)*, CEUR Workshop Proceedings, 2015; 1490: 234-241.
- [T02] S. Z. Tomov, *Adaptive methods for finite method approximations*. Ph.D. thesis, Texas A&M University, USA, 2002.
- [SMM10] L. Sun, S. R. Mathur, and J. Y. Murthy, An unstructured finite volume method for incompressible flows with complex immersed boundaries. *Numerical Heat Transfer, Part B*, 58: 217–241, 2010.
- [LWZ16] Z. Lai, B. Wu, and Q. Zou, Finite volume method on hybrid meshes for coastal ocean model. *International Journal of numerical analysis and modeling*, 13 (2016) 310-317.
- [O17] M. N. Özisik et al., *Finite difference methods in heat transfer (second edition)*. CRC Press, Taylor & Francis Group, LLC, USA, 2017.
- [NLS16] P. Nithiarasu, R. W. Lewis, and K. N. Seetharamu, *Fundamentals of the finite element method for heat and mass transfer (second edition)*. John Wiley & Sons, Ltd., United Kingdom, 2016.
- [LSK98] M. Ljungberg, S. E. Strand, M. A. King, *Monte Carlo calculations in nuclear medicine: applications in diagnostic imaging*. IOP Publishing Ltd., United Kingdom, 1998.
- [B01] A. F. Bielajew, *Fundamentals of the Monte Carlo method for neutral and charged particle transport*. The University of Michigan, USA, 2001.
- [FH77] S. K. Fraley, T. J. Hoffman, *A Monte Carlo method of solving heat conduction problems*. Ph. D. Thesis, University of Tennessee, USA, 1977.
- [B18] R. Bahadori et al., A mesh-free Monte-Carlo method for simulation of three-dimensional transient heat conduction in a composite layered material with temperature dependent thermal properties. *International Journal of Heat and Mass Transfer* 119 (2018) 533-541.
- [TK87] S. Tanaka, and T. Kunitomo, Numerical analysis of radiative-convective heat transfer from an extended surface by the Monte Carlo method. *Bulletin of the JSME*, 21 (1987) 258-265.
- [M19] J. R. Mahan, *The Monte Carlo ray-trace method in radiation heat transfer and applied optics*. ASME Press and John Wiley & Sons Ltd., USA, 2019.
- [D03] G. Demirkaya, *Monte Carlo solution of a radiative heat transfer problem in A 3-D rectangular enclosure containing absorbing, emitting, and anisotropically scattering medium*. M.Sc. thesis, The Middle East Technical University, Turkey, 2003.
- [V17] O. N. Vassiliev, *Monte Carlo methods for radiation transport*. Springer International Publishing, Switzerland, 2017

- [BK10] O. M. Belotserkovskii, Y. I. Khlopkov, Monte Carlo methods in mechanics of fluid and gas. World Scientific Publishing Co. Pte. Ltd., USA, 2010.
- [W11] J. C. Wagner et al., Review of hybrid (deterministic/Monte Carlo) radiation transport methods, codes, and applications at Oak Ridge National Laboratory. *Progress in Nuclear Science and Technology*, 2 (2011) 808-814.
- [P85] C. A. Philis et al., Monte-Carlo methods and applications in neutronics, photonics and statistical physics: proceedings of the joint Los Alamos National Laboratory-Commissariat à l'Energie Atomique. Springer Berlin Heidelberg, Lecture Notes in Physics 240, France, (1985) 22–26.
- [RR92] A. F. Rice, and R. W. Roussin, Deterministic methods in radiation transport. Oak Ridge National Laboratory. USA, 1992.
- [W03] M. L. Williams et al., Deterministic photon transport calculations in general geometry for external beam radiation therapy. *Medical Physics* (2003) 30(12):3183-95.
- [BG70] G. Bell, and S. Glasstone, Nuclear reactor theory. Litton Educational Publishing Inc., USA, 1970.
- [H21] Q. He et al., NECP-MCX: A hybrid Monte-Carlo-Deterministic particle-transport code for the simulation of deep-penetration problems. *Annals of Nuclear Energy* 151 (2021) 107978.
- [L21] M. Liu et al., An improved tracking method for particle transport Monte Carlo simulations. *Journal of Computational Physics*, 437 (2021) 110330.
- [D19] L. Deng et al., The coupled neutron transport calculation of Monte Carlo multi-group and continuous cross-section. *Annals of Nuclear Energy*, 127 (2019) 433-436.
- [GGOP21] V. Giménez-Alventosa, V. Giménez Gómez, S. Oliver, PenRed: An extensible and parallel Monte-Carlo framework for radiation transport based on PENELOPE. *Computer Physics Communications*, 267 (2021) 108065.
- [SIP13] R. Smith, H. Inomata, C. Peters, Heat transfer and finite-difference methods. *Supercritical Fluid Science and Technology* 4 (2013) 557-615.
- [M19] Z. Mehrdoost, Unstructured grid adaptation for multiscale finite volume method. *Computational Geosciences* 23 (2019) 1293–1316.
- [Q18] L. Qian et al., Introductory finite volume methods for PDEs. Bookboon, United Kingdom, 2018.
- [RG10] J. N. Reddy, and D. K. Gartling, The finite element method in heat transfer and fluid dynamics (third edition). Taylor and Francis Group, LLC, USA, 2010.
- [HU94] H. Huang, and A. S. Usmani, Finite element analysis for heat transfer. Springer-Verlag, United Kingdom, 1994.
- [B17a] R. Bahadori et al., Two-dimensional transient heat conduction in multi-layered composite media with temperature dependent thermal diffusivity using floating random walk Monte-Carlo method. *International Journal of Heat and Mass Transfer* 115 (2017) 570-580.
- [B17b] R. Bahadori et al., Monte Carlo method simulation for two-dimensional heat transfer in homogenous medium and proposed application to quench propagation simulation. *IEEE Transactions on Applied Superconductivity* 27 (2017) 1-5.
- [SB08] B. Sundén, and C. A. Brebbia, Advanced computational methods and experiments in heat transfer X. WIT Press, USA, 2008.
- [M17] A. A. Minea, Advances in new heat transfer fluids from numerical to experimental techniques. Taylor & Francis Group, LLC., USA, 2017.

- [PC18] W. R. Penney, and E. C. Clausen, Fluid mechanics and heat transfer inexpensive demonstrations and laboratory exercises. Taylor & Francis Group, LLC, USA, 2018.
- [T11] L. Theodore, Heat transfer applications for the practicing engineer. John Wiley & Sons, Inc., USA, 2011.
- [CHR03] W. Cao, W. Huang, R.D. Russell, Approaches for generating moving adaptive meshes: location versus velocity. *Applied Numerical Mathematics* 47 (2003) 121-138.
- [J96] H. Jasak, Error analysis and estimation for the finite volume method with applications to fluid flows, University of London, United Kingdom, 1996.
- [S11] I. Sezai, Lecture notes Fall 2011-2012. Methods for dealing with complex geometries, Part of the course in computational fluid dynamics at Eastern, Mediterranean University, Turkey, 2011.
- [W13] D.J. Van der Westhuizen, Gradient calculations of non-orthogonal meshes in the finite volume method, Potchefstroom Campus, North-West University, USA, 2013.
- [THLZ17] H. Tianliang, W. Hongchun, C. Liangzhi, L. Zhifeng, Finite volume method based neutronics solvers for steady and transient-state analysis of nuclear reactors, *Energy Procedia* 127 (2017) 275-283.
- [EGH00] R. Eymard, T. Gallouet, R. Herbin, Finite volume methods, in: *handbook of numerical analysis*. North-Holland, Netherland, 7 (2000) 713-1020. <https://old.i2m.univ-amu.fr/~herbin/PUBLI/bookevol.pdf>
- [E75] W.C. Edwards, Simultaneous heat and mass transfer in wet wood particles. M.Sc. thesis, University of British Columbia, Canada, 1975.
- [C02] Y. A. Cengel, Heat transfer. McGraw-Hill, USA, 2002.
- [MS06] W. J. Minkowycz, and E. M. Sparrow, Series in computational and physical processes in mechanics and thermal sciences. Taylor & Francis Group, LLC, 2006.
- [LS09] C. Long, and N. Sayma, Heat transfer. Bookboon, United Kingdom, 2009.
- [FT08] M. Favre-Marinet, and S. Tardu, Convective heat transfer. Hermes Science/Lavoisier, France, 2008.
- [F20] C. H. Forsberg, Heat transfer principles and applications. Academic Press, Elsevier Inc., USA, 2020.
- [NK09] G. Nellis, S. Klein, Heat transfer. Cambridge University Press, USA, 2009.
- [A77] Argonne Code Center, 1977. Benchmark Problem Book, Report ANL-7416 (Suppl. 2). Argonne National Laboratory, Argonne, IL
- [LLGC04] P. R. M. Lyra R. de C. F. de Lima, C. S. C. Guimarães, D. K. E. de Carvalho, An edge-based unstructured finite volume procedure for the numerical analysis of heat conduction applications. *Journal of the Brazilian Society of Mechanical Sciences and Engineering* 26 (2004) 160-169.
- [DNK11] A.I. Delis, I.K. Nikolos, and M. Kazolea, Performance and Comparison of Cell-Centered and Node-Centered Unstructured Finite Volume Discretizations for Shallow Water Free Surface Flows. *Archives of Computational Methods in Engineering* 18, 57–118 (2011). <https://doi.org/10.1007/s11831-011-9057-6>
- [DT11] B. Diskin, J. L. Thomas, Comparison of node-centered and cell-centered unstructured finite-volume discretizations: inviscid fluxes. *American Institute of Aeronautics and Astronautics Journal* 49 (2011) 836-854.
- [SB15] T. Siau, A. M. Bayen, An introduction to MATLAB programming and numerical methods for engineers. Academic Press, Elsevier Inc., USA, 2015.

- [E13] J. F. Epperson, An introduction to numerical methods and analysis (second edition). John Wiley & Sons, Inc., USA, 2013.
- [BFB16] R. L. Burden, J. D. Faires, A. M. Burden, Numerical analysis (tenth edition), Cengage Learning, USA, 2016.
- [S12] T. Sauer, Numerical analysis (second edition). Pearson Education, Inc., USA, 2012.
- [CC15] S. C. Chapra, R. P. Canale, Numerical methods for engineers (seventh edition). McGraw-Hill Education, USA, 2015.
- [B16] J. C. Butcher, Numerical methods for ordinary differential equations. John Wiley & Sons, Ltd, United Kingdom, 2016.
- [P18] G. F. Pinder, Numerical methods for solving partial differential equations: a comprehensive introduction for scientists and engineers, John Wiley and Sons, Inc., USA, 2018.
- [SW06] J. N. Stephen, and J. Wright, Numerical optimization (second edition), Springer Science+Business Media, LLC, USA, 2006.
- [EXFOR21] Experimental nuclear reaction data (EXFOR) (2021) <http://www.nds.iaea.org/exfor/>. Database Version of 2021
- [B15] J. Blazek, computational fluid dynamics principles and applications (third edition). Elsevier Ltd., 2015.
- [GGH16] P. M. Gerhart, A. L. Gerhart, J. I. Hochstein, Fundamentals of fluid mechanics (eighth edition). John Wiley & Sons, Inc. 2016.
- [Q22] G. Qin, Computational fluid dynamics for mechanical engineering. Taylor & Francis Group LLC, USA, 2022.
- [R17] B. E. Rapp, Microfluidics: modeling, mechanics, and mathematics. Elsevier Inc., 2017.
- [HP97] R.R. Huilgol, and N. Phan-Thien, Computational Viscoelastic Fluid Dynamics. Rheology Series, 6 (1997) 397-472.
- [BCHS08] S. Berg, A. W. Cense · J. P. Hofman, R. M. M. Smits. Two-phase flow in porous media with slip boundary condition. Transport in Porous Media 74 (2008) 275–292.
- [KSKM18] S. Koshizuka, K. Shibata, M. Kondo, T. Matsunaga, Moving particle semi-implicit method: a mesh free particle method for fluid dynamics. Academic Press, Elsevier Inc., USA, 2018.
- [VM07] H. K. Versteeg, and W. Malalasekera, An introduction to computational fluid dynamics: the finite volume method (second Edition). Pearson Education, United Kingdom, 2007.
- [T92] D. B. Thompson, Numerical methods 101- convergence of numerical models. USGS Staff -- Published Research. 115, 1992.
- [K17] D.R. Kiran, Total Quality Management, Chapter 27 - Reliability Engineering. Butterworth-Heinemann, United Kingdom, 2017.
- [P09] E.B. Podgorsak, Radiation physics for medical physicists (second edition). Springer-Verlag Berlin, 2009.
- [GMBM04] B. D. Guenther, A. Miller, L. Bayvel, J.E. Midwinter, Encyclopedia of modern optics. Elsevier Science Publishing Co Inc. 2004.
- [K84] B. G. Kyle, Chemical and process thermodynamics, Prentice-Hall, United States, 1984.
- [A07] S. N. Ahmed, Physics and engineering of radiation detection, Elsevier, United Kingdom, 2007

- [S13] R. H. H. Scott et al., Measuring fast electron spectra and laser absorption in relativistic laser-solid interactions using differential Bremsstrahlung photon detectors. *Review of Scientific Instrument* 84, 083505, 2013.
- [M14] A. Manninen, Clinical applications of radiophotoluminescence (RPL) dosimetry in evaluation of patient radiation exposure in radiology. Ph.D. thesis, University of Oulu, 2014.
- [NOBEL21] The Nobel Prize in Physics 1921. NobelPrize.org. Nobel Prize Outreach AB 2021. Tue. 7 Sep 2021. <<https://www.nobelprize.org/prizes/physics/1921/summary/>>
- [NKV10] M. Nečemer, P. Kump, K. Vogel-Mikuš, Use of x-ray fluorescence-based analytical techniques in phytoremediation, *Handbook of Phytoremediation*, Nova Science Publishers, Inc, 2010.
- [M16] C. Mahuvava, Monte Carlo evaluation of the dose perturbation effect of various hip prostheses during pelvic megavoltage photon radiotherapy. M.Sc. thesis, UFS & Universitas academic hospital, 2016.
- [P14] E. B. Podgoršak, *Compendium to radiation physics for medical physicists*. Springer-Verlag Berlin, 2014.
- [C07] N. J. Carron, *An introduction to the passage of energetic particles through matter*. Taylor & Francis Group, United States, 2007.
- [JC53] H. E. Johns, J. R. Cunningham, *The physics of radiology* (fourth edition), Charles C Thomas, United States, 1953.
- [L17] A. Lechner, Particle interactions with matter, *Proceedings of the CAS–CERN accelerator school: beam injection, extraction and transfer*, Italy, 2017.
- [FS20] C. W. Fabjan, H. Schopper, *Particle physics reference library; Volume 2: Detectors for particles and radiation*. Springer, Switzerland 2020.
- [E55] R. D. Evans, *The atomic nucleus*, McGraw-Hill, Inc. United States, 1955.
- [J17] T. E. Johnson, *Introduction to health physics* (fifth edition), McGraw-Hill, United States, 2017.
- [LR04] C. Leroy, P. Rancoita, *Principles of radiation interaction in matter and detection*. World Scientific Publishing Co. Pte. Ltd., Singapore, 2004.
- [RLK17] H. Rehman, J. Lee, Y. Kim, Comparison of the Laser-Compton scattering and the conventional Bremsstrahlung X-rays for photonuclear transmutation. *International Journal of Hydrogen Energy*, 2017. <https://doi.org/10.1016/j.ijhydene.2017.07.041>
- [P16] E. B. Podgoršak, *Radiation physics for medical physicists* (third edition). Springer International Publishing Switzerland, 2016.
- [R14] C. Rangacharyulu, *Physics of nuclear radiations concepts, Techniques and Applications*, y Taylor & Francis Group, LLC., United States, 2014.
- [PT73] H. W. Patterson, R. H. Thomas, *Accelerator health physics*, Academic Press, Inc., United States, 1973.
- [SHJ50] H. Steinwedel, J. Hans, D. Jensen, and P. Jensen, *Physical Review*, 79 (1950) 1019.
- [S07] M. G. Stabin, *Radiation protection and dosimetry: an introduction to health physics*. Springer Science+Business Media, LLC, 2007.
- [S14] M. Sherer, et al., *Radiation protection in medical radiography* (seventh edition), Elsevier Inc., United States, 2014.
- [P14] R. Prasad, *Nuclear physics*. Dorling Kindersley (India) Pvt. Ltd., India, 2014.
- [TL15] N. Tsoulfanidis, S. Landsberger, *Measurement & detection of radiation* (4th Edition), Taylor & Francis Group, LLC, United States, 2015.

- [MG05] J. Magill, J. Galy, Radioactivity radionuclides radiation. Springer-Verlag Berlin, 2005.
- [S55] K. Siegbahn, Beta and gamma –ray spectroscopy. North-Holland Publishing Company, Netherlands, 1955.
- [MDS18] J. Magill, R. Dreher, Zs. Soti, Karlsruher Nuklidkarte, 10. Edition, 2018.
- [N13] H. Naik, Photo-neutron reaction cross-section for  $^{93}\text{Nb}$  in the end-point Bremsstrahlung energies of 12-16 and 45-70 MeV. Nuclear Physics A 916, 168-182, 2013.
- [D88] K. Debertin, R.G. Helmer, Gamma-and x-ray spectrometry with semiconductor detectors. North-Holland, Netherlands, 1988.
- [K10] G. F. Knoll, Radiation detection and measurement (forth edition). John Wiley & Sons, Inc., United States 2010.
- [DNA13] N. Demir, Z. Nur Demirci, I. Akkurt, Monte Carlo simulations of Bremsstrahlung photon yields from thin targets with electron beams between 10 and 40 MeV. Radiation Effects & Defects in Solids, 168, 372–377, 2013.
- [C18] B. G. Cade et al., thermal design of a 100 kW electron to gamma converter at TRIUMF. Journal of Physics: Conference Series 1067 032023, 2018.
- [H07] E. M. A. Hussein, Radiation mechanics principles and practice, Elsevier Ltd. United Kingdom, 2007.
- [G48] M. Goldhaber, On nuclear dipole vibrations. Physical Review, 74, 1046-1049, 1948.
- [H70] E. Hayward, Photonuclear reactions. United States Department of Commerce. 1970.
- [DK14] P. Degtiarenko, G. Kharashvili, 2014. Proceedings, 12th meeting of task-force on shielding aspects of accelerators, targets and irradiation facilities (SATIF-12): United States, 284-290, 2014.
- [D12] P. Degtiarenko, “Electronuclear Interactions in FLUKA”, 2nd FLUKA advanced course and workshop – Vancouver, 2012.
- [DK14] P. Degtiarenko, G. Kharashvili, Contribution of the direct electronuclear processes to thin target activation. Fermi National Accelerator Laboratory (SATIF-12), United states, 2014.
- [TFS20] A. Tsechanskia, D. Fedorchenko, V. Starovoitova, On the contribution of the electronuclear reaction to the photonuclear production of Mo-99 and other radioisotopes. Radiation Physics and Chemistry 177, 109108, 2020.
- [PM] See: <https://www.matsusada.com/column/sem-tech1.html>
- [MKN96] X. Mao, K.R. Kase, W.R. Nelson, Giant dipole resonance neutron yields produced by electrons as a function of target material and thickness, SLAC-PUB-6628, 1996.
- [BNB16] M. Bobeica, D. Niculae et al., Radioisotope production for medical applications at ELI-NP. Romanian Reports in Physics 68, Supplement P. S847–S883, 2016.
- [M19] MEVEX The accelerator technology company. High Power Linacs for Isotope Production. [http://www.mevex.com/Brochures/Brochure\\_High\\_Energy.pdf](http://www.mevex.com/Brochures/Brochure_High_Energy.pdf) [accessed May 17, 2019]

The page features two large, overlapping blue triangles. One triangle is positioned in the upper right, pointing towards the bottom left. The other triangle is in the lower left, pointing towards the top right. They meet in the center, creating a white diamond-shaped area where the title is located.

## **Appendix A**

## **Benchmarking**



In this section of work, to verify the calculations' results, some problems (from literature) as a benchmark are presented and compared. The first two problems are concerning the Bremsstrahlung yield calculations for verification of the MCNP modeling, while the third presented problem is for validation of COMSOL Multiphysics software simulation.

**Problem1: Bremsstrahlung yield for high energetic electrons (MCNP code)**

**Bremsstrahlung yield for tungsten disc-shaped converter target with 30 MeV incident electron beam energy**

The first problem is a disc-shaped tungsten converter target with a 2 cm diameter and 3.5 mm thickness. The number of photons per incident electron was sampled, and the results showed that the difference between the two calculations (based on two simulations) is acceptable (around 5 percent). This difference can be due to using different nuclear libraries and code versions [20].

**Problem2: Bremsstrahlung yield for low energetic electrons (MCNP code)**

**Bremsstrahlung yield for tantalum disc-shaped converter target with 10 MeV incident electron beam energy**

The second problem is a tantalum disc-shaped converter target. An electron beam with 10MeV energy is incident on the target with 0.05 cm thickness. The Bremsstrahlung yield is obtained for photons emitted in the angular interval 0°to 90°and energy range of 0 to 10 MeV using MCNP code. A good agreement with the relative error of around 1 percent was obtained when two simulations were compared [19].

**Problem3: Temperature distribution determination (COMSOL Multiphysics software)**

**Temperature in beryllium disc for 40 MeV electron beam energy and 3.1 mA electron beam current**

The third problem is a beryllium disc shape with a thickness of 20 μm where an electron beam with an energy of 40 MeV, a current of 3.1 mA (Rhodotron) with 1mm FWHM (see chapter..., part...) hit it during 2.5 ms. According to the COMSOL Multiphysics software modeling, the temperature in the target rises to around 700 K. In order to compare the obtained results, a theoretical assessment can be employed as follows [18]:

$$\Delta T[K] = \frac{E[\text{Joule}]}{C[\frac{\text{Joule}}{\text{g.K}}].m[\text{g}]}$$

where C is the heat capacity, m is the mass of the irradiated volume in target, and E is the energy deposition. Considering the heat capacity of beryllium around  $1.82 [\frac{\text{Joule}}{\text{g.K}}]$ , 1mm beam

area with a corresponding fraction of total energy deposition ( $14.62 [\text{Joule} / \text{s}]$ ) in the target in 2.5 ms irradiation time, the temperature reaches around 710 K. The calculated temperature based on the COMSOL Multiphysics software, and theoretical assessment is quite similar to each other. The small temperature difference can be because, despite the theoretical

calculations, the heat conduction is considered in the COMSOL Multiphysics software (effect of the heat conduction term is small because of the short irradiation time).

#### **Problem4: Radionuclide yield calculation**

##### **<sup>225</sup>Ra yield calculation for 25 MeV pencil beam**

<sup>225</sup>Ra yield calculations comparison was performed for a 25 MeV pencil electron beam, 20 kW electron beam power, and 5 mm in diameter. The beam impinges on a tantalum converter target with 10 mm in diameter and 3 mm thickness. There is a 2 mm vacuum gap to the <sup>226</sup>Ra target, which is 10 mm in diameter, 2.6 mm thickness, and a mass of 1 g (equivalent to  $1.27 \text{ g/cm}^2$ ). The result of calculations presented in [89] and obtained using Fluka code is 5.36 Ci at (EOB) for a 10 days irradiation. The activity can be presented as  $0.99 \text{ GBq/kW.day}$ .

For a consistent comparison between the reference [89] and our calculations, proper modeling with the same parameters and geometries must be applied. On this basis, MCNP modeling with the same inputs described in the reference [89] was considered, and <sup>225</sup>Ra yield estimation using Eqs.2.2 and 2.3 revealed  $0.96 \text{ GBq/kW.day}$ . Comparing the results shows a relative error of about 3%, which can be due to using a different cross-section library or different simulation time (nps).



## **Appendix B**

### **Publications**





# European Patent

Title:

**High Power Converter Target Assembly, Related Facility and Method to  
Produce Bremsstrahlung for Photonuclear Reactions**

Patent No.: EP21212627.0

Submitted: 06.12.2021

# **A new moving-mesh Finite Volume Method for the efficient solution of two-dimensional neutron diffusion equation using gradient variations of reactor power**

*Nuclear Engineering and Technology* 51 (2019) 1181-1194

**Authors:** M. Vagheian, D.R. Ochbelagh\*, M. Gharib

**Abstract:** In this paper, a new numerical moving mesh method was developed to efficiently move the meshes in regions of interest based on a new discretization approach for the governing partial differential equations in two-dimensional geometries. According to the developed method, for the first time, the computational proposed framework was able to formulate the complex mathematical equations regarding the conventional moving mesh methods in a more straightforward algebraic form and reduce the computational time, leading to increasing the computational efficiency. The newly developed discretization algorithm, accuracy, and execution time were investigated for proper neutron population estimation in some nuclear reactors. The results confirmed that the proposed method is able to properly and accurately move the meshes in regions of interest automatically and, therefore, improve the accuracy in neutron flux estimation in a reasonable execution time.

**Contributions:** I conducted the entire mathematical derivation of the governing equations in the new discretized introduced moving mesh method. In addition, I performed programming in the MATLAB software with more than 80'000 programming lines. Moreover, I carried out the analysis and evaluation of the obtained results. Finally, I wrote the manuscript of this paper as the first author and performed the revisions after the journal's reviewers sent the feedback.

**License:** Authors can include their articles in dissertations for non-commercial purposes.



## Original Article

# A new moving-mesh Finite Volume Method for the efficient solution of two-dimensional neutron diffusion equation using gradient variations of reactor power

Mehran Vagheian, Dariush Rezaei Ochbelagh\*, Morteza Gharib

Department of Energy Engineering and Physics, Tehran Polytechnic University (Amirkabir University of Technology), P.O. Box 15875-4413, Tehran 009821, Iran

## ARTICLE INFO

## Article history:

Received 9 September 2018

Received in revised form

23 January 2019

Accepted 14 February 2019

Available online 16 February 2019

## Keywords:

New moving-mesh finite volume method  
Efficient form of control volume  
deformation

Gradient-based non-orthogonal calculations  
Efficient neutron diffusion calculations

## ABSTRACT

A new moving-mesh Finite Volume Method (FVM) for the efficient solution of the two-dimensional neutron diffusion equation is introduced. Many other moving-mesh methods developed to solve the neutron diffusion problems use a relatively large number of sophisticated mathematical equations, and so suffer from a significant complexity of mathematical calculations. In this study, the proposed method is formulated based on simple mathematical algebraic equations that enable an efficient mesh movement and CV deformation for using in practical nuclear reactor applications. Accordingly, a computational framework relying on a new moving-mesh FVM is introduced to efficiently distribute the meshes and deform the CVs in regions with high gradient variations of reactor power. These regions of interest are very important in the neutronic assessment of the nuclear reactors and accordingly, a higher accuracy of the power densities is required to be obtained.

The accuracy, execution time and finally visual comparison of the proposed method comprehensively investigated and discussed for three different benchmark problems. The results all indicated a higher accuracy of the proposed method in comparison with the conventional fixed-mesh FVM.

© 2019 Korean Nuclear Society, Published by Elsevier Korea LLC. This is an open access article under the CC BY-NC-ND license (<http://creativecommons.org/licenses/by-nc-nd/4.0/>).

## 1. Introduction

The neutron diffusion equation is the approximation of the neutron transport equation and indicates that the neutron current is proportional to the gradient of the neutron flux by considering a diffusion coefficient. Although the calculation of the neutron diffusion equation is simpler than the transport equation, the solutions cannot always be determined analytically and numerical approximation becomes essential for extracting quantitative solutions. On this basis, many numerical methods of solving the neutron diffusion equation have been introduced and among them, the FVM is always considered as an efficient discretization method if the number and the shape of CVs apply properly [1,2].

In terms of computational modeling, FVM usually concerns with different discretization and partitioning schemes. The cell-centered and vertex-centered are two major approaches for volume partitioning. In the former case, solutions are assumed to be stored in

the center of the primal grid cell in contrast to the latter one in which the solutions are assumed to be stored in the cell corner positions [3,4].

Previous studies in the nuclear reactor engineering have usually approached the neutron diffusion problems with the use of fixed-meshes due to their simplicity of implementation. However, a prerequisite for developing an efficient method of the neutron diffusion calculations is the ability to apply different mesh density resolution in regions of interest [5–9]. On this basis, some new methods have been developed and among them, the moving-mesh approach has priority on account of its new capabilities. To date, different approaches for generating moving adaptive methods have been introduced. It has been shown that the moving-mesh computational framework relying on the ability of mesh movement falls mainly into two main groups: the location-based method and the velocity-based method. The location-based method controls directly the location of mesh points whereas the velocity-based method targets directly the time derivative of the mapping or the mesh velocity. Each of these methods can also be divided into various sub-groups [10]. According to the proposed moving-mesh methods, it has been shown that the key to the success of the

\* Corresponding author.

E-mail address: [ddrezaey@aut.ac.ir](mailto:ddrezaey@aut.ac.ir) (D.R. Ochbelagh).

proposed moving-mesh methods lies in a suitable choice of a mesh density function and the dependency of the solution to the mesh history [10,11]. To date, few neutron diffusion works have been performed using the moving-mesh methods. In the following, some of the most important works are briefly presented. In 2015, a moving mesh method was developed for the numerical solution of the equilibrium radiation diffusion equations in two dimensions. It was shown that the method works well for radiation diffusion equations and can produce numerical solutions of good accuracy and stability. Due to the relatively considerable computational cost of the method, a two-level mesh movement strategy was proposed to increase the computational efficiency while maintaining a comparable accuracy [12]. In another work, a moving-mesh scheme based on local conservation was presented for a class of scale-invariant second-order nonlinear diffusion problems with moving boundaries that had the ability to preserve the scaling properties and be exact at the nodes for initial conditions sampled from similarity solutions. It was shown that superlinear convergence can be achieved for different initial conditions. However, the drawback of the method was that the accuracy of the solutions does not increase consistently with decreasing the time step intervals for both the porous medium equation (PME) and the simplistic glacier equation (SGE) that have been considered in the work [13]. According to the aforementioned proposed moving-mesh methods, they were developed for certain applications which are not related to the efficient neutronic assessment of the nuclear reactor cores. More importantly, almost all the aforementioned proposed methods relying on the ability of mesh movement employs a relatively large number of sophisticated mathematical equations [10–13]. However, for practical applications in nuclear reactors the

The main aim of this study is to introduce a new mesh movement and CV deformation technique for the accurate and efficient solution of the two-dimensional neutron diffusion equation. The proposed method employs the gradient-based calculations to determine the regions of interest. For the implementation of the stationary iterative neutron diffusion equation based on the moved-meshes, the discretization of the governing equations is performed regarding the over-relaxed cell-centered non-orthogonal FVM. To evaluate and assess the results of the calculations, including the power profile and  $k_{eff}$ , three different benchmark problems are finally considered. The main novelties of this work can accordingly be mentioned as: development of a new moving-mesh method based on the FVM, employing the over-relaxed cell-centered non-orthogonal method for the development of the proposed moving-mesh method, considering the gradient of power for the mesh movement and CV deformation and finally, development of a new mechanism for the boundary deformation of CVs. Apart from this fact that the proposed method is a new method, there is not also any similar method for the accurate and efficient neutron diffusion calculations by considering the gradient of power and using the moving-mesh method. Additionally, the developed moving-mesh method in this work is based on a very simple algebraic mathematical calculation that can be considered for practical application of the nuclear reactor core assessment.

## 2. Multi-group neutron diffusion equation

The General form of the steady-state, multi-group neutron diffusion equation can be described as [1,2,14]:

$$\left\{ \sum_{rg} (\mathbf{r}) \phi_g(\mathbf{r}) \right\} - \left\{ \text{div} \cdot D_g(\mathbf{r}) \text{grad} \phi_g(\mathbf{r}) \right\} = \sum_{g'=1}^G \left\{ \Sigma_{g' \rightarrow g}(\mathbf{r}) \phi_{g'}(\mathbf{r}) \right\} + \left\{ \frac{1}{k} \chi_g \left\{ \sum_{g'=1}^G \nu \Sigma_{fg'}(\mathbf{r}) \phi_{g'}(\mathbf{r}) \right\} \right\}, \quad g = 1, 2, \dots, G \quad (1)$$

computational cost, the complexity of implementation and sophisticated mathematical calculations associated with these methods could be overwhelming. Accordingly, development of an efficient neutron diffusion solver code for nuclear reactor applications that can move the meshes without any complexity of implementation is highly recommended.

where the terms from left to right are the removal, leakage, neutron in-scattering and fission production, respectively. It should be noted that Eq. (1) is a linear partial differential equation and can be transformed into a set of algebraic equations based on different discretization approaches. The finite volume scheme of the neutron diffusion equations starts with the integral form of Eq. (1) as:

$$\int_{\Omega_p} \left\{ \sum_{rg} (\mathbf{r}) \phi_g(\mathbf{r}) \right\} d\Omega - \int_{\Omega_p} \left\{ \text{div} \cdot D_g(\mathbf{r}) \text{grad} \phi_g(\mathbf{r}) \right\} d\Omega = \int_{\Omega_p} \sum_{g'=1}^G \left\{ \sum_{g'=1}^{g' \rightarrow g} (\mathbf{r}) \phi_{g'}(\mathbf{r}) \right\} d\Omega + \int_{\Omega_p} \left\{ \frac{1}{k} \chi_g \left\{ \sum_{g'=1}^G \nu \Sigma_{fg'}(\mathbf{r}) \phi_{g'}(\mathbf{r}) \right\} \right\} d\Omega, \quad g = 1, 2, \dots, G \quad (2)$$



where  $\Omega_p$  is the CV of cell  $P$ .

### 3. Mathematical formulation

The mathematical formulation for the discretization of the neutron diffusion equation is presented in this section. On this basis, this section of work has been divided into three different parts. The mathematical approximations based on the midpoint rule are presented in the first part. In the second part, the procedure of leakage term discretization is carried out in details regarding the over-relaxed decomposition method. In the final part of this section, the discretization of the removal, fission production and neutron in-scattering terms of the neutron diffusion equation are considered.

#### 3.1. The midpoint approximation

The midpoint approximation for the cell-centered FVM where the parameters are stored in the center of the cells can be considered as follows:

$$\int_{\Delta u} \psi(u) du = \bar{\psi} \Delta u, \quad (3)$$

in which  $\psi$  and  $u$  refer to an arbitrary function and independent variable, respectively. The volume-averaged and the face-averaged approximations of function  $\psi$  can be expressed as follows:

$$\iiint_{\Omega_p} -\text{div} \cdot \{D_g(\underline{r}) \underline{\text{grad}}(\phi_g(\underline{r}))\} d\Omega = - \sum_{f=1}^F \{ \tilde{D}_g(c_f) \underline{\text{grad}}(\tilde{\phi}_g(c_f)) \cdot S_f \underline{n}_f \}. \quad (8)$$

$$\bar{\psi} = \frac{\int_{\Omega_p} \psi(\Omega) d\Omega}{\int_{\Omega_p} d\Omega}, \quad (4)$$

$$\tilde{\psi} = \frac{\int_{S_p} \psi(s) ds}{\int_{S_p} ds}, \quad (5)$$

where  $\bar{\psi}$  and  $\tilde{\psi}$  denote the volume-averaged and face-averaged approximation of function  $\psi$ , respectively. In the following, the discretization procedure of the neutron diffusion equation is presented in details.

#### 3.2. Leakage term discretization

In the case of leakage term, an approximation of the gradients at the cell face of each CV requires to be determined. Considering the divergence theorem, the integral of the divergence over the CV  $\Omega_p$  will be as follows:

$$\iiint_{\Omega_p} -\text{div} \cdot \{D_g(\underline{r}) \underline{\text{grad}}(\phi_g(\underline{r}))\} d\Omega = \oint_{S_p} -D_g(\underline{r}) \underline{\text{grad}}(\phi_g(\underline{r})) \cdot \underline{n} ds, \quad (6)$$

where  $\underline{n}$  is the perpendicular vector to  $S_p$  at each point, pointing outward of the cell. Also,  $d\Omega$  and  $ds$  indicate infinitesimal elements of the volume and surface, respectively. The bonding surface  $S_p$  can be decomposed into  $F$  faces which are considered as  $S_f, f = 1, \dots, F$  ( $F = 4$  for two-dimensional rectangular geometries).

By considering the face-averaged diffusion coefficient using Eq. (5), the leakage term of the neutron diffusion equation can be expressed as follows:

$$\oint_{S_p} -D_g(\underline{r}) \underline{\text{grad}}(\phi_g(\underline{r})) \cdot \underline{n} ds = - \sum_{f=1}^F \{ \tilde{D}_g(c_f) \underline{\text{grad}}(\tilde{\phi}_g(c_f)) \cdot S_f \underline{n}_f \}, \quad (7)$$

where  $\underline{n}_f$  is the perpendicular vector to  $S_f$  for face  $f$ ,  $c_f$  is the center of face  $f$  and  $\tilde{\phi}_g(c_f)$  is the face-averaged of the scalar  $\phi_g$  over the face  $f$  in point of  $c_f$ . The coordinates of  $c_f$  for each face can be obtained using the arithmetic averaging between the coordinates of the vertices of each corresponding face. Eq. (7) can finally be written as:

In Eq. (8), computation of  $\{\underline{\text{grad}}(\tilde{\phi}_g(c_f))\}$  needs to be considered in each shared interface if boundaries are non-orthogonal. For determination of the gradient in the cell face, first, the gradients at the cell center meshes should be obtained. For this purpose, the Green-Gauss method which represents an intuitive and sound basis for gradient calculation has been considered. Regarding the Green-Gauss theorem, the average gradient of a scalar  $\phi_g$  in a closed volume  $\Omega_p$  can be obtained by:

$$\iiint_{\Omega_p} \underline{\text{grad}}(\phi_g(\underline{r})) d\Omega = \oint_{S_p} \phi_g(\underline{r}) \underline{n} ds, \quad (9)$$

$$\underline{\text{grad}}(\phi_g(\underline{r})) = \frac{1}{\Omega_p} \oint_{S_p} \phi_g(\underline{r}) \underline{n} ds, \quad (10)$$

where  $S$  refers to the surface area. For a 2nd order scheme with midpoint quadrature, the Green-Gauss method takes on the following discrete form for a polyhedral:

$$\underline{\text{grad}}(\phi_g(\underline{r})) = \frac{1}{\Omega_p} \sum_{f=1}^F \tilde{\phi}_g(c_f) \underline{n}_f S_f. \quad (11)$$

Up to this point, the average gradient of a linear function at the rectangular cell centroid is presented exactly by Eq. (11). The spatial gradient variations of the neutronic power for each CV can simply be determined from the neutron flux gradient as:

$$\underline{\text{grad}}(\text{power}_p) = \sum_{g=1}^G \underline{\text{grad}}(\phi_{g,p}) E \sum_{f \in g,P}, \quad (12)$$

where  $E$  is the constant fission energy released and  $\underline{\text{grad}}(\text{power}_p)$  is the gradient of power for CV  $P$ . To remove the impact of the absolute total reactor power from the results, Eq. (12) can be divided by the total reactor power (which can be considered as  $\text{Power}_{\text{Total}}$ ).

The next step is to deform the CVs regarding the spatial gradient variations of the reactor power. Note, in this step, the neutron diffusion equations should be derived and discretized regarding the non-orthogonal FVM. This, however, requires some advanced

$$\underline{\text{grad}}(\phi_g(r)) = \frac{1}{\Omega_P} \sum_{f=1}^F \tilde{\phi}_g(c_f) \underline{S}_f, \quad (14)$$

in which

$$\underline{S}_f = \underline{k}_f + \underline{A}_f, \quad (15)$$

where  $\underline{k}_f$  and  $\underline{A}_f$  denote non-orthogonal and orthogonal terms, respectively. By considering Eq. (13), and substituting Eq. (15) into Eq. (8) one can obtain the leakage term of the neutron diffusion equation as:

$$\begin{aligned} \iiint_{\Omega_P} -\text{div} \cdot \{D_g(r) \underline{\text{grad}}(\phi_g(r))\} d\Omega &= \sum_{f=1}^F \left\{ -\tilde{D}_g(c_f) \underline{\text{grad}}(\tilde{\phi}_g(c_f)) \cdot \underline{S}_f \right\} = \\ &= \left\{ \sum_{f=1}^F -\tilde{D}_g(c_f) (\underline{\text{grad}}(\tilde{\phi}_g(c_f))) \cdot \underline{A}_f \right\} + \left\{ \sum_{f=1}^F -\tilde{D}_g(c_f) (\underline{\text{grad}}(\tilde{\phi}_g(c_f))) \cdot \underline{k}_f \right\}. \end{aligned} \quad (16)$$

mathematical expression and consideration which have been presented and explained in the following.

The non-orthogonality of the FVM can be performed using the decomposition of the face area vector into two separate ones. Up to now, three main decomposition methods have been introduced and developed, namely, the minimum correction approach [15], the orthogonal correction approach [16] and the over-relaxed approach [17]. It has been shown that the last proposed method has superiority to the other ones [17–19]. On this basis, in the current study, the discretization of the leakage term is performed regarding the over-relaxed approach.

For obtaining the leakage term based on the over-relaxed approach, first, the following figure should be considered:

In this figure,  $\underline{S}_f$  and  $\underline{d}_f$  represent, respectively, the face area vector and a line connector between the centers of CVs. By considering the face area vector as:

For the sake of simplicity,  $\tilde{D}_g(c_f)$  and  $\tilde{\phi}_g(c_f)$  will be written as  $D_{g,f}$  and  $\phi_{g,f}$ , respectively. The first right-hand term of Eq. (16) can simply be obtained as:

$$\sum_{f=1}^F (-D_{g,f}) (\underline{\text{grad}}(\tilde{\phi}_{g,f})) \cdot \underline{A}_f = \sum_{f=1}^F (-D_{g,f}) \left| \underline{A}_f \right| \frac{\phi_{g,N} - \phi_{g,P}}{\left| \underline{d}_f \right|}, \quad (17)$$

in which  $\underline{A}_f$  is considered as:

$$\underline{A}_f = \frac{\underline{d}_f}{\underline{d}_f \cdot \underline{S}_f} \left| \underline{S}_f \right|^2. \quad (18)$$

In order to calculate  $\left| \underline{A}_f \right|$  one can have:

$$\left| \underline{A}_f \right| = \sqrt{\left( \frac{d_{f,x}}{(d_{f,x} S_{f,x} + d_{f,y} S_{f,y})} \left| \underline{S}_f \right|^2 \right)^2 + \left( \frac{d_{f,y}}{(d_{f,x} S_{f,x} + d_{f,y} S_{f,y})} \left| \underline{S}_f \right|^2 \right)^2}. \quad (19)$$

$$\underline{S}_f = \underline{n}_f S_f, \quad (13)$$

one can rewrite Eq. (11) and obtain  $\underline{\text{grad}}(\phi_g(r))$  as:

To obtain  $\left| \underline{S}_f \right|$  in Eq. (19) based on the non-orthogonal grid approach, the following figure should be considered (see Fig. 1).

As is shown in Fig. 2,  $\underline{S}_f$  has been decomposed into the vector components. So, it can be written as:

$$\underline{S}_f = S_{f,x} \underline{i} + S_{f,y} \underline{j}, \quad (20)$$

The orthogonal leakage term can then be given by:

$$\sum_{f=1}^F (-D_{g,f}) \{ \underline{\text{grad}}(\tilde{\phi}_{g,f}) \} \cdot \underline{\Delta}_f = \sum_{f=1}^F (-D_{g,f}) \left| \underline{\Delta}_f \right| \frac{\phi_{g,N} - \phi_{g,P}}{|\underline{d}_f|} =$$

$$\sum_{f=1}^F \left\{ \frac{(-D_{g,f}) \left\{ \sqrt{\left( \frac{d_{f,x}}{(d_{f,x}S_{f,x} + d_{f,y}S_{f,y})} |\underline{S}_f|^2 \right)^2 + \left( \frac{d_{f,y}}{(d_{f,x}S_{f,x} + d_{f,y}S_{f,y})} |\underline{S}_f|^2 \right)^2} \right\}}{|\underline{d}_f|} (\phi_{g,N} - \phi_{g,P}) \right\}. \quad (21)$$

The next step should be devoted to the non-orthogonal part of the leakage term (see Eq. (16)). The non-orthogonal term can be expanded in  $x$  and  $y$  directions as follows:

$$\sum_{f=1}^F (-D_{g,f}) \{ \underline{\text{grad}}(\phi_{g,f}) \} \cdot \underline{k}_f =$$

$$\sum_{f=1}^F \left\{ (-D_{g,f}) \{ \underline{\text{grad}}(\phi_{g,f,x}) \} \cdot k_{f,x} + (-D_{g,f}) \{ \underline{\text{grad}}(\phi_{g,f,y}) \} \cdot k_{f,y} \right\}, \quad (22)$$

where  $k_{f,x}$  and  $k_{f,y}$  refers to the non-orthogonal corrector factor for face  $f$  in  $x$  and  $y$  direction, respectively, and are specified by:

$$k_{f,x} = S_{f,x} - \Delta_{f,x}, \quad (23)$$

$$k_{f,y} = S_{f,y} - \Delta_{f,y}. \quad (24)$$

Regarding the aforementioned equations, the discretized form of the leakage term has been determined. The following section deals with the discretization procedure of other diffusion equation terms.

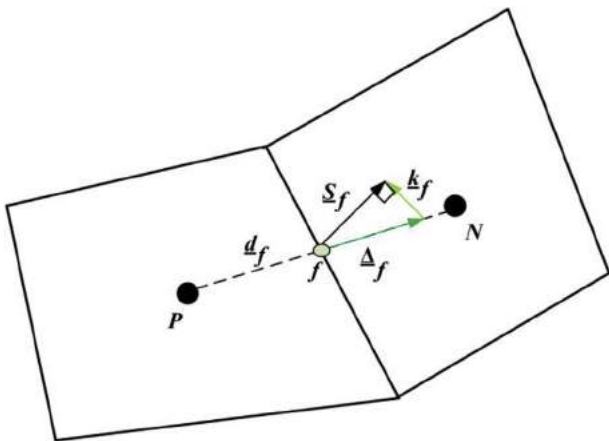


**Fig. 1.** The over-relaxed approach to the treatment of rectangular non-orthogonal finite volume scheme.

### 3.3. Discretization of the remaining neutron diffusion terms

The discretization of the remaining neutron diffusion terms is considered in this section. In order to discretize the terms of removal, neutron in-scattering and fission production of Eq. (2),

one can simply consider the midpoint rule (Eqs. (3), (4) and (5)) and obtain:

$$\iiint_{\Omega_P} \left\{ \sum_{g'} (\underline{r}) \phi_{g'}(\underline{r}) \right\} d\Omega = \overline{\left\{ \sum_{g'} (\underline{r}) \phi_{g',P} \right\}} \Omega_P, \quad (25)$$

$$\iiint_{\Omega_P} \sum_{g'=1}^G \left\{ \sum_{g'}^{g' \rightarrow g} (\underline{r}) \phi_{g'}(\underline{r}) \right\} d\Omega = \sum_{g'=1}^G \overline{\left\{ \Sigma_P^{g' \rightarrow g} \phi_{g',P} \right\}} \Omega_P, \quad (26)$$

$$\iiint_{\Omega_P} \left\{ \frac{1}{k} \chi_g \left\{ \sum_{g'=1}^G \nu \Sigma_{fg'}(\underline{r}) \phi_{g'}(\underline{r}) \right\} \right\} d\Omega$$

$$= \overline{\left\{ \frac{1}{k} \chi_{g,P} \left\{ \sum_{g'=1}^G \nu \Sigma_{fg',P} \phi_{g',P} \right\} \right\}} \Omega_P. \quad (27)$$

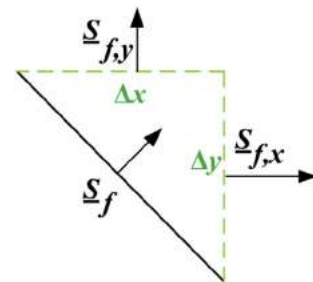


**Fig. 2.** Schematic view of the face area vector components.

### 3.4. BCs for the deformed CVs

In the neutron diffusion approximation, the BCs are divided into two groups, namely, Dirichlet BC and Von Neumann BC. The Dirichlet BC prescribes a zero fixed value at the boundary (known as zero flux BC) while the other one prescribes a fixed gradient at the boundary [14]. Both of these BCs and the corresponding discretization methodology have been considered in the following.

Based on the over-relaxed gradient-based approach, a CV with a boundary face can be illustrated as Fig. 3.

As is shown, the vector  $\underline{d}_f$  that already connects the centers of the CVs herein connects the center of the neighboring CV to the center of the boundary face.

To treat the gradient of a non-orthogonal mesh at the BCs, the vector  $\underline{d}_n$ , between the center of the CV and normal to the face needs to be determined and employed instead of  $\underline{d}_f$ . On this basis,  $|\underline{d}_n|$  can be written by considering Fig. 3 as:

$$|\underline{d}_n| = \cos(\alpha) |\underline{d}_f|. \quad (28)$$

So,  $\underline{d}_n$  can simply be given by:

$$\underline{d}_n = \frac{\underline{S}_f \underline{d}_f \cdot \underline{S}_f}{|\underline{S}_f| |\underline{S}_f|}. \quad (29)$$

Note, the orthogonal component  $\underline{A}_f$  is equal to the face area vector  $\underline{S}_f$  (see Fig. 3), and the non-orthogonal corrector factor  $\underline{k}_f$  no longer required to be considered.

The leakage term of the neutron diffusion equation by considering Dirichlet B.C. can be given as:

$$(-D_{gf}) \underline{A}_f \cdot \{\underline{\text{grad}}(\phi_{g,b})\} = (-D_{gf}) |\underline{A}_f| \frac{\phi_{g,b} - \phi_{g,p}}{|\underline{d}_n|}, \quad (30)$$

where  $|\underline{A}_f|$  can be obtained from Eq. (19). In Eq. (30),  $\phi_{g,b}$  is the flux at the boundary face and has been assumed valid along the entire boundary face. By considering  $\phi_b = 0$ , Eq. (30) can finally be written as:

$$(-D_{gf}) \underline{A}_f \cdot \{\underline{\text{grad}}(\phi_{g,b})\} = (-D_{gf}) |\underline{A}_f| \frac{(-\phi_{g,p})}{|\underline{d}_n|}. \quad (31)$$

In the following, the Von Neumann BC will be considered. The

Von Neumann B.C. is described as  $\{-D_{gf} \underline{S}_f \cdot \underline{\text{grad}}(\phi_{g,b})\}$ . Regarding the reflective BC ( $\underline{\text{grad}}(\phi_{g,b}) = 0$ ), one can assume that

$$(-D_{gf}) \underline{A}_f \cdot \{\underline{\text{grad}}(\phi_{g,b})\} = 0. \quad (32)$$

However, in the case of the albedo BC ( $\beta$ ) that defined as the ratio between the current out of the reflecting region to the current into the reflecting region [14], one can express that

$$(-D_{gf}) \underline{A}_f \cdot \{\underline{\text{grad}}(\phi_{g,b})\} = |\underline{A}_f| \left( \frac{1}{2} \frac{1-\beta}{1+\beta} \right) (\phi_{g,p}). \quad (33)$$

## 4. Mechanism and procedure of the mathematical calculations

The proposed mechanism and procedure of the mathematical calculations are presented in this section. The mathematical calculations for the solution of the stationary neutron diffusion equation are considered to be performed based on a new mesh movement and CV deformation technique. Additionally, an initial non-iterative gradient-based calculation needs to be carried out to obtain gradient value at each CV. On this basis, the general calculation procedure for implementation of the proposed method can be expressed as three different parts including the gradient-based calculations, mesh movement in addition to the CV deformation and finally stationary iterative neutron diffusion calculations. In the following, the required explanations for the implementation of the calculations have been presented in details.

### 4.1. Initial gradient-based calculations

The initial gradient-based calculations for the implementation of the proposed method are presented in this section. In order to determine the gradient variations of the reactor power at each CV, the gradient of neutron fluxes should be calculated based on Eq. (14). According to Eq. (14), in order to obtain the gradient of neutron fluxes, the neutron flux solution for all neutron energy groups is required to be determined. The solution of the neutron fluxes can be determined using the iterative stationary neutron diffusion calculation. The iterative solution strategy for the stationary neutron diffusion calculations has been described in the literature [14]. After determining the gradient variations of the neutron fluxes, one can simply obtain the gradient variations of the reactor power using Eq. (12).

### 4.2. Mesh movement and CV deformation

The mechanism of mesh movement and CV deformation is presented in this section. According to the proposed method, it has been assumed that the mesh density resolution and CV deformation is performed with respect to the relative gradient variations of the reactor power in the entire reactor core configuration.

The derived formulas in section 3 are based on the cell-centered FVM and are assumed that this assumption is also valid in the case of deformed CVs. In order to locate the moved-meshes in the middle of the CVs, the boundaries of all CVs should also be moved. For the movement of the cell boundaries, the coordinates of the two vertices meshes that form a cell boundary should be obtained. For this purpose, one can employ the coordinates of the moved-meshes that have been determined in the earlier steps. The entire procedure of refinement, including the mechanism of mesh movement, the cell boundary determination, and finally, the mesh point

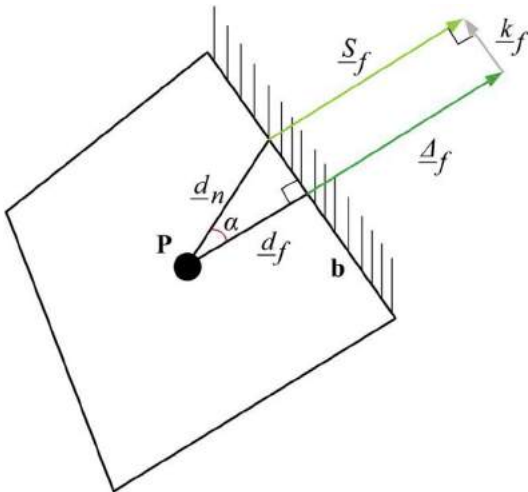


Fig. 3. CV of a non-orthogonal rectangular mesh with a boundary face.

reconsideration is presented in the following.

### Step 1. Mesh movement mechanism

The mechanism of mesh movement is the first step of the proposed moving-mesh FVM. In this step, the meshes should be moved based on the gradient variations of the reactor power. In the case of 2-D rectangular geometries, the new position of each cell center meshes in the  $x$ -direction can be given by:

$$X^{new} = X^{old} + \left\{ X^{old} \times \frac{1}{\left\{ \frac{\text{grad}\{power_{p,x}\}}{Power_{Total}} \right\}} \right\}, \quad (34)$$

where  $X^{old}$  and  $X^{new}$  are the position of the original (fixed) and new (moved) meshes, respectively. In Eq. (34),  $\text{grad}\{power_{p,x}\}$  is the gradient power of CV  $P$  in the  $x$ -direction. Additionally,  $Power_{Total}$  indicates the total neutronic reactor power and is applied to remove the dependence of the results on the reactor power. Similarly, in the  $y$ -direction, one can have:

$$Y^{new} = Y^{old} + \left\{ Y^{old} \times \frac{1}{\left\{ \frac{\text{grad}\{power_{p,y}\}}{Power_{Total}} \right\}} \right\}. \quad (35)$$

As is shown in Eqs. (34) and (35), the new cell center positions in each direction are in reverse relation to the calculated relative gradient of power in the same direction. To prevent any unwanted large value which can be obtained based on a small value of the denominator, a limitation is needed to be considered for the rising of the parameter. In this study, the limitation of the denominator was considered to be obtained based on the number of meshes that exist in each region of the reactor with the same material composition (i.e. group constants). To be more precise, because at least one mesh point should be located in each region of the reactor, so the limitation of the mesh movement is considered based on the number of meshes in each region and the complexity (dimensions of each region) of the problem.

### Step 2. Cell boundary determination

The cell boundary determination is the second step of the proposed moving-mesh FVM. In order to implement the cell boundary determination, the cell to cell refinement needs to be performed. On this basis, it is required to start from one cell and then consider the neighboring cells. The first cell is assumed to be the cell from the bottom-left corner (cell (1,1) in Fig. 4). Note, the short segments that are shown in Fig. 4, are the boundaries of the problem. Let these segments consider fixed, so, the coordinates of the three points of the cell (1,1) are known and the coordinate of only one point requires to be obtained (white triangular point in Fig. 4). This can simply be performed by the arithmetic averaging between four surrounded cell-centered meshes which in the case of the aforementioned cell, they are (1,1), (2,1), (1,2) and (2,2). The cell boundary determination of the other CVs can similarly be performed from left to right and then from bottom to top CVs.

Based on this step, the cell boundaries are moved and deformed with respect to the position of the moved-meshes. More precisely, although there is not any particular equation between the cell boundaries and gradient variations of power, there is a direct relationship between the density resolution of the CVs and meshes. Therefore, as can be observed later in the results section (section 5), there should be higher CV resolutions in regions with higher gradient variations of power.

It is interesting to note that one possible problem that can be happened during the procedure of the cell boundary determination is the overlapping of the cell centers with the cell boundaries. The

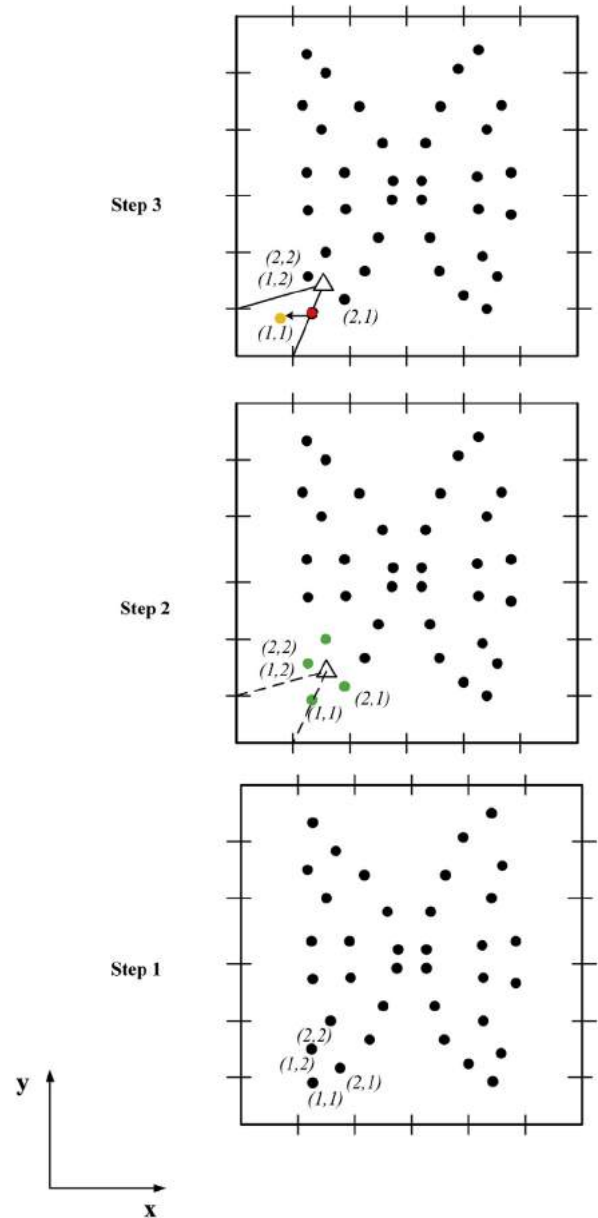


Fig. 4. Stepwise refinement illustration of the proposed algorithm.

schematic view of this problem has been shown in Fig. 4 (Step 2), where the right cell boundary is overlapped with the cell center (1,1). As is mentioned previously, locating of the meshes in the middle of the cells is important. This is the reason that the position of the moved-meshes should be checked and reconsidered. The mechanism of the mesh point reconsideration has been presented in the next step.

### Step 3. Mesh points reconsideration

The mesh point reconsideration is the last step of the proposed moving-mesh FVM. In fact, after the movement of the entire cell center meshes in the first step and cell boundary deformation in Step 2, a new mesh movement should be carried out to solve the possible overlapping problem that was discussed in Step 2. On this basis, in this part of the work, the new coordinates of the moved-meshes should be determined. This can be performed using the arithmetic averaging of the cell coordinate vertices. As is shown in Fig. 4 (Step 3), only by a simple arithmetic averaging of the four



coordinate vertices (where in the case of the cell (1,1) are the bottom and left segments in addition to the triangle mesh point and the left-bottom corner), the proper position of the cell center meshes can be obtained.

#### 4.3. Stationary iterative neutron diffusion calculations

The stationary iterative neutron diffusion calculations are considered in this section of the study. According to the previous discussion, the iterative neutron diffusion calculations are required to be implemented after the process of the mesh movement and CV deformation. The solution strategy and flow diagram of these calculations can be found in the literature [14]. To reduce the execution time of the proposed method, the solution of the stationary rough calculations from the first step that was based on the fixed-meshes is applied as the initial guess on the accurate stationary iterative neutron diffusion calculations based on the moved-meshes. The procedure used to transfer the solution from the fixed-meshes to the moved-meshes can be carried out based on the interpolation between the results of fixed-meshes (including the flux and power profiles). More precisely, owing to the fact that the position of the moved-meshes is different from those of the fixed-meshes, the solutions cannot be directly transformed and accordingly an interpolation requires to be considered.

### 5. Results and benchmarking

Results and benchmarking of the proposed moving-mesh FVM are presented in this section. It should be noted that the power iteration method and MATLAB software have been considered for the numerical calculation due to their simplicity of implementation and efficiency. Based on the power iteration method, neutron fluxes and  $k_{eff}$  are firstly considered as the initial guesses and then the equations are solved to obtain the correct values of the neutron fluxes and the corresponding  $k_{eff}$ . More precisely, the neutron flux for each mesh point and neutron energy group is searched iteratively (known as an inner iteration) and after converging the results,  $k_{eff}$  is calculated based on the updated values of neutron fluxes. If the relative difference of the new  $k_{eff}$  does not meet the dedicated convergence criteria, the new  $k_{eff}$  is used again to obtain new neutron fluxes (is called the outer iteration). This process will be repeated until the results all converged according to the dedicated values for the convergence criterion. In this work,  $4E-5$  and  $1E-8$  values are considered, respectively, as the inner and outer convergence criterion. More details about the stationary iterative calculations of the multi-group neutron diffusion equation can be found in the literature [8,9and14].

The general procedure for implementation of the calculations regarding the proposed moving-mesh FVM are summarized as the following:

In the first step, the initial stationary iterative neutron diffusion calculations are performed to obtain the neutron flux/power profile. Then, the gradient-based calculations for the entire CVs are carried out to obtain the gradient variations of the reactor power. Following this, the mesh movement and CV deformation regarding the proposed stepwise algorithm is implemented. In the last step, the stationary iterative neutron diffusion calculations are performed to obtain the power profile in addition to the corresponding  $k_{eff}$ .

In order to check the performance of the proposed method, three different well-known benchmark problems are considered. The first benchmark problem is the IAEA reactor problem, the second is the BWR fuel bundle problem, and finally, the third is the

BIBLIS reactor problem. The reactor core configurations, BCs and the group constants of these benchmark problems can be found in the literature [20].

For the solution of the benchmark problems, different arbitrary arrays of  $17 \times 17$ ,  $36 \times 36$  and  $34 \times 34$  CVs are employed for the IAEA, BWR fuel bundle and BIBLIS problems, respectively. In order to solve these benchmark problems based on the proposed method, the gradient-based calculations are performed according to the formulas that discussed in the previous sections. Figs. 5–7 show the relative power gradient distribution for the IAEA, BWR fuel bundle and BIBLIS benchmark problems, respectively.

After the gradient-based calculations, the meshes should be moved and the CVs should be deformed using the proposed triple stepwise algorithm. Figs. 8–10 show the visual mesh density resolution of the conventional FVM and the proposed moving-mesh FVM.

Regarding Figs. 8–10, a significant difference of the mesh density resolution can be found between the two aforementioned methods. Interestingly, it can be revealed that the meshes are moved with respect to the gradient variations of the reactor power. This result is quite revealing the capability of the proposed method for the mesh movement and CV deformation based on the gradient variations of the reactor power.

Tables 1–3 compare the results of  $k_{eff}$  between the conventional FVM and the proposed moving-mesh FVM for the IAEA, BWR fuel bundle and BIBLIS reactor test problems, respectively. The error of calculations has been investigated using the Relative Percent Error (RPE(%)) [8,9]. As Tables 1–3 show, there is a considerable difference between the error of calculations. More precisely, these tables reveal that the solutions based on the proposed method are more accurate compared with the conventional FVM. Tables 1–3 also compare the results of the execution times between the proposed moving-mesh FVM and the conventional FVM. Regarding the fact that execution time varies depending upon the computer, programming language and programming style in use, the relative execution time is considered for facilitating comparison between the proposed moving-mesh FVM and the conventional fixed-mesh FVM. Accordingly, the relative execution time of the proposed method with respect to the execution time of the orthogonal FVM has been presented in Tables 1–3. As is observable from these tables, there is no significant difference between the execution time of the two aforementioned methods. The reasons for the small

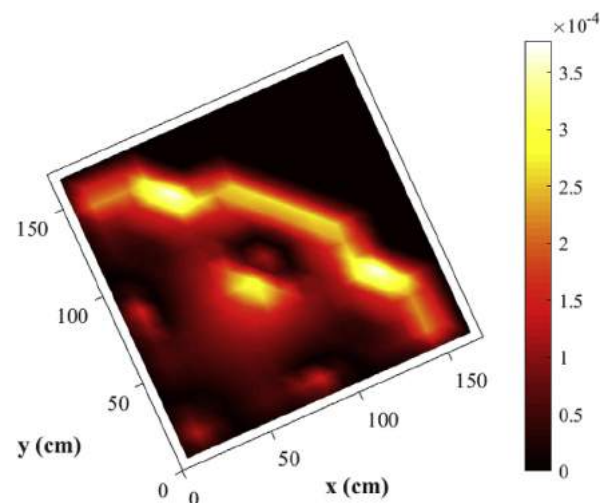


Fig. 5. Calculated relative power gradient distribution for the IAEA benchmark problem.

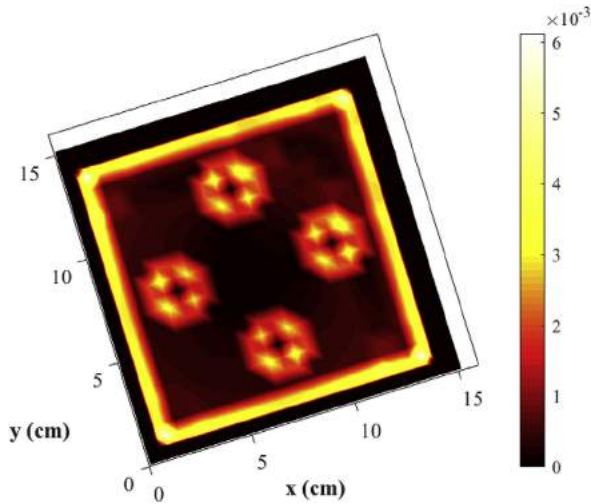


Fig. 6. Calculated relative power gradient distribution for the BWR fuel bundle benchmark problem.

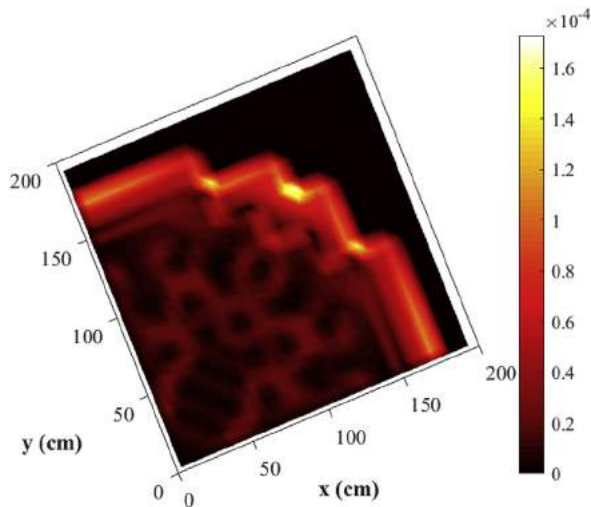


Fig. 7. Calculated relative power gradient distribution for the BIBLIS benchmark problem.

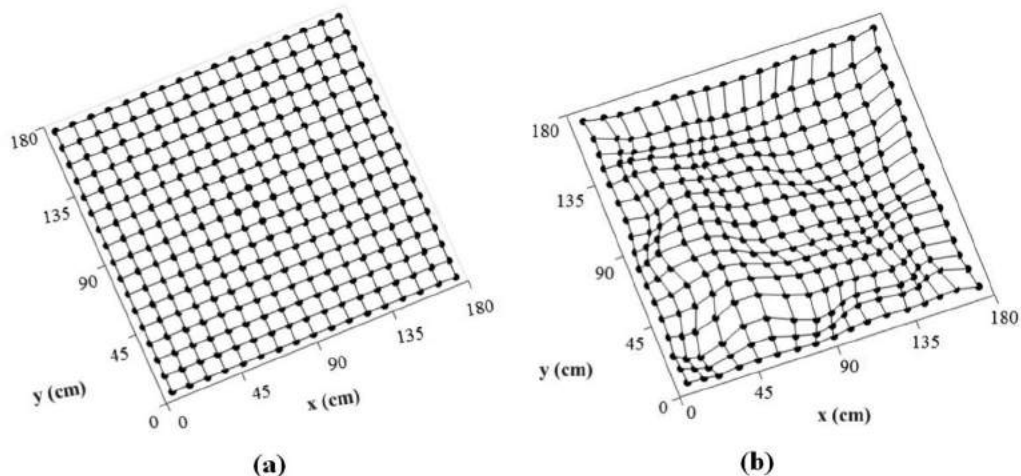


Fig. 8. Fixed (a) and moved (b) meshes of the IAEA benchmark problem.

difference of the execution time are investigated in section 5.1.

The results of the relative power distribution for the IAEA, BWR fuel bundle and BIBLIS reactor benchmark problems are presented in Figs. 11–13, respectively. Note that to obtain the power values, first, the normalization of the neutron fluxes proceeds as follows [8,9 and 20]:

$$\frac{1}{\Omega_{Core}} \int_{\Omega_{Core}} \sum_g \nu \sum_{fg} \phi_g d\Omega = 1. \quad (36)$$

Then, the calculated fluxes are employed to obtain the assembly powers [20]. The reference data for the IAEA benchmark problem is based on the results in reference [20]. It also should be noted that due to the lack of power values in the reference for the BWR fuel bundle problem, the reference solution of the relative power values has been obtained using the thermal and fast flux distribution which has been reported in the literature [20]. In the case of BIBLIS reactor benchmark problem, the reference data is the results that have been presented in the published work [21].

As is observable in Figs. 11–13, the results based on the proposed FVM have higher accuracy when compared to the conventional orthogonal FVM. Moreover, as is shown in Figs. 11–13, the accuracy of the calculations is more evident in the regions with high gradient variations of the reactor power. A possible explanation for these results might be related to the higher mesh density resolution in these regions compared to the other regions. Another important point in Figs. 11–13 are related to the non-orthogonal shape of CVs and orthogonal shape of reactor zones. To be more precise, the material zones in nuclear reactors are generally in orthogonal shapes (as is also the cases of the benchmark tests employed in this paper), however, the CVs based on the proposed method are in non-orthogonal shapes. On this basis, for facilitating consistent accuracy between the results of the conventional FVM and proposed moving-mesh FVM, the volume averaging technique was employed accordingly to Fig. 14:

As is observable in Fig. 14, regarding the volume averaging technique the value of each CV that are located in each zone of the reactor is taking into account with respect to its volume ratio to the volume of the corresponding zone. This technique was considered for presenting the results of power distribution in Figs. 11–13 for making comparison between the results obtained from the aforementioned methods.

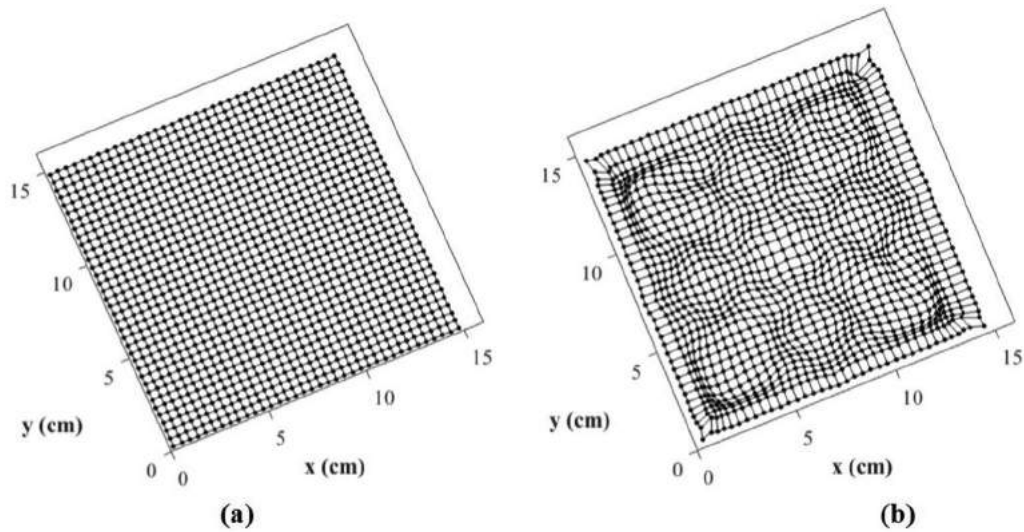


Fig. 9. Fixed (a) and moved (b) meshes of the BWR fuel bundle benchmark problem.

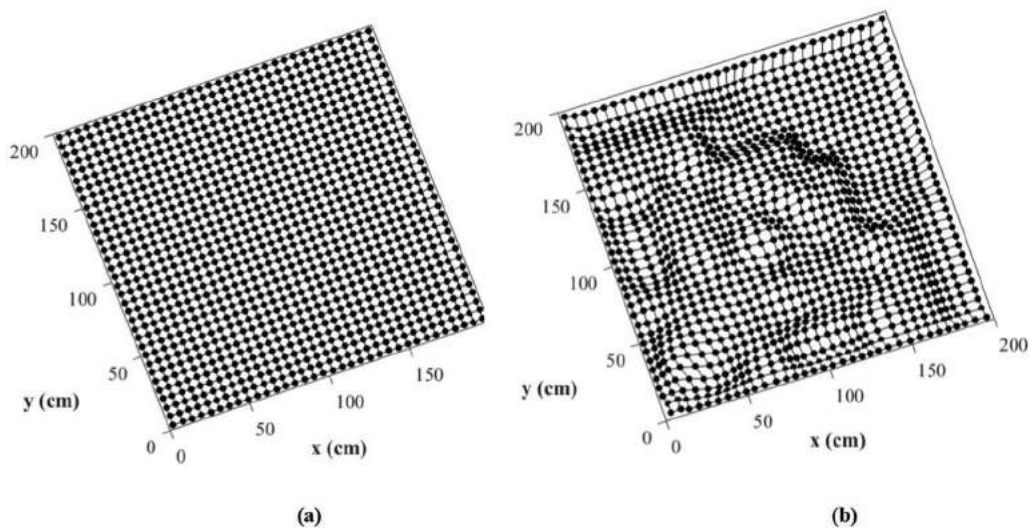


Fig. 10. Fixed (a) and moved (b) meshes of the BIBLIS benchmark problem.

**Table 1**

Comparison of the calculated  $k_{eff}$  and the relative execution time for the IAEA benchmark problem.

Method	$k_{eff}$	RPE(%)	Relative Execution Time
The proposed moving-mesh FVM	1.02968	0.00874	1.03
The conventional fixed-mesh FVM	1.02994	0.03399	...

$k_{eff}$  reference solution is 1.02959 [20].

**Table 2**

Comparison of the calculated  $k_{eff}$  and the relative execution time for the BWR fuel bundle benchmark problem.

Method	$k_{eff}$	RPE(%)	Relative Execution Time
The proposed moving-mesh FVM	1.08560	0.00921	1.06
The conventional fixed-mesh FVM	1.08613	0.05804	...

$k_{eff}$  reference solution is 1.0855 [20].

### 5.1. Execution time investigation

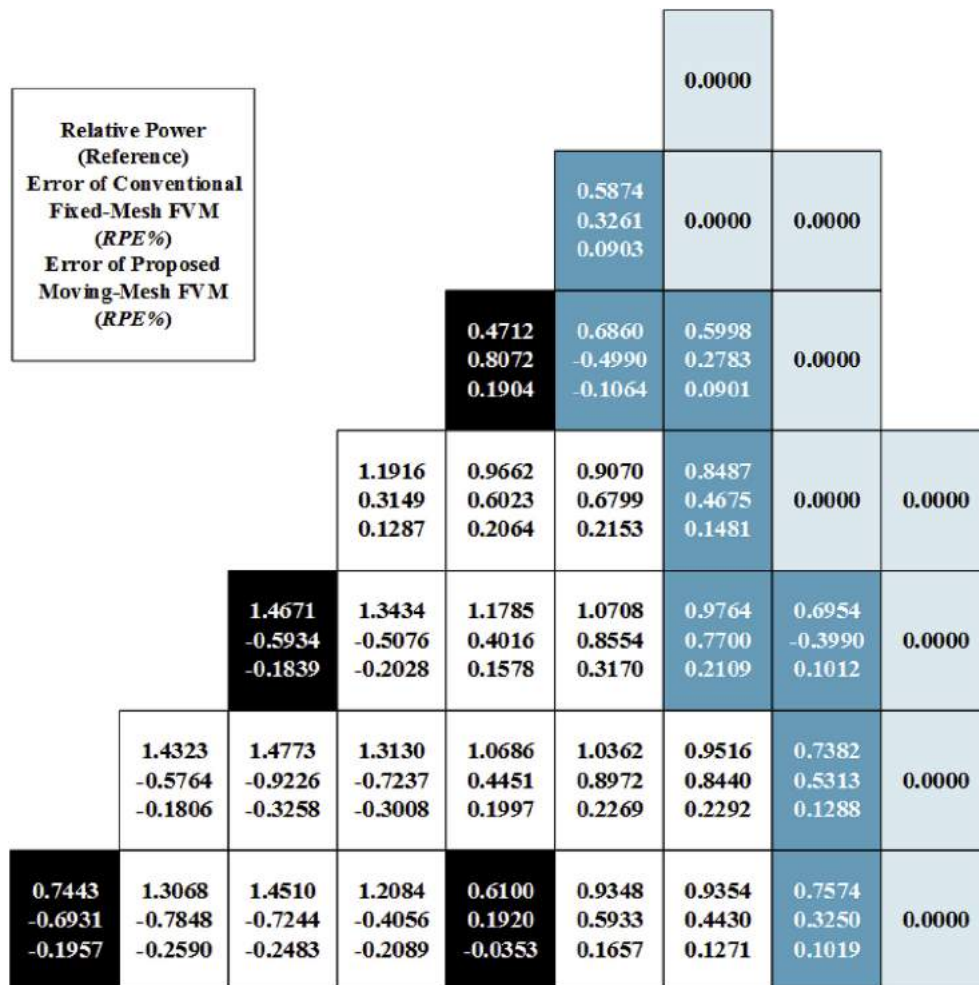
Regarding the fact that the execution time varies depending

upon the computer, programming language and programming style in use, the relative execution time is considered for facilitating comparison between the proposed moving-mesh FVM and



**Table 3**Comparison of the calculated  $k_{eff}$  and the relative execution time for the BIBLIS benchmark problem.

Method	$k_{eff}$	RPE(%)	Relative Execution Time
The proposed moving-mesh FVM	1.02530	0.01756	1.04
The conventional fixed-mesh FVM	1.02598	0.08389	...

 $k_{eff}$  reference solution is 1.02512 [21].**Fig. 11.** One-fourth view of relative power distribution in the IAEA benchmark problem.

conventional fixed-mesh FVM. The execution time in this work was considered based on the total time consumed from the point at which the input data have been read and initialize to the point that the solution of the calculations has been determined. The results of the execution time from Tables 1–3 show that the solution based on the proposed method requires a little more time to be executed than the other method due to the extra initial gradient-based calculations for the mesh movement and CV deformation. However, it is apparent from Tables 1–3 that there were no significant differences between the results of the execution times. It is also interesting to elaborate on the discussion by detailed comparisons of the number of outer and inner iterations between calculations with and without moving-mesh method. In the case of IAEA problem, it is found that the inner and outer iterations are, respectively, 167 and 49 for the conventional FVM, and 175 and 49 for the proposed method. In the case of the BWR problem, the inner and outer iterations are, respectively, 251 and 86 for the conventional FVM, and

262 and 88 for the proposed method. And finally, for the BIBLIS benchmark problem, the inner and outer iterations are obtained, respectively, 248 and 81 for the conventional FVM, and 260 and 82 for the proposed method. Regarding the number of iterations it can be observed that an explanation for the small difference between the execution times of the conventional FVM and the proposed method is due to the small difference between the total number of iterations. Additionally, it can be seen that the proposed method has almost the same number of outer iteration with the conventional FVM. This is due to the fact that the solution of the  $k_{eff}$  which were obtained initially using the fixed-meshes are then employed as the initial guess of the subsequent iterative neutron diffusion calculations based on the moved-meshes. In the case of inner iteration, it can be seen that the proposed method has higher number of inner iterations compared to the conventional FVM for each benchmark problems. This is due to the fact that the neutron flux values for the moved-meshes are almost different from the



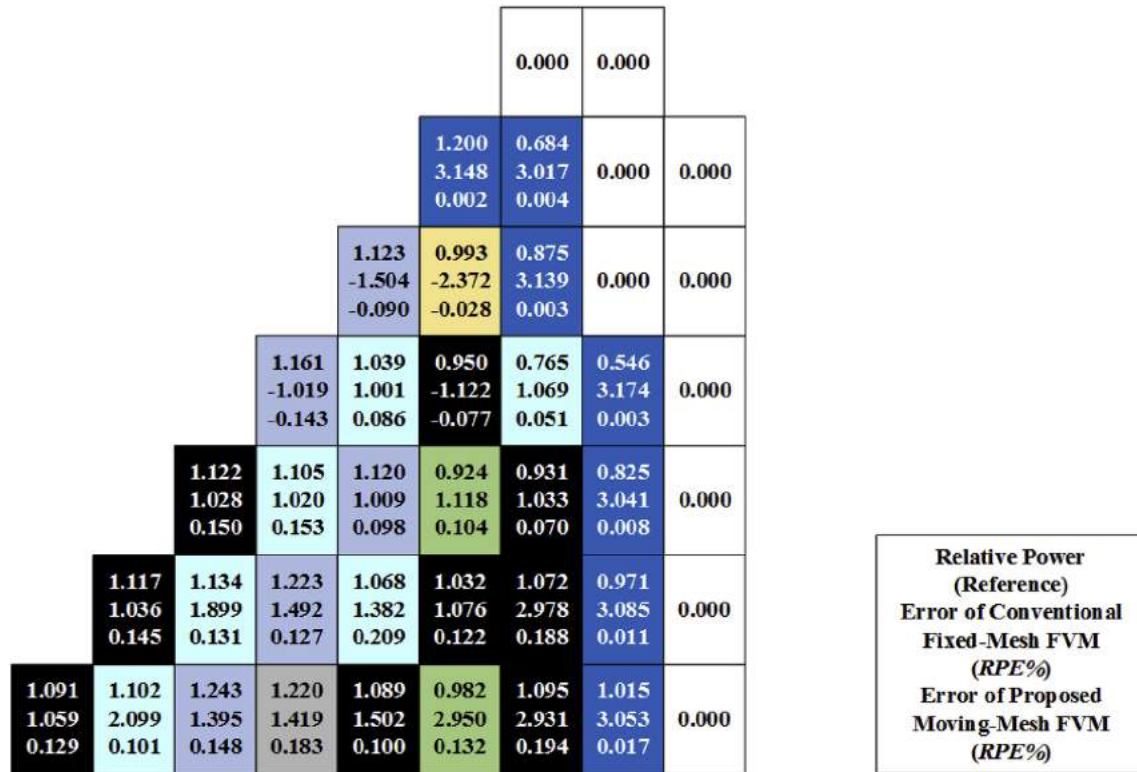


Fig. 13. One-fourth view of relative power distribution in the BIBLIS benchmark problem.

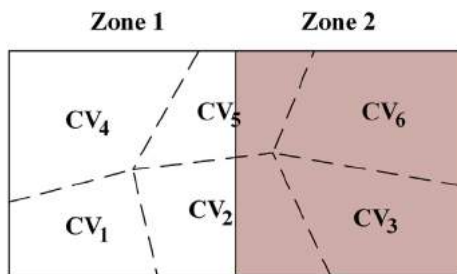
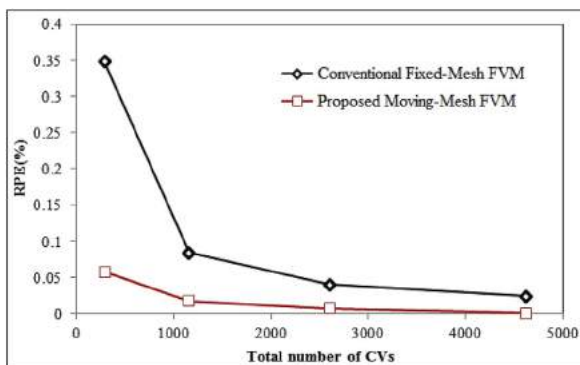


Fig. 14. Schematic view of the CVs position in each reactor zone regarding the proposed method.

Fig. 15. RPEs of the calculated  $k_{eff}$  based on orthogonal and proposed moving-mesh FVM for arrays of  $17 \times 17$ ,  $34 \times 34$ ,  $51 \times 51$  and  $68 \times 68$  CVs.

### 5.3. Performance assessment

In this paper, the accuracy of the proposed method for the power distribution along with the  $k_{eff}$  was investigated. It was shown that the proposed moving-mesh FVM is highly accurate. Moreover, the execution time in addition to the inner and outer iterations of the proposed method was considered and compared with the conventional FVM. It was revealed that not only the proposed method is highly accurate, but also is efficient. In order to check the performance of the proposed moving-mesh FVM, further array investigation was performed and compared to the conventional FVM. The results of the comparison indicated that the performance of the proposed method is more acceptable than the conventional FVM. The visual mesh density comparison between the proposed moving-mesh FVM and the conventional FVM also was shown that the mechanism of mesh movement and CV deformation based on the gradient variations of the reactor power is highly effective. In the case of programming effort, the use of the proposed moving-mesh FVM requires to introduce and calculate some extra parameters. More precisely, it requires some specific programming efforts which are not included in developing of the conventional FVM. However, it also should be noted that the proposed moving-mesh FVM developed based on a very simple algebraic mathematical equations which its complexities are not comparable to the previous proposed moving-mesh methods. The major advantage of the proposed new moving-mesh method accordingly appears to be due to highly accurate and efficient solution in addition to the simplicity of implementation.

From another point of view, the proposed moving-mesh FVM showed that it enables the mesh movement and CV deformation based on very simple algebraic mathematical equations. Unlike the fixed-mesh approach, this feature allows an efficient form of diffusion calculation for neutronic assessment of nuclear reactor

cores. Additionally, it is interesting to point out that the proposed moving-mesh FVM can be employed for different applications. More precisely, the proposed method can move meshes and deform CVs based on different parameters (only by changing Eqs. (34) and (35)).

## 6. Conclusion

The objective of this paper was to develop a new moving-mesh FVM for enhancing the accuracy of the two-dimensional neutron diffusion calculations. On this basis, the proposed method formulated for the first time based on a new mesh movement and CV deformation technique regarding the spatial gradient variations of the reactor power. The regions with high gradient variations of the reactor power almost considered as important regions in the neutronic assessment of the nuclear reactors. So, a higher accuracy of the calculations is almost required to be determined for the reactor core analysis.

The general procedure for implementation of the proposed method was expressed as three different parts including gradient-based calculations, mesh movement in addition to CV deformation and finally stationary iterative neutron diffusion calculations. Using the power iteration method, the  $k_{eff}$  along with the spatial reactor power distribution was calculated. The results were benchmarked against the exact results for IAEA, BWR fuel bundle and BIBLIS benchmark problems and then compared with the conventional fixed-mesh FVM. The accuracy of the proposed moving-mesh FVM was also assessed and checked for other arrays of CVs. In all cases, the results showed a higher accuracy of the proposed method than the conventional FVM, particularly in the regions with high gradient variations of the reactor power, where the accuracy of the power densities improved remarkably. The results also indicated that there was no significant difference in execution time between the proposed moving-mesh FVM and the conventional FVM. This was due to the simplicity of the proposed equations for the mesh movement and CV deformation in addition to the efficient procedure of implementation. Possible future works can include applying of this method for transient calculations by taking into account the fuel depletion in which the power gradient varies with the time evolution and can cause the time-dependent mesh movement and CV deformation.

## Appendix A. Supplementary data

Supplementary data to this article can be found online at <https://doi.org/10.1016/j.net.2019.02.011>.

## References

- [1] Hu Tianliang, Wu Hongchun, C. Liangzhi, Li Zhifeng, Finite volume method based neutronics solvers for steady and transient-state analysis of nuclear reactors, *Energy Procedia* 127 (2017) 275–283. <https://doi.org/10.1016/j.egypro.2017.08.102>.
- [2] R.S. Verga, Numerical solution of the two-group diffusion equation in x-y geometry, U.S. Atomic Energy Commission Report WAPD-159, Westinghouse Electric Corp., Atomic Power Division, Pittsburgh, Pa, 1956.
- [3] R. Eymard, T. Gallouet, R. Herbin, Finite volume methods, in: handbook of numerical analysis, vol. 7, North-Holland, Amsterdam, 2000, pp. 713–1020. <https://old.i2m.univ-amu.fr/~herbin/PUBLI/bookevol.pdf>.
- [4] B. Diskin, J.L. Thomas, Comparison of node-centered and cell-centered unstructured finite-volume discretizations: Viscous fluxes, *AIAA J* 49 (2011) 836–854. <https://doi.org/10.2514/1.44940>.
- [5] S.Z. Tomov, Adaptive methods for finite volume approximation, Texas A&M University, 2002.
- [6] G. Theler, Unstructured grids and the multigroup neutron diffusion equation, *Sci. Technol. Nucl. Install.* (2013). Article ID 641863, 26 pages, 2013, <https://doi.org/10.1155/2013/641863>.
- [7] C. Le Potier, A finite volume method for the approximation of highly anisotropic diffusion operators on unstructured meshes, *Finite Volumes for Complex Applications IV*, Marrakesh, Morocco, 2005.
- [8] M. Vagheian, N. Vosoughi, M. Gharib, Enhanced finite difference scheme for the neutron diffusion equation using the importance function, *Ann. Nucl. Energy* 96 (2016) 412–421. <https://doi.org/10.1016/j.anucene.2016.06.031>.
- [9] M. Vagheian, D. Rezaei Ochbelagh, M. Gharib, On an improved box-scheme finite difference method based on the relative event probabilities, *Prog. Nucl. Energy* 88 (2016) 33–42. <https://doi.org/10.1016/j.pnucene.2015.12.003>.
- [10] W. Cao, W. Huang, R.D. Russell, Approaches for generating moving adaptive meshes: location versus velocity, *Appl. Numer. Math.* 47 (2003) 121–138. [https://doi.org/10.1016/S0168-9274\(03\)00061-8](https://doi.org/10.1016/S0168-9274(03)00061-8).
- [11] W. Huang, R.D. Russell, Adaptive moving mesh methods, Springer, New York, 2010.
- [12] X. Yang, W. Huang, J. Qiu, A moving mesh finite difference method for equilibrium radiation diffusion equations, *J. Comput. Phys.* 298 (2015) 661–677. <https://doi.org/10.1016/j.jcp.2015.06.014>.
- [13] M.J. Baines, N. Sarahs, A moving-mesh finite difference scheme that preserves scaling symmetry for a class of nonlinear diffusion problems, *J. Comput. Appl. Math.* 340 (2018) 380–389. <https://doi.org/10.1016/j.cam.2018.02.040>.
- [14] J.J. Duderstadt, L.J. Hamilton, Nuclear reactor analysis, John Wiley & Sons, New York, 1991.
- [15] J. Stewart, Multivariable calculus early transcendentals, fifth ed., Thomson Brooks/Cole, 2003, p. 1168.
- [16] S. Menon, A numerical study of droplet formation and behaviour using interface tracking methods, University of Massachusetts, 2011.
- [17] H. Jasak, Error analysis and estimation for the finite volume method with applications to fluid flows, University of London, 1996.
- [18] I. Sezai, Lecture notes Fall 2011–2012. Methods for dealing with complex geometries, Part of the course in computational fluid dynamics at Eastern, Mediterranean University, 2011.
- [19] D.J. Van der Westhuizen, Gradient calculations of non-orthogonal meshes in the finite volume method, Potchefstroom Campus, North-West University, 2013.
- [20] Report ANL-7416 (Suppl.2), Argonne code center, Benchmark problem book, Argonne National Laboratory, Argonne, IL, 1977.
- [21] S.A. Hosseini, N. Vosoughi, Development of two-dimensional, multigroup neutron diffusion computer code based on GFEM with unstructured triangle elements, *Ann. Nucl. Energy* 51 (2013) 213–226. <https://doi.org/10.1016/j.anucene.2012.07.032>.

# **Introduction to the non-orthogonal gradient-based finite volume method for three-dimensional neutron diffusion calculations with application to the rectangular reactor core configurations**

*Annals of Nuclear Energy* 138 (2020) 107216.

**Authors:** M. Vagheian, D.R. Ochbelagh\*, M. Gharib

**Abstract:** In this paper, a new non-orthogonal Finite Volume Method was developed, relying on a new control volume deformation algorithm in the three-dimensional geometries. The new non-orthogonal Finite Volume Method was developed based on the over-relaxed decomposition method, Green-Gauss method, and gradient-based non-orthogonal method to allow for providing a computational framework to adaptively change the control volume configuration and concentrate them in regions of more importance. The developed method showed that it is able to perform the computations automatically based on the objective function. The method was applied on some benchmarks and showed its high capability in accuracy, performance, and execution time.

**Contributions:** I introduced and formulated the entire mathematical equations, including the discretization form of the governing equations using the new non-orthogonal gradient-based Finite Volume Method. Also, I programmed the entire presented problems using MATLAB software which was around 150'000 programming lines. At the final step, I wrote the manuscript as the first author and revised the paper after receiving the comments from the journal's reviewers.

**License:** Authors can include their articles in dissertations for non-commercial purposes.





# Introduction to the non-orthogonal gradient-based finite volume method for three-dimensional neutron diffusion calculations with application to the rectangular reactor core configurations

Mehran Vagheian, Dariush Rezaei Ochbelagh\*, Morteza Gharib

Amirkabir University of Technology (Tehran Polytechnic), Department of Energy Engineering & Physics, Hafez Avenue, Tehran, Iran



## ARTICLE INFO

### Article history:

Received 20 August 2018

Received in revised form 21 October 2019

Accepted 16 November 2019

Available online 27 November 2019

### Keywords:

New mesh movement method

New control volume deformation method

Three-dimensional neutron diffusion equations

Non-orthogonal hexahedron grids

Efficient FVM

Gradient-based adaptive method

## ABSTRACT

The objective of this research is to introduce a new adaptive non-orthogonal gradient-based Finite Volume Method (FVM) for the accurate solution of the multi-group three-dimensional neutron diffusion equations. This method of calculation is developed for the first time, based on a new method of mesh movement and Control Volume (CV) deformation using the spatial gradient variations of the reactor power. The mesh movement and CV deformation is developed for rectangular three-dimensional reactor core configurations and different boundary conditions.

For verification and evaluation of the proposed method, five benchmark problems have been considered and the results of calculations compared with the reference solutions. The results of solutions involved in obtaining reactor power as well as the corresponding effective multiplication factor showed that the proposed non-orthogonal gradient-based FVM is more accurate than the conventional FVM.

© 2019 Elsevier Ltd. All rights reserved.

## 1. Introduction

The multi-group neutron diffusion approximation of the transport equation has been widely used in nuclear reactor analysis. The analytical solution of this equation is mostly difficult and on this basis, various numerical methods have been developed in many years (Clark and Hansen, 1964; Duderstadt and Hamilton, 1991).

Achieve accurate results via numerical methods even with the current computation speeds has been always a challenging problem. And the high requirement for computation efficiency is yet to be satisfied for some important applications which need perform many times of calculations such as three-dimensional core analyses (Blanchon et al., 1988; Tianliang et al., 2017; Kang and Hansen, 1971).

Many methods of solving the neutron diffusion equations have been developed and introduced in the literature. Among them, the Finite Volume Method (FVM) has been always considered as an efficient form of discretization technique using the proper number and shape of CVs (Verga, 1956; Blanchon et al., 1988; Tianliang et al., 2017; Nakamura, 1977; Barth and Ohlberger, 2004).

Orthogonal and non-orthogonal finite volume schemes can be considered for the numerical solution of the neutron diffusion

equations. While, the standard finite volume approximation with orthogonal grid partitioning scheme is numerically interesting, mostly due to their simplicity for implementation, the other approach has some advantages such as ease of fitting grids around every irregular shape object and the ability to adapt the mesh density resolution in regions of interest (Lyra et al., 2002; Tomov, 2002; Theler, 2013; Droniou and Eymard, 2006; Bernal et al., 2015; Le Potier 2005; Eymard et al., 2000). In recent years, some new methods have been developed to present an efficient form of the finite volume scheme. However, it is interesting to note that almost all of them are based on orthogonal scheme may be due to their simplicity to solving complex mathematical and computational problems (Vagheian et al. 2016a; Vagheian et al., 2016b). In this work, a new adaptive non-orthogonal gradient-based finite volume scheme has been presented to compute the three-dimensional multi-group neutron diffusion equations. The proposed method allows to achieve a various mesh density resolution through the reactor core and also a non-orthogonal formation of hexahedron CVs during the process of calculation.

This paper is organized as follows: In Section 2 the required mathematical formulation of the neutron diffusion equations is presented briefly. Section 3 mainly deals with the development of the required mathematical expressions and formulas for discretization of the governing equations regarding the non-orthogonal finite volume scheme. Next, in Section 4 details on

\* Corresponding author.

E-mail address: [ddrezaey@aut.ac.ir](mailto:ddrezaey@aut.ac.ir) (D.R. Ochbelagh).

the procedure of implementation of the proposed non-orthogonal FVM have been presented. The results and discussion of the calculations are presented in Section 5. This paper is completed then with the conclusion of this study.

## 2. Neutron diffusion equation

In order to derive the discretized finite volume form of the steady-state multi-group neutron diffusion equations, one can consider the general form of the governing equation as (Christensen, 1985; Clifford, 2007; Lamarsh, 1965):

$$\left\{ \sum_{rg} (r) \phi_g(r) \right\} - \{ \nabla \cdot D_g(r) \nabla \phi_g(r) \} = \sum_{g'=1}^G \left\{ \Sigma_{s'}^{g'-g}(r) \phi_{g'}(r) \right\} + \left\{ \frac{1}{k} \chi_g \left\{ \sum_{g'=1}^G v \Sigma_{fg'}(r) \phi_{g'}(r) \right\} \right\}, \quad g = 1, 2, \dots, G \quad (1)$$

where the terms from left to right are the removal, leakage, neutron in-scattering and fission production, respectively, and all the other parameters have their usual meaning.

The starting point for discretization of the neutron diffusion equations is the integration of Eq. (1) on a CV  $P$  as:

$$\int_{\Omega_p} \left\{ \sum_{rg} (r) \phi_g(r) \right\} d\Omega - \int_{\Omega_p} \{ \nabla \cdot D_g(r) \nabla \phi_g(r) \} d\Omega = \int_{\Omega_p} \sum_{g'=1}^G \left\{ \sum_s^{g'-g} (r) \phi_{g'}(r) \right\} d\Omega + \int_{\Omega_p} \left\{ \frac{1}{k} \chi_g \left\{ \sum_{g'=1}^G v \Sigma_{fg'}(r) \phi_{g'}(r) \right\} \right\} d\Omega \quad g = 1, 2, \dots, G \quad (2)$$

in which  $\Omega_p$  denotes CV  $P$  and all of the parameters and terms have their usual meaning. The next step is to assume a three-dimensional rectangle CV with the six adjacent neighbors to have a seven-box scheme for discretization of the neutron diffusion terms. Accordingly, some required mathematical expressions and formulas for discretization of the steady-state neutron diffusion equation regarding the proposed non-orthogonal FVM have been presented in the following section.

## 3. Mathematical method

In this work, the CV-centered scheme of the FVM in which the parameters are stored in the center of the CVs has been considered. For applying the proposed non-orthogonal FVM on the entire CVs and in a three-dimensional system, the midpoint rule should be considered as follows:

$$\int_{\Delta u} \psi(u) du = \bar{\psi} \Delta u, \quad (3)$$

where  $\psi$  and  $u$  denote an arbitrary function and independent variable, respectively. Moreover, the volume-averaged and the face-averaged relations are considered as Eqs. (4) and (5):

$$\bar{\psi} = \frac{\int_{\Omega_p} \psi(\Omega) d\Omega}{\int_{\Omega_p} d\Omega}, \quad (4)$$

$$\bar{\psi}_f = \frac{\int_{S_p} \psi(s) ds}{\int_{S_p} ds}, \quad (5)$$

where  $\bar{\psi}$  and  $\bar{\psi}_f$  refer to the volume-averaged and face-averaged quantity of function  $\psi$ , respectively. The next step deals with the

result of integration of the neutron diffusion terms (see Eq. (2)) by considering the aforementioned approximations (Eqs. (3)–(5)) and some other mathematical techniques and expressions. So, in the following subsections, the discretization procedure of the governing equations in the three-dimensional Cartesian system by considering the non-orthogonality approach has been presented in details.

### 3.1. Leakage term discretization

In this subsection, the discretization procedure of the leakage term has been presented. In the first step, an approximation of the gradients at the CV face of each CV is obtained.

Considering the divergence theorem, the integral of the divergence over CV  $P$  is expressed as follows:

$$\iiint_{\Omega_p} -\nabla \cdot (D(r) \nabla (\phi(r))) d\Omega = \iint_{S_p} -D(r) \nabla (\phi(r)) \cdot \underline{n} ds, \quad (6)$$

where  $\underline{n}$  is the perpendicular vector to  $S_p$  at each point, pointing outward of the CV. Also,  $d\Omega$  and  $ds$  indicate infinitesimal elements of the volume and surface, respectively. The bonding surface  $S_p$  can be decomposed into  $F$  faces which are considered as  $S_f, f = 1, \dots, F$  ( $F = 6$  for three-dimensional geometries). The geometry of unstructured hexahedron CV  $P$  and the corresponding neighboring CVs has been shown in Fig. 1. As is observable,  $N$  stands the number of neighboring CVs which are numbered in anticlockwise order, and  $\underline{n}_f$  is the unit vector normal to face  $f$  pointing outward of CV  $P$ .

Thus, by considering Fig. 1, the leakage term of the neutron diffusion equation can be expressed as:

$$\iint_{S_p} -D(r) \nabla (\phi(r)) \cdot \underline{n} ds = - \sum_{f=1}^F \left( \underline{n}_f \cdot \iint_{S_f} D(r) \nabla (\phi(r)) ds \right). \quad (7)$$

However, one can rewrite Eq. (7) by considering Eq. (5), as follows:

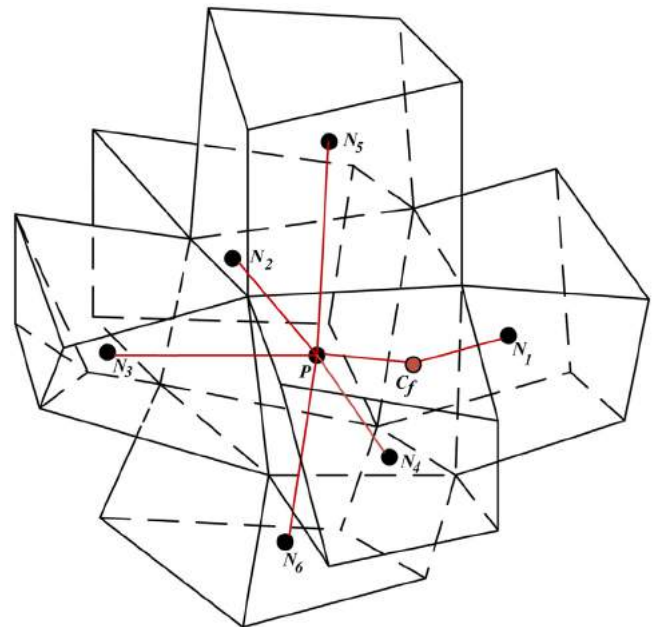


Fig. 1. The geometry of unstructured hexahedron CV  $P$  and the corresponding neighboring CVs.

$$\iiint_{\Omega_p} -\nabla \cdot (D(r) \nabla (\phi(r))) d\Omega = - \sum_{f=1}^F \left\{ \tilde{D}(c_f) \nabla \tilde{\phi}(c_f) \cdot S_f \underline{n}_f \right\} \quad (8)$$

In order to use Eq. (8), the gradient in CV faces ( $\nabla \tilde{\phi}(c_f)$ ) needs to be obtained. However, to obtain these gradient values, the gradients at entire CV centers first should be determined. Accordingly, the Green-Gauss method which represents an intuitive and sound basis for gradient calculation has been employed. Regarding the Green-Gauss theorem, the integral of scalar  $\phi$  in a closed CV  $\Omega_p$  can be determined as Eq. (9):

$$\iiint_{\Omega_p} \nabla(\phi(r)) d\Omega = \iint_{S_p} \phi(r) \underline{n} ds, \quad (9)$$

and accordingly, one can obtain the average gradient of  $\phi$  as Eq. (10):

$$\overline{\nabla(\phi(r))} = \frac{1}{\Omega_p} \iint_{S_p} \phi(r) \underline{n} ds, \quad (10)$$

where  $\underline{n}$  and  $S$  are the surface unit normal vector and the surface area, respectively. For a 2nd order scheme with midpoint quadrature, the Green-Gauss method takes on the following discrete form for a polyhedral:

$$\nabla(\phi(r)) = \frac{1}{\Omega_p} \sum_{f=1}^F \tilde{\phi}(c_f) \underline{n}_f S_f, \quad (11)$$

where  $F$  is the number of faces and  $\tilde{\phi}(c_f)$  denotes the face-averaged of the scalar  $\phi$  over face  $f$  in point of  $c_f$ . Up to this point, the average gradient of a linear function at the hexahedron CV centroid is presented exactly by Eq. (11). As is discussed previously, the mesh movement and CV deformation is based on the variations of power gradient. So, in this step it is worth to formulate the gradient of power from the gradient of flux. It can simply be seen that the spatial gradient variations of reactor power can be determined from the flux gradient:

$$\nabla(\text{power}_p) = \sum_{g=1}^G \nabla(\phi_{g,p}) E \sum_{fg,p}, \quad (12)$$

where  $E$  is the constant fission energy released and  $P$  denotes CV  $P$ . To remove the impact of the absolute total reactor power from the results, Eq. (12) can be divided by the  $\text{Power}_{\text{Total}}$ .

The next step is to treat the deformation of the CVs regarding the spatial gradient variations of the reactor power. Note, in this step, the neutron diffusion equations should be derived and discretized regarding the non-orthogonal FVM. This, however, requires some advanced mathematical expression and consideration which have been presented and explained in the following.

First of all, the non-orthogonality of FVM in three dimensions should be considered. The non-orthogonality of FVM can be implemented using decomposing the face area vector into two separate ones. A variety of decomposition methods have been used in the literature. Among them, the over-relaxed decomposition method which corresponds to the level of non-orthogonality achieved many positive results (Jasak, 1996). In 1996, Jasak introduced this method of decomposition in a two dimensional Cartesian system and then it has been shown that (Jasak, 1996; Sezai, 2011, Van der Westhuizen, 2013), in terms of stability, convergence rate and angles size of non-orthogonality, the over-relaxed decomposition method has superiority to the other similar methods such as the minimum correction approach (Stewart, 2003) and the orthogonal correction approach (Menon, 2011).

Regarding the above discussion, the over-relaxed decomposition method has been applied to the neutron diffusion equation.

Fig. 2 can be considered to formulate the leakage term based on the over-relaxed approach in the three-dimensional Cartesian system:

In this figure,  $\underline{S}_f$  and  $\underline{d}_f$  represent, respectively, the face area vector and the line connector vector between the centers of CVs. By considering the face area vector as Eq. (13), one can rewrite Eq. (11) in the form of Eq. (14):

$$\underline{S}_f = \underline{n}_f S_f \quad (13)$$

$$\nabla(\phi(r)) = \frac{1}{\Omega_p} \sum_{f=1}^F \tilde{\phi}(c_f) \underline{S}_f \quad (14)$$

in which  $\underline{S}_f$  can simply be expressed as:

$$\underline{S}_f = \underline{k}_f + \underline{\Delta}_f \quad (15)$$

where  $\underline{k}_f$  and  $\underline{\Delta}_f$  are the non-orthogonal and orthogonal terms (see Fig. 2), respectively, and they should be derived separately.

The leakage term of the neutron diffusion equation can now be driven by substituting Eq. (13) into Eq. (8), and then combining with Eq. (15) as:

$$\begin{aligned} \iiint_{\Omega_p} -\nabla \cdot (D(r) \nabla (\phi(r))) d\Omega &= - \sum_{f=1}^F \left\{ \tilde{D}(c_f) \nabla (\tilde{\phi}(c_f)) \cdot S_f \underline{n}_f \right\} \\ &= - \sum_{f=1}^F \left\{ \tilde{D}(c_f) \nabla (\tilde{\phi}(c_f)) \cdot \underline{S}_f \right\} \\ &= \left\{ \sum_{f=1}^F (-\tilde{D}(c_f)) \left( \nabla \tilde{\phi}_f \right) \cdot \underline{\Delta}_f \right\} + \left\{ \sum_{f=1}^F (-\tilde{D}(c_f)) \left( \nabla \tilde{\phi}_f \right) \cdot \underline{k}_f \right\} \end{aligned} \quad (16)$$

The first summation in the RHS of Eq. (16) will result in:

$$\sum_{f=1}^F \left\{ (-D_f) \left( \nabla \left( \tilde{\phi}_f \right) \right) \cdot \underline{\Delta}_f \right\} = \sum_{f=1}^F \left\{ (-D_f) |\underline{\Delta}_f| \frac{\phi_N - \phi_P}{|\underline{d}_f|} \right\} \quad (17)$$

in which  $\underline{\Delta}_f$  can be considered as:

$$\underline{\Delta}_f = \frac{\underline{d}_f}{\underline{d}_f \cdot \underline{S}_f} |\underline{S}_f|^2 \quad (18)$$

Moreover, one can simply obtain that

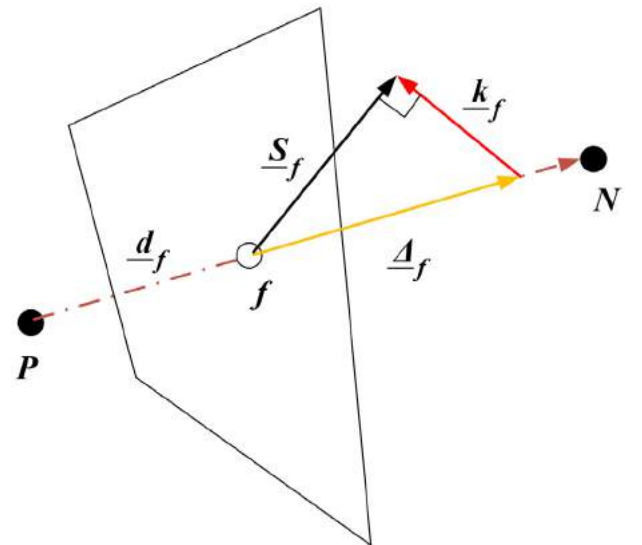


Fig. 2. The over-relaxed approach to the treatment of three dimensional non-orthogonal grids.



$$|\underline{\Delta}_{f,u}| \equiv \Delta_{f,u} \quad (19)$$

in which  $u$  represent  $x, y$  and  $z$ . Considering Eqs. (18) and (19), one can rewrite Eq. (18) as:

$$\Delta_{f,u} = \frac{d_{f,u}}{\sum_{u=x,y,z} d_{f,u} S_{f,u}} |\underline{S}_f|^2, \quad (20)$$

and finally formulate  $|\underline{\Delta}_f|$  as:

$$|\underline{\Delta}_f| = \sqrt{\sum_{u=x,y,z} \left( \frac{d_{f,u}}{\sum_{u=x,y,z} d_{f,u} S_{f,u}} |\underline{S}_f|^2 \right)^2}. \quad (21)$$

To obtain  $|\underline{S}_f|$  in Eq. (21) regarding the orthogonal grid approach, the following figure should be considered.

In non-orthogonal grids, the face area vector  $\underline{S}_f$  can be determined by considering Fig. 3 as:

$$\underline{S}_f = S_{f,x} \underline{i} + S_{f,y} \underline{j} + S_{f,z} \underline{k} \quad (22)$$

and also  $|\underline{S}_f|$  can be given by

$$|\underline{S}_f| = \sqrt{(S_{f,x})^2 + (S_{f,y})^2 + (S_{f,z})^2} \quad (23)$$

Finally, the orthogonal part of the leakage term is obtained as:

$$\begin{aligned} \sum_{f=1}^F \left\{ (-D_f) \left( \nabla \left( \frac{\phi}{f} \right) \right) \cdot \underline{\Delta}_f \right\} &= \sum_{f=1}^F \left\{ (-D_f) |\underline{\Delta}_f| \frac{\phi_N - \phi_P}{|\underline{d}_f|} \right\} \\ &= \sum_{f=1}^F (-D_f) \left\{ \frac{\left( \sum_{u=x,y,z} \left( \frac{d_{f,u}}{\sum_{u=x,y,z} d_{f,u} S_{f,u}} |\underline{S}_f|^2 \right)^2 \right)}{|\underline{d}_f|} \right\} (\phi_N - \phi_P). \end{aligned} \quad (24)$$

The next step should be devoted to the non-orthogonal part of the leakage term (see Eq. (16)). The non-orthogonal term can be expanded in  $x, y$  and  $z$  directions as follows:

$$\begin{aligned} \sum_{f=1}^F \left\{ (-D_f) \left\{ \nabla(\phi_f) \right\} \cdot \underline{k}_f \right\} &= \sum_{f=1}^F \left\{ (-D_f) \left\{ \nabla(\phi_{f,x}) \right\} k_{f,x} \right. \\ &\quad \left. + (-D_f) \left\{ \nabla(\phi_{f,y}) \right\} k_{f,y} + (-D_f) \left\{ \nabla(\phi_{f,z}) \right\} k_{f,z} \right\}, \end{aligned} \quad (25)$$

where  $k_{f,x}$ ,  $k_{f,y}$  and  $k_{f,z}$  are specified by Eq. (26), respectively as follows:

$$k_{f,u} = S_{f,u} - \Delta_{f,u}. \quad (26)$$

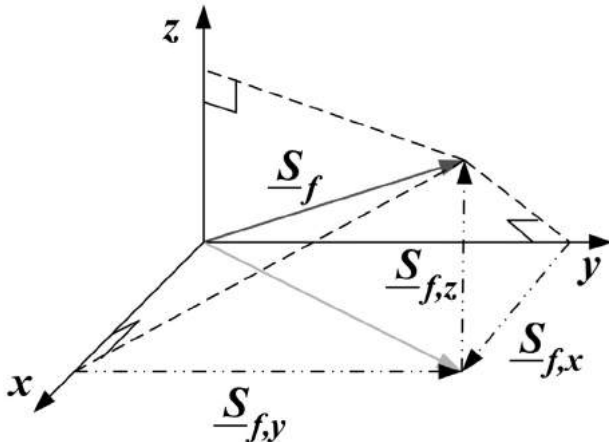


Fig. 3. Illustration of the face area vector components in three dimensions.

Also,  $\nabla(\phi_{f,x})$ ,  $\nabla(\phi_{f,y})$  and  $\nabla(\phi_{f,z})$  in Eq. (25) can be obtained by considering Fig. 4 as:

$$\nabla(\phi_{f,u}) = \frac{L_1}{L_1 + L_2} \{ \nabla(\phi_{P,u}) \} + \frac{L_2}{L_1 + L_2} \{ \nabla(\phi_{N,u}) \}, \quad (27)$$

where the first fraction in the RHS is the ratio of the distance between the center of the face and the center of the CV  $N$ , to the distance between the center of the owner (CV  $P$ ) and the center of the CV  $N$ . And the second fraction in the RHS is the ratio of the distance between the center of the face and the center of the CV  $P$ , to the distance between the center of the owner (CV  $P$ ) and the center of the CV  $N$  (Van der Westhuizen, 2013). Using this method of implementation for the calculation of gradient at the face, one can simply obtain all the gradients at the faces for all CVs. Due to the fact that these calculations are not iterative, they are efficient and of great interest. For more details about this method of approximation, one can refer to (Van der Westhuizen, 2013).

In order to obtain  $\nabla(\phi_{P,u})$  and  $\nabla(\phi_{N,u})$  in Eq. (27), one can employ Eq. (14) and have:

$$\nabla(\phi_{P,u}) = \frac{1}{\Omega_P} \sum_{f=1}^F S_{f,u} \phi_f, \quad (28)$$

$$\nabla(\phi_{N,u}) = \frac{1}{\Omega_N} \sum_{f=1}^F S_{f,u} \phi_f. \quad (29)$$

### 3.2. Remaining terms discretization of the neutron diffusion equation

This section of work is related to the discretization procedure of the remaining terms of the neutron diffusion equation (see Eq. (2)). The discretization procedure of the remaining terms can simply be performed using the midpoint rule (Eq. (3)) and formulated as the following equations:

$$\int_{\Omega_P} \left\{ \sum_{rg} (r) \phi_g(r) \right\} d\Omega = \left\{ \sum_{rg} \phi_{g,P} \right\} \Omega_P \quad (30)$$

$$\int_{\Omega_P} \sum_{g'=1}^G \left\{ \sum_{g''=1}^{g'-g} (r) \phi_{g''}(r) \right\} d\Omega = \sum_{g'=1}^G \left\{ \sum_{g''=1}^{g'-g} \phi_{g'',P} \right\} \Omega_P \quad (31)$$

$$\int_{\Omega_P} \left\{ \frac{1}{k} \chi_g \left\{ \sum_{g'=1}^G v \Sigma_{fg'}(r) \phi_{g'}(r) \right\} \right\} d\Omega = \left\{ \frac{1}{k} \chi_g \left\{ \sum_{g'=1}^G v \Sigma_{fg',P} \phi_{g',P} \right\} \right\} \Omega_P \quad (32)$$

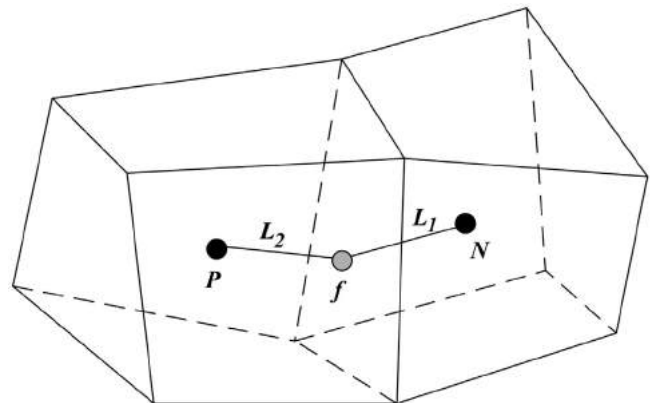


Fig. 4. Two adjacent non-orthogonal three-dimensional CVs.

### 3.3. Boundary conditions

According to the neutron diffusion approximation, the Boundary Conditions (BC) are divided into two groups, namely, Dirichlet B.C. and Von Neumann B.C. While, the first case prescribes a zero fixed value at the boundaries (known as zero flux B.C.), the second case prescribes a fixed value of gradient (Lamarsh, 1965; Duderstadt and Hamilton, 1991; Bell and Glasstone, 1970). Accordingly, this section of work is devoted to the boundary conditions and the corresponding mathematical formulation. Based on the over-relaxed gradient-based approach, a CV with a boundary face can be illustrated as Fig. 5.

As shown, the vector  $\underline{d}_f$  which already connects the centers of the CVs connects the center of the CV to the center of the boundary face. Because center of each bounded surface in space is unique, so  $\underline{d}_f$  which connects the center of the neighboring CV to the center of the boundary face is also a unique vector. To treat the gradient of a non-orthogonal mesh at the boundary conditions, the vector  $\underline{d}_n$  between the center of the CV and normal to the face should be determined and used instead of  $\underline{d}_f$ . Accordingly, one can obtain

$$|\underline{d}_n| = \cos(\alpha) |\underline{d}_f|, \quad (33)$$

where  $\alpha$  is the angle between the vectors  $\underline{d}_f$  and  $\underline{d}_n$ . Regarding Fig. 5, it can be also obtained that

$$\frac{S_f}{|S_f|} \equiv \frac{\underline{\Delta}_f}{|\underline{\Delta}_f|}. \quad (34)$$

So,  $\underline{d}_n$  can be given by:

$$\underline{d}_n = \frac{S_f}{|S_f|} \frac{\underline{d}_f \cdot S_f}{|S_f|}, \quad (35)$$

and based on the vector components:

$$|\underline{d}_n| = \frac{\sum_{u=x,y,z} \underline{d}_f \cdot \underline{S}_f \cdot \underline{u}}{\sqrt{\sum_{u=x,y,z} S_{f,u}^2}}. \quad (36)$$

As is shown in Fig. 5, the orthogonal component  $\underline{\Delta}_f$  is equal to the face area vector  $\underline{S}_f$ , and the non-orthogonal corrector factor  $k_f$  is then not used. So, the Dirichlet BC can be presented as:

$$(-D_f) \underline{\Delta}_f \cdot \{\underline{\nabla}(\phi_b)\} = (-D_f) |\underline{\Delta}_f| \frac{\phi_b - \phi_p}{|\underline{d}_n|}, \quad (37)$$

in which  $\phi_b$  stands the flux at the boundary and is assumed to be valid along the whole face. Note that  $|\underline{\Delta}_f|$  in Eq. (37) can be computed from Eq. (21). By considering  $\phi_b = 0$ , Eq. (37) becomes:

$$(-D_f) \underline{\Delta}_f \cdot \{\underline{\nabla}(\phi_b)\} = (-D_f) |\underline{\Delta}_f| \frac{(-\phi_p)}{|\underline{d}_n|}. \quad (38)$$

The Von Neumann BC can be given by  $(-D_f) \underline{S}_f \cdot \{\underline{\nabla}(\phi_b)\}$ . By considering the reflective B.C. ( $\underline{\nabla}(\phi_b) = \underline{0}$ ), one can have:

$$(-D_f) \underline{\Delta}_f \cdot \{\underline{\nabla}(\phi_b)\} = 0. \quad (39)$$

However, in the case of the albedo BC ( $\beta$ ) that defined as the ratio between the current out of the reflecting region to the current into the reflecting region (Duderstadt and Hamilton, 1991), one can express that:

$$(-D_f) \underline{\Delta}_f \cdot \{\underline{\nabla}(\phi_b)\} = |\underline{\Delta}_f| \left( \frac{1}{2} \frac{1-\beta}{1+\beta} \right) (\phi_p). \quad (40)$$

As is discussed previously, each individual CV needs flux value at the center of the neighbors to calculate the gradient at its own center. However, by considering the Von Neumann boundary condition, only a fixed gradient at the boundary is prescribed, and accordingly the flux values are not known. To deal with such condition, one can assume Fig. 6 and obtain the gradient of flux in the shared interface as Eq. (41):

$$\underline{\nabla}(\phi_f) = \left( \frac{L_1}{L_1 + L_2} \right) \underline{\nabla}(\phi_N) + \left( \frac{L_2}{L_1 + L_2} \right) \underline{\nabla}(\phi_P), \quad (41)$$

where  $\underline{\nabla}(\phi_N)$  is the gradient at the adjacent CV P and can be obtained by considering Fig. 6 as Eq. (42):

$$\underline{\nabla}(\phi_N) = \left( \frac{L_2}{L_2 + L_3} \right) \underline{\nabla}(\phi_{dn}) + \left( \frac{L_3}{L_2 + L_3} \right) \underline{\nabla}(\phi_f). \quad (42)$$

It can be argued that the flux face boundary value no longer required to be computed and instead, the fixed gradient value can be substituted properly.

### 4. Procedure of implementation

In this section, the procedure of implementation of the proposed method in addition to the flow diagrams is presented in details. Fig. 7 demonstrates the procedure of calculations including the gradient-based calculations, CVs deformation and finally

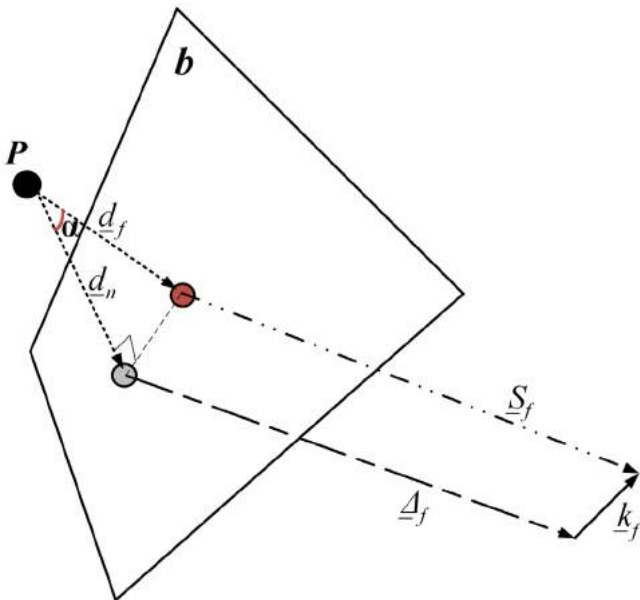


Fig. 5. Boundary face of a non-orthogonal three-dimensional CV.

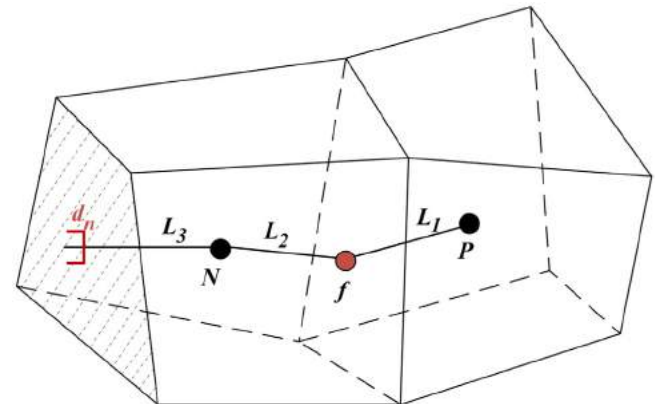


Fig. 6. A non-orthogonal three-dimensional CV with a boundary face regarding the Von Neumann B.C.

stationary iterative numerical calculations. Each of these parts has been considered separately in more details in the following.

#### 4.1. Gradient-based calculations

The gradient-based calculations are the first step for the implementation of the proposed method. According to the previously presented gradient-based formulation, flux profile is required for determination of gradient at each CV. To prevent iterative time-consuming computations, only a rough calculation for obtaining the shape of variations is considered to be performed (using the stationary iterative algorithm which is presented and discussed in Section 4.3). The gradient of flux at each CV is then obtained by considering Eq. (16) and finally, they are employed to determine the spatial gradient variations of power using Eq. (12). According to Fig. 7, the next step for implementation of the proposed method is the CV deformation which is presented in the following.

#### 4.2. CV deformation

The CV deformation is the main part of the study which is presented in this section. The mechanism for the CV implementation is that the mesh movement is firstly performed regarding the spatial gradient variations of the reactor power. Then, the corresponding CV boundaries deformed to establish proper boundaries between adjacent CV centered meshes. In the final step, all of the meshes are moved again so that they can be located in the middle

of the newly defined boundaries. The importance of the CV boundaries deformation is due to the fact that, CV center meshes move during the calculations regarding the proposed method, and accordingly if the corresponding boundaries do not move simultaneously, the meshes cannot be located in the center of the CVs anymore. This point is in contradiction with the assumption of the CV centered FVM, and should be corrected. To clarify the mechanism of determining the CV boundaries, Fig. 8 should be considered. As can be seen, a 3-dimensional  $4 \times 4 \times 4$  CV array (as an example) based on the CV-centered orthogonal FVM has been illustrated.

In the conventional CV-centered orthogonal FVM, first, the number of total mesh centers is determined (Fig. 8a), and then, the same number of CVs is considered (Fig. 8b), where each mesh point should be located in the middle of the corresponding CVs (Fig. 8c). In the final step, the CVs containing the mesh points should be located in the entire computational geometry to form

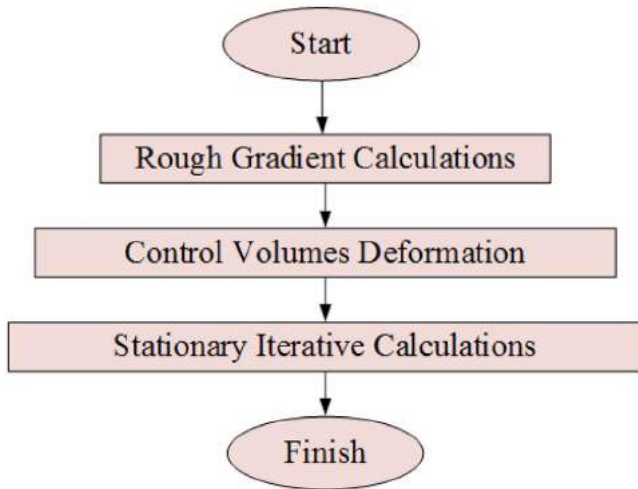


Fig. 7. Flow diagram of the procedure of implementation.

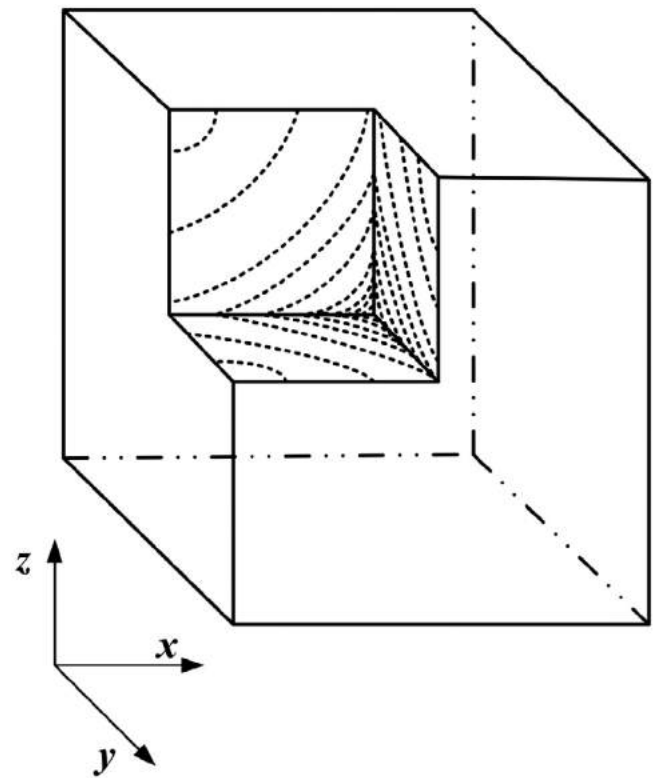


Fig. 9. Schematic view of the relative gradient variations of reactor power for the sample problem.

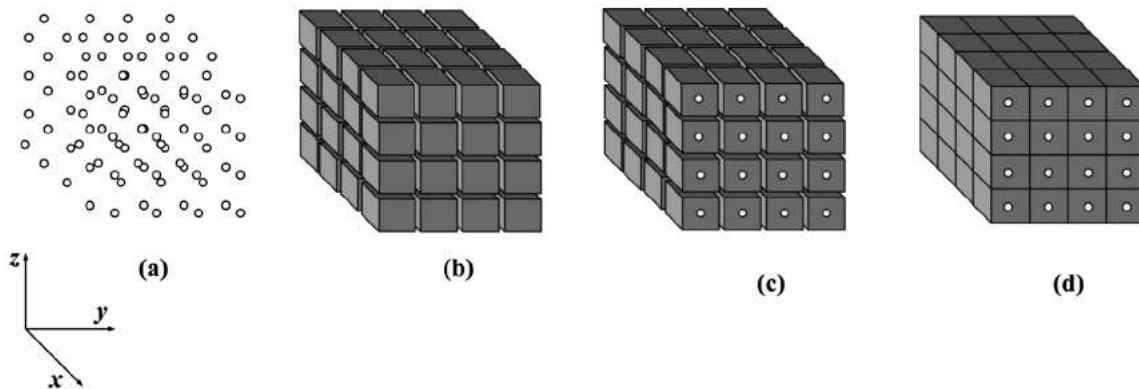
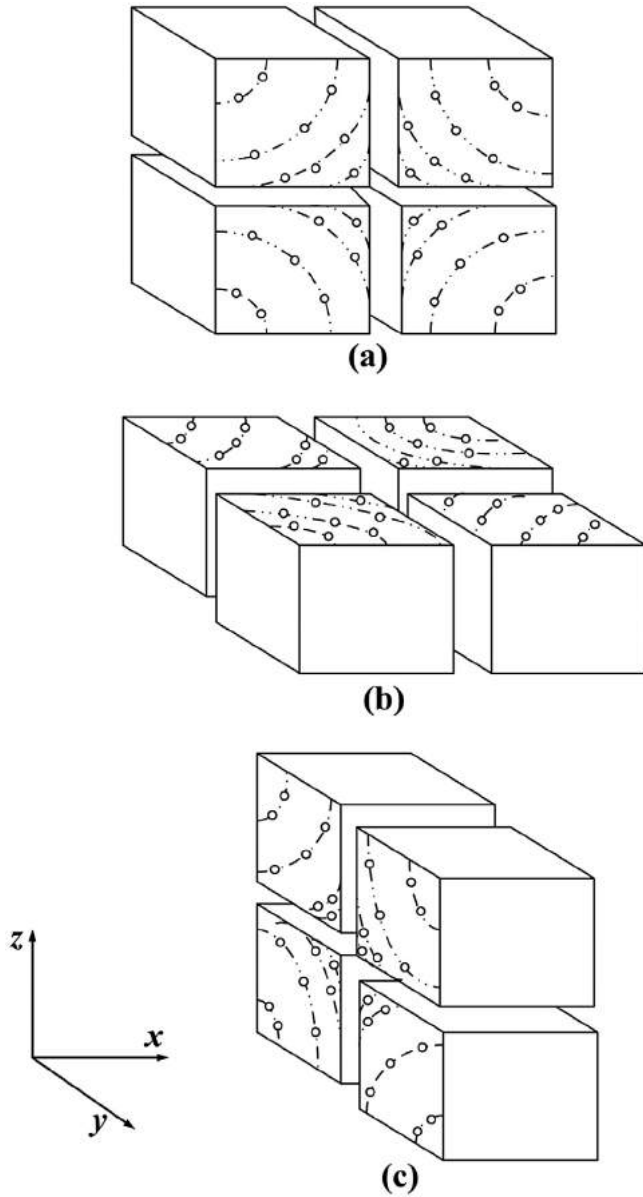


Fig. 8. Schematic view of the orthogonal CV partitioning procedure for an example of  $4 \times 4 \times 4$  array.



**Fig. 10.** Schematic view of the mesh movement in an adaptive form and in each direction without formation of the CVs for the considered sample problem.

a uniform orthogonal mesh grid structure (Fig. 8d). This procedure of implementation is very important when one wants to introduce and develop a new method. Accordingly, we present a sample problem in which the relative power gradient increases as it approaches the center of geometry according to Fig. 9. The following has been devoted to the explanation of the stepwise algorithm including the mesh movement, CV boundaries deformation mechanism and finally reconstruction of the mesh points.

#### 4.2.1. Step 1: mesh movement

Mesh movement is considered in the first step of the proposed algorithm. The CV-centered meshes will be moved towards the center position of the geometry (Fig. 10). It is assumed that the gradient value increases as the geometry center approaches. Fig. 10 shows a schematic view of the mesh movement toward the center of geometry in different directions.

In this work, for the first time, a new mechanism for the mesh movement is presented. The first step is the gradient calculations of the neutron fluxes in all neutron energy groups and CVs

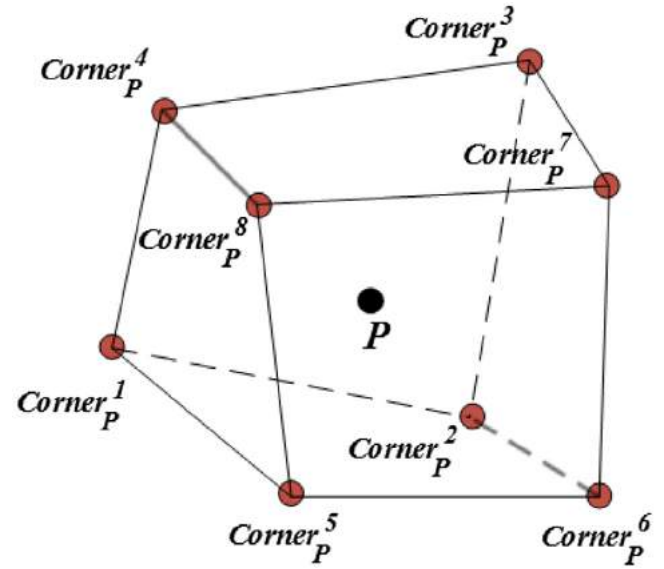


**Fig. 11.** Vertices numbering of CV  $P$ .

( $\nabla(\phi_p)$ ) using Eq. (16). Then, the gradient of power ( $\nabla(\text{power}_p)$ ) should be implemented for each CV based on Eq. (12). Regarding the fact that only the gradient variations of the power are required the impact of the total reactor power on the results should be eliminated. This can simply be performed as dividing the results of  $\nabla(\text{power}_p)$  by the total reactor power. The next step then is devoted to obtaining the new position of the CV centers. In the case of 3-D hexahedron geometries, the new position of each CV center in each direction can be given by

$$u^{\text{new}} = u^{\text{old}} + \left\{ u^{\text{old}} \times \frac{1}{\left\{ \frac{\nabla(\text{power}_{p,u})}{\text{Power}_{\text{Total}}} \right\}} \right\} \quad (43)$$

where  $\text{Power}_{\text{Total}}$  is the total reactor power and  $u$  can be  $x$ ,  $y$  or  $z$ . As is observable from Eq. (43), the new CV center positions in each direction are in reverse relation to the calculated relative gradient of power in the same direction. To prevent any unwanted large value which can be obtained based on a small value of the denominator, it is assumed that the rising of the parameter should be maintained in a limitation. After the mesh movement, the meshes should be surrounded by their new corresponding CV boundaries, because if the initial CV boundaries are considered then the meshes cannot be located in the middle of CVs. Because of the importance of this issue, the next section deals with the mechanism of the CV boundaries determination.

#### 4.2.2. Step 2: CV boundaries determination

CV boundaries determination is the second step of the proposed algorithm and is introduced for the first time in this work. In order to determine the entire CV boundaries, numbering of each vertex point is performed as Fig. 11. Also, the initial considered CV is assumed to be the corner bottom-left-back CV according to Fig. 12a. Moreover, faces and vertices that located on the boundaries of geometry are assumed to be fixed and accordingly cannot be moved or changed. By considering Figs. 11 and 12, it will be observed that in the case of the first CV, the coordinates of all vertex points are known except point 7. The coordinates of this point can be determined by using the coordinates of mesh  $P$  and its entire adjacent mesh center points. The coordinates of this point (vertex point 7 of the first CV) is the same with the coordinates of vertex point 8 of the next CV (see Fig. 12b). So, the coordinates

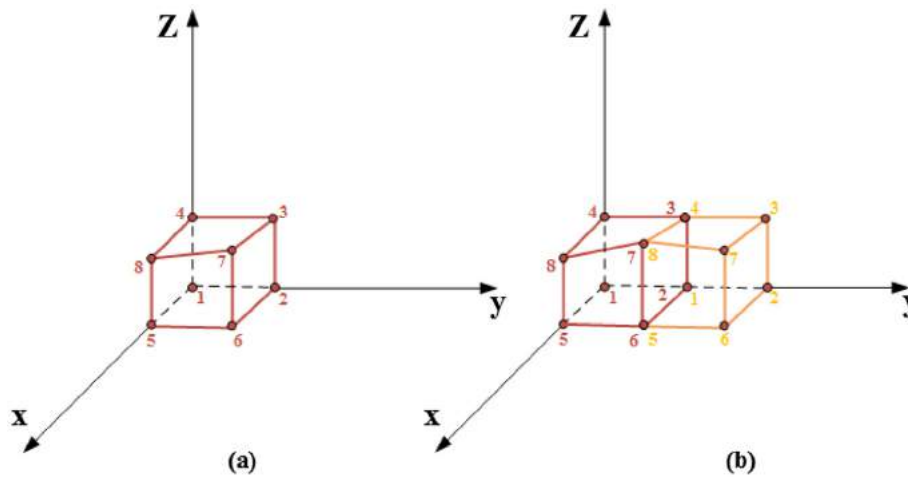


Fig. 12. Schematic view of the vertex points numbering.

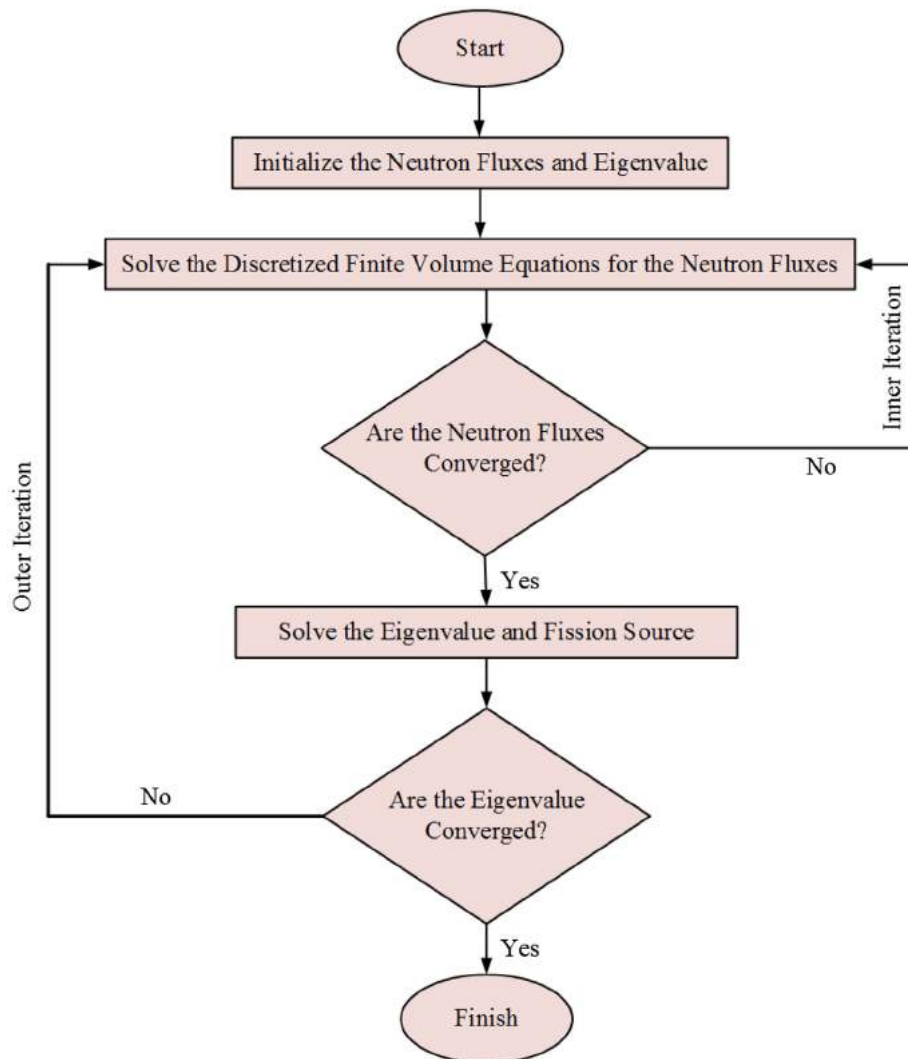


Fig.13. Flow diagram of the stationary iterative neutron diffusion calculations.

of all vertex points of the second CV are known except point 7 that can be obtained similar to the previous case. Using this method of implementation, the coordinates of all points can finally be determined if the CVs are considered from left to right and then from

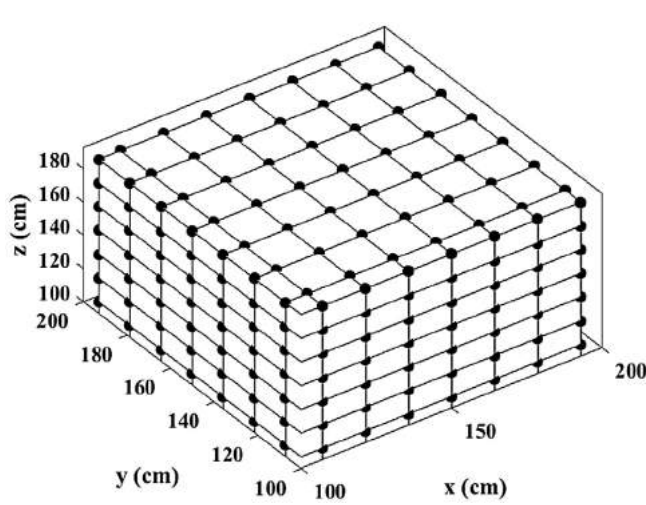
back to front and eventually from bottom to top. By considering this mechanism, the CV boundaries are moved and deformed with respect to the position of the meshes that were moved according to step 1. More precisely, although there is not any particular equa-



**Table 1**

Group constants of the test case 1 (Ferguson and Hansen, 1973).

Group Constants	$D_g(\text{cm})$	$\Sigma_{ag}(\text{cm}^{-1})$	$\nu_g \Sigma_{fg}(\text{cm}^{-1})$	$\Sigma_{g \rightarrow g+1}(\text{cm}^{-1})$
1	1.35	0.001382	0.00058322	0.0023
2	1.08	0.0054869	0.0098328	...

**Fig. 14.** One-eighth view of the applied orthogonal CV partitioning distribution for the solution of the relative power gradient calculations of test case 1.

tion between the CV boundaries and gradient variations of power, there is direct relationship between the density resolution of the CVs and meshes. Therefore, as can be observed later in the results section (Section 5), there should be higher CV resolutions in regions that have higher gradient variations of power.

Because the CV boundaries deformed, the position of the mesh centers is no longer in the middle of the CVs and they need to be moved again. Therefore, in addition to the previous two steps, it is necessary to take another step.

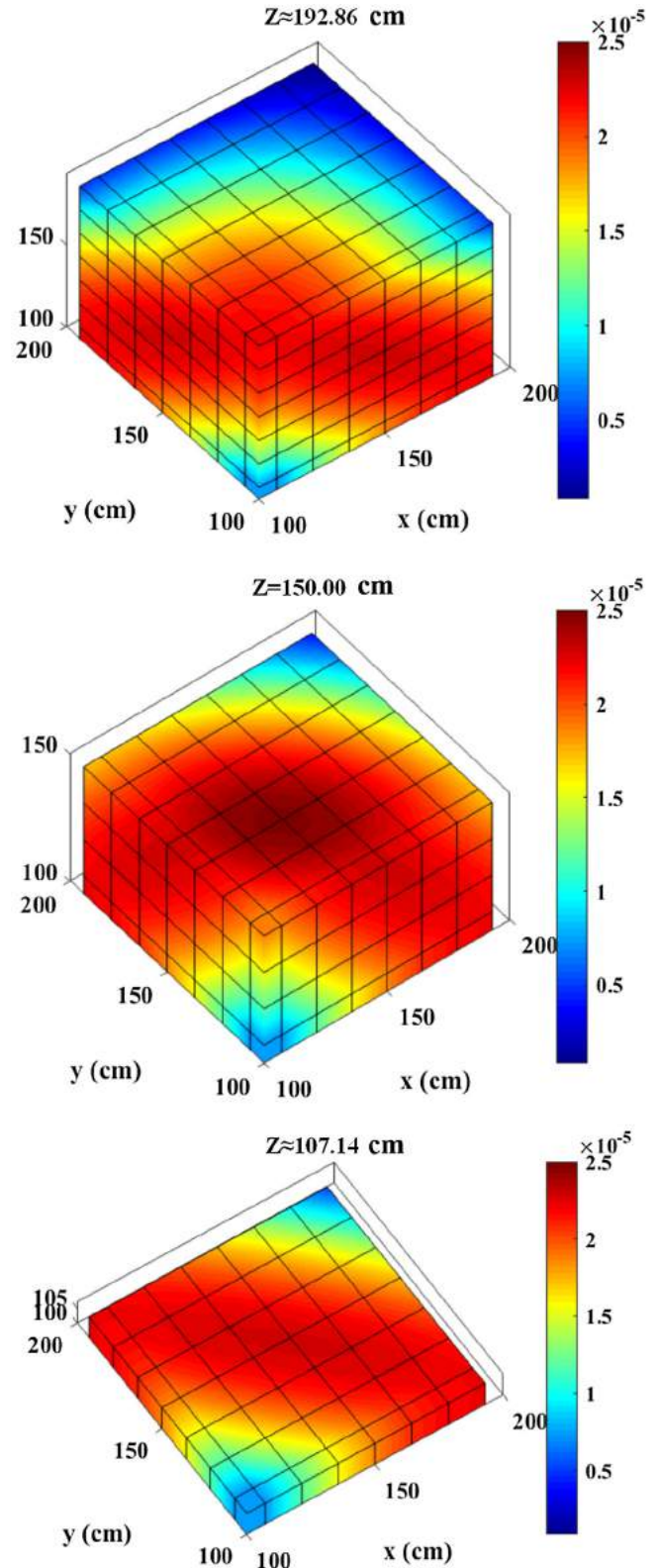
#### 4.2.3. Step 3: reconsideration of mesh points

Reconsideration of mesh points is the last step of the proposed algorithm. This step can be performed using the arithmetic averaging of the coordinates of vertex meshes. By performing this step, the coordinates of all meshes and boundaries are determined. In the following, five benchmark problems have been considered in order to assess and check the performance of the method.

#### 4.3. Stationary iterative calculations

The stationary iterative calculations for the solution of the neutron diffusion equation are presented in this section. In order to solve the governing equations iteratively, the power iteration method is employed. The flow diagram of the iterative calculations is shown in Fig. 13. As is shown in this figure, an initial flux profile in addition to the eigenvalue ( $k_{eff}$ ) should be applied. In the next step, neutron flux computations over all neutron energy groups are performed until the solution converges and meets the criteria (Eq. (44)). The new eigenvalue and fission source will then be updated regarding Eqs. (45) and (46), and subsequently the outer iteration will be performed to obtain the desired convergence criterion of the eigenvalue (Eq.(47)). This iterative strategy will be carried out once the eigenvalue in addition to the neutron flux profile converges at the same time.

$$\left| \frac{\phi_{g,p}^{m+1} - \phi_{g,p}^m}{\phi_{g,p}^{m+1}} \right| < \varepsilon_1, \quad (44)$$

**Fig. 15.** Calculated relative power gradient distribution as a three-dimensional form for test case 1.

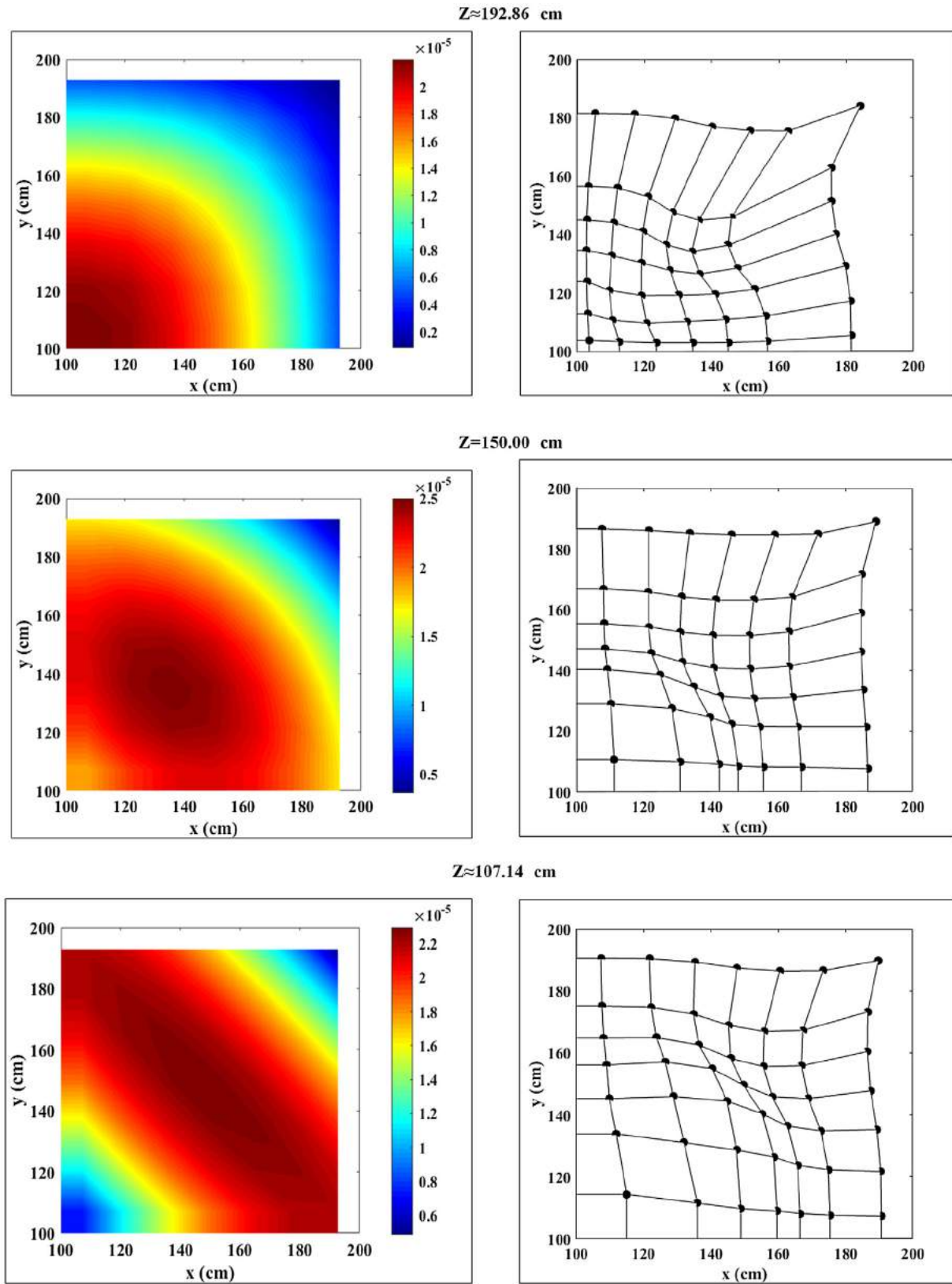


**Fig. 16.** Relative power gradient distributions (left) and the corresponding mesh density resolutions (right) for the test case 1.

**Table 2**Comparison of the calculated  $k_{eff}$  and its relative error with the reference value of test case 1.

Method	Effective Multiplication Factor ( $k_{eff}$ )	RPE(%)	Total execution time (s)
The proposed non-orthogonal gradient-based FVM	0.8932910	0.0309289 (~31 pcm)	77
The orthogonal FVM	0.8937029	0.00770536 (~77 pcm)	73

**Table 3**

Relative error (%) comparison of the calculated power for the test case 1.

CV	Z = 107.14 cm		Z = 150.00 cm		Z = 192.86 cm	
	Orthogonal Method	Non-Orthogonal Method	Orthogonal Method	Non-Orthogonal Method	Orthogonal Method	Non-Orthogonal Method
(1,1)	0.081	0.067	0.081	0.067	0.158	0.068
(2,1)	0.116	0.068	0.109	0.067	-0.150	-0.067
(3,1)	-0.131	-0.060	-0.108	0.061	-0.152	0.050
(4,1)	-0.130	-0.060	-0.128	-0.059	-0.149	-0.061
(5,1)	0.147	0.060	0.146	0.060	0.149	-0.050
(6,1)	-0.148	-0.048	-0.145	-0.062	-0.157	0.067
(7,1)	0.126	0.053	0.139	0.066	-0.159	-0.069
(2,2)	-0.108	-0.067	-0.116	-0.060	0.155	0.062
(3,2)	0.128	0.068	0.150	0.061	0.149	-0.050
(4,2)	-0.141	-0.058	0.152	0.068	0.150	0.061
(5,2)	0.156	0.039	0.150	0.056	0.125	0.050
(6,2)	0.146	0.049	0.151	0.062	0.144	0.061
(7,2)	-0.138	-0.066	0.141	-0.058	-0.150	-0.062
(3,3)	0.130	0.069	0.159	0.069	0.150	-0.064
(4,3)	0.159	0.059	0.151	0.065	0.140	0.046
(5,3)	-0.158	0.069	-0.153	0.063	-0.131	0.060
(6,3)	-0.145	-0.061	0.149	0.061	-0.140	0.059
(7,3)	0.150	0.060	0.150	0.052	0.150	-0.060
(4,4)	0.159	0.070	-0.149	-0.061	0.151	0.060
(5,4)	0.131	0.055	-0.141	0.052	0.150	-0.060
(6,4)	-0.148	-0.043	0.147	0.057	-0.150	-0.060
(7,4)	-0.154	-0.063	0.150	0.052	0.151	0.059
(5,5)	0.141	0.060	0.149	0.050	0.149	0.060
(6,5)	0.149	0.059	0.140	0.057	0.140	0.044
(7,5)	-0.148	-0.069	-0.150	-0.063	-0.149	0.050
(6,6)	0.153	0.057	0.151	0.060	-0.141	-0.059
(7,6)	-0.158	-0.065	-0.155	-0.062	-0.150	-0.059
(7,7)	0.150	-0.060	0.154	-0.060	0.143	-0.055

$$k_{eff}^{m+1} = \frac{\sum_{i=1}^N \sum_{g=1}^G v \sum_{fg} (i) \phi_g^{m+1}(i)}{\frac{1}{k_{eff}^m} \sum_{i=1}^N \sum_{g=1}^G v \sum_{fg} (i) \phi_g^m(i)}, \quad (45)$$

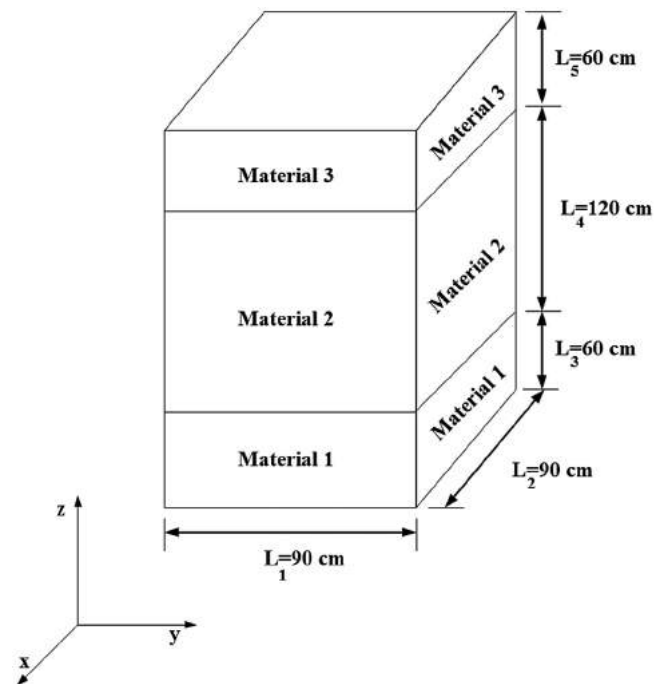
$$S^{m+1} = \frac{1}{k_{eff}^{m+1}} \sum_{i=1}^N \sum_{g=1}^G v \sum_{fg} (i) \phi_g^{m+1}(i), \quad (46)$$

$$\left| \frac{k_{eff}^{m+1} - k_{eff}^m}{k_{eff}^m} \right| < \varepsilon_2, \quad (47)$$

where  $m$  indicates the iteration number,  $N$  denotes the total number of CVs, and  $S$  is the neutron source term. It also should be noted that  $\varepsilon_1$  in Eq. (44) and  $\varepsilon_2$  in Eq. (47) are the convergence criterion of the neutron flux profile and the eigenvalue, respectively. In this work, in order to obtain the stationary iterative accurate solutions,  $4E-5$  and  $1E-8$  values are considered for the inner iteration (i.e.  $\varepsilon_1$ ) and outer iteration (i.e.  $\varepsilon_2$ ), respectively.

In Eq. (45), summations in both the numerator and denominator are on all neutron energy groups and CVs. This point also has been considered in Eq. (46) for calculating the neutron source term at each step of iteration. More details about the stationary iterative calculations for the multi-group neutron diffusion equation can be found in the literature (Duderstadt and Hamilton, 1991; Clark and Hansen, 1964).

It is interesting to point out that the aforementioned stationary iterative calculations should be performed two times. The first time is for determination of the gradient of power based on the original mesh resolution and the second time is for the

**Fig. 17.** Geometry configuration of test case 2.



**Table 4**  
Group constants of test case 2 (Miro et al., 2002).

Mat.	Group Constants	$D_g$ (cm)	$\Sigma_{ag}$ (cm <sup>-1</sup> )	$\nu_g \Sigma_{fg}$ (cm <sup>-1</sup> )	$\Sigma_{g \rightarrow g+1}$ (cm <sup>-1</sup> )
1	1	1.695310	0.0139530	0.013406855	0.0164444
	2	0.409718	0.2614097	0.342323710	...
2	1	1.695310	0.0139954	0.013406855	0.0164444
	2	0.409718	0.2614200	0.342323710	...
3	1	1.695310	0.0139523	0.013406855	0.0164444
	2	0.409718	0.2614095	0.342323710	...

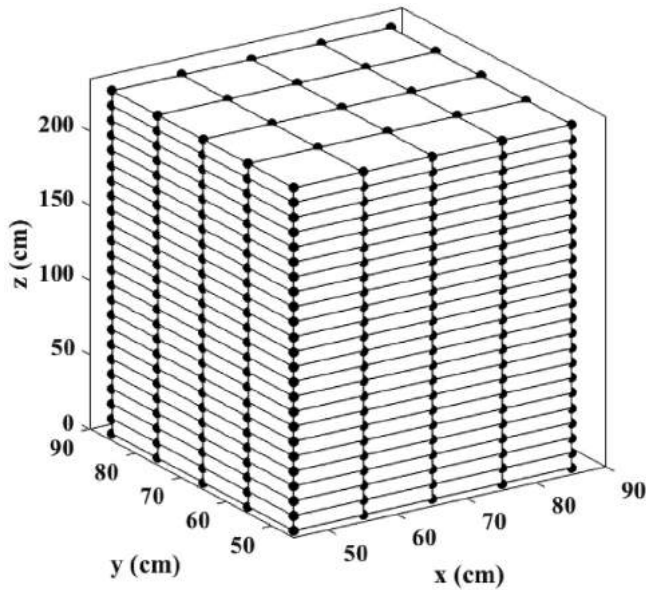


**Fig. 18.** One-fourth view of the applied orthogonal CV distribution for the gradient-based calculations of test case 2.

determination of flux and power profiles based on the moved meshes. To reduce the computational time and prevent the time consuming iterative calculations, only a rough calculation for obtaining the shape of variations is considered to be performed for the determination of the gradient of power. The results of the neutron fluxes and power profiles are then applied as the initial guess for the second iterative calculations after the mesh movement and CV deformation. This strategy can significantly reduce the computational cost for the implementation of the proposed method. This is due to the fact that in the first iterative calculations based on the original meshes, only a rough calculation is performed (which is not a relatively time-consuming calculation compared to the accurate solution), and in the second iterative calculations based on the moved meshes, the results of the original meshes are applied as the initial guess. The latter strategy similar to the former case can reduce the computational cost and improve the efficiency. The procedure used to transfer the solution from the original meshes to the moved meshes can be based on the interpolation between the results of original meshes (including the flux and power profiles). More precisely, owing to the fact that the position of the moved meshes is different from those of the original meshes, the solutions can not be directly transformed and accordingly an interpolation should be considered by the aid of the obtained flux/power profiles from the original meshes and knowing the position of the moved meshes. Although is approximation is not accurate, it can be acceptable as the initial guess for the subsequently iterative calculations.

## 5. Results and benchmarking

In this section of work, the proposed non-orthogonal gradient-based FVM is evaluated. Accordingly, a steady-state multi-group neutron diffusion solver code named the CITATION code is considered as the steady-state reference code for benchmarking of the results all. Note that all of the obtained results regarding the CITATION code are obtained based on the fine mesh simulation (Fowler, 1999).

The procedure of implementation is that an arbitrary number of CVs are first applied. Then, the gradient-based calculations are performed to determine the relative gradient variations of power. In the next step, the mesh movement and CV deformation are carried out. In the final step, the stationary iterative calculations are performed and the results are compared to the orthogonal FVM with the same number of CVs.

### 5.1. Test case 1

The first benchmark problem is a bare homogenous three-dimensional cube of length 200 cm on each side with two neutron energy groups. The boundary conditions of this reactor comprise of zero flux for the external boundaries. The group constants of this problem are presented in Table 1 (Ferguson and Hansen, 1973).

For the solution of the first benchmark problem, an arbitrary number of  $14 \times 14 \times 14$  CVs are considered. An-eighth view of the applied orthogonal CV partitioning distribution for the solution of the gradient calculations is presented in Fig. 14. Fig. 15 shows the calculated relative power gradient distribution as the three-dimensional form. In order to illustrate the mesh partitioning distribution of the proposed method based on the gradient-based calculations, Fig. 16 should be considered. This figure shows the mesh partitioning distribution in three different heights. As can be seen, each of the mesh partitioning distributions is properly adapted to the variations of power gradient.

After the mesh movements and CVs deformation, stationary iterative neutron diffusion calculations are performed regarding Fig. 13. To reduce the executing time of these calculations, the solution of the previous performed calculations based on the orthogonal FVM is considered as the initial guess.

In order to check the performance of the proposed method, the results that obtained based on the orthogonal FVM are compared to those obtained regarding the proposed non-orthogonal FVM. It is also worth to mention that the same number of CVs is considered to be compared for making consistent accuracy comparison between the aforementioned methods. In the case of the first benchmark problem, this array of CVs is  $14 \times 14 \times 14$ . Table 2 shows the results of comparison of the calculated  $k_{eff}$  between the proposed gradient-based non-orthogonal FVM and the conventional FVM. In order to compare the results, the relative percent error (RPE) is used and defined as (Vagheian and Talebi, 2019):

$$RPE(\%) = \frac{\text{calculated value} - \text{reference value}}{\text{reference value}} \times 100 \quad (48)$$

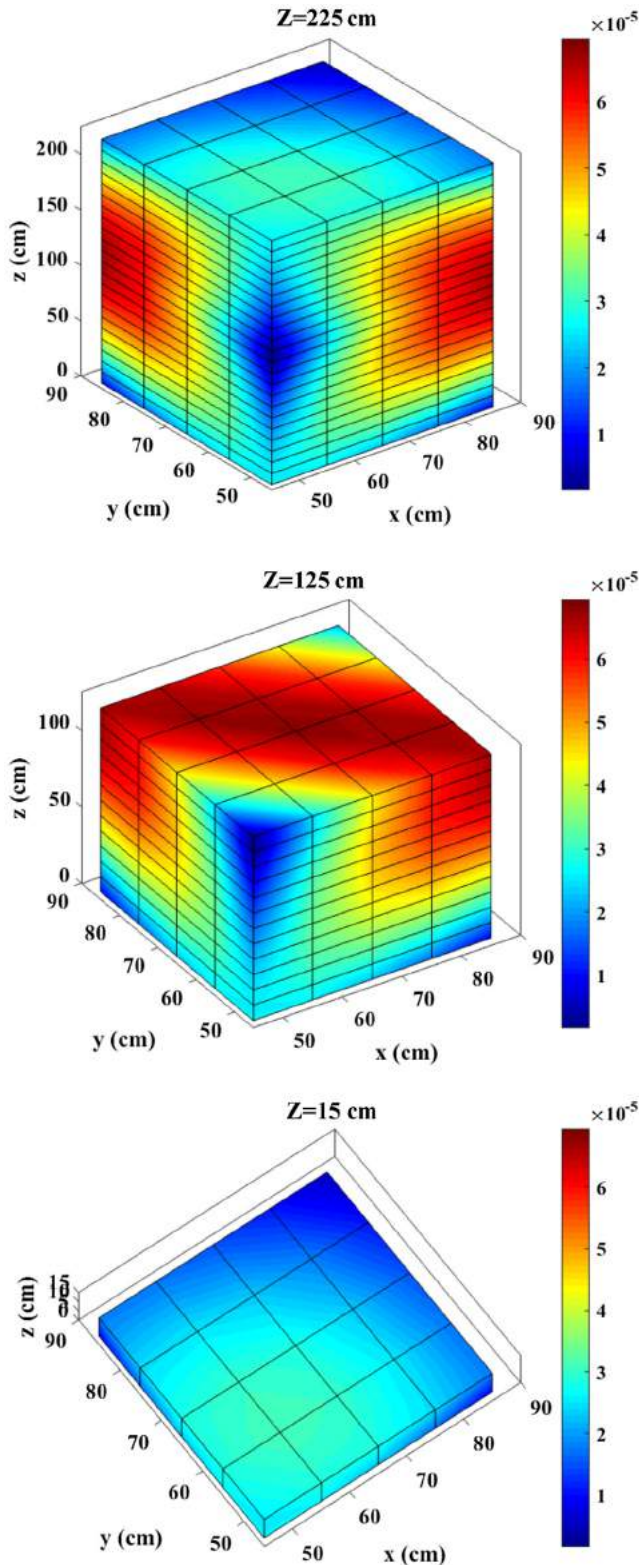


Fig. 19. Calculated relative power gradient distribution as a three-dimensional form for the test case 2.

The reference solution was obtained 0.8930148 using the fine mesh CITATION code.

As is observable, the calculated  $RPE(\%)$  based on the proposed method is significantly fewer than the orthogonal FVM. Table 2 also shows that the total execution time of the proposed

non-orthogonal gradient-based FVM is more than the other method. This is due to the higher required initial gradient-based calculations for deformation of the applied CVs. However, as can be seen, this difference is not significant because the aforementioned initial stationary iterative calculations based on the original meshes do not need to be implemented in an accurate form, and in fact, a rough calculation is enough for determination of the neutron flux/power profile. The solution of the neutron fluxes along with the  $k_{eff}$  is then used as the initial guess for the subsequent iterative neutron diffusion calculations based on the moved meshes to reduce the total execution time. Moreover, it should be noted that the gradient-based calculations for the implementation of the proposed method are not an iterative calculation. Accordingly, it can not be comparable to the execution time of the iterative calculations.

To verify the accuracy of the method, the relative errors of the calculated powers for the test case 1 are presented in Table 3. Note that to obtain the power values, first, the normalization of the neutron fluxes proceed as follows (Argonne Code Center, 1977, Vagheian et al., 2016a):

$$\frac{1}{\Omega_{Core}} \int_{\Omega_{Core}} \sum_g v \sum_{fg} \phi_g d\Omega = 1, \quad (49)$$

and then the calculated fluxes are employed to obtain power values. Additionally, it should be noted that the power value in each position compared with the corresponding position of the power value that obtained by the fine mesh solution of the CITATION code.

Table 3 clearly indicates that the proposed method can significantly reduce the error of calculations in comparison to the orthogonal FVM at entire reactor regions. Table 3 also reveals that the maximum error of power which is located at CV (4,4) in the height  $z = 107.14$  cm and is calculated based on the proposed method (0.070%) is fewer than that obtained from the orthogonal FVM (0.159%) in the same position. This is due to the fact that the mesh distribution according to the proposed method can properly cover regions with high gradient variations. In the case of the error of maximum power which is located at CV (1,1), the proposed method also showed a fewer amount of relative error (0.067%) than the conventional orthogonal FVM (0.081%).

## 5.2. Test case 2

The second benchmark problem is a three-dimensional reactor core with two neutron energy groups and total dimensions  $90 \times 90 \times 240$  cm<sup>3</sup>. Fig. 17, shows the geometry and configuration of this test case study. This reactor is made of three different materials. The boundary conditions of this reactor core comprise of zero flux for the external boundaries. The group constants of this problem are presented in Table 4 (Miro et al., 2002).

In order to solve the second benchmark problem, an arbitrary number of  $9 \times 9 \times 24$  CVs are considered. An-fourth view of the applied orthogonal CV distribution for the gradient-based calculations is presented in Fig. 18. Fig. 19 shows the calculated relative power gradient distribution as the three-dimensional form in three different heights.

Similar to the previous case study, the mesh partitioning distribution of the proposed method in each height is illustrated in Fig. 20. As can be seen, there is observable relation between the gradient distribution and mesh density resolution in each height. It is also interesting to note that, the mesh point distribution in the first and third heights are almost similar to each other. This is due to the fact that there is no significant observable difference between the obtained gradient variations in two considered heights. This point can be considered important from the point of view of checking the performance of the method. More precisely,

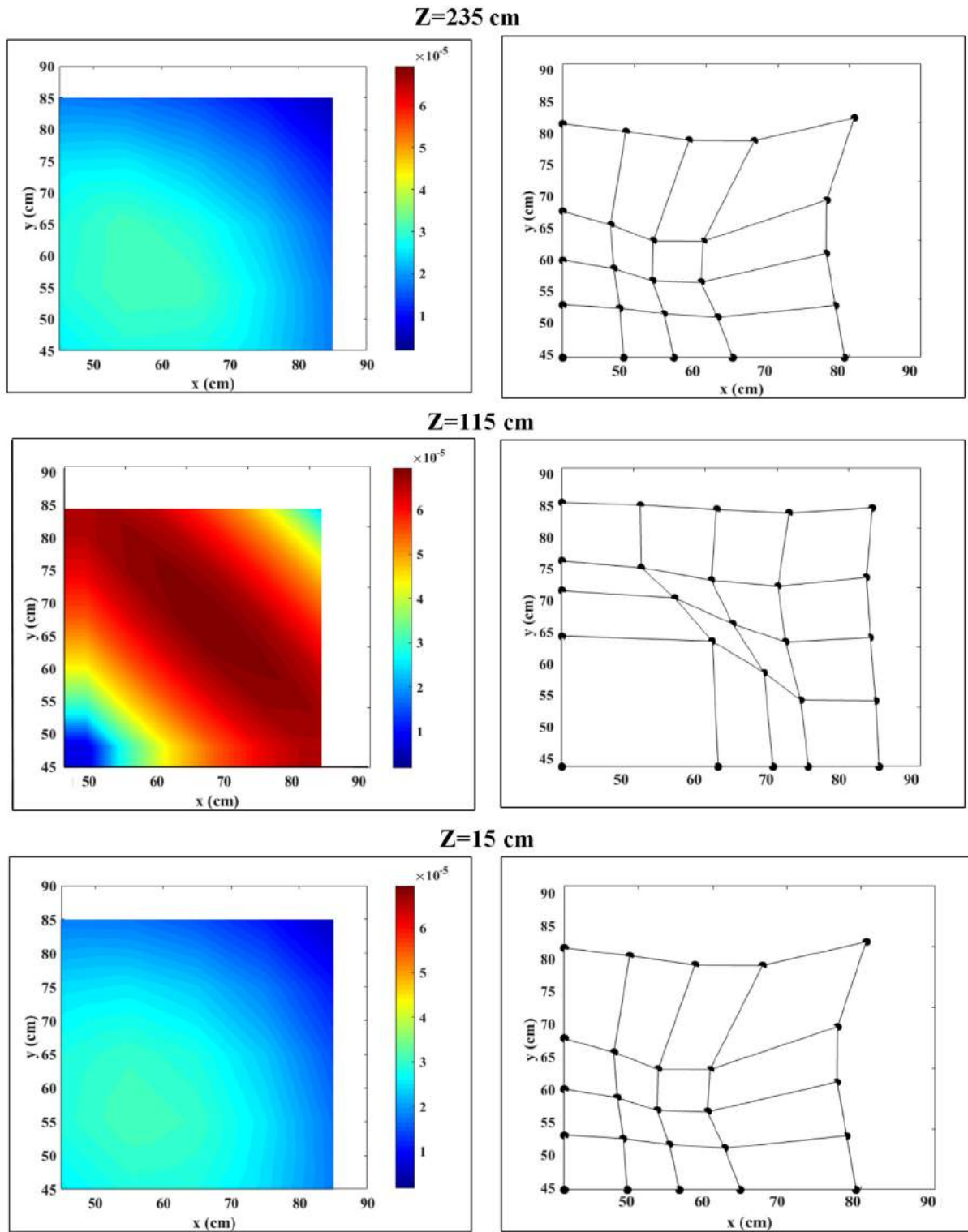


**Fig. 20.** Relative power gradient distributions (left) and the corresponding mesh density resolutions (right) for the test case 2.

this figure indicates that the proposed method can allow to accurate mesh movement and CV deformation even if the gradient variations have no uniform trend along the coordinate axes.

For evaluating the proposed method, the results that obtained based on the orthogonal FVM are compared to those obtained regarding the proposed non-orthogonal FVM. Also, it should be noted that in order to make consistent accuracy comparison, the same number of CVs is considered which in the case of the second

benchmark problem this array of CVs is  $9 \times 9 \times 24$ . The calculated effective multiplication factor is presented in Table 5. As can be seen, the calculated  $RPE(\%)$  based on the proposed method is significantly lower than that the other one. Table 5 also indicates that the total execution time of the proposed non-orthogonal gradient-based FVM is more than the other one. However, similar to the previous case study it can be observed that this difference is not considerable.

**Table 5**Comparison of the calculated  $k_{eff}$  and its relative error with the reference value of test case 2.

Method	Effective Multiplication Factor ( $k_{eff}$ )	RPE(%)	Total execution time (s)
The Proposed non-orthogonal gradient-based FVM	1.0006146	0.0582481 (~58 pcm)	92
The orthogonal FVM	1.0012130	0.1180862 (~118 pcm)	89

The reference solution was obtained 1.0000321 using the fine mesh CITATION code.

**Table 6**

Relative error (%) comparison of the calculated power for the test case 2.

CV	Z = 15 cm		Z = 115 cm		Z = 235 cm	
	Orthogonal Method	Non-Orthogonal Method	Orthogonal Method	Non-Orthogonal Method	Orthogonal Method	Non-Orthogonal Method
(1,1)	0.059	0.023	0.075	0.064	0.059	0.024
(2,1)	0.096	0.042	0.101	0.051	0.096	0.042
(3,1)	-0.086	0.050	-0.149	0.060	0.086	-0.050
(4,1)	-0.083	-0.046	-0.137	0.060	-0.083	-0.046
(2,2)	0.109	0.041	0.150	0.061	0.109	0.041
(3,2)	-0.087	-0.040	0.131	0.060	0.086	0.040
(4,2)	0.088	0.040	0.136	0.059	0.088	0.040
(3,3)	-0.094	-0.040	-0.142	-0.060	-0.094	-0.040
(4,3)	0.086	0.041	0.149	-0.060	0.086	0.041
(4,4)	0.091	0.041	0.142	0.059	0.092	0.041

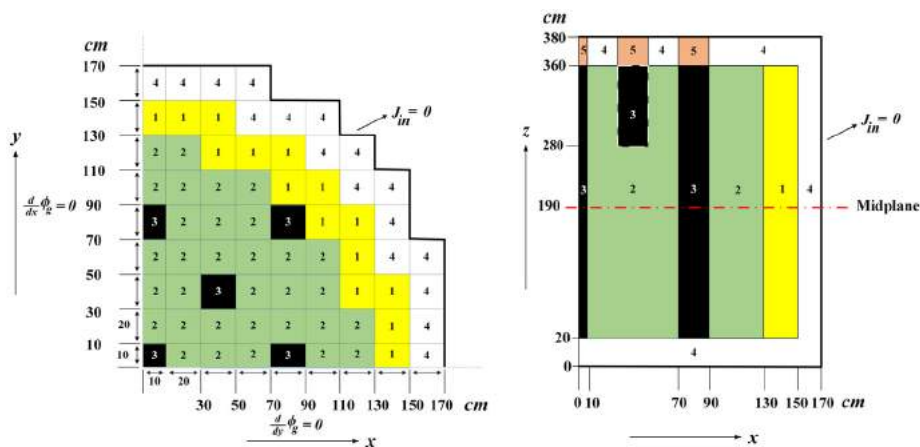
The results of power calculations are tabulated in Table 6. As is observable, all of the calculated errors based on the proposed method are fewer than those obtained from the conventional FVM. It is also worth to point out that in the case of the maximum error of power which is located at CV (2,2) and in the middle of the reactor's height, the proposed method showed a fewer amount of relative error (0.061%) than the conventional orthogonal FVM (0.150%).

Table 6 additionally reveals that the error of maximum power which is located at CV (1,1) in the height of  $z = 115$  cm and is

calculated based on the proposed method (0.064%) is fewer than that calculated regarding the conventional orthogonal FVM (0.075%) in the same position.

### 5.3. Test case 3

The third benchmark problem is the IAEA three-dimensional problem. One hundred and seventy-seven (177) fuel assemblies including nine (9) fully rodded fuel assemblies and four (4) partially rodded fuel assemblies compose the core. The core of the

**Fig. 21.** Geometry configuration of test case 3 (Argonne Code Center, 1977).**Table 7**

Group constants of test case 3 (Argonne Code Center, 1977).

Mat.	Group Constants	$D_g(\text{cm})$	$\Sigma_{og}(\text{cm}^{-1})$	$\nu\Sigma_{fg}(\text{cm}^{-1})$	$\Sigma_{g \rightarrow g+1}(\text{cm}^{-1})$
1	1	1.5	0.01	0.135	0.02
	2	0.4	0.08	...	...
2	1	1.5	0.01	0.135	0.02
	2	0.4	0.085	...	...
3	1	1.5	0.01	0.135	0.02
	2	0.4	0.13	...	...
4	1	2.0	0.00	0.00	0.04
	2	0.3	0.01	...	...
5	1	2.0	0.00	0.00	0.04
	2	0.3	0.055	...	...



IAEA benchmark problem is also surrounded by sixty-four (64) reflector assemblies with the axial and radial thickness of 20 cm (Argonne Code Center, 1977). The geometry and boundary conditions of this problem are shown in Fig. 21. Additionally, the group constants of the problem are shown in Table 7.

In Fig. 21, according to reference (Argonne Code Center, 1977), Material 1 (regions with yellow color) represents Fuel 1; Material 2 (regions with green color) represents Fuel 2; Material 3 (regions with black color) represents Fuel 2 + Rod; Material 4 (regions with white color) represents Reflector and finally Material 5 (regions with pink color) represents Reflector + Rod.

Fig. 22 shows one-fourth view of the applied orthogonal CV distribution for the gradient-based calculations of the test case 3. As is shown, an arbitrary number of  $17 \times 17 \times 38$  CVs are considered for the solution of this benchmark problem. The calculated relative power gradient distribution as the three-dimensional form is illustrated in Fig. 23.

The mesh partitioning distribution of the proposed method in each height is presented in Fig. 24. As is shown, the mesh movement and CV deformation is only observable in the height of 195 cm. This is due to the fact that there are not any power value and power gradient variations in the region of the reflector (material number 4,  $z = 15$  cm) and in the region of reflector and control rods (material number 5,  $z = 375$  cm). According to Fig. 24, it is also worth to note that the proposed algorithm enables the mesh movement and CV deformation when there is a gradient variation in each height and position.

To consider the performance of the proposed method for the test case 3, the results that obtained based on the orthogonal FVM are compared to those obtained based on the proposed non-orthogonal FVM for the same array of CVs ( $17 \times 17 \times 38$ ). Accordingly, the calculated  $k_{eff}$  based on the two methods is presented in Table 8. As is shown, the calculated  $RPE(\%)$  based on the proposed method is significantly fewer than that the other method. According to Table 8, it also can be observed that the difference of total execution time between the proposed non-orthogonal FVM and the conventional FVM is negligible. More precisely, by using the proposed method, higher accurate results without spending more

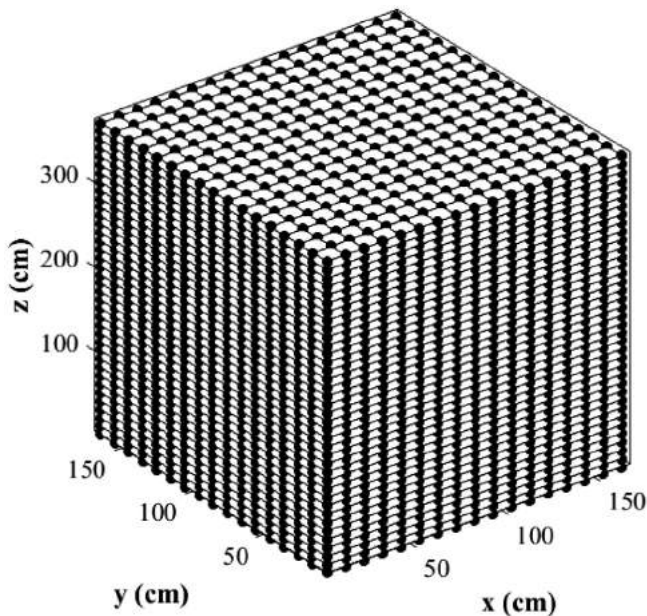


Fig. 22. One-fourth view of the applied orthogonal CV distribution for the gradient-based calculations of test case 3.

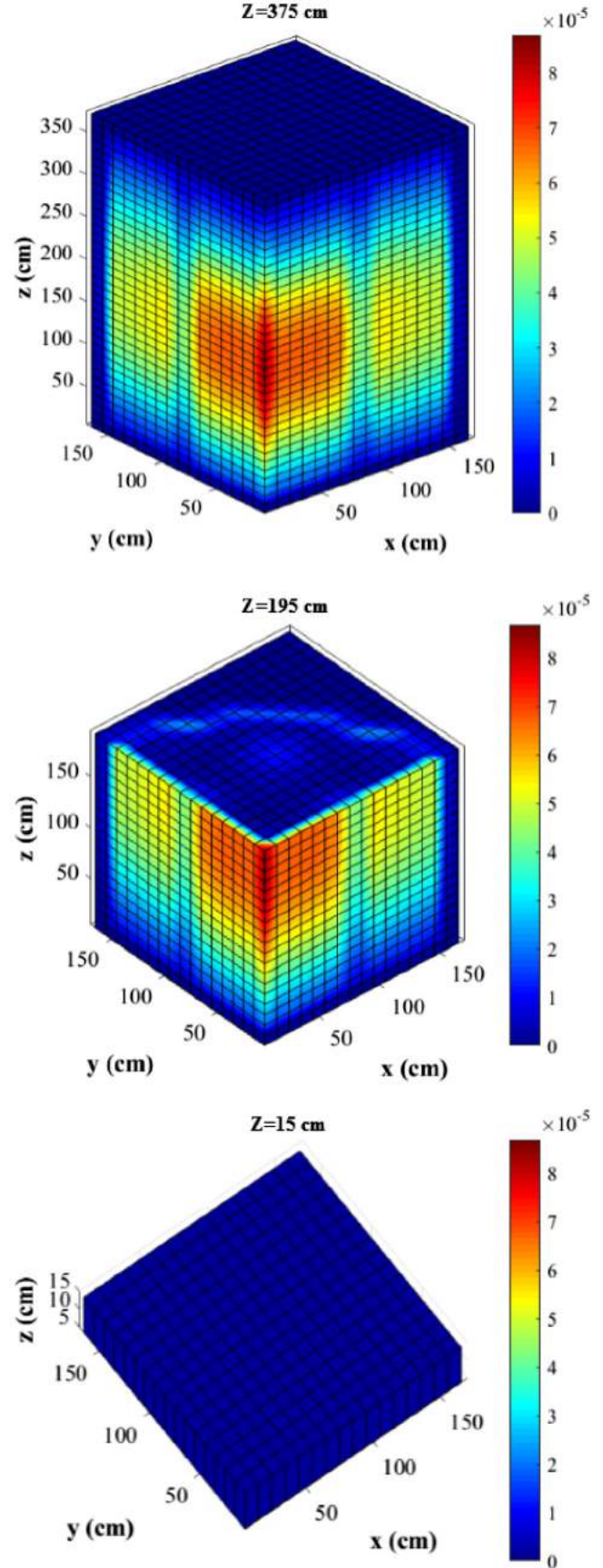
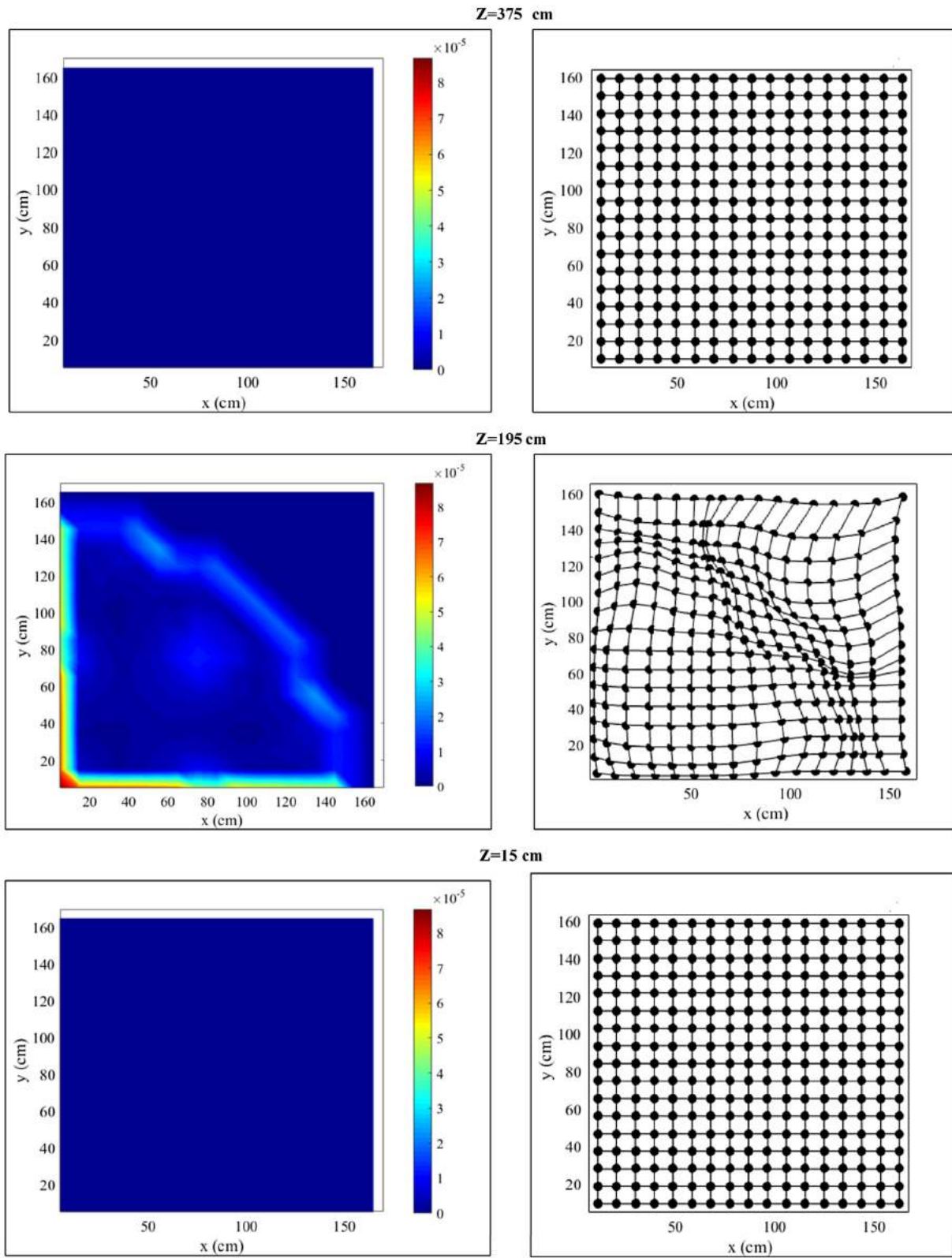


Fig. 23. Calculated relative power gradient distribution as a three-dimensional form for the test case 3.



**Fig. 24.** Relative power gradient distributions (left) and the corresponding mesh density resolutions (right) for the test case 3.

**Table 8**Comparison of the calculated  $k_{eff}$  and its relative error with the reference value of test case 3.

Method	Effective Multiplication Factor ( $k_{eff}$ )	RPE(%)	Total execution time (s)
The Proposed non-orthogonal gradient-based FVM	1.0295307	0.0422215 (~42 pcm)	129
The orthogonal FVM	1.0299073	0.0788167 (~79 pcm)	122

The reference solution was obtained 1.0290962 using the fine mesh CITATION code.

execution time can be achieved in comparison with the conventional FVM.

The results of power calculations for the test case 3 are tabulated in Table 9. As was previously discussed, because the mesh and CV scheme of the two illustrated heights (i.e.  $z = 15$  cm and  $z = 375$  cm) are the same with the orthogonal scheme, the difference between the results is not significant. Therefore, only the results of the power calculations for the height of  $z = 195$  cm are tabulated in Table 9. As is shown in this table, all of the calculated

errors based on the proposed method are fewer than those obtained from the conventional FVM. It is also worth to point out that in the case of the maximum error of power which is located at CV (1,1) and in the middle of the reactor's height, the proposed method showed fewer RPE% (0.328%) than the conventional orthogonal FVM (0.790%). Moreover, Table 9 shows that the error of the maximum power which is located at CV (4,4) and in the middle of the reactor's height is about 0.209% for the proposed method and 0.708% for the conventional orthogonal FVM. Accordingly, in

**Table 9**Relative error (%) comparison of the calculated power for the test case 3 and height  $z = 195$  cm.

CV	Orthogonal Method	Non-Orthogonal Method	CV	Orthogonal Method	Non-Orthogonal Method	CV	Orthogonal Method	Non-Orthogonal Method
(1,1)	0.790	0.328	(7,4)	0.720	0.211	(12,8)	0.731	0.251
(2,1)	0.771	0.302	(8,4)	-0.600	0.215	(13,8)	0.711	0.229
(3,1)	0.669	0.301	(9,4)	0.754	-0.221	(14,8)	...	...
(4,1)	-0.780	-0.295	(10,4)	0.739	0.200	(15,8)	...	...
(5,1)	0.761	0.283	(11,4)	0.748	0.205	(16,8)	...	...
(6,1)	0.549	-0.300	(12,4)	0.741	0.210	(17,8)	...	...
(7,1)	0.744	0.269	(13,4)	0.540	0.227	(9,9)	0.715	0.200
(8,1)	-0.752	-0.272	(14,4)	-0.743	0.219	(10,9)	0.729	0.231
(9,1)	0.749	0.267	(15,4)	0.739	0.218	(11,9)	-0.723	-0.243
(10,1)	0.741	0.275	(16,4)	...	...	(12,9)	0.740	0.219
(11,1)	-0.750	-0.280	(17,4)	...	...	(13,9)	0.740	0.220
(12,1)	-0.730	-0.298	(5,5)	-0.730	0.229	(14,9)	...	...
(13,1)	0.731	0.246	(6,5)	0.706	0.204	(15,9)	...	...
(14,1)	0.743	-0.217	(7,5)	-0.710	-0.201	(16,9)	...	...
(15,1)	0.721	0.235	(8,5)	0.600	0.210	(17,9)	...	...
(16,1)	0.734	...	(9,5)	-0.731	-0.211	(10,10)	0.746	0.240
(17,1)	0.750	...	(10,5)	-0.736	-0.206	(11,10)	0.735	0.241
(2,2)	0.776	0.230	(11,5)	0.736	-0.220	(12,10)	...	...
(3,2)	0.769	0.286	(12,5)	0.755	0.218	(13,10)	...	...
(4,2)	-0.761	-0.264	(13,5)	-0.661	0.219	(14,10)	...	...
(5,2)	-0.761	-0.291	(14,5)	-0.759	0.210	(15,10)	...	...
(6,2)	0.462	0.209	(15,5)	0.756	-0.200	(16,10)	...	...
(7,2)	0.751	0.257	(16,5)	...	...	(17,10)	...	...
(8,2)	0.751	0.255	(17,5)	...	...	(11,11)	0.720	0.200
(9,2)	0.651	0.206	(6,6)	-0.741	-0.229	(12,11)	...	...
(10,2)	-0.751	-0.251	(7,6)	-0.529	-0.231	(13,11)	...	...
(11,2)	0.747	0.219	(8,6)	-0.731	0.234	(14,11)	...	...
(12,2)	0.728	0.239	(9,6)	0.709	0.237	(15,11)	...	...
(13,2)	-0.738	0.240	(10,6)	0.713	0.218	(16,11)	...	...
(14,2)	-0.751	-0.239	(11,6)	-0.607	0.220	(17,11)	...	...
(15,2)	-0.733	0.237	(12,6)	0.750	-0.255	(12,12)	...	...
(16,2)	...	...	(13,6)	-0.753	-0.267	(13,12)	...	...
(17,2)	...	...	(14,6)	...	...	(14,12)	...	...
(3,3)	0.740	0.237	(15,6)	...	...	(15,12)	...	...
(4,3)	-0.639	0.188	(16,6)	...	...	(16,12)	...	...
(5,3)	-0.715	-0.221	(17,6)	...	...	(17,12)	...	...
(6,3)	0.728	0.209	(7,7)	0.779	0.250	(13,13)	...	...
(7,3)	0.738	0.241	(8,7)	0.771	0.264	(14,13)	...	...
(8,3)	0.741	-0.231	(9,7)	0.531	0.200	(15,13)	...	...
(9,3)	0.509	0.231	(10,7)	0.745	0.245	(16,13)	...	...
(10,3)	-0.621	-0.271	(11,7)	0.775	0.239	(17,13)	...	...
(11,3)	-0.737	-0.260	(12,7)	0.752	0.258	(14,14)	...	...
(12,3)	0.737	0.269	(13,7)	0.749	-0.255	(15,14)	...	...
(13,3)	0.749	-0.254	(14,7)	...	...	(16,14)	...	...
(14,3)	0.753	0.251	(15,7)	...	...	(17,14)	...	...
(15,3)	0.757	0.231	(16,7)	...	...	(15,15)	...	...
(16,3)	...	...	(17,7)	...	...	(16,15)	...	...
(17,3)	...	...	(8,8)	0.780	0.210	(17,15)	...	...
(4,4)	0.708	0.209	(9,8)	-0.779	0.229	(16,16)	...	...
(5,4)	-0.717	-0.210	(10,8)	-0.629	-0.260	(17,16)	...	...
(6,4)	0.722	0.201	(11,8)	0.747	-0.263	(17,17)	...	...



addition to the maximum error of power, the proposed method also has more accurate results for the error of the maximum power in comparison to the conventional orthogonal FVM.

As is observable from Table 9, some of the points have no values. This is due to the fact that they are located in regions (such as the reflector) that there is not any power value. Additionally, it should be noted that the power value in each position compared with the corresponding position of the power value that obtained by the fine mesh solution of the CITATION code. Note that based on this approach, some of the meshes might have been moved from the regions with no power values to the regions with power values that have fissionable materials. However, owing to the fact that there are not any comparable results between these moved meshes and the original meshes, they have not been indicated.

#### 5.4. Test case 4

The fourth benchmark problem is the static version of the transient benchmark problem of a light water reactor. This problem, the LMW (Langenbuch–Maurer–Werner) test problem, is modeled with two neutron energy groups. The layout of this LMW core is shown in Fig. 25. The core is a simplified pressurized water reactor (PWR) and is composed of two kinds of fuel assemblies whose dimensions are 20 cm × 20 cm × 160 cm (Langenbuch et al., 1977; Aoki et al., 2007).

In Fig. 25, Material 1 (regions with white color) represents Fuel 1; Material 2 (regions with green color) represents Fuel 1 + Rod composition; Material 3 (regions with light brown color) represents Fuel 2 and finally, Material 4 (regions with dark brown color) represents Reflector. The group constants the LMW benchmark problem are tabulated in Table 10.

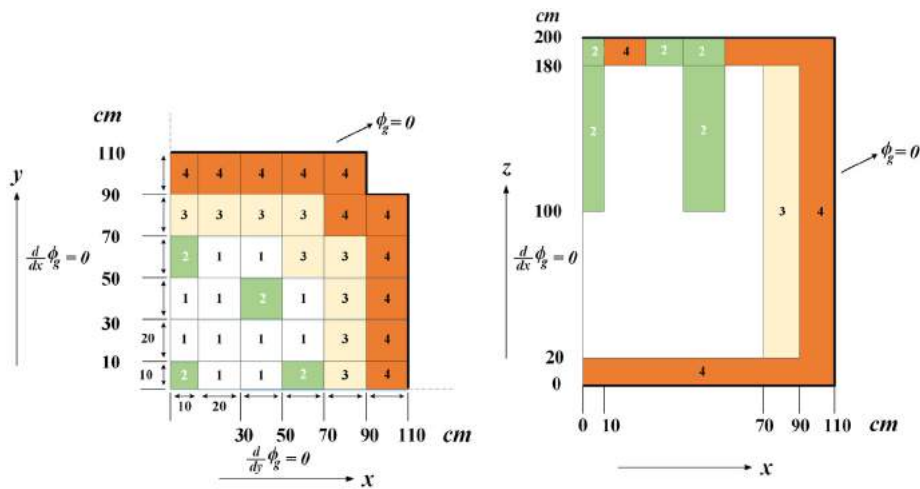


Fig. 25. Geometry configuration of test case 4 (Langenbuch et al., 1977; Aoki et al., 2007).

Table 10

Group constants of test case 4 (Langenbuch et al., 1977; Aoki et al., 2007).

Mat.	Group Constants	$D_g$ (cm)	$\Sigma_{ag}$ (cm <sup>-1</sup> )	$\nu\Sigma_{fg}$ (cm <sup>-1</sup> )	$\Sigma_{g \rightarrow g+1}$ (cm <sup>-1</sup> )
1	1	1.423913	0.01040206	0.006477691	0.01755550
	2	0.356306	0.08766217	0.112732800	...
2	1	1.423913	0.01095206	0.006477691	0.01755550
	2	0.356306	0.09146217	0.112732800	...
3	1	1.425611	0.01099263	0.007503284	0.01717768
	2	0.350574	0.09925634	0.137800400	...
4	1	1.634227	0.00266057	...	0.02759693
	2	0.264002	0.04936351	...	...

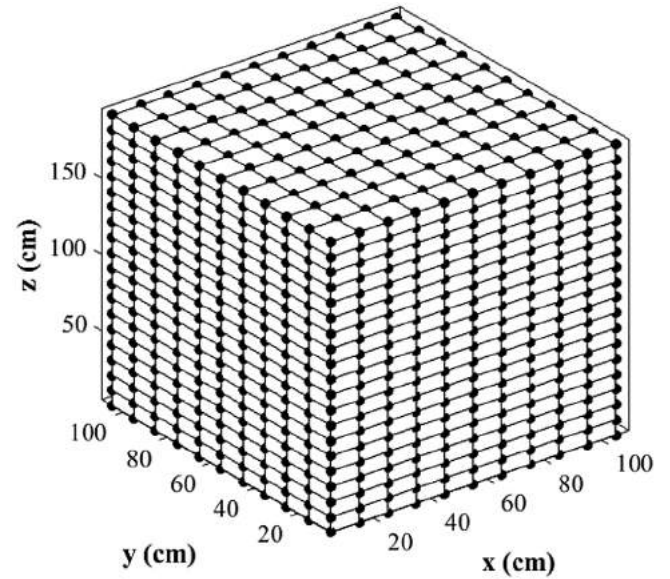


Fig. 26. One-fourth view of the applied orthogonal CV distribution for the gradient-based calculations of test case 4.

To solve this benchmark problem, an arbitrary number of  $11 \times 11 \times 20$  CVs are considered. An-fourth view of the applied orthogonal CV distribution for the gradient-based calculations of the fourth benchmark problem is shown in Fig. 26. Additionally, the calculated relative power gradient distribution as the three-dimensional form for three different heights is illustrated in



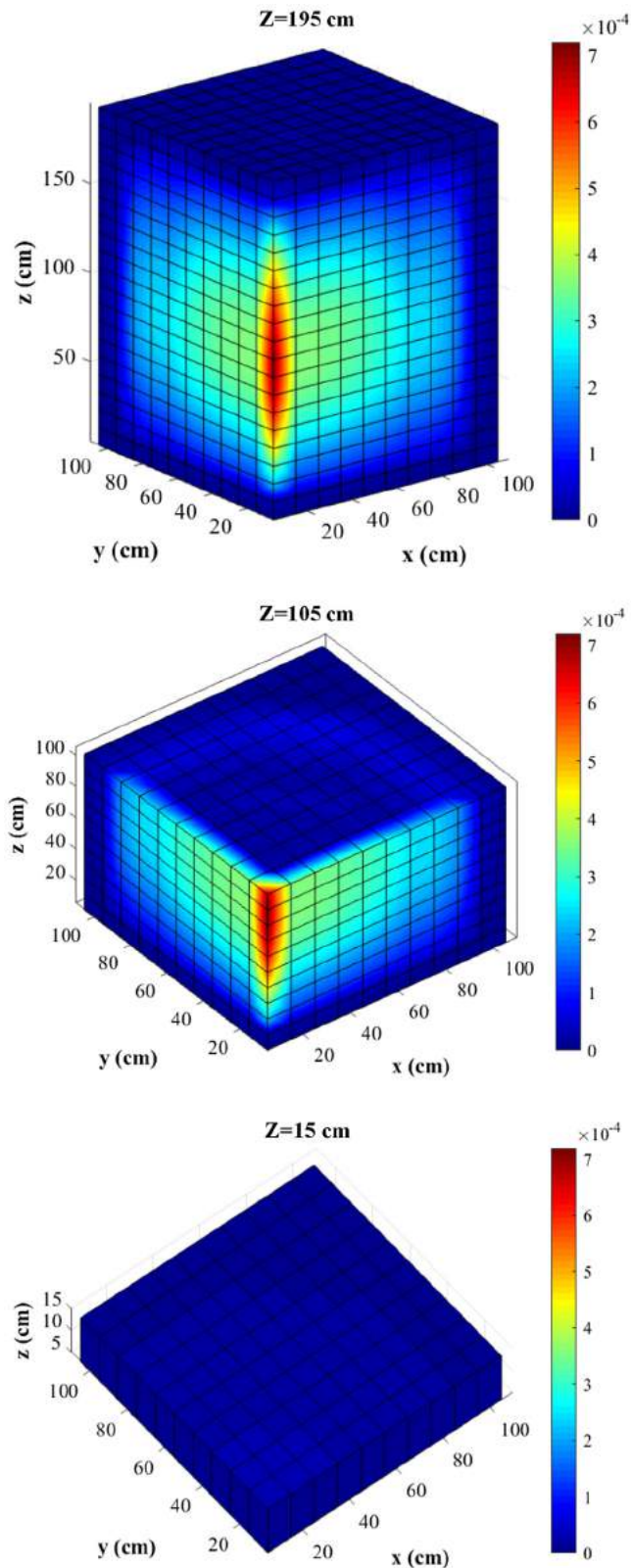


Fig. 27. Calculated relative power gradient distribution as a three-dimensional form for the test case 4.

Fig. 27. Moreover, the visual mesh density resolution of the proposed method in each height is shown in Fig. 28.

In order to make consistent accuracy comparison between the orthogonal FVM and proposed non-orthogonal FVM, again the

same number of CVs is considered (which for the test case 4 is  $11 \times 11 \times 20$ ). The results of the calculated  $k_{eff}$  between the proposed non-orthogonal gradient-based FVM and the conventional orthogonal FVM are presented in Table 11.

Table 11 reveals that the calculated  $RPE(\%)$  based on the proposed method is fewer than the orthogonal FVM. Additionally, similar to the previous test case studies it can be observed that there are no considerable differences in the execution time between the methods. The calculated power value for the test case 4 is presented in Table 12. Owing to the fact that there is not any power value in the reflector region, the results only are tabulated for  $z = 105$  cm and  $z = 195$  cm. According to this table, it is shown that the maximum error of power which is located at CV (1,1) and  $z = 105$  cm is 0.606% and 0.287% based on the conventional orthogonal FVM and proposed non-orthogonal FVM, respectively. Moreover, it can also be observed that the error of maximum power which is located in CV (2,2) and  $z = 105$  cm is 0.601% and 0.284% regarding the conventional orthogonal FVM and proposed non-orthogonal FVM, respectively.

### 5.5. Test case 5

The fifth benchmark problem is the OBLONG reactor with four neutron energy groups. The layout of this problem is shown in Fig. 29. In this figure, Material 1 (regions with black color) and 2 (regions with light brown color) are fuel. Material 1 is a highly enriched material while Material 3 (regions with red color) is a strong moderator. The group constants of this benchmark problem are presented in Table 13 (Aboanber and Nahla, 2007; Ferguson and Hansen, 1973).

In order to perform the iterative calculations, an arbitrary number of  $40 \times 20 \times 30$  CVs are considered for this benchmark problem. An-fourth view of the applied orthogonal CV distribution for the gradient-based calculations is presented in Fig. 30. Fig. 31 shows the calculated relative power gradient distribution as the three-dimensional form.

In order to show the performance of the proposed method, the relative power gradient distributions and the corresponding mesh density resolution in three different heights are illustrated in Fig. 32. As is observable, the proposed method allows covering the regions of interest based on the spatial gradient variations of the reactor power by aid of the proposed mesh movement and CV deformation algorithm.

Similar to the previous test case studies, the performance of the proposed method are considered. Accordingly, the same number of CVs ( $40 \times 20 \times 30$ ) are considered to ensure the consistent accuracy comparison between the orthogonal FVM and proposed non-orthogonal FVM. Table 14 shows the calculated  $k_{eff}$  for the two aforementioned methods. As is shown, the proposed method has higher accuracy than the conventional orthogonal FVM with almost the same execution time. In fact, the accuracy of the  $k_{eff}$  has been improved more than 2 times, while the execution time increased by only about 5%.

The comparison results of the power values is of interest similar to the previous benchmark problems. However, owing to the lots of CVs in each height ( $40 \times 20$ ) for this benchmark problem, only the results of two important parameters are discussed (i.e. the maximum error of power and the error of maximum power). Regarding the performed calculations, the maximum error of power obtained 0.521% and 0.2191% based on the orthogonal FVM and proposed non-orthogonal FVM, respectively. Moreover, the calculated error of maximum power obtained 0.472% and 0.184% regarding the orthogonal FVM and the proposed method, respectively. As is obvious, in addition to the  $k_{eff}$ , the proposed

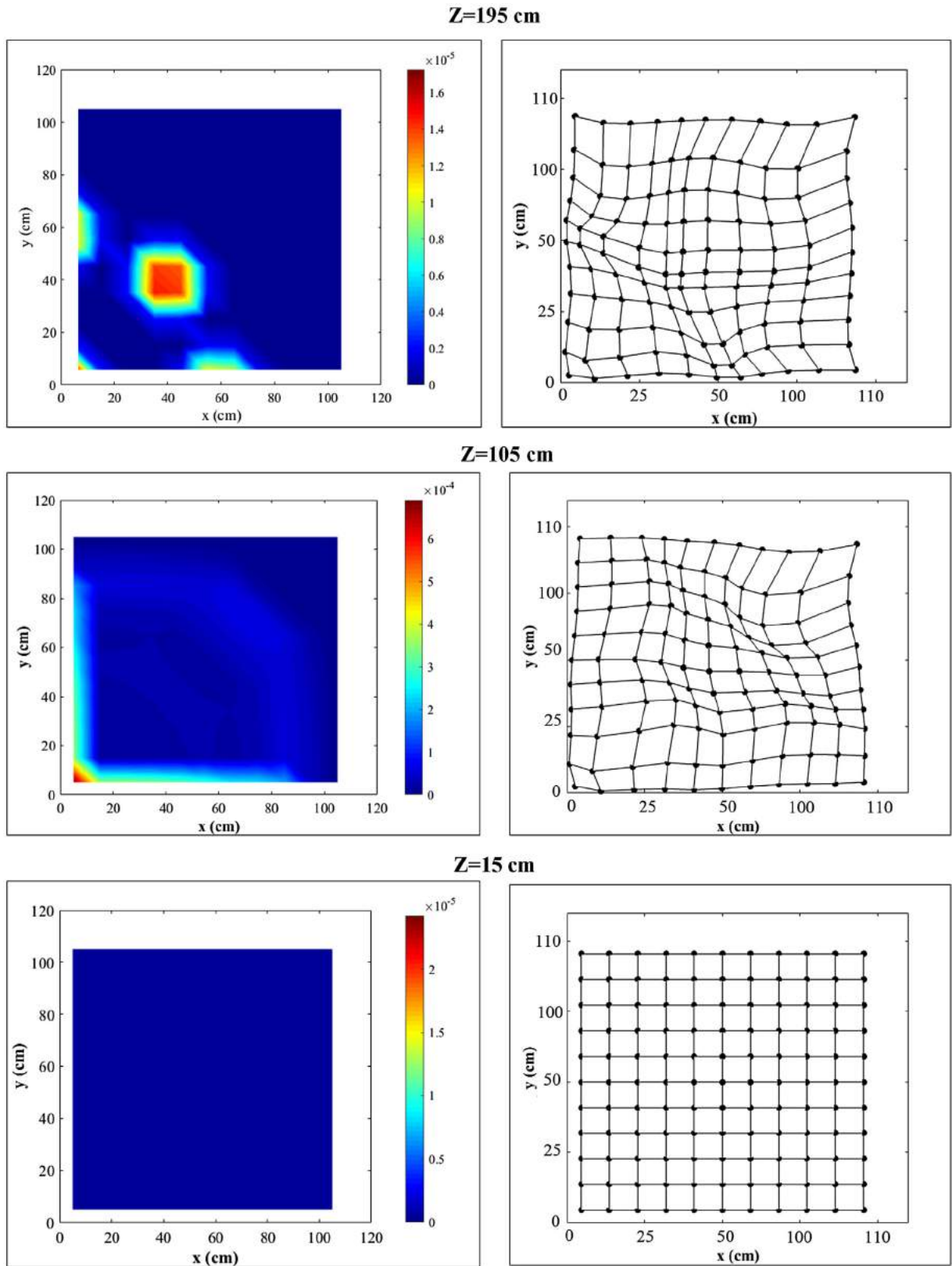


**Fig. 28.** Relative power gradient distributions (left) and the corresponding mesh density resolutions (right) for the test case 3.

**Table 11**Comparison of the calculated  $k_{eff}$  and its relative error with the reference value of test case 4.

Method	Effective Multiplication Factor ( $k_{eff}$ )	RPE(%)	Total execution time (s)
The Proposed non-orthogonal gradient-based FVM	1.0000825	0.0482493 (~48 pcm)	118
The orthogonal FVM	1.0005372	0.0937374 (~94 pcm)	111

The reference solution was obtained 0.9996002 using the fine mesh CITATION code.

**Table 12**Relative error (%) comparison of the calculated power for the test case 4 and heights  $z = 105$  cm and  $z = 195$  cm.

CV	Z = 105 cm		Z = 195 cm	
	Orthogonal Method	Non-Orthogonal Method	Orthogonal Method	Non-Orthogonal Method
(1,1)	0.606	0.287	0.553	0.229
(2,1)	0.603	0.286	...	...
(3,1)	0.504	0.217	...	...
(4,1)	0.601	0.287	...	...
(5,1)	0.602	0.286	...	...
(6,1)	0.604	0.275	0.507	0.220
(7,1)	-0.483	-0.275	-0.508	0.223
(8,1)	-0.603	-0.273	...	...
(9,1)	-0.603	-0.281	...	...
(10,1)	...	...	...	...
(11,1)	...	...	...	...
(2,2)	0.601	0.284	...	...
(3,2)	0.602	0.282	...	...
(4,2)	0.533	-0.282	...	...
(5,2)	0.603	0.285	...	...
(6,2)	0.601	0.284	...	...
(7,2)	0.604	0.287	...	...
(8,2)	-0.604	0.282	...	...
(9,2)	-0.603	0.278	...	...
(10,2)	...	...	...	...
(11,2)	...	...	...	...
(3,3)	0.608	0.282	...	...
(4,3)	0.570	0.283	...	...
(5,3)	0.602	0.284	...	...
(6,3)	-0.499	-0.284	...	...
(7,3)	-0.605	0.283	...	...
(8,3)	0.520	0.283	...	...
(9,3)	-0.604	0.283	...	...
(10,3)	...	...	...	...
(11,3)	...	...	...	...
(4,4)	0.609	0.282	0.548	0.221
(5,4)	0.608	0.282	0.531	0.220
(6,4)	0.609	-0.284	...	...
(7,4)	-0.595	-0.280	...	...
(8,4)	-0.607	0.279	...	...
(9,4)	-0.602	0.278	...	...
(10,4)	...	...	...	...
(11,4)	...	...	...	...
(5,5)	0.609	0.280	0.547	-0.221
(6,5)	0.605	0.282	...	...
(7,5)	-0.583	-0.281	...	...
(8,5)	-0.601	-0.281	...	...
(9,5)	0.604	0.279	...	...
(10,5)	...	...	...	...
(11,5)	...	...	...	...
(6,6)	0.609	0.280	...	...
(7,6)	-0.606	0.282	...	...
(8,6)	-0.609	-0.273	...	...
(9,6)	0.608	0.272	...	...
(10,6)	...	...	...	...
(11,6)	...	...	...	...
(7,7)	0.609	0.281	...	...
(8,7)	-0.605	-0.278	...	...
(9,7)	0.605	-0.277	...	...
(10,7)	...	...	...	...
(11,7)	...	...	...	...

Table 12 (continued)

CV	Z = 105 cm		Z = 195 cm	
	Orthogonal Method	Non-Orthogonal Method	Orthogonal Method	Non-Orthogonal Method
(8,8)	...	...	...	...
(9,8)	...	...	...	...
(10,8)	...	...	...	...
(11,8)	...	...	...	...
(9,9)	...	...	...	...
(10,9)	...	...	...	...
(11,9)	...	...	...	...
(10,10)	...	...	...	...
(11,10)	...	...	...	...
(11,11)	...	...	...	...

gradient-based non-orthogonal FVM has more accurate results in the case of the power values.

### 5.6. Further array investigation

To investigate the accuracy of the proposed non-orthogonal FVM for further arrays, three more arbitrary arrays have been considered to be applied on the second benchmark problem (as an example). Fig. 33 shows the comparison between the calculated RPEs of the effective multiplication factors based on the two methods and arrays of  $6 \times 6 \times 16$ ,  $9 \times 9 \times 24$ ,  $12 \times 12 \times 32$  and  $15 \times 15 \times 40$ .

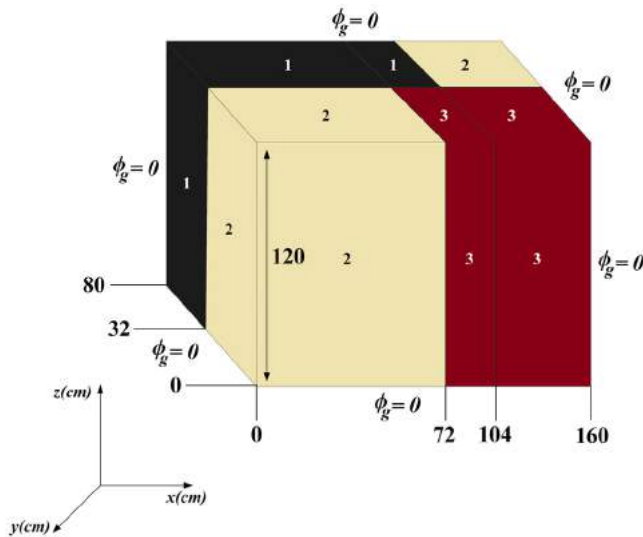


Fig. 29. Geometry configuration of test case 5 (Aboanber and Nahla, 2007; Ferguson and Hansen, 1973).

This figure clearly reveals the higher accuracy of the proposed non-orthogonal FVM than the other one for all considered arbitrary arrays. More precisely, the proposed method shows lower relative errors in comparison with the conventional orthogonal FVM at the same number of CVs. Moreover, Fig. 33 shows that the rate of reduction of relative error which is indicated by the slope of the error curves is different for the two applied methods. According to Fig. 33, it can also be found that there is an important relationship between the difference of accuracy of the methods and the number of total CVs. In fact, the difference between the results of the two methods decreases as the total number of CVs increase. This can be due to the fact that by increasing the number of CVs, the difference of CV density resolution in different regions decrease and accordingly the results of the calculations are close to each other.

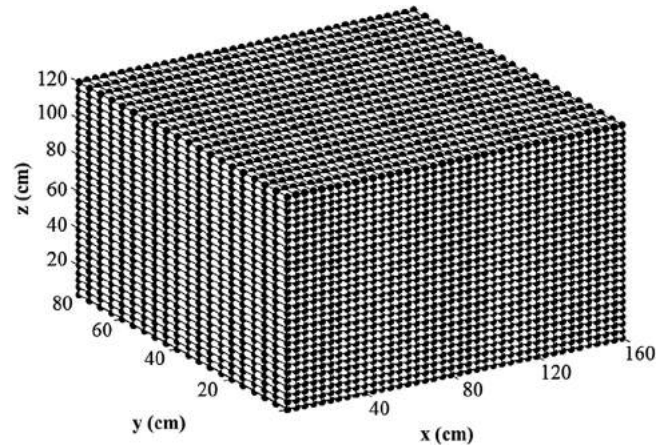


Fig. 30. One-fourth view of the applied orthogonal CV distribution for the gradient-based calculations of test case 5.

Table 13

Group constants of the test case 5 (Aboanber and Nahla, 2007; Ferguson and Hansen, 1973).

Mat.	Group Constants	$D_g(\text{cm})$	$\Sigma_{ag}(\text{cm}^{-1})$	$\nu\Sigma_{fg}(\text{cm}^{-1})$	$\Sigma_{g \rightarrow g+1}(\text{cm}^{-1})$
1	1	2.77778	0.00266	0.002176	0.0586
	2	1.07527	0.00297	0.003152	0.0828
	3	0.64103	0.0359	0.04192	0.0850
	4	0.16260	0.655	0.864	0.0
2	1	3.33333	0.00135	0.00112	0.0586
	2	1.38889	0.00140	0.00144	0.0828
	3	0.83333	0.0176	0.02096	0.0850
	4	0.20833	0.332	0.4384	0.0
3	1	4.16667	0.00077	0.0	0.0570
	2	2.08333	0.00072	0.0	0.0822
	3	1.07527	0.00051	0.0	0.0847
	4	0.26247	0.012	0.0	0.0



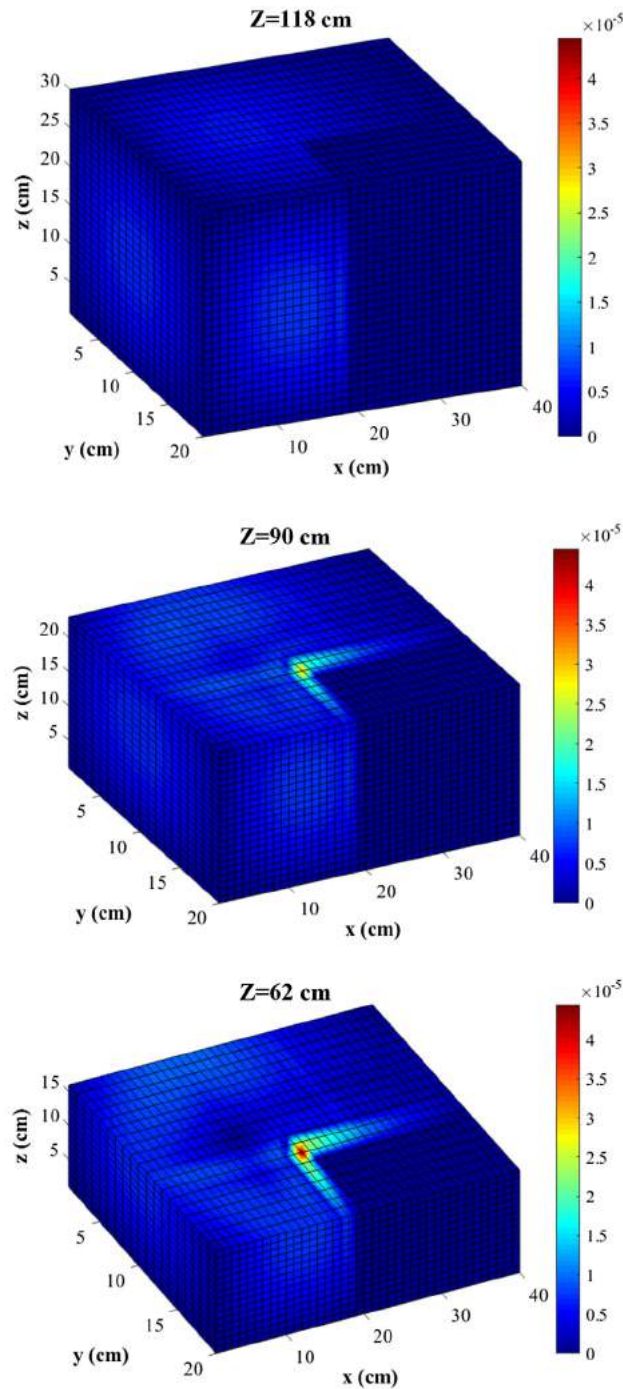


Fig. 31. Calculated relative power gradient distribution as a three-dimensional form for the test case 5.

### 5.7. Execution time

The execution time of the presented benchmark problems is of obvious interest. In making comparisons between the presented different computational methods, direct comparisons is often difficult because execution time varies depending upon the computer, programming language and programming style in use. On this basis, in addition to the proposed non-orthogonal gradient-based FVM, the solution of the conventional orthogonal FVM has been

obtained to insure the consistent accuracy comparison between the results. It is also worth to mention that the execution time herein is the total time consumed from the point at which the input data have been read and initialize to the point that the solution of the calculations determines.

The results of execution time from Tables 2,5,8,11 and 14 for the test cases 1,2,3,4 and 5, respectively, shows that the solution based on the proposed method requires a few more time to be executed than the conventional orthogonal FVM for all of the benchmark problems. This is due to the extra initial gradient-based calculations for the mesh movement and CV deformation. However, as is also observable in the aforementioned tables, this difference is not significant. One of the reason is that the initial gradient-based calculations are not iterative and accordingly the execution time is not considerable when compared to the iterative calculations. The second reason is that, the initial stationary iterative calculations do not need to be implemented in an accurate form, and in fact, a rough calculation is performed to obtain the shape of variations of flux/power. The last reason might be due to the fact that the initial guess for the subsequent iterative neutron diffusion calculations based on the moved meshes are provided by the initial solution of the proposed method both in terms of neutron flux/power and in terms of  $k_{eff}$ . This access reduces computational effort because it rapidly reduces the number of inner and outer iterations in which a large set of algebraic iterative equations should be solved numerically. This procedure accordingly was considered in this work and it was the main reason for the small difference of execution time between the orthogonal and non-orthogonal FVMs.

## 6. Conclusion

In this paper a new non-orthogonal gradient-based FVM was introduced to solve the multi-group three-dimensional neutron diffusion equations. The proposed method formulated based on a new method of calculation to achieve a various mesh density resolution in different regions. The regions of interest in this work were considered to be regions with the highly gradient variations of reactor power. The authors also introduced and developed a new method of mesh movement in addition to the CV deformation to accurately model and efficiently solve the neutron diffusion problems.

For facilitating comparison between the conventional FVM and that proposed in this work, five benchmark problems were considered. These benchmark problems had different features such as material compositions, neutron energy groups and boundary conditions. In the case of the complexity of the problems, they had different rectangular reactor core configurations including homogeneous, radially heterogeneous, axially heterogeneous and finally, axially-radially heterogeneous geometries. The results all including the error of effective multiplication factor, the maximum error of power and finally the error of maximum power revealed the superiority and effectiveness of the proposed method with respect to the orthogonal FVM.

Possible future works can be included, extending of the proposed method to different CV tessellations and reactor core geometries.

## Appendix A. Supplementary data

Supplementary data to this article can be found online at <https://doi.org/10.1016/j.anucene.2019.107216>.

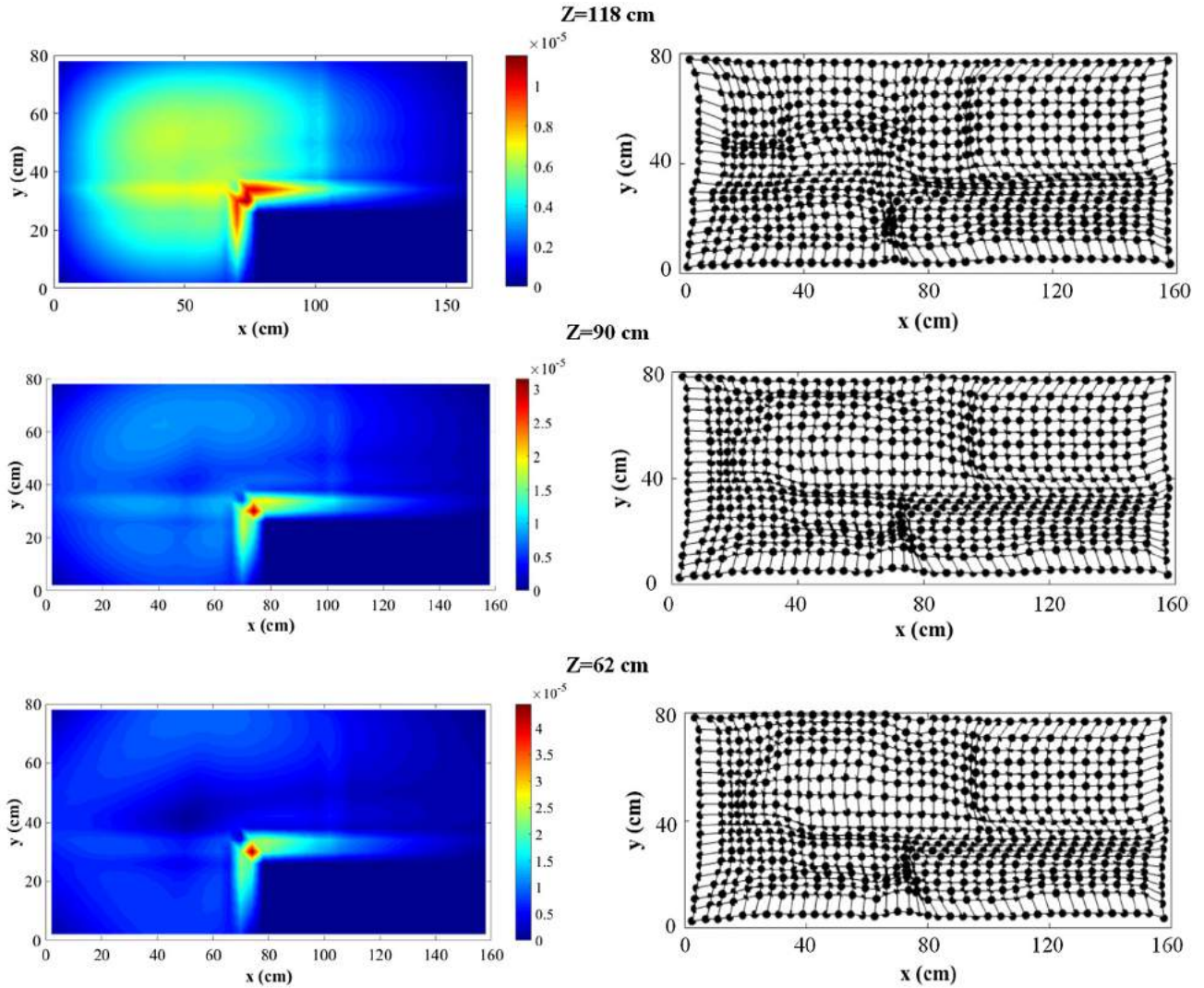


Fig. 32. Relative power gradient distributions (left) and the corresponding mesh density resolutions (right) for the test case 5.

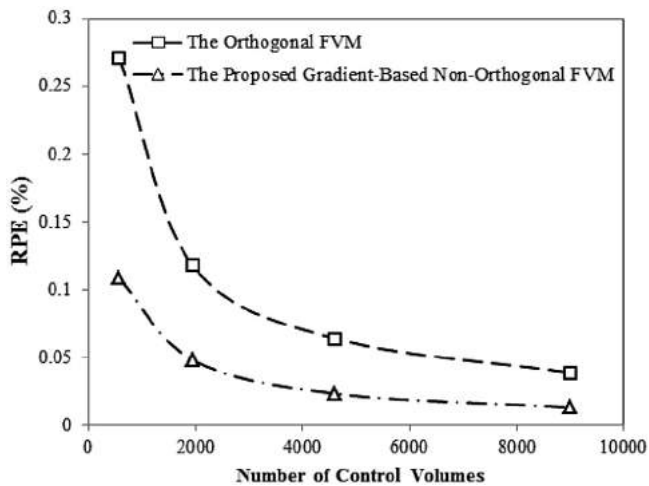


Fig. 33. RPEs of the calculated effective multiplication factor ( $k_{eff}$ ) versus the total number of CVs for the both of the orthogonal and non-orthogonal FVM and all considered arrays of  $6 \times 6 \times 16$ ,  $9 \times 9 \times 24$ ,  $12 \times 12 \times 32$  and  $15 \times 15 \times 40$ .

Table 14

Comparison of the calculated  $k_{eff}$  and its relative error with the reference value of the test case 5.

Method	Effective Multiplication Factor ( $k_{eff}$ )	RPE(%)	Total execution time (s)
The Proposed non-orthogonal gradient-based FVM	1.06638051	0.0339365 (~34 pcm)	98
The orthogonal FVM	1.06684219	0.0772454 (~77 pcm)	93

The reference solution was obtained 1.06601874 using the fine mesh CITATION code.

## References

- Aboanber, A.E., Nahla, A.A., 2007. Adaptive matrix formation (AMF) method of space-time multigroup reactor kinetics equations in multidimensional model. *Ann. Nucl. Energy* 34, 103–119.
- Argonne Code Center, 1977. Benchmark Problem Book, Report ANL-7416 (Suppl. 2). Argonne National Laboratory, Argonne, IL.
- Barth, T., Ohlberger, M., 2004. In: *Finite Volume Methods: Foundation and Analysis*, Encyclopedia of Computational Mechanics 1, 15. John Wiley & Sons, Ltd.. <https://doi.org/10.1002/0470091355.ecm010>.

- Bell, G.I., Glasstone, S., 1970. Nuclear Reactor Theory. Van Nostrand Reinhold Company, New York.
- Bernal, A., Roman, J.E., Miró, R., Ginestar, D., Verdú, G., 2015. Development of a finite volume inter-cell polynomial expansion method for the neutron diffusion equation. *J. Nucl. Sci. Technol.* <https://doi.org/10.1080/00223131.2015.1102661>.
- Blanchon, F., Ha-Duong, T., Planchard, J., 1988. Numerical methods for solving the reactor kinetic equations. *Prog. Nucl. Energy* 22, 173–180.
- Christensen, B., 1985. Three-dimensional Static and Dynamic Reactor Calculations by the Nodal Expansion Method PhD dissertation. Rise National Laboratory, Denmark.
- Clark, M., Hansen, K.F., 1964. Numerical Methods of Reactor Analysis. Academic Press Inc, New York.
- Clifford, I.D., 2007. Object-oriented Multi-physics Applied to Spatial Reactor Dynamics MSc dissertation. North-West University, Potchefstroom Campus.
- Droniou, J., Eymard, R., 2006. A mixed finite volume scheme for anisotropic diffusion problems on any grid. *Numerische Mathematik* 105, 35–71.
- Duderstadt, J.J., Hamilton, L.J., 1991. Nuclear Reactor Analysis. John Wiley & Sons, New York.
- Eymard, R., Gallouet, T., Herbin, R., 2000. Finite volume methods. In: *Handbook of Numerical Analysis*, pp. 713–1020. North-Holland, Amsterdam.
- Ferguson, D.R., Hansen, K.F., 1973. Solution of the space-dependent reactor kinetics equations in three dimensions. *Nucl. Sci. Eng.* 51 (2), 189–205.
- Fowler, T.B., 1999. CITATION-LDI2 Nuclear Reactor Core Analysis Code System, CCC643. ORNL, Oak Ridge, Tennessee.
- Jasak, H., 1996. Error Analysis and Estimation for the Finite Volume Method with Applications to Fluid Flows Dissertation. University of London, London.
- Kang, C.M., Hansen, K.F., 1971. Finite Element Methods for Space-time Reactor Analysis PhD dissertation. Massachusetts Institute of Technology, Massachusetts.
- Lamarsh, J.R., 1965. Introduction to Nuclear Reactor Theory. Addison-Wesley Publishing Company.
- Langenbuch, S., Maurer, W., Werner, W., 1977. Coarse-mesh flux-expansion method for the analysis of space-time effects in large light water reactor cores. *Nucl. Sci. Eng.* 63 (4), 437–456.
- Le Potier, C., 2005. A finite volume method for the approximation of highly anisotropic diffusion operators on unstructured meshes. *Finite Volumes for Complex Applications IV*, Marrakesh, Morocco.
- Lyra, P.R.M., de Lima, R.C.F., Guimarães, C.S.C., de Carvalho, D.K.E., 2002. An edge-based unstructured finite volume method for the solution of potential problems. *Mecanica Comput.* 11, 1213–1231.
- Menon, S., 2011. A Numerical Study of Droplet Formation and Behaviour using Interface Tracking Methods PhD dissertation. University of Massachusetts, Massachusetts.
- Miro, R., Ginestar, D., Verdu, G., Hennig, D., 2002. A nodal modal method for the neutron diffusion equation. Application to BWR instabilities analysis. *Ann. Nucl. Energy* 29, 1171–1194.
- Nakamura, S., 1977. Computational Methods in Engineering and Science with Applications to Fluid Dynamics and Nuclear Systems. Wiley Interscience, New York.
- Sezai, I., 2011. Lecture notes Fall 2011–2012. Methods for dealing with complex geometries (Part of the course in computational fluid dynamics at Eastern Mediterranean University).
- Aoki, Sh., Suemura, T., Ogawa, J., Takeda, T., 2007. The verification of 3 dimensional nodal kinetics code ANCK using transient benchmark problems. *J. Nucl. Sci. Technol.* 44, 862–868.
- Stewart, J., 2003. Multivariable Calculus Early Transcendentals. Thomson Brooks/Cole.
- Theler, G., 2013. Unstructured Grids and the Multigroup Neutron Diffusion Equation. *Science and Technology of Nuclear Installations*, Volume 2013, Article ID 641863, 26 pages. DOI:10.1155/2013/641863.
- Tianliang, Hu., Hongchun, Wu., Liangzhi, C., Zhifeng, Li, 2017. Finite volume method based neutronics solvers for steady and transient-state analysis of nuclear reactors. *Energy Procedia* 127, 275–283.
- Tomov, S.Z., 2002. Adaptive Methods for Finite Volume Approximation PhD dissertation. Texas A&M University, Texas.
- Vagheian, M., Talebi, S., 2019. Introduction to the slide modeling method for the efficient solution of heat conduction calculations. *JACM* 5, 680–695.
- Vagheian, M., Vosoughi, N., Gharib, M., 2016a. Enhanced finite difference scheme for the neutron diffusion equation using the importance function. *Ann. Nucl. Energy* 96, 412–421.
- Vagheian, M., Rezaei Ochbelagh, D., Gharib, M., 2016b. On an improved box-scheme finite difference method based on the relative event probabilities. *Prog. Nucl. Energy* 88, 33–42.
- Van der Westhuizen, D.J., 2013. Gradient Calculations of Non-orthogonal Meshes in the Finite Volume Method MSc dissertation. North-West University, Potchefstroom Campus.
- Verga, R.S., 1956. Numerical Solution of the Two-group Diffusion Equation in x-y Geometry U.S. Atomic Energy Commission Report WAPD-159. Westinghouse Electric Corp., Atomic Power Division, Pittsburgh, Pa.

## Introduction to the Slide Modeling Method for the efficient solution of heat conduction calculations

*Journal of Applied and Computational Mechanics*, 5(4) (2019) 680-695.

**Authors:** M. Vagheian\*, Saeed Talebi

**Abstract:** A new adaptive orthogonal Finite Volume Method, called Slide Modeling Method, was developed for the determination of the maximum temperature in one and two-dimensional geometries efficiently. The proposed numerical method was developed based on a pre-determined mesh density technique and applied to the heat conduction equation. In the proposed Slide Modeling Method, each homogeneous region (each region has a unique material) as a part of a large multi-region problem is divided into a few slices, and a different number of meshes are assigned to them regarding some calculated weighting factors. These weighting factors were obtained roughly before the beginning of the main numerical solution of the heat conduction equation based on the estimation of the temperature profile in each region. The proposed method was applied to different benchmark problems and confirmed its very high accuracy in a reasonable computational cost.

**Contributions:** I developed the proposed Slide Modeling Method and derived the entire algorithm. In addition, I discretized the mathematical heat conduction equation and programmed it in the MATLAB software. I sent the manuscript as the corresponding author after writing the entire sections of the manuscript as the first author and afterward revised the manuscript according to the received comments from the journal.

**License:** This work is licensed under a Creative Commons Attribution 4.0 International (CC BY 4.0). To see the license go to <http://jacm.scu.ac.ir>





## Journal of Applied and Computational Mechanics



Research Paper

# Introduction to the Slide Modeling Method for the Efficient Solution of Heat Conduction Calculations

Mehran Vagheian<sup>1</sup>, Saeed Talebi<sup>2</sup>

<sup>1</sup> Department of Energy Engineering and Physics, Amirkabir University of Technology (Tehran Polytechnic)  
424 Hafez Avenue, P.O. Box 15875-4413, Tehran, Iran, Email: mvagheian@aut.ac.ir

<sup>2</sup> Department of Energy Engineering and Physics, Amirkabir University of Technology (Tehran Polytechnic)  
424 Hafez Avenue, P.O. Box 15875-4413, Tehran, Iran, Email: sa.talebi@aut.ac.ir

Received October 23 2018; Revised December 19 2018; Accepted for publication January 12 2019.

Corresponding author: Mehran Vagheian, mvagheian@aut.ac.ir

© 2019 Published by Shahid Chamran University of Ahvaz

& International Research Center for Mathematics & Mechanics of Complex Systems (M&MoCS)

**Abstract.** Determination of the maximum temperature and its location is the matter of the greatest importance in many technological and scientific engineering applications. In terms of numerical calculations of the heat conduction equation by using uniform mesh increments in space, large computational cost is sometimes countered. However, adaptive grid refinement method could be computationally efficient both in terms of accuracy and execution time. In this work, the numerical solution of the heat conduction equation based on the slide modeling method (SMM) is introduced. This method is based on a pre-determined mesh density approach which divides each homogeneous region into different slides and then assigns higher mesh point densities to slides of interest regarding their relative importance by performing some mathematical calculations. The importance of each region is determined by some formulated weighting factors which rely on the estimation of temperature profiles in all regions and slides. To investigate the accuracy and efficiency of the proposed method, a number of different case studies have been considered. The results all revealed the strength of the proposed SMM in comparison with the conventional method (based on uniform mesh point distribution).

**Keywords:** Slide modeling method, Efficient finite volume method, Heat conduction calculations, Unstructured meshes.

## 1. Introduction

Determination of the maximum temperature and its location is the matter of the greatest importance in many technological and scientific engineering applications. This is mainly due to the fact that in a homogeneous region, required information, including the exact temperatures as well as the location of the maximum temperature are always essential to prevent local abnormal conditions [1, 2]. In consequence, there is a strong incentive to develop accurate and computationally efficient methods for obtaining these parameters.

A number of methods have been developed and introduced for solving the heat conduction equation such as the Finite Difference Method (FDM) [3], Finite Element Method (FEM) [4], Finite Volume Method (FVM) [5], Discrete Element Method (DEM) [6], Boundary Element Method (BEM) [7], Monte Carlo Method (MCM) [8] and Meshless Method [9]. Among the aforementioned methods, the FDM has been always the center of attention on account of its simplicity and satisfactory accuracy [10, 11].

Previous research findings suggests that the discretization forms of differential equations by the FDM can mainly be divided into two categories, namely Mesh-Edged and Mesh-Centered. It is also worth to mention that the latter, which is also called as the Box-Scheme FDM gives almost a more accurate numerical solution in comparison to the other one [11].

As is obvious, the accuracy of the FDM can significantly be impacted by changing the number of mesh elements. However,



it is also revealed that the position of mesh elements is a second key factor that should be considered. In fact, there are numbers of mesh adaptive approaches for optimizing mesh point positions and consequently, the selection and development of an innovative approach are the center of attention that has been discussed widely in the literature for different numerical problems [11-18].

Based on the arguments mentioned above, it is evident that distributing the mesh point positions is almost the center of attention, and accordingly a number of different perspectives have been applied for different applications. In 2015, Zhai et al. [14] has shown that an adaptive local mesh refinement could be considered with respect to the unknown variable errors along with its first derivatives where a higher mesh element density is applied in domain with rapid function variations in comparison to the other regions with relatively smooth variations. Recently, Zhai et al. [15] have also presented an improved scheme for the convection-dominated diffusion solution by using a non-uniform grid structure method. This work has also supported the fact that the accuracy of the non-uniform grids is significantly higher than those using uniform grids. Cao et al. [12] investigated a hybrid adaptive Finite Difference Method to form an unstructured-based mesh method by using the posteriori error estimation technique. Based on the suggested method, three principal numerical steps are considered, including: a finite difference solver, a posteriori error estimator, and a re-gridding re-coarsening tool. Here, the error estimation is determined by solving a local Neumann problem to form an error energy norm for guiding the mesh adaptation through the simultaneous mesh refinement process. It has been shown that by implementing this method, the global error magnitude has been eventually reduced. In addition to the error estimation approach, some researchers have introduced different types of view of methodology for optimization problems. In this connection, Lee et al. [13] developed a novel technique based on the finite difference moving mesh method to provide higher accuracy of the one-dimensional nonlinear initial value problems. According to this adaptive method, the mesh point distribution is adjusted to focus on areas of interest where the solution of the problem varies with rapid changes. The results showed that the accuracy of the solution has been significantly developed. The finite difference weighted essentially non-oscillatory method (WENO) may alternatively be used to refine mesh distributions [3]. Regarding this approach, it has been shown that the accuracy of the solution along with the performance of the numerical calculation can be remarkably improved by getting the way for using a new cell-based data structure to form the adaptive meshes of multi-dimensional denotation problems.

In 2016, a pre-determined mesh point position technique was developed to increase the efficiency and accuracy of the nuclear reactor calculations using an adaptive BSFDM [11]. This method considered the two key mentioned parameters concomitantly, i.e. the number of mesh elements and the adaptively mesh refinement. According to the proposed method, the mesh positions are pre-determined in all regions by considering each region's importance in the solution. In facilitating consistent accuracy comparison, the results of the proposed adaptive method and the standard FDM is presented for the same number of mesh elements. This method proved its strength on obtaining more accurate results for any arbitrary the same number of mesh elements.

Our application of interest is the determination of the maximum temperature and its corresponding locations using the heat conduction calculations based on the SMM. This proposed method is based on dividing each homogeneous region into different slides and then calculating the relative importance of them using the formulated weighting factors which rely on the estimation of temperature profiles in all slides. The formalism for derivation of the mathematical conduction equation is performed using the BSFDM (Box-Scheme Finite Difference Method) and solved numerically by the iteration method. To consider the strength of the proposed method properly, it accounts for different type of boundary conditions and mesh point numbers. For a quantitative comparison, the total involved CPU time is reported for the same level of accuracy between the proposed SMM method and the CM (based on uniform mesh distribution).

The current research is organized in six sections. In the second section, the adaptive discretization form of the governing equations for one and two-dimensional rectangular geometries are presented. These equations are derived based on the BSFDM used for iterative calculating. In section three, the proposed SMM method is completely introduced and followed by the required mathematical equations and methodology. In the fourth section, the proposed method is applied to five different problems, including the two aforementioned rectangular geometries to verify and evaluate the results of the calculations for different boundary conditions and temperature distributions. For facilitating comparison purpose, the total CPU time of the calculations has also been presented in this section to study the efficiency of the suggested SMM method. In the section five, the discussion of the obtained results has been presented and finally, in the last section a conclusion of the paper has been stated.

## 2. Mathematical Formulation

In this section, the numerical solution scheme for the temperature distributions with one and two-dimensional heat conduction equations are presented. This section, deals primarily with one-dimensional steady-state cases in which the discretization adaptive form of the governed equations based on the BSFDM is introduced. Following this, the process is repeated, beginning by illustrating the derivation of the governed equations for two-dimensional rectangular geometries by considering non-equal mesh box sides.

### 2.1. Adaptive one-dimensional heat conduction approach

In this subsection, the heat transfer by conducting in one-dimensional geometry is stressed. The general form of the mentioned equation is as the following [19, 20]:



$$U \frac{\partial^2 T}{\partial x^2} = -q''', \quad (1)$$

This equation is the stationary form of the heat transfer by conducting in one-dimensional geometry and known as Poisson's equation. In eq. (1),  $q'''$  is the volumetric thermal source strength and  $U$  is the heat conduction coefficient. The volumetric thermal source is applied in the heat transfer equation due to the consideration of possible existence of internal heat generation in the material. Hence, for the development of the proposed method in this work, a general heat conduction equation, which can be used to evaluate the heat transfer in any direction and with or without heat generation, is considered. In the following, the discretization procedure of the aforementioned equation is presented in details.

As can be observed from Fig.1, the implementation can be carried out by considering the two adjacent neighbors for  $i$ th mesh box, in such a way that in the resulting mesh, nodal points fell on in the center of a mesh box based on the BSFDM. It is noticeable that,  $\Delta^i$  and  $\Delta^j$  reflecting the side length of  $i$ th mesh box and the adjacent neighbors  $j=[1,2]$ , respectively.

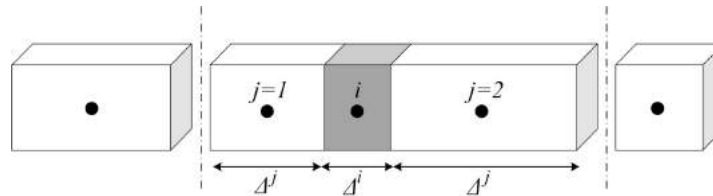


Fig. 1. Two adjacent neighbors of box ( $i$ ) in 1-D geometry

The discretized scheme of the one dimensional heat conduction equations can be widely found in the literature; however, we propose a reformulation of these equations using non-equal mesh box approach as follows:

$$\sum_{j=1}^2 \oint_s q'' ds = \int_V q''' dV, \quad (2)$$

where all parameters have their usual meaning. In order to obtain  $q''$  in eq. (2), one can employ eq. (3) and obtain eqs. (4) and (5):

$$q'' = -U \frac{dT}{dx}, \quad (3)$$

$$q''_{in} = -U^j \frac{T^j - T_s}{\Delta^j / 2}, \quad (4)$$

$$q''_{out} = -U^i \frac{T_s - T^i}{\Delta^i / 2}, \quad (5)$$

In eqs. (4) and (5),  $T_s$  is the temperature at shared interface between box ( $i$ ) and box ( $j$ ). Because, this parameter is not determined using the cell centered FVM, it should be substituted with another parameter. This can be performed regarding the fact that in the shared interface  $q''_{in} = q''_{out}$ , accordingly, one can obtain:

$$T_s = \frac{\left(\frac{U^i}{\Delta^i}\right)T^i + \left(\frac{U^j}{\Delta^j}\right)T^j}{\left(\frac{U^i}{\Delta^i} + \frac{U^j}{\Delta^j}\right)}. \quad (6)$$

By substituting  $T_s$  from eq. (6) into eqs. (4) and (5) and then considering  $q''_{net}$ , one has:

$$q''_{net} = \frac{-2U^j \times U^i}{U^j \times \Delta^i + U^i \times \Delta^j} (T^j - T^i), \quad (7)$$

Finally, by substituting eq. (7) into eq. (2) one can obtain the discretized form of the heat transfer equation on 1-D geometries and for box ( $i$ ) as:

$$\sum_{j=1}^2 \left[ 2 \frac{U^i \times U^j}{U^i \times \Delta^j + U^j \times \Delta^i} \right] \times T^i + \sum_{j=1}^2 \left[ -2 \frac{U^i \times U^j}{U^i \times \Delta^j + U^j \times \Delta^i} \right] \times T^j = q''' \times \Delta^i, \quad (8)$$

In eq. (8), all parameters have their usual meaning. It is noteworthy to mention that we want to apply our presented algorithm for 1 and 2 dimensional geometries considering different boundary conditions. More precisely, the capability of the proposed method has been the center of our attention to prove the effectiveness and efficiency of the method in different conditions. Regarding eq. (8), it is obvious and vivid that this equation is a general form of the 1-D heat conduction equation with two adjacent neighbors; however, it is rewarding to demonstrate the governed equations with respect to different boundary conditions for boundary CVs [1, 2]. In the first case, the mesh box ( $i$ ), is subjected to a constant and uniform wall temperature. So, one can rewrite eq. (7) for the boundary face as:

$$q_{net}^* = -\frac{U^i}{\Delta^i/2}(T_s - T^i), \quad (9)$$

So, the governing heat conduction equation for the boundary CV can be simply derived as the following:

$$\left[ \sum_{j=1}^2 2 \frac{U^i \times U^j}{U^i \times \Delta^j + U^j \times \Delta^i} + 2 \frac{U^i}{\Delta^i} \right] \times T^i + \left[ \sum_{j=1}^2 -2 \frac{U^i \times U^j}{U^i \times \Delta^j + U^j \times \Delta^i} \right] \times T^j + \left[ -2 \frac{U^i}{\Delta^i} \right] \times T_s = q^m \times \Delta^i. \quad (10)$$

In the same way, in the case of the insulation boundary condition [1, 2] one can have for the boundary face:

$$q_{net}^* = 0, \quad (11)$$

and subsequently one can express the discretized heat conduction equation for the boundary CV for node ( $i$ ) as follows:

$$\left[ \sum_{j=1}^2 2 \frac{U^i \times U^j}{U^i \times \Delta^j + U^j \times \Delta^i} \right] \times T^i + \left[ \sum_{j=1}^2 -2 \frac{U^i \times U^j}{U^i \times \Delta^j + U^j \times \Delta^i} \right] \times T^j = q^m \times \Delta^i. \quad (12)$$

We can now analyze problems in which a wall cooled by flowing fluid on one side of the boundary mesh box ( $i$ ). By considering this boundary condition, one can obtain for the boundary face:

$$\frac{-U^i}{\Delta^i/2}(T_s - T^i) = h(T_s - T_f), \quad (13)$$

By rearranging eq. (13), one can obtain:

$$T_s = \frac{\left( \frac{2U^i}{\Delta \times h} \right) T^i + T_f}{1 + \left( \frac{2U^i}{\Delta \times h} \right)}, \quad (14)$$

And then, rewrite the governing equation for the boundary CV ( $i$ ) as:

$$\left[ \sum_{j=1}^2 \frac{2 \times U^i \times U^j}{U^i \times \Delta^j + U^j \times \Delta^i} + \frac{2 \times U^i \times h}{\Delta^i \times h + 2 \times U^i} \right] \times T^i + \sum_{j=1}^2 \left[ -\frac{2 \times U^i \times U^j}{U^i \times \Delta^j + U^j \times \Delta^i} \right] \times T^j + \left[ \left( -\frac{2 \times U^i \times h}{\Delta^i \times h + 2 \times U^i} \right) \times T_f \right] = q^m \times \Delta^i, \quad (15)$$

Where  $h$  and  $T_f$  are the heat transfer coefficient and temperature of the flow, respectively. In addition to the discussed boundary conditions, one can also consider the mixed boundary conditions such as thermal radiation and heat convection. According to the procedure of discretization which has been presented previously in this work, the main step is obtaining the temperature of boundary face (i.e.  $T_s$ ) and then using it to obtain the discretized governing equation. On this basis, a boundary face that has thermal radiation and heat convection boundary conditions is considered regarding the assumption that these boundary conditions are separated and do not have any impact on each other. Accordingly, one can have:

$$-U^i \frac{T_s - T^i}{\Delta^i/2} = h(T_s - T_f) - \alpha \sigma T_f^4, \quad (16)$$

where all parameters have their usual meaning. By rearranging eq. (16), one can obtain:

$$T_s = \left( \frac{\left( \frac{2U^i}{\Delta} \right)}{h + \left( \frac{2U^i}{\Delta} \right)} \right) T^i + \frac{h}{h + \left( \frac{2U^i}{\Delta} \right)} T_f + \frac{\alpha \sigma}{h + \left( \frac{2U^i}{\Delta} \right)} T_f^4, \quad (17)$$

Using eq. (17) one can obtain the governing heat equation similar to the previous cases. Due to the fact that there are more mixed boundary conditions that can be also considered, we did not investigate further these kind of problems.

At this stage it is instructive to evaluate the temperature distributions using the BSFDM approximation. To solve the

discretized governing equations numerically, the mentioned parameters can be searched for an iterative process. This method consists of successive steps, where, at first estimating initial values typically proceed for the unknown temperatures at all nodal points and subsequently the temperatures are recalculated using the new adjacent and previous adjoining temperatures. This iterative process is continued until some convergence criteria regarding the temperatures all are fulfilled [10, 11, 19, and 20].

## 2.2. Adaptive two-dimensional heat conduction approach

In this section, introducing the discretization form of the two-dimensional heat conduction equations based on the BSFDM is presented. The general 2-D heat conduction equation is considered as follows [1, 2]:

$$U \frac{\partial^2 T}{\partial x^2} + U \frac{\partial^2 T}{\partial y^2} = -q''', \quad (18)$$

As can be seen, eq. (18) is the general form of the heat conduction equations and consequently it should be discretized similar to the case of 1-D geometry. Fig. 2 illustrates the 2-D structured rectangular geometry by considering the four adjacent neighbors.

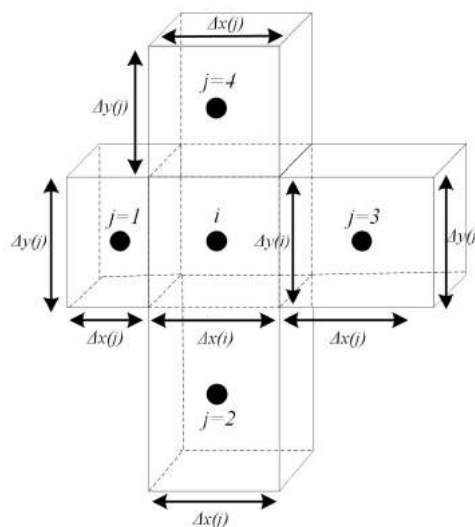


Fig. 2. Four adjacent neighbors of box (i) in 2-D geometry

As can be seen, each side of a mesh box is assumed to be differed from the surrounding boxes regarding the adaptive approach. From this figure, it is also clear that  $\Delta x$  and  $\Delta y$  imply the side lengths of a mesh box in  $x$  and  $y$  direction, respectively. For discretization of the governing heat conduction equation in 2-D geometries, one has:

$$\sum_{j=1}^4 \oint_s q'' ds = \int_V q''' dV, \quad (19)$$

Using eq. (19), the discretized form of the adaptive governing equation in the case of 2-D geometries can be obtained similar to the 1-D geometries as:

$$\sum_{j=1}^4 \left[ 2 \frac{U^i \times U^j}{U^i \times \Delta^j + U^j \times \Delta^i} \times S^i \right] \times T^i + \sum_{j=1}^4 \left[ -2 \frac{U^i \times U^j}{U^i \times \Delta^j + U^j \times \Delta^i} \times A^i \right] \times T^j = q''' \times V^i, \quad (20)$$

Here,  $S^i$  and  $V^i$  are the area and volume of  $i$ th mesh box, respectively. It is also noteworthy to mention that, in eq. (20)  $\Delta$  is as  $\Delta x$  or  $\Delta y$  depending on which direction is chosen. Moreover, as is shown in Fig. 2, one can reasonably argue that  $A$  is perpendicular to the side of  $\Delta$ . In order to obtain the governing discretized equation of the boundary CVs, each face of the CV should be treated separately similar to the 1-D geometries. In the following, discretization of one corner CV in a 2-D geometry is considered.

As is observable in Fig. (3), the right boundary face is exposed to a heat flux ( $q''_{Right}$ ) and the bottom boundary condition is reflective (i.e.  $\partial T / \partial y = 0$  on the boundary). So, one can simply consider:

$$\oint_{S_{Right}} q''_{Right} ds + \oint_{S_{Left}} q''_{Left} ds + \oint_{S_{Top}} q''_{Top} ds + \oint_{S_{Bottom}} q''_{Bottom} ds = \int_V q''' dV. \quad (21)$$

In the case of the corner CV, by considering the right and bottom boundary conditions, one can have:

$$\oint_{S_{Right}} q''_{Right} ds = q''_{Right} \times \Delta y^i, \quad (22)$$

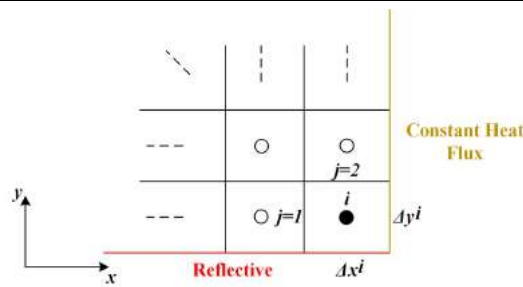


Fig. 3. Schematic view of the corner CV in 2-D geometries

$$\oint_{S_{Bottom}} q''_{Bottom} ds = 0. \quad (23)$$

In the case of the left and top boundary faces, previously the equations were derived (for 1-D geometries), So:

$$\oint_{S_{Left}} q''_{Left} ds = \frac{-2U^1 \times U^i}{U^1 \times \Delta x^i + U^i \times \Delta x^1} \times \Delta y^i \times (T_1 - T_i), \quad (24)$$

$$\oint_{S_{Top}} q''_{Top} ds = \frac{-2U^2 \times U^i}{U^2 \times \Delta y^i + U^i \times \Delta y^2} \times \Delta x^i \times (T_2 - T_i). \quad (25)$$

Thus, one can simple consider the discretized governing equation for the boundary corner CV as:

$$\begin{aligned} & \left\{ \frac{-2U^1 \times U^i}{U^1 \times \Delta x^i + U^i \times \Delta x^1} \times \Delta y^i \right\} \times T_1 + \left\{ \frac{-2U^2 \times U^i}{U^2 \times \Delta y^i + U^i \times \Delta y^2} \times \Delta x^i \right\} \times T_2 \\ & + \left\{ \left( \frac{+2U^1 \times U^i}{U^1 \times \Delta x^i + U^i \times \Delta x^1} \times \Delta y^i \right) + \left( \frac{+2U^2 \times U^i}{U^2 \times \Delta y^i + U^i \times \Delta y^2} \times \Delta x^i \right) \right\} \times T_i \\ & + \{ q''_{Right} \times \Delta y^i \} = q'' \times \Delta x^i \times \Delta y^i. \end{aligned} \quad (26)$$

To solve eq. (26), it is convenient to employ the numerical techniques including the iterative process which are formally mentioned in the previous section for one-dimensional calculations. It should be noted that the above equation is the general form of the 2-D heat conduction equation and consequently by considering the different boundary conditions, the corresponding formulas can simply be derived similar to the 1-D approach.

### 3. The Proposed SMM

The aim of this section is to introduce the SMM with application in the heat conduction calculations for both one and two-dimensional rectangular geometries. It is widely shown in the literature that in most engineering and industrial heat transfer problems such as irradiated slab media, nuclear plate-type fuel elements, cladding plate-type fuel elements, electrical equipment, mechanical equipment, and other uncomplicated structures which the temperature distribution is not varied dramatically, the temperature distribution mainly follows a quadratic curve in the presence of a space-independent volumetric heat source (it also depends on boundary conditions) [1, 2, 19 and 20]. Considering this point and the fact that, at least three points are always required to estimate a quadratic curve; each homogeneous region can be divided into three different slides and then a coarse heat conduction calculation can be implemented to determine the approximated distribution of the temperature profile in the regions and the corresponding slides. Using the results of these preliminary mathematical calculations, one can assign higher mesh point densities to slides of interest regarding their relative importance in each region. The importance of each slide can be determined by some formulated weighting factors which rely on the estimation of temperature profiles in all slides. On this basis, the maximum temperatures and their corresponding locations in different regions with different material properties can be determined by considering a higher spatial resolution. This method of implementation can provide high computational efficiency in addition to the global high accuracy. It is also worth pointing out that, another key feature which has been taken into account is the capability of using any arbitrary mesh point numbers in designing the proposed method. Needless to say that, this factor is essentially needed for evaluating the obtained results against the usual methods with the same number of nodal mesh points [11].

To explain the procedure of the developed method properly, this section has been divided into two parts. The first part deals with the one-dimensional approach, and the second part provides the adaptive mathematical formulation considering the two-dimensional geometry.

#### 3.1. One-dimensional SMM

Using the points mentioned above and considering the 1-D approach, the proposed adaptive method can be presented via the stepwise algorithm described below:





- 1) Divide the entire geometry of a homogeneous structure into three slides as eq. (27):

$$\text{Slide Dimension} = \frac{A}{3}, \quad (27)$$

where  $A$  refers to the dimension of region and Slide Dimension indicates the dimension of each slide in the region. Then, calculating the heat conduction equations to approximate the temperature profile is performed. It should be underlined that if a multi-structure with different materials is desired, each structure should be treated separately to form the mentioned slides in each homogeneous region as eq. (28).

$$\text{Slide Dimension}_m = \frac{A}{3}, \quad m = 1, 2, \dots, M \quad (28)$$

where  $m$  refers to the number of each homogeneous region in the problem.

- 2) Calculate a set of weighting factors to assign a fraction of the appropriate number of mesh points for each slide. These weighting factors are determined with respect to the obtained temperature values from the previous step as the following:

$$SWF_g = \sum_{g=1}^3 T^g, \quad g = 1, 2 \text{ and } 3 \quad (29)$$

where  $g$  is the slide number in each region and  $SWF_g$  refers to the Slide Weighting Factor  $g$ . Due to the fact that the weighting factor is a summation of a number of temperatures, accordingly, it has the dimension of Celsius degrees. By implementing this step, one can determine the importance of each slide in each region. In the case of multi-regions, there are three  $SWF$  for each region. Accordingly, one can rewrite eq. (29) as:

$$SWF_{m,g} = \sum_{g=1}^3 T^{m,g}, \quad g = 1, 2 \text{ and } 3 \quad (30)$$

where  $SWF_{m,g}$  and  $T^{m,g}$  are the Slide Weighting Factor of slide  $g$  in region  $m$  and temperature of slide  $g$  in region  $m$ . To assign different mesh resolutions in each slide with an arbitrary total mesh point number (determined by users), implantation of the next step is needed.

- 3) Determine the appropriate number of meshes corresponding to each slide as follows:

$$\frac{SWF_g}{\sum_g SWF_g} \times W = d_g, \quad (31)$$

where  $d_g$  is the mesh point numbers in the corresponding slide  $g$ , and  $W$  implies the total number of mesh elements. It is worth bearing in mind that, as is also mentioned before, the  $SWF_g$  needs to be calculated for each slide in a homogeneous region. In other words, in the case of a multi-region case, the weighting factors should be evaluated separately regarding the maximum temperature in each region. This allows to properly extract this parameter as accurate as possible in the respective regions. In fact, in the case of multi-region, one can rewrite eq. (31) as:

$$\frac{SWF_{m,g}}{\sum_g SWF_{m,g}} \times W_m = d_{m,g}, \quad (32)$$

here  $d_{m,g}$  is the mesh point numbers in slide  $g$  and region  $m$ , and,  $W_m$  implies the total number of mesh elements in region  $m$ .

### 3.2. Two-dimensional SMM

The stepwise steady-state heat conduction analysis based on the SMM of the two-dimensional rectangular geometry is presented by considering in turn the mentioned considerations in the previous section as follows:

- 1) Dividing each homogeneous region into three slides in each direction and then computing the heat conduction equations numerically using the iterative manner to approximate the temperature profiles (similar to eqs. (27) and (28)).

- 2) Using the initial calculations from the previous step, determining the corresponding weighting factors can be performed for each slide in  $x$  and  $y$  directions as:

$$SWF_l = \sum_{l;p=1}^3 T^{l,p}, \quad p = 1, 2 \text{ and } 3 \quad (33)$$

$$SWF_p = \sum_{p;l=1}^3 T^{l,p}, \quad l = 1, 2 \text{ and } 3 \quad (34)$$

where  $l$  and  $p$  are the total number of slides in  $x$  and  $y$  directions, respectively. Note also that  $CWF_l$  and  $RWF_p$  in eqs. (33)

and (34) refer to the slide Weighting Factor of column  $l$ , and row  $p$ , respectively. In the case of the 2-D multi-region geometries, eqs. (33) and (34) can be rewritten as:

$$SWF_{m,l} = \sum_{p=1}^3 T^{m,l,p}, \quad p = 1, 2 \text{ and } 3 \quad (35)$$

$$SWF_{m,p} = \sum_{l=1}^3 T^{m,l,p}, \quad l = 1, 2 \text{ and } 3 \quad (36)$$

Here  $T^{m,l,p}$  is temperature in row  $p$  and column  $l$  in region  $m$ . Additionally,  $CWF_{m,l}$  and  $RWF_{m,p}$  in eqs. (35) and (36) refer to, respectively, the Slide Weighting Factor of column  $l$  and row  $p$  in region  $m$ .

3) Assigning the appropriate mesh point numbers for each column and row, according to the obtained weighting factors as below:

$$\frac{SWF_l}{\sum_l SWF_l} \times R = n_l, \quad (37)$$

$$\frac{SWF_p}{\sum_p SWF_p} \times Z = n_p, \quad (38)$$

where  $n_l$  and  $n_p$  indicate the mesh point numbers in the corresponding column  $l$  and row  $p$ , respectively. Additionally, in the above equations,  $R$  refers to the total number of mesh elements in  $x$  direction and  $Z$  similarly is the total number of mesh elements in  $y$  direction. It should be also stressed that in the case of two-dimensional, multi-regions, similar to the one-dimensional approach each homogeneous region should be treated separately via dividing each existing region into three slides in both  $x$  and  $y$  direction. In the case of 2-D multi-region geometries, one can rewrite eqs. (37) and (38) as the following:

$$\frac{SWF_{m,l}}{\sum_l SWF_{ml}} \times R_m = n_{m,l}, \quad (39)$$

$$\frac{SWF_{m,p}}{\sum_p SWF_{m,p}} \times Z_m = n_{m,p}, \quad (40)$$

where  $R_m$  and  $Z_m$  refer to the total number of mesh elements in region  $m$  in  $x$  and  $y$  direction, respectively. Moreover,  $n_{m,l}$  and  $n_{m,p}$  indicate the mesh point numbers in region  $m$  and in column  $l$  and row  $p$ , respectively.

## 4. Numerical Results

In this section, some test cases are solved numerically by the iterative process based on the SMM and the Conventional Method (CM) which employ uniform mesh distribution. The obtained results, including the maximum temperature, the location of the maximum temperature and in addition the total CPU execution time have been demonstrated to evaluate the accuracy and efficiency of the proposed method. It should be also noted that, for a consistent accuracy comparison, the results determined by the two methods have been benchmarked against the reference (exact) solutions which obtained using the grid size of 100 and 100×100 mesh elements per region for one and two-dimensional geometries, respectively.

Similar to the previous sections, this section is also divided into two main sub-sections for one and two-dimensional geometries. Where, the results for a number of study cases have been provided in each sub-section.

### 4.1. One-dimensional results

In the following, some numerical problems are solved to consider and compare the results of the CM and the adaptive one against the accurate solutions. The first case relates to a homogeneous region with the volumetric thermal source strength ( $q'''$ ) of 900 (W/m<sup>3</sup>) and the heat conduction coefficient of 13 (W/m.K). The boundary conditions for this case study comprise of constant temperatures at the external boundaries which is presented in Fig.4.

The exact solution has a sharp peak at 0.79 (m) with the maximum temperature of 321.543 (K). Fig.5 displays the calculated temperature distributions of the CM (based on uniform distribution) and the improved one.

According to this figure, using the proposed three-step algorithm mentioned in section 3.1, a finer mesh grid is assigned to the sub-regions with corresponding higher temperature, stand in total contrast to CM. It is interesting to note that to evaluate the accuracy of the obtained results, the Relative Percent Error ( $RPE$ ) and the Apparent Absolute Error ( $AAE$ ) can be defined as the following equations:





$$RPE(\%) = \left| \frac{\text{calculated value} - \text{reference value}}{\text{reference value}} \right| \times 100, \quad (41)$$

$$AAE = |\text{calculated value} - \text{reference value}|. \quad (42)$$

The *RPE* and *AAE* results analysis for both the aforementioned methods has been given in Table 1 for 10 mesh box numbers.

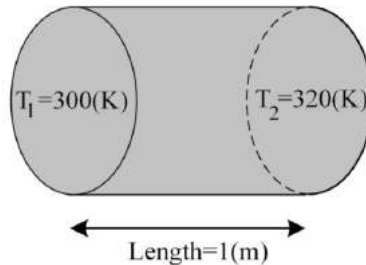


Fig. 4. Geometry of test case 1

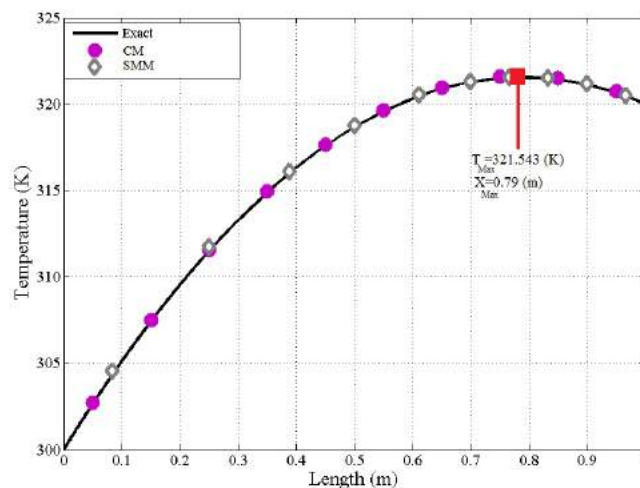


Fig. 5. Solution of the heat conduction equation based on the CM and proposed SMM for the test case 1

**Table 1.** *RPEs* of the calculated maximum temperatures, *AAEs* of the calculated location of maximum temperature and the total CPU execution time for the test case 1

Distribution	Number of boxes	<i>RPE</i> (%) of maximum temperature	<i>AAE</i> in location of the maximum temperature (m)	Total CPU time (s)
CM	10	0.011	0.039	0.06
SMM	10	0.007	0.022	0.06

As is evident, the obtained results by the proposed method with 0.022 (cm) is more accurate than that of the ordinary method with 0.039 (cm); on account of the fact that by optimizing the mesh point positions with respect to the trend of temperature profile, the locations of extreme values can more accurately be obtained.

The second case study is related to a one-dimensional geometry with two different regions. Fig. 6 represents the geometry and the boundary conditions of this problem.

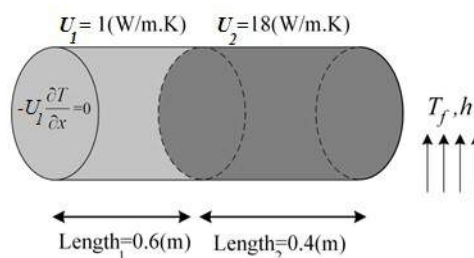


Fig. 6. Geometry of test case 2

where,  $q''$  for the region 1 is 300 and for the region 2 is 5 (W/m<sup>3</sup>). Additionally, the heat transfer coefficient and the flow temperature have been considered to be 2000 (W/m<sup>2</sup>.K) and 311 (K), respectively. The exact solution has a peak at the origin

of the region 1 with the maximum temperature of 369.093 (K) and a peak at 0.60 (m) with a maximum temperature of 315.368 (K) in the region 2. Similar to the previous case study, the proposed adaptive method and the CM (based on uniform distribution) have been applied to this problem to predict the desired considerations by performing the governed equations numerically. Here, the drawn mesh point distributions based on the mentioned methods are illustrated in Fig. 7. It has been also noted that, the accuracy and efficiency of the obtained results are given in Table 2.

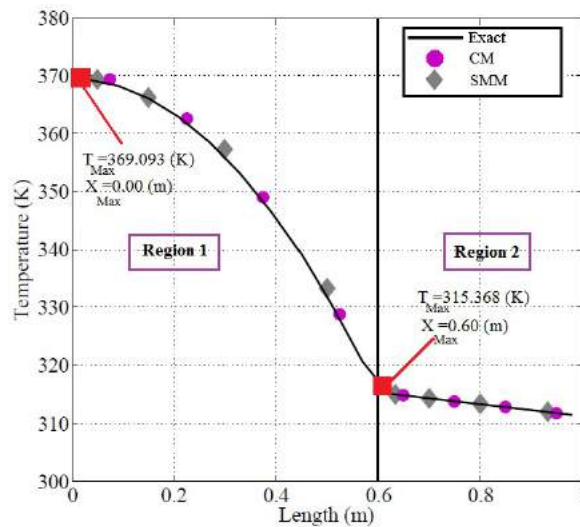


Fig.7. Solution of the heat conduction equation based on the CM and proposed SMM for the test case 2

Table 2. *RPEs* of the calculated maximum temperatures, *AAEs* of the calculated location of maximum temperature and the total CPU execution time for the test case 2

Region number	Distribution	Number of boxes	<i>RPE</i> (%) of maximum temperature	<i>AAE</i> in location of the maximum temperature (m)	Total CPU time (s)	
					CM	SMM
Region 1	CM	4	0.005	0.075	0.034	0.036
	SMM	4	0.002	0.050		
Region 2	CM	4	0.151	0.050		
	SMM	4	0.098	0.030		

As can apparently be seen, in the first region, the *RPE* results based on the proposed and ordinary method were 0.002 and 0.005, and in the second region, were 0.098 and 0.151, respectively. Moreover, as can be detected, the locations of the extreme values based on the mentioned methods have been compared to each other. Regarding the table in the first region the *AAE* of the proposed method was 0.050 m, while for the ordinary method it was 0.075 m. Also, the *AAEs* were 0.030 m and 0.050 m for the proposed and ordinary method in the second region, respectively.

The above-mentioned procedure is repeated for the test case 3, where the features of this case study are depicted in Fig.8.

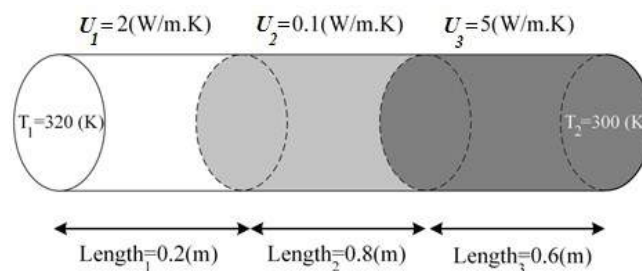


Fig. 8. Geometry of test case 3

As can be seen, this case study is comprised of three different regions with the volumetric thermal source strength of 60, 80 and 40 (W/m<sup>3</sup>) for the region 1, 2 and 3, respectively. The accurate solution has a peak at 0.20 (m) with the maximum temperature of 324.147 (K) in the region 1, a peak at 0.57 (m) with a maximum temperature of 378.865 (K) in the region 2, and, a peak at 1.00 (m) with a maximum temperature of 306.210 (K) in the region 3. It is worth to mention that the uniform and non-uniform mesh grid structures along with the corresponding temperature distributions have been displayed in Fig. 9. Having looked at the results tabulated in Table 3, the advantages of the novel mentioned algorithm in the case of determination of the maximum values and the corresponding locations are proven.

## 4.2 Two-dimensional results

This section comprises of two case studies for the two-dimensional heat conduction calculations. First, we present the results of a simple homogeneous region, which is shown in Fig. 10. The length of this problem both in *x* and *y* direction is 1



(m) and the heat conduction coefficient is 4 (W/m.K). Additionally, the volumetric thermal source strength is 100 (W/m<sup>3</sup>). The boundary conditions of this problem have been illustrated in Fig. 10. The accurate solution has the maximum temperature of 420 (K) that is located on the right side of the geometry (see Fig. 11).

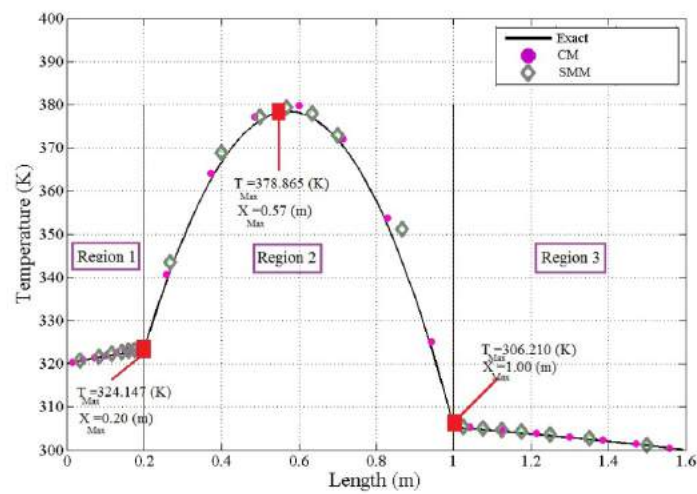


Fig. 9. Solution of the heat conduction equation based on the CM and proposed SMM for the test case 3

Table 3. RPEs of the calculated maximum temperatures, AAEs of the calculated location of maximum temperature and the total CPU execution time for the test case 3

Region number	Distribution	Number of boxes	RPE (%) of maximum temperature	AAE in location of the maximum temperature (m)	Total CPU time (s)	
					CM	SMM
Region 1	CM	7	0.014	0.056	0.051	0.056
	SMM	7	0.008	0.029		
Region 2	CM	7	0.028	0.265		
	SMM	7	0.015	0.118		
Region 3	CM	7	0.043	0.084		
	SMM	7	0.025	0.044		

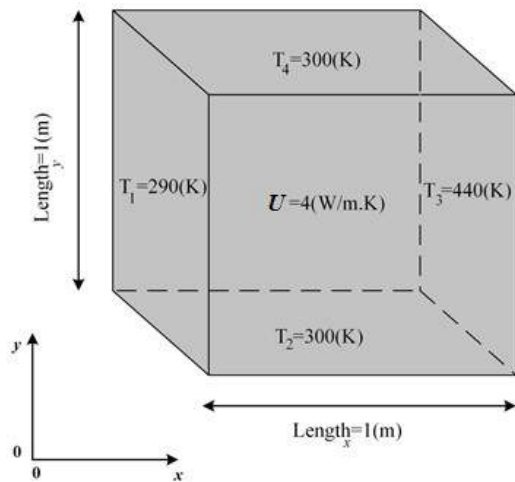
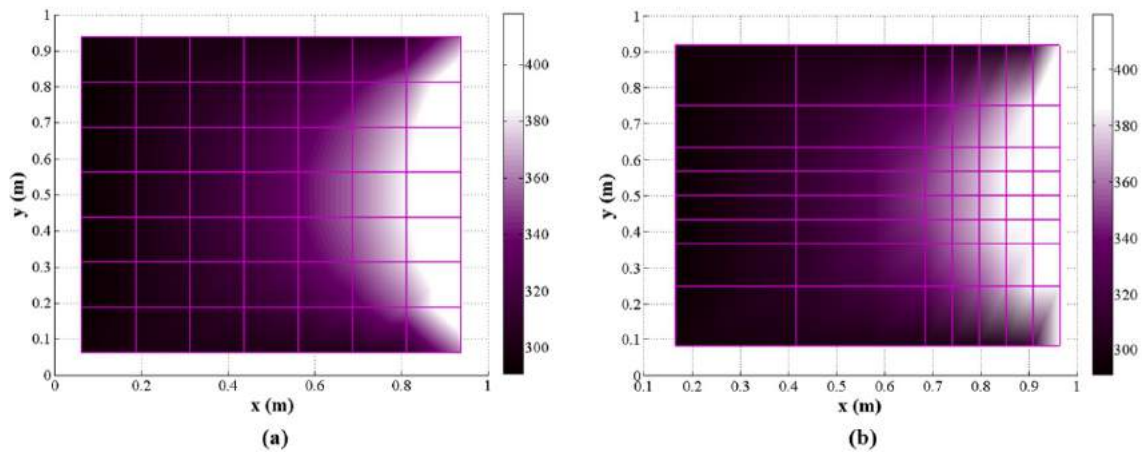


Fig. 10. Geometry of test case 4

For facilitating comparison between the mentioned methods, the results of the numerical calculations, including the errors of the obtained maximum temperatures and the corresponding locations are given in Table 4.

Table 4. RPEs of the calculated maximum temperatures, AAEs of the calculated location of maximum temperature and the total CPU execution time for the test case 4

Distribution	Number of boxes	RPE (%) of maximum temperature	AAE <sub>x</sub> in location of the maximum temperature (m)	AAE <sub>y</sub> in location of the maximum temperature (m)	Total CPU time (s)	
					CM	SMM
CM	8×8	0.017	0.049	0.042	0.081	0.085
SMM	8×8	0.009	0.025	0.026		



**Fig. 11.** Solution of the heat conduction equation based on the a) CM and b) proposed SMM for the test case 4 for grid size  $8 \times 8$

As it is observed, the locations of the extreme values which are obtained based on the aforementioned methods have been compared to each other for both  $x$  and  $y$  directions. This is due to the fact that by optimizing mesh point positions in 2-D geometries, the locations of extreme values will then be optimized in two directions, consequently.

The geometry and boundary conditions of the second problem (test case 5) are shown in Fig. 12; where the volumetric thermal source strength of region 1 and 2 are 400 and 100 ( $\text{W/m}^3$ ), respectively.

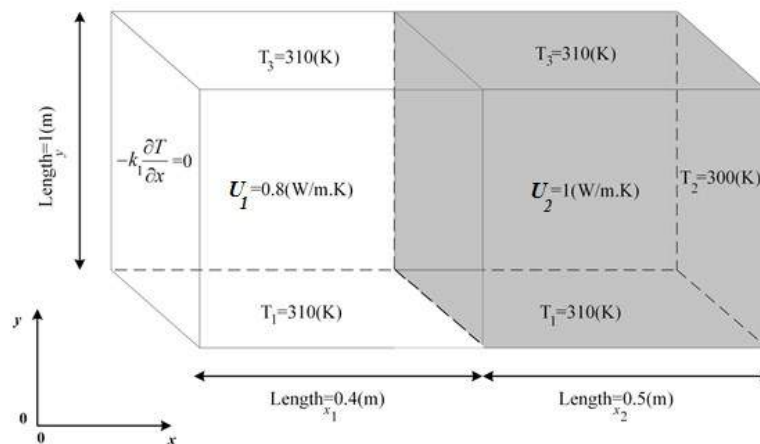


**Fig. 12.** Geometry of test case 5

The accurate solution has a peak at (0.00, 0.50) meter in the region 1 with the maximum temperature of 351.852 (K), and, a peak at (0.40, 0.50) meter with a maximum temperature of 334.851 (K) in the region 2. The obtained 2-D temperature distributions for uniform and non-uniform grid size  $14 \times 14$  are depicted in Fig. 13.

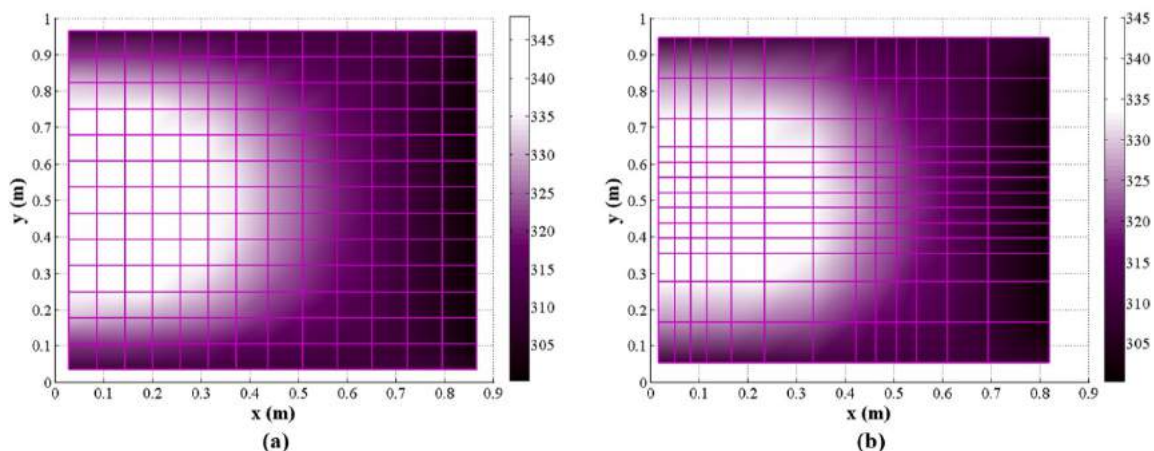


**Fig. 13.** Solution of the heat conduction equation based on the a) CM and b) proposed SMM for the test case 5 for grid size  $14 \times 14$

In Table 5, the calculated results for both region 1 and 2 using the developed method and the CM (based on uniform distribution) are compared with the accurate solution.



**Table 5.** *RPEs* of the calculated maximum temperatures, *AAEs* of the calculated location of maximum temperature and the total CPU execution time of the test case 5 for grid size 14×14

Region number	Distribution	Number of boxes	<i>RPE</i> (%) of maximum temperature	<i>AAE<sub>x</sub></i> in location of the maximum temperature (m)	<i>AAE<sub>y</sub></i> in location of the maximum temperature (m)	Total CPU time (s)	
						CM	SMM
Region 1	CM	7×7	0.021	0.090	0.088	0.901	0.912
	SMM	7×7	0.015	0.057	0.059		
Region 2	CM	7×7	0.034	0.089	0.095		
	SMM	7×7	0.019	0.069	0.070		

Furthermore, in order to check the capability and accuracy of this algorithm for any arbitrary number of mesh element boxes, the proposed SMM method has been applied to a different mesh element grid size of the last case study. Fig. 14 displays the temperature distribution for uniform and non-uniform grid structure of the grid size 22×22.

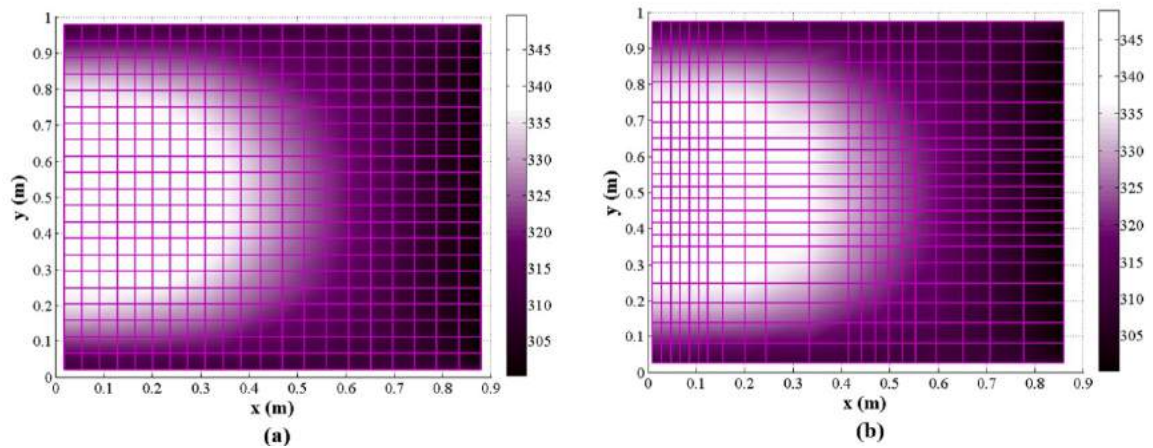


**Fig. 14.** Solution of the heat conduction equation based on the a) CM and b) proposed SMM for the test case 5 for grid size 22×22

The obtained results, including the *RPEs* of the maximum temperatures, *AAEs* of the location of maximum temperatures and the total CPU execution times have been tabulated for both the aforementioned distributions in the Table 6.

**Table 6.** *RPEs* of the calculated maximum temperatures, *AAEs* of the calculated location of maximum temperature and the total CPU execution time of the test case 5 for grid size 22×22

Region number	Distribution	Number of boxes	<i>RPE</i> (%) of maximum temperature	<i>AAE<sub>x</sub></i> in location of the maximum temperature (m)	<i>AAE<sub>y</sub></i> in location of the maximum temperature (m)	Total CPU time (s)	
						CM	SMM
Region 1	CM	11×11	0.009	0.078	0.093	1.701	1.740
	SMM	11×11	0.006	0.060	0.070		
Region 2	CM	11×11	0.011	0.090	0.100		
	SMM	11×11	0.008	0.059	0.082		

As is observed from this table, the calculated parameters have been given to the region 1 and 2, separately.

5. Discussion

As can be observed from Table 1, the *RPE* of the calculated maximum temperature based on the CM is 0.011 %, though; the obtained value of the SMM is 0.07 %. Furthermore, as is apparent the *AAEs* of the location of maximum temperature are 0.039 and 0.022 using the CM and the SMM, respectively. Similarly, it can be seen from the Tables 2, 3, 4, 5 and 6, that the suggested method gives more accurate results in comparison to the CM. However, it should be underlined that for a consistent comparison between the efficiency of the CM and the SMM, the total CPU execution time has been considered using a laptop computer with CPU 1.60 GHz.

The results (*RPEs*) in the tables indicate that the new method with non-uniform grid is indeed more accurate than the CM based on the uniform grids at a very comparable computational expense. All results presented in the paper are namely already calculated with the excellent accuracy in the order of *RPE*(%)<0.15% regardless of the method used. However, all the results indicated that about 50% improvement can be achieved by considering the proposed method without any significant extra computational CPU time. From a practical point of view, this improvement can be very useful in many technological and scientific engineering applications. For example, in nuclear safety analysis, there are some safety criteria for maintaining the maximum fuel and clad temperatures within certain limitations [21]. Accordingly, calculating and obtaining the mentioned extremes as accurate as possible without significant computational costs is vital. Additionally from a numerical point of view, it is worth bearing in mind that, for areas of interest where gradients vary significantly in space, using a fine grid over the domain can be computationally intensive. So it can be reasonably argued that using small mesh spacing where the function is varying large can be very useful. In this paper, we proposed an enhanced algorithm instead of applying complex mathematical



prospective to predict the extreme values and their corresponding locations in a number of different problems.

Based on the arguments mentioned above, it can be concluded that the proposed method has about 50% more accuracy than that of the ordinary method. Moreover, it should be noted that the total execution time of the proposed method is nearly equal to the other one. This is due to the fact that the computational cost of the primary calculations based on the SMM is not comparable with the iterative process. Consequently, one can argue that the adaptive proposed SMM is more efficient compared with CM.

From another point of view, the information about how much one has to condense the uniform grid (and concurrently increasing the computational expense) in order to obtain a similar accuracy of the results should be considered. Table 7 shows the number of additional boxes in CM, the corresponding computational cost for all of the presented benchmark problems.

**Table 7.** Comparison results between the CM and SMM for obtaining the same accuracy

Test Case Number	Methods	Number of boxes	<i>RRE</i> (%) of maximum temperature			in location of the maximum temperature (m)						Total CPU time (s)
			Region Number			Region Number						
			1	2	3	1		2		3		
						<i>AAE<sub>x</sub></i>	<i>AAE<sub>y</sub></i>	<i>AAE<sub>x</sub></i>	<i>AAE<sub>y</sub></i>	<i>AAE<sub>x</sub></i>	<i>AAE<sub>y</sub></i>	
1	CM	14	~0.007	...	...	~0.022	...	...	...	...	...	0.11
	SMM	10	0.007	...	...	0.022	...	...	...	...	...	0.06
2	CM	12	~0.002	~0.098	...	~0.050	...	~0.030	...	...	...	0.077
	SMM	8	0.002	0.098	...	0.050	...	0.030	...	...	...	0.036
3	CM	33	~0.008	~0.015	~0.025	~0.029	...	~0.118	...	~0.044	...	0.118
	SMM	21	0.008	0.015	0.025	0.029	...	0.118	...	0.044	...	0.056
4	CM	102	~0.009	...	...	~0.025	~0.026	...	...	...	...	0.193
	SMM	64	0.009	...	...	0.025	0.026	...	...	...	...	0.085
5	CM	332	~0.015	~0.019	...	~0.057	~0.059	~0.069	~0.070	...	...	1.907
	SMM	196	0.015	0.019	...	0.057	0.059	0.069	0.070	...	...	0.912
5	CM	820	~0.006	~0.008	...	~0.060	~0.070	~0.059	~0.082	...	...	3.801
	SMM	484	0.006	0.008	...	0.060	0.070	0.059	0.082	...	...	1.740

As is observable, more boxes and accordingly much more computational costs are needed if almost the same results are desired. This shows that the proposed SMM can improve the accuracy of the solutions in a reasonable running time.

Another important point that is worth to mention is that the proposed method is based on a simple discretization and efficient implementation. The benchmarks which were considered in this work have analytical solution [22]. However, the analytical solution relies on a relatively sophisticated mathematical solution and accordingly for practical applications, the computational cost, the complexity of implementation and sophisticated mathematical calculations associated with the analytical calculation could be overwhelming. In the following, the analytical solution of 2 dimensional heat conduction equation for a homogeneous material composition considering the constant temperature on the geometry boundaries is presented as:

$$T(x, y) = \sum_{n=1}^{\infty} \left\{ \frac{2}{a \sinh\left(\frac{n\pi b}{a}\right)} \int_0^a C \sin\left(\frac{n\pi}{a}x\right) dx \right\} \sin\left(\frac{n\pi}{a}x\right) \sinh\left(\frac{n\pi}{a}y\right), \quad (43)$$

where  $a$ ,  $b$  and  $C$  are, respectively, the dimension of the geometry in  $x$  and  $y$  direction and the temperature on the boundary of geometry in line  $b$ . Additionally, it should be noted that the temperature on other boundaries are considered to be zero. As is observable, the mathematical solution is sophisticated even for a simple homogeneous problem. On this basis, development of efficient solver codes for practical heat transfer applications is highly recommended.

## 6. Conclusion

The present work deals with an enhanced adaptive spatial mesh refinement approach for the heat conduction calculations using the SMM. This proposed method works based on dividing each homogeneous region into separate slides and then assigning different mesh point densities to slides of interest regarding their relative importance using some formulated weighting factors. These weighting factors comprise of terms which needs the approximated temperature profile in each region and slide. The proposed SMM, which allows for accurate and efficient solution of the heat conduction equation, is applied to some case studies with different geometries and boundary conditions. The numerical results showed high accuracy and efficiency of the proposed SMM compared to the Conventional Method (CM). It is also worthwhile to mention that the extra execution time for the primary required mathematical calculations was almost negligible in comparison with the total CPU time. Moreover, different grid sizes were used to consider the accuracy of the suggested method for any arbitrary mesh point numbers. Results of comparison between the SMM and the CM, proved the strength of the proposed SMM. According to the satisfactory results reported herein, it is very promising for future application of the proposed method to simulate a variety more challenging problems for which a pre-determined mesh position strategy can be established.

## Conflict of Interest

The author(s) declared no potential conflicts of interest with respect to the research, authorship and publication of this article.

## Funding

The author(s) received no financial support for the research, authorship and publication of this article.

## Nomenclature

BSFDM	Box-Scheme Finite Difference Method	$p$	Number of slides in $y$ direction for 2-D geometry
$U$	Heat conduction coefficient	$P$	Total No. of slides in $y$ direction for 2-D geometry
$T^i$	Temperature of mesh box $i$	$q'''$	Volumetric thermal source strength
$T^j$	Temperature of mesh box $j$	$W$	Total No. of mesh elements in 1-D
$T^g$	Average temp. of each slides (1D geometry)	$R$	Total No. of mesh elements in $x$ direction for 2-D
$\Delta^i$	Side length of mesh box $i$	$Z$	Total number of mesh elements in $y$ direction for 2-D
$\Delta^j$	Side length of mesh box $j$	$n_l$	Mesh point numbers for slide $l$
$S^i$	Area of mesh box $i$	$n_p$	Mesh point numbers for slide $p$
$V^i$	Volume of mesh box $i$	$SWF_g$	Slide Weighting Factor $g$
$g$	Number of slides in 1-D	$SWF_l$	Slide Weighting Factor for slide $l$
$l$	Number of slides in $x$ direction for 2-D geometry	$SWF_p$	Column Weighting Factor for slide $p$
$d_g$	Mesh point numbers in the corresponding slide $g$	$\sigma$	Stefan-Boltzmann constant
$\alpha$	Radiation absorptivity		

## References

- [1] Bergman, Th., Lavine, A. S., Incropera, F. P., Dewitt, D. P., *Fundamentals of heat and mass transfer*. The United States, John Wiley & Sons (2011)
- [2] Wakil, M. M. El., *Nuclear heat transport*. The United States, The Haddon Craftsmen Inc (1971)
- [3] Wang, C., Dong, X., Shu, C. H., Parallel adaptive mesh refinement method based on WENO finite difference scheme for the simulation of multi-dimensional detonation. *J Comput Phys* 298 (2015) 161–175
- [4] Fengzhi, L., Penghao, R., A novel solution for heat conduction problems by extending scaled boundary finite element method. *Int J Heat Mass Transf* 95 (2016) 678–688
- [5] Wang, P., Yu, B., Li, J., Zhao, Y., Shao, Q., A novel finite volume method for cylindrical heat conduction problems. *Int Commun Heat Mass* 63 (2015) 8–16
- [6] Haddad, H., Guessasma, M., Fortin, J., Heat transfer by conduction using DEM–FEM coupling method. *Comp Mater Sci* 81 (2014) 339–347
- [7] Yao, W., Yu, B., Gao, X., Gao, Q., A precise integration boundary element method for solving transient heat conduction problems. *Int J Heat Mass Transf* 78 (2014) 883–891
- [8] Kovtanyuk, A. E., Botkin, N. D., Hoffmann, K., Numerical simulations of a coupled radiative–conductive heat transfer model using a modified Monte Carlo method. *Int J Heat Mass Transf* 55 (2012) 649–654
- [9] Zhang, X., Xiang, H., A fast meshless method based on proper orthogonal decomposition for the transient heat conduction problems. *Int J Heat Mass Transf* 84 (2015) 729–739
- [10] Malmir, H., Moghaddam, N. M., Zahedinejad, E., Comparison between triangular and hexagonal modeling of a hexagonal-structured reactor core using box method. *Ann Nucl Energy* 38 (2011) 371–378
- [11] Vagheian, M., Ochbelagh, D. R., Gharib, M., On an improved box-scheme finite difference method based on the relative event probabilities. *Prog Nucl Energy* 88 (2016) 33–42
- [12] Cao, J., Zhoua, G., Wang, C., Dong, X., A hybrid adaptive finite difference method powered by a posteriori error estimation technique. *J Comput Appl Math* 259 (2014) 117–128
- [13] Lee, T. E., Baines, M. J., Langdona, S., A finite difference moving mesh method based on conservation for moving boundary problems. *J Comput Appl Math* 288 (2015) 1–17
- [14] Zhai, S. H., Weng, Z. H., Feng, X., An adaptive local grid refinement method for 2D diffusion equation with variable coefficients based on block-centered finite differences. *Appl Math Comput* 268 (2015) 284–294
- [15] Zhai, S. H., Qian, I., Gui, D., Fengd, X., A block-centered characteristic finite difference method for convection-dominated diffusion equation. *Int Commun Heat Mass* 61 (2015) 1–7
- [16] Mallik, R. K., Mahapatra, S. K., Sarkar, A., Neural-finite difference method (NFDm) in development of improved differential approximation (IDA) and its application for coupled conduction and radiation heat transfer in a square enclosure: An experimental validation. *Int J Heat Mass* 52 (2009) 504–515
- [17] Grzywiński, M., Sluzalec, A., Stochastic convective heat transfer equations in finite differences method. *Int J Heat Mass*

*Transf* 43 (2000) 4003-4008.

[18] Kalis, H., Efficient finite-difference scheme for solving some heat transfer problems with convection in multilayer media. *Int J Heat Mass Transf* 43 (2000) 4467-4474

[19] Talebi, S., Kazeminejad, H. A mathematical approach to predict dry-out in a rod bundle. *Nucl Eng Des* 249 (2012) 348–356

[20] Talebi, S., Kazeminejad, H., Davilu, H., Prediction of dry-out and post dry-out wall temperature using film thickness model. *Predict Eng Des* 244 (2012) 73–82

[21] IAEA-Safety Reports Series No. 30. Accident Analysis for Nuclear Power Plants with Pressurized Water Reactors. Austria: International Atomic Energy Agency (2004)

[22] Ordonez, Miranda J., Lemonnier, D., Ezzahri Y., Joulain K., Analytical description of the radiative-conductive heat transfer in a gray medium contained between two diffuse parallel plates. *Appl Math Model* 56 (2018) 51-64.



© 2019 by the authors. Licensee SCU, Ahvaz, Iran. This article is an open access article distributed under the terms and conditions of the Creative Commons Attribution-NonCommercial 4.0 International (CC BY-NC 4.0 license) (<http://creativecommons.org/licenses/by-nc/4.0/>).



## Enhanced finite difference scheme for the neutron diffusion equation using the importance function

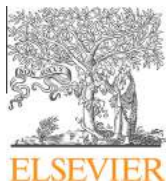
*Annals of Nuclear Energy* 96 (2016) 412–421.

**Authors:** M. Vagheian, N. Vosoughi\*, M. Gharib

**Abstract:** In this work, for the first time, the neutron importance function as the result of the adjoint numerical calculations was obtained to consider whether it can be employed for an adaptive mesh point distribution in the cell-centered Finite difference Method to improve the numerical accuracy. It was revealed that the objective function as the neutron importance function could provide a computational framework for the enhancement of the numerical solution using the power iteration method. The proposed method was applied to two-dimensional geometries for a number of benchmark problems. The results of simulations showed that a more accurate solution could be obtained using the developed method compared to the conventional numerical technique.

**Contributions:** I performed discretization of the governing equations and carried out the entire required programming (more than 70'000 programming lines). Then, I conducted the assessment of the obtained results and wrote the paper as the first author. In the final step, I revised the paper based on the comments sent by the journal.

**License:** Authors can include their articles in dissertations for non-commercial purposes.



# Enhanced finite difference scheme for the neutron diffusion equation using the importance function



Mehran Vagheian<sup>a</sup>, Naser Vosoughi<sup>b,\*</sup>, Morteza Gharib<sup>a</sup>

<sup>a</sup> Amirkabir University of Technology (Tehran Polytechnic), Department of Energy Engineering & Physics, Hafez Avenue, Tehran, Iran

<sup>b</sup> Sharif University of Technology, Department of Energy Engineering, Azadi Street, Tehran, Iran

## ARTICLE INFO

### Article history:

Received 2 June 2015

Received in revised form 29 April 2016

Accepted 28 June 2016

Available online 7 July 2016

### Keywords:

Neutron importance function

Enhanced finite difference method

Box scheme

Adjoint calculations

## ABSTRACT

Mesh point positions in Finite Difference Method (FDM) of discretization for the neutron diffusion equation can remarkably affect the averaged neutron fluxes as well as the effective multiplication factor. In this study, by aid of improving the mesh point positions, an enhanced finite difference scheme for the neutron diffusion equation is proposed based on the neutron importance function.

In order to determine the neutron importance function, the adjoint (backward) neutron diffusion calculations are performed in the same procedure as for the forward calculations. Considering the neutron importance function, the mesh points can be improved through the entire reactor core. Accordingly, in regions with greater neutron importance, density of mesh elements is higher than that in regions with less importance. The forward calculations are then performed for both of the uniform and improved non-uniform mesh point distributions and the results (the neutron fluxes along with the corresponding eigenvalues) for the two cases are compared with each other. The results are benchmarked against the reference values (with fine meshes) for Kang and Rod Bundle BWR benchmark problems. These benchmark cases revealed that the improved non-uniform mesh point distribution is highly efficient.

© 2016 Elsevier Ltd. All rights reserved.

## 1. Introduction

The adjoint equation has been widely used in sensitivity analysis and uncertainty propagation in the field of reactor core calculations. One of the important applications of the adjoint equation is in the neutron importance determination (Bell and Glasstone, 1970; Duderstadt and Hamilton, 1991).

Adjoint-based methods have a rich history in Monte-Carlo (MC) variance reduction technique. The excessively long runtime calculations and slow convergence of the fission source of the MC method led to develop some variance reduction techniques including adjoint-based methods. In this connection, recently it has been shown that the runtime MC calculations can be significantly speeded up by considering the Russian roulette technique and a weight window map to bias MC particles based on the adjoint information (Zhang and Abdel-Khalik, 2014).

Determination of the forward/adjoint effective multiplication factor ( $k_{eff}$  and  $k_{eff}^{\dagger}$ , respectively), in core neutronic calculations is of great importance. The effective multiplication factor is usually

determined using the power iteration method. The neutron diffusion equation can be solved by various numerical methods such as Box Scheme Finite Difference Method (Malmir et al., 2010, 2011), Direct Discrete Method (Ayyoubzadeh et al., 2012), Finite Element Method (Hosseini and Vosoughi, 2013), Nodal Expansion Method (Poursalehi et al., 2013). Among these, the Finite Difference Method (FDM) has priority on account of its simplicity. However, this method definitely is not more accurate than nodal or FEM methods.

The Box-Scheme Finite Difference Method (BSFDM) has been recently used for the forward/adjoint calculations owing to its efficiency (Malmir et al., 2010, 2011). This method is based on the neutron leakage calculation from each side of a mesh box.

To date various methods have been developed and introduced to use the adjoint-based mesh adaptivity methods in the case of posteriori error measurements (Ragusa and Wang, 2010; Lathouwers, 2011a; Wang and Ragusa, 2011). These error measures can be employed to determine the effective multiplication factor of the neutron transport equation efficiently (Lathouwers, 2011b). In the light of the fact that, mesh element positions have a great importance in the accuracy of the neutron diffusion calculations, the adjoint-based goal-oriented mesh adaptivity methods can be employed to optimize density of mesh elements through

\* Corresponding author.

E-mail address: [nvosoughi@sharif.edu](mailto:nvosoughi@sharif.edu) (N. Vosoughi).

the entire reactor core, though, at the cost of computing an adjoint solution (Ayyoubzadeh and Vosoughi, 2011).

The main aim of this study is to compare the results of the uniform and improved non-uniform mesh distribution for the steady state neutron diffusion calculations. Hence, two different benchmark problems, namely Kang (Kang and Hansen, 1971) and Rod Bundle BWR (Argonne Code Center, 1977), have been considered for this comparative study. The improved non-uniform mesh distribution is determined by a novel algorithm based on the well-known neutron importance function in each region and group. At first, it is necessary to perform the adjoint calculations for the aforementioned benchmark cases. Accordingly, the rectangular form of the Box-Scheme Finite Difference Method is applied to the matrix form of the forward/adjoint neutron diffusion equation. Then, using the power iteration method, the adjoint calculations are performed to determine the neutron importance function for the entire reactor core. For facilitating comparison, the forward calculations are performed numerically for both the uniform and improved non-uniform coarse mesh point distributions. Finally, all the results are benchmarked against the fine uniform mesh point distribution.

In the following and in Section 2, the matrix form of the BSFDM for the forward as well as the backward neutron diffusion equation is presented. The improved mesh point algorithm is explained in detail in Section 3. Section 4 contains the results of this method for two different benchmark problems. Finally, in Section 5, the conclusion of this study is presented.

## 2. Mathematical formulation

### 2.1. Discretization of the forward neutron diffusion equation

The two-group forward neutron diffusion equations are described in matrix form as follows (Malmir et al., 2011):

$$\begin{bmatrix} -\nabla \cdot D_1(r) \nabla + \Sigma_{a1}(r) + \Sigma_{s,1 \rightarrow 2}(r) & 0 \\ -\Sigma_{s,1 \rightarrow 2}(r) & -\nabla \cdot D_2(r) \nabla + \Sigma_{a2}(r) \end{bmatrix} \begin{bmatrix} \phi_1(r) \\ \phi_2(r) \end{bmatrix} = \frac{1}{k_{eff}} \begin{bmatrix} \nu_1 \Sigma_{f1}(r) & \nu_2 \Sigma_{f2}(r) \\ 0 & 0 \end{bmatrix} \begin{bmatrix} \phi_1(r) \\ \phi_2(r) \end{bmatrix}, \quad (1)$$

where subscripts 1 and 2 denote the fast and thermal neutron energy groups, respectively, and all the other parameters have their usual meaning.

Using the Box-Scheme Finite Difference Method one can discretize Eq. (1) for different geometries. The Box-Scheme Finite Difference Method was first developed for rectangular geometries (Nakamura, 1977). Then, Malmir et al. (2011) applied this method for triangular and hexagonal geometries. Fig. 1 properly shows the mesh box properties for the rectangular geometry.

Using the Box-Scheme Finite Difference Method one can consider Eq. (1) in 2-D 2-group as follows:

$$\begin{bmatrix} \sum_{j=1}^4 \frac{2 \times D_1^i \times D_1^j}{D_1^i \times \Delta^j + D_1^j \times \Delta^i} + (\Sigma_{a1}^i + \Sigma_{s,1 \rightarrow 2}^i) \Delta^i & 0 \\ -\Sigma_{s,1 \rightarrow 2}^i \Delta^i & \sum_{j=1}^4 \frac{2 \times D_2^i \times D_2^j}{D_2^i \times \Delta^j + D_2^j \times \Delta^i} + \Sigma_{a2}^i \Delta^i \end{bmatrix} \times \begin{bmatrix} \phi_1^i \\ \phi_2^i \end{bmatrix} + \sum_{j=1}^4 \begin{bmatrix} -\frac{2 \times D_1^i \times D_1^j}{D_1^i \times \Delta^j + D_1^j \times \Delta^i} & 0 \\ 0 & -\frac{2 \times D_2^i \times D_2^j}{D_2^i \times \Delta^j + D_2^j \times \Delta^i} \end{bmatrix} \times \begin{bmatrix} \phi_1^j \\ \phi_2^j \end{bmatrix} = \frac{1}{k_{eff}} \begin{bmatrix} \nu_1 \Sigma_{f1}^i \Delta^i & \nu_2 \Sigma_{f2}^i \Delta^i \\ 0 & 0 \end{bmatrix} \times \begin{bmatrix} \phi_1^i \\ \phi_2^i \end{bmatrix}, \quad (2)$$

where the mesh boxes ( $j$ ), [ $j = 1, \dots, 4$ ], represent the adjacent neighbors of the mesh box ( $i$ ) and  $\Delta$  is the size of one side of each mesh box as is depicted in Fig. 1.

### 2.2. Discretization of the adjoint neutron diffusion equation

To solve the adjoint neutron diffusion equation, firstly one can consider Eq. (2) as follows:

$$L\phi = \frac{1}{k_{eff}} F\phi \quad (3)$$

where  $L$  and  $F$  are called the loss and fission operators, respectively. Then, the transposition of Eq. (3) gives:

$$L^\dagger \psi = \frac{1}{k_{eff}} F^\dagger \psi, \quad (4)$$

in which  $L^\dagger$  and  $F^\dagger$  are the transposes of  $L$  and  $F$ , respectively. In addition,  $\psi$  refers to the neutron importance function (or the adjoint flux) (Bell and Glasstone, 1970; Lamarsh, 1965). Thus, considering Eqs. (2) and (4), the matrix form of the adjoint neutron diffusion equation can be written as follows:

$$\begin{bmatrix} \sum_{j=1}^4 \frac{2 \times D_1^i \times D_1^j}{D_1^i \times \Delta^j + D_1^j \times \Delta^i} + (\Sigma_{a1}^i + \Sigma_{s,1 \rightarrow 2}^i) \Delta^i & -\Sigma_{s,1 \rightarrow 2}^i \Delta^i \\ 0 & \sum_{j=1}^4 \frac{2 \times D_2^i \times D_2^j}{D_2^i \times \Delta^j + D_2^j \times \Delta^i} + \Sigma_{a2}^i \Delta^i \end{bmatrix} \times \begin{bmatrix} \psi_1^i \\ \psi_2^i \end{bmatrix} + \sum_{j=1}^4 \begin{bmatrix} -\frac{2 \times D_1^i \times D_1^j}{D_1^i \times \Delta^j + D_1^j \times \Delta^i} & 0 \\ 0 & -\frac{2 \times D_2^i \times D_2^j}{D_2^i \times \Delta^j + D_2^j \times \Delta^i} \end{bmatrix} \times \begin{bmatrix} \psi_1^j \\ \psi_2^j \end{bmatrix} = \frac{1}{k_{eff}} \begin{bmatrix} \nu_1 \Sigma_{f1}^i \Delta^i & 0 \\ \nu_2 \Sigma_{f2}^i \Delta^i & 0 \end{bmatrix} \times \begin{bmatrix} \psi_1^i \\ \psi_2^i \end{bmatrix}, \quad (5)$$

where  $\psi^i$  and  $\psi^j$  denote the neutron importance function for the mesh boxes ( $i$ ) and ( $j$ ), respectively. It should be noted that Eq. (5) can be obtained directly by the transposition of Eq. (2).

## 3. Methodology

To improve the mesh point positions based on the neutron importance function in the entire reactor geometry, firstly it is necessary to perform adjoint neutron diffusion calculations. These calculations are performed using the power iteration method. It should be noted that the convergence criteria, for the neutron flux and eigenvalue variations in the inner and outer iterations, can be chosen based on the reported benchmark values.

The main idea of the mesh improvement is that, in regions with higher neutron importance, higher density of mesh elements should be used than that in regions with lower importance. This can be expressed as follows:

Step 1. Determination of the fast and the thermal neutron importance functions using the power iteration method.

This step should be performed to obtain the neutron importance value for each mesh of the entire reactor geometry.

Step 2. Calculation of the average neutron importance function in all mesh points over the group energies, as follows:

$$\psi_{average}^{ij} = \frac{\psi_1^{ij} + \psi_2^{ij}}{2} \quad (6)$$

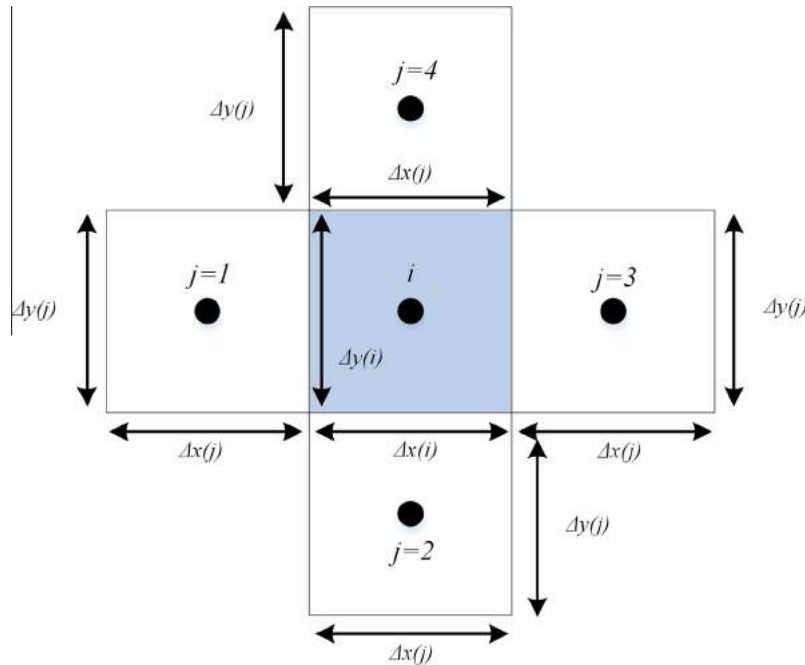


Fig. 1. Mesh geometric properties in rectangular 2-D cases.

Since, for each mesh the effect of the neutron importance function for both the fast and thermal groups should be considered as one number, the simple average of the two groups is used. Although instead of using the average importance function, one can use a weighted average.

Step 3. Dividing the entire reactor geometry into rows and columns and determination of the neutron importance function for each of them.

After determination of the average neutron importance function for each mesh of the entire reactor geometry from step 2, it is necessary to calculate the average neutron importance function for all rows and columns. It should be noted that in this study the terms “rows” and “columns” refer to all mesh boxes located in y and x directions, respectively (see Figs. 4 and 10).

Step 4. Determination of the appropriate number of mesh subdivisions to each row and columns based on their importance values.

The appropriate number of mesh subdivisions along the y-direction of the column (i), and along the x-direction for the row (j), can be obtained by the following formulas:

$$\frac{CI_i}{\sum_i \frac{CI_i dV_i}{V_{core}}} \times M = m_i \quad (7)$$

$$\frac{RI_j}{\sum_j \frac{RI_j dV_j}{V_{core}}} \times N = n_j \quad (8)$$

In fact, by considering Eqs. (7) and (8) each column is divided to  $m_i$  subdivisions along y-direction and each row is divided to  $n_j$  subdivisions along x-direction. Where in the aforementioned equations,  $CI_i$  and  $RI_j$  denote the importance values of the column (i) and the row (j), respectively. Then, by considering the reported number of mesh elements (the fine mesh) as the reference values, the value of  $M$  (or  $N$ ) can be obtained as follows:

Step 5. Considering the half number of the fine mesh elements (reference value) as the coarse mesh value.

Step 6. Distributing half of the coarse mesh value uniformly in each direction throughout the reactor core.

Step 7. Considering the remaining half value as  $M$  (or  $N$ ).

Thus, by substitution of  $M$  and  $N$ ,  $m_i$  and  $n_j$  can be calculated from Eqs. (7) and (8), respectively. Finally, the forward neutron diffusion calculations are performed using the power iteration method to determine neutron fluxes and corresponding eigenvalue for the improved non-uniform mesh distribution.

#### 4. Results and benchmarking

Adjoint calculations are performed in the following for two different benchmark problems, namely Kang and Rod Bundle BWR by considering the two neutron groups. The results are also averaged neutron flux.

##### 4.1. Kang reactor core

The Kang reactor core as a 2-D, 2-group model is considered as the first benchmark problem (Kang and Hansen, 1971). The geometry of this problem is depicted in Fig. 2 and the group constants are shown in Table 1.

The improvement of the mesh point positions is performed for this problem based on the proposed seven-step algorithm. Accordingly, the adjoint numerical calculations based on step 1, are performed in both the thermal and fast neutron groups as shown in Fig. 3. In addition, the average neutron importance function is determined over the two neutron groups for the entire reactor core based on step 2.

In order to calculate the neutron importance function, the normalization process should be performed as follows (Malmir et al., 2010):

$$\frac{1}{N_{fuel}} \sum_{i=1}^{N_{fuel}} \psi_i^i V_i = 1, \quad (9)$$

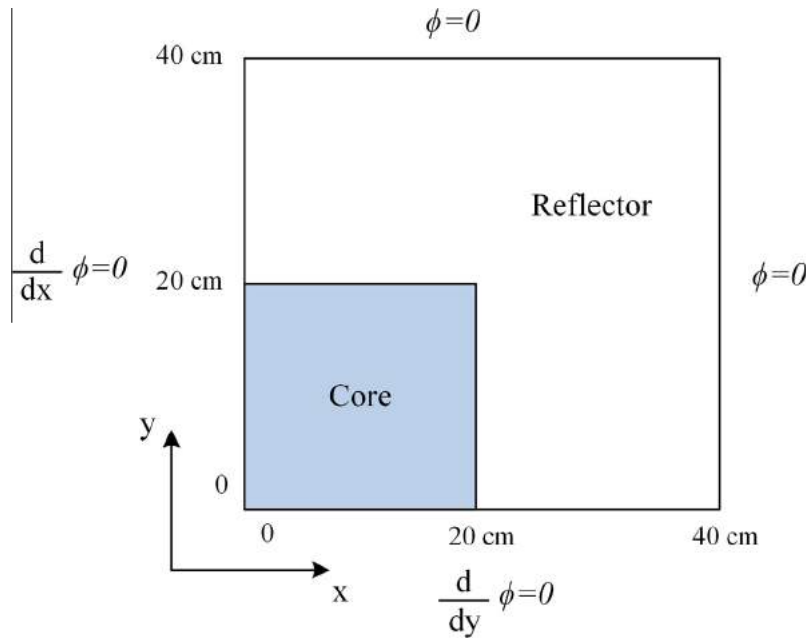


Fig. 2. One-fourth view of the Kang 2-D reactor core.

Table 1

Group constants of the core and reflector in two energy groups for the Kang reactor problem.

Energy Group	Material	$D_g$ (cm)	$\Sigma_{ag}$ (cm $^{-1}$ )	$\nu\Sigma_{fg}$ (cm $^{-1}$ )	$\Sigma_{sg \rightarrow g+1}$ (cm $^{-1}$ )
Fast	Core	1.5	0.0023	0.0	0.06
	Reflector	1.2	0.001	0.0	0.1
Thermal	Core	0.4	0.2	0.218	0.0
	Reflector	0.15	0.02	0.0	0.0

where  $N_{fuel}$  is the number of mesh boxes in the fuel region and  $V_i$  denotes the box volume ( $i$ ).

The third step of the algorithm is performed by dividing the entire reactor geometry in two numbers of rows and columns. In addition, the neutron importance values for each row and column

are determined based on step 4, using the average neutron importance function of each meshes.

As can be seen in Fig. 3, the neutron importance function in the core is greater than the reflector. Hence, higher mesh element density needs to be applied to this region than the reflector based on the presented algorithm.

By considering the last three steps of the proposed algorithm, the appropriate number of mesh subdivisions is assigned to the entire columns and rows. Fig. 4 shows the uniform and improved non-uniform mesh point positions. The forward calculations are then performed for the new mesh distribution in the entire reactor geometry.

Finally, the calculated values of the 2-group neutron fluxes can be normalized in each mesh box to obtain the actual ones as follows (Argonne Code Center, 1977):

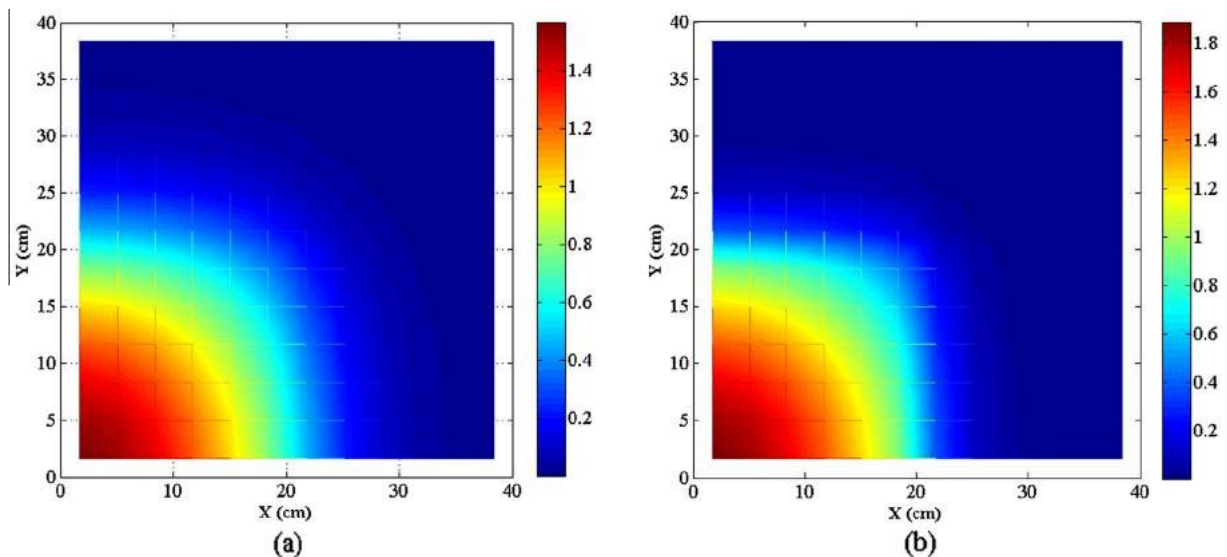


Fig. 3. Fast (a) and thermal (b) neutron importance function for the Kang reactor problem.

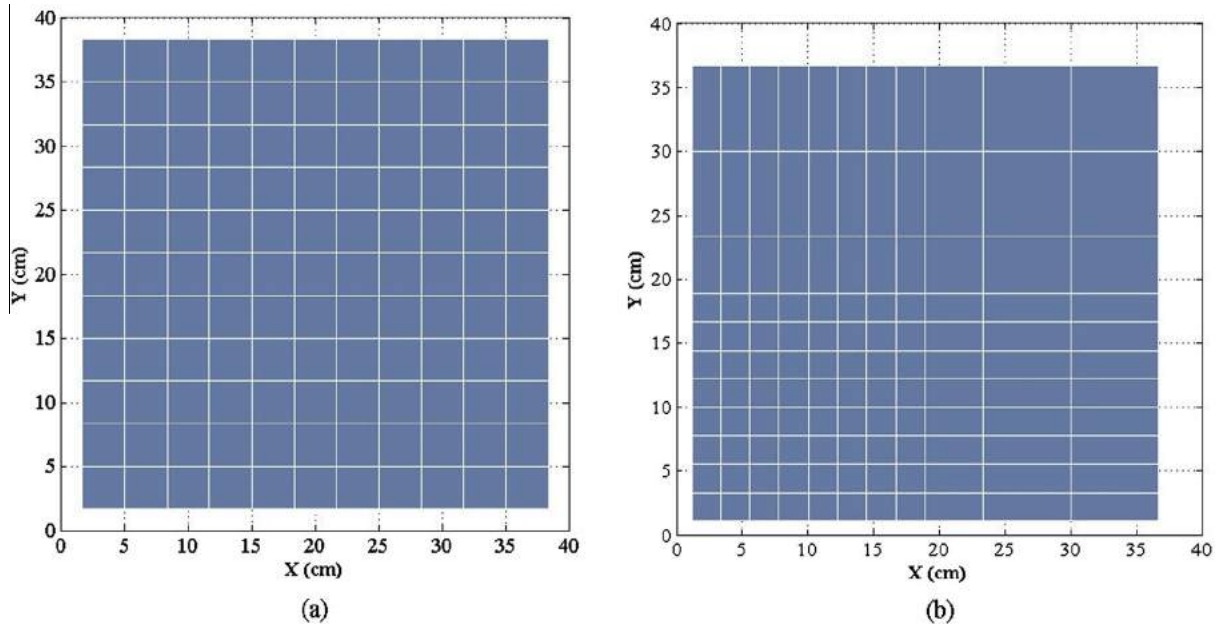


Fig. 4. Comparison between the ordinary uniform (a) and the improved non-uniform.

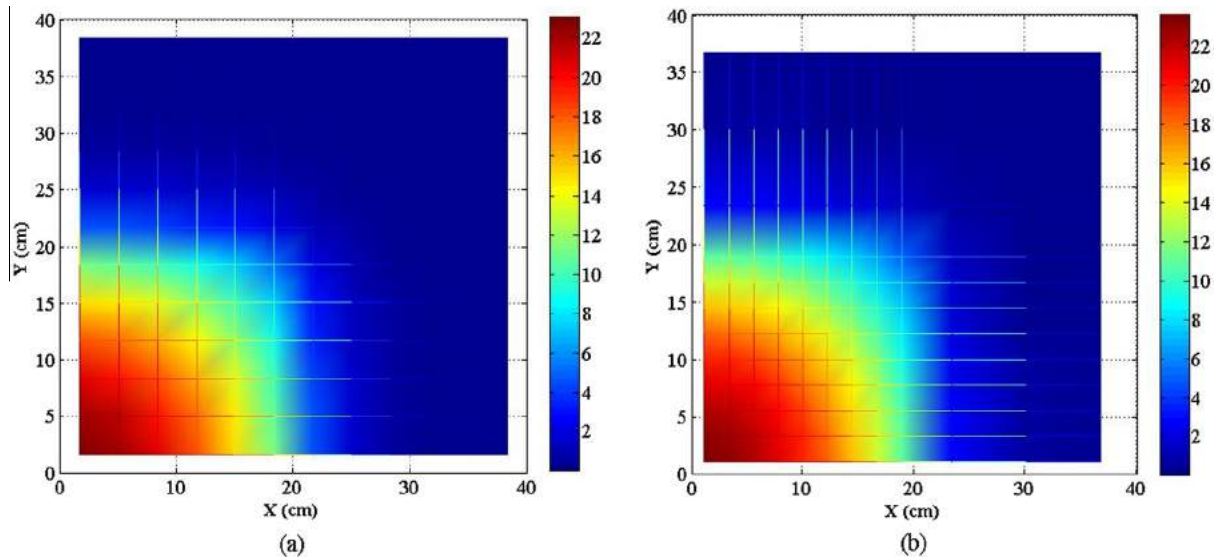


Fig. 5. Fast flux distributions for the ordinary uniform (a) and improved non-uniform (b) mesh point distribution for array  $12 \times 12$  for the Kang reactor problem.

$$\frac{1}{V_{core}} \sum_{i=1}^{N_{fuel}} [v_1 \Sigma_{f,1}^i \phi_1^i + v_2 \Sigma_{f,2}^i \phi_2^i] V_i = 1, \quad (10)$$

where all the parameters have their usual meaning. Figs. 5 and 6, show the fast and thermal fluxes, respectively, for both the two kinds of mesh point distributions.

It should be noted that the series (a) and (b) in Figs. 4–6, correspond to the uniform and improved non-uniform mesh point distributions, respectively.

Table 2, contains the calculated  $k_{eff}$  for the Kang reactor core compared to the ordinary uniform and improved non-uniform coarse mesh distributions against the fine reference value. It is observable that the improved non-uniform solution is more accurate than the other one. It is also noteworthy to mention that, for a

consistent comparison between the efficiency of the uniform mesh element distribution and that of the adaptive one, the total execution time has been considered using a laptop computer with CPU 1.60 GHz.

As is shown in Table 2, the total execution time of the adaptive (non-uniform) mesh element distribution which is adjoint plus forward execution time is higher than the other one. Because, the initial adjoint calculations based on the proposed algorithm are always needed. However, as a matter of the reduction computational time, the effective multiplication factor from the adjoint calculations has been used as a starting guess for subsequent forward calculations. To be more precise, the results in Table 2 indicate an about three and one half times improvement of accuracy compared to the uniform case but the differences are not too large. Although, the total execution time for the adaptive one, has been increased



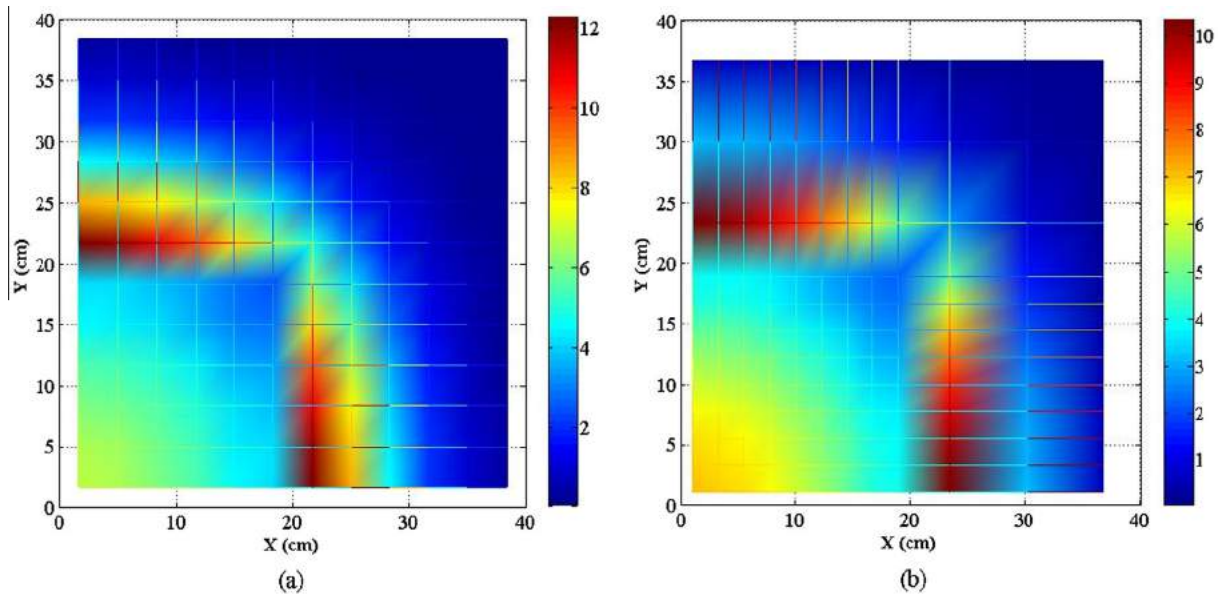


Fig. 6. Thermal flux distributions for the ordinary uniform (a) and improved non-uniform (b) mesh point distribution for array  $12 \times 12$  for the Kang reactor problem.

Table 2

Calculated forward multiplication factors for the Kang reactor problem.

Mesh zone types	$k_{eff}$	RPE (pcm)	Total execution time (s)
$12 \times 12$ Uniform	0.89389	–215	28
$12 \times 12$ Improved non-uniform	0.89525	–64	39
$24 \times 24$ Uniform* (reference)	0.89582	...	...

\* The reference  $k_{eff}$  is obtained using CITATION code.

only about one and half times in comparison with the other one. Accordingly, the proposed method can be considered as an efficient method for the neutron diffusion calculations.

In order to compare the flux results, one has to find the relative percent errors (RPE) which can be obtained by the following expression:

$$RPE(\%) = \frac{\text{calculated value} - \text{reference value}}{\text{reference value}} \times 100 \quad (11)$$

It is worth pointing out that the flux spatial distribution of the RPEs with respect to the reference values (CITATION code) has been depicted in Fig. 7. As is apparent, the results of the adaptive method are more accurate than the conventional method.

	0.105 1.847 1.322 0.633 1.780 1.173	
14.276 0.902 0.649 4.587 1.650 1.219	1.064 1.670 1.189 3.694 1.881 1.305	<b>Fast flux (Reference)</b> RPE (%) fast flux (Uniform) RPE (%) fast flux (Non-uniform) <b>Thermal flux (Reference)</b> RPE (%) thermal flux (Uniform) RPE (%) thermal flux (Non-uniform)

Fig. 7. RPEs of the fast and thermal neutron flux for the uniform and improved non-uniform mesh point distributions of lattice  $12 \times 12$  for the Kang reactor problem.

#### 4.2. Rod bundle BWR

The Rod Bundle BWR which is a 2-D, 2-G model is considered as the second benchmark problem. The boundary condition of this problem consists of perfect reflective for the symmetry line boundaries. The geometry of this problem is shown in Fig. 8.

In this figure, Material 19 (regions with red color) represents stainless steel; Material 20 (regions with white color) represents water; Material 5 (regions with black color) represents poison pins and the other regions (with yellow, brown and cream colors) represent different composition of fuel and other materials (Argonne Code Center, 1977). The group constants of the aforementioned regions are tabulated in Table 3.

Similar to the previous case (Kang reactor core), the seven-step algorithm is applied to improve the mesh point positions based on the neutron importance function for the entire reactor geometry. Accordingly, the adjoint neutron diffusion equation is solved numerically using the power iteration method for both the fast and thermal groups. In addition, the average neutron importance function for the two groups is obtained using Eq. (6). Fig. 9 shows the neutron importance function for fast and thermal groups. It should be noted that the fast and thermal neutron importance functions are normalized by the use of Eq. (9).

As can be seen from Fig. 8, the problem geometry is of the square array " $12 \times 12$ " (Argonne Code Center, 1977). Accordingly, 12 numbers of columns and rows is considered based on the third step of the algorithm. In addition, in order to determine the appropriate number of mesh subdivisions to each column and rows, the importance value of all columns and rows (i.e.  $Cl_i$  and  $Rl_j$ ) based on step 4 is calculated. Fig. 10 properly shows the difference between the ordinary uniform and the improved non-uniform mesh point distributions.

As can be seen from Fig. 10, uniform mesh point distribution over all regions regardless of their dimensions, increases the number of mesh elements in some parts of the reactor geometry which may have not necessarily a high neutron importance value (see Figs. 9 and 10).

As a matter of comparison, the forward calculations are performed numerically for both the uniform and improved non-uniform cases. Figs. 11 and 12, show the fast and thermal fluxes

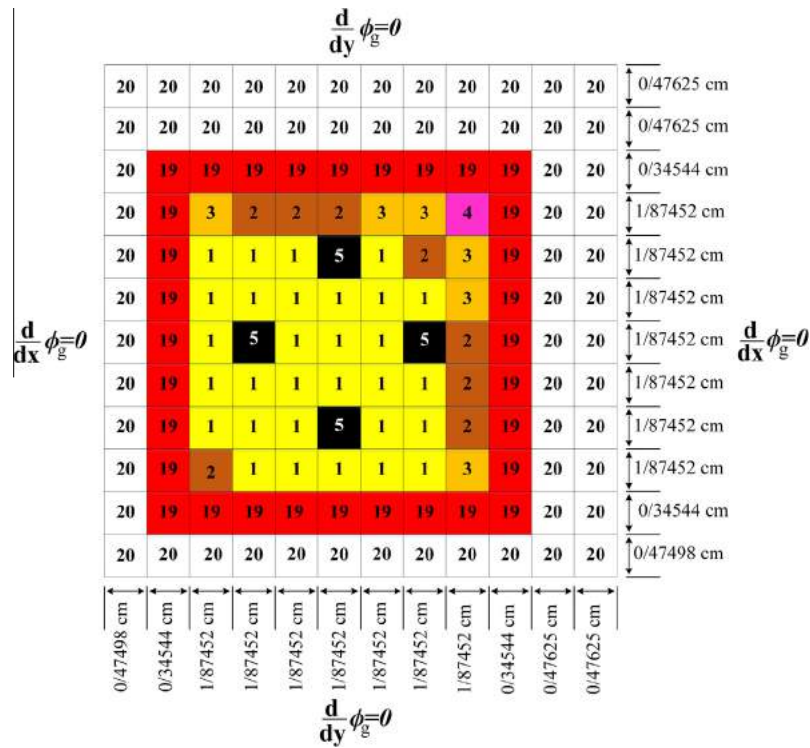


Fig. 8. View of the Rod Bundle BWR problem.

**Table 3**  
Group constants of Rod Bundle BWR in two energy groups.

Energy group	Material	$\Sigma_f$ (cm <sup>-1</sup> )	$\Sigma_{ag}$ (cm <sup>-1</sup> )	$\nu\Sigma_{fg}$ (cm <sup>-1</sup> )	$\Sigma_T$ (cm <sup>-1</sup> )	$\Sigma_{sg \rightarrow g+1}$ (cm <sup>-1</sup> )
Fast	1	2.281E-3	8.983E-3	5.925E-3	2.531E-1	1.069E-2
	2	2.003E-3	8.726E-3	5.242E-3	2.536E-1	1.095E-2
	3	1.830E-3	8.587E-3	4.820E-3	2.535E-1	1.112E-2
	4	1.632E-3	8.480E-3	4.337E-3	2.533E-1	1.113E-2
	5	2.155E-3	9.593E-3	5.605E-3	2.506E-1	1.016E-2
	19	...	1.043E-3	...	2.172E-1	9.095E-3
	20	...	1.983E-4	...	2.476E-1	3.682E-2
Thermal	1	4.038E-2	5.892E-2	9.817E-2	5.732E-1	...
	2	3.385E-2	5.174E-2	8.228E-2	5.767E-1	...
	3	2.962E-2	4.717E-2	7.200E-2	5.797E-1	...
	4	2.428E-2	4.140E-2	5.900E-2	5.837E-1	...
	5	9.968E-3	1.626E-1	2.424E-2	5.853E-1	...
	19	...	4.394E-3	...	4.748E-1	...
	20	...	7.796E-3	...	1.123E+0	...

for both the aforementioned distributions, respectively. It has to be noticed that the series (a) and (b) in Figs. 10–12, correspond to the uniform and improved non-uniform mesh point distributions, respectively. The mean and maximum flux variations in both mesh point distributions are shown in Table 4. Moreover, the calculated values of  $k_{eff}$  for the coarse uniform, improved non-uniform and fine reference value are presented in Table 5.

The RPEs and the total execution times for the aforementioned distributions are given in Table 5. As it is observable, all the RPEs which are obtained based on the proposed algorithm are more acceptable in comparison with the other one. However, the total execution time results are vice versa.

Although the proposed seven-step algorithm is applied to the certain number of mesh elements, it is executable for arbitrary mesh size arrays. Accordingly, the seven-step improvement pro-

cess is considered for two more mesh arrays, namely  $48 \times 48$  and  $96 \times 96$ , for the Rod Bundle BWR benchmark problem (Argonne Code Center, 1977).

To compare the  $k_{eff}$  results, consider the Apparent Absolute Error in  $k_{eff}$  as follows (Argonne Code Center, 1977):

$$\text{Apparent Absolute Error in } k_{eff} (\times 10^3) = (\text{calculated value} - \text{reference value}) \times 10^3 \quad (12)$$

Fig. 13 shows the results of  $k_{eff}$  in uniform and improved non-uniform mesh arrays  $24 \times 24$ ,  $48 \times 48$  and  $96 \times 96$  by considering the results of the infinite number of mesh elements as the reference value (Argonne Code Center, 1977).

It reveals that the effective multiplication factor for all mesh element arrays in the case of improved non-uniform mesh point



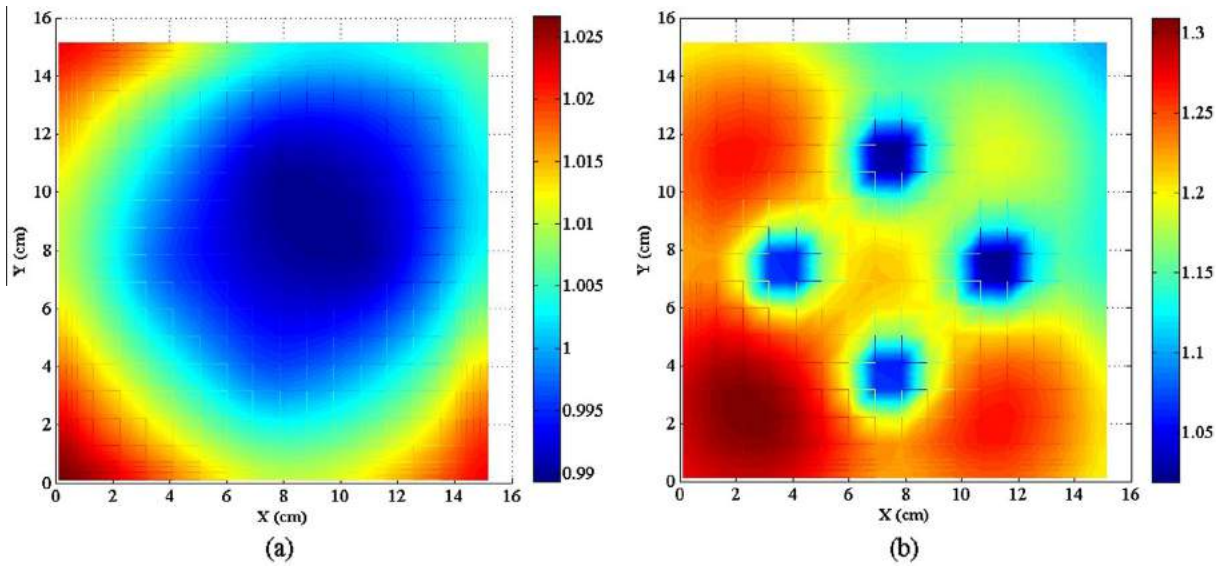


Fig. 9. Fast (a) and thermal (b) neutron importance function for the Rod Bundle BWR problem.

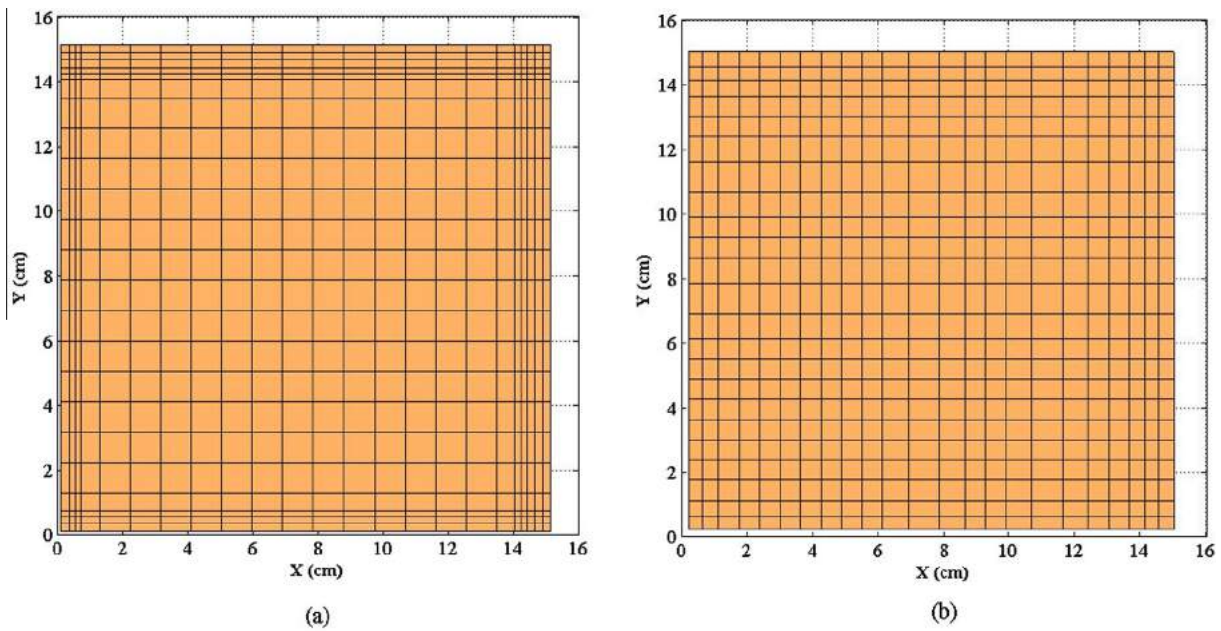


Fig. 10. Comparison between the ordinary uniform (a) and the improved non-uniform (b) mesh point distribution for array  $24 \times 24$  for the Rod Bundle BWR problem.

distribution is more accurate than that in the uniform distribution. Additionally, this figure shows that the rate of reduction of error indicated by the slope of the error curves is different. This can be due to the fact that, the coarse mesh solution by the conventional methods with uniform distributions is not accurate. By increasing the number of mesh elements, however, more accurate solutions can be determined. So, it can reasonably be argued that the rate of reduction of error should be decreased with increases the number of mesh elements significantly. Additionally, as the results clearly show, the accuracy of the solutions of the adaptive method is better than the other one of any number of mesh elements. This difference in accuracy, though, is dominant in lower mesh element numbers. The most obvious explanation for this might be from the

point of view of the relative number of improved mesh element positions to the total number of them. More precisely, in the case of total high number of mesh elements, the impact of a few number of adaptive mesh elements of the solution is lower. Based on the arguments cited above and as the results apparently indicate, the slop reduction of error for the adaptive case should be lower than the other one.

As can be reasonably argued, in order to calculate the weighting factors for the proposed algorithm, initial adjoint calculations are needed. So the efficiency is impacted. However, the accuracy of the neutron diffusion solutions by using the proposed method has been significantly better than the other one. Accordingly, the proposed algorithm based on the importance function can be

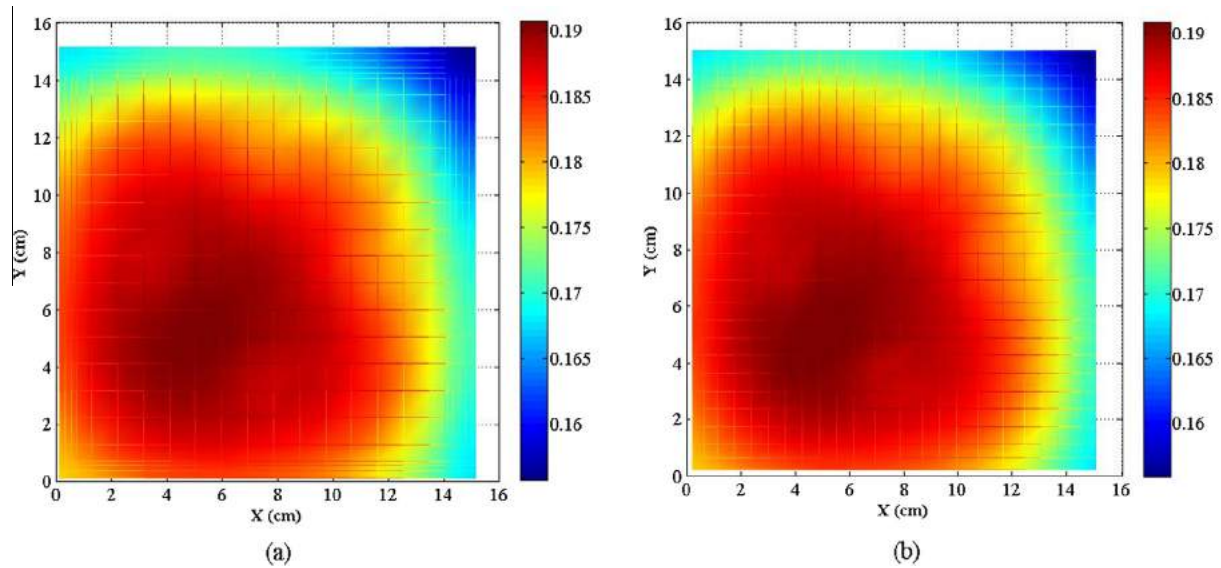


Fig. 11. Fast flux distributions for the ordinary uniform (a) and the improved non-uniform (b) mesh point distribution for array  $24 \times 24$  for the Rod Bundle BWR problem.

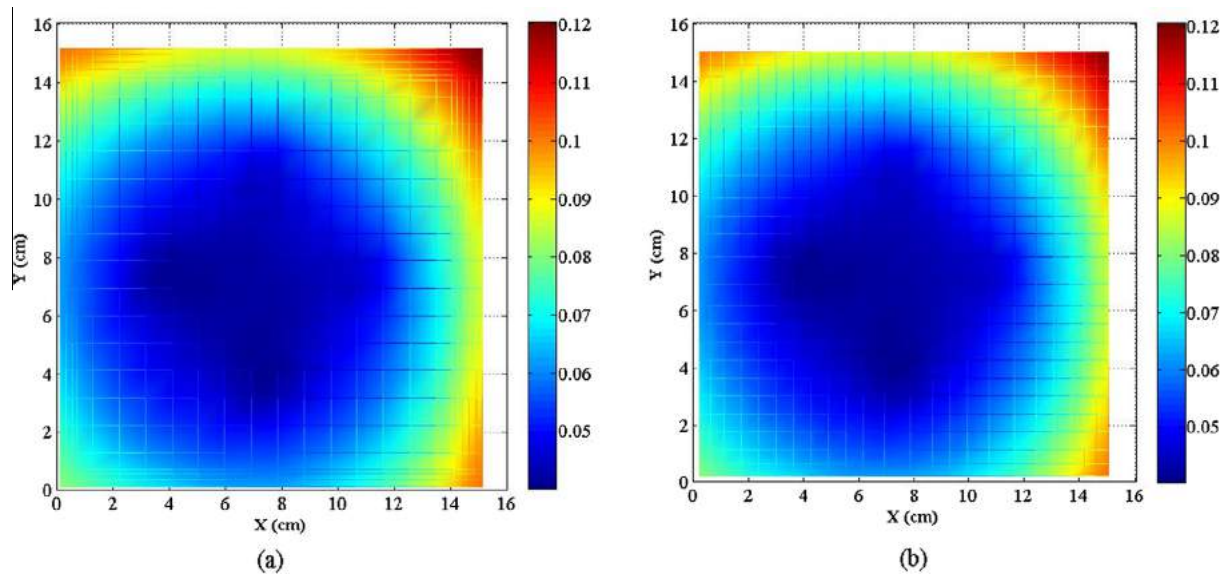


Fig. 12. Thermal flux distributions for the ordinary uniform (a) and the improved non-uniform (b) mesh point distribution for array  $24 \times 24$  for the Rod Bundle BWR problem.

Table 4

Fast and thermal neutron flux analysis for the Rod Bundle BWR problem.

Error analysis (RPE)	Fast	Thermal
Mean RPE(%) for Uniform $24 \times 24$	0.189	0.200
Max RPE(%) for Uniform $24 \times 24$	1.015	1.677
Mean RPE(%) for Improved non-uniform $24 \times 24$	0.130	0.133
Max RPE(%) for Improved non-uniform $24 \times 24$	1.001	1.362

Table 5

Calculated forward multiplication factors for the Rod Bundle BWR problem.

Mesh zone types	$k_{eff}$	RPE (pcm)	Total execution time (s)
$24 \times 24$ Uniform	1.08759	141	73
$24 \times 24$ Improved non-uniform	1.08696	83	95
$48 \times 48$ Uniform* (reference)	1.08606	...	...

\* The reference is reported by the Argonne Code Center (1977).

considered as an efficient method to obtain accurate results. Additionally, it should be noted that, this paper would benefit from the extension to unstructured meshes because local mesh refinement really shows all its benefits only for locally refined unstructured

meshes. This is due to the fact that mesh refinement in Cartesian meshes always entails refinement in the areas that doesn't need refinement.

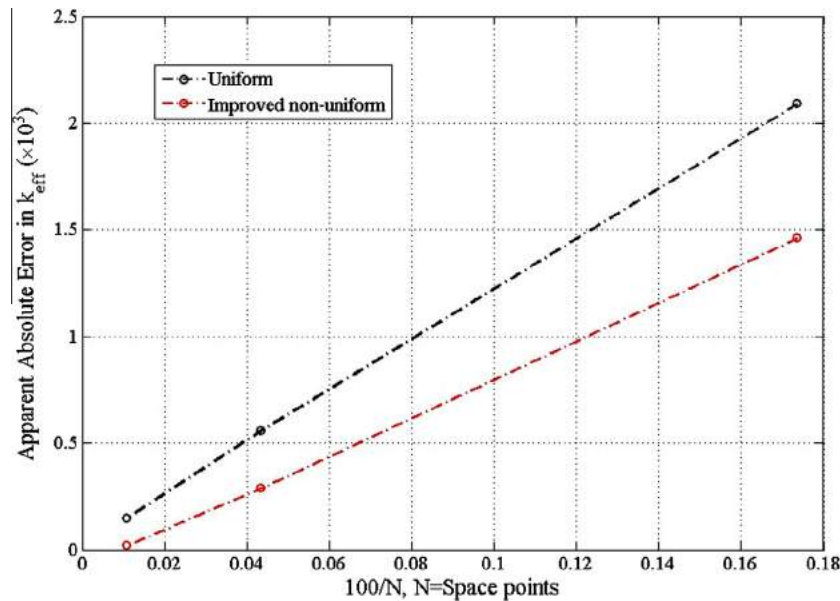


Fig. 13. Comparison of the  $k_{eff}$  for the uniform and improved non-uniform mesh point distribution for arrays  $24 \times 24$ ,  $48 \times 48$  and  $96 \times 96$  for the Rod Bundle BWR problem.

## 5. Conclusion

In this work, by aid of improving the mesh point positions, an enhanced finite difference scheme for the neutron diffusion equation was proposed based on the neutron importance function. The neutron importance function was determined using the adjoint (backward) neutron diffusion calculations. These calculations were performed in the same procedure as for the forward calculations. Considering the neutron importance function, the mesh points were improved through the entire reactor core. Accordingly, in regions with greater neutron importance, density of mesh elements was higher than that in regions with less importance. The forward calculations were performed for both of the ordinary uniform and improved non-uniform mesh point distributions and the results, including the neutron fluxes along with the corresponding eigenvalues for the two cases were compared with each other.

The results were benchmarked against the reference values (with fine meshes) for the Kang and Rod Bundle BWR benchmark problems. Furthermore, in order to check the capability and accuracy of this algorithm for any arbitrary number of mesh elements, it was applied to several numbers of mesh elements to the Rod Bundle BWR problem. Results all revealed that the improved non-uniform mesh element distribution was highly efficient.

To sum up, an improvement of the mesh element positions in Finite Difference Method (FDM) based on the suggested scheme of the neutron importance function can remarkably affect the averaged neutron fluxes as well as the effective multiplication factor for any arbitrary number of mesh elements. Possible future works can be included, extending of the suggested algorithm to different numerical methods such as the Finite Element Method (FEM) and Nodal Expansion Method (NEM). For the time-dependent cases, however, further developments are required and more works are recommended.

## References

- Argonne Code Center, 1977. Benchmark Problem Book, Report ANL-7416 (Suppl. 2). Argonne National Laboratory, Argonne, IL.
- Ayyoubzadeh, S.M., Vosoughi, N., 2011. Optimization of the Direct Discrete Method using the solution of the adjoint equation and its application in the multi-group neutron diffusion equation. AIP Conf. Proc. 1389, 1777–1781.
- Ayyoubzadeh, S.M., Vosoughi, N., Ayyoubzadeh, S.M., 2012. On an improved Direct Discrete Method and its application in two dimensional multi-group neutron diffusion equation. Ann. Nucl. Energy 44, 1–7.
- Bell, G.I., Glasstone, S., 1970. Nuclear Reactor Theory. Van Nostrand Reinhold Company, New York.
- Duderstadt, J.J., Hamilton, L.J., 1991. Nuclear Reactor Analysis. John Wiley & Sons, New York.
- Hosseini, S.A., Vosoughi, N., 2013. Development of two-dimensional, multigroup neutron diffusion computer code based on GFEM with unstructured triangle elements. Ann. Nucl. Energy 51, 213–226.
- Kang, C.M., Hansen, K.F., 1971. Finite Element Methods for Space-Time Reactor Analysis (PhD dissertation). Massachusetts Institute of Technology, Massachusetts, USA.
- Lamarsh, J.R., 1965. Introduction to Reactor Nuclear Reactor Theory. Addison-Wesley Publishing Company.
- Lathouwers, D., 2011a. Goal-oriented spatial adaptivity for the  $S_N$  equations on unstructured triangular meshes. Ann. Nucl. Energy 38, 1373–1381.
- Lathouwers, D., 2011b. Spatially adaptive eigenvalue estimation for the  $S_N$  equations on unstructured triangular meshes. Ann. Nucl. Energy 38, 1867–1876.
- Malmir, H., Vosoughi, N., Zahedinejad, E., 2010. Development of a 2-D 2-group neutron noise simulator for hexagonal geometries. Ann. Nucl. Energy 37, 1089–1100.
- Malmir, H., Moghaddam, N.M., Zahedinejad, E., 2011. Comparison between triangular and hexagonal modeling of a hexagonal-structured reactor core using box method. Ann. Nucl. Energy 38, 371–378.
- Nakamura, S., 1977. Computational Methods in Engineering and Science with Applications to Fluid Dynamics and Nuclear Systems. Wiley Interscience, New York.
- Poursalehi, N., Zolfaghari, A., Minuchehr, A., 2013. Development of a high order and multi-dimensional nodal code, ACNEC3D, for reactor core analysis. Ann. Nucl. Energy 55, 211–224.
- Ragusa, J.C., Wang, Y., 2010. A two-mesh adaptive mesh refinement technique for  $S_N$  neutral-particle transport using a higher-order DGFEM. J. Comput. Appl. Math. 233, 3178–3188.
- Wang, Y., Ragusa, J.C., 2011. Standard and goal-oriented adaptive mesh refinement applied to radiation transport on 2D unstructured triangular meshes. J. Comput. Phys. 230, 763–788.
- Zhang, Q., Abdel-Khalik, H.S., 2014. Global variance reduction for Monte Carlo reactor physics calculations. Nucl. Eng. Des. 280, 76–85.

## Experimental and theoretical investigation into X-ray shielding properties of thin lead films

*International Journal of Radiation Research*, 18 (2) (2020) 263-274.

**Authors:** M. Vagheian\*, D. Sardari, S. Saramad, D. Rezaei Ochbelagh

**Abstract:** In this work, X-ray shielding properties of different nanostructured and bulk-structured thick lead films have been considered experimentally and theoretically, respectively. The lead films were fabricated from 10 to 1000 nm thicknesses and exposed to 8 to 14 keV X-ray energies. From the theoretical point of view, the Monte-Carlo simulation using the MCNP code was employed to investigate the shielding properties of the samples. Due to the fact that the MCNP code is not able to consider the nanostructured films and indeed consider them as bulk-structured, the difference in photon transmission for the same thickness of the lead samples can give the impact of nanostructuring of the sample in photon shielding properties. By facilitating comparison between the experimental and theoretical results, it was revealed that the nanostructured lead thin films were able to attenuate the incident photons more than those samples considered as bulk-structured for the same thicknesses.

**Contributions:** I carried out the synthesis of the nanostructured thin lead films using the Physical Vapor Deposition (PVD) technique and performed the results obtained by the Energy Dispersive Spectroscopy (EDS), the Scanning Electron Microscopy (SEM), and the gamma detector measurements. I also performed the entire Monte-Carlo simulation and modeling using the MCNP code. Moreover, I conducted the analysis of most of the obtained results and then wrote the manuscript. As the corresponding author, I sent the manuscript and performed the revision based on the reviewer's comments.

**License:** This work is licensed under a Creative Commons Attribution 4.0 International (CC BY 4.0). To see the license go to <http://ijrr.com/en>



# Experimental and theoretical investigation into X-ray shielding properties of thin lead films

M. Vagheian<sup>1\*</sup>, D. Sardari<sup>2</sup>, S. Saramad<sup>1</sup>, D. Rezaei Ochbelagh<sup>1</sup>

<sup>1</sup>Tehran Polytechnic University (Amirkabir University of Technology), Tehran, Iran

<sup>2</sup>Azad University, Science and Research Branch, Tehran, Iran

## ABSTRACT

### ► Original article

#### \*Corresponding authors:

Mehran Vagheian, Ph.D.,

#### E-mail:

mehran.vagheian@gmail.com

Revised: June 2019

Accepted: August 2019

Int. J. Radiat. Res., April 2020;  
18(2): 263-274

DOI: 10.18869/acadpub.ijrr.18.2.263

**Background:** Among all of the radiations, X-ray has been always the center of attention due to the increasing availability of the X-ray tubes in industry, research institutes and medical centers. In this study, X-ray shielding properties of bulk and nanostructured thin lead films were investigated by means of Monte-Carlo computational and experimental methods, respectively. **Materials and Methods:** The lead samples were fabricated by the Physical Vapor Deposition technique (PVD) with different thickness of 10, 100 and 1000 nm. To investigate the radiation shielding properties of the nanostructured thin films, all of the prepared samples were subjected to the X-ray ranging from 8 to 14 keV. In order to consider the shielding properties of the bulk-structured thin films, the Monte-Carlo MCNPX code was employed. **Results:** The results indicated that, for low X-ray energies, the nanostructured thin lead films attenuate more than bulk-structured samples; however, the difference disappears as film thickness increases to 1000 nm or X-ray energy reaches 14 keV. **Conclusion:** Results imply that the nanostructured thin lead films attenuate more photons than the bulk-structured thin lead films with the same thicknesses.

**Keywords:** Nanostructured thin lead films, Advanced X-ray shielding design, MCNPX code, Thin lead film characterization.

## INTRODUCTION

Among all of the radiations, X-ray radiation has been always the center of attention due to the increasing availability of the X-ray tubes in industry, research institutes and medical centers. Photons of X-ray s can penetrate into the human body and cause cell injury and even cell death enclosing enclosing or shielding the X-ray generating units with a material which resists X-ray penetration, which is a requisite and concerning issue <sup>(1-3)</sup>.

Some recent studies compared the effect of nano-sized and micro-sized materials on the transmission of different X-ray energy beams. In 2013, Noor Azman *et al.* <sup>(4, 5)</sup>, considered and compared the attenuation ability of the nano-sized and micro-sized WO<sub>3</sub> as a filler loading component within the epoxy composites in

different X-ray energies. In a similar recent work, the mass attenuation coefficients of pure concrete and WO<sub>3</sub> added concrete with micro-sized and nano-sized particles were considered and compared with each other. It was observed that shielding properties of concrete doped with WO<sub>3</sub> increased. The results of mass attenuation coefficients also showed that the concrete doped with nano-WO<sub>3</sub> significantly improved shielding properties compared to micro-WO<sub>3</sub> <sup>(6)</sup>. In 2012, Kunzel and Okuno <sup>(7)</sup> investigated the effect of thickness and concentration of dispersed micro and nano-sized CuO powder within the polymer resin. They showed that the attenuation property of both the nano-sized and micro-sized CuO would increase by increasing the thickness and concentration. The aforementioned investigations additionally indicated a higher

attenuation ability of the nano-sized particles than those of the micro-sized ones in low X-ray energy ranges. More precisely, in high X-ray energies, almost no significant differences were observed between the nano-sized and micro-sized particles with the same weight percentages. In 2018, Tekin *et al.* <sup>(8)</sup>, investigated the influence of WO<sub>3</sub> and Bi<sub>2</sub>O<sub>3</sub> additives in micro and nano scales on the radiation shielding properties of hematite-serpentine concrete (HSC). The results showed that the values of  $\mu/\rho$  of nanoparticles were higher than those of micro-particles. In another research, the attenuation of nano lead oxide and EPDM composite was investigated for development of polymer-based radiation shielding material. The nano-sized lead oxide showed improvement in regard to the radiation shielding behavior of the EPDM material <sup>(9)</sup>.

The most important advantages of the nano-sized particles on the X-ray shielding properties of the materials are the maximization of surface to volume ratio and their high dispersion properties on the substrate. Both of these factors increase the surface electron density of the shield material, and therefore, raise the interaction probability of the impinged photons with the shield electrons which consequently leads to improving the shielding effectiveness <sup>(4-11)</sup>.

There are several reports of experimental and theoretical studies on X-ray radiation shielding with the usage of various materials; however, among all of the candidate materials, lead has long been considered as a highly effective material for X-ray radiation attenuation owing to its high density <sup>(1-3, 12)</sup>. Lead is available in a variety of forms such as bricks, sheets and plates. Several recent studies considered the effect of the lead nanoparticles as a filler loading component for enhancing the shielding properties of other materials including polymers, composites, etc. <sup>(13-21)</sup>. Despite these investigations, the features of the pure nanostructured lead thin films have never been considered and evaluated. Additionally, shielding properties of nanostructured materials around the electron shell energy ranges have not been adequately assessed. As the use of lead thin

films in radiation shielding is a promising way for the development of X-ray radiation protection, this work focused on investigation of lead shielding properties. More precisely, in the present research, the investigation of the X-ray radiation shielding of thin lead films in the case of both the nano and bulk-structured samples were considered. Importantly, the impact of the material thickness and X-ray energy on the shielding properties of thin lead films was evaluated. The main novelties of this research can accordingly be considered as: determination of the X-ray shielding properties of nanostructured thin lead films for the first time; investigation of the effect of different X-ray energies and thicknesses on the shielding properties of the films; and finally comparison of the results between the nanostructured and bulk-structured samples.

In the following section, the theoretical and computational aspects of the X-ray radiation shielding properties of materials in addition to the sample preparation and characterization are presented in details. Then, theoretical and experimental results regarding the irradiation of the nanostructured and bulk-structured thin lead films have been considered. After that, a detailed discussion regarding the obtain results have been presented. The last section is devoted to the conclusion of this study.

## MATERIALS AND METHODS

### Theoretical methodology

When a mono energy X-ray with an intensity of  $I_0$  incidents on the absorber with a thickness of  $x$ , the shielding ratio of the absorber can be considered as shown in equation 1 <sup>(2, 3, 12)</sup>:

$$1 - \frac{I}{I_0} = 1 - e^{-N\sigma_t x} \quad (1)$$

Where  $N$  and  $\sigma_t$  indicate the atomic number density and total photon microscopic cross section, respectively. The energy spectrum of X-ray photons emitted from an X-ray generating tube has different characteristic X-ray lines that are superimposed on the continuous

bremsstrahlung spectrum. Regarding the fact that the microscopic cross-section is considerably dependent on the incident photon energy, calculations of the shielding ratio of the X-ray spectra are a difficult and laborious issue. The Monte-Carlo photon transport calculation code is an internationally recognized code for analyzing such complex computational problems, which are presented in the following.

### MCNPX modeling and simulation

MCNPX code version 2.6 is employed to investigate the shielding ratio of the deposited lead thin films for different X-ray energies and material thicknesses. This code is based on the probabilistic transport Monte Carlo method as developed by the Los Alamos National Laboratory <sup>(22)</sup>. Printed with each tally bin is the relative error of the tally corresponding to one standard deviation. These errors cannot be believed reliable (hence, neither can the tally itself) unless the error is fairly low (below 5%). Additionally, MCNP performs a series of statistical tests to determine the statistical validity and convergence of tally scores and uncertainties. Tally fluctuation charts are printed to show how a tally mean, error, variance of the variance (an estimate of the error of the relative error), and slope of the largest history scores (the estimated exponent of the probability density function) fluctuate as a function of the number of histories run. MCNP additionally calculates a figure of merit (FOM)

for one tally bin of each tally as a function of the number of histories and prints the results in the tally fluctuation charts at the end of the output. The FOM should be approximately constant as the number of histories increases <sup>(22-25)</sup>.

### Sample preparation

High-pure commercial lead powder with the particle size smaller than 100 micrometers is supplied by the Merck Company to be used in this investigation. The lead thin films were fabricated with a different thickness of 10, 100 and 1000 nanometers using the Physical Vapor Deposition technique (PVD) <sup>(26)</sup>. The standard borosilicate thin cover slips with the thickness of approximately 130 micrometers were used as the substrate. The lead nanoparticles were deposited on the substrates with the deposition rate of 1 angstrom/s.

### Sample characterization

#### Energy Dispersive X-ray Spectroscopy Analysis

The aim of the Energy Dispersive X-ray Spectroscopy Analysis (EDS) was to investigate the purity of the prepared samples. The importance of this analysis is laid upon the fact that any undesirable impurities can remarkably impact the experimental results. Figure 1 illustrates the EDS spectra of the samples by providing information on the different lead electronic shells in addition to the absence of any impurities.

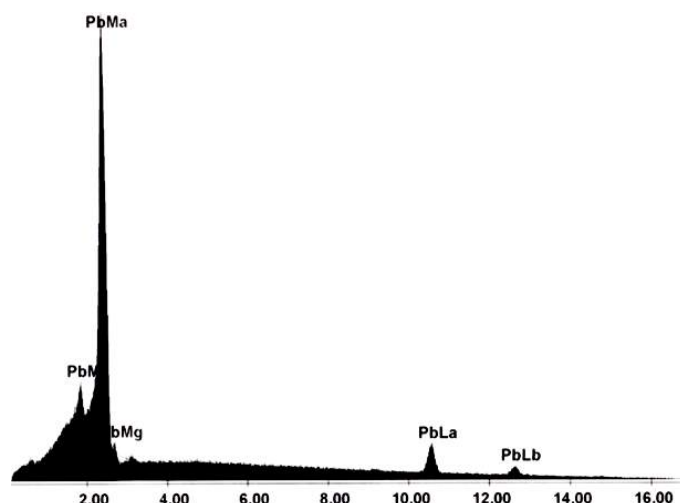


Figure 1. Measurement of lead purity using Energy Dispersive Spectroscopy (EDS).

### Scanning electron microscopy observations

To make sure the accuracy of the measured thickness by the PVD technique, the Scanning Electron Microscopy (SEM) (KYKY model EM 3200) was employed. Figure 2 shows the cross face view of the sample 100 nm and 1000 nm thicknesses. As is shown, the thickness measured by the SEM technique is in good agreement with those obtained by the PDV technique.

Figure 3 shows the SEM images of the surface morphology for all of the fabricated lead thin films (i.e., 10, 100 and 1000 nm thicknesses). As is shown, agglomeration is occurred both for the samples of 100 nm and 1000 nm thicknesses; however, for the sake of comparison, it is much more evident for the latter case. Moreover, it is worth pointing out that the nano lead particles are distributed much more uniformly for the

sample of 10 nm thickness than the other ones. Considering these observations, it seems that increasing the thickness of deposited lead films causes an increase in the agglomeration probability of nano lead particles which eventually leads to the reduction of surface electron density.

### Theoretical and experimental results

#### Validation and benchmarking

Firstly, for a consistent and accurate comparison between the experimental measurements and the simulation results, the same set up was considered according to figure 4. In this analysis, the shielding ratio of a bulk lead sheet with the thickness of 60 micrometers for both the experimental and simulation measurements was obtained and then compared with each other in different X-ray energies.

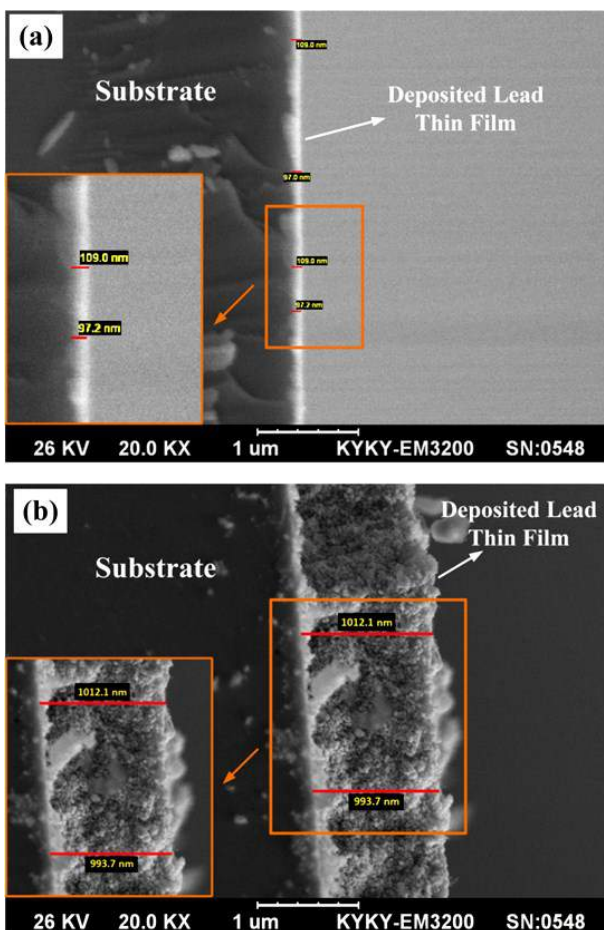


Figure 2. Cross face view of a) 100 nm and b) 1000 nm thickness of deposited lead thin film.

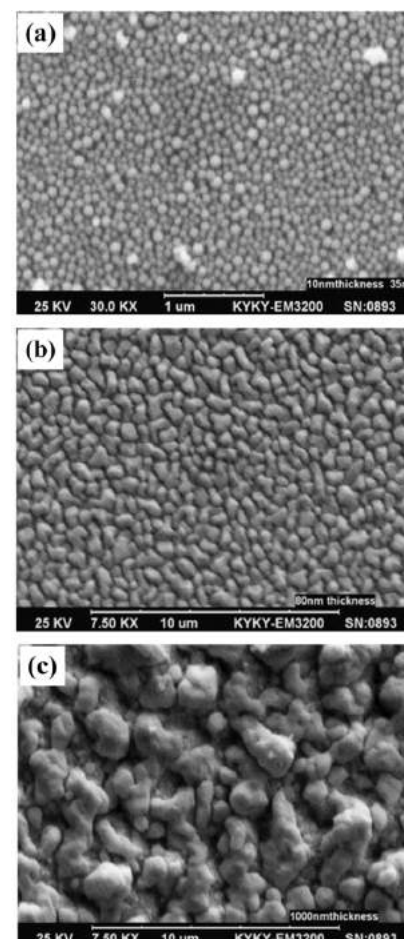


Figure 3. SEM images of a) 10 nm, b) 100 nm and c) 1000 nm thickness of the deposited lead thin film.



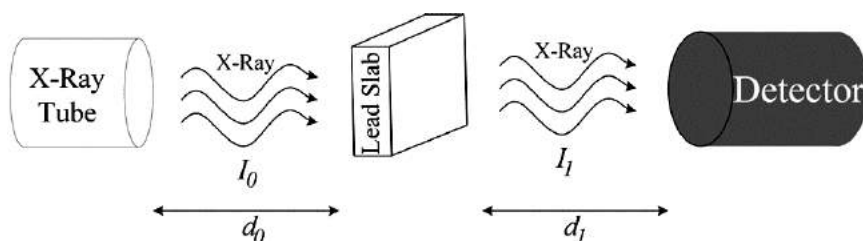


Figure 4. Schematic view of the experimental and simulation setups for benchmarking.

Figure 4 shows the simplified geometry configuration of the X-ray generating tube which has been used as the input for the MCNPX code. As can be observed,  $d_0$  is the distance from the X-ray window and the lead slab, and  $d_1$  is the distance from the lead slab and the detector. In order to consider the highest possible number of the transmitted and scattered photons, both  $d_0$  and  $d_1$  are considered to be less than 0.5 mm. As is shown, the X-ray generation is the first thing that should be obtained. Accordingly, a mono-energy electron beam was designed to impinge on the copper target with a  $45^\circ$  angle, and then the beryllium window was considered to be located at the  $90^\circ$  angle to the incident electron beam. The thickness and density of the beryllium window were assumed to be 125 microns and  $1.85 \text{ g/cm}^3$ , respectively.

The X-ray spectra were determined by F1: tally of MCNPX code and then the shielding ratio of the lead slab were obtained in different X-ray energies based on a combination of X-ray spectrum and energy-dependent attenuation coefficients. The configuration of the detector considered as the manufacturer design and

information so that the density of Mica window, the diameter of the housing, the diameter of the counter tube and counter tube length are  $1.75 \text{ (mg / cm}^2\text{)}$ , 22 mm, 15 mm and 76 mm, respectively. Additionally, it should be noted that the impact of detector's dead time on the results has been considered. The sample size was considered to be  $22 \times 22 \text{ mm}$  to properly be fitted the window of the counter tube.

To compare the experimental and theoretical results, the Apparent Absolute Error (AAE) in shielding ratio was calculated using equation 2 (27, 28):

$$\text{AAE (\%)} = |\text{Theoretical Value} - \text{Experimental Value}| \times 100 \quad (2)$$

High-pure commercial lead slab, purchased from the Hopkins and Williams Company, was used in this section of work as the absorber for validation and benchmarking. The thickness of the slab was 60 micrometers and the results all tabulated in table 1 for different irradiated X-ray energy voltage peaks.

Table 1. Theoretical and experimental results of the shielding ratio for 60 micrometer bulk Lead sheet.

Energy (keV)	Theoretical result (%)	Experimental result (%)	AAE (%)
8	99.81	99.79	1.89
9	99.76	99.74	1.70
10	99.65	99.63	1.50
11	99.40	99.39	1.43
12	99.13	99.12	1.28
13	98.69	98.68	1.12
14	98.14	98.13	0.75

As is shown, the MCNPX computational measurements are in good agreement with those obtained from the experiments.

#### Irradiation characterization

A typical X-ray tube (commercial RONTGENERAT German type X-ray tube) with

a target of copper was used to consider and characterize the X-ray shielding property of thin lead films. The tube currently in use can be set in the ranges 8 keV toward the 14 keV (due to the long-life of the tube). The built-in rate meter including counter-tube voltage supply enables direct measuring of photons using a Geiger-Muller counter tube. The employed Geiger Mueller tube (PHYWE model 09025-11) was considered to count the transmitted X-ray radiations; however by considering the detector's dead time effect.

In this work, three lead samples with a different thickness of 10, 100 and 1000 nm were

considered to investigate a wide range of thickness variations. As is shown in figure 5, each sample is located between the Geiger Mueller counter and the X-ray tube.

In order to obtain the shielding ratio of the nanostructured and bulk-structured thin lead films, firstly, the transmission of X-rays from the substrate has been determined. As is illustrated in figure 5(a), firstly, the number of transmitted X-rays from the substrate is counted and then the aforementioned lead samples are located between the counter and X-ray source. Figure 5 (b) and (c) show the schematic view of the experimental and theoretical setup, respectively.

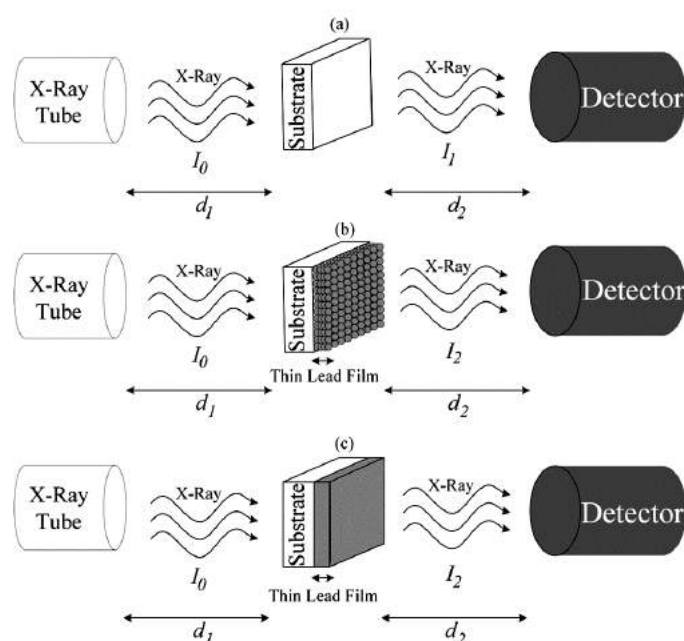


**Figure 5.** Schematic view of the irradiated and transmitted X-ray radiations **a)** through substrate **b)** through both substrate and thin lead film for the experimental setup **c)** through both substrate and thin lead film for the MCNPX setup.

Where;  $d_0$  is the distance between the X-ray tube and the substrate and  $d_2$  is the distance between the lead film and the detector. Similar to the previous experiment, the sample size was considered to be 22×22 mm to properly fit the window of the counter tube. It should be noted that each experiment was repeated 20 times. Regarding figure 5 and using equation(2), the shielding ratio of the experimental and theoretical measurements was calculated for different X-ray energies ranging from 8 to 14 keV using equation 3:

$$\text{Shielding Ratio}(\%) = \left(1 - \frac{I_2}{I_1}\right) \times 100, \quad (3)$$

Where;  $I_1$  and  $I_2$  are the transmitted X-rays from the substrate and from both substrate and thin lead films, respectively. The experimental and theoretical MCNPX results have been presented in figure 6. It should be noted that the required corrections to the experimental data due to the detector's dead time effect have been applied. Moreover, to reduce the counting uncertainty, the number of performed counts

and the acquisition time used in each measurement are considered to be 50 times and 120s, respectively.

Form a simulation point of view, the statistical uncertainty of the results based on the MCNPX code has been considered. It has been shown that all of the 10 statistical checks for the tally fluctuations have been passed. To be more precise, all of the results have a fewer relative

error of 2.0%, fewer Variance Of Variance (VOV) of 0.0001, near-constant large value and random behavior of FOM and finally constant slope value of 10.0.

To investigate the X-ray shielding ratio of the nanostructured and bulk-structured thin lead films versus thickness variations, the following results (figure 7) regarding the experimental and theoretical calculations are illustrated.

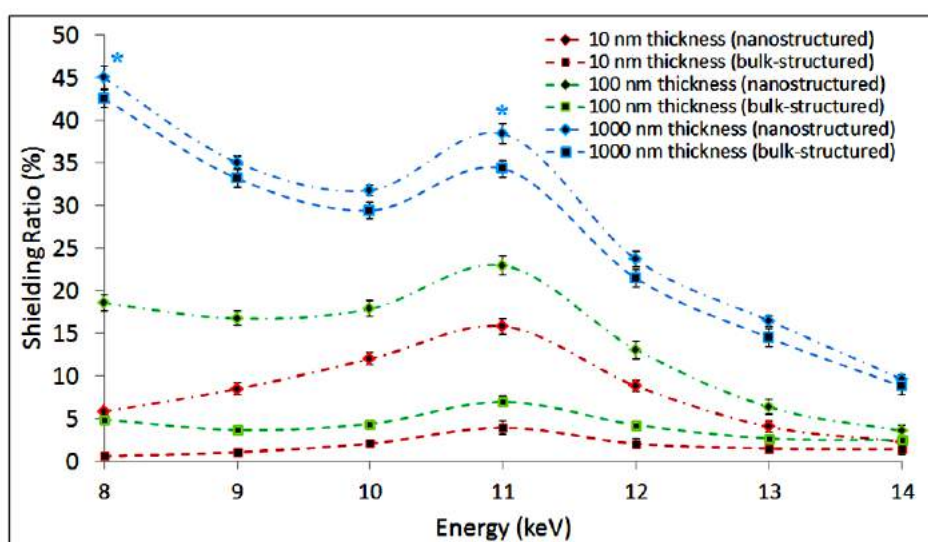
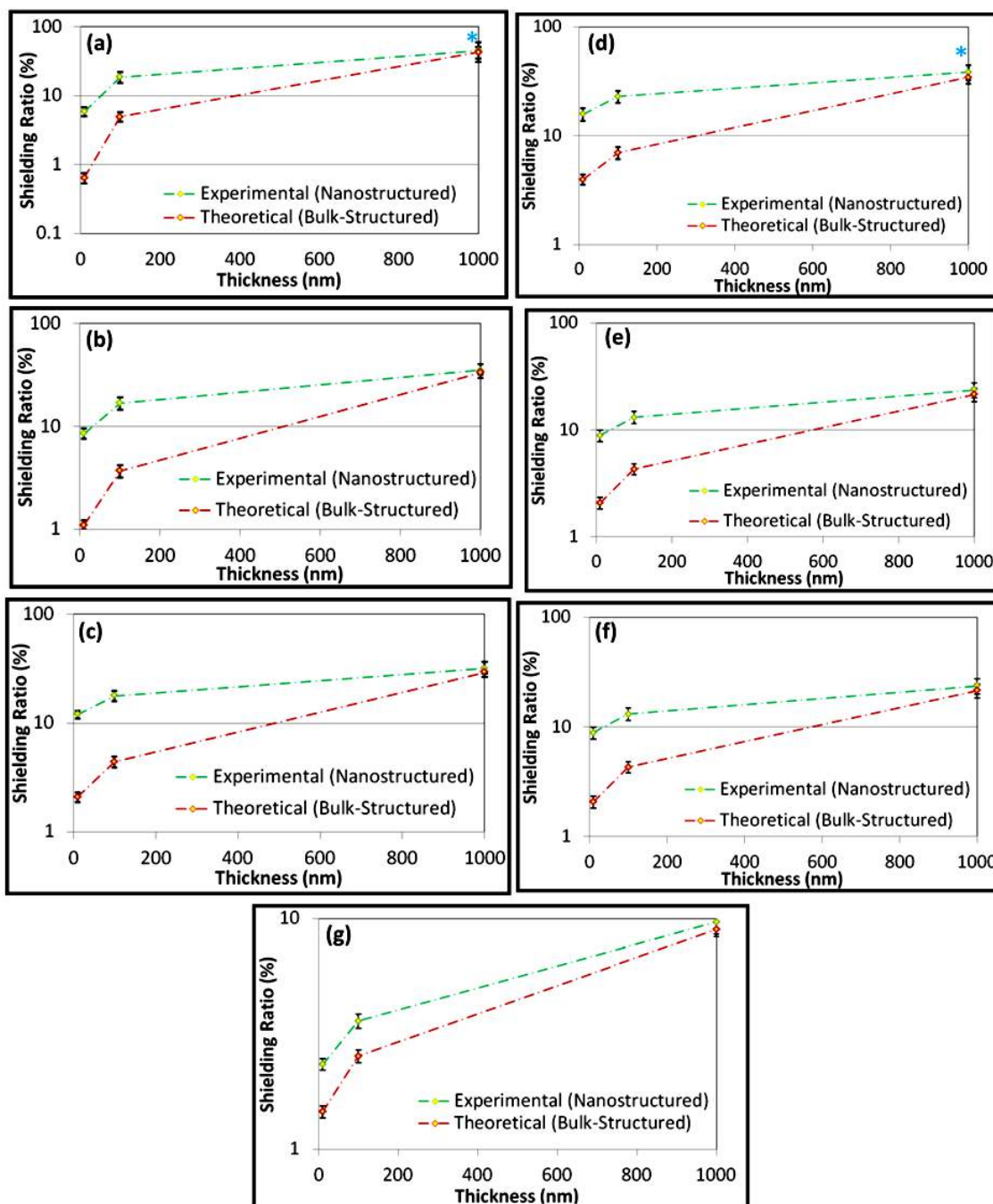


Figure 6. Shielding ratio comparison between the experimental and theoretical results for different X-ray energies.



**Figure 7.** Shielding ratio of the deposited lead thin films for 8 keV (a), 9 keV (b), 10 keV (c), 11 keV (d), 12 keV (e), 13 keV (f) and 14 keV (g) X-ray energy.

## DISCUSSION

Figure 6 shows that the shielding ratio of the nanostructured thin lead films is significantly higher than those calculated from the bulk-structured for all lead thicknesses and impinging X-ray energy ranges. This result is

almost the same as the result already obtained by other researchers with different materials (4-9). More precisely, in the case of  $\text{WO}_3$ , Noor Azman *et al.* (4 and 5), confirmed the superior attenuation ability of nano-sized  $\text{WO}_3$ -epoxy composites than they predicted. A similar result also was observed by Mesbahi and Ghiasi (6) and

*Int. J. Radiat. Res., Vol. 18 No. 2, April 2020*

they showed a higher photon attenuation coefficient of nano-sized particles of  $\text{PbO}_2$ ,  $\text{Fe}_2\text{O}_3$ ,  $\text{WO}_3$  and  $\text{H}_4\text{B}$  (Boronium) compared to the larger particle sizes. In the case of  $\text{CuO}$ , Kunzel and Okuno <sup>(7)</sup> also found that the X-ray absorption is higher for the nanostructured samples compared to the microstructured samples for all  $\text{CuO}$  concentrations. By taking into account of these works and the results presented in figure 7 for the lead material, one can reasonably argue that the results herein are consistent with those obtained by the other researchers. In fact, it has been shown that the shielding property of materials is increased only by nanosizing the particles. This superiority of the nanostructures; however, is more evident for the small thicknesses. In fact, the results indicate that the difference of the determined shielding ratio between the two structures decreases with increasing the lead thickness in almost each incident X-ray energy. The main reason for these observations can be explained by considering figure 3, in which the agglomeration of the nanoparticles was raised by increasing the thickness considerably. On this basis, the maximization of the surface to volume ratio, which is normally occurred by nanosizing the particles, will be decreased. This leads to the reduction of surface electron density and, eventually, reduction of the reaction rate of electrons with incident photons. This part of the results did not well investigate by other researchers even for other materials. This is due to the fact that the nano particles usually were distributed in a matrix as a filler by different concentrations, and accordingly, the higher thicknesses did not cause the higher agglomeration. On this basis, a new finding of the effect of agglomeration on the shielding properties of the materials is revealed. According to figures 3 and 6, the agglomeration of the nano particles causes a reduction in the discrepancy of the shielding properties between the nanostructured and bulk-structured samples. This means that the shielding properties of the materials increase by increasing the thickness of the shield in the case of both nanostructured and bulk-structured samples, however, the superiority of the

nanostructured thin lead films is reduced due to the agglomeration effect. This new aspect of the shielding properties of the nano materials has not been investigated previously mostly due to the fact that in all the previous studies the nano particles only have been employed as the additive component. For instance, Özdemir *et al.* <sup>(9)</sup> showed that the photon attenuation of EPDM increases consistently by increasing the thickness of the samples that contain  $\text{PbO}$  nanoparticles as the additive component. Similar results also were obtained in the case of other additive materials including  $\text{PbO}_2$ ,  $\text{PbO}$ , and  $\text{PbTiO}_3$  <sup>(13)</sup>,  $\text{WO}_3$  <sup>(4,5)</sup>,  $\text{Fe}_2\text{O}_3$  <sup>(6)</sup> and  $\text{CuO}$  <sup>(7)</sup>. However, according to our results, it can be revealed that not only the thickness of the shield but also the agglomeration effect of the nano particles is of great importance in X-ray shielding.

From a different point of view, figure 6 also shows that the difference between the nanostructured and bulk-structured thin lead films diminished by raising the X-ray energy in all sample thicknesses and was finally eliminated at 14 keV. These results are consistent with those obtained by previous works which showed a higher attenuation ability of the nano-sized particles than those of the micro-sized particles in low X-ray energy ranges (Noor Azman *et al.* for the energy range investigation of 10-40 keV <sup>(4)</sup> and also 22-120 keV <sup>(5)</sup> using  $\text{WO}_3$  nano particles, and also for the energy range investigation of 40-100 keV using W, Au and Pb nano particles <sup>(11)</sup>, Mesbahi and Ghiasi for the energy range investigation of 142-1250 keV using  $\text{PbO}_2$ ,  $\text{Fe}_2\text{O}_3$ ,  $\text{WO}_3$  and  $\text{H}_4\text{B}$  nano particles <sup>(6)</sup>, Kunzel and Okuno for the energy range investigation of 25-120 keV using  $\text{CuO}$  nano particles <sup>(7)</sup>, and Tekin *et al.* for the energy range investigation of 0.142–1.33 MeV using  $\text{WO}_3$  and  $\text{Bi}_2\text{O}_3$  nano particles <sup>(8)</sup>. This is due to the fact that the photon interaction probability decreases by increasing the incident photon energy, therefore, the superiority of the nanostructured samples which is due to the very high interactions of the incident photons with the electrons in the thin films are affected and eventually reduced. This leads to the almost similar number of interactions between the



incident photons and electrons in the thin lead films, and consequently, similar shielding properties of the nanostructured and bulk-structured samples in the same high X-ray energies. Another important point is that the nano and bulk-structured samples both have a sharp value around 11 keV in all lead thicknesses. This may be due to the existence of an electron shell in the lead material around 11 keV which was also observed previously by EDS spectra in figure 1. In fact, because, in this study, the X-ray energy range variations are 8 keV to 14 keV, the dominant interaction is, therefore, photoelectric, and consequently, the existence of an electron shell around 11 keV can lead to increasing the interaction probability and shielding ratio. This result can be very important from the point of view of shielding properties of nanostructured materials around the electron shells energy ranges. This observation is important also, because, in almost all of the previous works, the shielding properties of the nano materials were mostly investigated in much higher energy ranges than those considered in this work, and, accordingly, the behavior of nanostructured materials in low X-ray energies was unclear <sup>(5-9)</sup>. For instance, Noor Azman *et al.* studied the energy range of 22-120 keV <sup>(5)</sup> and also 40-100 keV <sup>(11)</sup>, Mesbahi and Ghiasi considered the energy range of 142-1250 keV <sup>(6)</sup>, and Tekin *et al.* investigated the energy range of 0.142-1.33 MeV <sup>(8)</sup>. Among all of the previous studies, a recent work on WO<sub>3</sub>-filled epoxy composites <sup>(4)</sup> considered the energy range investigation of 10-40 keV. According to their results, it was shown that the X-ray transmission is lower around 10 keV compared to higher X-ray energies. Although this observation did not explain and investigate in their work, it can be considered and explained according to our results. We have found that tungsten has an electron shell around 10 keV <sup>(29)</sup> and this is the reason for observation a higher X-ray attenuation in their work at 10 keV X-ray energy. Based on these results, it can reasonably be argued that the results of our work (for the Lead material) is consistent with those obtained by Noor Azman *et al.* <sup>(4)</sup> (for WO<sub>3</sub>).

Another important result that can be

obtained from figure 6 is that the nanostructured sample with the thickness of 10 nm has higher shielding properties compared to the bulk-structured sample with the thickness of 100 nm. This is an important observation that shows the effectiveness of the nanostructured thin lead films compared to the bulk-structured films even at different thicknesses. In other words, the low thickness of the nanostructured thin lead films can even be more effective than ten times more thick bulk-structured samples at the same X-ray energies.

In figure 6, also, Standard Deviation (SD) of the experimental measurements and theoretical calculations are presented. As can be observed, the theoretical SD is almost the same for different measurements. This is due to the fact that the SD in the theoretical calculations using the MCNPX code always kept below a certain value and if it exceeded, the calculations were again performed with more execution time and number of particle histories. Despite the theoretical calculations, SD is different regarding the number of recorded radiations in the detector and the number of repetition of the measurements.

The first thing that will be cleared from figure 7 is that, the shielding ratio for both nanostructured and bulk-structured thin films increases with increasing the thickness of lead layers in all incident X-ray energies due to the raising the fraction of deposition X-ray energies by growing the thickness of the shield. According to the results, it is also possible to observe that, the form of variations is in the form of Eq. (3) for both the aforementioned structures. However, the shielding ratio of the nanostructured films in all X-ray energies is significantly higher than of bulk-structured films, particularly for both samples of 10 and 100 nm thicknesses. In the case of 1000 nm lead thickness; however, the measured data almost reached to each other. Based on this argument, it may be inferred that by increasing the lead thickness, the difference between the nanostructured and bulk-structured lead thin films tends to be diminished. The most obvious explanation for this observation might be due to the agglomeration phenomenon. In fact, as is

shown in figure 3 and explained previously, the agglomeration of the deposited lead thin films increases with increasing the shield thickness remarkably. So, the surface electron density which was the main reason for the superiority of the nanostructured over the bulk-structured thin films will decrease. This leads to the reduction of the interaction probability between the incident photons and the lead electrons and consequently leads to the reduction of difference in the results. In figure 7, additionally, SD of the experimental measurements and theoretical calculations are shown. Similar to figure 6, SDs of the theoretical calculations are almost the same as each others. However, in the case of experimental measurements, the number of recorded radiations in the detector and the number of repetition of the measurements are the main reasons for the discrepancy between the obtained results. From the point of view of making a comparison, as it is observable in figures 6 and 7, the SDs in 8 keV and 11 keV for the 1000 nm thickness (with the blue sign of \* in figures 6 and 7) have the most discrepancy not only between experimental measurements but also between the experimental measurements and theoretical calculations. This is due to the fact that the shielding ratio is higher in these two energies. The higher shielding ratio leads to the lower recorded signals in the detector and eventually the higher SDs in the experimental measurements. When it compares to the theoretical calculations (which have almost the same SDs as explained previously), these discrepancies also are again observable at these two energies.

Regarding the above discussion, it can be concluded that, for low energy X-ray s (8-14 keV), the nanostructured thin lead films attenuate photons more compared to the bulk-structured films with the same thicknesses. However, the discrepancy disappears as film thickness increases to 1000 nm or the X-ray energy reaches 14 keV.

## CONCLUSION

In this study, investigation of the X-ray

shielding properties of bulk and nanostructured thin lead films was performed by means of Monte-Carlo calculations and experimental measurements. The results revealed that, for low energy X-ray s, the nanostructured thin lead films attenuate more than bulk-structured samples; however, the difference disappears as film thickness increases to 1000 nm or the X-ray energy reaches 14 keV.

**Conflicts of interest:** Declared none.

## REFERENCES

1. Knoll GF (2000) Radiation detection and measurement. John Wiley and Sons, Inc. New York.
2. Meyerhof WE (1967) Elements of nuclear physics. McGraw-Hill, New York.
3. Johns HE and Cunningham JR (1983) The physics of radiology. Charles C Thomas, Illinois.
4. Noor Azman NZ, Siddiqui SA, Low IM (2013) Characterisation of micro-sized and nano-sized tungsten oxide-epoxy composites for radiation shielding of diagnostic X-rays. *Mat Sci Eng C*, **33**: 4952-4957.
5. Noor Azman NZ, Siddiqui SA, Hart R Low IM (2013) Effect of particle size, filler loadings and X-ray tube voltage on the transmitted X-ray transmission in tungsten oxide epoxy composites *Appl Radiat Isot*, **71**: 62-67.
6. Mesbahi A and Ghiasi H (2018) Shielding properties of the ordinary concrete loaded with micro- and nano-particles against neutron and gamma radiations. *Appl Radiat Isot*, **136**: 27-31.
7. Kunzel R and Okuno E (2012) Effects of the particle sizes and concentrations on the X-ray absorption by CuO compounds. *Appl Radiat Isot*, **70**: 781-784.
8. Tekin HO, Sayyed MI, Issa SAM (2018) Gamma radiation shielding properties of the hematite-serpentine concrete blended with WO<sub>3</sub> and Bi<sub>2</sub>O<sub>3</sub> micro and nano particles using MCNPX code. *Radiat Phys Chem*, **150**: 95-100.
9. Özdemir T, Güngör A, Akbay IK, Uzun H, Babuçcuoglu Y (2018) Nano lead oxide and epdm composite for development of polymer based radiation shielding material: Gamma irradiation and attenuation tests. *Radiat Phys Chem*, **144**: 248-255.
10. Vagheian M, Saramad S, Rezaei-Ochbelagh D, Sardari D (2017) On an experimental study of the electron generation property of thin gold films. *J Chem*, **6**: 84-92.
11. Noor Azman NZ, Siddiqui SA, Ionescu MR Low IM (2012) Synthesis and characterisation of ion-implanted epoxy composites for X-ray shielding. *Nucl Instrum Methods Phys Res Sec B*, **287**: 120-123.
12. Chilton AB, Shultis JK, Faw RE (1984) Principles of radiation

- shielding. Prentice-Hall, Inc, Englewood Cliffs.
13. Hassan HE, Badran HM, Aydarous A, Sharshar T (2015) Studying the effect of nano lead compounds additives on the concrete shielding properties for  $\gamma$ -rays. *Nucl Instr Meth Phys Res B*, **360**: 81-89.
14. Alwaeli M (2017) Investigation of gamma radiation shielding and compressive strength properties of concrete containing scale and granulated lead-zinc slag wastes. *J Clean Prod*, **166**: 157-162.
15. Zhang X, Yang M, Zhang X, Wu H, Guo S, Wang Y (2017) Polymer-Composite materials for radiation protection. *Compos Sci Technol*, **150**: 16-23.
16. Mondala S, Gangulya S, Dasb P, Bhawala P, Dasa TK, Ravindrena R, Ghosha S, Dasa NCh (2017) Effect of thermal-air ageing treatment on mechanical properties and electromagnetic interference shielding effectiveness of low-cost nano-structured carbon filled chlorinated polyethylene. *Mater Sci Eng B*, **225**: 140-149.
17. La LBT, Leong Y, Leatherday C, Au PI, Haywarda KJ, Zhang L (2016) X-ray protection, surface chemistry and rheology of ball-milled submicron Gd<sub>2</sub>O<sub>3</sub> aqueous suspension. *Colloids Surf A*, **501**: 75-82.
18. Rezaei-Ochbelagh D and Azimkhani S (2012) Investigation of gamma-ray shielding properties of concrete containing different percentages of lead. *Appl Radiat Isot*, **70**: 2282-2286.
19. Kim J, Seo D, Lee BC, Seo YS, Miller WH (2014) Nano- W dispersed gamma radiation shielding materials. *Adv Eng Mater*, **16**: 1083-1089.
20. Botelho MZ, Kunzel R, Okuno E, Levenhagen RS, Basegio T, Bergmann CP (2011) X-ray transmission through nanostructured and microstructured CuO materials. *Appl Radiat Isot*, **69**: 527-530.
21. Adliene D, Cibulskaitė I, Meskinis S (2010) Low energy X-ray radiation impact on coated Si constructions. *Radiat Phys Chem*, **79**: 1031-1038.
22. MCNPX user's manual version 2.6.0 (2008). Los Alamos National Laboratory.
23. Briesmeister JF (1986) MCNP: a general Monte Carlo code for neutron and photon transport version 3A. Los Alamos National Laboratory.
24. Shultis JK and Faw RE (2011) An MCNP primer. Kansas State University.
25. Kiedrowski BC and Solomon CJ (2011) Statistical assessment of numerous Monte Carlo tallies. *International Conference on Mathematics and Computational Methods*, Brazil, ISBN 978-85-63688-00-2.
26. Mahan JE (2000) Physical vapor deposition of thin films. John Wiley & Sons, New York, ISBN 0-471-33001-9.
27. Vagheian M, Rezaei Ochbelagh D, Gharib M (2016) An improved box-scheme finite difference method based on the relative event probabilities. *Prog Nucl Energy*, **88**: 33-42.
28. Vagheian M, Vosoughi N, Gharib M (2016) Enhanced finite difference scheme for the neutron diffusion equation using the importance function. *Ann Nucl Energy*, **96**: 412-421.
29. Bearden JA and Burr AF (1967) Reevaluation of X-ray atomic energy levels. *Rev Mod Phys*, **39**: 125.



## Investigation of the production of the Auger electron emitter $^{135}\text{La}$ using medical cyclotrons

*Acta Physica Polonica B 51 (2020) 861-866.*

**Authors:** J. Jastrzębski, ..., M.Vagheian

**Abstract:** In this work,  $^{135}\text{La}$  production investigation from a  $^{\text{nat}}\text{BaCO}_3$  target irradiation was performed using a 16 MeV proton beam generated in a PETtrace cyclotron at the Heavy Ion Laboratory of the University of Warsaw. The Monte-Carlo production estimation of  $^{135}\text{La}$  through the  $^{\text{nat}}\text{Ba}(p,x)^{135}\text{La}$  reaction using the MCNP code showed that the theoretical results are in good agreement with the experimental measurements. For the MCNP modeling, the proton beam energy and intensity derived for the PETtrace cyclotron were considered to impinge to a natural  $^{\text{nat}}\text{BaCO}_3$  target. The geometry of the target and isotope abundance was calculated and considered as the input for modeling. The reaction rate estimation was then performed regarding the  $^{\text{nat}}\text{Ba}(p,x)^{135}\text{La}$  reaction for a variety of target designs and parameters. Facilitating comparison between the experimental and theoretical results showed that the production yield estimations are in good agreement. The developed MCNP model for the  $^{135}\text{La}$  production could be used in different target quantities, beam energy, and power at the Heavy Ion Laboratory.

**Contributions:** I performed the Monte-Carlo simulation and modeling using the MCNP code. I also carried out the analysis of the obtained results and contributed to the writing of the corresponding theoretical parts of the manuscript.

**License:** This work is licensed under a Creative Commons Attribution 4.0 International (CC BY 4.0). To see the license go to <https://www.actaphys.uj.edu.pl/index.html>

# INVESTIGATION OF THE PRODUCTION OF THE AUGER ELECTRON EMITTER $^{135}\text{La}$ USING MEDICAL CYCLOTRONS\*

J. JASTRZĘBSKI<sup>a,†</sup>, N. ZANDI<sup>a</sup>, J. CHOIŃSKI<sup>a</sup>, M. SITARZ<sup>a,b</sup>  
A. STOLARZ<sup>a</sup>, A. TRZCIŃSKA<sup>a</sup>, M. VAGHEIAN<sup>c</sup>

<sup>a</sup>Heavy Ion Laboratory, University of Warsaw, 02-093 Warszawa, Poland

<sup>b</sup>Faculty of Physics, University of Warsaw, 02-093 Warszawa, Poland

<sup>c</sup>Department of Energy Engineering and Physics  
Amirkabir University of Technology, Tehran, Iran

*(Received January 8, 2020)*

Possible reactions leading to the production of  $^{135}\text{La}$  are discussed in this study and corresponding theoretical yields calculated using Monte-Carlo (MCNPX) code are presented. The pilot  $^{135}\text{La}$  production was performed employing the 16 MeV protons provided by a PETtrace cyclotron and a  $^{\text{nat}}\text{BaCO}_3$  target.

DOI:10.5506/APhysPolB.51.861

## 1. Introduction

The Auger electron therapy is one of the most promising and important cancer therapies due to delivery of radiation dose only to individual cells [1]. Its effectiveness has been recently summarized in Refs. [2–4]. The Auger electron emitters cause much less off-target effects than  $\beta$  emitters [4].  $^{135}\text{La}$  with the half-life of 19.5 h and almost 100% decay to the stable  $^{135}\text{Ba}$  [1] by electron capture is one of the important candidates for this kind of therapy. It also emits only low-intensity gamma rays (predominantly 480.5 keV, 1.5%) which contribute to the patient dose at a negligible level.

$^{135}\text{La}$  can be produced using proton or deuteron bombardment of barium via  $^{135}\text{Ba}(p, n)^{135}\text{La}$ ,  $^{136}\text{Ba}(p, 2n)^{135}\text{La}$ ,  $^{134}\text{Ba}(d, n)^{135}\text{La}$ ,  $^{135}\text{Ba}(d, 2n)^{135}\text{La}$  reactions and alpha bombardment of cesium  $^{133}\text{Cs}(\alpha, 2n)^{135}\text{La}$ .

---

\* Presented at the XXXVI Mazurian Lakes Conference on Physics, Piaski, Poland, September 1–7, 2019.

† Deceased.

In 2015 and 2018, respectively, Mansel [5] and Fonslet [1] reported production of  $^{135}\text{La}$  using protons bombarding a barium target. Nevertheless, to date, only few research works have been performed to study  $^{135}\text{La}$  production routes. The cross sections are reported only for:  $^{\text{nat}}\text{Ba}(d, x)$ ,  $^{\text{nat}}\text{Ba}(p, x)$ ,  $^{\text{nat}}\text{La}(p, x)$  and  $^{133}\text{Cs}(\alpha, 2n)$  [2–10]. In this work, some possible routes of  $^{135}\text{La}$  radionuclide production have been analysed in terms of production yield regarding the small medical cyclotron facilities and cost of targets needed for the discussed reaction. The production yield was calculated using the Monte Carlo N-Particle eXtended (MCNPX) code [11, 12].

## 2. Materials and methods

### 2.1. Theoretical calculations of TTY

The assessment of the applicability of a  $^{135}\text{La}$  production route was mainly based on evaluation of Thick Target Yield (TTY) describing number of the produced radionuclides (activity) per unit of time and current of the applied beam. Theoretical TTY for production of the radionuclide of interest can be calculated using the following equation [13, 14]:

$$\text{TTY} = \frac{HN_A\lambda}{MZ e} \int_{E_1}^{E_2} \frac{\sigma(E)}{dE/d(x\rho)} dE, \quad (1)$$

where TTY is thick target production yield [Bq/Ah],  $N_A$  is the Avogadro number [1/mol],  $H$  is the isotope abundance of the target nuclide [%],  $M$  is the molar mass of the target element [g/mol],  $\sigma(E)$  is the cross section at energy  $E$  [ $\text{cm}^2$ ],  $dE/d(x\rho)$  is the stopping power [ $\text{MeV}/(\text{mg}/\text{cm}^2)$ ],  $\lambda$  is the decay constant of the product [1/h],  $E_1 - E_2$  is the energy deposited in the target material [MeV],  $Z$  is the atomic number of the projectile, and  $e$  is the elementary charge [As].

In our calculations, we used the cross sections from the TENDL-2017 nuclear data library based on the TALYS code [15]. The stopping powers used in the calculation were derived from the SRIM 2013 code (Stopping and Range of Ions in Matter) [16].

The activity produced at the given irradiation time or the irradiation time needed to produce the required activity can be calculated from the following relation (considering decays of the produced radionuclide):

$$A_{\text{EOB}} = \text{TTY} I \frac{1}{\lambda} \left( 1 - e^{-\lambda t_{\text{irr}}} \right), \quad (2)$$

where  $A_{\text{EOB}}$  — activity at the End Of Bombardment,  $I$  — beam current,  $\lambda$  — decay constant,  $t_{\text{irr}}$  — irradiation time.

2.2. TTY predictions for  $^{135}\text{La}$  production

$^{135}\text{Ba}(p, n)^{135}\text{La}$  and  $^{136}\text{Ba}(p, 2n)^{135}\text{La}$  reactions

The optimal proton energy range for the  $^{135}\text{Ba}(p, n)^{135}\text{La}$  reaction is of 16 to 5 MeV [15]. Since the natural abundance of  $^{135}\text{Ba}$  is relatively low (6.5%) (Table I), a highly enriched barium target would be necessary for efficient production of  $^{135}\text{La}$  in this reaction. The best energy range for the  $^{136}\text{Ba}(p, 2n)^{135}\text{La}$  reaction is between 35 to 12 MeV, however, it is worth mentioning that for the energy corresponding to the best range of the first reaction, the  $^{135}\text{La}$  production yield is of comparable level. In other words, using natural barium both  $^{135}\text{La}$  production channels have to be considered. The theoretical calculation shows the production yield at 16 to 5 MeV of proton energy range for the 100% enriched isotopes,  $^{135}\text{Ba}$  and  $^{136}\text{Ba}$  equals to 165.48 MBq/ $\mu\text{Ah}$  and 151 MBq/ $\mu\text{Ah}$ , respectively and 16 MBq/ $\mu\text{Ah}$  for a natural Ba target (Table II).

TABLE I

Natural abundance of barium isotopes.

Isotope	$^{132}\text{Ba}$	$^{134}\text{Ba}$	$^{135}\text{Ba}$	$^{136}\text{Ba}$	$^{137}\text{Ba}$	$^{138}\text{Ba}$
Abundance [%]	0.1	2.4	6.5	7.8	11.2	71.7

TABLE II

$^{135}\text{La}$  theoretical production yield in various reactions.

Reaction	Target yield [MBq/ $\mu\text{Ah}$ ]		Energy range [MeV]
	100% enrichment	Natural target	
$^{135}\text{Ba}(p, n)^{135}\text{La}$	165.48	16*	16 $\rightarrow$ 5
$^{136}\text{Ba}(p, 2n)^{135}\text{La}$	151.20		16 $\rightarrow$ 12
$^{135}\text{Ba}(d, 2n)^{135}\text{La}$	570.45		35 $\rightarrow$ 8
$^{134}\text{Ba}(d, n)^{135}\text{La}$	33.27		14 $\rightarrow$ 8
$^{133}\text{Cs}(\alpha, 2n)^{135}\text{La}$	38.28		40 $\rightarrow$ 16

\*This TTY value was calculated for 16  $\rightarrow$  5 MeV proton energy range, taking into account the contribution of the  $^{135}\text{Ba}(p, n)^{135}\text{La}$  and  $^{136}\text{Ba}(p, 2n)^{135}\text{La}$  reactions.

Taking into account composition of the natural barium, it makes the  $^{135}\text{La}$  production efficiency relatively high and considering the energy of protons delivered by cyclotrons such as PETtrace, C18/9 or Eclipse<sup>TM</sup>RD, this production route seems to be the most effective for the  $^{135}\text{La}$  production in PET centres.

### **$^{135}\text{Ba}(d, 2n)^{135}\text{La}$ reaction**

The efficient energy range for the  $^{135}\text{La}$  production in  $^{135}\text{Ba}(d, 2n)^{135}\text{La}$  reaction is between 35 to 8 MeV. The theoretical calculation shows that the production yield in this energy range is 570.45 MBq/ $\mu\text{Ah}$  (Table II). However, it requires high-energy deuterons that are not provided by the medical cyclotrons most commonly installed in the PET centres.

### **$^{134}\text{Ba}(d, n)^{135}\text{La}$ reaction**

The production energy range for the  $^{134}\text{Ba}(d, n)^{135}\text{La}$  reaction is of 14 to 8 MeV [15]. The theoretical calculation shows that the production yield in the mentioned energy range equals 33.27 MBq/ $\mu\text{Ah}$  (Table II). Due to the limited production efficiency and the very low abundance of  $^{134}\text{Ba}$  in natural barium (2.4%), which would require the use of expensive enriched target material, the reaction cannot be considered as a good candidate for the efficient production of  $^{135}\text{La}$ .

### **$^{133}\text{Cs}(\alpha, 2n)^{135}\text{La}$ reaction**

Regarding the best energy range of  $^{133}\text{Cs}(\alpha, 2n)^{135}\text{La}$  production route (40–16 MeV), the calculation shows that the production yield equals 38.28 MBq/ $\mu\text{Ah}$  (Table II). Taking into account that the yield is very low compared to other possible production routes, this reaction cannot be considered as a reasonable candidate.

## *2.3. Pilot production of $^{135}\text{La}$ using PETtrace cyclotron*

### **2.3.1. Proton beam energy and beam current measurements**

The verification of the experimental results requires measurements of the proton energy and the current of extracted beam. This is needed as well to optimize a target thickness and to reduce the radiation dose originating from the isotopes produced inside reactions [17].

Using the method proposed by Gagnon *et al.* [17], we verified the proton energy to be  $15.98 \pm 0.03$  MeV. The beam current was measured by irradiating the copper and titanium foils of the same thickness (11  $\mu\text{m}$ ) and evaluating the activity of each radionuclide ( $^{62}\text{Zn}$ ,  $^{65}\text{Zn}$  and  $^{48}\text{V}$ ) produced respectively in Cu and Ti [18]. The obtained average beam current was  $9.41 \pm 1.85$   $\mu\text{A}$  which we found consistent with Faraday Cup measurements ( $10.2 \pm 0.1$   $\mu\text{A}$ ).

### **2.3.2. Target and irradiation condition**

Considering the above TTY calculations and energy of protons delivered by PETtrace installed at HIL UW, the production of the  $^{135}\text{La}$  via the  $^{\text{nat}}\text{Ba}(p, x)^{135}\text{La}$  reaction was tested. Natural barium carbonate target ( $\text{BaCO}_3$ ) with thickness of 427 mg/ $\text{cm}^2$  prepared as a pellet [19] was

bombarded for 10 minutes at the PETtrace cyclotron solid state target station [20] with a proton beam of 15.7 MeV energy and 9.4  $\mu\text{A}$  intensity. The foils of Cu (11  $\mu\text{m}$ ) and Ti (11  $\mu\text{m}$ ) were placed in front of the barium carbonate pellet for off-line beam current verification. Target activity after irradiation was measured with a HPGe detector. Moreover, due to the fact that natural barium is composed of 6 stable isotopes (Table I), the co-produced impurities were also investigated.

3. Results and discussion

The activity of  $^{135}\text{La}$  produced in our pilot irradiation was equal to 9.57 MBq at EOB what corresponds to about 6 MBq/ $\mu\text{Ah}$  of TTY (Fig. 1, left panel). The activities of coproduced impurities (Fig. 1, right panel) namely  $^{132}\text{La}$  and  $^{132}\text{Cs}$  were measured as 0.43 MBq and 0.83 MBq, respectively (Table III).

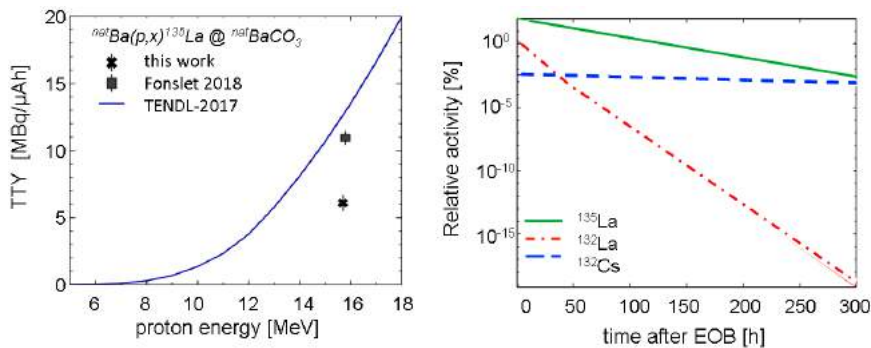


Fig. 1. Thick target yield for  $^{\text{nat}}\text{Ba}(p,x)^{135}\text{La}$  reaction and measured evolution of  $^{135}\text{La}$  activity relative to the activity of coproduced impurities.

TABLE III

Activity of  $^{135}\text{La}$  and impurities produced in natural Ba target.

Isotope	Half-life	Activity at EOB
$^{135}\text{La}$	19.5 h	$9.57 \pm 0.20$ MBq
$^{132}\text{La}$	4.72 h	$0.43 \pm 0.18$ MBq
$^{132}\text{Cs}$	6.48 d	$0.83 \pm 0.31$ MBq

4. Conclusion

The most important  $^{135}\text{La}$  production routes were considered based on the production yield and natural isotope abundance. The theoretical production yield for each reaction was obtained using the MCNPX code and

the results showed that  ${}^{\text{nat}}\text{Ba}(p, x){}^{135}\text{La}$  reaction represents a reasonable production route considering common facilities of the PET centres. The activity of  ${}^{135}\text{La}$  produced by bombarding a natural barium target with protons of 15.7 MeV (attenuated by Cu and Ti foils) for 10 minutes with the beam current of  $9.4\ \mu\text{A}$  was equal to 9.57 MBq with impurities on the level below 1% at EOB.

Work completed with ENSAR2 (grant agreement No. 654002) support.

## REFERENCES

- [1] J. Fonslet *et al.*, *Phys. Med. Biol.* **63**, 015026 (2018).
- [2] A.L. Kassis, *J. Nucl. Med.* **44**, 1479 (2003).
- [3] F. Buchegger, F. Perillo-Adamer, Y.M. Dupertuis, A.B. Delaloye, *J. Nucl. Med. Mol. Imaging* **33**, 1352 (2006).
- [4] B. Cornelissen, K.A. Vallis, *Curr. Drug Discov. Technol.* **7**, 263 (2010).
- [5] A. Mansel, K. Franke, *Radiochim. Acta* **103**, 759 (2015).
- [6] F. Tarkanyi *et al.*, *Nucl. Instrum. Methods Phys. Res. B* **414**, 18 (2018).
- [7] F. Tarkanyi *et al.*, *Appl. Radiat. Isot.* **68**, 1869 (2010).
- [8] K. Prescher *et al.*, *Nucl. Instrum. Methods Phys. Res. B* **53**, 105 (1991).
- [9] F. Tarkanyi, A. Hermanne, F. Ditroi, S. Takacs, *J. Radioanal. Nucl. Chem.* **312**, 691 (2017).
- [10] N.P.M. Sathik, M. Afzal Ansari, B.P. Singh, R. Prasad, *Pramana* **47**, 401 (1996).
- [11] MCNPX User's manual, version 2.4.0, Los Alamos National Laboratory, New Mexico, 2002.
- [12] A. Infantino, C. Hoeher, *AIP Conf. Proc.* **1845**, 020009 (2017).
- [13] M. Sitarz *et al.*, *Instruments* **3**, 7 (2019).
- [14] M. Sadeghi, N. Zandi, H. Afarideh, *J. Radioanal. Nucl. Chem.* **291**, 731 (2012).
- [15] A.J. Koning, D. Rochman, TENDL-2017: TALYS-based evaluated nuclear data library, Nuclear Research and Consultancy Group (NRG) Petten, The Netherlands, <http://www.talys.eu/tendl-2017>
- [16] J.F. Ziegler, J.P. Biersack, U. Littmark, The code of SRIM — the stopping and range of ions in matter, IBM Research, New York 2006.
- [17] K. Gagnon *et al.*, *Appl. Radiat. Isot.* **69**, 247 (2011).
- [18] A. Hermanne *et al.*, *Nucl. Data Sheets* **148**, 338 (2018).
- [19] A. Stolarz, *J. Radioanal. Nucl. Chem.* **299**, 913 (2014).
- [20] UP RP patent No. P.227402.

## **On an improved box-scheme finite difference method based on the relative event probabilities**

*Progress in Nuclear Energy* 88 (2016) 33-42.

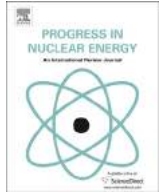
**Authors:** M. Vagheian\*, D.R. Ochbelagh, M. Gharib

**Abstract:** In this paper, a novel objective function as the relative event probabilities relying on the neutron importance function was defined. Then, an adaptive form of the Box-Scheme Finite Difference Method was developed. For the first time in this paper, the relative event probabilities were introduced and showed that they could give a quantitative estimation of the neutron importance function without performing the adjoint numerical calculations. The neutron importance function was able to give a scheme of the importance of regions for higher mesh density resolution. Adaptive mesh distribution can lead to an accurate numerical solution in a reasonable computational time. The simulation was applied for a number of different benchmark problems in different kinds of boundary conditions and parameters. The results confirmed the developed method's capabilities for accurate and fast numerical calculations with a low execution time.

**Contributions:** I proposed the probable use of the relative event probabilities and formulated the mathematical discretization of the governing equations using the Box-Scheme Finite Difference Method. Then, I performed the programming and the elaboration on the obtained results for some available IAEA benchmark problems. At the next step, I wrote the paper as the first author and sent it as the corresponding author. Finally, I revised the paper regarding the reviewer's comments.

**License:** Authors can include their articles in dissertations for non-commercial purposes.





# On an improved box-scheme finite difference method based on the relative event probabilities



Mehran Vagheian\*, Dariush Rezaei Ochbelagh, Morteza Gharib

Amirkabir University of Technology (Tehran Polytechnic), Department of Energy Engineering & Physics, Hafez Avenue, Tehran, Iran

## ARTICLE INFO

### Article history:

Received 4 August 2015  
Received in revised form  
7 November 2015  
Accepted 5 December 2015  
Available online 18 December 2015

### Keywords:

Improved box-scheme finite difference method  
Relative event probability  
Neutron diffusion calculations  
Power iteration method

## ABSTRACT

The accuracy of the neutron diffusion calculations can be significantly affected by changing mesh point positions in the Box-Scheme Finite Difference Method (BSFDM). Accordingly, optimizing mesh point positions with respect to the relative region's importance for the 2-D rectangular geometry, light water reactors are addressed in this paper.

In this study, we present a new algorithm approximation form based on the relative event probabilities (REPs), which can be directly used to evaluate the relative region's importance for optimizing mesh points positions in BSFDM. In accordance with this method, in regions with greater importance, the number of meshes is more than that in regions with less importance. So, the implementation of this method makes an adaptive nonuniform mesh point distribution through the entire reactor core unlike the usual methods. The results are benchmarked against two well-known solutions, namely the TWIGL seed-blanket and the Rod Bundle BWR.

The results all suggest that the proposed method has a better accuracy in all benchmarking cases compared to the usual method for any arbitrary mesh point numbers.

© 2015 Elsevier Ltd. All rights reserved.

## 1. Introduction

Designing a nuclear reactor properly needs to predict some measurable parameters such as neutron flux as well as the effective multiplication factor. These important parameters can be obtained using either the neutron diffusion or transport equations. Although, the neutron diffusion equation is an approximation of the transport equation, its solution can sufficiently be acceptable, accurate and owing to compute a minimum computational cost which is necessary in a practical reactor analysis (Lamarsh, 1965; Akcasu et al., 1971).

There have been various methods to solving the neutron diffusion equations (Vosoughi et al., 2004; Cavdar and Ozgener, 2004; Nakamura, 1977; Singh et al., 2014; Chiba et al., 2001; Bareiss and Antolak, 1981). One of these methods is the Finite Difference Method (FDM), which is worthful because of its simplicity and capability in determining numerical solutions. However, the efficiency of the standard FDM's is not very good (Duderstadt and Hamilton, 1991; Bell and Glasstone, 1970; Hosseini et al., 2015).

The two well-known models of the FDM are the mesh edged and mesh centered. However, it has been shown that the second model, which is called as the Box-Scheme Finite Difference Method (BSFDM), gives almost a more accurate numerical solution than that other one (Argonne Code Center, 1977; Malmir et al., 2011; Shen, 2012).

In 1977, Nakamura has developed the BSFDM to model the neutron diffusion equation for rectangular geometry based on the neutron leakage calculations from each side of a mesh box. Moreover, this method of discretization has been described in the excellent treatise for the hexagonal and triangular geometries (Malmir et al., 2010, 2011).

Mesh point positions in FDM have a great importance in the accuracy of the neutron diffusion calculations (Malmir et al., 2011). Although, in most applications, mesh point positions are preferred to be distributed uniformly throughout the system, it can be mannered in a different way to be distributed through the regions with respect to the corresponding region's importance (Ayyoubzadeh and Vosoughi, 2011). It has been shown that the importance of a region, regardless of its location in a reactor corresponds to the both fission and scattering event probabilities, whereas the capture event cannot play any role due to its incapability of producing any signals in detectors (Duderstadt and

\* Corresponding author. P.O. Box: 15875-4413.  
E-mail address: [mvagheian@aut.ac.ir](mailto:mvagheian@aut.ac.ir) (M. Vagheian).

Hamilton, 1991; Lamarsh, 1965; Bell and Glasstone, 1970).

The main purpose of present study is to introduce a novel algorithm based on REPs to improve the mesh point positions in BSFDM. A part of this, the time-dependent neutron diffusion equations in the presence of the six-group of delayed neutrons as well as the precursor equations is initially introduced. Then, the adaptive matrix spatial discretization form of the mentioned equations in two dimensional rectangular geometries is presented. So, the proposed novel algorithm based on the REPs is developed to distribute the mesh point positions throughout the reactor core. By way of analogy, the static neutron flux with corresponding eigenvalues for the both uniform and adaptive non-uniform mesh point distributions are then calculated using the power iteration method. Finally, for a consistent accuracy comparison between the standard BSFDM and the improved one, the same number of mesh points has been considered and the results are then benchmarked against two well-known different benchmark problems, namely the TWIGL two-dimensional seed-blanket (Christensen, 1985) and the Rod Bundle BWR (Argonne Code Center, 1977).

This paper is organized in six sections: In the second section, the adaptive spatial discretization form of the time-dependent neutron diffusion equations is presented. These equations comprise of six-group delayed neutrons as well as the precursor equations for two dimensional rectangular geometries using the BSFDM. In the section three, the static results of the final matrix form of the aforementioned equations are presented. The proposed algorithm based on the REPs is completely introduced in the section four. Two different examples with the corresponding results are illustrated to show the accuracy and efficiency of the proposed algorithm in the section five. Eventually, the sixth section gives the concluding remarks.

## 2. Mathematical formulation

In this section, the discretization matrix form of the time-dependent multigroup neutron diffusion equations, including six-group delay neutrons as well as the precursor equations are presented. The general forms of these equations are as Eqs. (1)–(3) (Christensen, 1985; Duderstadt and Hamilton, 1991; Akcasu et al., 1971):

$$\begin{aligned} \frac{1}{v_g} \frac{\partial}{\partial t} \phi_g(\vec{r}, t) &= \nabla \cdot D_g(\vec{r}, t) \nabla \phi_g(\vec{r}, t) - \left[ \sum_{ag} (\vec{r}, t) + \sum_{sg} (\vec{r}, t) \right] \phi_g(\vec{r}, t) \\ &+ \sum_{g'=1}^G \left[ \Sigma_{gg'}(\vec{r}, t) + (1 - \beta) \frac{\chi_{pg}}{k_{eff}} \nu \Sigma_{fg'}(\vec{r}, t) \right] \phi_{g'}(\vec{r}, t) \\ &+ \sum_{h=1}^H \lambda_h \chi_{dg}^i C_h(\vec{r}, t) \quad g \\ &= 1, 2, \dots, G \end{aligned} \quad (1)$$

$$\frac{\partial}{\partial t} C_h(\vec{r}, t) = \frac{1}{k_{eff}} \beta_h \sum_{g'=1}^G \nu \Sigma_{fg'}(\vec{r}, t) - \lambda_h C_h(\vec{r}, t) \quad h = 1, 2, \dots, H \quad (2)$$

where,

$$\beta = \sum_{h=1}^H \beta_h \quad (3)$$

Here,  $G$  is the number of neutron energy groups;  $H$  the number of

delayed neutron families and all the other parameters has their usual meaning.

The aforementioned equations are linear partial differential equations which one can transform them into a set of algebraic equations by using different methods (Hosseini and Vosoughi, 2013; Quintero-Leyva, 2014). Among these methods, here, the BSFDM is considered. This method is based on the calculation of the neutron leakage from each side of a mesh box for simulating numerically the neutron diffusion equation. The discrete form of this method has been widely pointed out in the literature (e.g., Clark and Hansen, 1964; Malmir et al., 2010, 2011; Duderstadt and Hamilton, 1991; Gado and Schmidt, 1987; Shen, 2012). However, there has been less attention to the derivation of these equations by considering non equal mesh box dimensions, possibly due to the fact that in the practical nuclear reactor analysis such accuracy of the conventional parameters is not almost required. Here, by using of derived equations in the aforementioned literature and considering various mesh box dimensions, one can rewrite the discretization form of the mentioned equations as follows:

$$\begin{aligned} \frac{V^i}{v_g \times \Delta t} \times (\phi_g^{i,n+1} - \phi_g^{i,n}) &- \sum_{j=1}^4 \frac{2 \times D_g^{i,n} \times D_g^{j,n}}{D_g^{i,n} \times \Delta_j^i + D_g^{j,n} \times \Delta_i^i} \times A^i \times (\phi_g^{j,n} \\ &- \phi_g^{i,n}) + \left( \sum_{ag}^{i,n} + \sum_{sg}^{i,n} \right) \times \phi_g^{i,n} \times V^i \\ &= \sum_{g'=1}^G \left[ \sum_{gg'}^{i,n} + (1 - \beta^i) \times \frac{\chi_{pg}^i}{k_{eff}} \times \nu \sum_{fg'}^{i,n} \right] \times \phi_{g'}^{i,n} \times V^i + \sum_{h=1}^H \lambda_h^i \\ &\times \chi_{dg}^i \times C_h^{i,n} \quad g \\ &= 1, 2, \dots, G \end{aligned} \quad (4)$$

$$\begin{aligned} C_h^{i,n+1} - C_h^{i,n} \times e^{-\lambda_h^i \times \Delta t} &= \frac{\beta_h^i}{k_{eff}} \times \frac{1 - e^{-\lambda_h^i \times \Delta t}}{\lambda_h^i} \sum_{g'=1}^G \nu \Sigma_{fg'}^{i,n} \phi_{g'}^{i,n} \quad h \\ &= 1, 2, \dots, H \end{aligned} \quad (5)$$

Where, superscript  $(i)$  and  $(j)$  denote the  $i$ th mesh box and the four adjacent neighbors  $j=[1,2,\dots,4]$ , respectively. As can be seen from Fig. 1, each of the mesh boxes has two dimensions of  $\Delta x$  and  $\Delta y$ ;

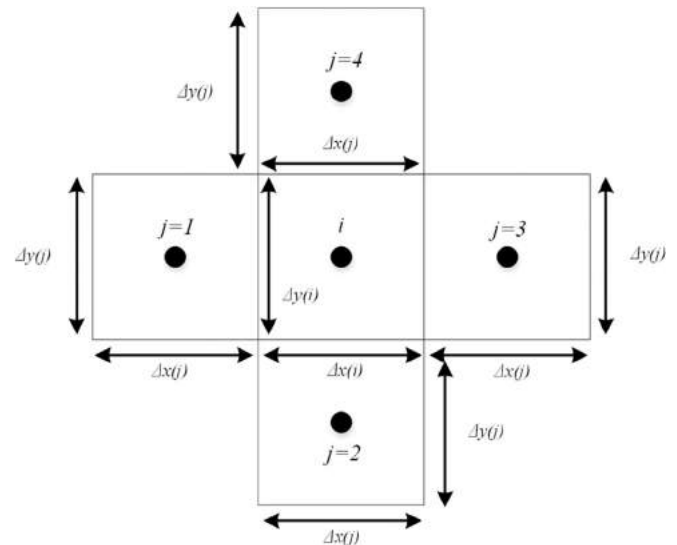


Fig. 1. Structured rectangular geometries with four adjacent neighbors.

where,  $A^i$  and  $V^i$  are the area and volume of the  $i$ th mesh box, respectively. Moreover,  $n$  is the time distinct number and all the other parameters have their usual meaning. It should be noted that based on the BSFDM, all parameters in Eqs. (4) and (5), are averaged over the volume of the mesh boxes.

### 3. Static calculations

In this section, the method of calculating the static fast and thermal neutron fluxes along with the corresponding effective multiplication factor ( $k_{eff}$ ) by considering one delayed neutron family is presented. These calculations are based on the BSFDM which are described in the section 2. The discretized matrix form of the static equations is illustrated below:

$$\begin{bmatrix} \sum_{j=1}^4 \frac{2 \times D_1^i \times D_1^j}{D_1^i \times \Delta^j + D_1^j \times \Delta^i} \times A^i + (\Sigma_{a1}^i + \Sigma_{s,1 \rightarrow 2}^i) \times V^i & 0 & 0 \\ -\Sigma_{s,1 \rightarrow 2}^i \times V^i & \sum_{j=1}^4 \frac{2 \times D_2^i \times D_2^j}{D_2^i \times \Delta^j + D_2^j \times \Delta^i} \times A^i + \Sigma_{a2}^i \times V^i & 0 \\ 0 & 0 & 1 \end{bmatrix} \times \begin{bmatrix} \phi_1^i \\ \phi_2^i \\ C^i \end{bmatrix} + \sum_{j=1}^4 \begin{bmatrix} -\frac{2 \times D_1^i \times D_1^j}{D_1^i \times \Delta^j + D_1^j \times \Delta^i} \times A^i & 0 & 0 \\ 0 & -\frac{2 \times D_2^i \times D_2^j}{D_2^i \times \Delta^j + D_2^j \times \Delta^i} \times A^i & 0 \\ 0 & 0 & 0 \end{bmatrix} \times \begin{bmatrix} \phi_1^j \\ \phi_2^j \\ C^j \end{bmatrix} = \frac{(1 - \beta^i)}{k_{eff}} \begin{bmatrix} \nu \Sigma_{f1}^i \times V^i & \nu \Sigma_{f2}^i \times V^i & \lambda^i \times V^i \\ 0 & 0 & 0 \\ \frac{\beta^i}{(1 - \beta^i) \times \lambda^i} \times \nu \Sigma_{f1}^i \times V^i & \frac{\beta^i}{(1 - \beta^i) \times \lambda^i} \times \nu \Sigma_{f2}^i \times V^i & 0 \end{bmatrix} \times \begin{bmatrix} \phi_1^i \\ \phi_2^i \\ C^i \end{bmatrix} \quad (6)$$

In order to solve Eq. (6) numerically, one can use the power iteration method owing to its high efficiency and simplicity (Duderstadt and Hamilton, 1991; Moghaddam et al., 2014, 2015; Malmir et al., 2010; Hosseini and Vosoughi, 2013). In this method, the aforementioned parameters can be searched for an iterative process. Accordingly, by considering the destruction and production operators as  $\underline{M}$  and  $\underline{F}$ , respectively, Eq. (6) can be written in an operator notation form as follows:

$$\underline{M} \times \underline{\phi} = \frac{1}{k_{eff}} \underline{F} \times \underline{\phi} \quad (7)$$

Then, by considering the term  $S = \underline{F} \times \underline{\phi}$  as the fission source and making an initial estimate of the fission source and the effective multiplication factor as  $S^{(0)}$  and  $k_{eff}^{(0)}$ , respectively, a new  $\underline{\phi}^{(n)}$  in which  $(n)$  indicate the iteration number, can be calculated on each

iteration using the previous values in the following equation:

$$\underline{\phi}^{(n)} = \underline{M}^{-1} \times \frac{1}{k_{eff}^{(n-1)}} S^{(n-1)} \quad (8)$$

where the new fission source ( $S^{(n)}$ ) and the new effective multiplication factor ( $k_{eff}^{(n)}$ ) can be calculated as the following:

$$S^{(n)} = \underline{F} \times \underline{\phi}^{(n)} \quad (9)$$

$$k_{eff}^{(n)} = \frac{S^{(n)}}{S^{(n-1)}} \times k_{eff}^{(n-1)} \quad (10)$$

It is worthful to mention that in the above equations (Eqs.

(7)–(10)), the flux operator,  $\underline{\phi}$ , comprises of neutron fluxes as well as the precursor concentration (see Eq. (6)) which for simplicity, it is shown as this notation. It also should be underlined that, because the aforementioned static formula (Eq. (6)) has been determined based on the time-dependent neutron diffusion equation (Eqs. (4) and (5)), so the precursor concentration has been considered. However, the calculation of the precursor concentration does not need to be included in the static neutron balance equation. The mentioned iterative procedure will be repeated until to obtain the desired convergence criterion of the fast and thermal neutron fluxes along with the corresponding eigenvalues. In this work, 4E-5 and 1E-7 values are considered for the inner and outer convergence criterion, respectively.

### 4. Improved box-scheme Finite Difference Method

In this section, a novel algorithm for improving mesh point positions in BSFDM is presented. This algorithm can effectively

reduce relative errors for neutron flux as well as the corresponding eigenvalues. One of the most important considerations has been taken into account in this algorithm that has the capability to use for any arbitrary mesh point numbers as the usual methods. To this end, based on the proposed algorithm, mesh point numbers should be assigned to each region by considering the region's relative importance values; which, unlike the conventional methods it causes non-uniform distribution of mesh points through the entire reactor core.

As pointed out in the introduction, it has been shown that the importance of a reactor region corresponds to the adjoint flux. The adjoint flux is a dimensionless parameter which is proportional to the detector response to a chain induced by one initial neutron with the same coordinates. Although determining the adjoint flux can be useful for our proposed algorithm, it needs to perform the adjoint neutron diffusion calculations which are almost considered as a costly further calculation (Bell and Glasstone, 1970; Duderstadt and Hamilton, 1991; Akcasu et al., 1971; Lamarsh, 1965; Stripling et al., 2013; Merton et al., 2013; Schunert et al., 2015). In this paper, we overcome this difficulty by an approximation calculation for determining the relative region's importance throughout the reactor. This method is based on the REP which is introduced in the literature (Lamarsh, 1965; Duderstadt and Hamilton, 1991; Bell and Glasstone, 1970).

The relative importance of a particular region can be specified by considering its REPs neglecting its different possible positions in a reactor. An initial neutron should be induced a chain to create a detector response, as is declared before. So, the relative fission event probability is in direct relation to the region's importance, whereas the scattering probability can indirectly take part in a fission chain event by providing the desire neutrons in the other energy groups. In the capture event, though, neutron will be

reaction rate can be calculated through each column ( $l$ ) and row ( $p$ ). It is noteworthy and worthwhile to declare that the terms columns and rows refer to all mesh boxes which are located in  $x$  and  $y$  directions, respectively.

- 2) Determining the total scattering reaction rate for two neutron energy groups for each column and row as bellows:

$$\sum_{l=1}^P \left[ \sum_{s,1 \rightarrow 2}^{l,p} \times \phi_1^{l,p} \right] \times V^{l,p} \quad l = 1, 2, \dots, L \quad (13)$$

$$\sum_{p=1}^L \left[ \sum_{s,1 \rightarrow 2}^{l,p} \times \phi_1^{l,p} \right] \times V^{l,p} \quad p = 1, 2, \dots, P \quad (14)$$

- 3) Calculating the total reaction rate by considering the two neutron energy groups over the entire reactor:

$$\sum_{p=1}^P \sum_{l=1}^L \left[ \sum_{t1}^{l,p} \times \phi_1^{l,p} + \sum_{t2}^{l,p} \times \phi_2^{l,p} \right] \times V^{l,p} \quad (15)$$

As can be seen from this equation, the summation operators are performed through the entire reactor regions including all mesh boxes in all directions. In fact, Eq. (15) gives the total reaction rate for the reactor.

- 4) Determination a weighting factor for each column and rows to assign an appropriate mesh point number for each of them.

Considering Eqs. (11)–(15), the appropriate weighting factor for each column and rows can be resulted in:

$$CWF_l = \frac{\sum_{l,p=1}^P \left[ \sum_{f1}^{l,p} \times \phi_1^{l,p} + \sum_{f2}^{l,p} \times \phi_2^{l,p} \right] \times V^{l,p} + \sum_{l,p=1}^P \left[ \sum_{s,1 \rightarrow 2}^{l,p} \times \phi_1^{l,p} \right] \times V^{l,p}}{\sum_{p=1}^P \sum_{l=1}^L \left[ \sum_{t1}^{l,p} \times \phi_1^{l,p} + \sum_{t2}^{l,p} \times \phi_2^{l,p} \right] \times V^{l,p}} \times \frac{V_{Column_l}}{V_{Reactor}} \quad (16)$$

absorbed without producing any new chain and thus any detector response (Bell and Glasstone, 1970). Consequently, it could be reasonably argued that the only two first aforementioned probabilities are proportional to region's importance. Based on the above discussion, mesh point positions can be distributed throughout the system as follows:

- 1) Dividing the entire reactor core into rows and columns to determine the total fission reaction rate for the two neutron energy groups as the following:

$$\sum_{l,p=1}^P \left[ \sum_{f1}^{l,p} \times \phi_1^{l,p} + \sum_{f2}^{l,p} \times \phi_2^{l,p} \right] \times V^{l,p} \quad l = 1, 2, \dots, L \quad (11)$$

$$\sum_{p,l=1}^L \left[ \sum_{f1}^{l,p} \times \phi_1^{l,p} + \sum_{f2}^{l,p} \times \phi_2^{l,p} \right] \times V^{l,p} \quad p = 1, 2, \dots, P \quad (12)$$

where  $L$  and  $P$  are the total number of the mesh boxes in  $x$  and  $y$  directions, respectively. According to Eqs. (11) and (12), the fission

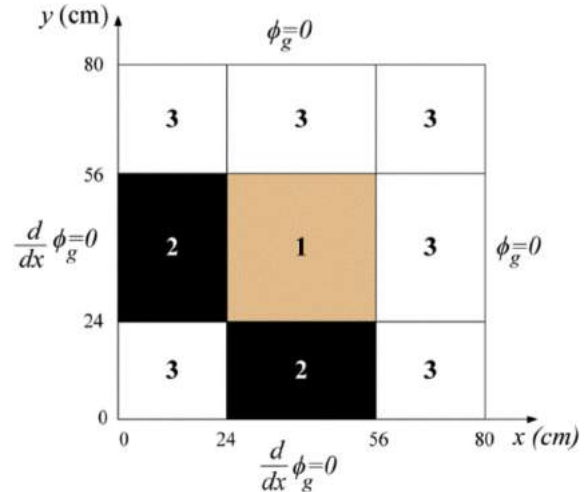


Fig. 2. One-fourth view of the TWIGL problem.

$$RWF_p = \frac{\sum_{l=1}^L \left[ \sum_{f1}^{l,p} \times \phi_1^{l,p} + \sum_{f2}^{l,p} \times \phi_2^{l,p} \right] \times V^{l,p} + \sum_{p:l=1}^L \left[ \sum_{s,1 \rightarrow 2}^{l,p} \times \phi_1^{l,p} \right] \times V^{l,p}}{\sum_{p=1}^P \sum_{l=1}^L \left[ \sum_{t1}^{l,p} \times \phi_1^{l,p} + \sum_{t2}^{l,p} \times \phi_2^{l,p} \right] \times V^{l,p}} \times \frac{V_{Row_p}}{V_{Reactor}} \quad (17)$$

where  $CWF_l$  and  $RWF_p$  represent the Column and Row Weighting Factor for the column ( $l$ ) and row ( $p$ ), respectively. Finally, the appropriate numbers of meshes for the column ( $l$ ),  $n_l$ , and for row ( $p$ ),  $n_p$ , become:

$$\frac{CWF_l}{\sum_l CWF_l} \times L = n_l \quad (18)$$

$$\frac{RWF_p}{\sum_p RWF_p} \times P = n_p \quad (19)$$

So, one can obtain the appropriate mesh point numbers for any arbitrary  $L$  and  $P$  values using the Eqs. (18) and (19), respectively. Note, in order to perform the calculations, at first it is necessary to determine the 2-G neutron fluxes. So, the uniform coarse mesh calculations firstly has to be performed, then by using the proposed algorithm, the non-uniform fine mesh calculations based on the proposed algorithm can be carried out using the power iteration method. Additionally, it should be noted that, in regions of strong absorptions (with no fission events and low scattering) the flux changes significantly so it is required more partitions in those regions to obtain accurate results, however the described weighting factors neglect that.

## 5. Results and benchmarking

To verify the steady-state results of the novel proposed method, two well-known benchmark problems are considered. The first is the TWIGL seed-blanket reactor (Christensen, 1985), and the second is the Rod Bundle BWR (Argonne Code Center, 1977). In the following, the obtained results such as thermal and fast neutron fluxes along with the corresponding effective multiplication factor for both the improved uniform and non-uniform cases are compared with the reference values.

### 5.1. Test case 1

The first case is a two-dimensional model of a 160 cm square unreflected seed-blanket reactor, which is modeled with two neutron energy groups and one-group delayed neutrons (Christensen, 1985). The boundary conditions of this reactor core comprise of zero flux for the external boundaries and perfect

reflective for the symmetry line boundaries. The geometry of this problem is shown in Fig. 2 and the neutronic properties of the materials are given in Tables 1 and 2.

Calculation of the coarse mesh 2-D 2-G neutron diffusion equations by corresponding one-group delayed neutrons has been carried out using Eq. (6). Later on, improving the mesh point positions is done by applying the four-step proposed algorithm. As seen from Figs. 3 and 4, the normalized fast and thermal fluxes are depicted for lattice  $12 \times 12$  for the both uniform, (a), and improved non-uniform, (b), mesh point positions, respectively. Where one can normalize the calculated flux values by multiplying them to the related 2-group power to flux ratios as follows (Malmir et al., 2010):

$$\sum_{i=1}^{N_{fuel}} [K_1(i) \times \phi_1(i) + K_2(i) \times \phi_2(i)] = P_{th} \quad (20)$$

Here,  $P_{th}$  and  $N_{fuel}$  are the total power of the reactor and the number of mesh boxes in the fuel region, respectively. Moreover,  $K_1(i)$  and  $K_2(i)$  are the power to flux ratios in the  $i$ th mesh box for fast and thermal neutron energy groups, respectively. In Table 3 the results of the eigenvalues benchmarking are given in the both mentioned distributions against the reported reference values, which is used more mesh point numbers. The benchmarking is performed by using the relative percent error (RPE) as follows (Hosseini and Vosoughi, 2013):

$$RPE(\%) = \frac{\text{calculated value} - \text{reference value}}{\text{reference value}} \times 100 \quad (21)$$

Moreover, for a consistent comparison between the efficiency of the BSFDM and that of the improved one, the total CPU time (TCT) has been considered using a laptop computer with CPU 1.60 GHz. As it is apparent from Table 3, the TCT of the uniform mesh point distribution is lower than the other one. In the case of being compulsory, an initial calculation of optimized mesh point positions based on the proposed algorithm is needed. More precisely, calculating a number of additional involved unknowns takes a little time. However, as a matter of the reduction computational time, the flux solution from the initial calculations of the proposed algorithm has been used as a starting guess for subsequent calculations. The RPEs of the relative powers are illustrated in Fig. 5. This figure shows that the RPEs which are obtained based on our proposed algorithm are more accurate in comparison with the other ones which are determined by using the usual method.

Although, the enhancement of the mesh point positions for the TWIGL problem has been considered for lattice  $12 \times 12$ , it can be carried out for any arbitrary mesh point numbers. So, in order to check the ability and accuracy of the proposed algorithm, the results of the two more lattices  $6 \times 6$  and  $9 \times 9$  has been studied. In order to compare the results of the eigenvalues, one has to find the

**Table 1**  
The material cross section of each region for TWIGL problem (Christensen, 1985).

Energy group	Material	$D_g$ (cm)	$\Sigma_{ag}$ ( $\text{cm}^{-1}$ )	$\nu\Sigma_{fg}$ ( $\text{cm}^{-1}$ )	$\Sigma_{sg \rightarrow g+1}$ ( $\text{cm}^{-1}$ )
Fast	1	1.4	0.01	0.007	0.01
	2	1.4	0.1	0.007	0.01
	3	1.3	0.008	0.003	0.01
Thermal	1	0.4	0.15	0.2	...
	2	0.4	0.15	0.2	...
	3	0.5	0.05	0.06	...

**Table 2**  
Parameters for delay neutrons for the TWIGL problem (Christensen, 1985).

Family	Delay fraction	Decay constant
1	0.0075	0.080



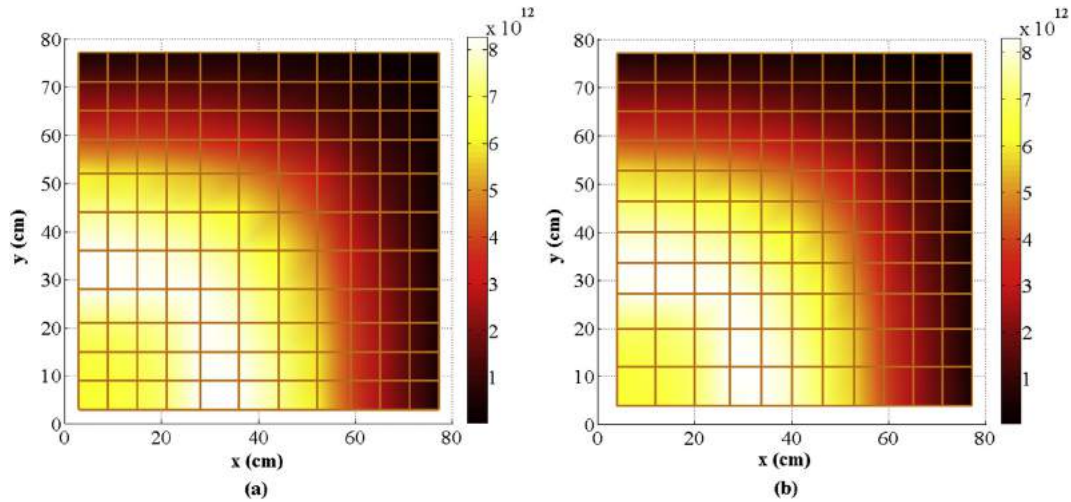


Fig. 3. Fast neutron flux for the uniform, (a), and improved non-uniform, (b), mesh point distributions of lattice  $12 \times 12$  for the TWIGL problem.

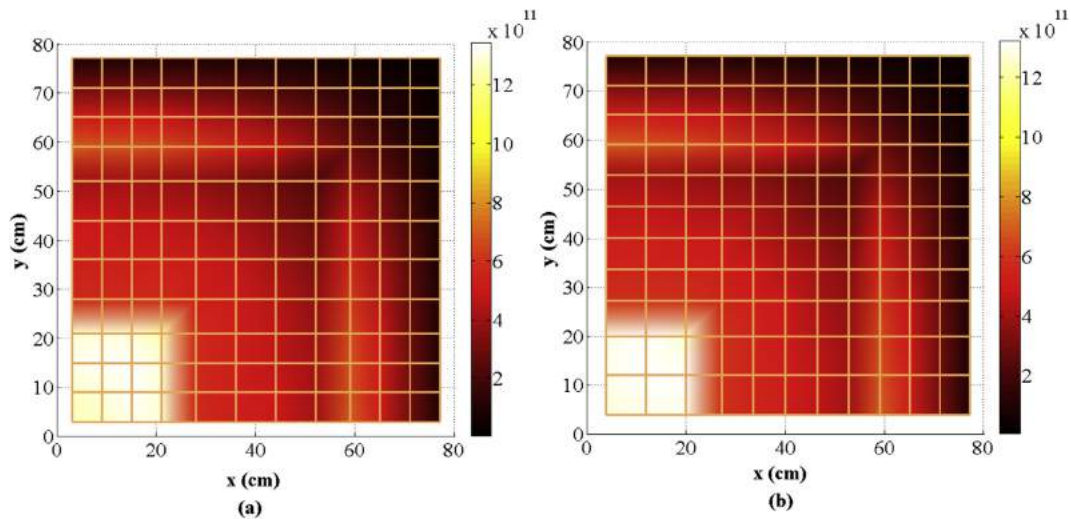


Fig. 4. Thermal neutron flux for the uniform, (a), and improved non-uniform, (b), mesh point distributions of lattice  $12 \times 12$  for the TWIGL problem.

**Table 3**  
Comparison of the calculated  $k_{eff}$  and its relative error with the reference for the TWIGL problem.

	Effective multiplication factor ( $k_{eff}$ )	Relative error (%)	Total CPU time (s)
Uniform $12 \times 12$	0.91331	0.014	19
Improved non-uniform $12 \times 12$	0.91315	−0.003	23

$k_{eff}$  reference solution by NEM Method (Christensen, 1985; page no. 162): 0.91318.

		0.100
		8.00
		8.00
	1.581	0.287
	8.37	6.11
	8.36	5.87
1.262	2.026	0.392
10.81	13.12	5.12
10.64	6.61	5.10

**Reference Power**  
**RPE Uniform (%)**  
**RPE Improved**  
**Non-Uniform (%)**

Fig. 5. RPEs of the relative powers for the uniform and improved non-uniform mesh point distributions of lattice  $12 \times 12$  for the TWIGL problem.

apparent absolute errors (AAEs) which can be obtained by the following definition (Argonne Code Center, 1977):

$$\text{Apparent Absolute Error in } k_{eff} (\times 10^3) = (\text{calculated value} - \text{reference value}) \times 10^3 \quad (22)$$

Accordingly, the results of the eigenvalues in the case of uniform and improved non-uniform mesh point distributions for the different above-mentioned lattices can be shown as Fig. 6.

As it is observed from Fig. 6, all the AAEs results in based on the proposed algorithm are more acceptable in contrast with the cases calculated by the usual method; which causing uniform mesh point distribution throughout the reactor core.

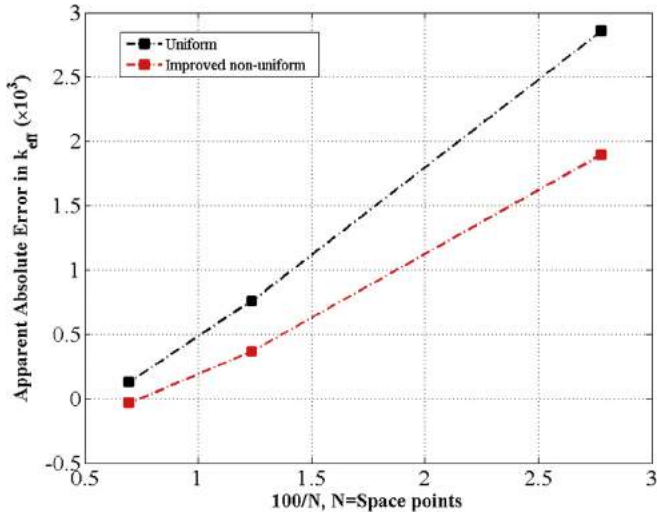


Fig. 6. The results of the  $k_{eff}$  for the uniform and improved non-uniform mesh point distributions for the lattice  $6 \times 6$ ,  $9 \times 9$  and  $12 \times 12$  for the TWIGL problem.

## 5.2. Test case 2

The second case is related to a two-dimensional reactor and two neutron energy groups (Argonne Code Center, 1977). Fig. 7 shows this reactor with perfect reflective conditions for the symmetry line boundaries. The group constants of this reactor are given in Table 4. Similar to the previous case study, the mesh point positions have been improved based on the proposed algorithm. Then, the neutron

diffusion equations have been solved numerically using the power iteration method for the both uniform and non-uniform mesh point distributions in the case of lattice  $48 \times 48$  (see Eqs. (7)–(10)). The relative errors and TCTs for the aforementioned distributions are given in Table 5. As it is observable, all the relative errors which are obtained based on the proposed algorithm are more acceptable in comparison with the other one. However, the TCT results are vice versa. The fast and thermal neutron flux variations for the aforementioned distributions has also been shown in Figs. 8 and 9, respectively; which the normalization is performed as below (Argonne Code Center, 1977):

$$\frac{1}{V_{core}} \sum_{i=1}^{N_{fuel}} [\nu \Sigma_{f1}(i) \phi_1(i) + \nu \Sigma_{f2}(i) \phi_2(i)] V_i = 1 \quad (23)$$

where  $N_{fuel}$  is the number of mesh boxes in the fuel region. As can be seen from the uniform cases, (a), from Figs. 8 and 9, it seems that the mesh points are not uniformly distributed, although this is not true. In fact, the mesh points are distributed uniformly through the regions, but because the surrounding regions (see Fig. 7) have smaller dimensions in comparison with the inner regions, this misperception can be occurred. It is noteworthy to underline that, RPEs of the fast and thermal neutron fluxes for the both uniform and non-uniform mesh point distributions are presented in Figs. 10 and 11, respectively. Data from these figures is quite revealing that the performed calculations based on the proposed algorithm have a more accurate result in contrast to the usual method.

The accuracy and ability of this problem also has been studied for two more lattices similar to the previous case study. Accordingly, the proposed algorithm has been applied to the lattice

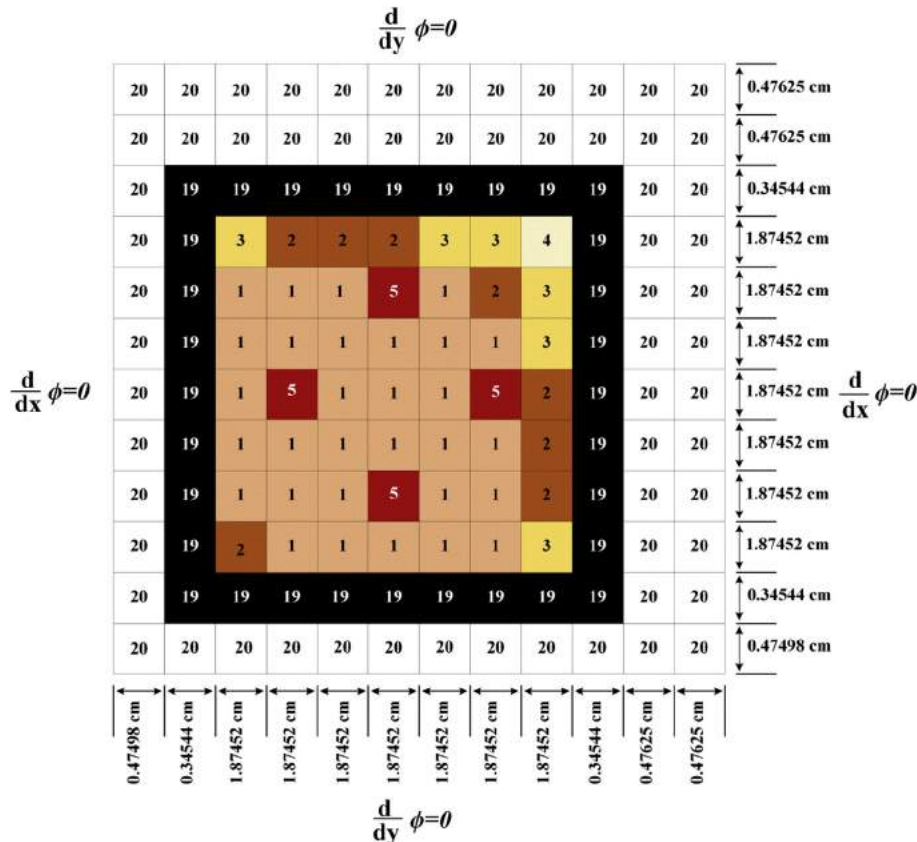


Fig. 7. One-fourth view of the Rod Bundle BWR problem.

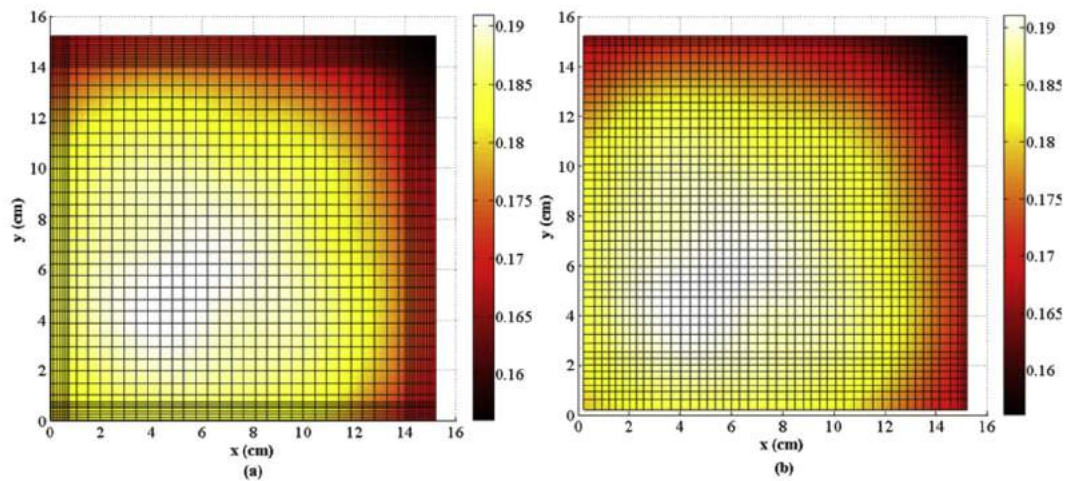
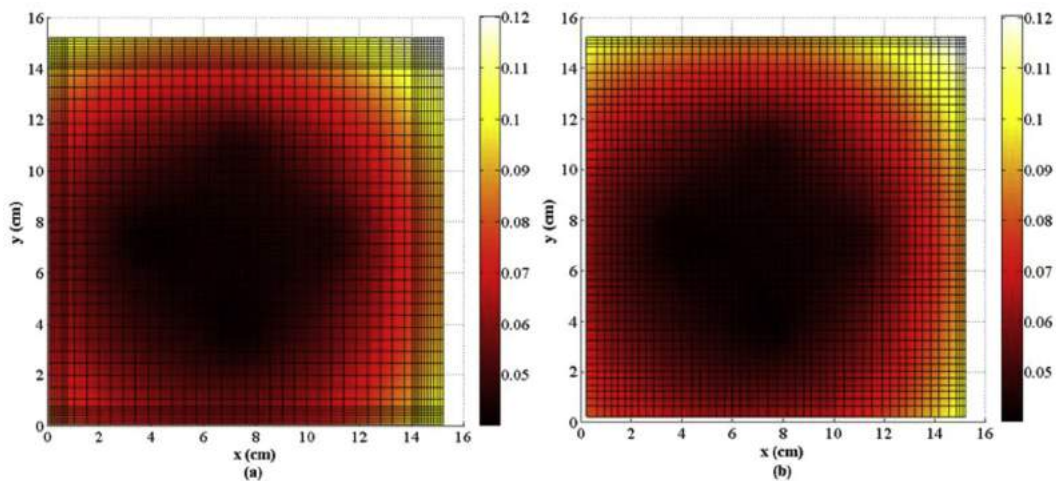
**Table 4**

Group constants of Rod Bundle BWR in two energy groups (Argonne Code Center, 1977).

Energy group	Material	$\Sigma_f$ ( $\text{cm}^{-1}$ )	$\Sigma_{ag}$ ( $\text{cm}^{-1}$ )	$\nu\Sigma_{fg}$ ( $\text{cm}^{-1}$ )	$\Sigma_T$ ( $\text{cm}^{-1}$ )	$\Sigma_{sg \rightarrow g+1}$ ( $\text{cm}^{-1}$ )
Fast	1	2.281E-3	8.983E-3	5.925E-3	2.531E-1	1.069E-2
	2	2.003E-3	8.726E-3	5.242E-3	2.536E-1	1.095E-2
	3	1.830E-3	8.587E-3	4.820E-3	2.535E-1	1.112E-2
	4	1.632E-3	8.480E-3	4.337E-3	2.533E-1	1.113E-2
	5	2.155E-3	9.593E-3	5.605E-3	2.506E-1	1.016E-2
	19	...	1.043E-3	...	2.172E-1	9.095E-3
Thermal	20	...	1.983E-4	...	2.476E-1	3.682E-2
	1	4.038E-2	5.892E-2	9.817E-2	5.732E-1	...
	2	3.385E-2	5.174E-2	8.228E-2	5.767E-1	...
	3	2.962E-2	4.717E-2	7.200E-2	5.797E-1	...
	4	2.428E-2	4.140E-2	5.900E-2	5.837E-1	...
	5	9.968E-3	1.626E-1	2.424E-2	5.853E-1	...
	19	...	4.394E-3	...	4.748E-1	...
	20	...	7.796E-3	...	1.123E+0	...

**Table 5**Comparison of the calculated  $k_{eff}$  and its relative error with the reference for the Rod Bundle BWR.

	Effective multiplication factor ( $k_{eff}$ )	Relative error (%)	Total CPU time (s)
Uniform $48 \times 48$	1.08606	0.052	68
Improved non-uniform $48 \times 48$	1.08553	0.003	79

 $k_{eff}$  reference solution by FDM (VENTURE code) (ANL-7416, page no. 541): 1.0855.**Fig. 8.** Fast neutron flux for the uniform, (a), and improved non-uniform, (b), mesh point distributions of lattice  $48 \times 48$  for the Rod Bundle BWR problem.**Fig. 9.** Thermal neutron flux for the uniform, (a), and improved non-uniform, (b), mesh point distributions of lattice  $48 \times 48$  for the Rod Bundle BWR problem.



16.82	16.84	16.96	17.11	17.12	17.01	16.80	16.47	16.01	15.74	15.66	15.62
1.90	2.06	2.05	1.93	2.15	2.08	1.92	1.15	1.61	1.92	1.29	1.44
1.90	2.06	2.05	1.92	2.14	2.08	1.92	1.15	1.61	1.91	1.29	1.44
16.90	16.93	17.06	17.23	17.24	17.12	16.91	16.58	16.11	15.81	15.72	
-1.18	-0.86	0.40	-0.31	-0.28	-0.10	-0.08	-0.27	0.06	-0.11	-0.03	
-1.18	-0.86	0.38	-0.31	-0.27	0.09	-0.08	-0.18	-0.06	0.10	0.02	
17.01	17.06	17.22	17.41	17.41	17.29	17.08	16.75	16.25	15.92		
-1.21	0.37	0.07	0.10	0.09	0.09	0.03	0.07	0.06	0.10		
-1.21	0.37	0.06	0.06	0.06	0.06	0.00	0.06	0.06	0.06		
17.38	17.46	17.71	17.74	17.93	17.78	17.58	17.26	16.70			
1.00	0.14	0.07	1.21	0.07	0.09	0.10	0.10	0.8			
1.00	0.12	0.06	1.18	0.06	0.06	0.06	0.06	0.06			
17.94	18.03	18.33	18.56	18.52	18.30	18.21	17.89				
-1.09	0.15	0.07	0.08	0.06	0.15	0.07	0.07				
-1.09	0.15	0.05	0.05	0.05	0.11	0.05	0.06				
18.25	18.34	18.61	18.82	18.85	18.74	18.57					
0.94	0.21	0.07	0.08	-0.08	0.09	0.06					
0.94	0.21	0.05	0.05	0.05	0.05	0.05					
18.40	18.48	18.72	18.86	18.99	18.95						
-1.17	0.07	0.09	1.87	0.07	0.08						
-1.17	0.07	0.05	1.81	0.05	0.05						
18.46	18.54	18.81	19.02	19.07							
-1.25	0.12	0.09	0.12	0.06							
-1.25	0.12	0.05	0.05	0.05							
18.39	18.48	18.78	19.03								
0.87	0.39	0.08	0.10								
0.87	0.34	0.05	0.05								
18.16	18.24	18.51									
-1.32	0.13	0.04									
-1.32	0.13	0.00									
17.98	18.04										
-1.42	0.07										
-1.42	0.07										
17.94											
-1.81											
-1.81											

Reference Power  
 RPE Uniform (%)  
 RPE Improved  
 Non-Uniform (%)

Fig. 10. RPEs of the fast neutron fluxes for the uniform and improved non-uniform mesh point distributions of lattice  $48 \times 48$  for the Rod Bundle BWR problem.

10.01	9.916	9.527	8.921	8.561	8.534	8.915	9.669	10.77	11.52	11.77	11.95
0.91	0.60	0.10	-0.18	-0.18	-0.18	-0.15	-0.20	0.17	0.28	0.78	0.37
0.90	0.58	0.10	-0.18	-0.16	-0.18	-0.15	-0.19	0.17	0.27	0.78	0.36
9.718	9.553	9.105	8.476	8.108	8.078	8.972	9.240	10.37	11.17	11.52	
1.64	1.74	1.74	1.92	1.87	1.80	-2.20	1.87	1.48	1.59	1.39	
1.61	1.72	1.70	1.92	1.87	1.70	-2.19	1.87	1.46	1.57	1.38	
9.335	9.090	8.612	7.956	7.580	7.546	7.955	8.739	9.901	10.72		
-1.47	-1.88	0.11	0.14	0.17	0.17	0.18	0.18	0.22	-0.27		
-1.47	-1.86	0.11	0.13	0.15	0.17	0.17	0.17	0.18	-0.26		
8.435	8.202	7.636	6.929	6.512	6.410	6.889	7.729	8.969			
1.59	-0.22	0.17	0.16	0.15	-0.15	0.16	0.14	0.14			
1.55	-0.19	0.14	0.14	0.15	-0.15	0.14	0.14	0.14			
7.216	6.966	6.350	5.616	5.134	4.793	5.469	6.400				
1.67	0.18	0.16	-0.16	-0.18	0.44	-0.16	-0.16				
1.63	0.14	0.13	-0.15	-0.17	0.42	-0.16	-0.16				
6.456	6.203	5.563	4.783	4.476	4.414	4.760					
1.44	0.19	0.18	-0.17	-0.19	-0.19	-0.17					
1.41	0.17	0.16	-0.16	-0.18	-0.17	-0.17					
6.119	5.862	5.175	4.205	4.167	4.241						
1.97	0.17	-0.26	0.37	-0.16	0.16						
1.94	0.15	-0.25	0.37	-0.15	0.15						
6.190	5.936	5.304	4.531	4.230							
1.86	0.16	-0.22	-0.20	-0.21							
1.85	0.15	-0.19	-0.19	-0.20							
6.589	6.338	5.731	5.001								
1.78	-0.18	-0.17	-0.21								
1.78	-0.16	-0.15	-0.18								
7.274	7.034	6.460									
1.70	-0.16	-0.13									
1.69	-0.15	-0.13									
7.765	7.534										
1.68	-0.18										
1.66	-0.18										
7.929											
1.97											
1.98											

Reference Power  
 RPE Uniform (%)  
 RPE Improved  
 Non-Uniform (%)

Fig. 11. RPEs of the thermal neutron fluxes for the uniform and improved non-uniform mesh point distributions of lattice  $48 \times 48$  for the Rod Bundle BWR problem.

$36 \times 36$  and  $24 \times 24$ . As can be seen from Fig. 12, the AAEs of the effective multiplication factors are then obtained and illustrated for the uniform and non-uniform mesh point distributions to compare with each other. This Figure shows a more acceptable accuracy of the proposed method based on the REPs in comparison with the usual method. Additionally, it could be acclaimed that, the two studied cases (see test cases 1 and 2) relevantly show that the proposed algorithm can be applied to any arbitrary mesh point numbers.

It is obvious and apparent, in order to calculate the weighting factors for the proposed algorithm, initial calculation of the static flux is needed. So the efficiency is impacted. In another word expression, calculating a number of additional involved unknowns takes a little time. However, by using the proposed method, the accuracy of the neutron diffusion calculation is significantly better than the other one. Accordingly, the proposed algorithm based on the REPs can be considered as a useful tool to obtain accurate results efficiently.

## 6. Conclusion

This paper deals with the development of a novel algorithm for improving the Box-Scheme Finite Difference Method (BSFDM); which was considered to the 2-D rectangular geometry light water reactors. The mesh point positions in the BSFDM have a significant effect on the accuracy of the neutron diffusion calculations. So based on the proposed method, mesh point positions were optimized through the entire reactor core by considering the relative region's importance. By using of this approach, in regions with greater importance, the number of meshes was more than that in regions with less importance, which making an adaptive nonuniform mesh point distribution unlike the usual method.

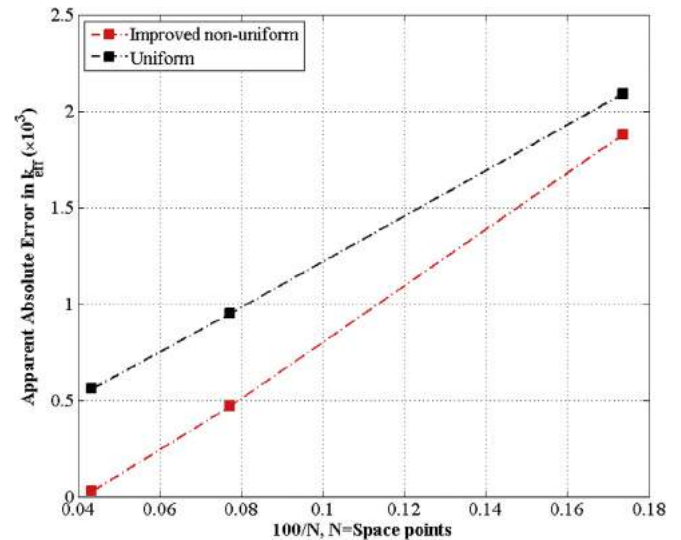


Fig. 12. The results of the  $k_{eff}$  for the uniform and improved non-uniform mesh point distributions for the lattice  $24 \times 24$ ,  $36 \times 36$  and  $48 \times 48$  for the Rod Bundle BWR problem.

The REPs were preferred and employed in the development of the suggested algorithm to determine the relative region's importance through the entire reactor core. Evaluating of the proposed algorithm was considered by using two different well-known benchmark problems, namely the TWIGL seed-blanket and the Rod Bundle BWR. Moreover, different mesh point numbers were used to consider the accuracy of this method for any arbitrary mesh

point numbers. Results of comparison between the adaptive nonuniform mesh point distributions based on the proposed method and the uniform distributions based on the usual method, proved the strength of suggested method considering accuracy involved in obtaining neutron fluxes as well as the corresponding eigenvalues. Possible future works can include applying of this method for the different geometries and reactor types.

## References

- Akcasu, Z., Lellouche, G.S., Shotkin, L.M., 1971. *Mathematical Methods in Nuclear Reactor Dynamics*. Academic Press, New York and London.
- Argonne Code Center, 1977. Benchmark Problem Book. Report ANL-7416 (Suppl. 2). Argonne National Laboratory, Argonne, IL.
- Ayyoubzadeh, S.M., Vosoughi, N., 2011. Optimization of the direct discrete method using the solution of the adjoint equation and its application in the multi-group neutron diffusion equation. *AIP Conf. Proc.* 1389, 1777–1781.
- Bareiss, E.H., Antolak, A.J., 1981. Solution of the transport equation by the BIF Method. *Prog. Nucl. Energy* 8, 295–307.
- Bell, G.I., Glasstone, S., 1970. *Nuclear Reactor Theory*. Van Nostrand Reinhold Company, New York.
- Cavdar, S., Ozgener, H.A., 2004. A finite element/boundary element hybrid method for 2-D neutron diffusion calculations. *Ann. Nucl. Energy* 31, 1555–1582.
- Chiba, G., Tsuji, M., Shimazu, Y., 2001. A hierarchical domain decomposition boundary element method with a higher order polynomial expansion for solving 2-D multiregion neutron diffusion equations. *Ann. Nucl. Energy* 28, 895–912.
- Christensen, B., 1985. Three-dimensional Static and Dynamic Reactor Calculations by the Nodal Expansion Method. PhD dissertation. Rise National Laboratory, Denmark.
- Clark, M., Hansen, K.F., 1964. *Numerical Methods of Reactor Analysis*. Academic Press INC, New York.
- Duderstadt, J.J., Hamilton, L.J., 1991. *Nuclear Reactor Analysis*. John Wiley & Sons, New York.
- Gado, J., Schmidt, F., 1987. Solution of the neutron diffusion equation in hexagonal geometries. *Ann. Nucl. Energy* 14, 83–97.
- Hosseini, S.A., Vosoughi, N., 2013. Development of two-dimensional, multigroup neutron diffusion computer code based on GFEM with unstructured triangle elements. *Ann. Nucl. Energy* 51, 213–226.
- Hosseini, M., Khalafi, H., Khakshornia, S., 2015. Development of a parallel analytic coarse mesh finite difference code for two group diffusion equation solution in two dimensional rectangular geometries. *Prog. Nucl. Energy* 78, 258–269.
- Lamarsh, J.R., 1965. *Introduction to Nuclear Reactor Theory*. Addison-Wesley Publishing Company.
- Malmir, H., Vosoughi, N., Zahedinejad, E., 2010. Development of a 2-D 2-group neutron noise simulator for hexagonal geometries. *Ann. Nucl. Energy* 37, 1089–1100.
- Malmir, H., Moghaddam, N.M., Zahedinejad, E., 2011. Comparison between triangular and hexagonal modeling of a hexagonal-structured reactor core using box method. *Ann. Nucl. Energy* 38, 371–378.
- Merton, S.R., Buchan, A.G., Pain, C.C., Smedley-Stevenson, R.P., 2013. An adjoint-based method for improving computational estimates of a functional obtained from the solution of the Boltzmann transport equation. *Ann. Nucl. Energy* 54, 1–10.
- Moghaddam, N.M., Afarideh, H., Espinosa-Paredes, G., 2014. On the numerical solution of the neutron fractional diffusion equation. *Ann. Nucl. Energy* 70, 1–10.
- Moghaddam, N.M., Afarideh, H., Espinosa-Paredes, G., 2015. Modifying the neutron diffusion equation using spatial fractional operators and developed diffusion coefficients. *Prog. Nucl. Energy* 83, 59–72.
- Nakamura, S., 1977. *Computational Methods in Engineering and Science with Applications to Fluid Dynamics and Nuclear Systems*. Wiley Interscience, New York.
- Quintero-Leyva, B., 2014. Solving the static-neutron diffusion equation in 2D-Cartesian geometry with Lagrange interpolation. *Ann. Nucl. Energy* 65, 370–375.
- Schunert, S., Wang, Y., Martineau, R., DeHart, M.D., 2015. A new mathematical adjoint for the modified SAAF-S<sub>N</sub> equations. *Ann. Nucl. Energy* 75, 340–352.
- Shen, W., 2012. On the better performance of the coarse-mesh finite-difference method for CANDU-type reactors. *Ann. Nucl. Energy* 46, 169–178.
- Singh, T., Mazumdar, T., Pandey, P., 2014. NEMSQR: a 3-D multi group diffusion theory code based on nodal expansion method for square geometry. *Ann. Nucl. Energy* 64, 230–243.
- Stripling, H.F., Anitescu, M., Adams, M.L., 2013. A generalized adjoint framework for sensitivity and global error estimation in time-dependent nuclear reactor simulations. *Ann. Nucl. Energy* 52, 47–58.
- Vosoughi, N., Salehi, A.A., Shahriari, M., 2004. Discrete formulation for two-dimensional multigroup neutron diffusion equations. *Ann. Nucl. Energy* 31, 231–253.

## **Declaration of consent**

on the basis of Article 30 of the RSL Phil.-nat. 18

Name/First Name:

Registration Number:

Study program:

Bachelor ☐

Master ☐

Dissertation ☐

Title of the thesis:

Supervisor:

I declare herewith that this thesis is my own work and that I have not used any sources other than those stated. I have indicated the adoption of quotations as well as thoughts taken from other authors as such in the thesis. I am aware that the Senate pursuant to Article 36 paragraph 1 litera r of the University Act of 5 September, 1996 is authorized to revoke the title awarded on the basis of this thesis.

For the purposes of evaluation and verification of compliance with the declaration of originality and the regulations governing plagiarism, I hereby grant the University of Bern the right to process my personal data and to perform the acts of use this requires, in particular, to reproduce the written thesis and to store it permanently in a database, and to use said database, or to make said database available, to enable comparison with future theses submitted by others.

Place/Date

Signature

A handwritten signature in black ink, appearing to be 'V. H. S.', written in a cursive style.

## **Declaration of Originality**

**Last name, first name:**

**Matriculation number:**

I hereby declare that this thesis represents my original work and that I have used no other sources except as noted by citations.

All data, tables, figures and text citations which have been reproduced from any other source, including the internet, have been explicitly acknowledged as such.

I am aware that in case of non-compliance, the Senate is entitled to withdraw the doctorate degree awarded to me on the basis of the present thesis, in accordance with the "Statut der Universität Bern (Universitätsstatut; UniSt)", Art. 69, of 7 June 2011.

Place, date

Signature

A handwritten signature in black ink, appearing to be 'Zurich' or similar, written in a cursive style.